

AUGUST 2018

AJNR

VOLUME 39 • PP 1385–1581

AJNR

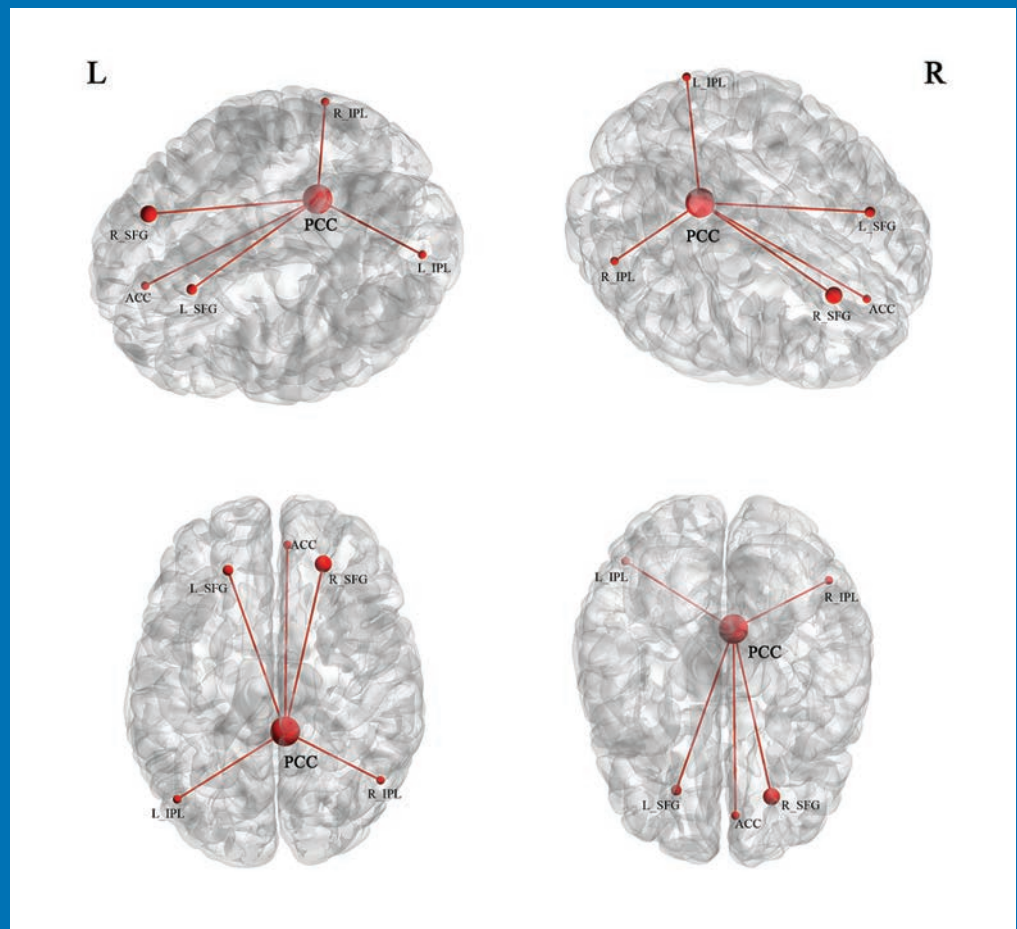
AMERICAN JOURNAL OF NEURORADIOLOGY

AUGUST 2018
VOLUME 39
NUMBER 8
WWW.AJNR.ORG

THE JOURNAL OF DIAGNOSTIC AND
INTERVENTIONAL NEURORADIOLOGY

Resting-state functional MRI
Contextual neuroradiology reporting
Angioplasty without stenting for intracranial stenosis

Official Journal ASNR • ASFNR • ASHNR • ASPNR • ASSR



A Complete Coil Portfolio

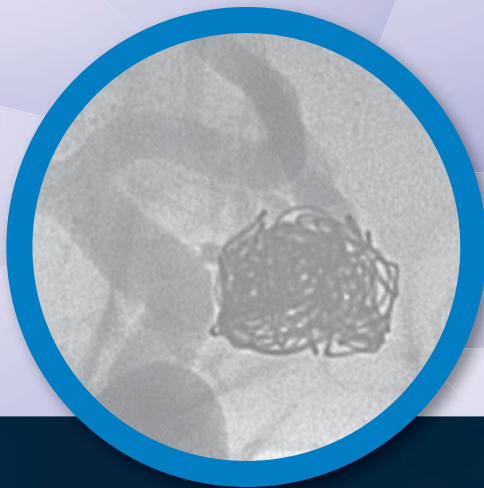
Hydrogel Embolic Coils & Platinum Coils

MicroVention's comprehensive portfolio features clinically proven Hydrogel coils, which can be used exclusively or in combination with our trusted Platinum coils to treat a wide range of aneurysms and neurovascular lesions.

Breakthrough Hydrogel Technology

- Less Recurrence
- Less Retreatment
- More Progressive Occlusion

Compared to platinum coils with comparable safety¹



REFERENCES:

1. Taschner et al. Second-Generation Hydrogel Coils for the Endovascular Treatment of Intracranial Aneurysm; A Randomized Controlled Trial. 2018;49:00-00. DOI:10.1161/STROKEAHA.117.018707

For more information or a product demonstration,
contact your local MicroVention representative:



**MicroVention Worldwide
Innovation Center**
35 Enterprise
Aliso Viejo, CA 92656 USA
MicroVention UK Limited
MicroVention Europe, S.A.R.L.
MicroVention Deutschland GmbH
microvention.com

PH +1.714.247.8000

PH +44 (0) 191 258 6777

PH +33 (1) 39 21 77 46

PH +49 211 210 798-0

The one to choose when you choose aspiration.



- **Easily find clot**
ClotFinder™ Specimen Cup retains the aspirated thrombus
- **High max vacuum**
Adjustable up to -713mmHg
- **Aspirate on demand**
Control aspiration from the sterile field

0.218in ID
AXS Universal
Aspiration Tubing



AXS Universal™
ASPIRATION SET

We're Inside Every Great Neuroradiologist!

ASNR MEMBERS RECEIVE

American Journal of Neuroradiology (AJNR)

The leading neuroradiology research journal, published monthly

Neurographics

Bimonthly educational journal with CME for members

ASNR Annual Meeting

Discounts for members on the field's premier conference

eCME

Online collection of lectures and articles with SA-CME and Category 1 credit

Advocacy

Coding/reimbursement, quality standards and practice guidelines; demonstrating neuroradiology's value!

Networking

Access to 5,000 peers

... And More!

TR 4730.0
TE 108.0
TA 03.27
BW 70.0
M/ND
A1
HL1.2;HS1.2
*tseR2d1_9 / 180
SP F17.7
SL 5.0
FoV 194*230
190*256s
Tra>Cor(8.7)
w 1469
c 705
MF 1.14
D
R
5cm
5cm

Join the leaders in neuroradiology today!

Learn more at www.asnr.org/join

ASNR

American Society of Neuroradiology

800 Enterprise Dr., Suite 205, Oak Brook, IL 60523 • (630)574-0220 • membership@asnr.org • www.asnr.org



American Society
of Pediatric
Neuroradiology

SAVE THE DATE

1st Annual Meeting of the

AMERICAN SOCIETY OF

Pediatric Neuroradiology

January 18-20, 2019

Royal Sonesta Hotel - New Orleans • New Orleans, Louisiana

Please contact Educational Symposia, at 813-806-1000 or ASPNR@edusymp.com or visit www.ASPNR.org for additional information.



Simplify the MOC Process



Manage your CME Credits Online

CMEgateway.org

Available to Members of Participating Societies

American Board of Radiology (ABR)
American College of Radiology (ACR)
American Roentgen Ray Society (ARRS)
American Society of Neuroradiology (ASNR)
Commission on Accreditation of Medical
Physics Educational Programs, Inc. (CAMPEP)
Radiological Society of North America (RSNA)
Society of Interventional Radiology (SIR)
SNM
The Society for Pediatric Radiology (SPR)

It's Easy and Free!

Log on to CME Gateway to:

- View or print reports of your CME credits from multiple societies from a single access point.
- Print an aggregated report or certificate from each participating organization.
- Link to SAMs and other tools to help with maintenance of certification.

American Board of Radiology (ABR) participation!

By activating ABR in your organizational profile, your MOC-fulfilling CME and SAM credits can be transferred to your own personalized database on the ABR Web site.

Sign Up Today!

go to CMEgateway.org

Go Green!

AJNR urges American Society of Neuroradiology members to reduce their environmental footprint by voluntarily suspending their print subscription.

The savings in paper, printing, transportation, and postage not only help members cut down on clutter, but go to fund new electronic enhancements and expanded content.

The digital edition of *AJNR* presents the print version in its entirety, along with extra features including:

- Publication Preview
- Case of the Week
- Podcasts
- Special Collections
- The *AJNR* Blog
- Weekly Poll

It also **reaches subscribers much faster than print**. An **electronic table of contents** will be sent directly to your mailbox to notify you as soon as it publishes.

Readers can **search, reference, and bookmark** current and archived content 24 hours a day on www.ajnr.org, rather than thumb through stacks of accumulated paper issues for articles and images they need.



<http://www.ajnr.org/cgi/feedback>

ASNR members who wish to opt out of print can do so by using the Feedback form on the *AJNR* Website (<http://www.ajnr.org/cgi/feedback>). Just type "Go Green" in the subject line to stop print and spare our ecosystem.

Dominant Flex Surgical Suction Pump

See package insert for complete indications, complications, warnings, and instructions for use.

INDICATIONS FOR USE

The intended use of the Dominant Flex suction pump is the creation of a constant vacuum for use in hospitals and clinics. This vacuum can be used for general suction, to aspirate and remove: surgical fluids, tissue (including bone), gases, bodily fluids or infectious materials and during specific procedures which may include, vacuum extraction, aesthetic body contouring, aspiration during flexible endoscopy, use with cardiac tissue stabilizers during off-pump coronary artery bypass, and epicardial ablation probes.

WARNINGS

- For use only by medically trained persons who have been adequately trained in suction procedures and in the use of aspirators.
- To avoid risk of electric shock, this equipment must only be connected to a fixed mains socket with protective earth.
- The device must not be used for suctioning explosive, easily flammable or corrosive liquids.
- The connecting tubing supplied with the device must never come into direct contact with the suction area. A sterile suction catheter must always be used (risk of infection).
- Before cleaning the device, pull the plug out of the fixed mains socket.

Copyright © 2018 Stryker
AP002176 v1.0 | Page 2 of 2

Trevo® XP ProVue Retrievers

See package insert for complete indications, complications, warnings, and instructions for use.

INDICATIONS FOR USE

1. The Trevo Retriever is indicated for use to restore blood flow in the neurovasculature by removing thrombus for the treatment of acute ischemic stroke to reduce disability in patients with a persistent, proximal anterior circulation, large vessel occlusion, and smaller core infarcts who have first received intravenous tissue plasminogen activator (IV t-PA). Endovascular therapy with the device should start within 6 hours of symptom onset.
2. The Trevo Retriever is intended to restore blood flow in the neurovasculature by removing thrombus in patients experiencing ischemic stroke within 8 hours of symptom onset. Patients who are ineligible for intravenous tissue plasminogen activator (IV t-PA) or who fail IV t-PA therapy are candidates for treatment.
3. The Trevo Retriever is indicated for use to restore blood flow in the neurovasculature by removing thrombus for the treatment of acute ischemic stroke to reduce disability in patients with a persistent, proximal anterior circulation, large vessel occlusion of the internal carotid artery (ICA) or middle cerebral artery (MCA)-M1 segments with smaller core infarcts (0-50cc for age < 80 years, 0-20cc for age ≥ 80 years). Endovascular therapy with the device should start within 6-24 hours of time last seen well in patients who are ineligible for intravenous tissue plasminogen activator (IV t-PA) or who fail IV t-PA therapy.

COMPLICATIONS

Procedures requiring percutaneous catheter introduction should not be attempted by physicians unfamiliar with possible complications which may occur during or after the procedure. Possible complications include, but are not limited to, the following: air embolism; hematoma or hemorrhage at puncture site; infection; distal embolization; pain/headache; vessel spasm, thrombosis, dissection, or perforation; emboli; acute occlusion; ischemia; intracranial hemorrhage; false aneurysm formation; neurological deficits including stroke; and death.

COMPATIBILITY

3x20mm retrievers are compatible with Trevo® Pro 14 Microcatheters (REF 90231) and Trevo® Pro 18 Microcatheters (REF 90238). 4x20mm retrievers are compatible with Trevo® Pro 18 Microcatheters (REF 90238). 4x30mm retrievers are compatible with Excelsior® XT-27® Microcatheters (150cm x 6cm straight REF 275081) and Trevo® Pro 18 Microcatheters (REF 90238). 6x25mm Retrievers are compatible with Excelsior® XT-27® Microcatheters (150cm x 6cm straight REF 275081). Recommended minimum vessel ID for all Retriever sizes is 2.5mm. Compatibility of the Retriever with other microcatheters has not been established. Performance of the Retriever device may be impacted if a different microcatheter is used.

Balloon Guide Catheters (such as Merc® Balloon Guide Catheter

- No modification of this equipment is allowed.
- Consult the indications for use and consider risk factors and contraindications before using the Dominant Flex. Failure to read and follow all instructions in this manual prior to use may result in serious or fatal injury of the patient.
- Do not connect this device to a passive drainage tube.
- Not suitable for setting at a low vacuum, as needed for example for thoracic drainage without specialized accessories. Not approved for outdoor use or transport applications.

PRECAUTIONS

- Incorrect use can cause pain and injury to the patient.
- Do not use sterile accessories when the sterile packaging is damaged.
- The use of mobile telephones, LAN / WLAN, walkie-talkies (two-way radios) and cordless telephones sets can affect the Dominant Flex pump. A safety distance of min. 3.3 ft (1 m) to the Dominant Flex pump is recommended.
- Portable and mobile RF communications equipment can affect medical devices.
- The rack version requires a minimum distance of 5 cm to the enclosure to prevent overheating of the device.
- The patient should be monitored regularly according to the physicians' instructions and facility guidelines. Objective indications or signs of a possible infection or complication must be met immediately (e.g. fever, pain, redness, increased warmth, swelling or purulent discharge).

and FlowGate® Balloon Guide Catheter) are recommended for use during thrombus removal procedures.

Retrievers are compatible with the Abbott Vascular DOC® Guide Wire Extension (REF 22260).

Retrievers are compatible with Boston Scientific Rotating Hemostatic Valve (Ref 421242).

SPECIFIC WARNINGS FOR INDICATION 1

- The safety and effectiveness of the Trevo Retrievers in reducing disability has not been established in patients with large core infarcts (i.e. ASPECTS ≤ 7). There may be increased risks, such as intracerebral hemorrhage, in these patients.
- The safety and effectiveness of the Trevo Retrievers in reducing disability has not been established or evaluated in patients with occlusions in the posterior circulation (e.g., basilar or vertebral arteries) or for more distal occlusions in the anterior circulation.

SPECIFIC WARNINGS FOR INDICATION 2

- To reduce risk of vessel damage, take care to appropriately size Retriever to vessel diameter at intended site of deployment.

SPECIFIC WARNINGS FOR INDICATION 3

- The safety and effectiveness of the Trevo Retrievers in reducing disability has not been established in patients with large core infarcts (i.e., ASPECTS ≤ 7). There may be increased risks, such as intracerebral hemorrhage, in these patients.
- The safety and effectiveness of the Trevo Retrievers in reducing disability has not been established or evaluated in patients with occlusions in the posterior circulation (e.g., basilar or vertebral arteries) or for more distal occlusions in the anterior circulation.
- Users should validate their imaging software analysis techniques to ensure robust and consistent results for assessing core infarct size.

WARNINGS APPLIED TO ALL INDICATIONS

- Administration of IV t-PA should be within the FDA-approved window (within 3 hours of stroke symptom onset).
- To reduce risk of vessel damage, adhere to the following recommendations:
 - Do not perform more than six (6) retrieval attempts in same vessel using Retriever devices.
 - Maintain Retriever position in vessel when removing or exchanging Microcatheter.
- To reduce risk of kinking/fracture, adhere to the following recommendations:
 - Immediately after unsheathing Retriever, position Microcatheter tip marker just proximal to shaped section. Maintain Microcatheter tip marker just proximal to shaped section of Retriever during manipulation and withdrawal.
 - Do not rotate or torque Retriever.
 - Use caution when passing Retriever through stented arteries.
- The Retriever is a delicate instrument and should be handled

- Non-observance can lead to considerable danger of the patient. Monitor the Dominant Flex frequently for operating status.
- To prevent the device from overheating, the exhaust at the bottom of the unit must be unobstructed when the unit is operational.

AXS Universal™ Liner Set and Aspiration Tubing

See package insert for complete indications, complications, warnings, and instructions for use.

INDICATIONS FOR USE

AXS Universal Liner Set and Aspiration Tubing is suitable for the safe collection and disposal of suctioned fluids. It is allowed for use only by medically trained staff who are aware of the in-house hygienic regulations. Medela can only guarantee the safe function if used in combination with Medela components.



Stryker Neurovascular
47900 Bayside Parkway
Fremont, CA 94538

strykerneurovascular.com

Date of Release: JUN/2018

EX_EN_US

carefully. Before use and when possible during procedure, inspect device carefully for damage. Do not use a device that shows signs of damage. Damage may prevent device from functioning and may cause complications.

- Do not advance or withdraw Retriever against resistance or significant vasospasm. Moving or torquing device against resistance or significant vasospasm may result in damage to vessel or device. Assess cause of resistance using fluoroscopy and if needed resheath the device to withdraw.
- If Retriever is difficult to withdraw from the vessel, do not torque Retriever. Advance Microcatheter distally, gently pull Retriever back into Microcatheter, and remove Retriever and Microcatheter as a unit. If undue resistance is met when withdrawing the Retriever into the Microcatheter, consider extending the Retriever using the Abbott Vascular DOC guidewire extension (REF 22260) so that the Microcatheter can be exchanged for a larger diameter catheter such as a DAC® Catheter. Gently withdraw the Retriever into the larger diameter catheter.
- Administer anti-coagulation and anti-platelet medications per standard institutional guidelines.
- Users should take all necessary precautions to limit X-radiation doses to patients and themselves by using sufficient shielding, reducing fluoroscopy times, and modifying X-ray technical factors where possible.

PRECAUTIONS

- Prescription only – device restricted to use by or on order of a physician.
- Store in cool, dry, dark place.
- Do not use open or damaged packages.
- Use by "Use By" date.
- Exposure to temperatures above 54°C (130°F) may damage device and accessories. Do not autoclave.
- Do not expose Retriever to solvents.
- Use Retriever in conjunction with fluoroscopic visualization and proper anti-coagulation agents.
- To prevent thrombus formation and contrast media crystal formation, maintain a constant infusion of appropriate flush solution between guide catheter and Microcatheter and between Microcatheter and Retriever or guidewire.
- Do not attach a torque device to the shaped proximal end of DOC® Compatible Retriever. Damage may occur, preventing ability to attach DOC® Guide Wire Extension.

DOC is a trademark of Abbott Laboratories.



Stryker Neurovascular
47900 Bayside Parkway
Fremont, CA 94538

strykerneurovascular.com

Date of Release: APR/2018

EX_EN_US

Copyright © 2018 Stryker
AP002078 v1.0 | Page 2 of 2

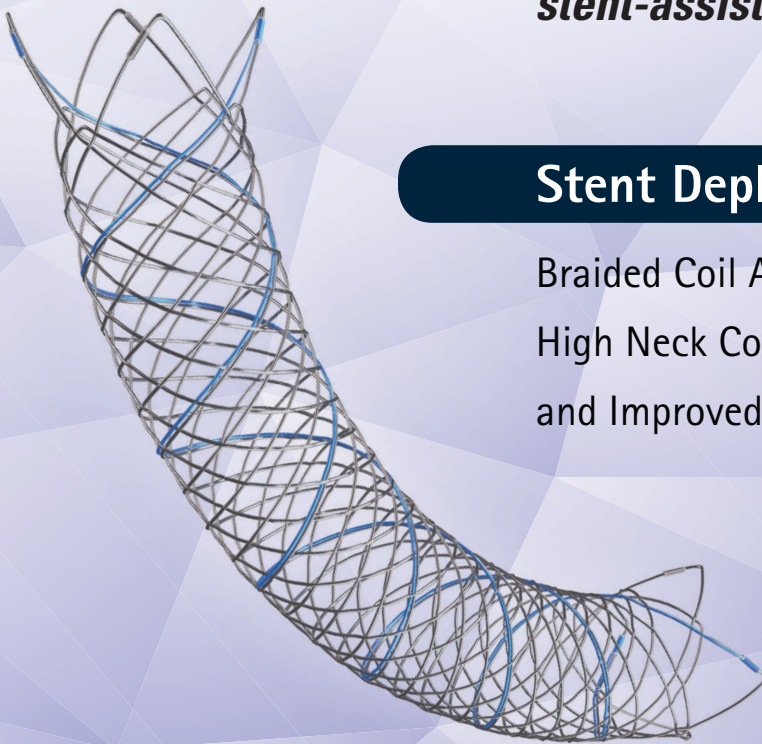


Aneurysm
Therapy
Solutions

LVIS[®]

Intraluminal Support Device

*The first and only stent with
Premarket Approval (PMA) for use in
stent-assisted coil embolization*



Stent Deployment. Refined.

Braided Coil Assist Stents with
High Neck Coverage, Excellent Visibility
and Improved Conformability*

Low-profile Visualized Intraluminal Support



INDICATIONS FOR USE:

The LVIS[®] and LVIS[®] Jr. devices are indicated for use with neurovascular embolization coils in patients ≥ 18 years of age for the treatment of wide-neck (neck width ≥ 4 mm or dome to neck ratio < 2) saccular intracranial aneurysms arising from a parent vessel with a diameter ≥ 2.0 mm and ≤ 4.5 mm.

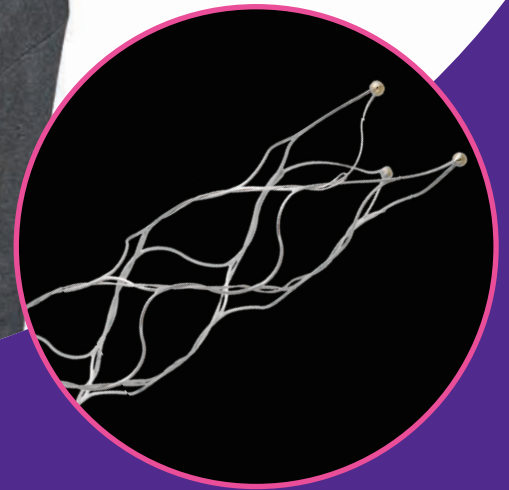
Rx Only: Federal (USA) law restricts this device to sale by or on the order of a physician.

The HydroCoil[®] Embolic System (HES) and MicroPlex[®] Coil System (MCS) are intended for the endovascular embolization of intracranial aneurysms and other neurovascular abnormalities such as arteriovenous malformations and arteriovenous fistulae. The HES and MCS are also intended for vascular occlusion of blood vessels within the neurovascular system to permanently obstruct blood flow to an aneurysm or other vascular malformation and for arterial and venous embolizations in the peripheral vasculature.

The device should only be used by physicians who have undergone pre-clinical training in all aspects of HES/MCS procedures as prescribed by MicroVention.

stryker

Now you have **24 hours** to make a lifetime of difference in stroke patients like Nora



The Trevo Retriever is the only device cleared to **reduce disability in stroke patients up to 24 hours** from time last seen well.

For more information, visit strykerneurovascular.com/trevo24hours

Trevo[®] XP
PROVUE RETRIEVER

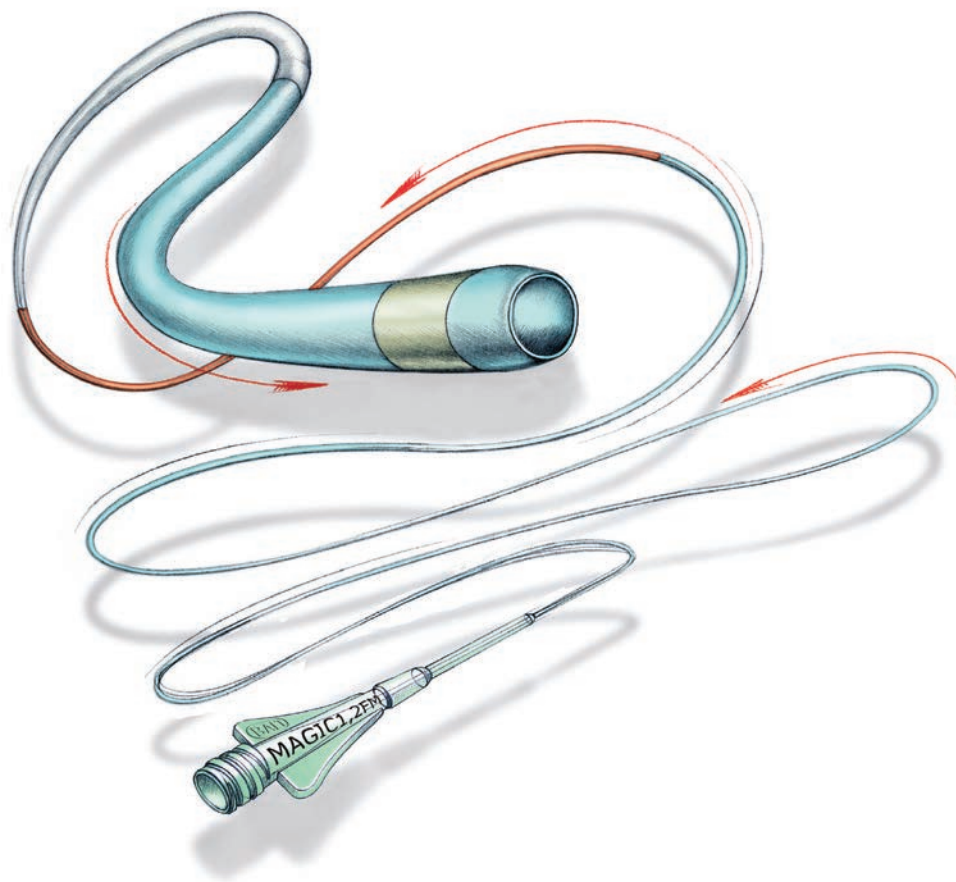
Copyright © 2018 Stryker
AP002078 v1.0

Magic



FLOW-DEPENDENT MICROCATHETER

NOW AVAILABLE THROUGH BLOCKADE™ MEDICAL



ORDERMAGICS@BLOCKADEMEDICAL.COM

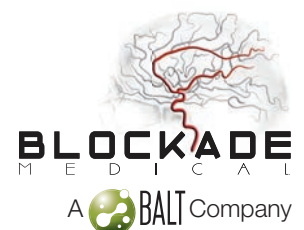
MAGIC catheters are designed for general intravascular use. They may be used for the controlled, selective regional infusion of therapeutic agents or embolic materials into vessels.¹

1. Magic Catheters IFU – Ind 19

MKTG-068 Rev. A

18 Technology Drive #169, Irvine Ca 92618

P 949.788.1443 | F 949.788.1444



AJNR

AMERICAN JOURNAL OF NEURORADIOLOGY

AUGUST 2018
VOLUME 39
NUMBER 8
WWW.AJNR.ORG

Publication Preview at www.ajnr.org features articles released in advance of print. Visit www.ajnrblog.org to comment on AJNR content and chat with colleagues and AJNR's News Digest at <http://ajnrndigest.org> to read the stories behind the latest research in neuroimaging.

1385 **PERSPECTIVES** *A. Gordhan*

EDITORIAL

1386 **Think A-Head Campaign of Image Gently: Shared Decision-Making in Pediatric Head Trauma** *N. Kadom, et al.*

REVIEW ARTICLE

 1390 **Resting-State Functional MRI: Everything That Nonexperts Have Always Wanted to Know** *H. Lv, et al.* **FUNCTIONAL**

PATIENT SAFETY

  1400 **Noncontrast Head CT in Children: National Variation in Radiation Dose Indices in the United States** *G. Sadigh, et al.* **PEDIATRICS**

PRACTICE PERSPECTIVES

    1406 **Contextual Radiology Reporting: A New Approach to Neuroradiology Structured Templates** *M.D. Mamlouk, et al.*

GENERAL CONTENTS

 1415 **Clinical Value of Vascular Permeability Estimates Using Dynamic Susceptibility Contrast MRI: Improved Diagnostic Performance in Distinguishing Hypervascular Primary CNS Lymphoma from Glioblastoma** *B. Lee, et al.* **ADULT BRAIN**

 1423 **Added Value of Spectroscopy to Perfusion MRI in the Differential Diagnostic Performance of Common Malignant Brain Tumors** *A. Vallée, et al.* **ADULT BRAIN**

  1432 **Brain Perfusion Measurements Using Multidelay Arterial Spin-Labeling Are Systematically Biased by the Number of Delays** *M. van der Thiel, et al.* **ADULT BRAIN**

   1439 **Clinically Relevant Imaging Features for MGMT Promoter Methylation in Multiple Glioblastoma Studies: A Systematic Review and Meta-Analysis** *C.H. Suh, et al.* **ADULT BRAIN**

 1446 **MR Imaging Features of Anaplastic Pleomorphic Xanthoastrocytoma Mimicking High-Grade Astrocytoma** *D. She, et al.* **ADULT BRAIN**

AJNR (Am J Neuroradiol ISSN 0195–6108) is a journal published monthly, owned and published by the American Society of Neuroradiology (ASNR), 800 Enterprise Drive, Suite 205, Oak Brook, IL 60523. Annual dues for the ASNR include \$170.00 for journal subscription. The journal is printed by Cadmus Journal Services, 5457 Twin Knolls Road, Suite 200, Columbia, MD 21045; Periodicals postage paid at Oak Brook, IL and additional mailing offices. Printed in the U.S.A. POSTMASTER: Please send address changes to American Journal of Neuroradiology, P.O. Box 3000, Denville, NJ 07834, U.S.A. Subscription rates: nonmember \$400 (\$470 foreign) print and online, \$320 online only; institutions \$460 (\$530 foreign) print and basic online, \$915 (\$980 foreign) print and extended online, \$380 online only (basic), extended online \$825; single copies are \$35 each (\$40 foreign). Indexed by PubMed/Medline, BIOSIS Previews, Current Contents (Clinical Medicine and Life Sciences), EMBASE, Google Scholar, HighWire Press, Q-Sensei, RefSeek, Science Citation Index, SCI Expanded, and Meta/CZI. Copyright © American Society of Neuroradiology.

-

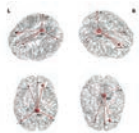
LETTERS

- E90 **Medullary Edema and Enhancement with a Straight Upper Border in Cases of Dural Arteriovenous Fistulas** *D. Byrne, et al.*
- E92 **Another Important Pitfall in the Diagnosis of Dural Sinus Thrombosis in Neonates** *A. Hakim, et al.*
- E93 **Rapid-Sequence MRI of the Brain: A Distinct Imaging Study** *C.M. Pfeifer*
- E95 **Regarding: “Localized Marked Elongation of the Distal Internal Carotid Artery with or without PHACE Syndrome: Segmental Dolichoectasia of the Distal Internal Carotid Artery”** *W. Brinjikji, et al.*
- E96 **Reply** *Z.Y. Zia, et al.*
- E97 **Laryngeal Cartilage Invasion** *L.E. Ginsberg*
- E98 **Reply** *H. Kuno, et al.*

BOOK REVIEWS

R.M. Quencer, Section Editor

Please visit www.ajnrblog.org to read and comment on Book Reviews.



Brain maps showing group average spatial representation of a seed-based functional connectivity. The posterior cingulate cortex was set as a seed. Nodes represent brain area; lines represent functional connectivity between nodes; PCC, posterior cingulate cortex; ACC, anterior cingulate cortex; SFG, superior frontal gyrus; IPL, inferior parietal lobule.

- ★ Indicates Editor's Choices selection
- ✍ Indicates Fellows' Journal Club selection
- 🔑 Indicates open access to non-subscribers at www.ajnr.org
- ☰ Indicates article with supplemental on-line table
- 🖼 Indicates article with supplemental on-line photo
- 📺 Indicates article with supplemental on-line video
- EBM 1 Evidence-Based Medicine Level 1
- EBM 2 Evidence-Based Medicine Level 2

Official Journal:

American Society of Neuroradiology
American Society of Functional Neuroradiology
American Society of Head and Neck Radiology
American Society of Pediatric Neuroradiology
American Society of Spine Radiology

EDITOR-IN-CHIEF

Jeffrey S. Ross, MD

Professor of Radiology, Department of Radiology,
Mayo Clinic College of Medicine, Phoenix, AZ

SENIOR EDITORS

Harry J. Cloft, MD, PhD

Professor of Radiology and Neurosurgery,
Department of Radiology, Mayo Clinic College of
Medicine, Rochester, MN

Thierry A.G.M. Huisman, MD

Professor of Radiology, Pediatrics, Neurology, and
Neurosurgery, Chairman, Department of Imaging
and Imaging Science, Johns Hopkins Bayview,
Director, Pediatric Radiology and Pediatric
Neuroradiology, Johns Hopkins Hospital,
Baltimore, MD

Yvonne W. Lui, MD

Associate Professor of Radiology,
Chief of Neuroradiology,
New York University School of Medicine,
New York, NY

C.D. Phillips, MD, FACR

Professor of Radiology, Weill Cornell Medical
College, Director of Head and Neck Imaging,
New York-Presbyterian Hospital, New York, NY

Pamela W. Schaefer, MD

Clinical Director of MRI and Associate Director of
Neuroradiology, Massachusetts General Hospital,
Boston, Massachusetts, Associate Professor,
Radiology, Harvard Medical School, Cambridge, MA

Charles M. Strother, MD

Professor of Radiology, Emeritus, University of
Wisconsin, Madison, WI

STATISTICAL SENIOR EDITOR

Bryan A. Comstock, MS

Senior Biostatistician,
Department of Biostatistics,
University of Washington, Seattle, WA

EDITORIAL BOARD

Ashley H. Aiken, Atlanta, GA
Lea M. Alhilali, Phoenix, AZ
Kubilay Aydin, Istanbul, Turkey
John D. Barr, Dallas, TX
Ari Blitz, Baltimore, MD
Barton F. Branstetter IV, Pittsburgh, PA
Jonathan L. Brisman, Lake Success, NY
Keith Cauley, Danville, PA
James Y. Chen, San Diego, CA
Asim F. Choudhri, Memphis, TN
Daniel Chow, Irvine, CA
J. Matthew Debnam, Houston, TX
Seena Dehkharghani, New York, NY
Yonghong Ding, Rochester, MN
Clifford J. Eskey, Hanover, NH
Saeed Fakhraan, Phoenix, AZ
Massimo Filippi, Milan, Italy
Reza Forghani, Montreal, Quebec, Canada
Nils D. Forkert, Calgary, Alberta, Canada
Wende N. Gibbs, Los Angeles, CA
Christine M. Glastonbury, San Francisco, CA
John L. Go, Los Angeles, CA
Philipp Göltz, Erlangen, Germany
Allison Grayev, Madison, WI
Brent Griffith, Detroit, MI
Ajay Gupta, New York, NY
Rakesh Kumar Gupta, Haryana, India
Lotfi Hacein-Bey, Sacramento, CA
Christopher P. Hess, San Francisco, CA
Andrei Holodny, New York, NY
Benjamin Huang, Chapel Hill, NC
Mahesh V. Jayaraman, Providence, RI
Valerie Jewells, Chapel Hill, NC
Christof Karmonik, Houston, TX
Timothy J. Kaufmann, Rochester, MN
Hillary R. Kelly, Boston, MA
Toshibumi Kinoshita, Akita, Japan
Kenneth F. Layton, Dallas, TX
Alexander Lerner, Los Angeles, CA
Michael Lev, Boston, MA
Karl-Olof Lovblad, Geneva, Switzerland
Franklin A. Marden, Chicago, IL
Joseph C. McGowan, Merion Station, PA
Stephan Meckel, Freiburg, Germany
Christopher J. Moran, St. Louis, MO
Takahisa Mori, Kamakura City, Japan
Suresh Mukherji, Ann Arbor, MI
Alexander J. Nemeth, Chicago, IL
Renato Hoffmann Nunes, Sao Paulo, Brazil

Sasan Partovi, Cleveland, OH
Laurent Pierot, Reims, France
Jay J. Pillai, Baltimore, MD
Whitney B. Pope, Los Angeles, CA
Joana Ramalho, Lisbon, Portugal
Otto Rapalino, Boston, MA
Álex Rovira-Cañellas, Barcelona, Spain
Paul M. Ruggieri, Cleveland, OH
Amit M. Saindane, Atlanta, GA
Erin Simon Schwartz, Philadelphia, PA
Lubdha M. Shah, Salt Lake City, UT
Maksim Shapiro, New York, NY
Timothy Shepherd, New York, NY
Mark S. Shiroishi, Los Angeles, CA
Bruno P. Soares, Baltimore, MD
Maria Vittoria Spampinato, Charleston, SC
Khin Khin Tha, Sapporo, Hokkaido, Japan
Krishnamoorthy Thamburaj, Hershey, PA
Cheng Hong Toh, Taipei, Taiwan
Aquila S. Turk, Charleston, SC
Anja G. van der Kolk, Madison, WI
Willem Jan van Rooij, Tilburg, Netherlands
Arastoo Vossough, Philadelphia, PA
Elysa Widjaja, Toronto, Ontario, Canada
Max Wintermark, Stanford, CA
Ronald L. Wolf, Philadelphia, PA
Kei Yamada, Kyoto, Japan
Carlos Zamora, Chapel Hill, NC
Vahe M. Zohrabian, New Haven, CT

EDITORIAL FELLOW

Alireza Radmanesh, New York, NY

SPECIAL CONSULTANTS TO THE EDITOR

AJNR Blog Editor

Neil Lall, Denver, CO

Case of the Month Editor

Nicholas Stence, Aurora, CO

Case of the Week Editors

Juan Pablo Cruz, Santiago, Chile
Sapna Rawal, Toronto, Ontario, Canada

Classic Case Editor

Sandy Cheng-Yu Chen, Taipei, Taiwan

Health Care and Socioeconomics Editor

Pina C. Sanelli, New York, NY

Physics Editor

Greg Zaharchuk, Stanford, CA

Podcast Editor

Wende N. Gibbs, Los Angeles, CA

Twitter Editor

Jennifer McCarty, Houston, TX

Founding Editor

Juan M. Taveras

Editors Emeriti

Mauricio Castillo, Robert I. Grossman,
Michael S. Huckman, Robert M. Quencer

Managing Editor

Karen Halm

Assistant Managing Editor

Laura Wilhelm

Marketing and Social Media Manager

Kylie Mason

Executive Director, ASNIR

Mary Beth Hepp



Title: David Davis Mansion, Bloomington Illinois. Plein air painting in oil. The Victorian home of Senator David Davis, friend and appointee of President Abraham Lincoln to the Supreme Court (1862–1877).

Ajeet Gordhan, Endovascularneuro LLC, Advocate Bromenn Medical Center, Normal, Illinois, and OSF St. Joseph Medical Center, Bloomington, Illinois

Think A-Head Campaign of Image Gently: Shared Decision-Making in Pediatric Head Trauma

N. Kadom, B.L. Vey, D.P. Frush, J.S. Broder, K.E. Applegate, and Members of the Image Gently Think A-Head Campaign Committee

When children present with head trauma, as with any imaging examination, it is necessary to consider the risks, costs, and benefits of testing. In many instances of pediatric head trauma, imaging studies are used for “confirming” or “excluding” certain diagnoses.¹ However, imaging tests, specifically radiographs (x-rays) and CT expose children to ionizing radiation, which, at relatively high doses (much higher than typical doses from diagnostic imaging), does have a small increased risk of cancer.² For children who experience head injury, there are now scientifically validated criteria that can help decide whether imaging tests are beneficial or can be avoided. This type of information is essential when providers discuss the use of imaging tests and other options with caregivers and patients during the shared decision-making process. Of note, the recommendations discussed in this article do not pertain to patients with head trauma in suspected child abuse.

Diagnostic imaging following head trauma serves several purposes: diagnosis, treatment planning, prognosis, and reassurance. In some cases, imaging of subtle injuries not requiring intervention can be avoided (Canadian CT Head Rule; Pediatric Emergency Care Applied Research Network [PECARN]). Clinical Decision Rules (CDRs) are intended to inform management partly by obviating unhelpful diagnostic imaging; clinical outcomes of patients are based on history and examination features. In pediatric head trauma, it is understood that children meeting low-risk criteria for head injury do not need diagnostic imaging because they do not require any additional interventions, such as additional observation, or neurosurgical procedures to achieve good neurologic outcomes.³

Concerns by caregivers, patients, and medical providers about potential carcinogenic effects of radiation exposure, even given relatively low doses during medical imaging, must be weighed against the risk of missing a clinically significant head injury that could harm a child if CT is deferred. Parents, patients, and caregivers may over- or underestimate the risk of radiation from CT relative to the risk of an undiagnosed brain injury.⁴ Physicians should use scientific evidence to estimate injury risk (using the Clinical Decision Rules described below), and the best available evidence about the radiation risk of CT to assist in shared decision-making.⁵

When one counsels patients, it is important to remember that the current knowledge on radiation risk for a given imaging study should not be downplayed or overemphasized to manipulate families into making what the physician believes to be the “right” decision. Rather, the best available scientific evidence should be used to estimate the risk of missing an important injury without imaging and the benefit

of defining the extent of a known significant injury with imaging. The imaging test benefit may vary for each patient scenario. The benefit of reassurance following normal CT findings may also be an important consideration. The Image Gently Alliance (www.imagegently.org) multispecialty, collaborative “Think A-Head” campaign (Figure) promotes the use of evidence-based guidelines when deciding whether children with head trauma need imaging and, if so, which imaging test (technique) would be appropriate.

Appropriate imaging modalities available for evaluating the head in children with trauma include radiography, CT, and MR imaging. Existing evidence-based clinical decision rules refer to the use of CT, which is widely available and can be accessed quickly in most US medical centers. Increasingly fast CT examination times obviate sedation in most cases, which is an important consideration, especially for serial patient evaluations in the emergency setting. MR imaging is not established for routine use in acute pediatric brain trauma yet, though several studies have validated the ability of MR imaging to detect relevant pathology and have shown the feasibility of rapid MR imaging protocols.⁶⁻⁸ The use of radiographs in minor pediatric head trauma is controversial. In patients with linear skull fractures on radiographs and who are asymptomatic, there may still be small intracranial hemorrhages, but these would not require neurosurgical intervention.⁹ In children younger than 2 years of age with minor head trauma, there is a higher risk of skull fracture, but neuro-observation without initial CT imaging is considered safe.¹⁰ In general, skull radiographs should not be used routinely in children with minor head trauma.¹⁰ The American College of Radiology appropriateness criteria for head trauma in children provide further information about the appropriate choice of imaging studies, depending on clinical scenarios.¹¹

Clinical Decision Rules

Clinical Decision Rules are clinical care guides intended to improve the appropriateness of care based on scientific evidence. CDRs reduce the use of unnecessary advanced testing (with associated cost, time, and risks such as further downstream investigations of incidental imaging findings and ionizing radiation) without compromising patient outcomes. CDRs typically use readily available information from the history and physical examination to risk-stratify patients. Other benefits of CDRs include the ability to create standardized care pathways, which can help reduce variation of practice by individual providers. In the case of traumatic brain injury, CDRs are expected to detect serious injury requiring intervention. Some rules by intention attempt to detect all injuries, regardless of the requirement for treatment, while others intentionally do not aim to detect injuries that would not progress or require explicit therapy, such as minimally displaced skull fractures. In general, an increase in the diagnostic sensitivity of a rule results in reduced specificity, usually leading to only a small-to-moderate reduction of imaging/testing use. Rules that ultimately achieve clinical adoption usually have a sensitivity for serious injury exceeding 99%, with more modest specificity (often 60%–70%) and reductions in imaging use (of 3%–40%).¹²

Many decision rules have been tested for validity in specific populations, such as children.^{13,14} Most professional medical societies

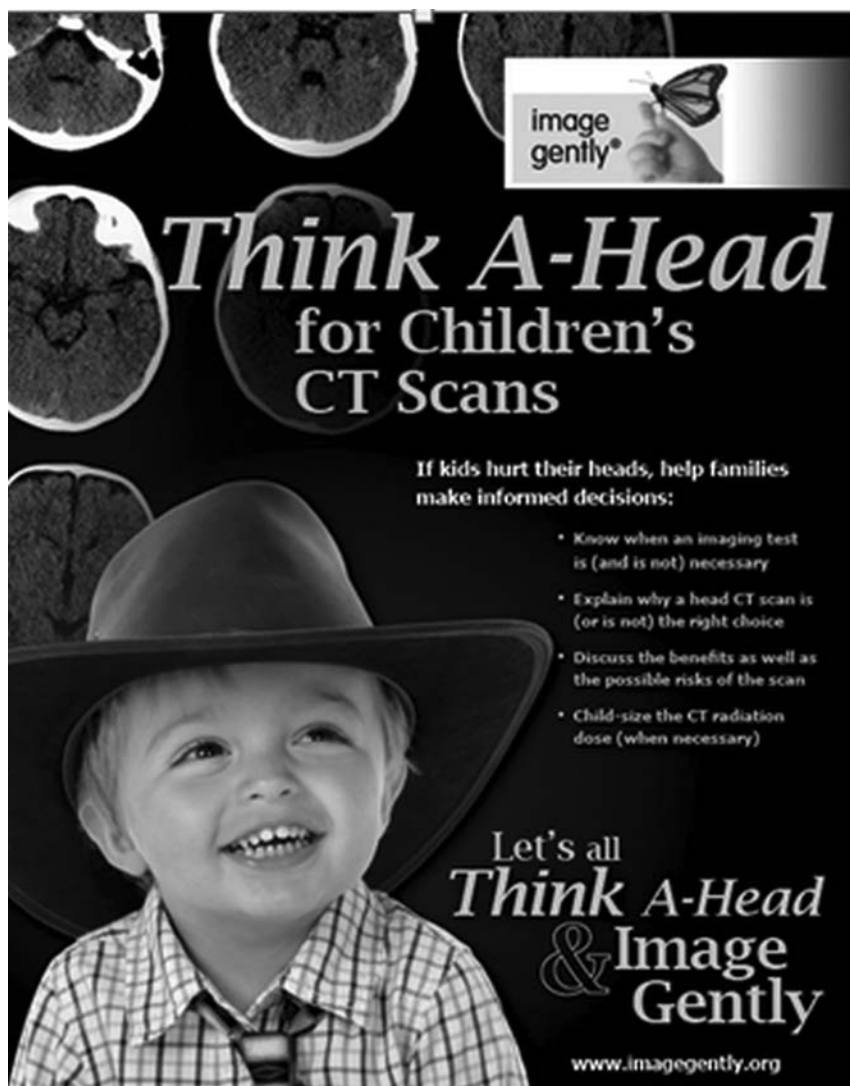


FIGURE. The Think A-Head campaign poster (www.imagegently.org). Poster design courtesy of the American Society of Radiologic Technologists.

endorse decision rules and help inform health care professionals of their existence. Locally, processes should be in place to enable training and promote compliance of care providers with decision rules that were locally adopted. Ideally, the health system should support quality monitoring and take opportunities to share stories of “harm and charm” to foster further improvement in care. Finally, medical providers and patient safety organizations can collaborate to share the best practice information so that parents and caregivers of children become partners in the care process, as promoted by the Choosing Wisely Campaign (www.choosingwisely.org).

For pediatric head trauma, several important decision rules have been developed and validated during the past 15 years (Tables 1 and 2): PECARN; the Canadian Assessment of Tomography for Childhood Head injury (CATCH); and the Children’s Head injury Algorithm for the prediction of Important Clinical Events (CHALICE).

Pediatric Emergency Care Applied Research Network

The strength of the PECARN decision rule is that it identifies children who are at low risk for brain injury and do not need brain imaging with a sensitivity of 100%.¹⁵ These results are based on a

multicenter prospective cohort study performed in 42,412 patients younger than 18 years of age and with a Glasgow Coma Scale (GCS) score of 14–15. The study yielded several clinical criteria that were predictive of clinically important traumatic brain injury. The study showed, with a 99.95%–100% negative predictive value,^{16,17} that children without clinical criteria for clinically important traumatic brain injury did not need neuroimaging. In the study, application of the PECARN rule could have reduced CT use by approximately 20% by identifying patients at extremely low risk of clinically important traumatic brain injury.¹⁶ Advantages of the PECARN decision tool over other decision tools include the PECARN rule being validated and the validation cohort including 20% of children younger than 2 years of age.^{16,18}

Canadian Assessment of Tomography for Childhood Head Injury

CATCH guidelines are based on a prospective multicenter cohort study performed in 3866 patients younger than 16 years of age with a GCS score of 13–15. These guidelines identified 7 risk factors for the presence of brain injury on CT scans in children with minor head injury with 98.1% sensitivity (95% confidence interval, 94.6%–99.4%) and 50.1% specificity (95% confidence interval, 48.5%–51.7%).¹⁹

Children’s Head Injury Algorithm for the Prediction of Important Clinical Events

CHALICE guidelines were published in 2006²⁰ and are the result of a prospective multicenter cohort study in England, performed in patients 16 years of age and younger. The goal of this study was to derive a decision rule to aid in identification of children at risk who should undergo CT of the brain. The rule was applied to children regardless of the GCS score and was shown to have a sensitivity of 98% (95% confidence interval, 96%–100%) and a specificity of 87% (95% confidence interval, 86%–87%) for the prediction of clinically significant head injury.²⁰

Risks

The most widely adopted decision rule in children is the PECARN rule, probably because it is the only rule that has been validated in children. Of note, the PECARN rule has been shown to have a negative predictive value of 100%, meaning that the likelihood of negative head CT findings in a child meeting the PECARN low-risk criteria is 100%. This means that there will still be a sizeable

Table 1: Decision rule comparison of predictor variables, modified after Lyttle et al^{16,18-20}

PECARN	CATCH	CHALICE
Mechanism of injury Severe mechanism of injury (MVC with patient ejection, death of another passenger, or rollover; pedestrian/bicyclist without helmet struck by motorized vehicle; falls >1.5 m [if younger than 2 yr, fall >0.9 m]; head struck by high-impact object)	Dangerous mechanism of injury (eg, MVC; fall from elevation of ≥3 feet [≥0.91 m] or 5 stairs; fall from bicycle with no helmet).	High-speed road traffic collision: pedestrian, cyclist, occupant (>40 miles/h or 64 km/h); fall >3 m in height; high-speed injury from projectile or object
History Any or suspected LOC History of vomiting	History of worsening headache	Witnessed LOC >5 min ≥3 Vomits after head injury (discrete episodes)
If age younger than 2 years LOC ≥5 sec Not acting normally per parent		Amnesia (anterograde/retrograde >5 min) Suspicion of nonaccidental injury Seizure in patient with no history of epilepsy
Physical examination Clinical signs of basilar skull fracture	GCS < 15, two hours after injury	GCS < 14, pediatric GCS < 15 if younger than 1 yr of age
If younger than 2 years age: Palpable or unclear skull fracture Occipital, parietal, or temporal scalp hematoma Large boggy scalp hematoma	Irritability on examination Any sign of basal skull fracture Suspected open or depressed skull fracture	Abnormal drowsiness (more than that expected by examining doctor) Positive focal neurology Signs of basal skull fracture Suspicion of penetrating or depressed skull injury or tense fontanelle Presence of bruise/swelling/laceration >5 cm if younger than 1 yr of age

Note:—MVC indicates motor vehicle collision; LOC, loss of consciousness.

Table 2: Comparison of reported statistics for CATCH, CHALICE, and PECARN rules

Decision Rule	Sensitivity (95% CI)	Specificity (95% CI)	Reference
CATCH	98.1% (94.6%–99.4%)	50.1% (48.5%–51.7%)	Osmond et al 2010 ¹⁹
CHALICE	98% (96%–100%)	87% (86%–87%)	Dunning et al 2006 ²⁰
PECARN	100% (84%–100%)	62% (59%–66%)	Babl et al 2014 ¹⁵
	NPV = 99.95%–100%		Kuppermann et al 2009 ¹⁶ Mihindu et al 2014 ¹⁷

Note:—NPV indicates negative predictive value.

percentage of children who meet the clinical criteria for CT imaging according to PECARN but who will not have imaging findings. For example, Mihindu et al¹⁷ found, after retrospectively applying the PECARN criteria, that 85% of CTs that were indicated per PECARN had negative findings; only 15% had positive findings; and of these, most did not require any medical interventions. Both CHALICE and CATCH rules may miss clinically important traumatic brain injury. In a comparison study, it was shown that the median likelihood for CATCH and CHALICE to miss important traumatic brain injury was 4%.³

Using tools to increase physician compliance can aid in successful adoption of CDRs in clinical practice. For example, at a regional level I trauma center, the emergency department achieved a 95% compliance with the PECARN rule regarding the use of CT in children with head trauma. This could be achieved using a provider scorecard and a peer-learning feedback system.²¹ Practices and institutional consensus of relevant stakeholders should determine whether decision rules are needed and which rules are the most appropriate. Auditing both impact and adherence to rules should also be part of this process.

CONCLUSIONS

All 3 CDRs for pediatric traumatic head injury describe high sensitivity with low specificity. This diagnostic performance of the

CDRs should not be surprising for the clinical scenario of head trauma in which it is critical not to miss this injury. The most commonly used decision rule in the United States today is the PECARN rule.

The Think A-Head Collaborative Campaign by Image Gently

The Image Gently Alliance, American Academy of Pediatrics, American College of Emergency Physicians, American Association of Neurologic Surgeons/Congress of Neurologic Surgeons Joint Section on Pediatric Neurosurgery, and other allied medical organizations launched the Think A-Head campaign to help providers appropriately obtain and perform CT in children with minor head injuries (www.imagegently.org/Procedures/Minor-CT-in-Head-Injuries). The effort will also equip providers and parents with resources to help them communicate effectively about when CT may be the best option for a proper diagnosis and provide balanced information and resources on medical radiation use and potential risks in children (www.imagegentlyparents.org; www.imagegentlyproviders.org).

The Think A-Head campaign provides tools and resources to accomplish the following (Figure):

- Help providers ensure that ordering patterns comply with latest evidence-based medical guidelines.
- Help providers explain to parents/caregivers why an imaging scan is (or is not) necessary.
- Help parents ask questions to better inform decision-making if their child is prescribed a head CT scan.
- Help imaging professionals use an appropriate examination radiation dose.

REFERENCES

1. Barrett TW, Rising KL, Bellolio MF, et al. **The 2016 Academic Emergency Medicine Consensus Conference, “Shared Decision Making in the Emergency Department: Development of a Policy-relevant Patient-centered Research Agenda” Diagnostic Testing Breakout Session Report.** *Acad Emerg Med* 2016;23:1354–61 CrossRef Medline
2. Pearce MS, Salotti JA, Little MP, et al. **Radiation exposure from CT scans in childhood and subsequent risk of leukaemia and brain tumours: a retrospective cohort study.** *Lancet* 2012;380:499–505 CrossRef Medline
3. Easter JS, Bakes K, Dhaliwal J, et al. **Comparison of PECARN, CATCH, and CHALICE rules for children with minor head injury: a prospective cohort study.** *Ann Emerg Med* 2014;64:145–52, 152.e1–5 CrossRef Medline
4. Lee CI, Haims AH, Monico EP, et al. **Diagnostic CT scans: assessment of patient, physician, and radiologist awareness of radiation dose and possible risks.** *Radiology* 2004;23:393–98 Medline
5. Lam DL, Larson DB, Eisenberg JD, et al. **Communicating potential radiation-induced cancer risks from medical imaging directly to patients.** *AJR Am J Roentgenol* 2015;205:962–70 CrossRef Medline
6. Cohen AR, Caruso P, Duhaime AC, et al. **Feasibility of “rapid” magnetic resonance imaging in pediatric acute head injury.** *Am J Emerg Med* 2015;33:887–90 CrossRef Medline
7. Mehta H, Acharya J, Mohan AL, et al. **Minimizing radiation exposure in evaluation of pediatric head trauma: use of rapid MR imaging.** *AJNR Am J Neuroradiol* 2016;37:11–18 CrossRef Medline
8. Sheridan DC, Newgard CD, Selden NR, et al. **QuickBrain MRI for the detection of acute pediatric traumatic brain injury.** *J Neurosurg Pediatr* 2017;19:259–64 CrossRef Medline
9. Erlichman DB, Blumfield E, Rajpathak S, et al. **Association between linear skull fractures and intracranial hemorrhage in children with minor head trauma.** *Pediatr Radiol* 2010;40:1375–79 CrossRef Medline
10. Arneitz C, Sinzig M, Fasching G. **Diagnostic and clinical management of skull fractures in children.** *J Clin Imaging Sci* 2016;6:47 CrossRef Medline
11. Palasis S, Saigal G, Singer AD, et al. **ACR Appropriateness Criteria head trauma—child.** *J Am Coll Radiol* 2014;11:939–47 CrossRef Medline
12. Stiell IG, Wells GA. **Methodologic standards for the development of clinical decision rules in emergency medicine.** *Ann Emerg Med* 1999;33:437–47 CrossRef Medline
13. Stiell IG, Greenberg GH, Wells GA, et al. **Prospective validation of a decision rule for the use of radiography in acute knee injuries.** *JAMA* 1996;275:611–15 Medline
14. Stiell IG, Greenberg GH, Wells GA, et al. **Derivation of a decision rule for the use of radiography in acute knee injuries.** *Ann Emerg Med* 1995;26:405–13 CrossRef Medline
15. Babl FE, Lyttle MD, Bressan S, et al; PREDICT research network. **A prospective observational study to assess the diagnostic accuracy of clinical decision rules for children presenting to emergency departments after head injuries (protocol): the Australasian Paediatric Head Injury Rules Study (APHIRST).** *BMC Pediatr* 2014;14:148 CrossRef Medline
16. Kuppermann N, Holmes JF, Dayan PS, et al; Pediatric Emergency Care Applied Research Network (PECARN). **Identification of children at very low risk of clinically-important brain injuries after head trauma: a prospective cohort study.** *Lancet* 2009;374:1160–70; Erratum in: *Lancet* 2014;383:308 CrossRef
17. Mihindu E, Bhullar I, Tepas J, et al. **Computed tomography of the head in children with mild traumatic brain injury.** *Am Surg* 2014;80:841–43 Medline
18. Lyttle MD, Crowe L, Oakley E, et al. **Comparing CATCH, CHALICE and PECARN clinical decision rules for paediatric head injuries.** *Emerg Med J* 2012;29:785–94 CrossRef Medline
19. Osmond MH, Klassen TP, Wells GA, et al; Pediatric Emergency Research Canada (PERC) Head Injury Study Group. **CATCH: a clinical decision rule for the use of computed tomography in children with minor head injury.** *CMAJ* 2010;182:341–48 CrossRef Medline
20. Dunning J, Daly JP, Lomas JP, et al; Children’s head injury algorithm for the prediction of important clinical events study group. **Derivation of the children’s head injury algorithm for the prediction of important clinical events decision rule for head injury in children.** *Arch Dis Child* 2006;91:885–91 CrossRef Medline
21. Jain S, Frank G, McCormick K, et al. **Impact of physician scorecards on emergency department resource use, quality, and efficiency.** *Pediatrics* 2015;136:e670–79 CrossRef Medline

Resting-State Functional MRI: Everything That Nonexperts Have Always Wanted to Know

H. Lv, Z. Wang, E. Tong, L.M. Williams, G. Zaharchuk, M. Zeineh, A.N. Goldstein-Piekarski, T.M. Ball, C. Liao, and M. Wintermark



ABSTRACT

SUMMARY: Resting-state fMRI was first described by Biswal et al in 1995 and has since then been widely used in both healthy subjects and patients with various neurologic, neurosurgical, and psychiatric disorders. As opposed to paradigm- or task-based functional MR imaging, resting-state fMRI does not require subjects to perform any specific task. The low-frequency oscillations of the resting-state fMRI signal have been shown to relate to the spontaneous neural activity. There are many ways to analyze resting-state fMRI data. In this review article, we will briefly describe a few of these and highlight the advantages and limitations of each. This description is to facilitate the adoption and use of resting-state fMRI in the clinical setting, helping neuroradiologists become familiar with these techniques and applying them for the care of patients with neurologic and psychiatric diseases.

ABBREVIATIONS: ALFF = Amplitude of Low Frequency Fluctuations; BOLD = blood oxygen level–dependent; FCD = functional connectivity density; ICA = independent component analysis; ReHo = regional homogeneity; rs-fMRI = resting-state fMRI

The brain controls all the complex functions in the human body. Structurally, the brain is organized grossly into different regions specialized for processing and relaying neural signals; functionally, the brain is subspecialized for perceptual and cognitive processes. Working in concert, these subspecialized areas orchestrate complex bodily functions and allow human behavior.

Neurons do not contain any internal reserves of energy, either in the form of glucose or oxygen. When activated, they are provided with more energy by the adjacent capillaries through a process called the hemodynamic response, which supplies them with increased regional cerebral blood flow and an increase in oxygen supply, usually even greater than their needs.^{1,2} This process results in a change in terms of the relative levels of oxyhemoglobin

and deoxyhemoglobin that can be detected by MR imaging on the basis of their differential magnetic susceptibilities. This imaging approach is called blood oxygen level–dependent (BOLD) contrast imaging. Conventionally, BOLD signal change has been known to be modulated by the arterial partial pressure of CO₂ level. More recent research suggests that BOLD signal is determined by both the arterial partial pressure of O₂ and CO₂, rather than CO₂ alone.³ The change in the BOLD signal is the cornerstone of functional MR imaging,^{4,5} which is traditionally used to construct maps indicating subspecialized brain regions that are activated by certain tasks or reacting to a stimulus at a low frequency (0.01–0.1 Hz). The frequencies of neural activity fluctuations measured by fMRI (which are low-frequency and indirectly measured using BOLD signal) and of neural firing measured in neurophysiologic studies (which are high-frequency and are directly measured) are different.^{6,7}

The biologic significance of the neural activity fluctuations was first described by Biswal et al in 1995.⁸ When the subjects were asked to perform bilateral finger tapping in that experiment, researchers identified a highly correlated BOLD time course between the left somatosensory cortex and the homologous areas in the contralateral hemisphere.⁸ Since then, fMRI has been widely used in both healthy subjects and patients with neurologic and psychiatric disorders to analyze synchronous, spontaneous fluctuations of various resting-state networks.⁹ Because of the neurovascular coupling, the BOLD signal, while vascular in nature, is strongly related to neuronal activity.¹⁰ However, the delay of the hemodynamic response following neural activation is responsible

From the Department of Radiology (H.L., Z.W.), Beijing Friendship Hospital, Capital Medical University, Beijing, China; Department of Radiology (H.L., G.Z., M.Z., M.W.), Neuroradiology Division, and Department of Psychiatry and Behavioral Sciences (L.M.W., A.N.G.-P., T.M.B.), Stanford University, Stanford, California; Department of Radiology (E.T.), Neuroradiology Section, University of California, San Francisco, San Francisco, California; and Department of Radiology (C.L.), Yunnan Tumor Hospital (The Third Affiliated Hospital of Kunming Medical University), Kunming, Yunnan Province, China.

Dr Ball is supported by grant T32MH019938 from the National Institute of Mental Health.

The content of this article is solely the responsibility of the authors and does not necessarily represent the official views of the National Institutes of Health.

Please address correspondence to Max Wintermark, MD, MAS, MBA, Stanford University, Department of Radiology, Neuroradiology Division, 300 Pasteur Dr, Room S047, Stanford, CA 94305-5105; e-mail: Max.Wintermark@gmail.com; @StanfordNRAD

Indicates open access to non-subscribers at www.ajnr.org

<http://dx.doi.org/10.3174/ajnr.A5527>

for the relatively poor temporal resolution of fMRI,¹¹ and the BOLD signal can be altered in brain regions where the blood circulation is altered.¹²⁻¹⁴ For example, pathologic conditions such as traumatic brain injury¹⁵⁻¹⁷ or anoxic brain injury¹⁸⁻²¹ might affect neurovascular coupling and therefore make fMRI suboptimal to assess neural activity in these pathologic conditions. Therefore, these factors should be taken into consideration when designing calibrated BOLD experiments and interpreting functional connectivity data, especially in patients with vascular pathologies.³

As opposed to paradigm- or task-based functional MR imaging, resting-state fMRI (rs-fMRI) is acquired in the absence of a stimulus or a task, in other words at rest. The principle of rs-fMRI is also based on the BOLD signal fluctuation, which is the same as for active-task fMRI. rs-fMRI focuses on spontaneous BOLD signal alterations. Data can be acquired with a dedicated scan, in which individuals are instructed to simply rest, or by inferring resting-state data from periods of rest embedded within a series of tasks.²² The lack of a task makes rs-fMRI particularly attractive for patients who may have difficulty with task instructions, such as those with neurologic, neurosurgical, and psychiatric conditions, as well as for pediatric patients. Thus, the application of rs-fMRI in the research and clinical setting has been growing for the past 2 decades.^{9,23}

There are multiple ways to analyze rs-fMRI data, and each approach has implications in terms of what information can be extracted from the data. This article attempts to provide a broad overview of major analysis methods that are used in rs-fMRI. We will systematically describe these approaches, their advantages, and limitations. This work will help nonexperts become familiar with rs-fMRI techniques and how to apply them to the benefit of patients with neurologic, neurosurgical, and psychiatric disorders.^{24,25}

Analytic Methods

rs-fMRI analysis is challenging due to the massive amount of data and the need for sophisticated analysis. Before one applies any of the analytic methods, realignment and removal of confounding artifacts (eg, head motion, CSF signal) are important preprocessing steps. Other main preprocessing steps are required on rs-fMRI data, including removing the first 10~20 time points, slice timing, data normalization, and band-pass filtering. Other possible procedures, including smoothing, may be performed in different sequences according to the analytic method applied. Several software packages, including but not limited to statistical parametric mapping, Analysis of Functional Neuro Images (AFNI; <http://afni.nimh.nih.gov/afni>), the CONN toolbox (<https://www.nitrc.org/projects/conn/>), MELODIC (<https://fsl.fmrib.ox.ac.uk/fsl/fslwiki/MELODIC>), and Group ICA of fMRI Toolbox Software (GIFT; <http://mialab.mrn.org/software/gift/>), are commonly used to analyze rs-fMRI data. Pipelines^{26,27} have also been developed to analyze data almost automatically, which make the data analysis much easier for nonexperts.

Proper interpretation of rs-fMRI data results requires an understanding of anatomy, pathophysiology, and neuroscience, to make logical inferences. For easy understanding, the large amount of information contained in the rs-fMRI data can be compared

with a map.²⁸ When one looks at a map, one can focus on finding cities or highways linking cities with each other. Similarly, when one analyzes rs-fMRI data, one can extract information on the function of specific brain regions or the functional connectivity between different brain regions. Analytic approaches can be broadly divided into 2 types: functional segregation and functional integration.^{29,30} Functional segregation focuses on the local function of specific brain regions and is mainly used for brain mapping. Functional integration focuses on the functional relationships or connectivity between different brain areas and assesses the brain as an integrated network. Functional segregation techniques rely on the analysis of rs-fMRI activity, while functional integration techniques rely on the analysis of rs-fMRI connectivity. By comparing the rs-fMRI results with the way we look at a map, one can understand these different methods more intuitively.

Functional Segregation Methods for Identifying Neural Networks

Functional segregation divides the brain into regions according to their specific functions³⁰: Amplitude of Low Frequency Fluctuations (ALFF) and regional homogeneity (ReHo) are methods commonly used in functional segregation assessments. Fractional-ALFF and ReHo reflect different aspects of regional neural activity (“cities”) but do not provide information on functional connectivity (“highways”). Although they are similar in many ways, they reveal different aspects of brain abnormalities in clinical populations.³¹⁻³⁴ The combined application of these 2 methods provides more information than either method alone. We next discuss each of these methods and their advantages and disadvantages and how they complement each other.

ALFF Analysis

The ALFF method measures the total power of the BOLD signal within the low-frequency range between 0.01 and 0.1 Hz (Fig 1A³⁵; the results are visualized with the REST Slice Viewer; <http://www.restfmri.net>³⁶). ALFF is proportional to regional neural activity.³⁵ Fractional-ALFF is a variant that measures the power within the low-frequency range (0.01–0.1 Hz) divided by the total power in the entire detectable frequency range and represents the relative contribution of the low-frequency oscillations.³⁷ ALFF and fractional-ALFF measure regional brain activity only (like traffic in cities on a map, ALFF reveals the density of “traffic” as an absolute value, while fractional-ALFF looks at the density of traffic as a proportion in cities). Thus, they do not provide information on functional connectivity between brain regions.

Subsets of frequency bands have been reported as follows: 1) Frequencies between 0.010 and 0.027 Hz may reflect cortical neuronal activity, 2) frequencies between 0.027 and 0.073 Hz may reflect basal ganglia activity, and 3) frequencies between 0.073 and 0.198 Hz and 0.198 and 0.250 Hz have been associated with physiologic noise and white matter signal, respectively.³⁸⁻⁴² However, there is an active ongoing debate about whether rs-fMRI can actually detect white matter activity. Reasons for white matter fMRI activation remain controversial and require further investigation.¹³ Mounting evidence supports the spatial properties of the white matter being assessed using functional correlation tensor

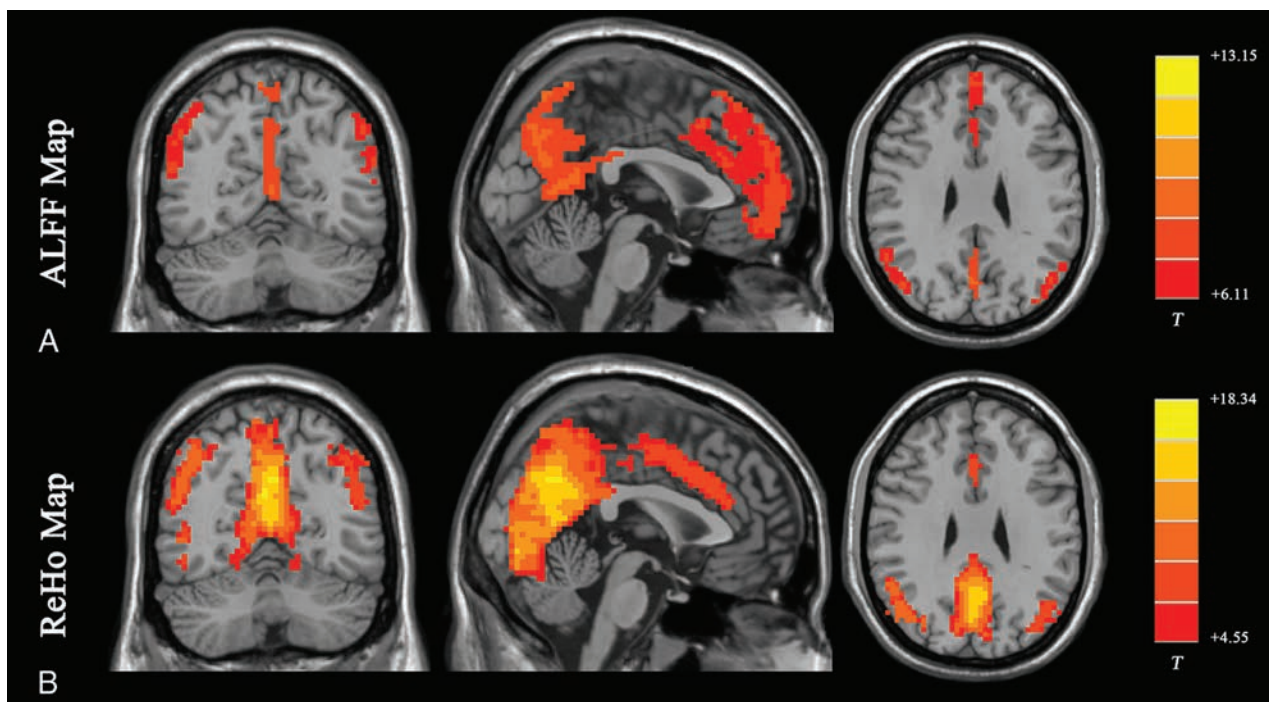


FIG 1. Results of ALFF and ReHo studies (1-sample *t* test results of 200 healthy volunteers [M.W., unpublished data, February 6, 2017]). A, ALFF results. B, ReHo results. Results of increased ALFF and ReHo are mostly overlapped with the default mode network, which is activated at resting-state in healthy volunteers. (For different kinds of patients, abnormal ALFF or ReHo findings may be detected in other brain areas in the resting-state.) Both ALFF and ReHo results reflect regional neural activities. ALFF is focused on measuring the strength of the activity, while ReHo is more specific for coherence and centrality of regional activity. T indicates peak intensity.

analysis based on rs-fMRI data.^{43,44} Functional correlation tensor results showed similarities to those of diffusion tensor imaging but represent a separate entity. Future studies involving functional correlation tensor analysis of rs-fMRI data may provide insight into the network interaction features of the brain within the white matter.

The advantage of the ALFF and fractional-ALFF methods lies in the simplicity of the analysis without any underlying hypothesis. Both ALFF and fractional-ALFF show remarkably high temporal stability⁴⁵ and long-term (about 6 months) test-retest reliability.⁴⁶ Fractional-ALFF is reportedly more specific to gray matter³⁷; however, it has slightly lower test-retest reliability.⁴⁶ Therefore, both measurements are commonly reported together to maximize the reliability across subjects, with sufficient specificity to examine individual differences.

Regional Homogeneity Analysis

ReHo analysis is a voxel-based measure of the similarity between the time-series of a given voxel and its nearest neighbors, as calculated by the Kendall coefficient of concordance of the BOLD time-series. It measures the synchrony of adjacent regions (equivalent to the concordance of traffic between “downtown” and the “suburbs” in a city) (Fig 1B).⁴⁷ A higher ReHo value represents higher coherence and centrality of regional brain activity. Higher coherence and centrality are usually associated with, but not necessarily, equal-to-high activity. Thus, the results of fractional-ALFF and ReHo should be discussed separately.⁴⁸ Areas that overlap in ALFF and ReHo represent regions that are not only active at the same time frequency but are also active in

sync with neighboring voxels. This representation means that the regions are not only active but also engaging a relatively large group of neurons.⁴⁷

ReHo is usually calculated within a low-frequency range, typically between 0.01 Hz and 0.1 Hz. It can be subdivided into different frequency bands. Lower frequency (0.01–0.04 Hz) ReHo is more sensitive for cortical activity.⁴⁹ The exact biologic meaning of ReHo measurements in different frequency bands still needs further exploration. Several studies demonstrated the frequency dependence of the ReHo changes in different neurologic conditions.^{42,50–52} Future rs-fMRI research focusing on the biologic meaning of ReHo should be conducted in both healthy subjects and patients with specific conditions using spectrum-specific analytic strategies.

The test-retest reliability of the ReHo method is very high, even when subjects are rescanned after a long interval (6 months).⁴⁶ Zuo et al⁵³ developed a ReHo computation method along 2 dimensions (surface) using cortical surface-based fMRI analysis after projecting individual preprocessed data into a cortical surface space. It is more reliable than a method based on conventional 3D (volume) because of the following: 1) It could accurately calculate the ReHo value on the cortical surface by avoiding a mixture of gray and white matter; and 2) by avoiding mixing adjacent brain tissues in 3D space due to the highly folded human cortex, it could more precisely characterize functional homogeneity within a brain region. Like ALFF, ReHo does not require an a priori definition of the ROI and can provide information about regional activity throughout the brain. ALFF and ReHo may also be applied together to reveal

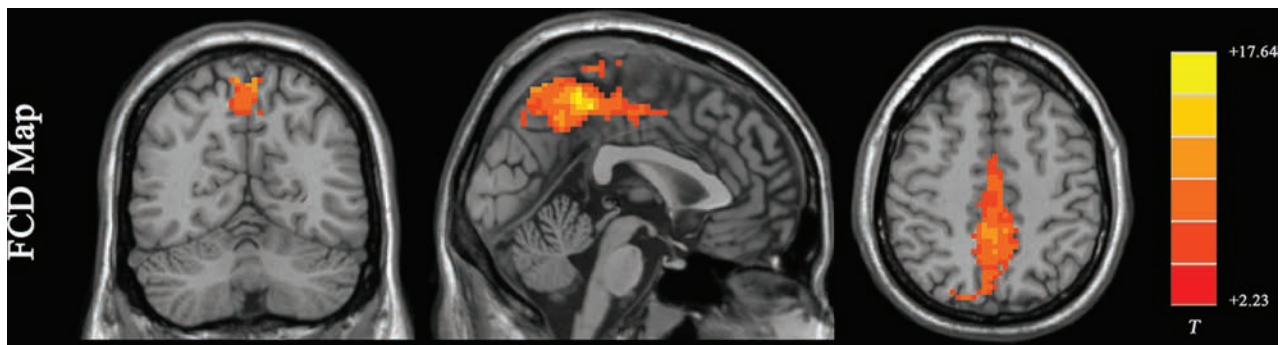


FIG 2. Results of an FCD study (1-sample *t* test results of 200 healthy volunteers [M.W., unpublished data, February 6, 2017]). The FCD reaches its highest value in the posterior cingulate cortex/precuneus, reflecting the highest density of functional connectivity of these voxels in healthy subjects. Results are like those of previous studies reviewed by Tomasi.⁵⁸ FCD parameters: $T_{\text{SNR}} = 50$ and $T_c = 0.6$.

different aspects of brain regional function and abnormalities arising in clinical populations.^{31,33,34,54,55}

Both ALFF and ReHo methods can be used to reveal local neural activity of the brain. Those methods are used to define an ROI for seed-based functional connectivity analysis (further discussed below). However, because the brain is more appropriately studied as an integrated network rather than isolated clusters, the excitement for stand-alone functional segregation methods has gradually receded in favor of functional integration methods. Another limitation of ReHo is the relatively unclear biologic meaning of ReHo in the different frequency bands.

Functional Integration Methods for Identifying Neural Networks

Functional integration focuses on the functional connectivity (highways on the map) between different regions of the brain. Functional connectivity measures the degree of synchrony of the BOLD time-series between different brain regions. The connectivity can be the result of a direct anatomic connection or an indirect path⁵⁶ via a mediating region or may have no known anatomic correlate. Functional connectivity can also be due to a common source of input signals. Of note, with rs-fMRI, the highways may not be directly visualized, only the brain regions presumably connected by these paths. Separate research effort focuses on directly visualizing the highways using different MR imaging modalities, including diffusion tensor imaging and tractography. Functional integration is the foundation of information transfer between different brain areas.^{30,57}

For assessing functional integration features, commonly used computational methods include functional connectivity density analysis, ROI-based functional connectivity analysis, independent component analysis (ICA), and graph analysis.

Functional Connectivity Density Analysis

Functional connectivity density (FCD) is the most basic measurement of functional connectivity.⁵⁸ FCD analysis attempts to identify the highly connected functional hubs (Fig 2). FCD reveals only how connected a voxel is but not the regions with which this voxel is connected. FCD analysis calculates the correlation of the BOLD time-series between each voxel and all the other voxels in the brain. Short-range and long-range FCD maps can be calculated.^{59,60} The cutoff distance is typically 75 mm.^{59,60} Short-range FCD is measured by the correlation analysis of the BOLD time-

series between each voxel and the voxels around it within a distance of 75 mm (and represents some kind of long-range ReHo). The short-range FCD may reflect the regional functional connectivity plasticity around this voxel.⁶⁰ The long-range FCD is the result of the global FCD minus the short-range FCD and could reflect long-distance functional connectivity plasticity.

FCD analysis is straightforward. It does not need any model assumptions to be performed. It can reveal the importance of functional hubs of brain connectivity but does not indicate which regions are connected. FCD should be interpreted with caution due to its moderate long-term (about 6 months) test-retest reliability.⁴⁶

Seed-Based Functional Connectivity Analysis

Seed-based functional connectivity, also called ROI-based functional connectivity, finds regions correlated with the activity in a seed region. In seed-based analysis, the cross-correlation is computed between the time-series of the seed and the rest of the brain (telling us where the traffic is communicating between selected cities) (Fig 3, the results are visualized with the BrainNet Viewer; <https://www.nitrc.org/projects/bnv/>⁶¹). Several metrics (eg, the cross-correlation coefficient, partial correlations, multiple regressions, and synchronization likelihood) can be used to assess associations between time-series of brain areas. The coupling of activation between different brain areas indicates that they are involved in the same underlying functional process and thus interpreted as functionally connected. These brain regions may not be directly connected by neural fibers. The overall connectivity of the brain with this method can be visualized using a connectivity matrix, showing the strength of all connections between seed regions within the brain (Fig 3). Such a matrix has been commonly used in clinical applications, (eg, presurgical localization, identification of patients with Alzheimer disease, or distinction of different types of dementia).⁶² Such clinical applications of rs-fMRI have been extensively described in previous reviews.⁶³⁻⁶⁵

Seed analysis requires a priori determination of the seeds, which is often based on a hypothesis or prior results. Seeds may also be derived from ALFF or ReHo calculations. Seed time-series may also be performance or physiologic variables (such as breathing or heart rate). The main advantage of seed analysis is that the computation is simple and the interpretation of the results is intuitive. However, when the seed region changes, the results of the

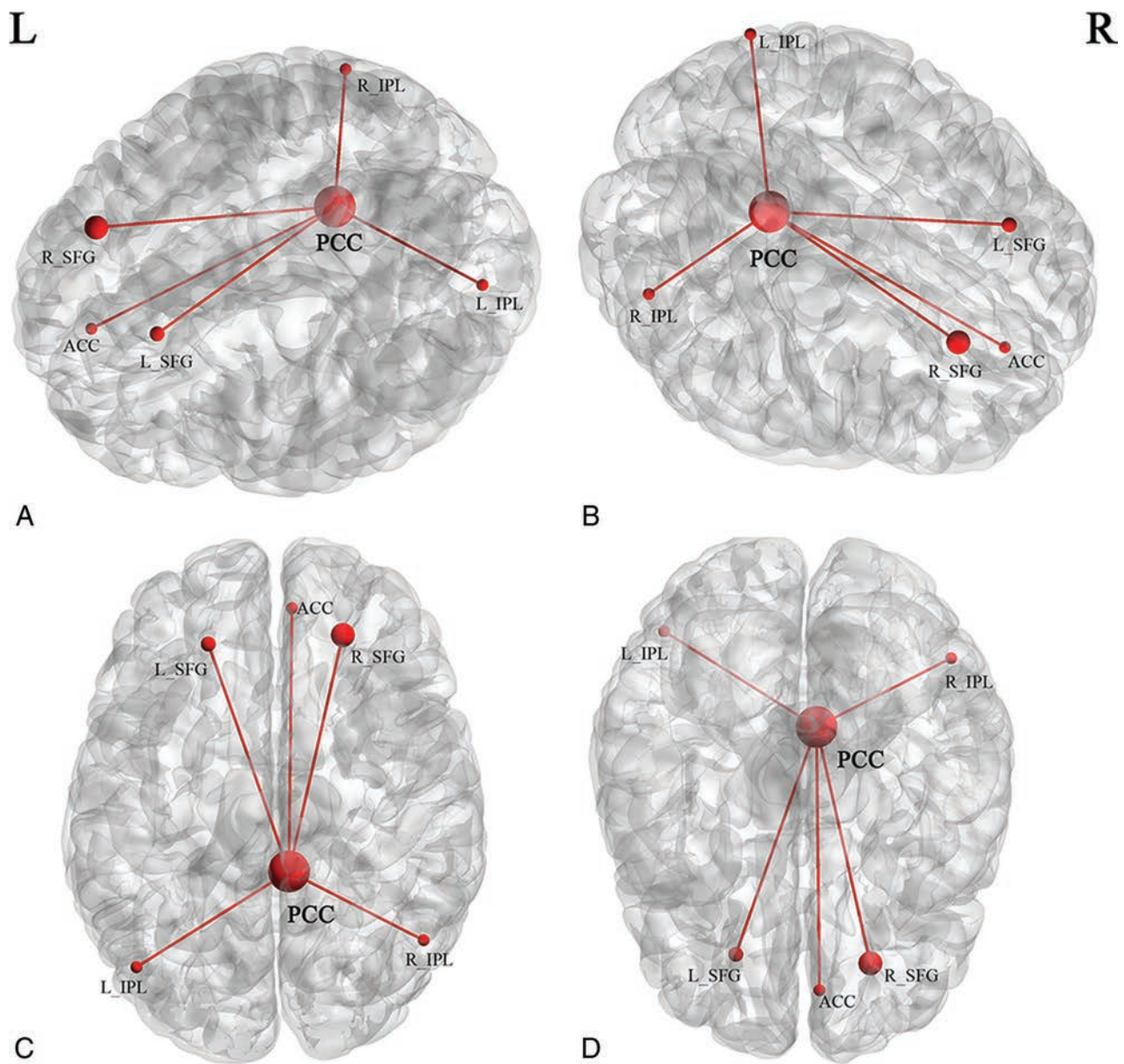


FIG 3. Brain maps show the group average spatial representation of the results of a seed-based functional connectivity study (results of 200 healthy volunteers [M.W., unpublished data, October 6, 2017]). The posterior cingulate cortex was set as a seed. *Nodes* represent brain area; *lines* represent functional connectivity between *nodes*. *A*, Left view. *B*, Right view. *C*, Upper view. *D*, Lower view. R indicates right; L, left; PCC, posterior cingulate cortex; ACC, anterior cingulate cortex; SFG, superior frontal gyrus; IPL, inferior parietal lobule.

functional connectivity analysis will also change, and sometimes obviously. Thus, the disadvantage of seed analysis is its dependence on the selection of seeds, which makes it vulnerable to bias.

Independent Component Analysis

Independent component analysis uses multivariate decomposition to separate the BOLD signal into several independent functional networks in the form of spatial maps, which are temporally correlated.⁶⁶⁻⁶⁸ Each functional network (component) embodies an independent network of neurons with synchronized BOLD activity (network of cities with high traffic between them). Each functional network is reported as a spatial map of the *z* scores derived from the correlation between the time-series of each voxel

and the mean time-series of that brain network. The average *z* score for each network indicates the magnitude of functional connectivity within the network.

There are several resting-state networks that commonly emerge from ICA analysis in rs-fMRI studies, including but not limited to the default mode network, auditory network, salience network, executive control network, medial visual network, lateral visual network, sensorimotor cortex, dorsal visual stream (frontoparietal attention network), basal ganglia network, limbic network, and precuneus network.⁶⁸⁻⁷⁰ These networks show resting-state connectivities, some of which are observed to be up- or down-regulated during specific cognitive tasks.

ICA is data-driven as opposed to seed-based analysis, which is ROI-driven. ICA can be performed without any a priori assump-

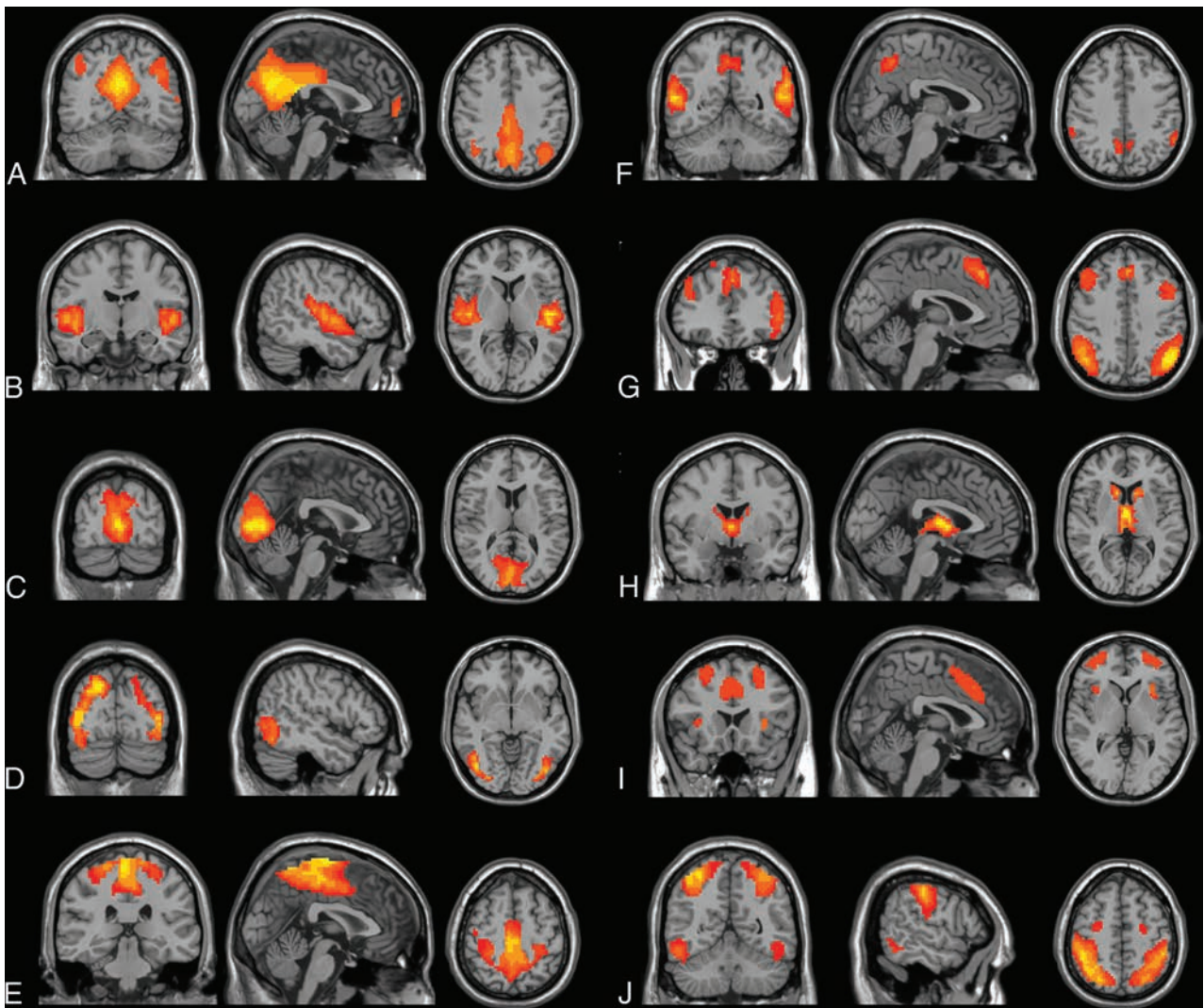


FIG 4. Typical reported networks (results of 200 healthy volunteers [M.W., unpublished data, February 6, 2017]). *A*, Default mode network. *B*, Auditory network. *C*, Medial visual network. *D*, Lateral visual network. *E*, Sensorimotor network. *F*, Precuneus network. *G*, Dorsal visual stream (frontoparietal attention network). *H*, Basal ganglia network. *I*, Executive control network. *J*, Visuospatial network.

tions, except the selection of the number of independent components to identify. While seed analysis extracts only the regions functionally connected to the ROI, ICA extracts all detectable networks within the subject (Fig 4). ICA analysis shows relatively high test-retest reliability for both the short term (<45 minutes) and the long term (5~16 months).⁷¹ However, the underlying cause of the perceived synchrony within the functional networks may be non-neural in origin (such as breathing or pulsation). This inherent property of ICA complicates the interpretation of ICA results. ICA only presents brain networks one by one. It does not show between-module connections or communications between different brain networks.⁷² Additional issues are that a single network could be broken into subnetworks, depending on the number of independent components specified, and that using ICA requires either manual or computer-driven identification of specific networks.

Independent vector analysis⁷³⁻⁷⁵ is a recent extension of ICA. Like ICA, independent vector analysis maximizes the dependence between associated components from different datasets. These components are conceptually regrouped into so-called source component vectors. The ability of independent vector analysis to

capture variability in spatial components across individuals and groups may be superior to that of ICA.⁷⁶⁻⁷⁸ Independent vector analysis can also be applied in the analysis of spatiotemporal dynamic features of brain networks.

Graph Analysis

Graph theory has been extensively used to examine the properties of complex networks. A small-world network (or “clique”), which was first described in social networks, is characterized as graphs with attenuated local connections and few long connections.⁷⁹ A small-world network is one in which most nodes (ie, regions) are not connected to one another, but nodes can be reached from every other node through a small number of connections. In other words, there are small networks of highly connected nodes in clusters (cities in 1 “state”) working together (“brain moduli”⁷² or states) to carry out a specific task or perform a specific cognitive function, with a few connections (limited number of highways between states) between these networks exhibiting prominent small-world organization and facilitating efficient information delivery at low wiring and energy costs.⁸⁰

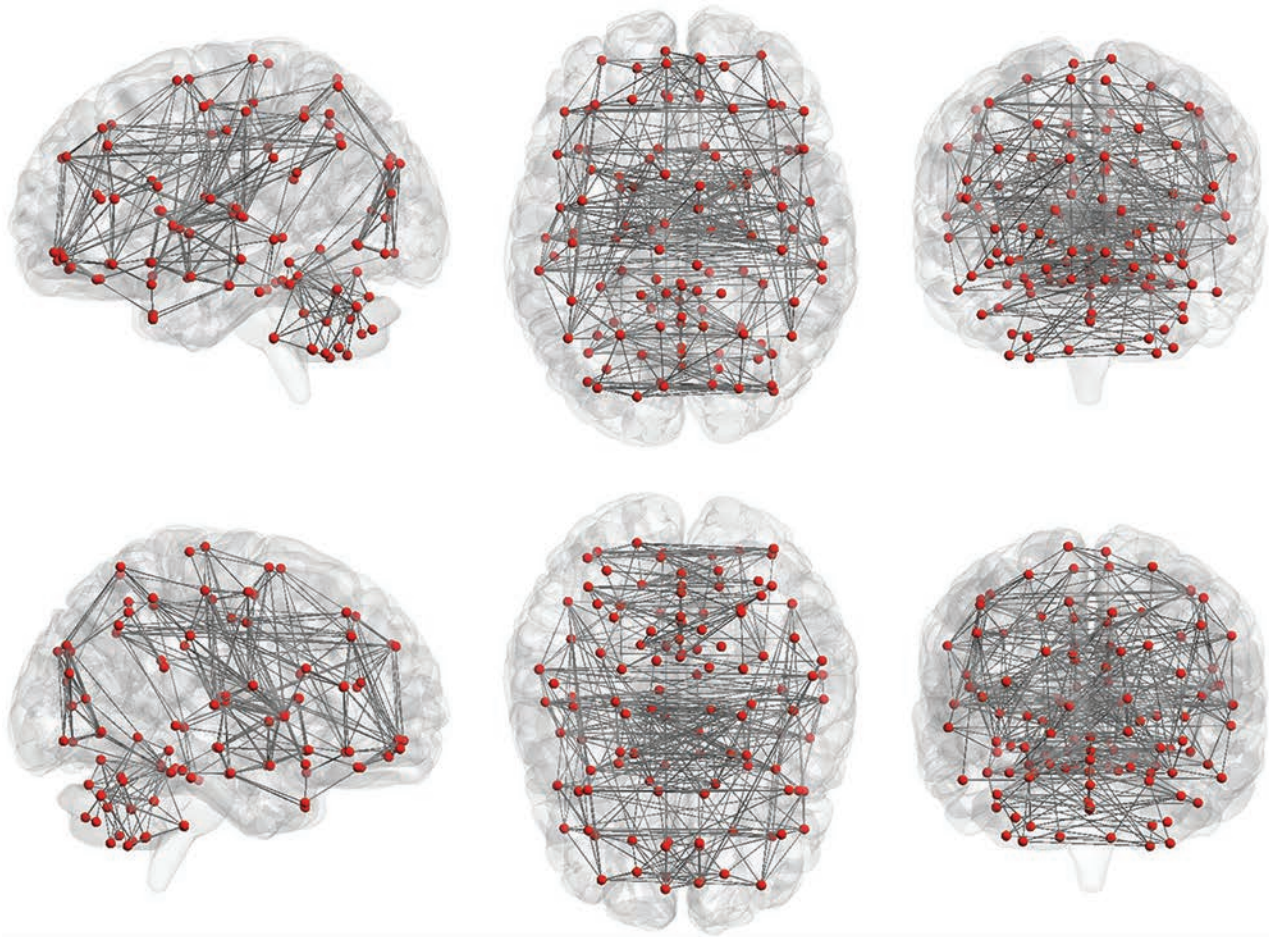


FIG 5. Nodes and functional connections are the basis of graph analysis. The whole brain includes 116 seeds (red dots; 45 nodes in each hemisphere of the cerebrum and 26 nodes in cerebellum) set on the basis of the anatomic parcellation defined by the Automated Anatomical Labeling atlas. Lines represent possible functional connections between those seeds.

Graph theory provides a theoretic framework for analyzing the topology of brain networks by examining both the local and global organization of neural networks.⁸⁰⁻⁸² In graph theory, functional brain networks can be defined as a graph (G) as a function of nodes (V) and functional connections (E), represented by $G = f(V, E)$.^{59,83,84} Nodes (V) may represent voxels or ROIs. The Automated Anatomical Labeling atlas, which contains 116 regions (90 nodes in the cerebrum and 26 nodes in the cerebellum, Fig 5), can be used to define the nodes for this analysis, but there are also many other parcellation schemes available for general use.^{69,85-87} The level of functional connectivity (E) between 2 nodes is computed by the correlation between the time-series of the 2 nodes. First, the functional connectivity between all possible node-pairs is computed. A graph representation of the functional brain network is then constructed using a predefined cutoff threshold of E . The following are some of the key graph analysis parameters:

1) “Clustering coefficient” describes the level of local neighborhood clustering. It reflects the level of local connectedness of a network.

2) “Characteristic path length” describes the average number of connections between all pairs of nodes. It reflects the global connectivity of the network, which reflects the efficiency of the network.

3) “Node degree” describes the number of connections of a node. It helps identify the highly connected nodes within the network.

4) “Centrality” describes the number of short-range connections for each node. Nodes with higher centrality contribute more to the overall efficiency of the network.

5) “Modularity” describes the extent to which groups of nodes are connected to the members of their own group. It reflects the existence of subnetworks within the full network.

Graph analysis of rs-fMRI reveals a highly efficient organization of the brain network optimized toward a high level of local and global efficiency,^{81,82} often referred to as small-world topology. The small-world topology could characterize the whole-brain map as well as different brain networks. Graph analysis can be automatically performed using published software,⁸⁸ without any a priori assumptions and with minimal bias. However, the results are often not intuitive and may be difficult to interpret.

Combined Study Recommendations

rs-fMRI has been widely used to characterize neuropsychiatric disorders using many of the methods described above.⁸⁹ There are multiple methods available to identify networks within rs-fMRI data on the basis of the connectivity using data-driven parcellation and on anatomic priors. Each method emphasizes different

approaches to defining brain connectivity. There is no single method currently considered a criterion standard on its own. Thus, these different methods are complementary to each other. The application of rs-fMRI is facilitated by methods that use a priori definitions of brain regions and brain networks. Combining different methods is one opportunity for yielding a more complete data-driven characterization of whole-brain resting connectivity than may be possible using one of the currently available single methods. An example of such a combination is the use of FCD, fractional-ALFF, or ReHo analysis, based on a graph theory framework, to identify ROIs for the functional connectivity analysis, as described above.

New Horizons

rs-fMRI is a rapidly evolving field with new analytic techniques introduced on a very regular basis. One such new methodology currently being proposed is the “chronnectome.”⁹⁰ So far, researchers mainly focused on the temporal properties of functional connectivity between different brain regions, implicitly assuming that functional connectivity (or traffic between cities) during the scanning time is relatively static. The chronnectome approach is based on a different assumption, that of temporal evolution of spatial properties of functional connectivity (dynamic, nonstationary patterns of traffic between cities) during the scanning time. Chronnectome approaches have shown promising results for studying the spatiotemporal dynamic features of brain networks in healthy subjects⁹¹⁻⁹⁵ and patients.^{43,96-101}

CONCLUSIONS

rs-fMRI is an imaging technique that plays a growing role in characterizing normal and abnormal functional brain connectivity in a variety of clinical conditions. To date, there are several different approaches and techniques to analyze rs-fMRI data, and the number of available methods is continually expanding. The different analysis methods are complementary, and applying several methods to the same dataset may yield better results compared with applying 1 method alone. A better understanding of each processing method is helpful in interpreting the common/divergent findings reported in the rs-fMRI literature.

Disclosures: Leanne M. Williams—UNRELATED: Board Membership: PsyberGuide, Comments: member of the Scientific Advisory Board; Grants/Grants Pending: National Institutes of Health*; Payment for Lectures Including Service on Speakers Bureaus: University of Minnesota, Comments: Grand Rounds. Greg Zaharchuk—UNRELATED: Grants/Grants Pending: National Institutes of Health, GE Healthcare. Michael Zeineh—UNRELATED: Grants/Grants Pending: National Institutes of Health, Doris Duke Charitable Foundation, Dana Foundation, Foundation of the ASNR, GE Healthcare*. Tali M. Ball—RELATED: Grant: National Institute of Mental Health, Comments: Salary support was provided by National Institute of Mental Health training grant T32MH019938; UNRELATED: Other: PsyberGuide, Comments: one-time payment to provide content for their Web site. Max Wintermark—UNRELATED: Board Membership: GE NFL Advisory Board. *Money paid to the institution.

REFERENCES

1. Handwerker DA, Bandettini PA. Hemodynamic signals not predicted? Not so: a comment on Sirotnin and Das (2009). *Neuroimage* 2011;55:1409–12 CrossRef Medline
2. Sirotnin YB, Das A. Anticipatory haemodynamic signals in sensory cortex not predicted by local neuronal activity. *Nature* 2009;457:475–79 CrossRef Medline
3. Nasrallah FA, Yeow LY, Biswal B, et al. Dependence of BOLD signal

fluctuation on arterial blood CO₂ and O₂: implication for resting-state functional connectivity. *Neuroimage* 2015;117:29–39 CrossRef Medline

4. Ogawa S, Lee TM, Kay AR, et al. Brain magnetic resonance imaging with contrast dependent on blood oxygenation. *Proc Natl Acad Sci U S A* 1990;87:9868–72 CrossRef Medline
5. Kwong KK, Belliveau JW, Chesler DA, et al. Dynamic magnetic resonance imaging of human brain activity during primary sensory stimulation. *Proc Natl Acad Sci U S A* 1992;89:5675–79 CrossRef Medline
6. Hyder F, Rothman DL. Neuronal correlate of BOLD signal fluctuations at rest: err on the side of the baseline. *Proc Natl Acad Sci U S A* 2010;107:10773–74 CrossRef Medline
7. Schölvinck ML, Maier A, Ye FQ, et al. Neural basis of global resting-state fMRI activity. *Proc Natl Acad Sci U S A* 2010;107:10238–43 CrossRef Medline
8. Biswal B, Yetkin FZ, Haughton VM, et al. Functional connectivity in the motor cortex of resting human brain using echo-planar MRI. *Magn Reson Med* 1995;34:537–41 CrossRef Medline
9. Smith K. Brain imaging: fMRI 2.0. *Nature* 2012;484:24–26 CrossRef Medline
10. Hermes D, Nguyen M, Winawer J. Neuronal synchrony and the relation between the blood-oxygen-level dependent response and the local field potential. *PLoS Biol* 2017;15:e2001461 CrossRef Medline
11. Koch C, Reid RC. Neuroscience: observatories of the mind. *Nature* 2012;483:397–98 CrossRef Medline
12. Christen T, Jahanian H, Ni WW, et al. Noncontrast mapping of arterial delay and functional connectivity using resting-state functional MRI: a study in Moyamoya patients. *J Magn Reson Imaging* 2015;41:424–30 CrossRef Medline
13. Gawryluk JR, Mazerolle EL, D’Arcy RC. Does functional MRI detect activation in white matter? A review of emerging evidence, issues, and future directions. *Front Neurosci* 2014;8:239 CrossRef Medline
14. Beissner F. Functional MRI of the brainstem: common problems and their solutions. *Clin Neuroradiol* 2015;25(Suppl 2):251–57 CrossRef Medline
15. Wintermark M, Sanelli PC, Anzai Y, et al; American College of Radiology Head Injury Institute. Imaging evidence and recommendations for traumatic brain injury: advanced neuro- and neurovascular imaging techniques. *AJNR Am J Neuroradiol* 2015;36:E1–E11 CrossRef Medline
16. Mayer AR, Bellgowan PS, Hanlon FM. Functional magnetic resonance imaging of mild traumatic brain injury. *Neurosci Biobehav Rev* 2014;49:8–18 CrossRef Medline
17. Stevens MC, Lovejoy D, Kim J, et al. Multiple resting state network functional connectivity abnormalities in mild traumatic brain injury. *Brain Imaging Behav* 2012;6:293–318 CrossRef Medline
18. Ishaque M, Manning JH, Woolsey MD, et al. Functional integrity in children with anoxic brain injury from drowning. *Hum Brain Mapp* 2017;38:4813–31 CrossRef Medline
19. Arngnim N, Hougaard A, Schytz HW, et al. Effect of hypoxia on BOLD fMRI response and total cerebral blood flow in migraine with aura patients. *J Cereb Blood Flow Metab* 2017 Jan 1. [Epub ahead of print] CrossRef Medline
20. Lv Y, Margulies DS, Cameron CR, et al. Identifying the perfusion deficit in acute stroke with resting-state functional magnetic resonance imaging. *Ann Neurol* 2013;73:136–40 CrossRef Medline
21. Amemiya S, Kunimatsu A, Saito N, et al. Cerebral hemodynamic impairment: assessment with resting-state functional MR imaging. *Radiology* 2014;270:548–55 CrossRef Medline
22. Korgaonkar MS, Ram K, Williams LM, et al. Establishing the resting state default mode network derived from functional magnetic resonance imaging tasks as an endophenotype: a twins study. *Hum Brain Mapp* 2014;35:3893–902 CrossRef Medline
23. Smith K. Brain decoding: reading minds. *Nature* 2013;502:428–30 CrossRef Medline

24. Williams LM. **Defining biotypes for depression and anxiety based on large-scale circuit dysfunction: a theoretical review of the evidence and future directions for clinical translation.** *Depress Anxiety* 2017;34:9–24 CrossRef Medline
25. Khazaee A, Ebrahimzadeh A, Babajani-Feremi A. **Classification of patients with MCI and AD from healthy controls using directed graph measures of resting-state fMRI.** *Brain Behav Res* 2017;322:339–50 CrossRef Medline
26. Schirner M, Rothmeier S, Jirsa VK, et al. **An automated pipeline for constructing personalized virtual brains from multimodal neuroimaging data.** *Neuroimage* 2015;117:343–57 CrossRef Medline
27. Chao-Gan Y, Yu-Feng Z. **DPARF: a MATLAB toolbox for “Pipeline” data analysis of resting-state fMRI.** *Front Syst Neurosci* 2010;4:13 CrossRef Medline
28. Dance A. **Neuroscience: connectomes make the map.** *Nature* 2015;526:147–49 CrossRef Medline
29. Liu Y, Gao JH, Liotti M, et al. **Temporal dissociation of parallel processing in the human subcortical outputs.** *Nature* 1999;400:364–67 CrossRef Medline
30. Tononi G, Sporns O, Edelman GM. **A measure for brain complexity: relating functional segregation and integration in the nervous system.** *Proc Natl Acad Sci U S A* 1994;91:5033–37 CrossRef Medline
31. Han L, Zhaohui L, Fei Y, et al. **Disrupted neural activity in unilateral vascular pulsatile tinnitus patients in the early stage of disease: evidence from resting-state fMRI.** *Prog Neuropsychopharmacol Biol Psychiatry* 2015;59:91–99 CrossRef Medline
32. Premi E, Cauda F, Gasparotti R, et al. **Multimodal fMRI resting-state functional connectivity in granulin mutations: the case of fronto-parietal dementia.** *PLoS One* 2014;9:e106500 CrossRef Medline
33. An L, Cao QJ, Sui MQ, et al. **Local synchronization and amplitude of the fluctuation of spontaneous brain activity in attention-deficit/hyperactivity disorder: a resting-state fMRI study.** *Neurosci Bull* 2013;29:603–13 CrossRef Medline
34. Lei D, Ma J, Du X, et al. **Spontaneous brain activity changes in children with primary monosymptomatic nocturnal enuresis: a resting-state fMRI study.** *Neurourol Urodyn* 2012;31:99–104 CrossRef Medline
35. Zang YF, He Y, Zhu CZ, et al. **Altered baseline brain activity in children with ADHD revealed by resting-state functional MRI.** *Brain Dev* 2007;29:83–91 CrossRef Medline
36. Song XW, Dong ZY, Long XY, et al. **REST: a toolkit for resting-state functional magnetic resonance imaging data processing.** *PLoS One* 2011;6:e25031 CrossRef Medline
37. Zou QH, Zhu CZ, Yang Y, et al. **An improved approach to detection of Amplitude of Low-Frequency Fluctuation (ALFF) for resting-state fMRI: fractional ALFF.** *J Neurosci Methods* 2008;172:137–41 CrossRef Medline
38. Buzsáki G, Draguhn A. **Neuronal oscillations in cortical networks.** *Science* 2004;304:1926–29 CrossRef Medline
39. Zuo XN, Di Martino A, Kelly C, et al. **The oscillating brain: complex and reliable.** *Neuroimage* 2010;49:1432–45 CrossRef Medline
40. Xue SW, Li D, Weng XC, et al. **Different neural manifestations of two slow frequency bands in resting functional magnetic resonance imaging: a systemic survey at regional, interregional, and network levels.** *Brain Connect* 2014;4:242–55 CrossRef Medline
41. Liu X, Wang S, Zhang X, et al. **Abnormal amplitude of low-frequency fluctuations of intrinsic brain activity in Alzheimer’s disease.** *J Alzheimers Dis* 2014;40:387–97 CrossRef Medline
42. Xue S, Wang X, Wang W, et al. **Frequency-dependent alterations in regional homogeneity in major depression.** *Brain Behav Res* 2016;306:13–19 CrossRef Medline
43. Chen X, Zhang H, Zhang L, et al. **Extraction of dynamic functional connectivity from brain grey matter and white matter for MCI classification.** *Hum Brain Mapp* 2017;38:5019–34 CrossRef Medline
44. Zhang L, Zhang H, Chen X, et al. **Learning-based structurally-guided construction of resting-state functional correlation tensors.** *Magn Reson Imaging* 2017;43:110–21 CrossRef Medline
45. Küblböck M, Woletz M, Höflich A, et al. **Stability of low-frequency fluctuation amplitudes in prolonged resting-state fMRI.** *Neuroimage* 2014;103:249–57 CrossRef Medline
46. Zuo XN, Xing XX. **Test-retest reliabilities of resting-state FMRI measurements in human brain functional connectomics: a systems neuroscience perspective.** *Neurosci Biobehav Rev* 2014;45:100–18 CrossRef Medline
47. Zang Y, Jiang T, Lu Y, et al. **Regional homogeneity approach to fMRI data analysis.** *Neuroimage* 2004;22:394–400 CrossRef Medline
48. Zang YF, Zuo XN, Milham M, et al. **Toward a meta-analytic synthesis of the resting-state fMRI literature for clinical populations.** *Biomed Res Int* 2015;2015:435265 CrossRef Medline
49. Song X, Zhang Y, Liu Y. **Frequency specificity of regional homogeneity in the resting-state human brain.** *PLoS One* 2014;9:e86818 CrossRef Medline
50. Liu ZR, Miao HH, Yu Y, et al. **Frequency-specific local synchronization changes in paroxysmal kinesigenic dyskinesia.** *Medicine (Baltimore)* 2016;95:e3293 CrossRef Medline
51. Huang Z, Wang Z, Zhang J, et al. **Altered temporal variance and neural synchronization of spontaneous brain activity in anesthesia.** *Hum Brain Mapp* 2014;35:5368–78 CrossRef Medline
52. Yu R, Hsieh MH, Wang HL, et al. **Frequency dependent alterations in regional homogeneity of baseline brain activity in schizophrenia.** *PLoS One* 2013;8:e57516 CrossRef Medline
53. Zuo XN, Xu T, Jiang L, et al. **Toward reliable characterization of functional homogeneity in the human brain: preprocessing, scan duration, imaging resolution and computational space.** *Neuroimage* 2013;65:374–86 CrossRef Medline
54. Cui Y, Jiao Y, Chen YC, et al. **Altered spontaneous brain activity in type 2 diabetes: a resting-state functional MRI study.** *Diabetes* 2014;63:749–60 CrossRef Medline
55. Premi E, Cauda F, Gasparotti R, et al. **Multimodal fMRI resting-state functional connectivity in granulin mutations: the case of fronto-parietal dementia.** *PLoS One* 2014;9:e106500 CrossRef Medline
56. Lanting CP, de Kleine E, Langers DR, et al. **Unilateral tinnitus: changes in connectivity and response lateralization measured with fMRI.** *PLoS One* 2014;9:e110704 CrossRef Medline
57. Friston KJ. **Modalities, modes, and models in functional neuroimaging.** *Science* 2009;326:399–403 CrossRef Medline
58. Tomasi D, Volkow ND. **Functional connectivity density mapping.** *Proc Natl Acad Sci U S A* 2010;107:9885–90 CrossRef Medline
59. Achard S, Salvador R, Whitcher B, et al. **A resilient, low-frequency, small-world human brain functional network with highly connected association cortical hubs.** *J Neurosci* 2006;26:63–72 CrossRef Medline
60. He Y, Chen ZJ, Evans AC. **Small-world anatomical networks in the human brain revealed by cortical thickness from MRI.** *Cereb Cortex* 2007;17:2407–19 CrossRef Medline
61. Xia M, Wang J, He Y. **BrainNet Viewer: a network visualization tool for human brain connectomics.** *PLoS One* 2013;8:e68910 CrossRef Medline
62. Lee MH, Smyser CD, Shimony JS. **Resting-state fMRI: a review of methods and clinical applications.** *AJNR Am J Neuroradiol* 2013;34:1866–72 CrossRef Medline
63. Wilson PH, Smits-Engelsman B, Caeyenberghs K, et al. **Cognitive and neuroimaging findings in developmental coordination disorder: new insights from a systematic review of recent research.** *Dev Med Child Neurol* 2017;59:1117–29 CrossRef Medline
64. Koyama MS, Parvaz MA, Goldstein RZ. **The adolescent brain at risk for substance use disorders: a review of functional MRI research on motor response inhibition.** *Curr Opin Behav Sci* 2017;13:186–95 CrossRef Medline
65. Gravel N, Harvey BM, Renken RJ, et al. **Phase-synchronization-based parcellation of resting state fMRI signals reveals topograph-**

- ically organized clusters in early visual cortex. *Neuroimage* 2017 Sep 1. [Epub ahead of print] CrossRef Medline
66. Kiviniemi V, Kantola JH, Jauhiainen J, et al. **Independent component analysis of nondeterministic fMRI signal sources.** *Neuroimage* 2003;19:253–60 CrossRef Medline
 67. van de Ven VG, Formisano E, Prvulovic D, et al. **Functional connectivity as revealed by spatial independent component analysis of fMRI measurements during rest.** *Hum Brain Mapp* 2004;22:165–78 CrossRef Medline
 68. Beckmann CF, DeLuca M, Devlin JT, et al. **Investigations into resting-state connectivity using independent component analysis.** *Philos Trans R Soc Lond B Biol Sci* 2005;360:1001–13 CrossRef Medline
 69. Shirer WR, Ryali S, Rykhlevskaia E, et al. **Decoding subject-driven cognitive states with whole-brain connectivity patterns.** *Cereb Cortex* 2012;22:158–65 CrossRef Medline
 70. Seeley WW, Menon V, Schatzberg AF, et al. **Dissociable intrinsic connectivity networks for salience processing and executive control.** *J Neurosci* 2007;27:2349–56 CrossRef Medline
 71. Zuo XN, Kelly C, Adelman JS, et al. **Reliable intrinsic connectivity networks: test-retest evaluation using ICA and dual regression approach.** *Neuroimage* 2010;49:2163–77 CrossRef Medline
 72. Bertolero MA, Yeo BT, D'Esposito M. **The modular and integrative functional architecture of the human brain.** *Proc Natl Acad Sci U S A* 2015;112:E6798–807 CrossRef Medline
 73. Anderson M, Fu GS, Phlypo R, et al. **Independent vector analysis: identification conditions and performance bounds.** *IEEE Trans Signal Process* 2014;62:4399–410 CrossRef
 74. Lee JH, Lee TW, Jolesz FA, et al. **Independent vector analysis (IVA): multivariate approach for fMRI group study.** *Neuroimage* 2008;40:86–109 CrossRef Medline
 75. Anderson M, Adali T, Li XL. **Joint blind source separation with multivariate Gaussian model: algorithms and performance analysis.** *IEEE Trans Signal Process* 2012;60:1672–83
 76. Laney J, Westlake KP, Ma S, et al. **Capturing subject variability in fMRI data: a graph-theoretical analysis of GICA vs. IVA.** *J Neurosci Methods* 2015;247:32–40 CrossRef Medline
 77. Ma S, Phlypo R, Calhoun VD, et al. **Capturing group variability using IVA: a simulation study and graph-theoretical analysis.** *Proc IEEE Int Conf Acoust Speech Signal Process* 2013:3128–32 CrossRef
 78. Allen EA, Erhardt EB, Wei Y, et al. **Capturing inter-subject variability with group independent component analysis of fMRI data: a simulation study.** *Neuroimage* 2012;59:4141–59 CrossRef Medline
 79. Watts DJ, Strogatz SH. **Collective dynamics of 'small-world' networks.** *Nature* 1998;393:440–42 CrossRef Medline
 80. Liao X, Vasilakos AV, He Y. **Small-world human brain networks: perspectives and challenges.** *Neurosci Biobehav Rev* 2017;77:286–300 CrossRef Medline
 81. Bullmore E, Sporns O. **Complex brain networks: graph theoretical analysis of structural and functional systems.** *Nat Rev Neurosci* 2009;10:186–98 CrossRef Medline
 82. Sporns O, Honey CJ, Kotter R. **Identification and classification of hubs in brain networks.** *PLoS One* 2007;2:e1049 CrossRef Medline
 83. van den Heuvel MP, Stam CJ, Boersma M, et al. **Small-world and scale-free organization of voxel-based resting-state functional connectivity in the human brain.** *Neuroimage* 2008;43:528–39 CrossRef Medline
 84. Achard S, Bullmore E. **Efficiency and cost of economical brain functional networks.** *PLoS Comput Biol* 2007;3:e17 CrossRef Medline
 85. Glasser MF, Coalson TS, Robinson EC, et al. **A multi-modal parcellation of human cerebral cortex.** *Nature* 2016;536:171–78 CrossRef Medline
 86. Zalesky A, Fornito A, Harding IH, et al. **Whole-brain anatomical networks: does the choice of nodes matter?** *Neuroimage* 2010;50:970–83 CrossRef Medline
 87. Li W, Andreasen NC, Nopoulos P, et al. **Automated parcellation of the brain surface generated from magnetic resonance images.** *Front Neuroinform* 2013;7:23 CrossRef Medline
 88. Wang J, Wang X, Xia M, et al. **GRETNA: a graph theoretical network analysis toolbox for imaging connectomics.** *Front Hum Neurosci* 2015;9:386 CrossRef Medline
 89. Menon V. **Large-scale brain networks and psychopathology: a unifying triple network model.** *Trends Cogn Sci* 2011;15:483–506 CrossRef Medline
 90. Calhoun VD, Miller R, Pearlson G, et al. **The chronnectome: time-varying connectivity networks as the next frontier in fMRI data discovery.** *Neuron* 2014;84:262–74 CrossRef Medline
 91. Griffa A, Ricaud B, Benzi K, et al. **Transient networks of spatio-temporal connectivity map communication pathways in brain functional systems.** *Neuroimage* 2017;155:490–502 CrossRef Medline
 92. AbróL A, Damaraju E, Miller RL, et al. **Replicability of time-varying connectivity patterns in large resting state fMRI samples.** *Neuroimage* 2017;163:160–76 CrossRef Medline
 93. AbróL A, Chaze C, Damaraju E, et al. **The chronnectome: evaluating replicability of dynamic connectivity patterns in 7500 resting fMRI datasets.** *Conf Proc IEEE Eng Med Biol Soc* 2016;2016:5571–74 CrossRef Medline
 94. Thompson WH, Fransson P. **The frequency dimension of fMRI dynamic connectivity: network connectivity, functional hubs and integration in the resting brain.** *Neuroimage* 2015;121:227–42 CrossRef Medline
 95. Chen Y, Wang W, Zhao X, et al. **Age-related decline in the variation of dynamic functional connectivity: a resting state analysis.** *Front Aging Neurosci* 2017;9:203 CrossRef Medline
 96. Park BY, Moon T, Park H. **Dynamic functional connectivity analysis reveals improved association between brain networks and eating behaviors compared to static analysis.** *Brain Behav Res* 2018; 337:114–21 CrossRef Medline
 97. Cheng JC, Bosma RL, Hemington KS, et al. **Slow-5 dynamic functional connectivity reflects the capacity to sustain cognitive performance during pain.** *Neuroimage* 2017;157:61–68 CrossRef Medline
 98. Damaraju E, Allen EA, Belger A, et al. **Dynamic functional connectivity analysis reveals transient states of dysconnectivity in schizophrenia.** *Neuroimage Clin* 2014;5:298–308 CrossRef Medline
 99. Hutchison RM, Womelsdorf T, Allen EA, et al. **Dynamic functional connectivity: promise, issues, and interpretations.** *Neuroimage* 2013;80:360–78 CrossRef Medline
 100. Preti MG, Bolton TA, Van De Ville D. **The dynamic functional connectome: state-of-the-art and perspectives.** *Neuroimage* 2017; 160:41–54 CrossRef Medline
 101. Lindquist MA, Xu Y, Nebel MB, et al. **Evaluating dynamic bivariate correlations in resting-state fMRI: a comparison study and a new approach.** *Neuroimage* 2014;101:531–46 CrossRef Medline

Noncontrast Head CT in Children: National Variation in Radiation Dose Indices in the United States

G. Sadigh, N. Kadom, P. Karthik, D. Sengupta, K. J. Strauss, D. Frush, and K.E. Applegate



ABSTRACT

BACKGROUND AND PURPOSE: Radiologists should manage the radiation dose for pediatric patients to maintain reasonable diagnostic confidence. We assessed the variation in estimated radiation dose indices for pediatric noncontrast head CT in the United States.

MATERIALS AND METHODS: Radiation dose indices for single-phase noncontrast head CT examinations in patients 18 years of age and younger were retrospectively reviewed between July 2011 and June 2016 using the American College of Radiology CT Dose Index Registry. We used the reported volume CT dose index stratified by patient demographics and imaging facility characteristics.

RESULTS: The registry included 295,296 single-phase pediatric noncontrast head CT studies from 1571 facilities (56% in male patients and 53% in children older than 10 years of age). The median volume CT dose index was 33 mGy (interquartile range = 22–47 mGy). The volume CT dose index increased as age increased. The volume CT dose index was lower in children's hospitals (median, 26 mGy) versus academic hospitals (median, 32 mGy) and community hospitals (median, 40 mGy). There was a lower volume CT dose index in level I and II trauma centers (median, 27 and 32 mGy, respectively) versus nontrauma centers (median, 40 mGy) and facilities in metropolitan locations (median, 30 mGy) versus those in suburban and rural locations (median, 41 mGy).

CONCLUSIONS: Considerable variation in the radiation dose index for pediatric head CT exists. Median dose indices and practice variations at pediatric facilities were both lower compared with other practice settings. Decreasing dose variability through proper management of CT parameters in pediatric populations using benchmarks generated by data from registries can potentially decrease population exposure to ionizing radiation.

ABBREVIATIONS: CTDI_{vol} = CT dose index volume; DIR = Dose Index Registry; DLP = dose-length product; IQR = interquartile range

In 2011, eighty-five million CT scans were performed in the United States; approximately 5%–11% of these scans were performed on children.^{1,2} A more recent study using the American College of Radiology Dose Index Registry (DIR) reported that approximately 6% of CT scans performed in participating facilities the United States were performed on children.³ CT scans

alone accounted for about 50% and 75% of the radiation doses in adults and in children, respectively.⁴ The most frequently imaged pediatric body part was the head.³ The most common indication was trauma, followed by headache, convulsions, and syncope.^{5,6} In the past 2 decades, there has been an increase in the use of CT scans in pediatric patients in emergency departments, which includes both first-time and repeat head CT scans.^{6–8}

Many attempts have been made to quantify risks associated with ionizing radiation use in medical imaging. Some studies have suggested that the radiation dose from pediatric head CT scans may increase the risk of developing leukemia or other solid tumors.^{9–12} Another study has suggested that the radiation dose to the lens of the eye from head and neck CT scans may increase the risk of cataracts.¹³ A recent cohort study of nuclear medicine technologists suggested a higher risk of cataracts from their occupational radiation exposures.¹⁴ Children are more radiosensitive than adults and, therefore, have a higher risk of developing cataracts.¹⁵ They are also more likely to be affected by cancers such as leukemia, brain, breast, skin, and thyroid cancer as well as cardiovascular diseases after high doses of

Received February 11, 2018; accepted after revision May 18.

From the Department of Radiology and Imaging Sciences (G.S., N.K.), Emory University School of Medicine, Atlanta, Georgia; American College of Radiology (P.K., D.S.), Reston, Virginia; Department of Radiology (K.J.S.), University of Cincinnati School of Medicine, Cincinnati, Ohio; Department of Radiology (D.F.), Duke University Medical Center, Durham, North Carolina; and Department of Radiology (K.E.A.), University of Kentucky, Lexington, Kentucky.

Abstract previously presented as a poster at: Annual Meeting of the American College of Radiology, May 21–25, 2017; Washington, DC.

Please address correspondence to Gelareh Sadigh, MD, Department of Radiology and Imaging Sciences, Emory University School of Medicine, 1364 Clifton Rd NE, Atlanta, GA 30322; email: gsadigh@emory.edu; @GelarehSadigh



Indicates article with supplemental on-line table.



Indicates article with supplemental on-line photo.

<http://dx.doi.org/10.3174/ajnr.A5719>

radiation from therapies. Interpretation of some of the literature is controversial as they associate cancer risks with ionizing radiation on the basis of myriad assumptions.¹⁶⁻¹⁸ Nevertheless, pediatric patients do have a longer expected lifetime during which diseases and radiation-related complications might occur, which may or may not be linked to ionizing radiation.

The As Low As Reasonably Achievable principle guides radiologists to use the lowest radiation dose on any given imaging examination that will answer the clinical question, yet preserve the radiologist's ability to make a diagnosis. This diagnostic capability can be influenced by many practical issues, including patient factors such as motion or the degree of medical illness/complexity, technical factors, and the level of training and experience of the interpreting radiologist. Therefore, there is an expected wide variability of imaging practices within a framework of best practice. The radiation dose from head CT and its variation in the pediatric population has had a limited focus, with small institutional studies or surveys¹⁹⁻²² each demonstrating substantial variation in radiation dose. However, the optimal current practices and the magnitude of variation in the radiation dose delivered by pediatric noncontrast head CT have not been assessed at the national level. Participation in dose registries allows those providers who care for children the opportunity to compare their performance against published national benchmarks.²³

The purpose of this study was to assess variations in estimated radiation dose indices for pediatric noncontrast head CT in the United States using the American College of Radiology DIR.

MATERIALS AND METHODS

Study Design

This was a retrospective analysis of pediatric noncontrast head CT examinations in the American College of Radiology DIR from July 1, 2011, through June 30, 2016. Because this study qualified as “nonhuman subject” research, institutional review board oversight was not required by our institution.

Dose Index Registry

The DIR launched in mid-2011 by the American College of Radiology is a national data base of dose indices associated with CT scans, which allows facilities to compare their dose indices with those at other facilities as well as other population and geographic denominations and to improve their practices when appropriate.^{24,25} Given that different facilities may use different examination names for the same imaging test, when a facility submits data to the DIR, every CT examination name used at that facility is mapped to a standardized list of examination names used by the DIR, using the RadLex Playbook identifiers (https://www.rsna.org/RadLex_Playbook.aspx).²⁴ All of the data presented in this study came from facilities that submit their data to the DIR data base.

Study Setting and Population

We included noncontrast head CT examinations performed in patients 18 years of age or younger during the study period. Multiphase examinations (ie, with and without contrast examinations) were excluded to avoid overestimating the radiation dose index. Furthermore, these examinations are not routine in pediatric head CT.

Study Protocol

We used the following examination names submitted by participating facilities mapped in the DIR to define noncontrast head CT examinations: “CT BRN WO IVCON,” “CT HEAD BRN WO IVCON,” “CT HEAD BRN DUAL ENG CT WO IVCON,” “CT HEAD MLTPL AREA SM BDY REG WO IVCON,” “CT PEDS HEAD WO IVCON,” “CT HEAD TRAUMA WO IVCON,” “CT PEDS HEAD BRN WO IVCON,” “CT HEAD WO IVCON.” These examinations included noncontrast head CT using routine or low-dose protocols. Of note, institutions may name CT examinations differently, and the name under which an examination was listed in the DIR may not reflect whether a low-dose protocol was actually used.

The 2 primary CT dose indices, which can be used to calculate estimates of the radiation dose to the patient during head scans, were analyzed in this study. The first, CT dose index volume (CTDI_{vol}) is an indication of the average absorbed radiation within the scan volume for a standardized cylindrical CTDI phantom.²⁶ In children, this is made of Plexiglas (<https://www.plexiglas-shop.com/shopselect.htm>) with a diameter of 16 cm. The second, dose-length product (DLP), is the product of CTDI_{vol} and scan length along the z-axis of the patient, which estimates the total energy delivered to the CTDI phantom during the examination. The scan length can be estimated by dividing the DLP by the CTDI_{vol}.²⁶

We obtained additional information including patient demographics (age, sex), characteristics of the imaging facility, and the year the examination was performed using the DIR data base. Age groups were defined on the basis of previous work⁵ and were as follows: 0–2, 3–6, 7–10, 11–14, and 15–18 years of age. Imaging facility characteristics included hospital type (academic, community hospital, multispecialty clinic, freestanding center, children's hospital, and other), trauma designation (I, II, III, IV, and not applicable), facility location (metropolitan, suburban, and rural), and census regions (Northeast, Midwest, South, and West) based on the US Census Bureau categorization.²⁷ Because facilities can designate only a single hospital type, facilities designated as academic and community were further assigned as pediatric if they used “children” in the name or if they performed at least 75% of the total examinations on children 18 years of age or younger⁵ as defined by the DIR.

Data Analysis

We used summary statistics to describe the patient and hospital characteristics, including number and frequency. The CTDI_{vol} and DLPs were reported as median and interquartile range (IQR). The median CTDI_{vol} was compared among the categories for each variable using the Kruskal-Wallis test. We further compared the median CTDI_{vol} among facility types adjusting on the basis of patient age and sex using the ANOVA test. The data analysis for this article was generated using SAS software (SAS Institute, Cary, North Carolina). *P* values ≤ .05 were considered statistically significant. The results were displayed graphically using 5 pediatric age categories (0–2, 3–6, 7–10, 11–14, and 15–18 years of age) that the American College of Radiology DIR provides to all enrolled facilities.

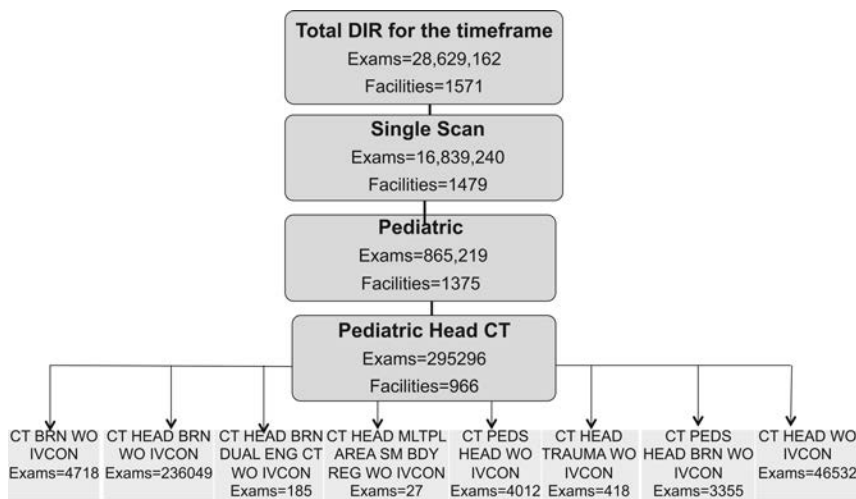


FIG. Head CT examinations included in the study cohort from the DIR.

RESULTS

Patient Population

Of the 28,629,162 CT examinations within the DIR data base, 59% ($n = 16,839,240$) were performed as a single scan, and 5% of these single scans ($n = 865,219$) were obtained in patients 18 years of age or younger. Of these pediatric single scans, 34% ($n = 295,296$) were noncontrast head CT scans (Figure).

Examinations in male patients represented 56% ($n = 165,482$) of examinations (On-line Table). The distribution of head CTs across patients in pediatric age groups was as follows: 21% ($n = 62,933$) in 0–2 years, 13% ($n = 38,144$) in 3–6 years, 13% ($n = 38,847$) in 7–10 years, 20% ($n = 58,091$) in 11–14 years, and 33% ($n = 97,281$) in 15–18 years.

Hospitals

There were a total of 1571 facilities in the DIR during the study period, and 966 facilities (61%) performed pediatric single noncontrast head CT scans (Figure). Most of these facilities (55%; 533/966) were community hospitals and 24% (226/966) were designated as trauma levels I and II.

While only 42% (404/966) of facilities performing pediatric single noncontrast head CT scans were in metropolitan areas, 65.7% ($n = 194,155$) of these examinations were performed in these facilities. Furthermore, 32% of the facilities (304/966) were in the Southern regions and 43% ($n = 126,874$) of examinations were performed in this area. More detailed information on patient demographics and characteristics of the imaging facilities are listed in the On-line Table.

Radiation Dose Indices

Across all pediatric single noncontrast head CT examinations, the median $CTDI_{vol}$ was 33 mGy (IQR = 22–47 mGy), with approximately 107% difference between the 25th and 75th percentiles. The median $CTDI_{vol}$ was higher for older age groups, as expected (On-line Table). The variations in the median $CTDI_{vol}$ for examinations were statistically significant among facility types ($P < .0001$). The pediatric facilities had a lower median $CTDI_{vol}$ (26 mGy, IQR = 19–33 mGy) compared with other facility types. Even though statistical tests showed that when controlling for age

group, sex, and other facility characteristics, the mean $CTDI_{vol}$ was statistically significantly different among facility types ($P < .0001$), lower age groups of 0–2 and 3–6 years did not have any clinically significant variations in their mean $CTDI_{vol}$ among facility types (On-line Figure). Community hospitals, which had the largest proportion of examinations, had a median $CTDI_{vol}$ of 40 mGy (IQR = 27–52 mGy). The variations in the median $CTDI_{vol}$ for examinations were also statistically significant among facility trauma designations ($P < .0001$). Trauma levels I and II had the lowest median $CTDI_{vol}$ (27 mGy for level I and 32 mGy for level II) compared with other hospitals. The facilities with average monthly examinations of ≤ 100 had

higher median $CTDI_{vol}$ compared with facilities with > 100 examinations (On-line Table).

For all pediatric single noncontrast head CT examinations, the median DLP was 543 mGy \times cm (IQR = 357–758 mGy \times cm), with an approximately 112% difference between the 25th and 75th percentiles. This finding corresponds to a median scan length of 16.5 cm along the z-axis of the patient for a pediatric head examination regardless of age. Accordingly, the median scan length for the 0–2 years of age group was 14.7 cm compared with a range of 16.2–16.7 cm for all patients older than 2 years of age.

DISCUSSION

The results of the current national study of radiation dose indices for pediatric single-phase noncontrast head CT showed variations in radiation dose estimates as measured by $CTDI_{vol}$ and DLP, with approximately 107% and 112% difference between the 25th and 75th percentiles, respectively. As expected, the $CTDI_{vol}$ increased with patient age. The median dose indices were lower at pediatric facilities compared with other facility types and lower in metropolitan areas compared with suburban and rural facilities.

Our results are similar to findings from prior studies (Table 1) showing practice variations among imaging facilities. Prior studies have reported that the dose indices of pediatric hospitals were less than those in general hospitals²¹ or trauma centers.¹⁹ A national survey of US hospitals using the American Hospital Association 2010 annual survey data base showed that 82% of hospitals reported doses of < 40 mGy.²¹ Practice variations were found in a survey of trauma centers in the state of Washington, which showed a large proportion of level III–V trauma facilities tended to have higher milliamperes-second values due to late adoption of dose-reduction strategies, resulting in larger median $CTDI_{vol}$ values.²⁰ Our results showed that facilities in metropolitan areas had lower median $CTDI_{vol}$ compared with urban and rural locations ($P < .0001$) possibly due to the poorer quality imaging equipment (eg, low-resolution equipment) in the smaller, rural facilities,²⁸ which requires a greater patient dose to produce acceptable images. Imaging facilities in the metropolitan areas may also be academic centers, which continually try to follow benchmarks

Table 1: Studies of radiation dose indices for pediatric noncontrast head CT

Study	Publication		Findings
	Year	Type	
Kanal et al ²¹	2015	National survey	Pediatric hospitals had lower dose indices compared with general hospitals
Kanal et al ²⁰	2011	Washington State survey	Level I–II trauma centers had lower dose indices compared with Levels III–V
King et al ¹⁹	2009	Bi-institutional studies	Regional pediatric hospitals had lower dose indices compared with trauma centers
Current study	2018	National study of ACR DIR	Pediatric hospitals had lower dose indices compared with other facility types Level I–II trauma centers had lower dose indices compared with level III–IV trauma centers or nontrauma hospitals Facilities in metropolitan areas had lower dose indices compared with urban and rural locations

Note:—ACR indicates American College of Radiology.

Table 2: Suggested dose-reduction strategies

Roles of radiologists and imaging center staff
Imaging pediatric patients in a dedicated pediatric imaging department with dedicated pediatric team including
Pediatric radiologists
Certified CT technologists with experience in pediatric populations
Qualified medical physicists to help manage complex equipment
Child life specialists to work with families of patients
Frequent use of information created by the Image Gently Alliance regarding radiation dose reduction
Referring clinician role
Careful consideration of evidence-based clinical algorithms that can help assess the risk versus benefit of not obtaining a CT scan and choosing an imaging modality that provides necessary diagnostic information and does not use ionizing radiation
Considering referring children to pediatric facilities when available

and compete with other centers. This effort can be facilitated by national, educational, or institutional campaigns.²²

As expected, our results show that both CTDI_{vol} and DLP increase with age. However, younger patients are expected to experience increases in DLP due to both an increase in CTDI_{vol} and scan length, given increasing head sizes. The scan lengths were 14.7 and 16.4 cm for the 0- to 2-year and 3- to 6-year age groups, respectively. The scan length in patients younger than 6 years of age being only slightly shorter than that in adult-sized heads, suggests that the total energy deposited in the small pediatric patients' heads could possibly be reduced further by more careful control of the beginning and end of the chosen scan length by the operator. In addition, the smaller the child, the more likely that radiosensitive organs are included within the imaging area of interest.²⁹

Multiple causes result in a wide range of patient radiation doses, including variability of equipment makes and models,^{30,31} patient positioning,³² and anatomic coverage (eg, scan length versus length of patient anatomy of interest).³³ All factors controlled by the technologist (eg, voltage, tube current, rotation time, pitch, scan length, bow-tie filter, and so forth) can affect the range of patient doses when not set properly.³⁴

Imaging pediatric patients with a dedicated pediatric team that includes pediatric radiologists, certified CT technologists with experience in the pediatric population, qualified medical physicists to help manage complex equipment, and child life specialists to work with families of patients in a dedicated pediatric imaging department may result in improved pediatric CT protocols that reduce the patient dose while maintaining image quality (Table 2).³⁵ The Image Gently Alliance has created information to help facilities achieve these types of goals.^{36–38}

While radiologists, medical physicists, and CT technologists directly manage CT imaging techniques, clinicians can influence the patients' radiation doses by careful consideration of evidence-based clinical algorithms, which can help assess the risk versus

benefit of not obtaining a CT examination and choosing an imaging technique that provides the necessary diagnostic information and does not use ionizing radiation. Clinicians may also consider referring children to pediatric facilities when available (Table 2).^{5,39}

Our study has several limitations. First, both CT dose indices for the head and CTDI_{vol} and DLP stored by the DIR are estimates of the dose to a standard plastic phantom as opposed to the patient. However, these are the only 2 CT dose indices available until the American Association for Physicists in Medicine finishes its development of a size-specific dose estimate to serve the same purpose for the head as the size-specific dose estimate currently serves for the trunk.²⁶ When the head-size-specific dose estimate is available, it will be expressed as a function of the size of the head, which correlates better to patient dose than the age of the patient.⁴⁰ Second, because participation in the DIR is voluntary, there may be a selection bias in our study population.⁵ Facilities involved in the DIR may be more likely to audit their practices and follow dose-reduction protocols and dose-modification techniques; therefore, our dose-estimate results may be an underestimate of both CT doses and the variation in current CT practices.⁵ Third, data collected in the early years of the DIR (2011 launch) may contain some systematic errors that were reduced or eliminated with more experience. Fourth, institutions may name CT examinations differently, which can be associated with inconsistent or incorrect mapping to the standardized list of examinations used by the DIR.⁴¹ Furthermore, the name under which an examination was listed in the DIR may not reflect whether a low-dose protocol was used. It is possible that pediatric facilities perform low-dose head CT examinations more commonly for evaluation of ventricular shunt catheters; therefore, their median CTDI_{vol} is lower compared with nonpediatric facilities. Finally, facilities continually change their protocols with time, especially as more

attention is given to the importance of checking doses and having appropriate protocols.

CONCLUSIONS

Practice variations in the radiation dose index for pediatric head CT exist. Less variation occurred in pediatric compared with adult facilities and in metropolitan areas compared with suburban/rural facilities. Decreasing dose variability through proper management of CT parameters in pediatric populations using benchmarks generated by data from registries may help decrease population exposure to ionizing radiation.

Disclosures: Keith J. Strauss—UNRELATED: Consultancy: Phillips Medical Systems of North America, Comments: assisted with assignments as a medical physics consultant as requested by the entity.

REFERENCES

1. Miglioretti DL, Johnson E, Williams A, et al. **The use of computed tomography in pediatric and the associated radiation exposure and estimated cancer risk.** *JAMA Pediatr* 2013;167:700–07 CrossRef Medline
2. Mettler FA Jr, Wiest PW, Locken JA, et al. **CT scanning: patterns of use and dose.** *J Radiol Prot* 2000;20:353–59 CrossRef Medline
3. Wildman-Tobriner B, Strauss KJ, Bhargavan-Chatfield M, et al. **Using the American College of Radiology Dose Index Registry to evaluate practice patterns and radiation dose estimates of pediatric body CT.** *AJR Am J Roentgenol* 2018;210:641–47 CrossRef Medline
4. Mettler FA Jr, Thomadsen BR, Bhargavan M, et al. **Medical radiation exposure in the U.S. in 2006: preliminary results.** *Health Phys* 2008;95:502–07 CrossRef Medline
5. Marin JR, Sengupta D, Bhargavan-Chatfield M, et al. **Variation in pediatric cervical spine computed tomography radiation dose index.** *Acad Emerg Med* 2015;22:1499–505 CrossRef Medline
6. Larson DB, Johnson LW, Schnell BM, et al. **Rising use of CT in child visits to the emergency department in the United States, 1995–2008.** *Radiology* 2011;259:793–801 CrossRef Medline
7. Hollingworth W, Vavilala MS, Jarvik JG, et al. **The use of repeated head computed tomography in pediatric blunt head trauma: factors predicting new and worsening brain injury.** *Pediatr Crit Care Med* 2007;8:348–56; CEU quiz 357 CrossRef Medline
8. Statler KD, Keenan H. **How many are too many? Repeat head computed tomography after traumatic brain injury.** *Pediatr Crit Care Med* 2007;8:402–03 CrossRef Medline
9. Pearce MS, Salotti JA, Little MP, et al. **Radiation exposure from CT scans in childhood and subsequent risk of leukaemia and brain tumours: a retrospective cohort study.** *Lancet* 2012;380:499–505 CrossRef Medline
10. Boice JD Jr. **Radiation epidemiology and recent paediatric computed tomography studies.** *Ann ICRP* 2015;44:236–48 CrossRef Medline
11. The National Academics. **Beir VII: Health Risks from Exposure to Low Levels of Ionizing Radiation.** <https://www.nap.edu/read/11340/chapter/1>. Accessed June 10, 2018
12. Mathews JD, Forsythe AV, Brady Z, et al. **Cancer risk in 680,000 people exposed to computed tomography scans in childhood or adolescence: data linkage study of 11 million Australians.** *BMJ* 2013;346:f2360 CrossRef Medline
13. Yuan MK, Tsai DC, Chang SC, et al. **The risk of cataract associated with repeated head and neck CT studies: a nationwide population-based study.** *AJR Am J Roentgenol* 2013;201:626–30 CrossRef Medline
14. Bernier MO, Journy N, Villoing D, et al. **Cataract risk in a cohort of U.S. radiologic technologists performing nuclear medicine procedures.** *Radiology* 2018;286:592–601 CrossRef Medline
15. Nakashima E, Neriishi K, Minamoto A. **A reanalysis of atomic-bomb cataract data, 2000–2002: a threshold analysis.** *Health Phys* 2006;90:154–60 CrossRef Medline
16. Gardavaud F, Luciani A, Rahmouni A. **CT scans in childhood and risk of leukaemia and brain tumours.** *Lancet* 2012;380:1735; author reply 1736–37 CrossRef Medline
17. Zopf DA, Green GE. **CT scans in childhood and risk of leukaemia and brain tumours.** *Lancet* 2012;380:1735–36; author reply 1736–37
18. United States Nuclear Regulatory Commission. **Radiation Exposure and Cancer.** <https://www.nrc.gov/about-nrc/radiation/health-effects/rad-exposure-cancer.html>. Accessed February 4, 2018
19. King MA, Kanal KM, Relyea-Chew A, et al. **Radiation exposure from pediatric head CT: a bi-institutional study.** *Pediatr Radiol* 2009;39:1059–65 CrossRef Medline
20. Kanal KM, Vavilala MS, Raelson C, et al. **Variation in pediatric head CT imaging protocols in Washington state.** *J Am Coll Radiol* 2011;8:242–50 CrossRef Medline
21. Kanal KM, Graves JM, Vavilala MS, et al. **Variation in CT pediatric head examination radiation dose: results from a national survey.** *AJR Am J Roentgenol* 2015;204:W293–301 CrossRef Medline
22. Graves JM, Kanal KM, Rivara FP, et al. **Dose reduction efforts for pediatric head CT imaging in Washington State trauma centers: follow-up survey results.** *J Am Coll Radiol* 2014;11:161–68 e3 CrossRef Medline
23. Kanal KM, Butler PF, Sengupta D, et al. **U.S. diagnostic reference levels and achievable doses for 10 adult CT examinations.** *Radiology* 2017;284:120–33 CrossRef Medline
24. American College of Radiology. **Dose Index Registry.** <http://www.acr.org/Quality-Safety/National-Radiology-Data-Registry/Dose-Index-Registry>. Accessed October 13, 2017
25. Morin RL, Coombs LP, Chatfield MB. **ACR Dose Index Registry.** *J Am Coll Radiol* 2011;8:288–91 CrossRef Medline
26. American Association of Physicist in Medicine. **The Measurement, Reporting, and Management of Radiation Dose in CT.** Report of AAPM Task Group 23 of the Diagnostic Imaging Council CT Committee. January 2008. https://www.aapm.org/pubs/reports/RPT_96.pdf. Accessed January 25, 2018
27. U.S. Census Bureau. **Census Regions and Divisions of the United States.** http://www2.census.gov/geo/pdfs/maps-data/maps/reference/us_regdiv.pdf. Accessed October 13, 2017
28. Ginde AA, Foianini A, Renner DM, et al. **Availability and quality of computed tomography and magnetic resonance imaging equipment in U.S. emergency departments.** *Acad Emerg Med* 2008;15:780–83 CrossRef Medline
29. Image Gently. **Image Gently launches the Think-A-head Campaign.** https://rpop.iaea.org/RPOP/RPOP/Content/News/10-Image_Gently.htm. Accessed October 19, 2017
30. Jaffe TA, Yoshizumi TT, Toncheva G, et al. **Radiation dose for body CT protocols: variability of scanners at one institution.** *AJR Am J Roentgenol* 2009;193:1141–47 CrossRef Medline
31. Mayo-Smith WW, Hara AK, Mahesh M, et al. **How I do it: managing radiation dose in CT.** *Radiology* 2014;273:657–72 CrossRef Medline
32. Brink M, de Lange F, Oostveen LJ, et al. **Arm raising at exposure-controlled multidetector trauma CT of thoracoabdominal region: higher image quality, lower radiation dose.** *Radiology* 2008;249:661–70 CrossRef Medline
33. Campbell J, Kalra MK, Rizzo S, et al. **Scanning beyond anatomic limits of the thorax in chest CT: findings, radiation dose, and automatic tube current modulation.** *AJR Am J Roentgenol* 2005;185:1525–30 CrossRef Medline
34. Harri PA, Moreno CC, Nelson RC, et al. **Variability of MDCT dose due to technologist performance: impact of posteroanterior versus anteroposterior localizer image and table height with use of automated tube current modulation.** *AJR Am J Roentgenol* 2014;203:377–86 CrossRef Medline
35. Borders HL, Barnes CL, Parks DC, et al. **Use of a dedicated pediatric CT imaging service associated with decreased patient radiation dose.** *J Am Coll Radiol* 2012;9:340–43 CrossRef Medline
36. Goske MJ, Applegate KE, Boylan J, et al. **The ‘Image Gently’**

- campaign: increasing CT radiation dose awareness through a national education and awareness program.** *Pediatr Radiol* 2008;38:265–69 CrossRef Medline
37. Goske MJ, Applegate KE, Boylan J, et al. **The Image Gently campaign: working together to change practice.** *AJR Am J Roentgenol* 2008;190:273–74 CrossRef Medline
38. Strauss KJ, Goske MJ, Kaste SC, et al. **Image Gently: ten steps you can take to optimize image quality and lower CT dose for pediatric patients.** *AJR Am J Roentgenol* 2010;194:868–73 CrossRef Medline
39. American College of Radiology. Appropriateness Criteria. <https://acsearch.acr.org/list>. Accessed January 25, 2018
40. Kleinman PL, Strauss KJ, Zurakowski D, et al. **Patient size measured on CT images as a function of age at a tertiary care children's hospital.** *AJR Am J Roentgenol* 2010;194:1611–19 CrossRef Medline
41. Bohl M. Dose Index Registry Exam Name Mapping Review Made Easy. <https://www.linkedin.com/pulse/dose-index-registry-exam-name-mapping-review-made-easy-michael-bohl/> 2017. Accessed April 13, 2018

Contextual Radiology Reporting: A New Approach to Neuroradiology Structured Templates

 M.D. Mamlouk,  P.C. Chang, and  R.R. Saket



ABSTRACT

SUMMARY: Structured reporting has many advantages over conventional narrative reporting and has been advocated for standard usage by radiologic societies and literature. Traditional structured reports though are often not tailored to the appropriate clinical situation, are generic, and can be overly constraining. Contextual reporting is an alternative method of structured reporting that is specifically related to the disease or examination indication. Herein, we create a library of 50 contextual structured reports for neuroradiologists and emphasize their clinical value over noncontextual structured reporting. These templates are located in the On-line Appendix, and a downloadable PowerScribe 360 file may be accessed at <https://drive.google.com/open?id=1AIPUmfAXPzjkMFcHf7vGKF4Q-vldpflT>.

ABBREVIATIONS: MAGNIMS = Magnetic Resonance Imaging in Multiple Sclerosis; PHACE = posterior fossa malformations, hemangiomas, arterial anomalies, cardiac defects, and eye abnormalities

Recent literature and several radiology organizations advocate the use of structured templates as a new standard for radiology reporting.¹⁻⁵ Structured reporting has many advantages over traditional free-text, narrative reporting, including improved consistency, increased clarity, decreased grammar and speech recognition errors, increased ability to mine data for research, and greater financial rewards.⁶⁻¹⁰ On the other hand, advantages of narrative or prose reporting include flexibility, personalization, and familiarity for radiologists. While structured reporting is not perfect, referring providers have expressed greater satisfaction with the implementation of structured reporting.⁸ Despite this impetus, there are few data that objectively demonstrate the added clinical value over narrative reporting.¹¹

Not all structured reporting is created equally. Many of the published structured templates are technique- or examination-based.³ For example, in CT abdomen and pelvis imaging, structured reports are organized by a litany of organs.³ Similarly within neuroimaging, a sample published MR imaging brain template contains 16 anatomic items within the findings section, and nearly all the fields are filled in with “normal.”¹² While these reports may be versatile, they do not guide the radiologist during image interpretation but simply provide fields to report in a “structured” fashion. In addition, some radiologists are reluctant to use structured reporting because they think that the reports are too generic or simplistic and often not appropriately tailored to the clinical scenario.¹³

Contextual Structured Reporting

Contextual reporting is an alternative method of structured reporting that is specifically related to the disease or examination indication. These disease-specific reports provide content focused on the clinical diagnosis or symptom, discuss appropriate differential diagnoses, and highlight pertinent positives and negatives. Contextual reports are flexible; pick lists can be created within the templates to permit different options for the radiologist. Depending on the reporting software, tiered concepts can also be managed to trigger other macros that can be inserted on the basis of specific keywords or selection of pick lists. Contextual reporting also does not preclude some free-text dictation within the appropriate contextual fields. No template can perfectly fit every clinical scenario; thus, contextual templates should not be overly restrictive. This feature is another negative that some radiologists have found with traditional structured reporting.¹⁴

Received January 19, 2018; accepted after revision April 20.

From the Department of Radiology (M.D.M., R.R.S.), The Permanente Medical Group, Kaiser Permanente Medical Center Santa Clara, Santa Clara, California; Department of Radiology and Biomedical Imaging (M.D.M., R.R.S.), University of California, San Francisco, San Francisco, California; and Department of Radiology (P.C.C.), The Permanente Medical Group, Kaiser Permanente Medical Center South San Francisco, South San Francisco, California.

Paper previously presented as an education exhibit at: Annual Meeting of the Radiological Society of North America, November 26–December 1, 2017; Chicago, Illinois. It received the Magna Cum Laude award.

Please address correspondence to Mark D. Mamlouk, MD, Department of Radiology, The Permanente Medical Group, Kaiser Permanente Medical Center Santa Clara, 700 Lawrence Expressway, Santa Clara, CA 95051; e-mail: mark.d.mamlouk@kp.org, mark.mamlouk@ucsf.edu; @MarkMamloukMD

 Indicates open access to non-subscribers at www.ajnr.org

 Indicates article with supplemental on-line appendix.

 Indicates article with supplemental on-line photos.

<http://dx.doi.org/10.3174/ajnr.A5697>

Contextual structured reporting has only been applied to a handful of diseases, including pancreatic cancer, pulmonary embolism, pediatric Crohn disease, prostate cancer, rectal cancer, infertility, and interstitial lung disease.^{11,15-20} To the authors' knowledge, contextual templates for multiple sclerosis, thyroid imaging, and head trauma are the only contextual structured reports developed within neuroimaging.²¹⁻²³ The purpose of this article was to create a library of 50 contextual structured reports for neuroradiologists and emphasize their clinical value over non-contextual structured reporting through the use of selective imaging examples.

Template Creation Process

The contextual templates were created in a systematic process that spanned >1 year, which is similar to processes in other institutions.^{24,25} Our institution (Kaiser Permanente, Santa Clara, California) is part of a 21-hospital network comprising 300 radiologists, 50 of whom are neuroradiologists. Led by a committee chairperson, a committee search was initiated to identify radiologists interested and knowledgeable about structured reporting and informatics. The subspecialty regional leaders of neuroradiology within brain, neurovascular, head/neck, pediatric neuroradiology, and spine imaging were recruited. After the committee was created, common examination indications and diseases within neuroradiology were culled from examination data, and templates were drafted. For each template created, the committee members provided revisions and ensured that the templates contained content contextual to the disease process or examination indication. Following committee voting and approval, each of the templates was sent to a subspecialty clinician who was an expert in the specific topic to provide additional suggestions. Before template publication within our radiology dictation software (Radiator; Napa, California), the informatics leader of the committee coded the template, ensuring the templates were practical to use and creating pick list options when appropriate.

The templates were mapped to the procedural codes of our institution within the radiology information system, which are closely modeled after the current procedural terminology codes, with the exception of more granularity to permit more complex associations between the procedures and structured templates. This mapping permits the template to automatically load in the reporting software when the examination is opened for interpretation. The templates were then made available to all radiologists to use in clinical practice, and a hyperlink was inserted within the dictation software for users to provide suggestions for change, which were reviewed and revised when appropriate. To orient the radiologists with the contextual templates at the onset of deployment, the template committee gave a lecture on the types of templates developed, the advantages of contextual reporting, and reference to available imaging guides for certain templates.

For the purposes of this publication and to make the contextual templates easily accessible to other radiologists without our proprietary reporting software, the templates were also created in Nuance Powerscribe360 (Burlington, Massachusetts). A downloadable Powerscribe 360 file can be accessed here (<https://drive>.

[google.com/open?id=1AIPUmfAXPzjkMFcHf7vGKF4Q-vIdpflT](https://drive.google.com/open?id=1AIPUmfAXPzjkMFcHf7vGKF4Q-vIdpflT)) and is compatible with versions 3.5 and 4.0.

Contextual Structured Reporting Templates

The advantages of contextual templates are 3-fold: They are individually tailored to the diagnosis, they ensure that all pertinent points are addressed in a checklist fashion, and they educate trainees by providing a systematic approach for clinical interpretation.

Contextual Templates Individually Tailored to the Diagnosis

Multiple Sclerosis Screening. Our institution abides by the Magnetic Resonance Imaging in Multiple Sclerosis (MAGNIMS) consensus guidelines for diagnostic and follow-up imaging.^{26,27} MR imaging criteria to establish disease dissemination in space are characterized as having at least 2 of the 5 findings: ≥ 3 periventricular lesions, ≥ 1 infratentorial lesion, ≥ 1 spinal cord lesion, ≥ 1 optic nerve lesion, and ≥ 1 cortical/juxtacortical lesion. These specific criteria render them suitable for a contextual template (Fig 1), one that is focused solely on multiple sclerosis and is supported by evidence-based medicine. This template is used in screening examinations with a unique imaging screening protocol to determine whether the patient has multiple sclerosis. At the end of the template, the MAGNIMS criteria are listed for a convenient reminder to the ordering provider. This contextual multiple sclerosis template addresses items similar to those in the previously reported multiple sclerosis templates,^{21,22} though the actual templates in these articles are not published for definite comparison.

Multiple Sclerosis Follow-Up. Evaluating disease progression or stability in the follow-up of multiple sclerosis can sometimes be cumbersome to the radiologist, especially when the disease burden is high. Because of this occasional difficulty, reporting can also be vexing. On the other hand, contextual reporting for multiple sclerosis has been anecdotally the easiest and most rapid template to fill out because it mainly focuses on the presence of new or active demyelinating lesions (Fig 2). Many of the fields can be quickly tabbed through, and a final report can often be crafted in a few minutes or less after reviewing the images.

Head and Neck Cancer. Reporting examinations for head and neck cancer warrant a thorough discussion of the primary tumor and nodal metastases. Contextual templates can assist with reporting by directing the radiologist to the pertinent findings relevant to staging by the American Joint Committee on Cancer. The template, which can be used for both MR imaging and CT, is divided into 2 sections: tumor and nodal characteristics (Fig 3), which provide the referring provider a clear and focused assessment. Also, by reporting in a systematic fashion, this template enables the radiologist to synthesize the findings and include the clinical staging in the impression section of the report. While some radiologists and institutions may not prefer to include the clinical staging within their radiology reports, it is still paramount to report all the pertinent positives and negatives so that the clinical stage can be established by the referring provider or within the hospital tumor board. As a final note, initially, contextual templates were created for each of the neck cancer sites; however, given the various presentations of each tumor and the several structures potentially

FINDINGS:
BRAIN PARENCHYMA:
T2 hyperintense white matter lesions:
***Periventricular:** [No|1-2|3 or more] lesions contacting the ependymal surface
***Juxtacortical/Cortical:** [None|Present]
***Infratentorial:** [None|Present involving the [brainstem|cerebellum|brainstem and cerebellum]]
***Optic Nerve:** [None|Present]
***Cervicomedullary Junction:** [None|Present]

Enhancing Lesions: [<# of enhancing lesions and locations>None]
Reduced Diffusion: [None|Present (describe)]
Overall Disease Burden: [None|<10 lesions|10-20 lesions|>20 lesions]

Parenchymal Atrophy: [None|Mild|Moderate|Severe]
Callosal Atrophy: [None|Mild|Moderate|Severe]

OTHER FINDINGS: [None]

IMPRESSION:
 [Normal MRI brain.|Multiple white matter lesions that are [typical|atypical|not consistent] with demyelinating disease.]

2016 MAGNIMS MRI criteria to establish disease dissemination in space in multiple sclerosis (Lancet Neurol. 2016 Mar;15(3):292-303)
 Involvement of at least two of five areas of the CNS as follows:
 * Three or more periventricular lesions
 * One or more infratentorial lesion
 * One or more spinal cord lesion
 * One or more optic nerve lesion
 * One or more cortical or juxtacortical lesion

FIG 1. Contextual template for multiple sclerosis screening. The template is individually tailored to the diagnosis of multiple sclerosis and is evidence-based, abiding by MAGNIMS criteria.

FINDINGS:
BRAIN PARENCHYMA:
New T2 hyperintense Lesions: [<new lesion number and location>None]
Enhancing Lesions: [<# of enhancing lesions and locations>None]
Reduced Diffusion: [None|Present (describe)]

Overall Disease Burden: [<10 lesions|10-20 lesions|>20 lesions]. [No change in multiple [periventricular|periventricular and juxtacortical|periventricular and infratentorial|periventricular, juxtacortical and infratentorial] white matter lesions compatible with known demyelinating disease].

T1 Hypointensities (Black Holes): [Absent|<5|>5] and [unchanged|increased] compared to prior exam].

Parenchymal Atrophy: [None|Mild|Moderate|Severe]
Callosal Atrophy: [None|Mild|Moderate|Severe]

OTHER FINDINGS: [<other>None]

IMPRESSION:
 Demyelinating disease in the [supratentorial|supratentorial and infratentorial] brain, [without|with] active disease and [no change|change] compared to [<PriorExamDate>].

FIG 2. Contextual template for multiple sclerosis follow-up. Because the template focuses on items germane to the clinical indication, reporting can be accomplished rapidly, permitting quick tabbing through the fields.

involved in each case, the templates were found to be constraining and time-consuming to report. Therefore, a single neck cancer template was created to provide report uniformity but also radiologist reporting flexibility.

Fetal Brain MR Imaging. Fetal neuroimaging naturally poses unique items for the radiologist to inspect and report that are different from those in postnatal imaging. Contextual structured reports for fetal MR brain imaging consist of 3 main areas: fetal positioning, biometry, and brain parenchyma (On-line Fig 1). Many of the items can be quickly selected through pick list options, which is an inherent advantage of structured reporting. In the event of a major fetal anomaly, these findings can be added to the corresponding field.

Contextual Templates Ensuring All Pertinent Points Addressed in a Checklist Fashion

Preoperative Sinus CT. Detecting sinonasal variants is an important assessment on preoperative sinus CT before endoscopic surgery. Despite published literature on sinonasal variants, radiology reporting of these variants is highly variable. Consequently, some otolaryngologists are dissatisfied with radiology reporting in this setting and even caution other otolaryngologists not to rely on the radiology report to manage their patients.²⁸ This reporting variability is likely, in part, attributed to the difficulty in remembering all the sinonasal variants. A contextual preoperative sinus template helps with this dilemma by providing a checklist approach to remind the user of all the pertinent points (Fig 4). Our group has also added a hyperlink in our dictation software with a concise imaging guide of all the described sinonasal variants for easy access while reporting.

Preoperative Pituitary MR Imaging. A presurgical checklist is also important in pituitary surgery because certain anatomic variants can greatly impact the surgical approach. A discussion of the pituitary lesion is common throughout radiology reporting, though anecdotal experience from our surgeon colleagues reveals that radiologists do not often re-

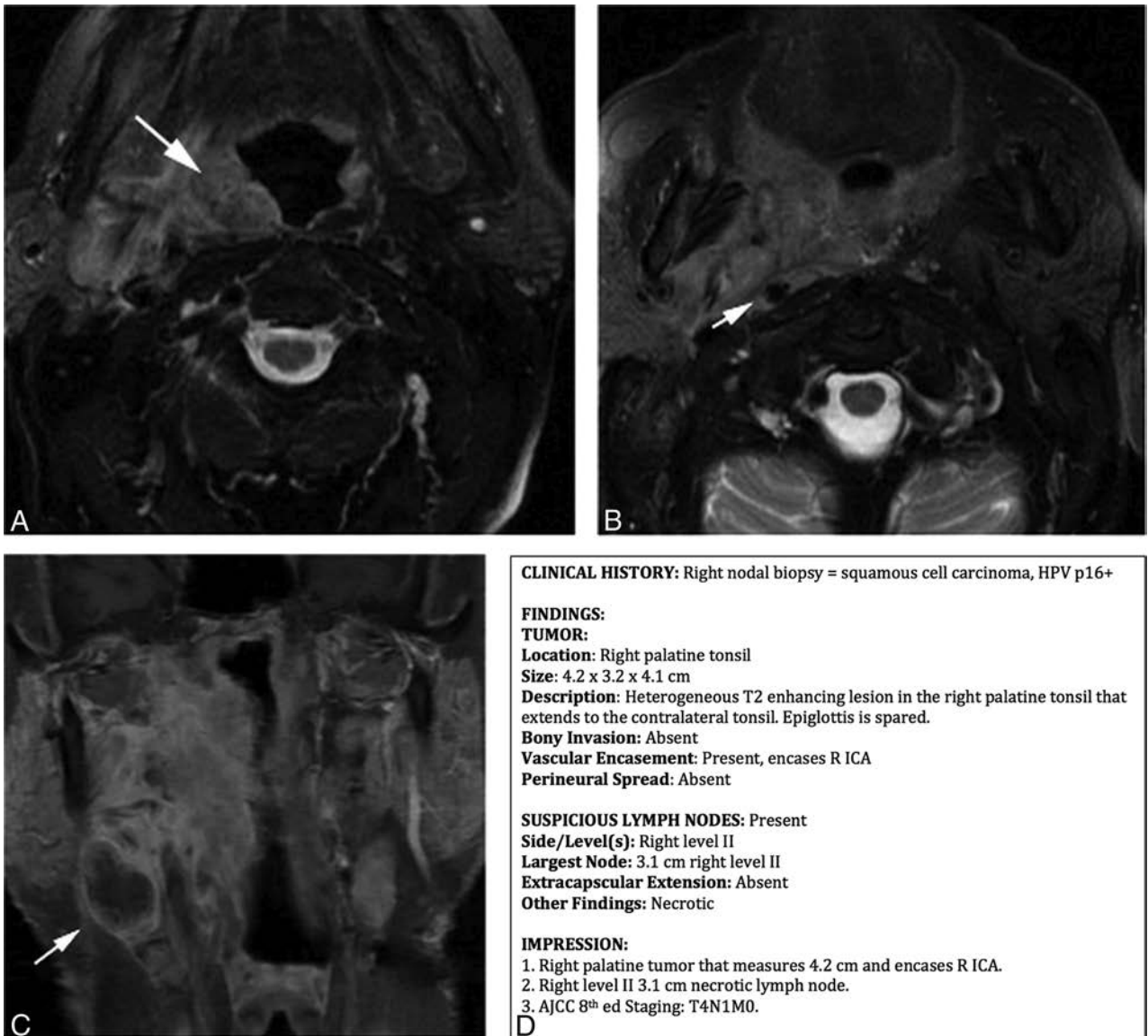


FIG 3. Value of a contextual template for neck cancer. *A* and *B*, Axial fat-suppressed T2-weighted images show a right palatine tumor (*long arrow*) encasing the right internal carotid artery (*short arrow*), while *C* shows a right level II node (*arrow*) on coronal contrast-enhanced fat-suppressed T1-weighted imaging. *D*, A contextual neck cancer template with all the fields concisely filled out and tailored to clinical staging.

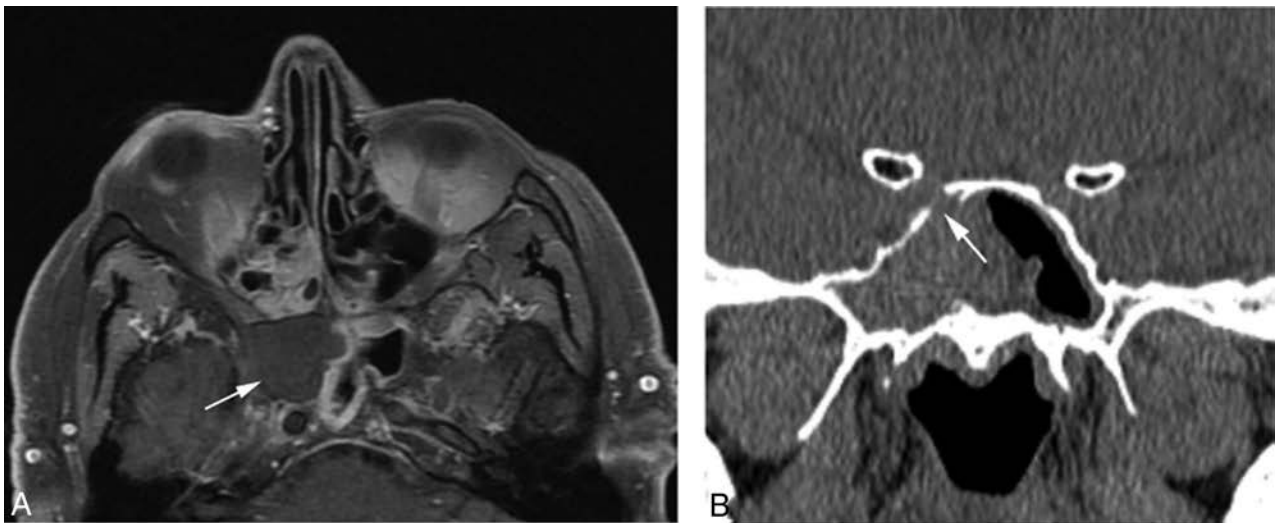
port anatomic variants in this setting. Similar to the presurgical sinus CT template, a contextual pituitary template can establish a checklist reminder for the interpreting radiologist (On-line Fig 2). Anatomic variants discussed within the template include the following: aberrant vasculature such as persistent trigeminal artery, a narrowed intercarotid distance, sphenoid sinus pneumatization, and the intersphenoid septum. In the event that these items are not well evaluated on the interpreting MR imaging, review of prior imaging can usually provide confirmation, if available. Depending on the surgeon's preference, the extent of the pituitary lesion, and the patient anatomy, a neuronavigation CT can be performed afterward. Nonetheless, these items within the contextual MR imaging template can provide an initial framework for the surgical approach. For this template, our institution also created a short summary guide of the anatomic variants accessible within the dictation software to aid the interpreting radiologist.

Trigeminal Neuralgia. The imaging work-up of trigeminal neu-

ralgia necessitates careful inspection for pathologies extending from the brain stem to the mandible. A contextual template facilitates this detailed evaluation in a succinct manner. The radiologist will remember where to identify potential causes, and the referring provider will be satisfied that the main diagnostic causes were assessed. Conversely, traditional free text or noncontextual structured templates could omit commentary on important elements and could also address unnecessary items, thereby cluttering the report. Figure 5 highlights this difference using a non-contextual structured template¹² versus a contextual template for trigeminal neuralgia.

Contextual Templates Educate Trainees by Providing a Systematic Approach for Clinical Interpretation

Developmental Delay, Dementia, and Pulsatile Tinnitus. Certain entities, such as developmental delay, dementia, and pulsatile tinnitus, have several common etiologies that the radiologist must



FINDINGS:
SINUS INFLAMMATORY DISEASE:
 ...

SINUS ANATOMY/VARIANTS:
Carotid and optic canals [are not|are] dehiscent.
 Sphenoid septum [does not insert|inserts] onto the carotid canal.
 [No evidence|Evidence] of Keros type III cribriform plate (lateral lamella 8-16 mm). [No cribriform plate asymmetry.]
 Anterior ethmoid canals [do not traverse|traverse] through the ethmoid air cells.
 [Lamina papyracea are intact.|There is a remote medial orbital wall fracture with prolapse of orbital fat into the [left|right] ethmoid sinus.]

[No evidence of sphenoethmoidal (Onodi) cell.|Sphenoethmoidal (Onodi) cell on the [left|right] with the optic nerve coursing through it.]
 [No evidence of infraorbital ethmoid (Haller) cell.|Infraorbital ethmoid (Haller) cell on the left|right] that narrows the infundibulum.]
 [No concha bullosa.|Concha bullosa present.]

OTHER: [None.]

IMPRESSION:
 [Normal CT sinus.]

C

FIG 4. Value of a contextual template for preoperative sinus CT. A, Axial contrast-enhanced fat-suppressed T1-weighted image shows diffuse paranasal sinus opacification, with nonenhancement in the right sphenoid sinus (*arrow*), compatible with invasive sinusitis. Preoperative sinus CT imaging was performed (B) and shows a dehiscent right carotid canal (*arrow*) that could have been overlooked without a contextual template (C). Remembering all the sinus variants can be difficult, but a contextual template can aid in this dilemma by providing a checklist approach. To improve education and usage of this template, a hyperlink can be added to the dictation software with imaging examples showing these sinonasal variants.

systematically inspect on imaging. Without a reference or guide, it is foreseeable that trainees may not be able to identify the important findings for these entities and synthesize them into a cohesive process. Contextual templates satisfy this need by serving as an adjunct guide to the attending radiologist. In fact, the instructing radiologist can teach trainees a systematic diagnostic approach to such cases with the template viewed in tandem with the imaging (Fig 6 and On-line Figs 3 and 4). The contextual templates will help reinforce knowledge that trainees need for their careers and board examinations.

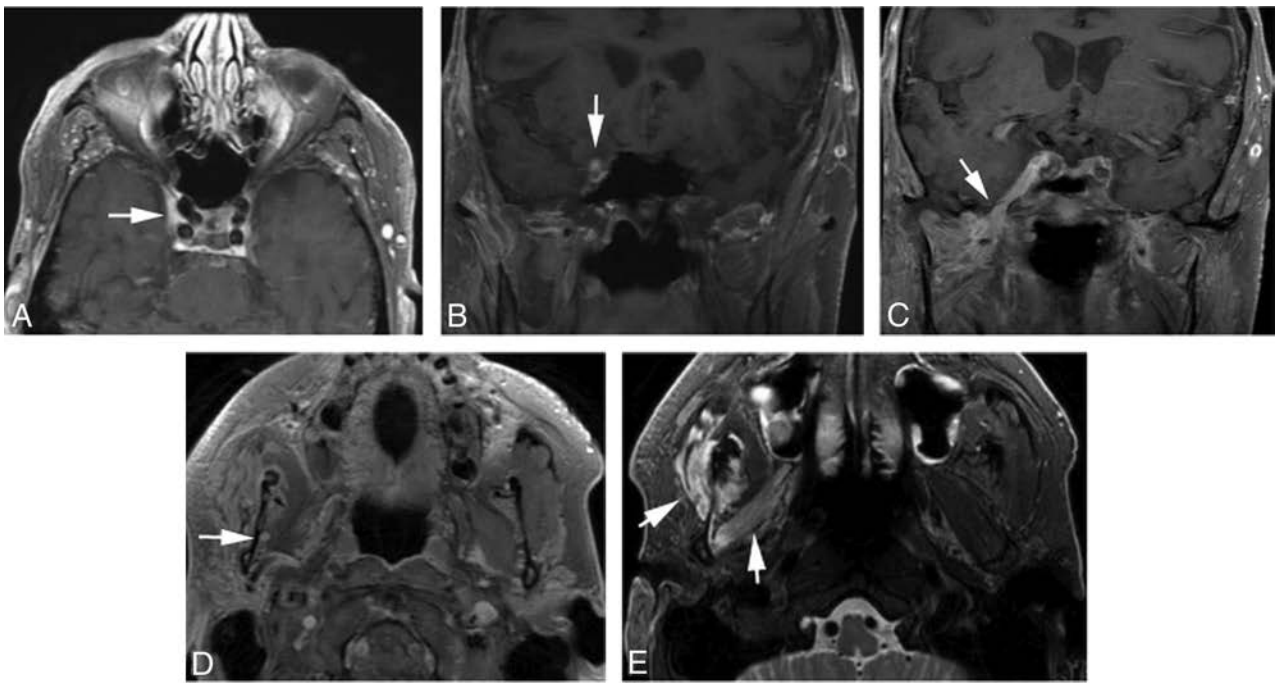
This method will also educate trainees on reporting. It has been reported that radiology residents receive no more than 1 hour of didactic instruction in radiology reporting per year.²⁹ Contextual templates can help with this deficient teaching by pro-

viding trainees with a solid foundation on effective radiology reporting.

Last, contextual templates that emphasize a systematic approach to interpretation can help mitigate the cognitive bias of “satisfaction of search.”³⁰ This error occurs when a radiologist identifies a finding and overlooks additional findings due to complacency. Contextual reporting will remind the user to look at all described entities regardless of whether 1 finding is already identified.

Contextual Templates for “Bread and Butter” Neuroradiology

Many examinations in neuroradiology are performed for routine conditions such as stroke CT, low back pain, and cervical radiculopathy. We created templates for these 3 entities as well (On-line Figs 5–7).



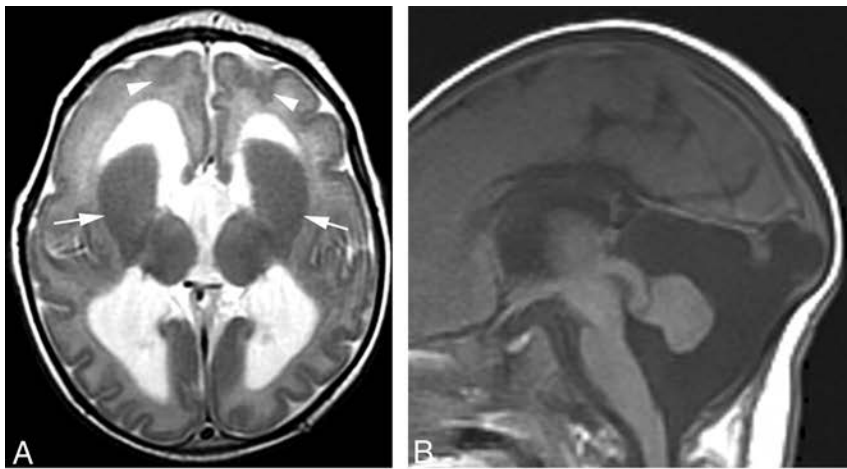
<p>FINDINGS: Extra-axial spaces: Normal in size and morphology for the patient's age. Intracranial hemorrhage: None. Ventricular system: Normal in size and morphology for the patient's age. Basal cisterns: Normal. Cerebral parenchyma: Normal. Midline shift: None. Cerebellum: Normal. Brainstem: Normal. Calvarium: Normal. Vascular system: Normal flow voids, without atheroma, occlusion, or dissection. Paranasal sinuses and mastoid air cells: Clear. Visualized orbits: Normal. Visualized upper cervical spine: Normal. Sella: Normal. Skull base: There is abnormal enhancement within the right cavernous sinus, foramen rotundum, and foramen ovale. Marrow: Normal.</p> <p>IMPRESSION: Abnormal enhancement within the right cavernous sinus, foramen rotundum, and foramen ovale, compatible with perineural spread of tumor from skin cancer.</p> <p>F</p>	<p>FINDINGS TRIGEMINAL NERVE Vascular Loop: Absent.</p> <p>Posterior Fossa Mass: Absent.</p> <p>Pons: No mass, acute infarct, or demyelinating lesion.</p> <p>Perineural Enhancement: Abnormal enhancement within the right foramen rotundum and foramen ovale.</p> <p>Cavernous Sinus: Abnormal enhancement on the right.</p> <p>Mandible: Enhancement and enlargement of the right inferior alveolar nerve.</p> <p>Muscles of Mastication: Right-sided denervation atrophy.</p> <p>REMAINING BRAIN PARENCHYMA: No acute infarct or hemorrhage. No mass effect or herniation.</p> <p>VENTRICLES/EXTRA-AXIAL SPACES: No hydrocephalus or extra-axial fluid collections.</p> <p>IMPRESSION:</p> <ol style="list-style-type: none"> 1. Abnormal enhancement within the right cavernous sinus, foramen rotundum, foramen ovale, and inferior alveolar nerve, compatible with perineural spread of tumor from skin cancer. 2. Denervation atrophy of the right muscles of mastication. <p>G</p>
--	--

FIG 5. Value of a contextual structured template for trigeminal neuralgia over a noncontextual structured template. *A–D*, Axial and coronal contrast-enhanced fat-suppressed imaging in a patient with skin cancer shows extensive perineural enhancement (*arrows*). *E*, Axial fat-suppressed T2-weighted image shows denervation atrophy in the right muscles of mastication (*arrows*). A noncontextual structured template (*F*) and a contextual structured template (*G*) describe the findings. Note that the noncontextual template is unnecessarily lengthy, and the skull base field is the only field conceivably relevant to trigeminal neuralgia, as opposed to the multiple relevant fields within the concise contextual template. Furthermore, discussion of the inferior alveolar nerve enhancement and muscular denervation atrophy could have been overlooked in the noncontextual template because there are no fields to describe them.

Additional Contextual Templates

In addition to the listed templates in this article, several other contextual templates were created (On-line Appendix). We made the following contextual adult brain MR imaging templates: rou-

tine brain, stroke/TIA, headache, epilepsy, sella, orbits, cranial nerves III-IV-VI, cranial nerve VII, hearing loss, vestibular schwannoma follow-up, cholesteatoma, skull base, paranasal sinus, and temporomandibular joints. We created the following



CLINICAL HISTORY: 6 wk old, term, developmental delay, microcephaly, seizures

FINDINGS:
BRAIN PARENCHYMA: No acute infarct or hemorrhage. Markedly enlarged caudate with absent internal capsule, resulting in fused striata bilaterally.

CORTEX: Bifrontal band heterotopias are seen as well as bioccipital pachygyria.

SULCATION: Delayed for age.

WHITE MATTER: Reduced volume. Myelination is delayed for age.

CORPUS CALLOSUM: Thinned.

VENTRICLES: Enlarged.

CEREBELLUM: Hypoplastic.

VERMIS: Hypoplastic.

BRAINSTEM: Hypoplastic pons.

MRS:
 NAA:choline ratio: Normal.
 Lactate Peak: Absent.

IMPRESSION:
 Combination of abnormal basal ganglia, malformations of cortical development, microcephaly, and a small cerebellum/brainstem are compatible with a tubulinopathy.

FIG 6. Contextual template for developmental delay. A, Axial T2-weighted image of the brain shows fused corpus striata (arrows) and bifrontal band heterotopia (arrowheads). B, Sagittal T1-weighted image shows a hypoplastic corpus callosum, pons, and cerebellum. The contextual template (C) arrives at the rare diagnosis of a tubulinopathy by systematically inspecting each of the important structures in a patient with developmental delay and synthesizing them together. This method aids in diagnosis and can also teach trainees how to approach challenging cases.

contextual pediatric brain MR imaging templates: routine brain; fast protocol; epilepsy; and posterior fossa malformations, hemangiomas, arterial anomalies, cardiac defects, and eye abnormalities (PHACE syndrome). Contextual MR imaging neck templates included neck pain/swelling, cancer follow-up, and Horner syndrome. Contextual spine templates included the following: multiple sclerosis initial and follow-up, brachial and lumbosacral plexus, tethered cord, drop metastases, thoracic pain, and sagittal

screening MR imaging. CT head contextual templates included the following: acute injury/ischemia, sinus, temporal bone, preoperative cochlear implant, CT angiogram head/neck, and CT venogram. 4D parathyroid adenoma and neck pain/swelling contextual templates were created for the CT neck category.

Analysis of Contextual Templates

To test the qualitative benefits of our contextual structured reports, we anonymously surveyed referring providers and radiologists in our hospital network (Tables 1 and 2). Referring providers consisted of neurologists, otolaryngologists, radiation oncologists, and neurosurgeons. Ninety-three percent of surveyed providers favored the contextual structured reports (either strongly agreed or agreed). Ninety-five percent of providers thought the pertinent findings were easy to understand, and 96% thought the impression was easy to understand. When asked how the reports compared with traditional narrative reporting, 83% preferred the contextual structured reports. In an optional commentary section of the survey, some providers highly praised our effort at standardization and uniformity, and other providers were pleased that certain important elements relevant to a specific disease process were always addressed, limiting second opinion communications.

For the survey of radiologists, both neuroradiologists and non-neuroradiologists were surveyed regarding contextual neuroradiology structured reports because non-neuroradiologists interpret a small percentage of neuroradiology examinations in our hospital network. Sixty-five percent of surveyed radiologists favored the contextual reports, while 24% were neutral and 11% were dissatisfied. Sixty percent thought the contextual templates made reporting more thorough and relevant for complex entities, 55% wanted contextual

reports to be created for other radiology subspecialties, and 53% thought that the contextual reports made their reporting more efficient. When asked if he or she thought radiology report standardization was necessary, 66% of respondents agreed.

In our study, the referring providers' satisfaction was greater than radiologists' satisfaction, which has also been witnessed in other publications.^{8,31-33} One of these publications surveyed 265 academic radiologists from the United States, and only 60% were

Table 1: Referring provider survey on contextual structured reporting (n = 85)^a

Question	Strongly Agree	Agree	Neither Agree nor Disagree	Disagree	Strongly Disagree
Do you have a positive overall impression of the new disease-specific structured radiology reports as they pertain to your specialty?	64 (75)	15 (18)	4 (5)	2 (2)	0 (0)
On average, it is easy for me to understand the pertinent findings from the structured radiology reports	58 (68)	23 (27)	3 (4)	1 (1)	0 (0)
On average, it is easy for me to understand the main impression from the structured radiology reports	55 (65)	26 (31)	3 (4)	1 (1)	0 (0)
Do you prefer structured radiology reporting to the previous prose, narrative reporting style you are accustomed to?	52 (61)	19 (22)	13 (15)	1 (1)	0 (0)

^a Thirty-eight neurologists, 34 otolaryngologists, 10 radiation oncologists, and 3 neurosurgeons. Data are number (percentage).

Table 2: Radiologist survey on contextual structured reporting (n = 100)^a

Question	Strongly Agree	Agree	Neither Agree nor Disagree	Disagree	Strongly Disagree
Do you have a positive overall impression of the new disease-specific structured radiology reports as they pertain to your specialty?	33 (33)	32 (32)	24 (24)	8 (8)	3 (3)
Do you feel that using contextual structured neuroradiology templates for complex entities makes your reporting more thorough and relevant?	28 (28)	32 (32)	29 (29)	7 (7)	4 (4)
Do you think that the contextual structured reports increase your efficiency?	22 (22)	30 (30)	20 (20)	23 (23)	5 (5)
Would you like contextual structured reports to be created for other radiology subspecialties (eg, body, musculoskeletal, and so forth)?	28 (28)	27 (27)	24 (24)	14 (14)	7 (7)
Do you think radiology report standardization is necessary?	27 (27)	39 (39)	15 (15)	16 (16)	3 (3)

^a Data are number (percentage).

satisfied with structured reports, whereas 27% were neutral and 13% were dissatisfied.³² We suspect that some of our radiologists were not in favor of the contextual reports because they were also not in favor of report standardization: Approximately one-third of respondents did not favor report standardization, and one-third did not favor the contextual reports. By filtering the data to those respondents who favored report standardization, the survey question percentages markedly improved. Eighty-eight percent of radiologists favored contextual reporting, 80% thought the contextual templates made reporting more thorough and relevant for complex entities, 79% wanted contextual reports to be created for other radiology subspecialties, and 71% thought the contextual templates increased their efficiency. Thus, our data show that most radiologists who believe in report standardization also favored the contextual templates.

One potential reason that some radiologists did not believe in report standardization and contextual reporting is familiarity with narrative reporting. Narrative reporting has existed since the early 1900s and naturally has become ingrained in our profession.³⁴ Other potential reasons for radiologists' dissatisfaction could be that structured reporting restricts autonomy, potentially undermines curiosity, and limits personalization.^{6,35} Despite these findings, we believe that radiologists' satisfaction will continue to increase as familiarity with contextual reports increases. Moreover, our stakeholders, the referring providers, demanding structured reporting will also be a great incentive.

Most radiologists who believed in report standardization also believed that contextual reporting increased their efficiency. This increased speed is likely because all the major items are discussed within the contextual template, thereby limiting actual dictation. We also observed a unique advantage of contextual reporting with normal or near-normal study findings, in that the template can be quickly signed. Our dictation software has a feature to default all

the fields with normal findings using a simple voice command. The default values within each template field were established when each template was created. With regard to noncontextual structured templates, theoretically, these reports can also be signed quickly in the setting of normal examination findings, but the content is less meaningful.

Contextual reporting and our article have limitations. One potential limitation to contextual structured reporting is the phenomenon of "eye dwell," in which the radiologist is inclined to keep his or her eye on the report template rather than the images.⁶ We believe that this issue can occur in all structured reporting but should resolve with time after the radiologist becomes more accustomed to the template. Another limitation is when a patient has 2 disease entities, making it difficult to choose which contextual template to follow. In these cases, the single best template can be used and supplemented with additional content either in the "Other" section of the report or by inserting phrases from another template. With regard to the article, we did not measure radiologists' compliance in using the templates. While we encourage and advocate the use of the aforementioned templates, we are unable to force radiologists to use a specific template at our institution.

Future Directions

Because this proof of concept was favorable with the neuroradiology contextual templates, our group is planning to develop contextual templates for other radiology subspecialty diseases. Our group believes that contextual reporting is the next generation of structured reporting.

Contextual reporting could theoretically have a substantial role in data tracking and machine learning. Because contextual reports are disease-specific and structured, common data elements can be gathered from the reports so that computers can read and understand the content. These natural language-pro-

cessing techniques could permit data extraction to populate national registries and aid research.^{36,37} Furthermore, contextual reports could also potentially be the framework for computer-generated reports if machine learning can reliably interpret certain radiologic examinations. Further studies are needed to substantiate these ideas.

CONCLUSIONS

Contextual reporting is a method of structured reporting specifically related to the disease or examination indication. Contextual templates are individually tailored to the diagnosis, they ensure that all pertinent points are addressed in a checklist fashion, and they educate trainees by providing a systematic approach for clinical interpretation. The included library of neuroradiology contextual templates can help neuroradiologists transition to a new method of structured reporting.

REFERENCES

- Kahn CE Jr, Langlotz CP, Burnside ES, et al. **Toward best practices in radiology reporting.** *Radiology* 2009;252:852–56 CrossRef Medline
- Radiological Society of North America Radiology Reporting Initiative. https://www.rsna.org/Reporting_Initiative.aspx. Accessed January 5, 2018
- Radiological Society of North America Informatics Reporting. www.radreport.org. Accessed January 5, 2018
- Bosmans JM, Peremans L, Menni M, et al. **Structured reporting: if, why, when, how-and at what expense? Results of a focus group meeting of radiology professionals from eight countries.** *Insights Imaging* 2012;3:295–302 CrossRef Medline
- Douglas PS, Hendel RC, Cummings JE, et al; American College of Cardiology Foundation (ACCF). **ACCF/ACR/AHA/ASE/ASNC/HRS/NASCI/RSNA/SAIP/SCAI/SCCT/SCMR 2008 Health Policy Statement on Structured Reporting in Cardiovascular Imaging.** *J Am Coll Cardiol* 2009;53:76–90 CrossRef Medline
- Ganeshan D, Duong PT, Probyn L, et al. **Structured reporting in radiology.** *Acad Radiol* 2018;25:66–73 CrossRef Medline
- Langlotz CP. **Structured radiology reporting: are we there yet?** *Radiology* 2009;253:23–25 CrossRef Medline
- Schwartz LH, Panicek DM, Berk AR, et al. **Improving communication of diagnostic radiology findings through structured reporting.** *Radiology* 2011;260:174–81 CrossRef Medline
- Hawkins CM, Hall S, Hardin J, et al. **Prepopulated radiology report templates: a prospective analysis of error rate and turnaround time.** *J Digit Imaging* 2012;25:504–11 CrossRef Medline
- Duzak R Jr, Nossal M, Schofield L, et al. **Physician documentation deficiencies in abdominal ultrasound reports: frequency, characteristics, and financial impact.** *J Am Coll Radiol* 2012;9:403–08 CrossRef Medline
- Brook OR, Brook A, Vollmer CM, et al. **Structured reporting of multiphase CT for pancreatic cancer: potential effect on staging and surgical planning.** *Radiology* 2015;274:464–72 CrossRef Medline
- Radiological Society of North America Informatics Reporting. MR Brain Template. <http://www.radreport.org/txt-mrrt/0000045>. Accessed January 5, 2018
- Boland GW, Duzak R Jr. **Structured reporting and communication.** *J Am Coll Radiol* 2015;12:1286–88 CrossRef Medline
- Johnson AJ, Chen MY, Swan JS, et al. **Cohort study of structured reporting compared with conventional dictation.** *Radiology* 2009;253:74–80 CrossRef Medline
- Sabel BO, Plum JL, Kneidinger N, et al. **Structured reporting of CT examinations in acute pulmonary embolism.** *J Cardiovasc Comput Tomogr* 2017;11:188–95 CrossRef Medline
- Wildman-Tobriner B, Allen BC, Davis JT, et al. **Structured reporting of magnetic resonance enterography for pediatric Crohn's disease: effect on key feature reporting and subjective assessment of disease by referring physicians.** *Curr Probl Diagn Radiol* 2017;46:110–14 CrossRef Medline
- Magnetta MJ, Donovan AL, Jacobs BL, et al. **Evidence-based reporting: a method to optimize prostate MRI communications with referring physicians.** *AJR Am J Roentgenol* 2018;210:108–12 CrossRef Medline
- KSAR Study Group for Rectal Cancer. **Essential Items for Structured Reporting of Rectal Cancer MRI: 2016 Consensus Recommendation from the Korean Society of Abdominal Radiology.** *Korean J Radiol* 2017;18:132–51 CrossRef Medline
- Montoliu-Fornas G, Marti-Bonmati L. **Magnetic resonance imaging structured reporting in infertility.** *Fertil Steril* 2016;105:1421–31 CrossRef Medline
- Sverzellati N, Odone A, Silva M, et al; Italian Structured Report on Fibrosing Lung Disease Consort. **Structured reporting for fibrosing lung disease: a model shared by radiologist and pulmonologist.** *Radiol Med* 2018;123:245–53 CrossRef Medline
- Dickerson E, Davenport MS, Syed F, et al; Michigan Radiology Quality Collaborative. **Effect of template reporting of brain MRIs for multiple sclerosis on report thoroughness and neurologist-rated quality: results of a prospective quality improvement project.** *J Am Coll Radiol* 2017;14:371–79.e1 CrossRef Medline
- Alessandrino F, Pichiecchio A, Mallucci G, et al. **Do MRI structured reports for multiple sclerosis contain adequate information for clinical decision making?** *AJR Am J Roentgenol* 2018;210:24–29 CrossRef Medline
- American College of Radiology. Reporting and Data Systems. <https://www.acr.org/Clinical-Resources/Reporting-and-Data-Systems>. Accessed January 5, 2018
- Goldberg-Stein S, Walter WR, Amis ES, et al. **Implementing a structured reporting initiative using a collaborative multistep approach.** *Curr Probl Diagn Radiol* 2017;46:295–99 CrossRef Medline
- Larson DB, Towbin AJ, Pryor RM, et al. **Improving consistency in radiology reporting through the use of department-wide standardized structured reporting.** *Radiology* 2013;267:240–50 CrossRef Medline
- Rovira A, Wattjes MP, Tintoré M, et al; MAGNIMS study group. **Evidence-based guidelines: MAGNIMS consensus guidelines on the use of MRI in multiple sclerosis-clinical implementation in the diagnostic process.** *Nat Rev Neurol* 2015;11:471–82 CrossRef Medline
- Filippi M, Rocca MA, Ciccarelli O, et al; MAGNIMS study group. **MRI criteria for the diagnosis of multiple sclerosis: MAGNIMS consensus guidelines.** *Lancet Neurol* 2016;15:292–303 CrossRef Medline
- Deuschmann MW, Yeung J, Bosch M, et al. **Radiologic reporting for paranasal sinus computed tomography: a multi-institutional review of content and consistency.** *Laryngoscope* 2013;123:1100–05 CrossRef Medline
- Sistrom C, Lanier L, Mancuso A. **Reporting instruction for radiology residents.** *Acad Radiol* 2004;11:76–84 CrossRef Medline
- Lin E, Powell DK, Kagetsu NJ. **Efficacy of a checklist-style structured radiology reporting template in reducing resident misses on cervical spine computed tomography examinations.** *J Digit Imaging* 2014;27:588–93 CrossRef Medline
- Weiss DL, Langlotz CP. **Structured reporting: patient care enhancement or productivity nightmare?** *Radiology* 2008;249:739–47 CrossRef Medline
- Powell DK, Silberzweig JE. **State of structured reporting in radiology: a survey.** *Acad Radiol* 2015;22:226–33 CrossRef Medline
- Faggioni L, Coppola F, Ferrari R, et al. **Usage of structured reporting in radiological practice: results from an Italian online survey.** *Eur Radiol* 2017;27:1934–43 CrossRef Medline
- Reiner BI, Knight N, Siegel EL. **Radiology reporting, past, present, and future: the radiologist's perspective.** *J Am Coll Radiol* 2007;4:313–19 CrossRef Medline
- Gunderman RB, McNeive LR. **Is structured reporting the answer?** *Radiology* 2014;273:7–9 CrossRef Medline
- Rubin DL, Kahn CE Jr. **Common data elements in radiology.** *Radiology* 2017;283:837–44 CrossRef Medline
- Chen MC, Ball RL, Yang L, et al. **Deep learning to classify radiology free-text reports.** *Radiology* 2018;286:845–52 CrossRef Medline

Clinical Value of Vascular Permeability Estimates Using Dynamic Susceptibility Contrast MRI: Improved Diagnostic Performance in Distinguishing Hypervascular Primary CNS Lymphoma from Glioblastoma

 B. Lee,  J.E. Park,  A. Bjørnerud,  J.H. Kim,  J.Y. Lee, and  H.S. Kim



ABSTRACT

BACKGROUND AND PURPOSE: A small subset of primary central nervous system lymphomas exhibits high cerebral blood volume, which is indistinguishable from that in glioblastoma on dynamic susceptibility contrast MR imaging. Our study aimed to test whether estimates of combined perfusion and vascular permeability metrics derived from DSC-MR imaging can improve the diagnostic performance in differentiating hypervascular primary central nervous system lymphoma from glioblastoma.

MATERIALS AND METHODS: A total of 119 patients (with 30 primary central nervous system lymphomas and 89 glioblastomas) exhibited hypervascular foci using the reference method of leakage-corrected CBV (reference-normalized CBV). An alternative postprocessing method used the tissue residue function to calculate vascular permeability (extraction fraction), leakage-corrected CBV, cerebral blood flow, and mean transit time. Parameters were compared using Mann-Whitney *U* tests, and the diagnostic performance to distinguish primary central nervous system lymphoma from glioblastoma was calculated using the area under the curve from the receiver operating characteristic curve and was cross-validated with bootstrapping.

RESULTS: Hypervascular primary central nervous system lymphoma showed similar leakage-corrected normalized CBV and leakage-corrected CBV compared with glioblastoma ($P > .05$); however, primary central nervous system lymphoma exhibited a significantly higher extraction fraction ($P < .001$) and CBF ($P = .01$) and shorter MTT ($P < .001$) than glioblastoma. The extraction fraction showed the highest diagnostic performance (the area under the receiver operating characteristic curve [AUC], 0.78; 95% confidence interval, 0.69–0.85) for distinguishing hypervascular primary central nervous system lymphoma from glioblastoma, with a significantly higher performance than both CBV (AUC, 0.53–0.59, largest $P = .02$) and CBF (AUC, 0.72) and MTT (AUC, 0.71).

CONCLUSIONS: Estimation of vascular permeability with DSC-MR imaging further characterizes hypervascular primary central nervous system lymphoma and improves diagnostic performance in glioblastoma differentiation.

ABBREVIATIONS: AUC = area under the receiver operating characteristic curve; CBV_{res} = leakage-corrected CBV derived using the proposed residue function-based correction method; DCE = dynamic contrast-enhanced; EF = extraction fraction; K^{trans} = contrast agent transfer constant; $nCBV_{ref}$ = leakage-corrected normalized CBV derived using the reference-correction method; PCNSL = primary central nervous system lymphoma

A common manifestation in primary central nervous system lymphoma (PCNSL) on dynamic susceptibility contrast MR imaging is low cerebral blood volume,^{1–6} which distinguishes PCNSL from glioblastoma with a diagnostic accuracy as high as 90.9%.³ This can be explained by less prominent neovasculariza-

tion and higher vascular permeability in histopathologic specimens compared with glioblastoma.^{7,8} Also, low cerebral blood volume (CBV) can be explained by the signal response in DSC-MR imaging, in which the T1-shortening effect in interstitial tissue from the extravasated contrast agent can overwhelm the T2* effect, thereby reducing apparent $CBV^{9,10}$ in PCNSLs if leakage-correction is not applied. Moreover, a small subset of PCNSLs may exhibit high CBV, comparable with the CBV of high-grade

Received January 24, 2018; accepted after revision May 1.

From the Department of Radiology (B.L.), Seoul Metropolitan Government-Seoul National University, Boramae Medical Center, Seoul, Korea; Department of Radiology and Research Institute of Radiology (J.E.P., H.S.K.), University of Ulsan College of Medicine, Asan Medical Center, Seoul, Korea; Department of Diagnostic Physics (A.B.), Rikshospitalet University Hospital, Oslo, Norway; NordicNeuroLab (J.H.K.), Seoul, Korea; and Department of Radiology (J.Y.L.), Soonchunhyang University Bucheon Hospital, Bucheon, Korea.

This research was supported by the National Research Foundation of Korea grant funded by the Korean government (Ministry of Science, ICT and Future Planning) (grant number: NRF-2017RIC1B2007258) and by a grant from the National R&D Program for Cancer Control, Ministry of Health and Welfare, Republic of Korea

(1720030). The funders had no role in the study design, data collection and analysis, decision to publish, or preparation of the article.

Please address correspondence to Ji Eun Park, MD, PhD, Department of Radiology and Research Institute of Radiology, University of Ulsan College of Medicine, Asan Medical Center, 43 Olympic-ro 88, Songpa-Gu, Seoul 05505, Korea; e-mail: jieunp@gmail.com

 Indicates open access to non-subscribers at www.ajnr.org

<http://dx.doi.org/10.3174/ajnr.A5732>

gliomas^{11,12}; this so-called hypervascular PCNSL thus becomes indistinguishable from glioblastoma using CBV.

Among the important vascular parameters of tumor vascularity and vessel permeability, PCNSL exhibits a distinctive difference in vascular permeability compared with glioblastoma. The T1-dominant leakage has been shown using dynamic contrast-enhanced (DCE) MR imaging in that substantial blood-brain barrier leakage and higher contrast agent transfer constant (K^{trans}) and K_{ep} (flux rate constant) values⁷ were observed in PCNSL than in glioblastoma. Histopathologic evaluation revealed intact vascular integrity in glioblastoma despite endothelial proliferation, whereas the PCNSL exhibited destroyed vessel architecture, thereby leading to differences in DCE parameters. Meanwhile, glioblastoma shows a dominant T2* effect from rapid and abundant accumulation of contrast in the interstitial space, which is known to be greater than the T1-shortening effect.^{7,13} The addition of DCE-MR imaging could thus potentially aid in the differentiation of hypervascular PCNSL from glioblastoma. However, the addition of this technique in addition to DSC-MR imaging would require a double contrast agent injection and additional complex image processing steps. An alternative strategy is therefore to derive both perfusion- and permeability-related metrics from the single DSC-MR imaging acquisition.

A combined perfusion/permeability analysis method by DSC-MR imaging was recently proposed by Bjørnerud et al.¹³ In this approach, both perfusion and permeability metrics are obtained by fitting appropriate kinetic models to the tissue residue function obtained by deconvolution with an automatically derived arterial input function.^{14,15} In addition to providing estimates of cerebral blood flow, mean transit time (MTT), and the extraction fraction (EF), the method also provides leakage-corrected CBV values, which are unaffected by variations in MTT.¹⁴ Given the substantial contrast agent leakage in both glioblastoma and PCNSL, CBV needs to be leakage-corrected, and the most established method of correction is the approach first proposed by Weisskoff et al¹⁶ and later tested for clinical performance by Boxerman et al.¹⁰ In this reference-correction method, extravasation is estimated by voxelwise deviation from a nonleaky reference tissue–response curve. The method is thus inherently sensitive to deviations in tumor mean transit time compared with the reference tissue.¹³ The alternative approach tested here is therefore hypothesized to have advantages over the reference method in that it provides additional perfusion- and extraction-related parameters and a more unbiased estimate of leakage-corrected CBV.

Thus, the purpose of our study was to test whether estimates of combined perfusion and permeability metrics obtained from DSC-MR imaging using the proposed method improve diagnostic performance in differentiating hypervascular PCNSL from glioblastoma.

MATERIALS AND METHODS

Patients

Our institutional (Asan Medical Center, Seoul, Korea) review board approved this retrospective study, and the requirement for informed consent was waived. From November 2006 to December 2016, we retrospectively reviewed patients from the data base

of our institution who were diagnosed with pathologically proved PCNSL ($n = 363$) and underwent DSC imaging before treatment. Inclusion criteria for PCNSL were as follows: 1) no prior history of chemotherapy, radiation therapy, or corticosteroid treatment; and 2) appropriate DSC imaging quality. Then, 2 experienced neuroradiologists (J.Y.L. and J.E.P.), who did not participate in any other image review, independently determined the vascularity of PCNSL based on the CBV maps, as visualized in the PACS, which were processed using the reference method of Weisskoff et al¹⁶ and Boxerman et al¹⁰ as part of the routine workflow. In case of a discrepancy, they discussed the issue with a senior radiologist (H.S.K., with 18 years of experience) to reach a consensus. Hypervascular PCNSLs were defined as showing higher CBV foci in the solid-enhancing tumor portion compared with the contralateral cortex. Among 363 patients with PCNSL, 30 patients (16 men; median age, 61.9 years; range, 56.5–67.3 years) were selected. As a comparison, a consecutive enrollment of patients with pathologically proved, newly diagnosed glioblastoma ($n = 105$) was performed using the radiologic data base from March 2015 to November 2016. The same criterion of visual assessment for hypervascular foci was applied, and 89 patients (54 men; mean age, 55.9 years of age; age range, 53.7–58.2 years) with glioblastoma were included in the study.

MR Imaging

All MR imaging studies were performed on a 3T unit (Achieva; Philips Healthcare, Best, the Netherlands) using an 8-channel head coil. The brain tumor imaging protocol consisted of the following sequences: T1-weighted, T2-weighted, fluid attenuated inversion recovery, diffusion-weighted, contrast-enhanced T1-weighted, and DSC-MR imaging.

A contrast-enhanced high-resolution anatomic 3D volume image was obtained using a gradient-echo T1-weighted sequence with the following parameters: TR/TE, 9.8/4.6 ms; flip angle, 10°; FOV, 256 mm; matrix, 512 × 512; and slice thickness, 1 mm with no gap. Then, DSC-MR imaging was performed using a gradient-echo, echo-planar sequence during the injection of a standard dose of 0.1 mmol/kg of intravenous gadoterate meglumine (Dotarem; Guerbet, Aulnay-sous-Bois, France) at a rate of 4 mL/s. The bolus injection of contrast material was followed by a 20-mL bolus injection of saline at the same injection rate. The DSC-MR imaging parameters were as follows: TR/TE, 1808/40 ms; flip angle, 35°; FOV, 24 cm; slice thickness/gap, 5/2 mm; matrix, 128 × 128; total acquisition time, 1 minute 54 seconds. Subsequently, a postcontrast T1-weighted 3D gradient-echo sequence was acquired with following parameters: TR/TE, 9.8/4.6 ms; flip angle, 8°; matrix, 512 × 512; slice thickness, 3 mm; FOV, 22–26 cm.

Image Postprocessing

DSC-MR imaging data were transferred to an independent workstation and processed using nordicICE (Version 4.0.6; Nordic-NeuroLab, Bergen, Norway) software. The postprocessing method is shown in Fig 1.

First, the reference method of Weisskoff et al¹⁶ and Boxerman et al¹⁰ was applied to calculate leakage-corrected CBV. Here, deconvolution is performed with respect to a “mean tissue curve,” which is assumed to be unaffected by extravasation; the mean

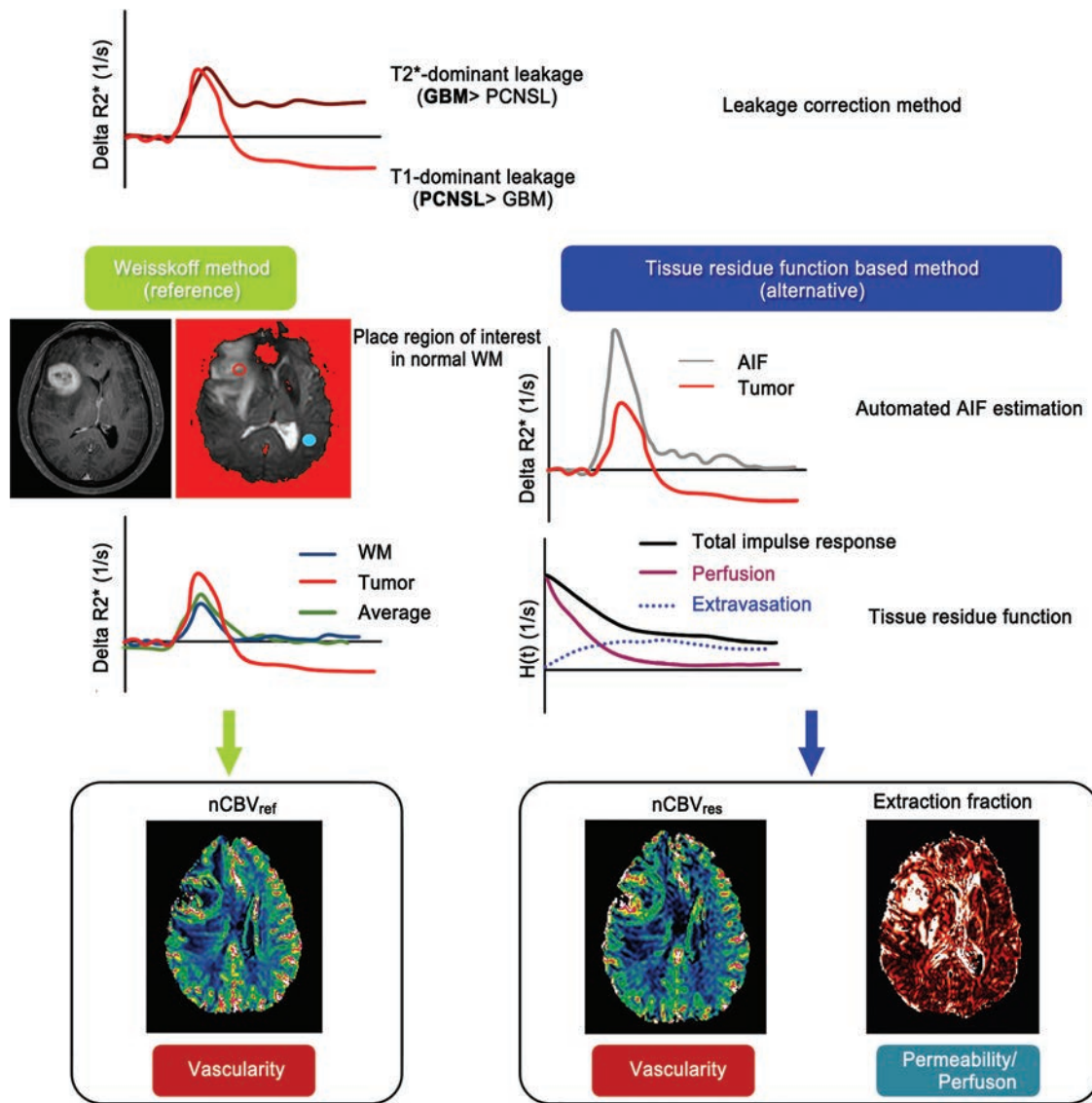


FIG 1. Workflow of the 2 presented analysis approaches: the reference Weisskoff method and the alternative tissue residue function–based method. In the reference method, an ROI is placed on the normal-appearing white matter and normalized cerebral blood volume is calculated. In the alternative method, both arterial input function and tissue residue function are estimated. The tissue residue function comprises both apparent tissue extravasation and a perfusion component. Then, leakage-corrected cerebral blood volume, reflecting tissue perfusion, and extraction fraction, reflecting the ratio of permeability/perfusion, are calculated. AIF indicates arterial input function; GBM, glioblastoma multiforme; R2*, gradient echo relaxation.

transit times of the reference tissue and leakage-corrected tissues are assumed to be identical. For CBV calculation, the dynamic signal-intensity curve was converted to a time–relaxation rate curve, and relative CBV was estimated from the area under the time–relaxation rate curve.¹³ Pixel-wise relative CBV values were then normalized relative to the mean value of the ROI placed on the contralateral normal-appearing white matter (size range, 30–50 mm²), resulting in a normalized CBV map (nCBV_{ref}). This process was performed in a fully automated batch mode, and motion-correction was applied before analysis.

Second, an alternative method, here called the residue function–based contrast leakage-correction method, was applied.¹³ This method is based on fitting of the tissue residue function to the 2-compartment uptake kinetic model.¹⁷ This provides a closed functional description of the resulting leakage-affected tis-

sue residue function.¹⁴ The general equation for the relationship between arterial input function and tissue response is then given by

$$1) \quad C_t(t) = F \times C_a(t) \otimes H(t),$$

where $C_t(t)$ and $C_a(t)$ are the tissue response and arterial input functions, respectively, \otimes is the convolution operator, and F is fractional tissue perfusion. $H(t)$ describes the probability of a tracer being present in a tissue at time t following an instantaneous tracer bolus. The product $F \times H(t) = R(t)$ can be estimated using standard deconvolution techniques, and F is then obtained from the peak height of the resulting $R(t)$.¹³ The 2-compartment uptake model accounts for continuous extravasation along the length of the capillaries but assumes negligible reflux of the contrast agent from the extracellular extravascular space to the

plasma space during the observation period.¹⁷ Then the residue function can be expressed by

$$2) \quad H(t) = \exp\left(-\frac{t}{T_p}\right) + E_x \left[1 - \exp\left(-\frac{t}{T_p}\right) \right],$$

where T_p is the plasma mean transit time and E_x is the extraction fraction describing the fraction of contrast agent that is extracted during the first passage through tissue. E_x can be expressed as the ratio

$$3) \quad E_x = K^{\text{trans}} / F,$$

where K^{trans} is the contrast agent transfer constant. $H(t)$ estimated from deconvolution was then fitted to Equation 2 using a nonlinear least-squares algorithm, giving T_p and E_x .

The capillary mean transit time is related to the time constant T_p according to

$$4) \quad MTT = \frac{T_p}{1 - E_x}.$$

From the central volume principle, the tissue volume fraction is given by $V = F \times MTT$, and capillary blood volume fraction (independent of extravasation) is thus given by

$$CBV_{\text{res}} = \varsigma \times F \frac{T_p}{1 - E_x},$$

where ς is a scaling factor (including tissue density and time unit conversion) and F is fractional tissue perfusion as defined in Equation 1, from the peak height of the residue function, as obtained from deconvolution using singular-value decomposition.¹³ Because leakage-corrected CBV (CBV_{res}) is calculated by deconvolution with (and automatically determined by) an arterial input function, no further normalization was applied here.¹³

Image Analysis

Among the DSC parameters, the parameter that relates to vascular permeability was the extraction fraction, which describes the fraction of the contrast agent that is extracted during the first passage through the tissue. We hypothesized that the EF can show discriminatory power in hypervascular PCNSL showing high CBV. Also, other macroscopic perfusion parameters of CBV, CBF, and MTT were analyzed. All parametric maps, $nCBV_{\text{ref}}$, CBV_{res} , MTT, and EF, were coregistered to the contrast-enhanced T1 images. The volume of interest was drawn section by section on the contrast-enhancing T1-weighted images using the semiautomated segmentation method with the nordicICE software. This includes all contrast-enhancing areas, excluding the vessels and necrosis. The VOI was drawn by a neuroradiologist (B.E.L., with 2 years of experience in neuroradiology) and confirmed by a senior radiologist (J.E.P., with 5 years of experience) to ensure proper segmentation. The overall value of each VOI in DSC parameters was obtained automatically with the software by summing up all values from each axial slice, which was then averaged.

Statistical Analysis

Clinical characteristics of patients with hypervascular PCNSLs and glioblastoma were compared with the χ^2 test. Values are expressed as mean \pm SD for continuous variables, and all continu-

Table 1: Clinical characteristics of the study patients^a

	PCNSL (n = 30)	Glioblastoma (n = 89)	P Value
No. of male patients	16 (46.7%)	54 (60.7%)	.48
Age (yr)	61.9 \pm 2.6	55.9 \pm 10.8	.04
Tumor volume (mL)	14.9 \pm 14.5	13.9 \pm 11.4	.70

^a Data are expressed as means for continuous variables. Numbers in parentheses are percentages.

Table 2: Comparisons of dynamic susceptibility contrast imaging parameters between hypervascular PCNSLs and glioblastomas^a

Parameter	Hypervascular		P Value
	PCNSL	Glioblastoma	
EF (%)	7.88 \pm 4.31	3.87 \pm 1.46	<.001 ^b
CBV _{res} (relative units)	2.85 \pm 1.32	2.73 \pm 1.10	.44
MTT (sec)	5.77 \pm 1.85	7.40 \pm 2.22	<.001 ^b
rCBF (relative units)	2.88 \pm 1.24	2.10 \pm 1.32	.01 ^b
nCBV _{ref} (relative units)	2.67 \pm 1.15	2.93 \pm 0.99	.14

Note:—rCBF indicates relative CBF.

^a Data are means.

^b Significant.

ous variables were assessed for normality using the Shapiro-Wilk test. Because continuous variables showed unequal variances and unequal sample sizes, the Mann-Whitney U test was performed to compare DSC parameters between hypervascular PCNSLs and glioblastoma.

Diagnostic performance to distinguish hypervascular PCNSLs from glioblastomas was calculated using receiver operating characteristic curve analysis. For receiver operating characteristic curve analysis, optimal thresholds of the imaging parameters were determined by maximizing the Youden index (sum of the sensitivity and 1-specificity values),¹⁸ which was calculated to differentiate the 2 entities. Diagnostic performance of the DSC parameters was further validated using leave-one-out cross-validation with 100-fold bootstrapping. This procedure assigns 1 subject as the validating set and the other subjects as the training set and repeats the calculation until every case has been selected as the validation set, with replacement allowed. For the comparison of the areas under the curve (AUCs) and cross-validation with bootstrap resampling, the pROC and cvTools packages in R, Version 3.3.3 (<http://www.r-project.org>) were used. P values <.05 indicated a significant difference.

RESULTS

Patient characteristics are summarized in Table 1. Patients with hypervascular PCNSL were older than those with glioblastoma (61.9 years versus 55.9 years, $P = .04$). There was no significant difference in tumor volume between the 2 groups.

Comparison of DSC Parameters between Hypervascular PCNSL and Glioblastoma

Table 2 summarizes the results of DSC parameter comparison. Hypervascular PCNSLs demonstrated significantly higher EF (7.88% \pm 4.31%) compared with glioblastomas (3.87% \pm 1.46%, $P < .001$). For CBV, there was not a significant difference between hypervascular PCNSLs and glioblastomas for either $nCBV_{\text{ref}}$ (2.67 \pm 1.15 versus 2.93 \pm 0.99; $P = .14$) or CBV_{res} (mean, 2.85 \pm 1.32 versus 2.73 \pm 1.10; $P = .44$).

Also, hypervascular PCNSLs showed shorter MTT (5.77 \pm 1.85 seconds) and higher relative CBF (2.88 \pm 1.24) compared

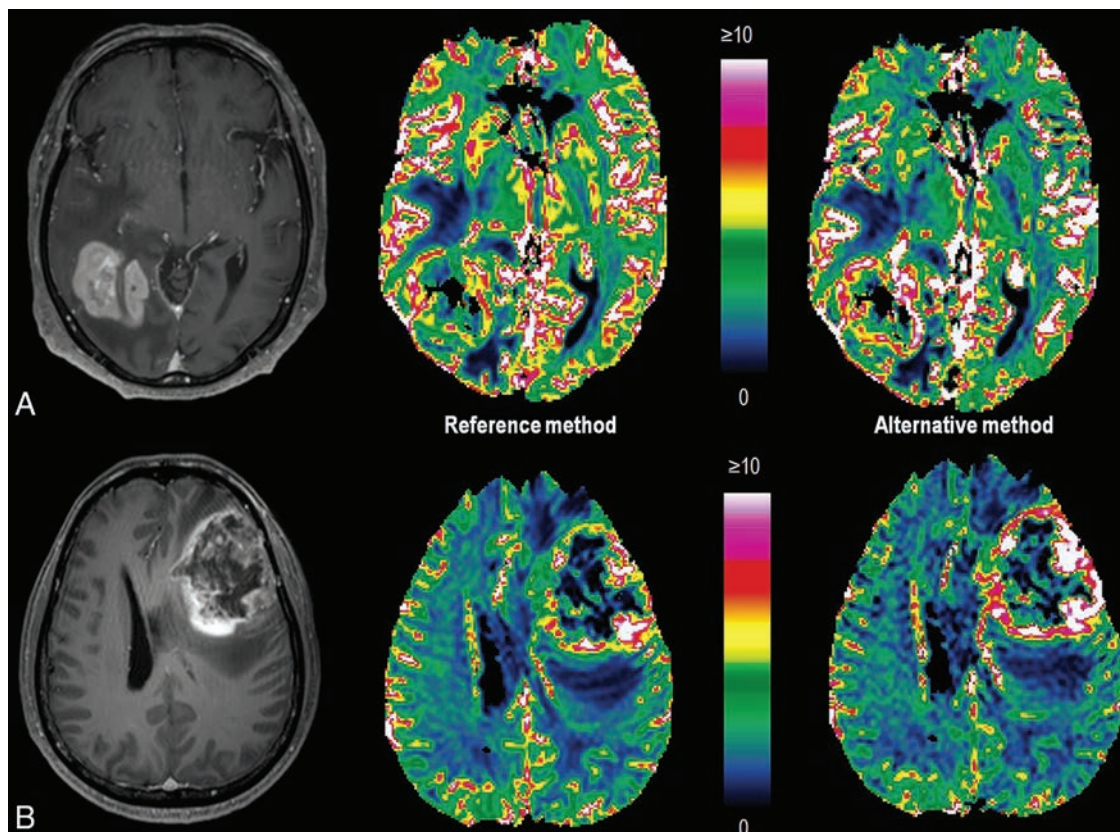


FIG 2. Comparison of cerebral blood volume between hypervascular PCNSL and glioblastoma. A, PCNSL shows homogeneous contrast enhancement and increased CBV in the right parietotemporal lobe. Note that the CBV is slightly increased in the alternative method (CBV_{res}) (right) compared with the reference method ($nCBV_{ref}$) (left). B, Glioblastoma shows heterogeneous enhancement and increased CBV in the left frontal lobe. Note that the CBV is similar with both methods.

with glioblastomas (MTT, 7.40 ± 2.22 seconds; $P < .001$; and relative CBF, 2.10 ± 1.32 , $P < 0.01$).

Figures 2 and 3 show representative DSC parameters from the patients with hypervascular PCNSL and glioblastoma.

Comparison of Diagnostic Performance Using DSC Parameters to Distinguish PCNSL from Glioblastoma

Among the DSC-MR imaging parameters tested, EF showed the highest diagnostic performance (AUC, 0.78; 95% confidence interval, 0.6–0.85) for differentiating hypervascular PCNSL from glioblastoma. The optimal threshold for EF was 6.25, with a sensitivity of 70.0%, specificity of 89.9%, and diagnostic accuracy of 84.9% (Table 3).

Diagnostic performances using CBV were generally poor, both for CBV_{res} (AUC, 0.53; 95% CI, 0.43–0.62) and $nCBV_{ref}$ (AUC, 0.59; 95% CI, 0.50–0.68) with EF significantly improving diagnostic performance compared with both CBV_{res} ($P = .002$) and $nCBV_{ref}$ ($P = .02$).

Moreover, EF indicated better diagnostic performance compared with MTT (AUC, 0.71; 95% CI, 0.62–0.79) and relative CBF (AUC, 0.72; 95% CI, 0.63–0.79), but these differences were not statistically significant.

The leave-one-out cross-validation demonstrated the same trend, in which EF showed the highest diagnostic performance in distinguishing hypervascular PCNSL from glioblastoma.

DISCUSSION

In this proof-of-concept study, we have applied a novel analysis approach to estimate both perfusion- and permeability-related metrics from a single DSC-MR imaging acquisition. About 8.3% of PCNSLs exhibited hypervascularity in our patient population, with comparable or higher CBV than in glioblastomas on DSC-MR imaging. The conditions of these patients would be indistinguishable with conventional processing methods. The main finding of the study is that estimation of the contrast agent extraction fraction using this approach can aid in the differentiation of hypervascular PCNSLs from glioblastomas. The EF showed higher diagnostic performance in differentiating hypervascular PCNSL from glioblastoma compared with all other metrics investigated (leakage-corrected CBV, MTT, and CBF). Thus, estimates of vascular permeability from DSC-MR imaging have clinical value to further characterize hypervascular PCNSLs and improve glioblastoma differentiation.

Previous DCE-MR imaging studies have shown increased vascular permeability, reflected in higher K^{trans} in PCNSLs, suggesting a greater degree of blood-brain barrier breakdown.^{6,7} Poor neovascularization and angiocentric growth patterns in PCNSL compared with glioblastoma result in increased permeability^{19,20} and support the observed increased EF in hypervascular PCNSL. Because the extraction fraction reflects the ratio of permeability to flow, the measured elevated EF in hypervascular PCNSL com-

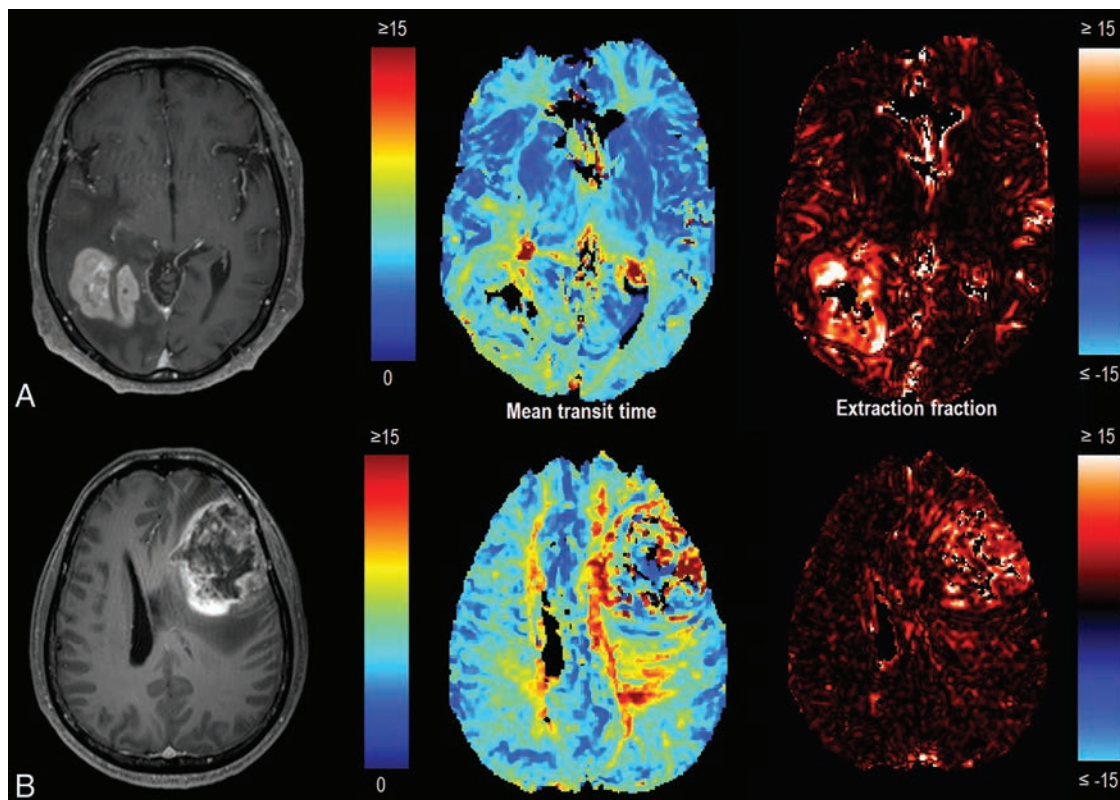


FIG 3. Comparison of the extraction fraction and mean transit time between hypervascular PCNSL and glioblastoma. *A*, PCNSL shows low MTT and a high extraction fraction. *B*, Glioblastoma shows high MTT and a low extraction fraction. There are distinct differences in the EF and MTT between the 2 tumors.

Table 3: Comparison of diagnostic performance among DSC parameters in distinguishing hypervascular PCNSL from glioblastoma

Parameter	AUC	95% CI	Standard Error	Optimal Threshold	Cross-Validated AUC
EF	0.78	0.69–0.85	0.06	6.25	0.76
CBV _{res}	0.53	0.43–0.62	0.06	3.71	0.49
MTT	0.71	0.62–0.79	0.05	6.81	0.73
rCBF	0.72	0.63–0.79	0.05	1.86	0.72
nCBV _{ref}	0.59	0.50–0.68	0.06	1.90	0.55

Note:—rCBF indicates relative CBF.

pared with glioblastoma suggests that permeability increases relatively more than perfusion in these tumors. EF is <10% in both tumor types, suggesting that K^{trans} is a permeability-limited parameter and not perfusion-limited in both gliomas and PCNSLs.²¹

The alternative method separates T1- or T2*-dominant leakage using the tissue residue function, whereby T1-dominant leakage results in a negative tail and T2*-dominant leakage results in a positive tail^{13,14} in the residue function. The reference method was originally developed to only correct for T1-dominant leakage, but a modified version of the algorithm was used here, which also corrects for T2*-dominant leakage.¹³ Regardless of the correction approach used, 1 inherent limitation of using DSC-MR imaging to derive permeability parameters is that the dominant relaxation effect following contrast agent extravasation is poorly defined and unpredictable. If a combination of T1 and T2* effects are present, then permeability will be underestimated because the 2 relaxation effects will have an opposing influence on the magnitude of the resulting permeability parameters. To obtain correct permeability

estimates from DSC-MR imaging, one would therefore ideally like to completely eliminate T1 effects following extravasation. Previous studies have shown that T1 effects can be reduced by injecting a small prebolus contrast agent to saturate T1 effects or by reducing the flip angle of the DSC sequence.²²

In the current study, a small flip angle (35°) method was used to reduce the sensitivity to the T1 leakage effect compared with the large flip angle T1-sensitive method. On the other hand, a preload bolus method is a widely accepted protocol to minimize the initial tissue T1 effects; the only concern for a prebolus method is a residual baseline level of contrast agent with a T2* effect,²³ which may increase relative CBV.²⁴ Along with permeability differences, hypervascular PCNSLs demonstrated shorter MTT and higher CBF compared with glioblastomas. These findings differ from those in previous studies, which either demonstrated no difference in CBF between PCNSL and high-grade glioma²⁵ or higher CBF in glioblastoma compared with PCNSL.²⁶ This difference may come from a unique population of hypervascular PCNSLs because most manifest a lower CBV than glioblastomas.

Our results further illustrate the inherent biologic differences in PCNSL relative to glioblastoma; however, hypervascular PCNSL presents as tumor infiltration around pre-existing vessels, which may result in lower MTT and higher CBF compared with glioblastoma.⁸ Conversely, glioblastomas with heterogeneous microvascular density may result in increased MTT.²⁷ Higher MTT and lower CBF in glioblastomas can be explained by previous pathologic studies revealing the chaotic architecture of the neovessels with arteriovenular shunts and compromised capillary

paths²⁸ that increase capillary transit time and decrease tissue perfusion²⁹ in the contrast-enhancing tumor portion. These hemodynamic parameters are difficult to obtain from a reference leakage-correction method¹⁶ because the model assumes that mean transit time and bolus arrival time are the same in tumor and normal tissues.^{13,15}

Our study is limited in that it used a small amount of patient data, especially regarding hypervascular PCNSLs. Second, direct correlations are lacking between perfusion parameters and histologic features such as microvessel density and endothelial ultrastructure. Third, permeability parameters and the relative contributions of T1- versus T2*-dominant leakage effects in the different tumor subgroups should be investigated in a separate study to validate their significance. Because the estimation of perfusion (F) is theoretically independent of leakage,¹³ varying contributions of the 2 relaxation effects postextravasation would directly influence the magnitude of the resulting EF value. Fourth, previous studies in patients with glioblastoma have indicated a nonlinear relationship between the “true” K^{trans} obtained from DCE-MR imaging compared with that obtained by DSC-MR imaging,^{13,30} which is probably due to the mixed contributions from the 2 relaxation effects in DSC-MR imaging as described above. A previous study showed that the microvessel area indicated by histopathology showed moderate correlation with the phase-derived vascular input function obtained from DCE-MR imaging and non-normalized blood volume from DSC-MR imaging³¹; but this correlation was not tested with the new processing method. Therefore, the microvascular permeability as derived from DSC-MR imaging should be validated against more established DCE-MR imaging-based approaches, and further studies are warranted before application of the new processing method in a clinical setting.

CONCLUSIONS

By means of a novel analysis approach, estimates of combined perfusion- and vascular permeability-related metrics were obtained from a single DSC-MR imaging acquisition. The contrast agent extraction fraction derived by this method showed improved diagnostic performance in differentiating hypervascular PCNSL from glioblastoma compared with the conventional CBV-based analysis. The analysis approach can be achieved with a single dose of gadolinium-based contrast and can be implemented in a clinical setting.

Disclosures: Atle Bjørnerud—UNRELATED: Consultancy: NordicNeuroLab AS, Comments: software development; Patents (Planned, Pending or Issued): Oslo University Hospital. Comments: patent applications relating to perfusion analysis methods*; Royalties: NordicNeuroLab AS, Comments: royalties from patents*; Stock/Stock Options: NordicNeuroLab AS. *Money paid to the institution.

REFERENCES

- Hartmann M, Heiland S, Harting I, et al. **Distinguishing of primary cerebral lymphoma from high-grade glioma with perfusion-weighted magnetic resonance imaging.** *Neurosci Lett* 2003;338:119–22 CrossRef Medline
- Lee IH, Kim ST, Kim HJ, et al. **Analysis of perfusion weighted image of CNS lymphoma.** *Eur J Radiol* 2010;76:48–51 CrossRef Medline
- Xu W, Wang Q, Shao A, et al. **The performance of MR perfusion-weighted imaging for the differentiation of high-grade glioma from primary central nervous system lymphoma: a systematic review and meta-analysis.** *PLoS One* 2017;12:e0173430 CrossRef Medline
- Liang R, Li M, Wang X, et al. **Role of rCBV values derived from dynamic susceptibility contrast-enhanced magnetic resonance imaging in differentiating CNS lymphoma from high grade glioma: a meta-analysis.** *Int J Clin Exp Med* 2014;7:5573–77 Medline Medline
- Kremer S, Grand S, Remy C, et al. **Cerebral blood volume mapping by MR imaging in the initial evaluation of brain tumors.** *J Neuroradiol* 2002;29:105–13 Medline
- Lu S, Gao Q, Yu J, et al. **Utility of dynamic contrast-enhanced magnetic resonance imaging for differentiating glioblastoma, primary central nervous system lymphoma and brain metastatic tumor.** *Eur J Radiol* 2016;85:1722–27 CrossRef Medline
- Kickingederer P, Sahm F, Wiestler B, et al. **Evaluation of microvascular permeability with dynamic contrast-enhanced MRI for the differentiation of primary CNS lymphoma and glioblastoma: radiologic-pathologic correlation.** *AJNR Am J Neuroradiol* 2014;35:1503–08 CrossRef Medline
- Koeller KK, Smirniotopoulos JG, Jones RV. **Primary central nervous system lymphoma: radiologic-pathologic correlation.** *Radiographics* 1997;17:1497–526 CrossRef Medline
- Zaharchuk G. **Theoretical basis of hemodynamic MR imaging techniques to measure cerebral blood volume, cerebral blood flow, and permeability.** *AJNR Am J Neuroradiol* 2007;28:1850–58 CrossRef Medline
- Boxerman J, Schmainda K, Weisskoff R. **Relative cerebral blood volume maps corrected for contrast agent extravasation significantly correlate with glioma tumor grade, whereas uncorrected maps do not.** *AJNR Am J Neuroradiol* 2006;27:859–67 Medline
- Dandois V, De Coene B, Laloux P, et al. **Increased relative cerebral blood volume (rCBV) in brain lymphoma.** *J Neuroradiol* 2011;38:191–93 CrossRef Medline
- Sugahara T, Korogi Y, Shigematsu Y, et al. **Perfusion-sensitive MRI of cerebral lymphomas: a preliminary report.** *J Comput Assist Tomogr* 1999;23:232–37 CrossRef Medline
- Bjørnerud A, Sorensen AG, Mouridsen K, et al. **T1- and T2*-dominant extravasation correction in DSC-MRI: part I, theoretical considerations and implications for assessment of tumor hemodynamic properties.** *J Cereb Blood Flow Metab* 2011;31:2041–53 CrossRef Medline
- Bjørnerud A, Emblem K. **Estimation of contrast agent extravasation from the tissue residue function: application to tumor perfusion imaging.** In: *Proceedings of the Scientific Meeting and Exhibition of the International Society of Magnetic Resonance in Medicine*, Honolulu, Hawaii. April 18–24, 2009
- Emblem KE, Bjørnerud A, Mouridsen K, et al. **T(1)- and T(2)(*)-dominant extravasation correction in DSC-MRI: part II—predicting patient outcome after a single dose of cediranib in recurrent glioblastoma patients.** *J Cereb Blood Flow Metab* 2011;31:2054–64 CrossRef Medline
- Weisskoff RM BJ, Sorensen AG, Kulke ST, et al. **Simultaneous blood volume and permeability mapping using a single Gd-based contrast injection.** In: *Proceedings of the Annual Meeting of the Society of Magnetic Resonance*, San Francisco, California. August 6–12, 1994
- Sourbron S, Ingrisch M, Siefert A, et al. **Quantification of cerebral blood flow, cerebral blood volume, and blood-brain-barrier leakage with DCE-MRI.** *Magn Reson Med* 2009;62:205–17 CrossRef Medline
- Park SH, Goo JM, Jo CH. **Receiver operating characteristic (ROC) curve: practical review for radiologists.** *Korean J Radiol* 2004;5:11–18 CrossRef Medline
- Molnár PP, O'Neill BP, Scheithauer BW, et al. **The blood-brain barrier in primary CNS lymphomas: ultrastructural evidence of endothelial cell death.** *Neuro Oncol* 1999;1:89–100 Medline
- Jain R. **Perfusion CT imaging of brain tumors: an overview.** *AJNR Am J Neuroradiol* 2011;32:1570–77 CrossRef Medline
- Tofts PS, Brix G, Buckley DL, et al. **Estimating kinetic parameters from dynamic contrast-enhanced T(1)-weighted MRI of a diffus-**

- able tracer: standardized quantities and symbols. *J Magn Reson Imaging* 1999;10:223–32 CrossRef Medline
22. Boxerman JL, Paulson ES, Prah MA, et al. **The effect of pulse sequence parameters and contrast agent dose on percentage signal recovery in DSC-MRI: implications for clinical applications.** *AJNR Am J Neuroradiol* 2013;34:1364–69 CrossRef Medline
 23. Paulson ES, Schmainda KM. **Comparison of dynamic susceptibility-weighted contrast-enhanced MR methods: recommendations for measuring relative cerebral blood volume in brain tumors.** *Radiology* 2008;249:601–13 CrossRef Medline
 24. Levin JM, Kaufman MJ, Ross MH, et al. **Sequential dynamic susceptibility contrast MR experiments in human brain: residual contrast agent effect, steady state, and hemodynamic perturbation.** *Magn Reson Med* 1995;34:655–63 CrossRef Medline
 25. Schramm P, Xyda A, Klotz E, et al. **Dynamic CT perfusion imaging of intra-axial brain tumours: differentiation of high-grade gliomas from primary CNS lymphomas.** *Eur Radiol* 2010;20:2482–90 CrossRef Medline
 26. Onishi S, Kajiwara Y, Takayasu T, et al. **NIMG-2: analysis of perfusion CT parameters for differentiating among glioblastoma, primary central nervous system lymphoma and brain metastasis.** *Neuro-Oncology* 2017;19:vi146 CrossRef
 27. Ulmer S, Liess C, Otto N, et al. **The mean transit time (MTT) reflects the amount of blood brain barrier breakdown due to microvascular proliferation in glioblastoma demonstrated by perfusion weighted imaging (PWI).**
 28. Tietze A, Mouridsen K, Lassen-Ramshad Y, et al. **Perfusion MRI derived indices of microvascular shunting and flow control correlate with tumor grade and outcome in patients with cerebral glioma.** *PLoS One* 2015;10:e0123044 CrossRef Medline
 29. Mouridsen K, Hansen MB, Østergaard L, et al. **Reliable estimation of capillary transit time distributions using DSC-MRI.** *J Cereb Blood Flow Metab* 2014;34:1511–21 CrossRef Medline
 30. Skinner JT, Moots PL, Ayers GD, et al. **On the Use of DSC-MRI for measuring vascular permeability.** *AJNR Am J Neuroradiol* 2016;37:80–87 CrossRef Medline
 31. Nguyen T, Cron G, Bezzina K, et al. **Correlation of tumor immunohistochemistry with dynamic contrast-enhanced and DSC-MRI parameters in patients with gliomas.** *AJNR Am J Neuroradiol* 2016;37:2217–23 CrossRef Medline

Added Value of Spectroscopy to Perfusion MRI in the Differential Diagnostic Performance of Common Malignant Brain Tumors

A. Vallée, C. Guillevin, M. Wager, V. Delwail, R. Guillevin, and J.-N. Vallée



ABSTRACT

BACKGROUND AND PURPOSE: Perfusion and spectroscopic MR imaging provide noninvasive physiologic and metabolic characterization of tissues, which can help in differentiating brain tumors. We investigated the diagnostic role of perfusion and spectroscopic MR imaging using individual and combined classifiers of these modalities and assessed the added performance value that spectroscopy can provide to perfusion using optimal combined classifiers that have the highest differential diagnostic performance to discriminate lymphomas, glioblastomas, and metastases.

MATERIALS AND METHODS: From January 2013 to January 2016, fifty-five consecutive patients with histopathologically proved lymphomas, glioblastomas, and metastases were included after undergoing MR imaging. The perfusion parameters (maximum relative CBV, maximum percentage of signal intensity recovery) and spectroscopic concentration ratios (lactate/Cr, Cho/NAA, Cho/Cr, and lipids/Cr) were analyzed individually and in optimal combinations. Differences among tumor groups, differential diagnostic performance, and differences in discriminatory performance of models with quantification of the added performance value of spectroscopy to perfusion were tested using 1-way ANOVA models, receiver operating characteristic analysis, and comparisons between receiver operating characteristic analysis curves using a bivariate χ^2 , respectively.

RESULTS: The highest differential diagnostic performance was obtained with the following combined classifiers: maximum percentage of signal intensity recovery–Cho/NAA to discriminate lymphomas from glioblastomas and metastases, significantly increasing the sensitivity from 82.1% to 95.7%; relative CBV–Cho/NAA to discriminate glioblastomas from lymphomas and metastases, significantly increasing the specificity from 92.7% to 100%; and maximum percentage of signal intensity recovery–lactate/Cr and maximum percentage of signal intensity recovery–Cho/Cr to discriminate metastases from lymphomas and glioblastomas, significantly increasing the specificity from 83.3% to 97.0% and 100%, respectively.

CONCLUSIONS: Spectroscopy yielded an added performance value to perfusion using optimal combined classifiers of these modalities, significantly increasing the differential diagnostic performances for these common brain tumors.

ABBREVIATIONS: AUC = area under the ROC curve; $\Delta R2^*$ = relaxation rate; GBM = high-grade gliomas (glioblastomas); Lac = lactate; Lip = lipids; max = maximum; min = minimum; PCNSL = primary central nervous system lymphoma; PRESS = point-resolved spectroscopic sequence; PSR = percentage of signal intensity recovery; rCBV = relative cerebral blood volume; ROC = receiver operating characteristic

Primary central nervous system lymphomas (PCNSLs), glioblastomas (GBMs), and metastases are the most commonly identified brain tumors in adults. Management of these malig-

nancies can differ substantially depending on lesion type; however, their preoperative characterization and differentiation can be challenging due to the overlapping of their imaging characteristics.

Conventional MR imaging is very limited in making the distinction. Contrast enhancement on T1-weighted images is dependent on blood-brain barrier disruption and neovascularity regardless of the pathologies. FLAIR MR imaging can depict a large

Received September 6, 2017; accepted after revision May 1, 2018.

From the Délégation à la Recherche Clinique et à l'innovation (A.V.), Hôpital Foch, 92150 Suresnes, France; DACTIM-MIS, UMR CNRS 7348 (A.V., C.G., R.G., J.-N.V.), Laboratory of Mathematics and Applications (LMA), University of Poitiers, 86000 Poitiers, France; Institut National de la Santé et de la Recherche Médicale (INSERM) U-1084 (M.W.), Experimental and Clinical Neurosciences Laboratory, University of Poitiers, 86000 Poitiers, France; Departments of Radiology (C.G., R.G.), Neurosurgery (M.W.), and Haematology (V.D.), Poitiers University Hospital, University of Poitiers, 86000 Poitiers, France; and Department of Diagnostic and Interventional Neuroradiology (J.-N.V.), Amiens University Hospital, University Picardie Jules Verne of Amiens, 80054 Amiens, France.

Please address correspondence to J.-N. Vallée, MD, PhD, Department of Diagnostic and Interventional Neuroradiology, Amiens University Hospital, University Picardie Jules Verne of Amiens (UPJV), 80054 Amiens, France; UMR CNRS 7348, Laboratory of Mathematics and Applications, University of Poitiers, Poitiers, France; e-mail: valleejn@gmail.com

<http://dx.doi.org/10.3174/ajnr.A5725>

fraction of the tumor but lacks specificity.¹ Advanced MR imaging modalities such as perfusion-weighted imaging and proton MR spectroscopy (¹H-MR spectroscopy) provide a physiologic and metabolic noninvasive characterization of brain tumors, which can help in the differentiation of these lesions.^{2,3} According to a recent meta-analysis, the apparent diffusion coefficient measured in diffusion MR imaging, in particular ADC_{mean}, correlated with glioma cellularity, but too weakly with lymphoma to be used as a biomarker of cellularity in this entity and with no evident data for metastases provided.⁴

The histopathologic differences in the tumor capillary structure are the origin of the variability in perfusion MR imaging, which may provide the basis for a possible differential diagnosis. PWI provides hemodynamic parameter measurements such as the relative cerebral blood volume (rCBV) as an index of microvasculature and neoangiogenesis correlated with the aggressiveness and malignancy of tumors, and the percentage of signal intensity recovery (PSR) as an index of the tissue capillary permeability.^{3,5} rCBV in PCNSLs is considerably lower than in GBMs and metastases; however, there is an overlap in rCBV values with regard to GBMs and metastases.^{3,6,7} Tumor rCBV measurements reflect gross tumor blood volume but do not provide any information regarding capillary permeability.⁸ Mangla et al³ reported that PSR appears to be a useful parameter to differentiate PCNSLs from GBMs and metastases, or metastases from PCNSLs and GBMs, but not GBMs from PCNSLs and metastases.

¹H-MR spectroscopy allows in vivo detection and characterization of brain metabolites, such as choline, a cellular membrane turnover marker involved in the metabolism of the phospholipid membrane structure (phosphatidylcholine and sphingomyelin) reflecting an increased need for membrane renewal due to alteration/destruction or membrane proliferation; *N*-acetylaspartate, a quantitative neuronal viability marker, its decrease reflecting an indirect measure of neuronal loss or degradation; creatine, a marker of intracellular energetic metabolism; lactate (Lac), usually undetectable by MR imaging in the healthy brain, its presence reflecting a product of anaerobic glycolysis; mobile lipids (Lip), absent in the normal brain, their concentration indicating the extent of necrosis and apoptosis. Changes in these brain metabolites often precede the structural abnormalities of the tumor. By means of characteristic changes in the metabolite profile in certain tumors compared with the normal CNS profile, ¹H-MR spectroscopy has the potential to provide a biochemical differential diagnosis. Thus, ¹H-MR spectroscopy could yield added value to perfusion MR imaging, increasing the reliability of the preoperative differentiation of PCNSLs, GBMs, and metastases.

We investigated the usefulness of the diagnostic role of perfusion and spectroscopic MR imaging using individual and combined classifiers of these modalities based on physiologic and biometabolic differences of tumors. Then, we assessed and quantified the added performance value that spectroscopy can provide to perfusion using optimal combined classifiers that have the highest differential diagnostic performance to discriminate lymphomas, glioblastomas, and metastases.

MATERIALS AND METHODS

Patients

Sixty-one consecutive patients with histopathologically proved PCNSL, GBM, or solitary metastases were evaluated from January 2013 to January 2016, after obtaining prior approval of the institutional review board (CHU Poitiers, France) and informed consent of each patient. Six patients were excluded because of artifacts on perfusion data (3 patients), uninterpretable spectral data (2 patients), and an immunocompromised condition (1 patient). Thus, we included 55 patients (23 women, 32 men; mean age, 63.8 ± 13.7 years); 28 previously untreated immunocompetent patients with PCNSL, 14 with GBM, and 13 with solitary metastases (5 originating from lung; 3, from breast; 2, from thyroid; 2, from melanoma; 1, from the esophagus) were analyzed.

Imaging Protocol

Conventional MR Imaging. All patients underwent an MR imaging examination according to the same protocol using a whole-body system (Verio 3T; Siemens, Erlangen, Germany) and the following features: sagittal 3D-FLAIR (TR/TE/TI = 5000/402/1800 ms, FOV = 260 mm, matrix = 156 × 128), axial 3D-T1 postcontrast (TR/TE/TI = 1900/2.93/900 ms, flip angle = 9°, FOV = 255 mm, matrix = 256 × 256), and axial postcontrast T1-weighted FSE imaging (TR/TE = 308/2.48 ms, FOV = 220 mm, matrix = 272 × 352).

PWI. Dynamic-susceptibility perfusion contrast-enhanced T2*-weighted gradient-echo echo-planar images (TR/TE = 1980/30 ms, 4.0-mm thick sections, 0.8-mm gap, FOV = 220 mm, matrix = 128 × 128, flip angle = 90°, phases = 75) were acquired during the first pass of a standard-dose (0.1 mmol/Kg) bolus of gadoteric acid at 0.5 mmol/mL. Contrast material was injected at a rate of 6 mL/s for all patients, with a 10-second delay. From 7 to 12 sections were selected on T2 FLAIR-weighted images, depending on the volume of the tumor.

¹H-MR Spectroscopy. All the spectroscopic data were obtained after intravenous administration of gadoteric acid using a point-resolved spectroscopic sequence (PRESS: TR = 1500 ms/TEs = 35/135 ms, 156 scans). CBV cartographies derived from PWI processing were used to position the excitation box sized from 10 to 15 mm in all 3 dimensions, depending on the volume of the lesion. Voxels were positioned within the ROI that allowed the maximal value of rCBV. Another equally sized voxel was symmetrically positioned in the healthy contralateral parenchyma. We selected the VOI to include the lesion and areas of healthy contralateral brain parenchyma while avoiding the scalp, skull, and sinuses.

Postprocessing

rCBV measurements from DSC MR imaging data were performed using syngo.via software (Siemens). During the first pass of a bolus of contrast agent, T2*-weighted signal intensity decreased. The change in the relaxation rate ($\Delta R2^*$, ie, the change in the reciprocal of T2*) can be calculated from the signal intensity as follows: $\Delta R2^*(t) = \{-\ln[S(t)/S_0]\}/TE$, where $S(t)$ is the signal intensity at time t , and S_0 the unenhanced signal intensity. $\Delta R2^*$ is proportional to the concentration of contrast agent in the tissue, and CBV is proportional to the area under the curve of $\Delta R2^*(t)$,

provided there is no recirculation or leakage of contrast agent. In general, these assumptions are violated, but the effects can be reduced by fitting a γ -variate function to the measured $\Delta R2^*$ curve. This function approximates the curve that would have been obtained without recirculation or leakage. CBV can then be estimated from the area under the fitted curve rather than from the original data. ROIs of standardized size (4.5-mm radius) were placed in regions of maximal CBV on CBV color overlay maps for targeting and were referenced to the symmetrically contralateral parenchyma (normal white or gray matter) for the calculation of relative maximal CBV, $rCBV_{max} = CBV_{lesion}/CBV_{contralateral}$. Volume averaging with the blood vessels was carefully avoided, confounding factors in the CBV analysis were minimized, and the size of the ROIs was kept constant. Because the maximally perfused regions of gliomas are suggestive of aggressiveness,^{3,5,6} we analyzed the PWI data from the maximally perfused regions of the tumors by drawing from 5 to 27 ROIs to cover the entire tumor volume, depending on the tumors.

PSR measurements were performed using syngo.via software. ROIs were drawn on the gray-scale perfusion maps overlaid on contrast-enhancing tumor on T1-weighted images. An ROI of 30–40 mm² was moved within the tumor area to look for the highest and lowest recoveries on T2*-weighted signal intensity curves and was selected for maximum and minimum PSR, respectively. For normalization, an ROI of approximately 30–50 mm² was also placed in the symmetrically contralateral parenchyma, and ratios were obtained. The PSR was calculated as described by Cha et al:⁷ $PSR = 100\% \times (S_1 - S_{min}) / (S_0 - S_{min})$, where S_1 , S_0 , and S_{min} are postcontrast, precontrast, and minimum T2*-weighted signal intensities, respectively.

¹H-MR spectroscopy raw data were analyzed with jMRUI (<http://www.jmrui.eu/>)⁹ postprocessing software using the AMARES algorithm¹⁰ for accurate relative quantification. The data were normalized using the contralateral creatine resonance signal from the symmetric healthy parenchyma. Cho (3.22 ppm), NAA (2.02 ppm), Cr (3.02 ppm), and Lac (1.33 ppm) resonances were assessed at an intermediate TE (135 ms), and free Lip (0.9–1.3 ppm) resonances were assessed at a short TE (35 ms). Both long TE and short TE spectra were used because the lactate doublet was inverted at 13-ms TE due to the J-coupling, thus allowing the separation and the correct quantification of lactate and lipids.

The structural image-processing tool FSL (<http://www.fmrib.ox.ac.uk/fsl>) was used to estimate the gray matter, white matter, and CSF content of each voxel and to correct for the partial volume effects on the metabolite data. Brain tissue images were extracted by removing the outer skull and scalp surfaces using the FSL Brain Extraction Tool (<http://fsl.fmrib.ox.ac.uk/fsl/fslwiki/BET>).¹¹ Finally, the FAST/FIRST tool (<https://fsl.fmrib.ox.ac.uk/fsl/fslwiki/FAST>; <http://fsl.fmrib.ox.ac.uk/fsl/fslwiki/FIRST>) was used to calculate the segmented tissue percentage in the VOI. Coregistration between the spectroscopic VOI and the segmented image was performed with a user-developed Matlab program (MathWorks, Natick, Massachusetts).

Statistical Analysis

The variables assessed included tumor groups (PCNSLs, GBMs, metastases), maximum perfusion parameters ($rCBV_{max}$,

PSR_{max}), and spectroscopic concentration ratios (Lac/Cr, Cho/NAA, Cho/Cr, Lip/Cr). Differences among groups were tested using 1-way ANOVA and the Fisher PLSD post hoc test (Fisher's Protected Least Significant Difference) (SAS 9.1; SAS Institute, Cary, North Carolina).

ROC analysis was performed for individual classifiers of spectroscopy and perfusion regarding their predictive ability to discriminate these tumors. For each classifier, the ability of the logistic regression models to allow discrimination was quantified by the area under the ROC curve (AUC). The maximum Youden index, $J = \max_c [Se(c) + Sp(c) - 1]$, was chosen to determine the optimal decision thresholds (c) for the discrimination.

Next, combined ROC analysis was performed for the classifiers resulting from the different combinations between a spectroscopy classifier and a perfusion classifier using the Logistic Regression Multivariate Effect Likelihood Ratio Tests¹² (SAS 9.1) to assess the discriminatory performance (AUC) for the differential diagnosis of these tumors. The classifiers used for the combination of classifiers were identified among those previously screened with the ROC analysis for individual classifiers of spectroscopy and perfusion with a level of $P < .05$.

Differences between the AUC values of ROC curves were tested for significance using a bivariate χ^2 test (SAS 9.1) to determine the differences among the predictive abilities in discriminatory performance (AUC) of classifiers (individual and combined) for the differential diagnosis of PCNSLs, GBMs, and metastases and to quantify the added performance value of spectroscopy to perfusion.

Mean values were expressed with their SDs. Significance was $P < .05$.

RESULTS

Perfusion and Spectroscopy Parameters and Signal Intensity Curves

Mean values of perfusion parameters ($rCBV$, PSR_{max}) and spectroscopic concentration ratios (Cho/Cr, Cho/NAA, Lac/Cr, Lip/Cr) in the tumor groups PCNSL, GBM, and metastases are shown in Table 1 and Fig 1; and signal intensity curves and cerebral MR imaging maps with postprocessing, in Fig 2. One-way ANOVA of the mean and SD derived for the perfusion and spectroscopy parameters showed significant differences among the 3 groups of lesions for all parameters studied. The Fisher PLSD test for pairwise comparisons demonstrated, in PCNSLs versus GBMs and metastases, significantly higher values of PSR_{max} ($P = .001$, respectively) and lower values of Cho/NAA ($P = .001$); in GBMs versus PCNSLs and metastases, significantly higher values of $rCBV$ ($P = .001$, respectively) and Cho/NAA ($P = .001$); and in metastases versus PCNSLs and GBMs, significantly lower values of PSR_{max} ($P = .001$, .02, respectively), Cho/Cr ($P = .002$, .03, respectively), and Lac/Cr ($P = .001$, .01, respectively) and higher values of Lip/Cr ($P = .04$, .03, respectively) (Table 1 and Fig 1).

Accuracy of Individual Classifiers

The AUCs obtained from ROC curves and decision thresholds for individual classifiers of perfusion and spectroscopy are shown in Table 2. The accuracy of the classifiers Cho/NAA and PSR_{max} was not significantly different (AUC = 0.835, 0.940, $P = .82$) and was

Table 1: Mean values of perfusion parameters and spectroscopic concentration ratios in differentiating brain tumors

Oncotype of Lesions/ P and F Values	rCBV	PSR _{max}	Cho/Cr	Cho/NAA	Lac/Cr	Lip/Cr
PCNSL	2.126 ± 0.335	106.857 ± 19.165	3.092 ± 1.752	2.007 ± 1.613	2.529 ± 2.334	3.379 ± 4.522
GBM	3.573 ± 0.851	74.857 ± 7.564	2.723 ± 0.732	3.703 ± 0.878	2.297 ± 1.102	2.865 ± 3.371
Metastases	2.445 ± 0.805	60.545 ± 7.634	1.568 ± 0.282	—	0.186 ± 0.336	6.346 ± 3.533
P (ANOVA)	<.001 ^a	<.001 ^a	.009 ^a	.001 ^a	.003 ^a	.07
F (ANOVA)	26.083	45.876	5.208	13.024	6.680	2.712
P PCNSL vs GBM	<.001 ^a	<.001 ^a	.40	.001 ^a	.73	.70
P PCNSL vs metastases	.15	<.001 ^a	.002 ^a	—	.001 ^a	.04 ^a
P GBM vs metastases	<.001 ^a	.02 ^a	.03 ^a	—	.001 ^a	.03 ^a

Note: — NAA was undetectable at 2.02 ppm in metastases.

^a Significant.

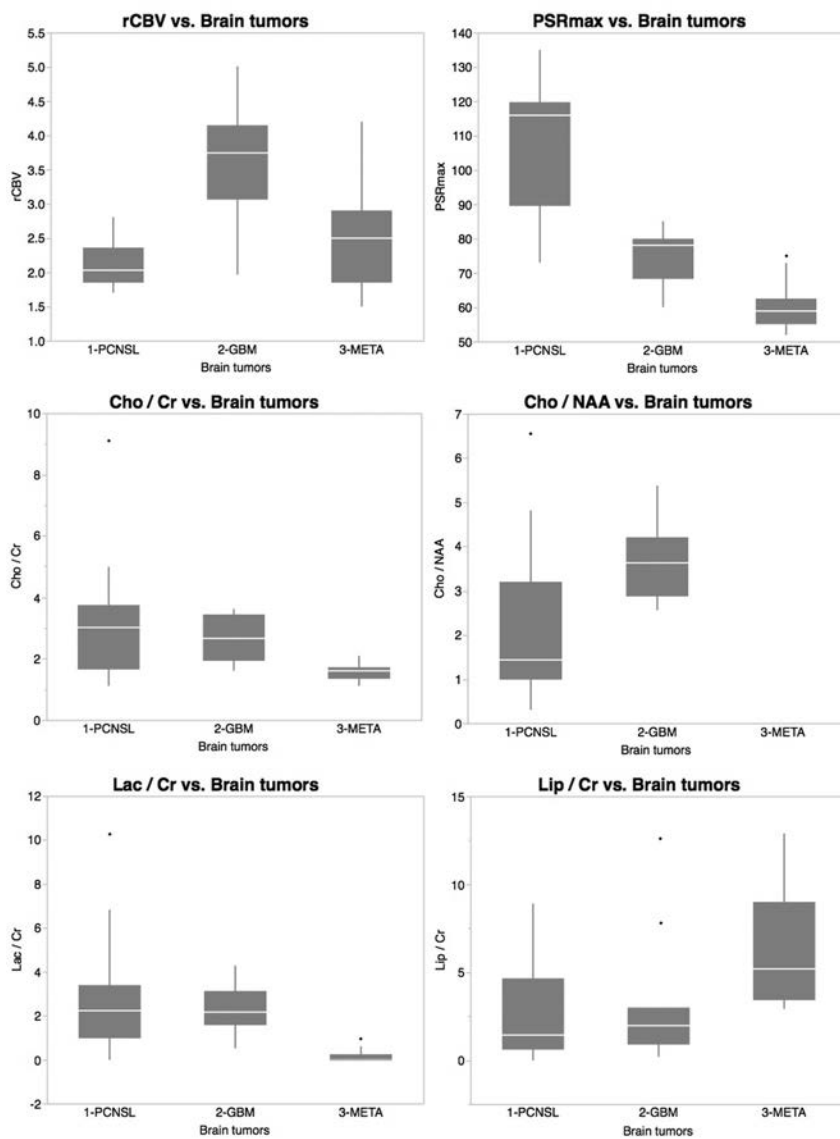


FIG 1. Boxplots of perfusion parameters and spectroscopic concentration ratios from MR imaging in differentiating brain tumors.

higher than that of other MR imaging classifiers ($P < .05$) to differentiate PCNSLs from GBMs and metastases. The accuracy of the classifiers Cho/NAA and rCBV was not significantly different ($AUC = 0.835, 0.911, P = .41$) and was higher than that of other MR imaging classifiers ($P < .05$) to differentiate GBMs from PCNSLs and metastases. The accuracy of the classifiers Lac/Cr,

Cho/Cr, and PSR_{max} was not significantly different ($AUC = 0.957, 0.868, 0.969, P = .11, .69, .16$) and was higher than that of other MR imaging classifiers ($P < .05$) to differentiate metastases from PCNSLs and GBMs (Fig 3).

Accuracy of Combined Classifiers

Comparisons between AUCs obtained from ROCs for the individual and combined classifiers showed that the combined classifier PSR_{max}-Cho/NAA had the highest differential diagnostic performance to discriminate PCNSLs from GBMs and metastases with significantly higher accuracy than that of the best individual classifiers, PSR_{max} and Cho/NAA ($AUC = 0.988$ versus 0.940 and $0.835; P < .001$ and $.02$, respectively), a sensitivity of 95.7%, and a specificity of 100%, thus significantly increasing the sensitivity of perfusion (82.1%) and spectroscopy (73.9%) to 95.7%. In the differentiation of GBMs and PCNSLs and metastases, the combined classifier rCBV-Cho/NAA had the highest differential diagnostic performance with significantly higher accuracy than that of the best individual classifiers, rCBV and Cho/NAA ($AUC = 0.960$ versus 0.911 and $0.835; P = .001$ and $.005$, respectively), a sensitivity of 85.7%, and a specificity of 100%, thus significantly increasing the specificity of perfusion (92.7%) and spectroscopy (73.9%) to 100%. In the differentiation of metastases versus PCNSLs and GBMs, the combined classifiers (PSR_{max}-Lac/Cr) and (PSR_{max}-Cho/Cr) had the highest differential diagnostic performances with accuracies not significantly different ($AUC = 0.988$ and $1; P = .89$), but significantly higher than those of the best individual classifiers PSR_{max}, Lac/Cr, and Cho/Cr ($AUC = 0.969, 0.957$ and $0.868; P = .001, .001, .04$ and $.001, .001, .02$, respectively), a sensitivity of 100%, respectively, and specificities of

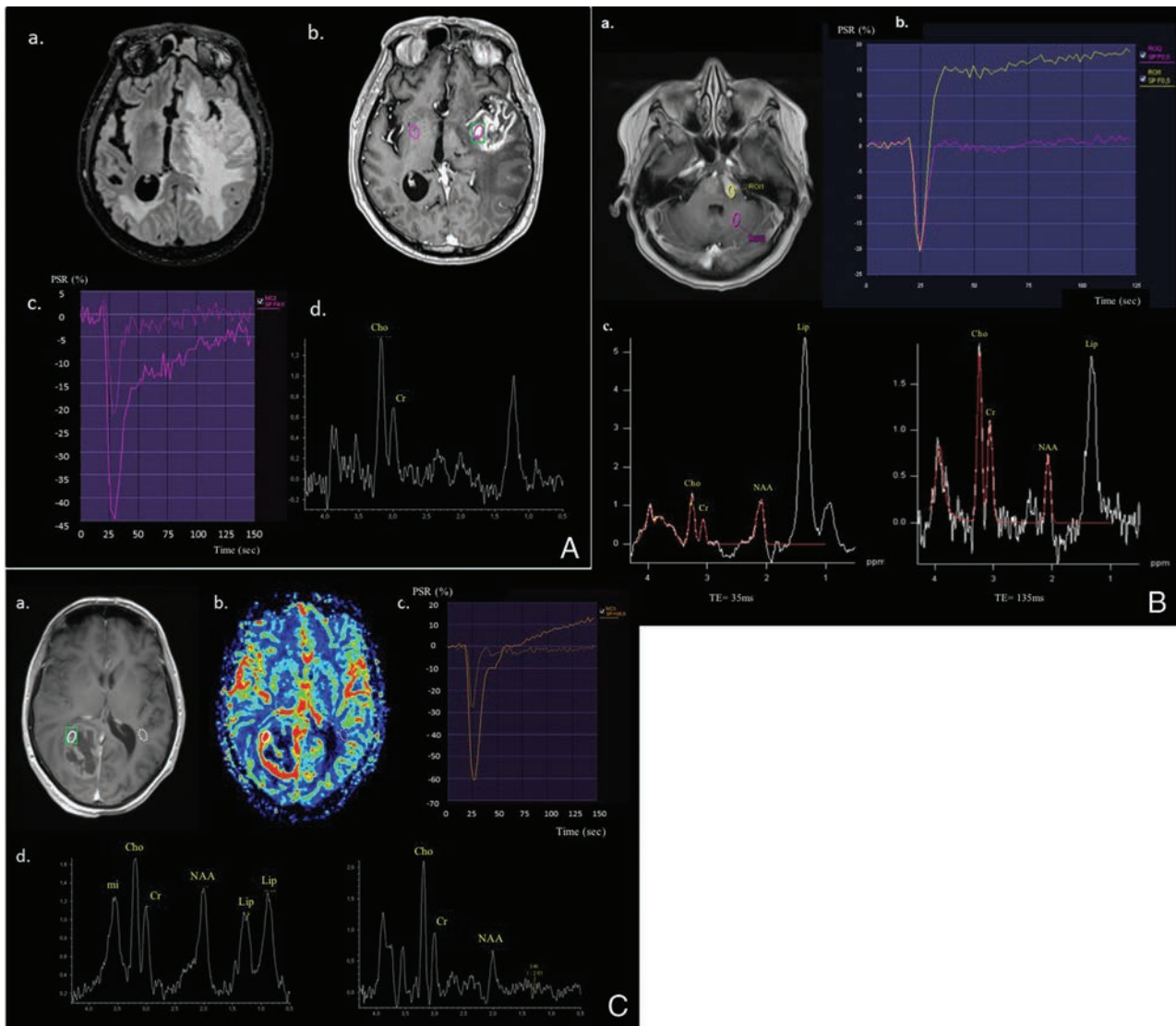


FIG 2. Cerebral MR imaging with postprocessing using syngo.via software shows the following: **A**, A 77-year-old man with histologically proved left insula metastasis from lung cancer who has extensive peritumoral edema on the T2-weighted FLAIR image (a), a heterogeneous contrast enhancement with necrosis on the postcontrast T1-weighted image (b), PSR_{max} at 65% with $rCBV_{max}$ at 2.5 on PWI γ function (c), and the Cho/Cr ratio at 1.8 with the resonance of free lipids still visible at TE = 135ms on 1H -MR PRESS spectra (d). **B**, A 56-year-old man with histologically proved PCNSL within the pons who has a homogeneous hyperintense lesion on postcontrast T1-weighted image (a), PSR_{max} at 125% with no increase in $rCBV_{max}$ on PWI γ function (b), and a strong resonance of free lipids at a short TE = 35ms, as well as at a long TE = 135 ms on 1H -MR PRESS spectra. Note also a strong increase of Cho/NAA and Cho/Cr at TE = 135 ms (c). **C**, A 52-year-old woman with histologically proved right occipital glioblastoma who has a heterogeneous necrotic lesion on the postcontrast T1-weighted image (a), with a ring of hyperperfusion (b), PSR_{max} at 80% with $rCBV_{max}$ at 4.1 on the PWI γ function (c), and a strong resonance of free lipids at TE = 35 ms and lactate with ratios of Cho/Cr at 3.1 and Cho/NAA at 3.5 on 1H -MR PRESS spectra (d).

97.0% and 100%, respectively, thus significantly increasing the specificity of perfusion (83.3%) and spectroscopy (81.8%) to 97.0% using the classifier PSR_{max} -Lac/Cr and 100% using the classifier PSR_{max} -Cho/Cr (Table 2 and Fig 3).

DISCUSSION

In our study, we have given special attention to the clinical application of our results by the determination of MR imaging classifiers that have the maximum differential diagnostic performance to discriminate brain tumor pathologies, which is more useful and closer to reasoning for the decision-making in daily clinical practice.

Differentiation of PCNSLs from GBMs and Metastases

Our study showed that the increased capillary permeability (PSR_{max}) was significantly greater in PCNSLs than that in GBMs and metastases and is concordant with several studies.^{3,7,8} These findings suggest that contrast material leakage into the interstitial space is more pronounced in PCNSLs than in GBMs and metastases.^{1,13} Mangla et al³ and Paulson and Schmainda¹⁴ reported that the intensity of signal for DSC imaging is the combined result of the T2* and T1 shortening effect from the accumulated contrast agent in the interstitial space. The T2* effects cause lower signal intensity recovery, while the T1 effects lead to higher signal intensity recovery. The signal intensity increases and even exceeds

baseline when the T1 shortening effect of the accumulation of contrast material in the interstitial space dominates the T2* effect. Xing et al,⁸ reported that in PCNSLs, the contrast accumulation might be slow and T1 and T2* shortening effects are not apparent during the first pass. Only after the first pass does the T1 shortening effect overwhelm the T2* shortening effect, resulting in a higher PSR. In most GBMs and metastases of high vessel density, the T2* effect from rapid and abundant accumulation of contrast agent in the interstitial space is considerably greater than the T1 shortening effect during and even after the first-pass period, leading to a lower PSR.

The markedly increased PSR in PCNSLs has so far not been

clearly explained.^{9,14-16} In contrast to GBMs and metastases, the tumor hypercellularity according to the angiocentric growth pattern, in which the PCNSL cells tend to cluster around pre-existing brain vessels and form multiple thick layers around the host vessels associated with widening of the perivascular space with smaller extravascular spaces and absence of neoangiogenesis, might explain the faster signal recovery.¹⁷

PCNSLs demonstrated significantly lower rCBV values and higher PSR values compared with GBMs and metastases, consistent with some authors.^{1-3,13,18,19} These differences have been attributed to the lack of neoangiogenesis and the angiocentric growth pattern in PCNSLs, resulting in lower microvessel density and higher vascular

permeability, whereas GBMs or brain metastases are characterized by tumor microvasculature and angiogenesis.^{3,13,20}

However, some authors^{3,8,19} have demonstrated that PSR was a significantly more accurate predictor than rCBV in differentiating PCNSLs from GBMs and metastases, which is in agreement with our findings, with an accuracy of 0.940 and 0.789, respectively.

In our study, the Cho/Cr ratio increased in both PCNSLs and GBMs without a significant difference between the 2 groups. However, the Cho/NAA ratio increased both in PCNSLs and GBMs but with significantly lower values in PCNSLs than in GBMs. The NAA/Cr ratio decreased less in PCNSLs than in GBMs. Thus, neuronal structures were less affected by PCNSLs than GBMs.

A trend toward higher Lip/Cr levels in PCNSLs compared with GBMs proved to be statistically nonsignificant. Some authors²¹⁻²³ stated that markedly elevated

Table 2: AUC from the ROC for individual and combined classifiers and decision thresholds, to discriminate brain tumors

	AUC	P Value	Thresholds	Sensitivity	Specificity
PCNSL vs GBM, metastases					
PSR _{max}	0.940	<.001 ^a	≥87.00	82.1	100.0
Cho/NAA	0.835	<.001 ^a	≤2.07	73.9	100.0
rCBV	0.789	<.001 ^a	≤2.59	92.9	63.0
Lac/Cr	0.728	.006 ^a	≥0.87	87.0	56.5
Cho/Cr	0.665	.01 ^a	≥2.84	56.5	77.8
Lip/Cr	0.638	.32			
PSR _{max} -Cho/NAA	0.988	<.001 ^a		95.7	100.0
GBM vs PCNSL, metastases					
rCBV	0.911	<.001 ^a	≥2.86	85.7	92.7
Cho/NAA	0.835	<.001 ^a	≥2.57	100.0	73.9
Lac/Cr	0.710	.40			
Cho/Cr	0.648	.68			
PSR _{max}	0.633	.18			
Lip/Cr	0.629	.19			
rCBV-Cho/NAA	0.960	<.001 ^a		85.7	100.0
Metastases vs PCNSL, GBM					
PSR _{max}	0.969	<.001 ^a	≤75.00	100.0	83.3
Lac/Cr	0.957	<.001 ^a	≤0.95	100.0	81.8
Cho/Cr	0.868	<.001 ^a	≤1.80	92.3	81.1
Lip/Cr	0.813	.02 ^a	≥2.90	100.0	64.9
rCBV	0.532	.51			
PSR _{max} -Lac/Cr	0.988	<.001 ^a		100.00	97.0
PSR _{max} -Cho/Cr	1.000	<.001 ^a		100.00	100.0

^a Significant.

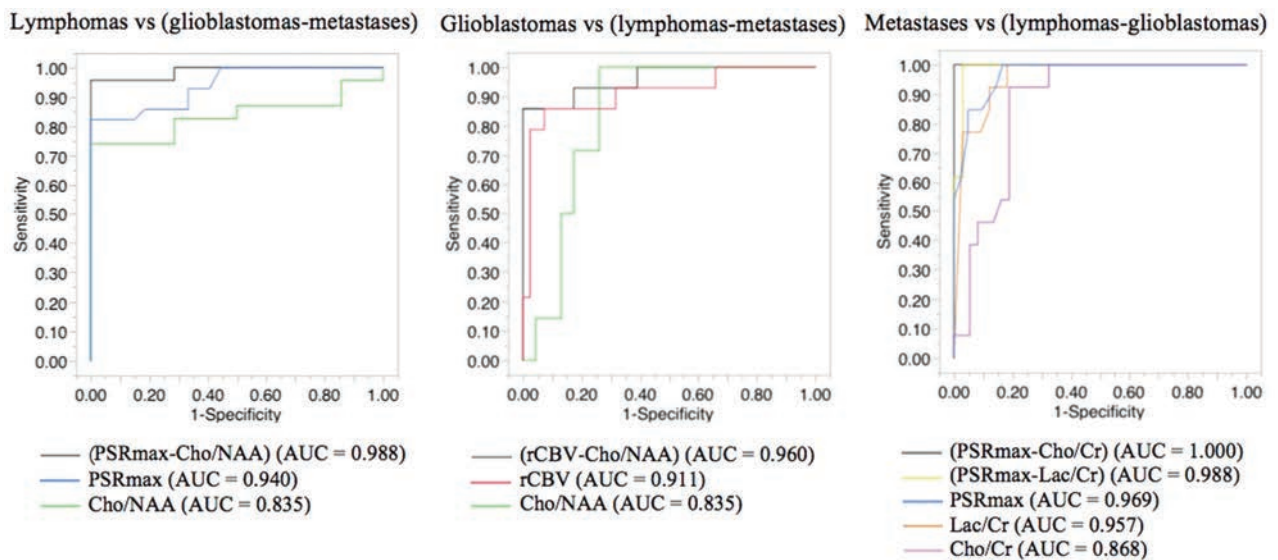


FIG 3. Differential diagnostic performances and the differences in discriminatory performance of classifiers of spectroscopy and perfusion to discriminate lymphomas, glioblastomas, and metastases.

lipid and choline in PCNSLs might be helpful in differentiating them from GBMs. Although the origin of the lipid is still unclear, an increase in lipid resonance is usually associated with necrosis and membrane breakdown as a signature of cell death.²⁴ However, a lipid-dominated spectrum found in PCNSLs is not macroscopically necrotic²³ and may result from the contribution of numerous macrophages and the increased turnover of the membrane components in transformed lymphoid cells rather than from necrosis.²⁵

Thus, our study demonstrated that the combined assessment of capillary permeability and cellular membrane turnover by proliferating cells relative to the viability of neuronal structures using the combined classifier $PSR_{max}-Cho/NAA$ was the underlying physiologic and metabolic characteristic that provides the best differential diagnostic performance to discriminate PCNSLs from GBMs and metastases.

Differentiation of GBMs from PCNSLs and Metastases

Our study showed that rCBV increased in GBMs with significantly higher values than in PCNSLs and metastases. The ultrastructure of GBMs^{2,6,26} is characterized by tumor microvasculature and extensive angiogenesis, including glomeruloid capillaries, simple vascular hyperplasia, delicate neocapillaries, and blood-brain barrier disruption, which may explain an increase in rCBV within the tumor compared with normal white or gray matter.²⁷ Increased rCBV, considerably higher in GBMs, correlates with the neoangiogenesis of malignant gliomas^{3,5} and has been used in the grading of gliomas.⁶

The Cho/NAA ratio increased in GBMs with significantly higher values than in PCNSLs. Thus, in GBMs, the decreased neuronal and axonal viability was significantly greater than that in PCNSLs because the Cho/Cr ratio was not significantly different between PCNSLs and GBMs, indicating that neuronal loss or degradation was significantly higher in GBMs than in PCNSLs.

PSR was not a sufficiently accurate classifier to exploit the difference in tumor capillary permeability between GBMs and the other common brain tumors such as PCNSLs and metastases; this finding is in agreement with those reported by Mangla et al.³ This may be explained by the disparity in capillary permeability characteristics between PCNSLs and metastases, with higher PSR values in PCNSLs and lower PSR values in metastases, compared with GBMs, and the difference in PSR values between PCNSLs and metastases being significantly different.

Thus, combined assessment of microvasculature and angiogenesis and cellular membrane turnover reflecting cell proliferation relative to neuronal viability using the combined classifier $rCBV-Cho/NAA$ was the underlying physiologic and metabolic characteristic that provided the best differential diagnostic performance to discriminate GBMs from PCNSLs and metastases.

Differentiation of Metastases from PCNSLs and GBMs

Our study showed that PSR_{max} increased in metastases, but with significantly lower values than those in PCNSLs and GBMs, a finding consistent with those in some reports.⁷ The capillary ultrastructure of metastases, characterized by a vascular structure similar to that of the primary tumor, absence of similarity to normal brain capillaries, prominent capillary fenestrations, and complete lack of BBB components may result in a higher permeability and render metastases far more susceptible to leakage.²⁶ The T2*

effects from markedly decreased intravascular contrast agent concentration and an increased volume of distribution result in an increase in effective compartment size during the first pass, and it, in turn, alters the signal intensity in a complex way, leading to lower PSR in metastases.³

The Lac/Cr ratio increased in metastases but with significantly lower values than those in PCNSLs and GBMs. Lactate detection precedes cellular injury and reflects pathologic conditions associated with an increased energy demand: impaired cellular capability for oxidative phosphorylation, which indicates an increase in anaerobic metabolism; and the presence of ischemic processes and macrophage invasion.²⁸ In our study, these pathologic conditions in metastases appeared significantly less important than those in PCNSLs and GBMs. J-coupling was used between TEs of 35 and 135 ms to extract the lactate resonance by subtraction between the overall co-resonance of lactate + free lipids at TE = 35 ms and the reversed lactate resonance with respect to the baseline at TE = 135 ms, thus allowing the separation and the correct quantification of lactate and lipids.

The Cho/Cr ratio increased in metastases but with significantly lower values than those in PCNSLs and GBMs. In tumors, Cho levels correlated with the degree of malignancy, reflective of cellularity.²⁹ Increased phosphocholine turnover due to membrane biosynthesis by proliferating cells in metastases was significantly less than that in PCNSLs and GBMs. However, some studies reported that the Cho/Cr ratio alone is not reliable in differentiating brain metastases from GBMs.³⁰ The prevailing view is that an elevated choline peak is a surrogate marker of increased cell membrane turnover caused by tumor growth or normal cell destruction; however, an alternative view suggests that the choline signal may, in part, be elevated because of increased production through phospholipase upregulation.³¹

Free lipids increased in metastases with significantly higher values than in PCNSLs and GBMs. This finding is consistent with those in previous studies that demonstrated a significant correlation between lipid levels and the amount of necrosis in GBMs and metastases irrespective of their primary origin.³²⁻³⁴ Sjøbakk et al³⁴ also confirmed the cytoplasmic origin of MR imaging-visible lipid signals in metastases because a cellular response to stressful stimuli from the tumor microenvironment can result in accumulation of neutral lipids in cytoplasm. MR imaging-visible lipid signals in non-necrotic brain tumor biopsies were mobile lipid droplets of cytoplasmic origin.^{34,35} Furthermore, apoptosis and hypoxic cells have been reported to contribute to elevated spectral lipid signals.³⁶

In our study, the Lip/Cr ratio was a discriminant classifier but with a moderate accuracy of 0.813 and a low specificity of 64.9% to discriminate metastases from PCNSLs and GBMs. While brain metastases demonstrated an elevated lipid peak,^{20,27} this peak was not reliable to discriminate brain metastases from GBMs, which may also be necrotic.³⁷

rCBV was not a sufficiently accurate classifier to exploit the difference in tumor angiogenesis between metastases and the other common brain tumors such as PCNSLs and GBMs; this finding is in agreement with those reported by Mangla et al.³ This may be explained by the disparity in angiogenesis characteristics between PCNSLs and GBMs, with lower rCBV values in PCNSLs

and higher rCBV values in GBMs compared with metastases and the difference in rCBV values between GBMs and PCNSLs being significantly different. With regard to GBMs and some hematogenous brain metastases, there may be an overlap in rCBV values because both have high rCBVs.⁷ Several prior studies have reported that rCBV may not be helpful for discrimination of GBMs and brain metastases.^{2,9} These findings may be attributed to brain metastases increasing tumor angiogenesis, as is the case with GBMs, leading to increased rCBV during the process of growth and invasion.^{14,32} However, depending on the origin and histopathology of the metastases, rCBV values within the tumor tissue may vary over a large range because hypervascular metastases such as renal cell carcinoma and melanoma may have a markedly high rCBV compared with less vascularized metastases.³⁸

Thus, combined assessment of capillary permeability and anaerobic metabolism or cellular membrane turnover reflecting cellular proliferation using the combined classifiers $PSR_{max}\text{-Lac/Cr}$ or $PSR_{max}\text{-Cho/Cr}$ was the underlying physiologic and metabolic characteristic that provided the best differential diagnostic performance to discriminate metastases from PCNSLs and GBMs.

Our study may have a few potential limitations, including the small sample size. Furthermore, rCBV measurements using DSC MR imaging in regions of disrupted BBB with consecutive leakage of contrast agent into the interstitial space may not be entirely accurate. The T1-related signal increase of the contrast agent leakage can partly compensate for the T2*-related signal decrease, which may lead to an under- or overestimation of hemodynamic parameters.^{6,8}

CONCLUSIONS

Our results show that perfusion and spectroscopic MR imaging highlighted salient features in lymphomas, glioblastomas, and metastases. Moreover, spectroscopy yielded added value to perfusion using optimal combined classifiers of these modalities, significantly increasing the differential diagnostic performance with a high accuracy for these common brain tumors in daily clinical practice.

REFERENCES

1. Wang S, Kim S, Chawla S, et al. **Differentiation between glioblastomas, solitary brain metastases, and primary cerebral lymphomas using diffusion tensor and dynamic susceptibility contrast-enhanced MR imaging.** *AJNR Am J Neuroradiol* 2011;32:507–14 CrossRef Medline
2. Law M, Yang S, Wang H, et al. **Glioma grading: sensitivity, specificity, and predictive values of perfusion MR imaging and proton MR spectroscopic imaging compared with conventional MR imaging.** *AJNR Am J Neuroradiol* 2003;24:1989–98 Medline
3. Mangla R, Kolar B, Zhu T, et al. **Percentage signal recovery derived from MR dynamic susceptibility contrast imaging is useful to differentiate common enhancing malignant lesions of the brain.** *AJNR Am J Neuroradiol* 2011;32:1004–10 CrossRef Medline
4. Surov A, Meyer HJ, Wienke A. **Correlation between apparent diffusion coefficient (ADC) and cellularity is different in several tumors: a meta-analysis.** *Oncotarget* 2017;8:59492–99 CrossRef Medline
5. Shin JH, Lee HK, Kwun BD, et al. **Using relative cerebral blood flow and volume to evaluate the histopathologic grade of cerebral gliomas: preliminary results.** *AJR Am J Roentgenol* 2002;179:783–89 CrossRef Medline
6. Aronen HJ, Gazit IE, Louis DN, et al. **Cerebral blood volume maps of**

gliomas: comparison with tumor grade and histologic findings. *Radiology* 1994;191:41–51 CrossRef Medline

7. Cha S, Lupo JM, Chen MH, et al. **Differentiation of glioblastoma multiforme and single brain metastasis by peak height and percentage of signal intensity recovery derived from dynamic susceptibility-weighted contrast-enhanced perfusion MR imaging.** *AJNR Am J Neuroradiol* 2007;28:1078–84 CrossRef Medline
8. Xing Z, You RX, Li J, et al. **Differentiation of primary central nervous system lymphomas from high-grade gliomas by rCBV and percentage of signal intensity recovery derived from dynamic susceptibility-weighted contrast-enhanced perfusion MR imaging.** *Clin Neuroradiol* 2014;24:329–36 CrossRef Medline
9. Stefan D, Cesare FD, Andrasescu A, et al. **Quantitation of magnetic resonance spectroscopy signals: the jMRUI software package.** *Measurement Science and Technology* 2009;20:104035 CrossRef
10. Vanhamme L, van den Boogaart A, Van Huffel S. **Improved method for accurate and efficient quantification of MRS data with use of prior knowledge.** *J Magn Reson* 1997;129:3–43 Medline
11. Smith SM. **Fast robust automated brain extraction.** *Hum Brain Mapp* 2002;17:143–55 CrossRef Medline
12. Haker S, Wells WM 3rd, Warfield SK, et al. **Combining classifiers using their receiver operating characteristics and maximum likelihood estimation.** *Med Image Comput Comput Assist Interv* 2005;8 (Pt 1):506–14 Medline
13. Liao W, Liu Y, Wang X, et al. **Differentiation of primary central nervous system lymphoma and high-grade glioma with dynamic susceptibility contrast-enhanced perfusion magnetic resonance imaging.** *Acta Radiol* 2009;50:217–25 CrossRef Medline
14. Paulson ES, Schmainda KM. **Comparison of dynamic susceptibility-weighted contrast-enhanced MR methods: recommendations for measuring relative cerebral blood volume in brain tumors.** *Radiology* 2008;249:601–13 CrossRef Medline
15. Levin JM, Wald LL, Kaufman MJ, et al. **T1 effects in sequential dynamic susceptibility contrast experiments.** *J Magn Reson* 1998;130:292–95 CrossRef Medline
16. Runge VM, Kirsch JE, Wells JW, et al. **Repeat cerebral blood volume assessment with first-pass MR imaging.** *J Magn Reson Imaging* 1994;4:457–61 CrossRef Medline
17. Kleihues P, Burger PC, Scheithauer BW. *Histological Typing of Tumours of the Central Nervous System.* Berlin: Springer; 1993
18. Hakyemez B, Erdogan C, Bolca N, et al. **Evaluation of different cerebral mass lesions by perfusion-weighted MR imaging.** *J Magn Reson Imaging* 2006;24:817–24 CrossRef Medline
19. Toh CH, Wei KC, Chang CN, et al. **Differentiation of primary central nervous system lymphomas and glioblastomas: comparisons of diagnostic performance of dynamic susceptibility contrast-enhanced perfusion MR imaging without and with contrast-leakage correction.** *AJNR Am J Neuroradiol* 2013;34:1145–49 CrossRef Medline
20. Hardee ME, Zagzag D. **Mechanisms of glioma-associated neovascularization.** *Am J Pathol* 2012;181:1126–41 CrossRef Medline
21. Fellows GA, Wright AJ, Sibtain NA, et al. **Combined use of neuroradiology and 1H-MR spectroscopy may provide an intervention limiting diagnosis of glioblastoma multiforme.** *J Magn Reson Imaging* 2010;32:1038–44 CrossRef Medline
22. Guillemin R, Menuel C, Abud L, et al. **Proton MR spectroscopy in predicting the increase of perfusion MR imaging for WHO grade II gliomas.** *J Magn Reson Imaging* 2012;35:543–50 CrossRef Medline
23. Harting I, Hartmann M, Jost G, et al. **Differentiating primary central nervous system lymphoma from glioma in humans using localised proton magnetic resonance spectroscopy.** *Neurosci Lett* 2003;342:163–66 CrossRef Medline
24. Howe FA, Barton SJ, Cudlip SA, et al. **Metabolic profiles of human brain tumors using quantitative in vivo 1H magnetic resonance spectroscopy.** *Magn Reson Med* 2003;49:223–32 CrossRef Medline
25. Tang YZ, Booth TC, Bhogal P, et al. **Imaging of primary central nervous system lymphoma.** *Clin Radiol* 2011;66:768–77 CrossRef Medline

26. Long DM. **Capillary ultrastructure in human metastatic brain tumors.** *J Neurosurg* 1979;51:53–58 CrossRef Medline
27. Roberts HC, Roberts TP, Bollen AW, et al. **Correlation of microvascular permeability derived from dynamic contrast-enhanced MR imaging with histologic grade and tumor labeling index: a study in human brain tumors.** *Acad Radiol* 2001;8:384–91 CrossRef Medline
28. Matsumura A, Isobe T, Takano S, et al. **Non-invasive quantification of lactate by proton MR spectroscopy and its clinical applications.** *Clin Neurol Neurosurg* 2005;107:379–84 CrossRef Medline
29. Bertholdo D, Watcharakorn A, Castillo M. **Brain proton magnetic resonance spectroscopy: introduction and overview.** *Neuroimaging Clin N Am* 2013;23:359–80 CrossRef Medline
30. Chawla S, Zhang Y, Wang S, et al. **Proton magnetic resonance spectroscopy in differentiating glioblastomas from primary cerebral lymphomas and brain metastases.** *J Comput Assist Tomogr* 2010;34:836–41 CrossRef Medline
31. Al-Okaili RN, Krejza J, Wang S, et al. **Advanced MR imaging techniques in the diagnosis of intraaxial brain tumors in adults.** *RadioGraphics* 2006;26(Suppl 1):S173–89 CrossRef Medline
32. Opstad KS, Griffiths JR, Bell BA, et al. **Apparent T(2) relaxation times of lipid and macromolecules: a study of high-grade tumor spectra.** *J Magn Reson Imaging* 2008;27:178–84 CrossRef Medline
33. Opstad KS, Bell BA, Griffiths JR, et al. **An investigation of human brain tumour lipids by high-resolution magic angle spinning 1H MRS and histological analysis.** *NMR Biomed* 2008;21:677–85 CrossRef Medline
34. Sjøbakk TE, Vettukattil R, Gulati M, et al. **Metabolic profiles of brain metastases.** *Int J Mol Sci* 2013;14:2104–18 CrossRef Medline
35. Delikatny EJ, Chawla S, Leung DJ, et al. **MR-visible lipids and the tumor microenvironment.** *NMR Biomed* 2011;24:592–611 CrossRef Medline
36. Righi V, Mucci A, Schenetti L, et al. **Identification of mobile lipids in human cancer tissues by ex vivo diffusion edited HR-MAS MRS.** *Oncol Rep* 2009;22:1493–96 Medline
37. Server A, Josefsen R, Kulle B, et al. **Proton magnetic resonance spectroscopy in the distinction of high-grade cerebral gliomas from single metastatic brain tumors.** *Acta Radiol* 2010;51:316–25 CrossRef Medline
38. Faehndrich J, Weidauer S, Pilatus U, et al. **Neuroradiological viewpoint on the diagnostics of space-occupying brain lesions.** *Clin Neuroradiol* 2011;21:123–39 CrossRef Medline

Brain Perfusion Measurements Using Multidelay Arterial Spin-Labeling Are Systematically Biased by the Number of Delays

M. van der Thiel, C. Rodriguez, P. Giannakopoulos, M.X. Burke, R. Marc Lebel, N. Gninenko, D. Van De Ville, and S. Haller



ABSTRACT

BACKGROUND AND PURPOSE: Multidelay arterial spin-labeling is a promising emerging method in clinical practice. The effect of imaging parameters in multidelay arterial spin-labeling on estimated cerebral blood flow measurements remains unknown. We directly compared 3-delay versus 7-delay sequences, assessing the difference in the estimated transit time and blood flow.

MATERIALS AND METHODS: This study included 87 cognitively healthy controls (78.7 ± 3.8 years of age; 49 women). We assessed delay and transit time–uncorrected and transit time–corrected CBF maps. Data analysis included voxelwise permutation-based between-sequence comparisons of 3-delay versus 7-delay, within-sequence comparison of transit time–uncorrected versus transit time–corrected maps, and average CBF calculations in regions that have been shown to differ.

RESULTS: The 7-delay sequence estimated a higher CBF value than the 3-delay for the transit time–uncorrected and transit time–corrected maps in regions corresponding to the watershed areas (transit time–uncorrected = 27.62 ± 12.23 versus 24.58 ± 11.70 mL/min/100 g, Cohen's $d = 0.25$; transit time–corrected = 33.48 ± 14.92 versus 30.16 ± 14.32 mL/min/100 g, Cohen's $d = 0.23$). In the peripheral regions of the brain, the estimated delay was found to be longer for the 3-delay sequence (1.52408 ± 0.25236 seconds versus 1.47755 ± 0.24242 seconds, Cohen's $d = 0.19$), while the inverse was found in the center of the brain (1.39388 ± 0.22056 seconds versus 1.42565 ± 0.21872 seconds, Cohen's $d = 0.14$). Moreover, 7-delay had lower hemispheric asymmetry.

CONCLUSIONS: The results of this study support the necessity of standardizing acquisition parameters in multidelay arterial spin-labeling and identifying basic parameters as a confounding factor in CBF quantification studies. Our findings conclude that multidelay arterial spin-labeling sequences with a high number of delays estimate higher CBF values than those with a lower number of delays.

ABBREVIATIONS: ASL = arterial spin-labeling; d = Cohen's d ; PLD = postlabeling delay

Arterial spin-labeling (ASL) is a noninvasive MR imaging technique capable of measuring perfusion and quantifying cerebral blood flow. ASL uses water in the blood as an endogenous

tracer by inversion of proximal inflowing spins,^{1,2} which are exchanged with tissue water, giving rise to the perfusion signal in the inversion images.³ The arterial transit time is reflective of the time it takes for blood to travel from the labeling to imaging plane. The time between labeling and acquisition is called the postlabeling delay (PLD).⁴ The use of different PLDs is implemented in ASL to account for the arterial transit time.⁵ The measurement of the cerebral blood flow without incorporating the estimated PLD gives rise to the transit time–uncorrected maps, while the transit time–corrected maps refer to the measurement of CBF corrected for the estimated PLD. Not considering the arterial transit time can lead to underestimation of the CBF signal,⁶ indicating the importance of correction for the transit time.

In practice, the arterial transit time is found to be a considerable source of error in the evaluation of perfusion.^{3,7} Customarily, ASL measurements are administered using a single PLD.⁸ However, when the distribution of transit times is wide, as observed in cerebrovascular diseases with multiple arterial lesions and proxi-

Received November 16, 2017; accepted after revision May 9, 2018.

From the Faculty of Medicine of the University of Geneva (M.v.d.T., P.G., N.G., D.v.d.V., S.H.), Geneva, Switzerland; Institute of Bioengineering (M.v.d.T., N.G., D.v.d.V.), School of Engineering, École Polytechnique Fédérale de Lausanne, Lausanne, Switzerland; Division of Institutional Measures (C.R., P.G.), Medical Direction, University Hospitals of Geneva, Geneva, Switzerland; Affidea Centre de Diagnostic Radiologique de Carouge (S.H.), Geneva, Switzerland; Department of Surgical Sciences and Radiology (S.H.), Uppsala University, Uppsala, Sweden; and GE Healthcare (M.X.B., M.L.), Little Chalfont, UK.

This work was supported by Swiss National Foundation grants SNF 3200B0-1161193 and SPUM 33CM30-124111 and an unrestricted grant from the Association Suisse pour la Recherche Alzheimer.

Please address correspondence to Sven Haller, MD, Faculty of Medicine of the University of Geneva, Switzerland. Affidea Centre de Diagnostic Radiologique de Carouge, Geneva, Switzerland. Department of Surgical Sciences and Radiology, Uppsala University, Uppsala, Sweden; e-mail: sven.haller@gmail.com

Indicates open access to non-subscribers at www.ajnr.org

<http://dx.doi.org/10.3174/ajnr.A5717>

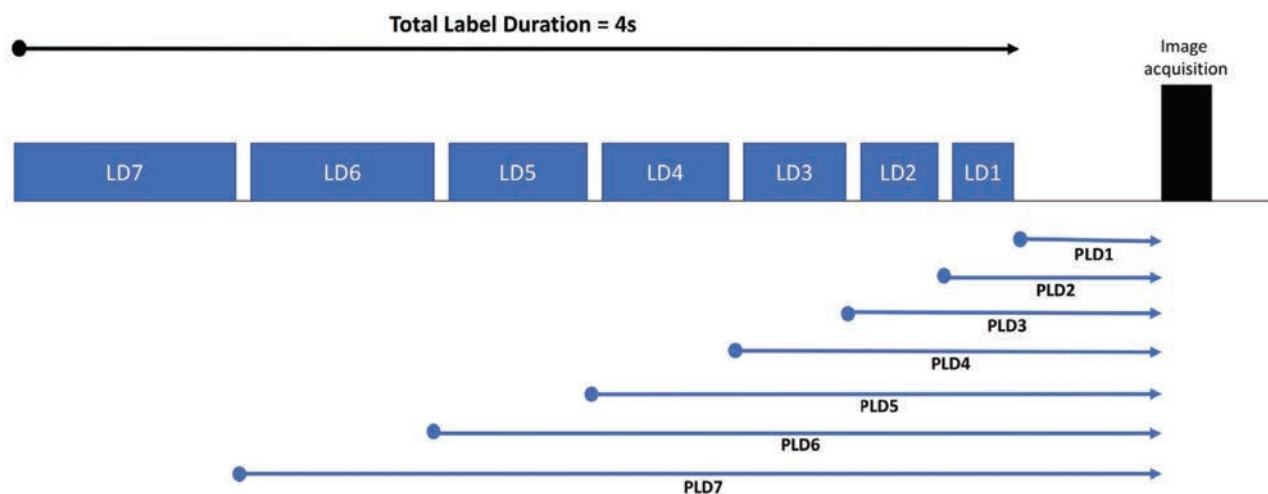


FIG 1. Seven pulsed continuous arterial spin-labeling periods of different durations: labeling duration (LD) = 0.22, 0.26, 0.30, 0.37, 0.48, 0.68, and 1.18 seconds was used to acquire perfusion-weighted images at postlabeling delays of 1.00, 1.22, 1.48, 1.78, 2.15, 2.62, and 3.32 seconds. When we used only 3 labeling periods, LD = 0.57, 0.89, 2.04 seconds and PLD = 1.00, 1.57, and 2.46 seconds.

mal vascular stenosis (a frequent finding in older subjects^{6,9}), these methods will be imprecise. One of the difficulties regarding the PLD is the modification of the optimal PLD during the life span. In general, children and young adults have good cardiac output and consequently a short optimal PLD. During aging, cardiac output decreases and vascular comorbidity increases, so a longer PLD is recommended for elderly participants.¹⁰ The PLD being too short may lead to a false underestimation of the CBF.

This problem can be partially solved by acquiring images at multiple PLDs, thereby sampling several points along the ASL uptake and decay curve.⁴ Multidelay ASL using a Hadamard-encoding scheme generates ASL images with several postlabeling delay times and enables quantification of both perfusion and arterial transit time.¹¹ In addition, the increased data averaging within the Hadamard-encoding scheme results in a higher SNR and reduces physiologic background noise.¹¹ Furthermore, knowledge of the transit time permits more robust CBF quantification than methods naive to the arrival time. Multiple PLDs are expected to improve the accuracy of CBF quantification¹² but sacrifice SNR efficiency due to short label durations.⁹ Conversely, a sequence with fewer delays will have a higher SNR per time point compared with many delays; nevertheless, it might sacrifice the specificity of the delay estimates, leading to a less accurate correction for this delay. The appropriate number of delay times to balance accurate transit-time estimates and precise CBF quantification is unclear.

The current study will examine the impact of the number of delays and transit-time correction on the estimation of CBF in ASL. The results of 3-delay and 7-delay sequences will be compared, and the effect of the transit-time correction on 3-delay and 7-delay sequences will be considered independently.

MATERIALS AND METHODS

Participants

The data used in this article were retrieved from an ongoing large population-based longitudinal study. The study encompassed a comprehensive neuropsychological evaluation, as described in detail previously.¹³ The final sample included 87 participants, classified as

cognitively healthy controls (mean age, 78.7 ± 3.8 years; 49 women). All participants gave written informed consent after formal approval by the local ethics committee.

MR Imaging

Imaging was performed on a 3T MR750w scanner (GE Healthcare, Milwaukee, Wisconsin) using a 32-channel head array coil. Perfusion images were acquired with a background-suppressed 3D stack-of-spirals FSE sequence preceded by a Hadamard-encoded pseudocontinuous arterial spin-labeling module (modified to acquire an additional control-only phase). A total label duration of 4 seconds was encoded into either 3 or 7 sub-blocks (Fig 1). The label durations of the 7 labeling blocks were 0.22, 0.26, 0.30, 0.37, 0.48, 0.68, and 1.18 seconds; postlabeling delays were 1.00, 1.22, 1.48, 1.78, 2.15, 2.62, and 3.32 seconds.

The total scan time was 4.02 minutes. When we used only 3 labeling blocks, label durations were 0.57, 0.89, and 2.04 seconds and postlabeling delays were 1.00, 1.57, and 2.46 seconds, resulting in a total scan time of 3.37 minutes.

Key imaging parameters were the following: FOV = 22.0 cm, slice thickness = 4.0 mm, 32 slices, bandwidth = ± 62.5 kHz, 4 arms with 640 points each. Images with 3 labeling blocks were acquired with a TE of 0.0105 seconds and a TR of 5.978 seconds; and for the 7 labeling blocks, these were 0.0105 ms and 5.936 seconds, respectively. Acquisition included a proton-density-weighted reference image with matched parameters for quantification. Image reconstruction was performed using an IDL-based RECON code, and reconstructed images were stored as DICOM images in the data base of the scanner.

Images were created at all delay times. The combined delay map consisted of the sum of the delay times per subject. In addition, a transit-delay map reflecting the transit time of blood from the labeling plane to the imaging plane was estimated using the signal-weighted delay method described by Dai et al.¹⁴ Transit time–uncorrected CBF was computed using the combined delay image. Transit time–corrected CBF maps were calculated by incorporating the combined delay image and the transit delay (δ):

$$CBF = \frac{6000e^{\delta / T_{1a}}}{2\varepsilon T_{1a} (e^{-\max(PLD - \delta, 0) / T_{1r}} - e^{-\max(LD + PLD - \delta, 0) / T_{1r}})} \frac{P}{R_s}$$

where CBF reflects the cerebral blood flow in milliliters/100 g/min, PLD is the shortest postlabeling delay (1.0 seconds), LD is the entire labeling duration (4.0 seconds), T_{1a} is the longitudinal relaxation of arterial blood (1.6 seconds), T_{1r} is the longitudinal relaxation of gray matter (1.2 seconds), ε is the combined efficiency of labeling and background suppression (0.6375), P is the signal intensity in the perfusion-weighted image, and R is the signal intensity of the reference image.

The reference image is scaled by $s_r = \lambda(1 - e^{-2/1.2})$ to account for the combined effect of the blood-brain partition coefficient ($\lambda = 0.9$) and the partial GM signal recovery in a 2-second saturation-recovery reference image. The in-plane resolution of the resulting images was $1.88 \times 1.88 \times 4$ mm.

Statistical Analysis

Data Preprocessing. The ASL data were processed using the fMRIB Software Library (FSL, Version 5.0.9; <http://fsl.fmrib.ox.ac.uk/fsl>). The combined delay image was obtained per participant, and nonbrain tissue was removed using the FSL Brain Extraction Tool (<http://fsl.fmrib.ox.ac.uk/fsl/fslwiki/BET>). The brain-extracted combined delay maps were normalized to the Montreal Neurological Institute standard space using an echoplanar image template from the Statistical Parametric Mapping SPM8 (<http://www.fil.ion.ucl.ac.uk/spm/software/spm12>) toolbox standard space using linear registration (FMRIB Linear Image Registration Tool; <http://www.fmrib.ox.ac.uk/fslwiki/FLIRT>, part of FSL). The concatenated transformation matrix of the transit-delay maps was then applied to the uncorrected flow maps, the transit time-corrected flow maps, and the transit-delay maps to spatially normalize the data to the EPI template.

The normalized ASL images were smoothed with a 5-mm full width at half maximum Gaussian kernel using a dilated 2-mm brain-extracted Montreal Neurological Institute mask (FSLUTILS; ftp://surfer.nmr.mgh.harvard.edu/pub/dist/freesurfer/tutorial_packages/OSX/fsl_501/doc/wiki/Fslutils.html, part of FSL).

3-Delay versus 7-Delay

First, the 7-delay and 3-delay sequences were compared using a voxelwise permutation-based testing (Randomise; <http://fsl.fmrib.ox.ac.uk/fsl/fslwiki/Randomise>, part of FSL), with threshold-free cluster enhancement correction for multiple comparisons applied¹⁵ and $P < .05$ considered significant.

Five thousand permutations were executed per contrast. The dilated Montreal Neurological Institute 2-mm brain-extracted mask was used during randomization for masking of nonbrain voxels. A repeated measures design was administered with age and sex as nonexplanatory coregressors.¹⁶ Age was defined as the difference in days between the date of birth and the day of scanning.

Second, the voxels that showed either a positive or negative significant difference between the 7-delay and 3-delay signal were masked by a threshold of 0.95 per direction of the difference (FSLUTILS). The mean values of all participants combined for the 7-delay and the 3-delay within the resulting masks were cal-

culated (FSLUTILS). The Cohen d was determined to imply the effect size of the discrepancy between sequences.

Corrected-versus-Uncorrected Flow Maps

The preprocessed transit-uncorrected and transit-corrected flow images of the 7-delay sequence and, independently, of the 3-delay sequence were likewise compared using voxelwise permutation-based testing (Randomise). The mean values of all participants within the resulting masks of the uncorrected and the corrected maps were calculated separately (FSLUTILS).

Laterality Index

The laterality index is a way to indicate hemispheric dominance. With the expectation of a symmetric perfusion distribution within the brain, an unbiased estimate of this would result in a laterality index of approximately zero.¹⁷ The laterality index for the transit time-corrected flow maps was determined for the 7-delay sequences and the 3-delay sequences. The right and left hemispheres were masked separately, and the mean CBF value per hemisphere was calculated within participants. The laterality index (LI) was determined as described in Seghier¹⁷:

$$LI = \frac{Q_{LH} - Q_{RH}}{Q_{LH} + Q_{RH}}$$

where Q_{LH} and Q_{RH} are representative quantities for the left and right hemisphere contributions of CBF, respectively. A positive laterality index will represent a left-lateralization effect, and a negative value stands for right-hemisphere dominance. A paired t test was applied to compare the laterality indices of the 2 sequences.

RESULTS

Voxelwise Comparison between 3-Delay and 7-Delay

Transit Time-Uncorrected Flow Maps. The 7-delay sequence provided a higher estimation of CBF in the peripheral brain regions and the center of the brain and regions between them compared with the 3-delay sequence. Most interesting, this difference was profound in the watershed areas of the brain (Fig 2A).¹⁸ Within the voxels that had a significant difference, the 7-delay sequences estimated an 11% higher average CBF value compared with the 3-delay estimates (27.62 ± 12.23 versus 24.58 ± 11.70 mL/min/100 g, 11.00% difference, Cohen's $d = 0.25$) (Fig 2B).

The voxelwise comparison of the transit time-uncorrected flow maps of the 3-delay with the 7-delay established a 7-delay CBF with an estimate of half of the CBF value of the estimate of the 3-delay estimate within the right insular region of the brain (19.20 ± 21.29 versus 12.57 ± 18.66 mL/min/100 g, 52.70% difference, $d = 0.33$).

Transit Time-Corrected Flow Maps. The average CBF estimates of the 7-delay transit-corrected flow maps were found to be significantly higher than the 3-delay estimates in the regions corresponding approximately to the results of the transit-uncorrected flow maps (Fig 2A). For the uncorrected maps, the discrepancy between the 7-delay and 3-delay was found to be more global, but lower estimated CBF values were determined within these voxels, as illustrated in Fig 2B (33.48 ± 14.92 versus 30.16 ± 14.32 mL/min/100 g, 9.91% difference, $d = 0.23$). The voxelwise compari-

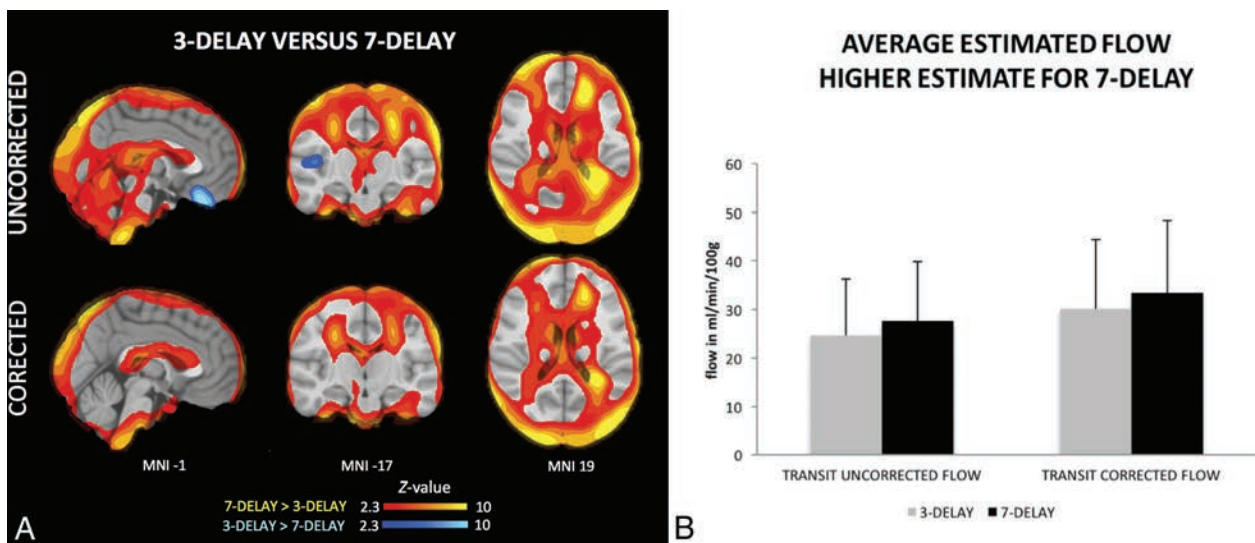


FIG 2. A, The spatial distribution of the differences between the 7-delay sequence and the 3-delay sequence for the uncorrected and corrected flow maps. The higher estimation value for the 7-delay over the 3-delay sequences is presented in the areas corresponding to the watershed areas (yellow). The 7-delay CBF estimates were found to be half the value of the 3-delay transit time–corrected flow maps within the right insular region of the brain and frontal regions (blue). The transit time–corrected maps show a higher value for the 7-delay sequence in the regions overlapping the uncorrected maps. However, the transit time–uncorrected maps show a broader signal for the difference between the 2 sequences, including more posterior regions of the brain. B, The average estimated transit-uncorrected flow and the transit-corrected flow in milliliters/minute/100 g for the 7-delay and 3-delay sequences within the voxels that displayed a significantly higher estimate for the 7-delay sequences. For these voxels, an average perfusion value of 27.62 ± 12.23 is estimated by the 7-delay versus 24.58 ± 11.70 mL/min/100 g for the 3-delay sequences in the uncorrected maps, and a perfusion value of 33.48 ± 14.92 is estimated by the 7-delay versus 30.16 ± 14.32 mL/min/100 g for the 3-delay sequences of the corrected flow maps.

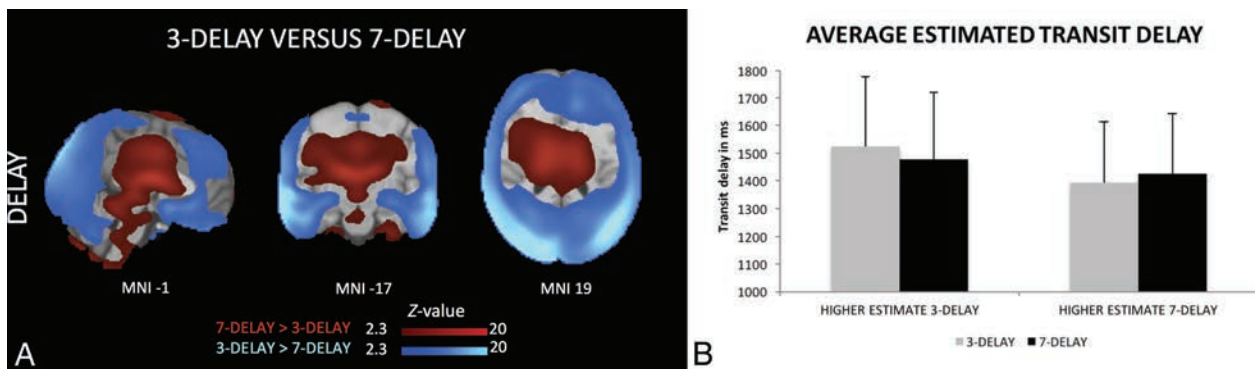


FIG 3. A, The spatial distribution of the differences between the 7-delay sequence and the 3-delay sequence for the delay maps. The estimation of the 7-delay as inferior to the 3-delay sequence (blue) concerns peripheral areas of the brain. In contrast, within the central regions of the brain, the averaged transit-time estimates are longer for the 7-delay sequences compared with the 3-delay sequences (red). B, The average estimated transit time delay in milliseconds of the voxels that displayed a significantly higher estimate for the 7-delay and those that showed a higher estimate for the 3-delay, respectively. This figure shows the difference between the 7-delay and the 3-delay within these corresponding regions. For the regions where the 7-delay estimated a smaller arterial transit time delay than the 3-delay sequence, an average arterial transit time of 1.47755 ± 0.24242 seconds is found for the 7-delay versus 1.52408 ± 0.25236 seconds for the 3-delay. Regions with a longer arterial transit time delay for the 7-delay compared to 3-delay resulted in an average arterial transit time estimation of 1.42565 ± 0.21872 seconds by the 7-delay sequence and 1.39388 ± 0.22056 seconds by the 3-delay sequences for the transit-time delay.

son of the corrected CBF maps testing for lower estimates for the 7-delay sequences compared with the 3-delay sequences was found to be statistically nonsignificant within the whole brain.

Transit-Delay Maps. In the peripheral regions of the brain, the transit-time estimates were found to be significantly shorter for the 7-delay sequence compared with the 3-delay sequence (Fig 3A). The mean difference between the delay sequences within the significant voxels corresponds to a medium effect size (1.47755 ± 0.24242 seconds versus 1.52408 ± 0.25236 seconds, 3.15% difference, $d = 0.19$) (Fig 3B).

Most interesting, in the center of the brain (Fig 3A), the 7-de-

lay sequence led to a significantly longer estimated transit time than the 3-delay measurements (1.42565 ± 0.21872 seconds versus 1.39388 ± 0.22056 seconds, 2.23% difference, $d = 0.14$) (Fig 3B).

Voxelwise Comparison between Transit-Corrected and -Uncorrected Maps

On average across the entire brain, the transit time–corrected flow maps provided an estimation of almost 20%, exceeding the CBF value of the corresponding uncorrected flow maps, for both the 7-delay and 3-delay sequences (7-delay: 34.56 ± 13.58 versus $28.60 \pm$

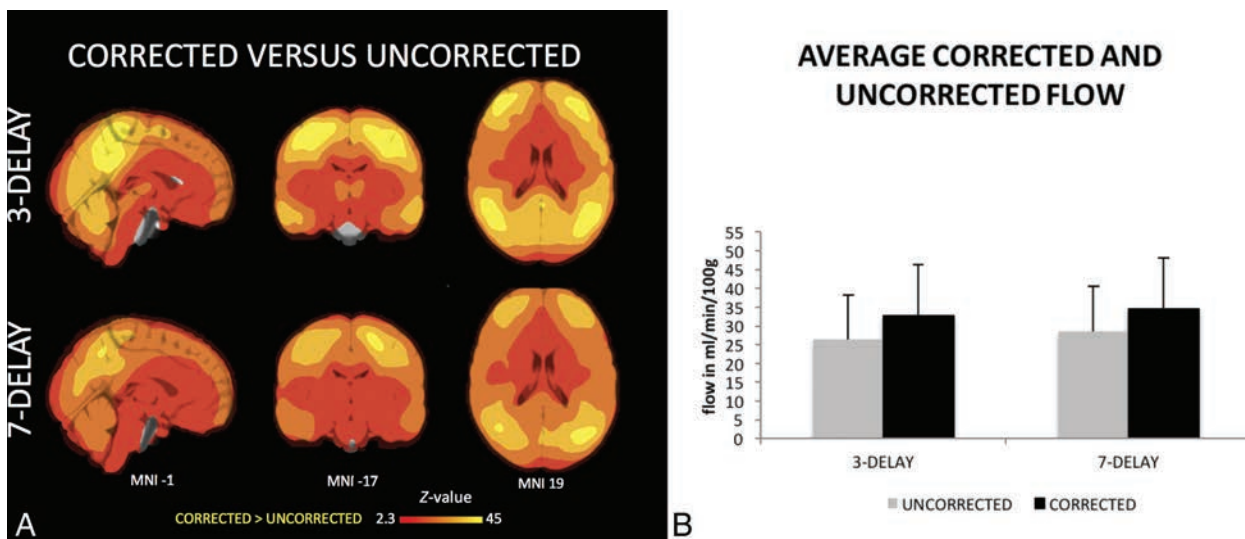


FIG 4. A, The spatial distribution of the differences between the uncorrected and corrected flow maps for the 7-delay and 3-delay sequences. On average, the transit-corrected flow maps provided a higher value for both the 7-delay and 3-delay compared with the corresponding uncorrected flow maps across the entire brain. B, The average estimated transit-uncorrected flow and the transit-corrected flow in milliliters/minute/100 g within the voxels that showed a significantly higher estimate for the transit-corrected sequences than for the 7-delay and the 3-delay sequences. This figure shows the difference between the uncorrected and corrected maps. The 7-delay sequences estimated a mean perfusion value of 28.60 ± 11.91 mL/min/100 g for the uncorrected versus 34.56 ± 13.58 mL/min/100 g for the corrected flow maps. For the 3-delay sequences, the uncorrected flow map resulted in an average perfusion estimation of 26.38 ± 11.74 mL/min/100 g versus the corrected map of 32.78 ± 13.44 mL/min/100 g. The corrected flow maps estimate for both sequences almost an additional 20% of the perfusion value of the uncorrected flow maps.

11.91 mL/min/100 g, 17.25% difference, $d = 0.47$; 3-delay: 32.78 ± 13.44 versus 26.38 ± 11.74 mL/min/100 g, 19.52% difference, $d = 0.53$ (Fig 4).

Laterality Index. The 7-delay and 3-delay sequences both represented a higher CBF signal in the right hemisphere. A more symmetric pattern was found for the 7-delay (mean = -0.013 ± 0.035) compared with the greater average hemispheric asymmetry of the 3-delay sequence of 2.3% (mean = -0.023 ± 0.35). The right lateralization was established as significantly lower in the 7-delay sequence compared with the 3-delay sequence (t -value = 3.89, $P < .001$).

DISCUSSION

The current study looked at 3-delay and 7-delay sequences by comparing the corrected, uncorrected, and delay maps. A greater CBF signal was found for both the uncorrected and corrected flow maps of the 7-delay sequence compared with the 3-delay sequence. These findings led us to conclude that multidelay ASL sequences with high numbers of delays lead to an estimation of higher CBF values than those with lower numbers of delays.

Comparison of 3-Delay versus 7-Delay on the Corrected and Uncorrected Flow Maps

Most interesting, the 7-delay surpassed the 3-delay in both the transit-uncorrected and transit-corrected flow maps in regions relating to the borderzone or watershed areas of the brain. The watershed areas are at distal parts of each vascular territory and therefore have a longer and more variable arterial transit time than other portions of each vascular territory.¹⁸ In consequence, estimation of the arterial transit time within these regions tends to be more challenging. A delay sequence with a higher number of

delays solves this problem by acquiring images at multiple PLD times, thereby measuring the entire delay curve more precisely.⁴ The advantages of a multidelay ASL sequence with a higher number of delays especially is seen when the distribution of transit times is wide, like that observed in older populations, as well as in some pathologies and cerebrovascular diseases with multiple arterial lesions.^{6,9} The elderly sample used in the current study would be sensitive to the effects of the advantage of a sequence with a higher number of PLDs, highlighting the effects of PLD choice on the estimated CBF signal within the watershed areas.

However, the precision of arterial transit time estimation by a sequence with more delay could be at the expense of the signal-to-noise ratio per unit of time.⁵ In line with these statements, the current study determined a lower estimation of the 7-delay sequence than the 3-delay, within the right insular region of the brain in the transit time-corrected flow maps. The insular region is the center of the vascularization and is one of the first regions to be vascularized.¹⁹ Thus, these areas will benefit less from the advantage in the estimation of longer arterial transit times of the sequence with a high number of delays. The CBF within the insular region might be underestimated by the 7-delay sequence, whereas the watershed areas benefit by obtaining a higher CBF signal.

Most interesting, this lower estimation of the 7-delay as opposed to the 3-delay is not observed within the uncorrected flow maps. A possible conclusion would be that correction for the transit time increases the overestimation of the 3-delay sequence within the right insular region.

In addition to the effects of the chosen number of delays, the current study showed the impact of the combination of different multidelays and correction for arterial transit time. We found a

larger increase in the estimated CBF value after correction for arterial transit time with the 7-delay sequence than with the 3-delay sequence. These findings suggest a stronger effect of transit-time correction on the delay sequence with a higher number of delays. Not only is the collection of parameters for the multidelay ASL important, but also the choice of combining different parameters can further influence CBF results.

Comparison of 3-Delay versus 7-Delay on the Transit-Delay Maps

The 3-delay and 7-delay sequences were further compared by looking at the transit-delay maps. The 7-delay demonstrated a shorter arterial transit time in the peripheral region sequence and a longer transit time in the central regions of the brain compared with the 3-delay. Most interesting, the central regions of the brain where this effect is apparent receive their blood supply mainly from the middle cerebral artery,¹⁸ suggesting an effect of the vascularization on these findings.

In addition, with a short PLD time, arterial signal is likely to artificially decrease the estimated transit delay in regions with substantial contamination.¹¹ This decrease in estimated transit delay will propagate into low transit-corrected CBF values. Our results show a shorter transit delay in the central regions of the brain with the 3-delay protocol, which are more likely to be contaminated by arterial signal. Additionally, regions like the insular cortex may be prone to arterial contamination, which could also explain why the 3-delay protocol displays greater CBF than the 7-delay protocol in this area. We chose not to use vascular crushing in this study. The risk with using vascular crushing is a substantially reduced SNR,³ enhanced sensitivity to motion, and possible removal of important clinical information.¹¹

Another point of influence might be the distribution of scans into the different time bins in the multidelay sequences. In a lower number of delays, more averages can be taken per each time bin, resulting in a higher SNR for each bin. This comes at the cost of having fewer time points. Therefore, time-related measures such as the delay maps are estimated less accurately. Not only are there fewer time bins, but also each time bin is longer; this feature results in a lower accuracy for estimating time-derived parameters for the 3-delay versus the 7-delay protocol.

The observed local differences in the delay maps of the 3-delay and the 7-delay sequences could be explained by this difference in time bins.

Comparison of 3-Delay versus 7-Delay in the Laterality Index

Both the 7-delay and 3-delay sequences represented a higher CBF signal in the right hemisphere compared with the left hemisphere; nevertheless, the mean laterality index determined within the 3-delay sequence was found to be significantly greater than the asymmetry of the 7-delay. This asymmetry of the CBF measures could have possibly led to the asymmetric findings within the corrected flow maps regarding the right insular region.

With the expectation of a symmetric perfusion distribution within the brain, one might argue that the 7-delay sequence provides a less biased global CBF approximation in comparison with the more asymmetric measurement of the 3-delay sequence.

However, the observed difference is relatively small (2%), and multiple other explanations could be argued, such as the acclimatization of the patient to the MR imaging environment rather than the sequence. Although there is an obvious explanation for these findings, it could be of interest to study the effects of number of delays on hemispherical differences in CBF estimation in more detail in future studies.

Comparison of the Transit-Corrected versus -Uncorrected Flow Maps

The current study investigated the effect of transit-time correction by comparing the transit-corrected flow maps with the transit-uncorrected flow maps. We established a higher average estimated CBF value for the corrected flow maps than for the uncorrected flow maps within the whole brain. This effect was constant in both the 7-delay and 3-delay sequences.

Although there was no regional variation found within the brain, the correction for delayed flow evidently influences the CBF signal measured.⁸ Hence, this study highlights the importance of applying arterial transit time correction.

The current study identified a 10% difference in CBF estimates between the 3-delay and 7-delay sequence. In clinical practice, where the differences between healthy subjects and patients are usually of a lower value than this 10%, the chosen number of delays in multidelay ASL could have an influential impact on the diagnostic process. In other respects, the quantification of CBF values could become biased by the mixed use of the different multidelay ASL sequences.

Limitations

The current study investigated a 7-delay and a 3-delay sequence to validate the effect of transit-time correction. Future research is recommended to access numerous different multidelay ASL sequences to confirm our conclusions and to find the optimal PLD for a specific region or research objective.

In addition, only the single ASL protocol was applied in this study. To further generalize the findings, one should investigate the scanners from distinct vendors and assess protocols variant to pulsed continuous arterial spin-labeling. Moreover, we acknowledge that the dynamic range of transit-delay mapping differs between the 3- and 7-delay protocols in the current study. The alternative (using equally spaced delays) provides images with diminishing SNR and increasing PLD.

A recent work by Guo et al²⁰ compared 3- and 7-delay ASL with linear and exponential delay spacing. They demonstrated that linear spacing outperformed exponential spacing. Their results are consistent with our findings when the relative SNR is greater than 2: Seven-delays provide a higher transit time delay estimate and higher CBF than 3-delays. Further work should focus on optimizing the minimum PLD, the delay spacing, and the use of vascular crushers.

Moreover, future studies are recommended to investigate differences between a low- and high-number multidelay sequence by investigating a sample with subjects of various ages. It is important to consider the relatively older sample size used to determine the advantage of a higher number delay sequence in this study. Nevertheless, for the investigation of elderly and pathologic pop-

ulations, as is the custom in clinical practice, the 7-delay sequence seems to be strongly preferable to the 3-delay sequence.

CONCLUSIONS

The results of this study support the necessity of standardizing acquisition parameters in multidelay ASL and identifying basic parameters as a confounding factor in CBF quantification studies. Additionally, the importance of applying arterial transit time correction was highlighted.

Disclosures: Merel van der Thiel—*RELATED: Grant:* This work is supported by Swiss National Foundation grants SNF 3200B0-1161193 and SPUM 33CM30-124111 and an unrestricted grant from the Association Suisse pour la Recherche Alzheimer.* Michael X. Burke—*UNRELATED: Employment:* GE Healthcare, *Comments:* full-time employee. R. Marc Lebel—*UNRELATED: Employment:* GE Healthcare; *Stock/Stock Options:* GE Healthcare, *Comments:* R.M.L. is a shareholder in GE. *Money paid to institution.

REFERENCES

1. Detre JA, Leigh JS, Williams DS, et al. **Perfusion imaging.** *Magn Reson Med* 1992;23:37–45 CrossRef Medline
2. Williams DS, Detre JA, Leigh JS, et al. **Magnetic resonance imaging of perfusion using spin inversion of arterial water.** *Proc Natl Acad Sci U S A* 1992;89:212–16 CrossRef Medline
3. Petcharunpaisan S, Ramalho J, Castillo M. **Arterial spin labeling in neuroimaging.** *World J Radiol* 2010;2:384–98 CrossRef Medline
4. Petersen ET, Lim T, Golay X. **Model-free arterial spin labeling quantification approach for perfusion MRI.** *Magn Reson Med* 2006;55: 219–32 CrossRef Medline
5. Detre JA, Alsop DC. **Perfusion magnetic resonance imaging with continuous arterial spin labeling: methods and clinical applications in the central nervous system.** *Eur J Radiol* 1999;30:115–24 CrossRef Medline
6. Ferré JC, Bannier E, Raoult H, et al. **Arterial spin labeling (ASL) perfusion: techniques and clinical use.** *Diagn Interv Imaging* 2013; 94:1211–23 CrossRef Medline
7. Alsop DC, Detre JA. **Reduced transit-time sensitivity in noninvasive magnetic resonance imaging of human cerebral blood flow.** *J Cereb Blood Flow Metab* 1996;16:1236–49 CrossRef Medline
8. MacIntosh BJ, Filippini N, Chappell MA, et al. **Assessment of arterial arrival times derived from multiple inversion time pulsed arterial spin labeling MRI.** *Magn Reson Med* 2010;63:641–47 CrossRef Medline
9. Haller S, Zaharchuk G, Thomas DL, et al. **Arterial spin-labeling perfusion of the brain: emerging clinical applications.** *Radiology* 2016; 281:337–56 CrossRef
10. Alsop DC, Detre JA, Golay X, et al. **Recommended implementation of arterial spin-labeled perfusion MRI for clinical applications: a consensus of the ISMRM perfusion study group and the European consortium for ASL in dementia.** *Magn Reson Med* 2015;73:102–16 CrossRef Medline
11. Wells JA, Lythgoe MF, Gadian DG, et al. **In vivo Hadamard encoded continuous arterial spin labeling (H-CASL).** *Magn Reson Med* 2010; 63:1111–18 CrossRef Medline
12. Wang DJ, Alger JR, Qiao JX, et al; UCLA Stroke Investigators. **Multi-delay multi-parametric arterial spin-labeled perfusion MRI in acute ischemic stroke: comparison with dynamic susceptibility contrast enhanced perfusion imaging.** *Neuroimage Clin* 2013;3:1–7 CrossRef Medline
13. Haller S, Montadon ML, Rodriguez C, et al. **APOE*4 is associated with gray matter loss in the posterior cingulate cortex in healthy elderly controls subsequently developing subtle cognitive decline.** *AJNR Am J Neuroradiol* 2017;38:1335–42 CrossRef Medline
14. Dai W, Robson PM, Shankaranarayanan A, et al. **Reduced resolution transit delay prescan for quantitative continuous arterial spin labeling perfusion imaging.** *Magn Reson Med* 2012;67: 1252–65 CrossRef Medline
15. Smith SM, Nichols TE. **Threshold-free cluster enhancement: addressing problems of smoothing, threshold dependence and localization in cluster inference.** *Neuroimage* 2009;44:83–98 CrossRef Medline
16. Liu Y, Zhu X, Feinberg D, et al. **Arterial spin labeling MRI study of age and gender effects on brain perfusion hemodynamics.** *Magn Reson Med* 2012;68:912–22 CrossRef Medline
17. Seghier M. **Laterality index in functional MRI: methodological issues.** *Magn Reson Imaging* 2008;26:594–601 CrossRef Medline
18. Liebeskind DS. **Collateral circulation.** *Stroke* 2003;34:2279–84 CrossRef Medline
19. Türe U, Yaşargil MG, Al-Mefty O, et al. **Arteries of the insula.** *J Neurosurg* 2000;92:676–87 CrossRef Medline
20. Guo J, Lebel M, Holdsworth S, et al. **Hadamard-encoded multi-delay PCASL: should the bolus durations be T1-Hadamard-encoded adjusted?** In: *Proceedings of the Annual Meeting and Exhibition of the International Society for Magnetic Resonance in Medicine*, Honolulu, Hawaii. April 22–27, 2017

Clinically Relevant Imaging Features for *MGMT* Promoter Methylation in Multiple Glioblastoma Studies: A Systematic Review and Meta-Analysis

C.H. Suh, H.S. Kim, S.C. Jung, C.G. Choi, and S.J. Kim



ABSTRACT

BACKGROUND: *O6-methylguanine methyltransferase (MGMT)* promoter methylation status has been reported as a prognostic biomarker in clinical trials.

PURPOSE: Our aim was to systematically evaluate imaging features of *MGMT* promoter methylated glioblastoma and to determine the diagnostic performance of MR imaging for prediction of *MGMT* promoter methylation in patients with newly diagnosed glioblastoma.

DATA SOURCES: A computerized search of Ovid MEDLINE and EMBASE up to February 27, 2018, was conducted.

STUDY SELECTION: We selected studies evaluating imaging features of *MGMT* promoter methylated glioblastoma and the diagnostic performance of MR imaging for prediction of *MGMT* promoter methylation.

DATA ANALYSIS: Pooled estimates of sensitivity and specificity were calculated using a hierarchic logistic regression model. Meta-regression and sensitivity analysis were performed.

DATA SYNTHESIS: Twenty-two articles including 2199 patients were included. *MGMT* promoter methylated glioblastoma is likely to show less edema, high ADC, and low perfusion. Ten articles including 753 patients were included in the meta-analysis. The summary sensitivity was 79% (95% CI, 72%–85%), and the summary specificity was 78% (95% CI, 71%–84%). In the meta-regression, *MGMT* promoter methylation and mean age were associated with heterogeneity. Sensitivity analysis excluding 1 study resolved the heterogeneity.

LIMITATIONS: Included studies used a variety of different MR imaging techniques to predict *MGMT* promoter methylation.

CONCLUSIONS: *MGMT* promoter methylated glioblastoma is likely to show less aggressive imaging features than *MGMT* promoter unmethylated glioblastoma. Despite the variety of different MR imaging techniques used, MR imaging in patients with newly diagnosed glioblastoma was shown to have the potential to predict *MGMT* promoter methylation noninvasively.

ABBREVIATIONS: DCE = dynamic contrast-enhanced imaging; HSROC = hierarchic summary receiver operating characteristic; *IDH* = isocitrate dehydrogenase; *MGMT* = *O6-methylguanine methyltransferase*; PRISMA = Preferred Reporting Items for Systematic Reviews and Meta-Analyses; QUADAS-2 = Quality Assessment of Diagnostic Accuracy Studies-2; WHO = World Health Organization

Epigenetic silencing of the *O6-methylguanine methyltransferase (MGMT)* gene by promoter methylation compromises DNA repair,¹ and *MGMT* promoter methylation status has been identified as a predictive biomarker for an alkylating chemotherapy response.^{2,3} In addition, *MGMT* promoter methylation status has been reported as a prognostic biomarker in clinical trials,^{4,5} and a

molecular-based recursive partitioning analysis model has recently been introduced as a potentially superior stratification variable in a clinical trial.⁶ Moreover, there is increasing evidence of the value of temozolomide monotherapy as a reasonable alternative to radiation therapy in elderly patients with *MGMT* promoter methylation.^{7,8} Furthermore, *MGMT* promoter methylation status has been reported as a strong predictor of pseudoprogression.⁹

Methylation-specific polymerase chain reaction of histopathologic specimens is considered a criterion standard method

Received November 30, 2017; accepted after revision May 8, 2018.

From the Department of Radiology and Research Institute of Radiology, University of Ulsan College of Medicine, Asan Medical Center, Seoul, Republic of Korea.

This work was supported by a grant from the National R&D Program for Cancer Control, Ministry of Health and Welfare, Republic of Korea (1720030).

Please address correspondence to Ho Sung Kim, MD, PhD, Department of Radiology and Research Institute of Radiology, University of Ulsan College of Medicine, Asan Medical Center, 86 Asanbyeongwon-Gil, Songpa-Gu, Seoul 138-736, Republic of Korea; e-mail: radhskim@gmail.com

Indicates open access to non-subscribers at www.ajnr.org

Indicates article with supplemental on-line tables.

Indicates article with supplemental on-line photos.

<http://dx.doi.org/10.3174/ajnr.A5711>

for the diagnosis of *MGMT* promoter methylation.² However, tissue-based genomics or epigenomics is generally invasive, and spatial and/or temporal intratumoral heterogeneity may reduce the value of invasive tissue-based genomic or epigenomic analysis. In cases of glioblastoma, a repeat operation or tissue sampling is also rarely performed at tumor recurrence.¹⁰ These tumor heterogeneities may provide opportunities for medical imaging, which could characterize the entire tumor in a noninvasive and repeatable way. Therefore, noninvasive, comprehensive, and repetitive assessments to predict *MGMT* promoter methylation may have great potential in routine clinical practice and may help in assessing prognosis or treatment response in patients with newly diagnosed glioblastoma.

Several studies have reported the imaging features and/or the diagnostic performance of MR imaging for the prediction of *MGMT* promoter methylation in patients with newly diagnosed glioblastoma.^{11–32} A diverse array of MR imaging modalities, including conventional MR imaging, diffusion-weighted imaging, diffusion tensor imaging, dynamic susceptibility-weighted contrast-enhanced imaging, dynamic contrast-enhanced imaging (DCE), arterial spin-labeling, susceptibility-weighted imaging, and amide proton transfer, have been used for such purposes. Recently, radiomics approaches using high-throughput quantitative imaging features have also been reported from various institutions.^{13,14,17,18,31}

However, the imaging prediction of *MGMT* promoter methylation has not yet been systematically evaluated, to our knowledge. Therefore, we systematically evaluated the imaging features of *MGMT* promoter methylated glioblastoma and determined the diagnostic performance of MR imaging for the prediction of *MGMT* promoter methylation in patients with newly diagnosed glioblastoma.

MATERIALS AND METHODS

This study was performed and reported in accordance with the Preferred Reporting Items for Systematic Reviews and Meta-Analyses (PRISMA) guidelines.³³ We established the following research questions: What are the imaging features of *MGMT* methylated glioblastoma in patients with newly diagnosed glioblastoma, and what is the diagnostic performance of MR imaging for prediction of *MGMT* promoter methylation?

Literature Search

A computerized search of Ovid MEDLINE and EMBASE up to February 27, 2018, was conducted to identify studies evaluating the imaging features of *MGMT* promoter methylated glioblastoma and the diagnostic performance of MR imaging for the prediction of *MGMT* promoter methylation in patients with newly diagnosed glioblastoma. The search terms combined synonyms for “glioblastoma,” “*MGMT*,” and “MR imaging” as follows: ((glioblastoma*) OR (glioma*)) AND ((methylguanine-DNA-methyltransferase) OR (O6-methylguanin-DNA-methyltransferase) OR (*MGMT*)) AND ((MR imaging) OR (MR imaging) OR (MR imaging)). The bibliographies of identified studies were screened manually to expand the search. The systematic search was limited to English-language publications.

Inclusion Criteria

Studies were included if they satisfied all of the following criteria: 1) patients with newly diagnosed glioblastoma (grade IV glioma based on the World Health Organization [WHO] classification criteria^{34,35}); 2) patients who underwent preoperative MR imaging including conventional MR imaging, advanced MR imaging, or a radiomics approach using high-throughput quantitative imaging features; 3) a reference standard based on methylation-specific polymerase chain reaction for *MGMT* promoter methylation; and 4) sufficient detail for acquisition of the imaging features of *MGMT* promoter methylated glioblastoma or reconstruction of 2×2 tables for determination of the diagnostic performance of MR imaging for prediction of *MGMT* promoter methylation in patients with newly diagnosed glioblastoma.

Exclusion Criteria

Studies were excluded if they met any of following criteria: 1) case reports/series including <10 patients; 2) conference abstracts, reviews, editorials, letters, or comments; 3) a study population including patients with recurrent glioblastoma; 4) studies focusing on subjects in whom techniques other than the MR imaging were used to diagnose *MGMT* promoter methylation; and 5) studies with a partially overlapping population (for the meta-analysis). In the event of an overlapping population or study period, the largest and latest study population was used. Authors of the studies were contacted for provision of further data when 2×2 tables could not be calculated.

Data Extraction and Quality Assessment

A standardized form was used to extract the following information from the selected studies—1) patient characteristics: sample size, number of patients with *MGMT* promoter methylation, histology of underlying disease (WHO grade), mean age (range), and male/female ratio; 2) study characteristics: authors, publication year, institution, patient recruitment period, study design (prospective versus retrospective), study enrollment (consecutive versus nonconsecutive), the reference standard, interval between MR imaging and the reference standard, and blinding to the reference standard; 3) MR imaging characteristics: magnetic field strength, scanner manufacturer, scanner model, number of head coil channels, types of MR imaging techniques, specific technical parameters, imaging features of *MGMT* promoter methylated glioblastoma; 4) MR imaging interpretation: number of readers, reader experience, and blinding to the reference standard; and 5) cutoff values for diagnosing *MGMT* promoter methylation and diagnostic performance of MR imaging for prediction of *MGMT* promoter methylation in patients with newly diagnosed glioblastoma.

Methodologic quality assessment was evaluated according to the Quality Assessment of Diagnostic Accuracy Studies-2 (QUADAS-2) criteria.³⁶ The literature selection, data extraction, and quality assessment were conducted independently by 2 reviewers (C.H.S. and H.S.K.). If disagreement occurred, a third reviewer (S.J.K.) was consulted to reach a consensus.

Data Synthesis and Analysis

Identification of the imaging features of *MGMT* promoter methylated glioblastoma and the diagnostic performance of MR imag-

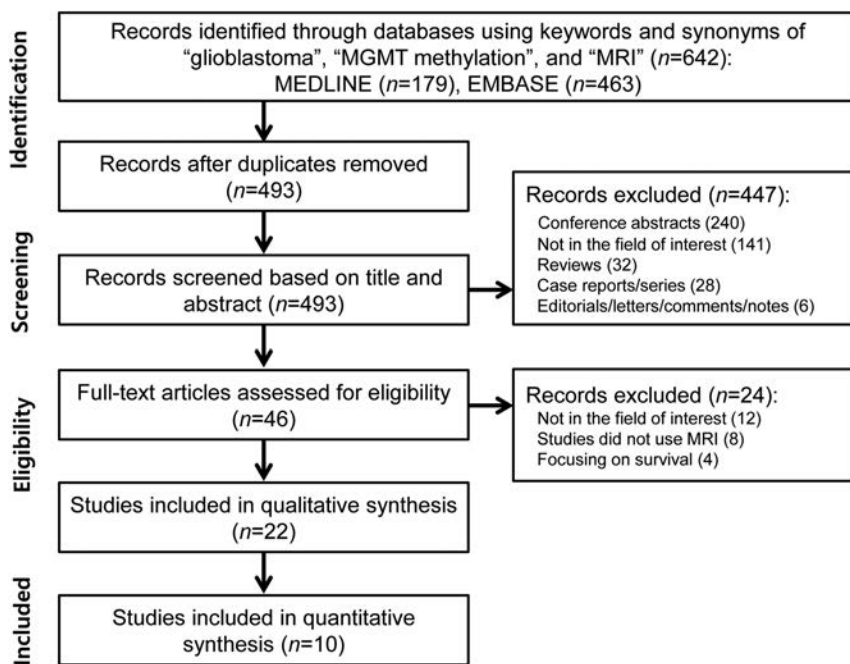


FIG 1. Flow diagram of the study-selection process.

ing for the prediction of *MGMT* promoter methylation in patients with newly diagnosed glioblastoma were the primary outcomes of the study. To identify their sensitivities and specificities, we reconstructed 2×2 tables from the included studies. If the diagnostic performances of several MR imaging techniques or multiple readers were assessed separately, the results with higher diagnostic performance were chosen.

Heterogeneity was evaluated by means of the following: 1) the Cochran Q test, with $P < .05$ indicating the presence of heterogeneity; 2) the Higgins inconsistency index (I^2) test, with the degree of heterogeneity being interpreted as follows: $I^2 = 0\%–40\%$, heterogeneity might not be important; $30\%–60\%$, moderate heterogeneity may be present; $50\%–90\%$, substantial heterogeneity may be present; and $75\%–100\%$, considerable heterogeneity³⁷; 3) visual assessment of a coupled forest plot for the presence of a threshold effect—that is, a positive correlation between sensitivity and the false-positive rate; and 4) a Spearman correlation coefficient of >0.6 implying a considerable threshold effect.³⁸

The pooled summary estimates of sensitivity and specificity were calculated using hierarchic logistic regression modeling—that is, bivariate and hierarchic summary receiver operating characteristic (HSROC) modeling.^{39–41} An HSROC curve with 95% confidence and prediction regions was plotted, and the area under the HSROC curve was calculated. Publication bias was analyzed using the Deeks funnel plot, and statistical significance was tested using the Deeks asymmetry test.⁴²

A meta-regression was performed to explain the effects of study heterogeneity. The following covariates were analyzed for the bivariate model: 1) the percentage of *MGMT* promoter methylation in the study population ($<49.5\%$ [median value of the included studies] versus $\geq 49.5\%$); 2) mean age (younger than 59 years [median value of the included studies] versus 59 years or older); 3) number of MR imaging readers (1 versus ≥ 2); 4) blind- ing to the reference standard for MR imaging readers; 5) magnetic

field strength (3T versus 1.5T); and 6) the use of radiomics approaches. Sub- group analyses according to studies using apparent diffusion coefficient and perfusion were conducted. In addition, sensitivity analyses were reassessed with the exclusion of 1 study with a lower diagnostic performance.

All statistical meta-analyses were performed by one of the authors (C.H.S., with 4 years of experience in conducting systematic reviews and meta-analyses) using the “midas” and “metandi” modules in STATA 10.0 (StataCorp, College Station, Texas) and the “mada” package in R statistical and computing software, Version 3.4.1 (<http://www.r-project.org>). P values $< .05$ indicated statistical significance.

RESULTS

Literature Search

The study selection process is described in Fig 1 and the On-line Appendix.

Twenty-two original articles evaluating the imaging features of *MGMT* promoter methylated glioblastoma, including 2199 patients, were included in this study.^{11–32}

Characteristics of the Included Studies

The patient and study characteristics of the included studies are listed in On-line Table 1. The size of the study populations ranged from 17 to 406 patients. Twenty-one of 22 studies included patients with newly diagnosed glioblastoma (WHO grade IV), and 1 study included high-grade glioma (WHO grades III and IV).²⁵ One study was prospective in design.²⁶ Twenty studies were retrospective,^{11–25,27,28,30–32} and 1 study did not explicitly state the design.²⁹ Study enrollment was consecutive in 3 studies^{16,18,25} and not explicit in the remaining studies. Fifteen of 22 studies used methylation-specific polymerase chain reaction as a reference standard to detect *MGMT* methylation,^{11,14–16,19–24,27,28,30–32} with the other studies using DNA methylation analysis,¹⁸ pyrosequencing,¹³ immunohistochemical staining,²⁹ or multiplex ligation-dependent probe amplification,²⁶ with the method not being stated in 3 studies.^{12,17,25}

MR Imaging Characteristics of the Included Studies

The MR imaging characteristics are shown in On-line Table 2. Ten studies used 3T scanners,^{12,13,15,16,18–21,23,25} 5 studies used 1.5T scanners,^{22,24,29–31} 3 studies used 1.5T and 3T scanners,^{17,27,28} and 4 studies did not state the scanner strength.^{11,14,26,32} A variety of different MR imaging techniques was used to predict *MGMT* promoter methylation: conventional MR imaging in 11 studies,^{11,13,14,17,26–32} DWI in 4 studies,^{19,20,22,24} CT/DWI/DTI/DSC in 1 study,²⁵ DWI/DSC/SWI in 1 study,¹⁸ DCE/DTI in 1 study,²¹ DWI/arterial spin-labeling in 1 study,¹² DSC in 1 study,²³ DCE in 1 study,¹⁶ and amide proton transfer in 1 study.¹⁵ Five studies used radiomics approaches from machine learning–based classification.^{13,14,17,18,31} MR imaging

was interpreted by 1–3 readers, with the level of experience of the readers ranging from 3 to 25 years. In 14 of 22 studies, the readers were blinded to the *MGMT* promoter methylation status of patients^{11–14,16,17,20,21,25,28–32}; however, this was not stated in the remaining studies.

Quality Assessment

The results of the quality assessment according to the QUADAS-2 criteria are described in On-line Fig 1. The quality of the studies was considered moderate, with 14 of the 22 studies satisfying at least 4 of the 7 QUADAS-2 domains. In the patient-selection domain, 20 of 22 studies were considered to have an unclear risk of bias because of nonconsecutive enrollment.^{11–15,17,19–32} In the index test domain, there was an unclear risk of bias in 8 studies because it was unclear whether MR imaging analysis was performed blinded to the reference standard.^{15,18,19,22–24,26,27} In the reference standard domain, the reference standard was not reported in 3 studies.^{12,17,25} In the flow and timing domain, the time intervals between MR imaging and the reference standard were not reported in 15 studies.^{11–14,16,17,19,20,25,27–32}

Imaging Features of *MGMT* Promoter Methylated Glioblastoma: A Systematic Review

Studies using conventional MR imaging demonstrated a variety of imaging features of *MGMT* promoter methylated glioblastoma (On-line Table 3). Two such studies revealed that *MGMT* promoter methylated glioblastoma showed less edema than *MGMT* promoter unmethylated glioblastoma.^{27,29} One study showed that mixed-nodular enhancement was significantly more frequent in *MGMT* promoter methylated glioblastoma,³² while ring enhancement was more frequent in *MGMT* promoter unmethylated glioblastoma.^{30,32} One study also showed that *MGMT* promoter methylated glioblastoma was lateralized to the left hemisphere, while *MGMT* promoter unmethylated glioblastoma was lateralized to the right hemisphere.²⁷ Furthermore, 1 study reported that glioblastoma with a higher rate of *MGMT* promoter protein expression (> 20%) was less necrotic than glioblastoma negative for, or with a lower rate of, *MGMT* promoter protein expression.²⁶

On DWI, *MGMT* promoter methylated glioblastoma showed higher ADC values than *MGMT* promoter unmethylated glioblastoma.^{12,25} In addition, *MGMT* promoter methylated glioblastoma also had a higher minimum ADC value than *MGMT* promoter unmethylated glioblastoma.^{20,24} Regarding perfusion, studies using DSC demonstrated that the normalized relative tumor blood volume was significantly lower in *MGMT* promoter methylated glioblastoma than in *MGMT* promoter unmethylated glioblastoma.²³ In addition, studies using arterial spin-labeling demonstrated that relative cerebral blood flow was also significantly lower in *MGMT* promoter methylated glioblastoma than in *MGMT* promoter unmethylated glioblastoma.¹²

Diagnostic Performance of MR Imaging for Prediction of *MGMT* Promoter Methylation: A Meta-Analysis

Ten original articles, which included 753 patients, evaluated the diagnostic performance of MR imaging in the imaging prediction of *MGMT* promoter methylation in patients with glioblastoma.^{12–15,17,18,21,23,24,30} The sensitivities and specificities of the

individual studies were 56% to 90% and 61% to 91%, respectively. A Q test demonstrated that heterogeneity was absent ($Q = 0.222$, $P = .447$). The Higgins I^2 statistic revealed moderate heterogeneity regarding both the sensitivity ($I^2 = 71.02\%$) and specificity ($I^2 = 65.71\%$). A coupled forest plot of the sensitivity and specificity showed no threshold effect (Fig 2). The Spearman correlation coefficient between the sensitivity and false-positive rate was -0.285 (95% CI, -0.775 – 0.420), also demonstrating no threshold effect.

The summary sensitivity for all 10 studies was 79% (95% CI, 72%–85%), and the summary specificity was 78% (95% CI, 71%–84%; Fig 2). There was a small difference between the 95% confidence and prediction regions in the HSROC curve, demonstrating a low possibility for the presence of heterogeneity among the studies (On-line Fig 2). The area under the HSROC curve was 0.86 (95% CI, 0.82–0.88). The Deeks funnel plot showed that the likelihood of publication bias was low ($P = .40$ for the slope coefficient; On-line Fig 3).

Exploration of the Heterogeneity

A meta-regression was performed to explain the causes of heterogeneity (On-line Table 4). Among the potential covariates, *MGMT* promoter methylation and mean age were associated with heterogeneity. Number of MR imaging readers, blinding to the reference standard for MR imaging readers, magnetic field strength, and studies using a radiomics approach were not shown to be significant factors affecting the heterogeneity.

Subgroup analysis according to studies using ADC showed that the summary sensitivity was 83% (95% CI, 71%–96%) and the summary specificity was 84% (95% CI, 74%–95%).^{12,24} Subgroup analysis according to studies using perfusion showed that the summary sensitivity was 72% (95% CI, 57%–88%) and the summary specificity was 82% (95% CI, 72%–92%).^{12,21,23}

One study showed a relatively low diagnostic performance (a sensitivity of 57% and specificity of 61%) in comparison with the other studies.¹⁸ When a sensitivity analysis was performed with the exclusion of this study,¹⁸ the heterogeneity in the sensitivity and specificity was resolved, with a recalculated pooled sensitivity of 82% (95% CI, 77%–86%; $I^2 = 28.36\%$) and a specificity of 80% (95% CI, 74%–86%; $I^2 = 36.43\%$).

DISCUSSION

Our study found that *MGMT* promoter methylated glioblastoma is likely to show less edema, high ADC, and low perfusion. In addition, this study revealed that the diagnostic performance of MR imaging for prediction of *MGMT* promoter methylation in patients with newly diagnosed glioblastoma was within a clinically acceptable range, even though various MR imaging techniques were used. The summary sensitivity was 79% (95% CI, 72%–85%), the summary specificity was 78% (95% CI, 71%–84%), and the area under the HSROC curve was 0.86 (95% CI, 0.82–0.88). In the meta-regression, heterogeneity was demonstrated in *MGMT* promoter methylation and mean age. In the sensitivity analysis, the heterogeneities of the sensitivity and specificity were resolved by removal of 1 study with outlying values, resulting in a recalculated pooled sensitivity of 82% (95% CI, 77%–86%) and a specificity of 80% (95% CI, 74%–86%). Despite the variety of MR

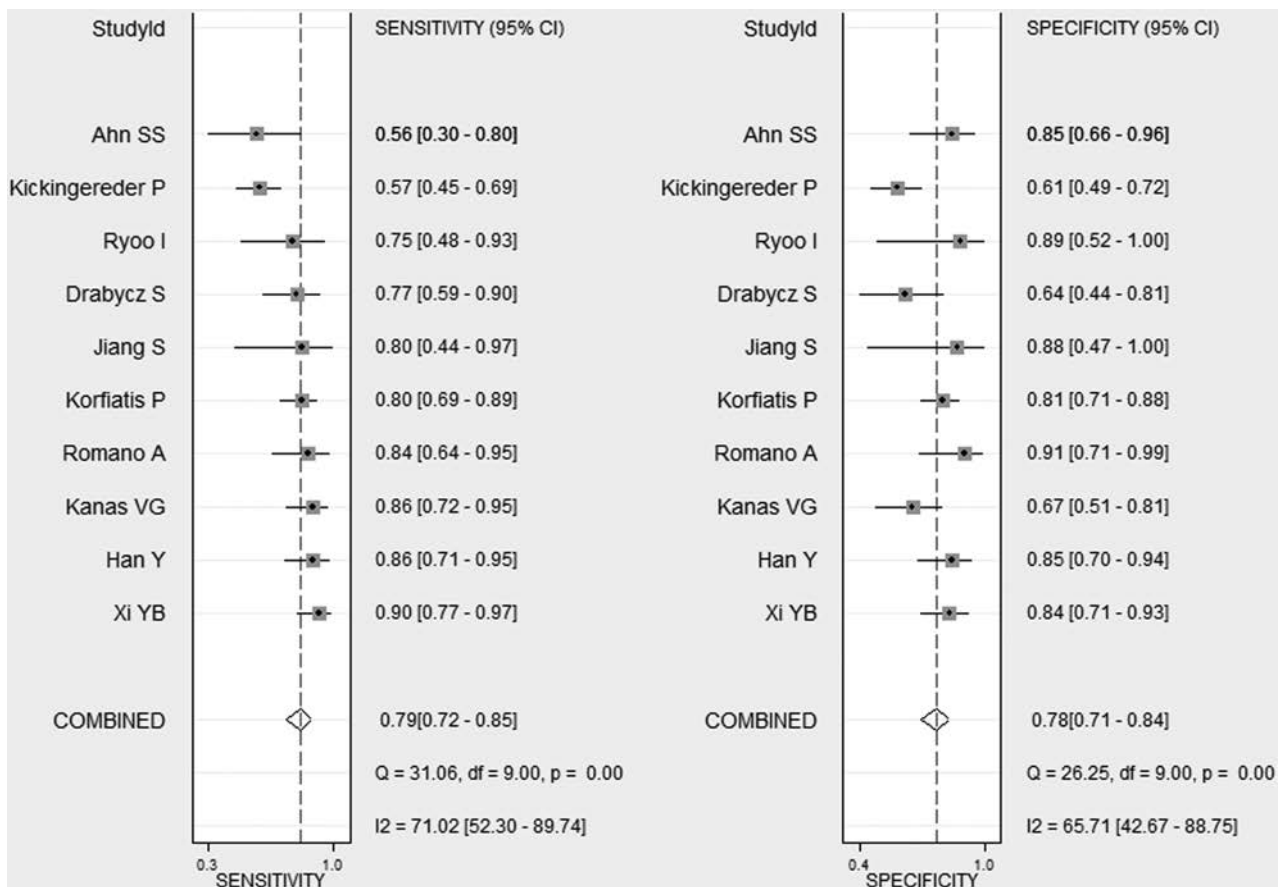


FIG 2. Coupled forest plots of the pooled sensitivity and specificity for the diagnostic performance of MR imaging for prediction of *MGMT* promoter methylation in patients with newly diagnosed glioblastoma. Numbers are pooled estimates with 95% confidence intervals in parentheses and horizontal lines indicating 95% CIs.

imaging techniques used, MR imaging in patients with newly diagnosed glioblastoma was shown to have the potential for noninvasive prediction of *MGMT* promoter methylation.

Imaging prediction of *MGMT* promoter methylated glioblastoma has not been widely used because of a lack of standardization in reporting, lack of standardization in imaging sequence, and uncertainty in terms of the criterion standard pathologic diagnosis of *MGMT* methylation status. In our study, we found that *MGMT* promoter methylated glioblastoma is likely to show less edema, high ADC, and low perfusion. In addition, studies using ADC or perfusion showed clinically acceptable diagnostic performance to predict *MGMT* promoter methylated glioblastoma. Therefore, imaging sequences including ADC or perfusion and corresponding reports of the results should be included. In terms of the reference standard, 15 of 22 studies used methylation-specific polymerase chain reaction. Therefore, we cautiously recommend methylation-specific polymerase chain reaction for the detection of *MGMT* methylation status. Although a variety of imaging sequences or reference standards was used, we believe our study may help in guiding future research.

Although there are multiple studies describing the distinctive imaging features of *MGMT* promoter methylated glioblastoma,^{16,19-24,26,27,29,30,32} some discrepancies do exist among them. In our understanding, an exact mechanism for the imaging prediction of *MGMT* promoter methylation has not been estab-

lished. The present study tried to focus on the imaging features of *MGMT* promoter methylated glioblastoma and the overall diagnostic performance of the various MR imaging techniques. We found that *MGMT* promoter methylated glioblastoma is likely to show less edema, high ADC, and low perfusion. The potential association between the imaging features and the overall diagnostic performance of MR imaging for the determination of *MGMT* promoter methylation status may have a predictive value for the evaluation of treatment response in newly diagnosed glioblastoma. This study revealed that MR imaging has a clinically acceptable diagnostic performance in the prediction of *MGMT* promoter methylation, with a summary sensitivity of 79% (95% CI, 72%–85%) and a summary specificity of 78% (95% CI, 71%–84%). Therefore, MR imaging in patients with newly diagnosed glioblastoma may potentially provide a noninvasive comprehensive and repetitive assessment for *MGMT* promoter methylation. However, due to the paucity of information regarding imaging features of *MGMT* promoter methylated glioblastoma, further study will be needed.

MGMT promoter methylation has been proposed as a predictive biomarker for benefit from alkylating agent chemotherapy in patients with *isocitrate dehydrogenase (IDH)* wild-type, but not *IDH*-mutant gliomas. This is due to the close correlation between *IDH* mutations and the presence of *MGMT* promoter methylation.^{43,44} One of the explanations for this correlation is that *IDH*

mutation is associated with a CpG island methylator phenotype in glioma.^{43,44} Therefore, the determination of *MGMT* promoter methylation status is clinically relevant in *IDH* wild-type lower grade gliomas as well as *IDH* wild-type glioblastoma. However, only 20%–30% of lower grade gliomas are *IDH* wild-type; therefore, due to the paucity of information reported so far, we could not include *IDH* wild-type lower grade gliomas. Further studies will be needed to answer the clinically relevant question.

The current study highlights 4 studies that evaluated the diagnostic performance of radiomics approaches in combination with machine-learning methods.^{13,14,17,18} With increases in the use of combined multiple imaging parameters to predict molecular characteristics, many researchers have used advanced statistical methods to increase the performance of such multiparametric imaging parameters. In particular, machine learning–based classification models have been popular; these aim to establish predictive models for molecular parameters by integrating all the available information from various MR imaging features.¹⁸ The present study revealed a summary sensitivity of 79% (95% CI, 70%–88%) and a summary specificity of 73% (95% CI, 66%–81%) for radiomics approaches, which is within a clinically acceptable range. However, studies using radiomics approaches showed slightly lower summary specificity than the other studies without statistical significance (87% [95% CI, 80%–94%]; $P = .42$). A possible reason for this significant difference is that radiomics approaches, which are data-driven, may be extensively affected by data quality. In addition, the step-by-step processes of radiomics approaches, which include imaging technique, feature extraction, feature selection, and classification by machine learning, vary substantially across institutions. Moreover, 3 studies used conventional MR imaging,^{13,14,17} while another study used multiparametric and multiregional MR imaging, including advanced techniques.¹⁸ Further effort to achieve the standardization of radiomics approaches is required.

This study revealed moderate heterogeneity across the included studies in both the sensitivity ($I^2 = 71.02\%$) and the specificity ($I^2 = 65.71\%$) measures. A meta-regression showed that *MGMT* promoter methylation and mean age were associated with heterogeneity. In addition, sensitivity analysis also demonstrated that the heterogeneities in the sensitivity and specificity were resolved when a study with outlying values was removed ($I^2 = 28.36\%$ and $I^2 = 36.43\%$, respectively). Although our meta-regression and sensitivity analysis may have explained some of the heterogeneity, further heterogeneity remains unexplained. A wide variety of MR imaging techniques was used to predict *MGMT* promoter methylation across the included studies: conventional MR imaging,^{13,14,17,30} DWI/DSC/SWI,¹⁸ DWI/arterial spin-labeling,¹² DCE/DTI,²¹ DWI,²⁴ DSC,²³ and amide proton transfer.¹⁵ The use of these different MR imaging techniques across the included studies is considered a major cause of study heterogeneity. To use MR imaging as a potential imaging predictor for molecular classification, the standardization of MR imaging acquisition, processing, and image analysis should be established.

This study is subject to several limitations. First, 22 studies were included in the systematic review; however, only 10 studies were included in the meta-analysis. In terms of imaging features of *MGMT* promoter methylated glioblastoma, a small number of

studies for each technique were included. However, these studies were the only currently available articles, and future studies will be needed. Second, the included studies used a variety of different MR imaging techniques to predict *MGMT* promoter methylation, and heterogeneity was reported in the sensitivity and specificity. To identify the source of the heterogeneity, we conducted a meta-regression and sensitivity analysis. We conducted our systematic review and meta-analysis using robust methodology (hierarchical logistic regression modeling^{39–41}) and reported the study results according to prestigious guidelines: PRISMA,³³ the Agency for Healthcare Research and Quality,⁴⁵ and the Handbook for Systematic Reviews of Diagnostic Test Accuracy published by the Cochrane Collaboration.⁴⁶

CONCLUSIONS

MGMT promoter methylated glioblastoma is likely to show less aggressive imaging features than *MGMT* promoter unmethylated glioblastoma. Despite the variety of different MR imaging techniques used, MR imaging in patients with newly diagnosed glioblastoma was shown to have the potential to predict *MGMT* promoter methylation noninvasively.

REFERENCES

1. Esteller M, Herman JG. **Generating mutations but providing chemosensitivity: the role of O6-methylguanine DNA methyltransferase in human cancer.** *Oncogene* 2004;23:1–8 CrossRef Medline
2. Hegi ME, Diserens AC, Gorlia T, et al. **MGMT gene silencing and benefit from temozolomide in glioblastoma.** *N Engl J Med* 2005;352:997–1003 CrossRef Medline
3. Esteller M, Garcia-Foncillas J, Andion E, et al. **Inactivation of the DNA-repair gene MGMT and the clinical response of gliomas to alkylating agents.** *N Engl J Med* 2000;343:1350–54 CrossRef Medline
4. Brandes AA, Tosoni A, Franceschi E, et al. **Recurrence pattern after temozolomide concomitant with and adjuvant to radiotherapy in newly diagnosed patients with glioblastoma: correlation with MGMT promoter methylation status.** *J Clin Oncol* 2009;27:1275–79 CrossRef Medline
5. Weller M, Tabatabai G, Kastner B, et al; DIRECTOR Study Group. **MGMT promoter methylation is a strong prognostic biomarker for benefit from Dose-Intensified Temozolomide Rechallenge in Progressive Glioblastoma: the DIRECTOR trial.** *Clin Cancer Res* 2015;21:2057–64 CrossRef Medline
6. Bell EH, Pugh SL, McElroy JP, et al. **Molecular-based recursive partitioning analysis model for glioblastoma in the temozolomide era: a correlative analysis based on NRG oncology RTOG 0525.** *JAMA Oncol* 2017;3:784–92 CrossRef Medline
7. Perry JR, Laperriere N, O'Callaghan CJ, et al; Trial Investigators. **Short-course radiation plus temozolomide in elderly patients with glioblastoma.** *N Engl J Med* 2017;376:1027–37 CrossRef Medline
8. Zarnett OJ, Sahgal A, Gosio J, et al. **Treatment of elderly patients with glioblastoma: a systematic evidence-based analysis.** *JAMA Neurol* 2015;72:589–96 CrossRef Medline
9. Brandes AA, Franceschi E, Tosoni A, et al. **MGMT promoter methylation status can predict the incidence and outcome of pseudoprogression after concomitant radiochemotherapy in newly diagnosed glioblastoma patients.** *J Clin Oncol* 2008;26:2192–97 CrossRef Medline
10. Weller M, Cloughesy T, Perry JR, et al. **Standards of care for treatment of recurrent glioblastoma: are we there yet?** *Neuro Oncol* 2013;15:4–27 CrossRef Medline
11. Li HY, Sun CR, He M, et al. **Correlation between tumor location and clinical properties of glioblastomas in frontal and temporal lobes.** *World Neurosurg* 2018;112:e407–14 CrossRef Medline
12. Han Y, Yan LF, Wang XB, et al. **Structural and advanced imaging in**

- predicting MGMT promoter methylation of primary glioblastoma: a region of interest based analysis. *BMC Cancer* 2018;18:215 CrossRef Medline
13. Xi YB, Guo F, Xu ZL, et al. Radiomics signature: a potential biomarker for the prediction of MGMT promoter methylation in glioblastoma. *J Magn Reson Imaging* 2018;47:1380–87 CrossRef Medline
 14. Kanas VG, Zacharaki EI, Thomas GA, et al. Learning MRI-based classification models for MGMT methylation status prediction in glioblastoma. *Comput Methods Programs Biomed* 2017;140:249–57 CrossRef Medline
 15. Jiang S, Rui Q, Wang Y, et al. Discriminating MGMT promoter methylation status in patients with glioblastoma employing amide proton transfer-weighted MRI metrics. *Eur Radiol* 2018;28:2115–23 CrossRef Medline
 16. Choi YS, Ahn SS, Lee HJ, et al. The initial area under the curve derived from dynamic contrast-enhanced MRI improves prognosis prediction in glioblastoma with unmethylated MGMT promoter. *AJNR Am J Neuroradiol* 2017;38:1528–35 CrossRef Medline
 17. Korfiatis P, Kline TL, Coufalova L, et al. MRI texture features as biomarkers to predict MGMT methylation status in glioblastomas. *Med Phys* 2016;43:2835–44 CrossRef Medline
 18. Kickingereder P, Bonekamp D, Nowosielski M, et al. Radiogenomics of glioblastoma: machine learning-based classification of molecular characteristics by using multiparametric and multiregional MR imaging features. *Radiology* 2016;281:907–18 CrossRef Medline
 19. Choi YS, Ahn SS, Kim DW, et al. Incremental prognostic value of ADC histogram analysis over MGMT promoter methylation status in patients with glioblastoma. *Radiology* 2016;281:175–84 CrossRef Medline
 20. Rundle-Thiele D, Day B, Stringer B, et al. Using the apparent diffusion coefficient to identify MGMT promoter methylation status early in glioblastoma: importance of analytical method. *J Med Radiat Sci* 2015;62:92–98 CrossRef Medline
 21. Ahn SS, Shin NY, Chang JH, et al. Prediction of methylguanine methyltransferase promoter methylation in glioblastoma using dynamic contrast-enhanced magnetic resonance and diffusion tensor imaging. *J Neurosurg* 2014;121:367–73 CrossRef Medline
 22. Sunwoo L, Choi SH, Park CK, et al. Correlation of apparent diffusion coefficient values measured by diffusion MRI and MGMT promoter methylation semiquantitatively analyzed with MS-MLPA in patients with glioblastoma multiforme. *J Magn Reson Imaging* 2013;37:351–58 CrossRef Medline
 23. Ryoo I, Choi SH, Kim JH, et al. Cerebral blood volume calculated by dynamic susceptibility contrast-enhanced perfusion MR imaging: preliminary correlation study with glioblastoma genetic profiles. *PLoS One* 2013;8:e71704 CrossRef Medline
 24. Romano A, Calabria LF, Tavanti F, et al. Apparent diffusion coefficient obtained by magnetic resonance imaging as a prognostic marker in glioblastomas: correlation with MGMT promoter methylation status. *Eur Radiol* 2013;23:513–20 CrossRef Medline
 25. Moon WJ, Choi JW, Roh HG, et al. Imaging parameters of high grade gliomas in relation to the MGMT promoter methylation status: the CT, diffusion tensor imaging, and perfusion MR imaging. *Neuroradiology* 2012;54:555–63 CrossRef Medline
 26. Iliadis G, Kotoula V, Chatzizotiriou A, et al. Volumetric and MGMT parameters in glioblastoma patients: survival analysis. *BMC Cancer* 2012;12:3 CrossRef Medline
 27. Ellingson BM, Cloughesy TF, Pope WB, et al. Anatomic localization of O6-methylguanine DNA methyltransferase (MGMT) promoter methylated and unmethylated tumors: a radiographic study in 358 de novo human glioblastomas. *Neuroimage* 2012;59:908–16 CrossRef Medline
 28. Carrillo JA, Lai A, Nghiemphu PL, et al. Relationship between tumor enhancement, edema, IDH1 mutational status, MGMT promoter methylation, and survival in glioblastoma. *AJNR Am J Neuroradiol* 2012;33:1349–55 CrossRef Medline
 29. Li WB, Tang K, Zhang W, et al. Relationship between magnetic resonance imaging and molecular pathology in patients with glioblastoma multiforme. *Chin Med J (Engl)* 2011;124:2589–92 Medline
 30. Drabycz S, Roldán G, de Robles P, et al. An analysis of image texture, tumor location, and MGMT promoter methylation in glioblastoma using magnetic resonance imaging. *Neuroimage* 2010;49:1398–405 CrossRef Medline
 31. Levner I, Drabycz S, Roldan G, et al. Predicting MGMT methylation status of glioblastomas from MRI texture. *Med Image Comput Comput Assist Interv* 2009;12(Pt 2):522–30 Medline
 32. Eoli M, Menghi F, Bruzzone MG, et al. Methylation of O6-methylguanine DNA methyltransferase and loss of heterozygosity on 19q and/or 17p are overlapping features of secondary glioblastomas with prolonged survival. *Clin Cancer Res* 2007;13:2606–13 CrossRef Medline
 33. Liberati A, Altman DG, Tetzlaff J, et al. The PRISMA statement for reporting systematic reviews and meta-analyses of studies that evaluate health care interventions: explanation and elaboration. *Ann Intern Med* 2009;151:W65–94 Medline
 34. Louis DN, Ohgaki H, Wiestler OD, et al. The 2007 WHO classification of tumours of the central nervous system. *Acta Neuropathol* 2007;114:97–109 CrossRef Medline
 35. Louis DN, Perry A, Reifenberger G, et al. The 2016 World Health Organization Classification of Tumors of the Central Nervous System: a summary. *Acta Neuropathol* 2016;131:803–20 CrossRef Medline
 36. Whiting PF, Rutjes AW, Westwood ME, et al; QUADAS-2 Group. QUADAS-2: a revised tool for the quality assessment of diagnostic accuracy studies. *Ann Intern Med* 2011;155:529–36 CrossRef Medline
 37. Higgins J, Green S. *Cochrane Handbook for Systematic Reviews of Interventions*, Version 5.1.0. The Cochrane Collaboration. <http://handbook-5-1.cochrane.org/>. Updated March 2011. Accessed October 9, 2017
 38. Devillé WL, Buntinx F, Bouter LM, et al. Conducting systematic reviews of diagnostic studies: didactic guidelines. *BMC Med Res Methodol* 2002;2:9 CrossRef Medline
 39. Suh CH, Park SH. Successful publication of systematic review and meta-analysis of studies evaluating diagnostic test accuracy. *Korean J Radiol* 2016;17:5–6 CrossRef Medline
 40. Kim KW, Lee J, Choi SH, et al. Systematic review and meta-analysis of studies evaluating diagnostic test accuracy: a practical review for clinical researchers, Part 1: general guidance and tips. *Korean J Radiol* 2015;16:1175–87 CrossRef Medline
 41. Lee J, Kim KW, Choi SH, et al. Systematic review and meta-analysis of studies evaluating diagnostic test accuracy: a practical review for clinical researchers, Part 2: statistical methods of meta-analysis. *Korean J Radiol* 2015;16:1188–96 CrossRef Medline
 42. Deeks JJ, Macaskill P, Irwig L. The performance of tests of publication bias and other sample size effects in systematic reviews of diagnostic test accuracy was assessed. *J Clin Epidemiol* 2005;58:882–93 CrossRef Medline
 43. Wick W, Meisner C, Hentschel B, et al. Prognostic or predictive value of MGMT promoter methylation in gliomas depends on IDH1 mutation. *Neurology* 2013;81:1515–22 CrossRef Medline
 44. van den Bent MJ, Erdem-Eraslan L, Idbaih A, et al. MGMT-STP27 methylation status as predictive marker for response to PCV in anaplastic oligodendrogliomas and oligoastrocytomas: a report from EORTC study 26951. *Clin Cancer Res* 2013;19:5513–22 CrossRef Medline
 45. Trikalinos TA, Balion CM, Coleman CI, et al. Chapter 8: meta-analysis of test performance when there is a “gold standard”. *J Gen Intern Med* 2012;27(Suppl 1):S56–66 CrossRef Medline
 46. Deeks JJ, Bossuyt PM, Gatsonis C, eds. *2013 Cochrane Handbook for Systematic Reviews of Diagnostic Test Accuracy*, Version 1.0.0. The Cochrane Collaboration. <http://srdta.cochrane.org/handbook-dta-reviews>. Accessed October 9, 2017

MR Imaging Features of Anaplastic Pleomorphic Xanthoastrocytoma Mimicking High-Grade Astrocytoma

D. She, J. Liu, Z. Xing, Y. Zhang, D. Cao, and Z. Zhang



ABSTRACT

BACKGROUND AND PURPOSE: Anaplastic pleomorphic xanthoastrocytoma, which has been recently defined as a distinct entity in the 2016 World Health Organization classification, may exhibit aggressive clinical behavior and relatively worse prognosis than pleomorphic xanthoastrocytoma. This study aimed to investigate whether there were any differences in MR imaging characteristics between these 2 tumors.

MATERIALS AND METHODS: This retrospective study included 9 patients with anaplastic pleomorphic xanthoastrocytoma and 10 patients with pleomorphic xanthoastrocytoma who underwent MR imaging before an operation. DWI was performed in 17 patients (8 with anaplastic pleomorphic xanthoastrocytoma, 9 with pleomorphic xanthoastrocytoma); and DSC-PWI, in 9 patients (5 with anaplastic pleomorphic xanthoastrocytoma, 4 with pleomorphic xanthoastrocytoma). Demographics, conventional imaging characteristics (location, size, cystic degeneration, enhancement, peritumoral edema, and leptomeningeal contact), minimum relative ADC ratio, and maximum relative CBV ratio were evaluated between the anaplastic pleomorphic xanthoastrocytoma and pleomorphic xanthoastrocytoma groups.

RESULTS: Anaplastic pleomorphic xanthoastrocytoma was more likely to demonstrate high-grade features than pleomorphic xanthoastrocytoma, including greater maximum tumor diameter (4.7 ± 0.6 cm versus 3.1 ± 1.1 cm, $P = .001$), more frequent heterogeneous contrast enhancement of solid portions (88.9% versus 20.0%, $P = .01$), more obvious peritumoral edema (2.3 ± 0.9 cm versus 1.0 ± 0.9 cm, $P = .008$), lower minimum relative ADC on DWI (1.0 ± 0.2 versus 1.5 ± 0.4 , $P = .008$), and higher maximum relative CBV on DSC-PWI (2.6 ± 0.8 versus 1.6 ± 0.2 , $P = .036$).

CONCLUSIONS: Anaplastic pleomorphic xanthoastrocytomas often have more aggressive MR imaging features mimicking high-grade astrocytomas than pleomorphic xanthoastrocytomas. DWI and DSC-PWI might be useful in the characterization and differentiation of anaplastic pleomorphic xanthoastrocytoma and pleomorphic xanthoastrocytoma.

ABBREVIATIONS: APXA = anaplastic pleomorphic xanthoastrocytoma; PXA = pleomorphic xanthoastrocytoma; $rADC_{min}$ = minimum relative ADC; $rCBV_{max}$ = maximum relative CBV; WHO = World Health Organization

Pleomorphic xanthoastrocytoma (PXA) is a rare circumscribed glioma composing <1% of all astrocytic tumors, usually occurring in children and young adults.¹ It was first described in 1979 by Kepes et al² and was recognized as a distinct brain tumor

by the World Health Organization (WHO) in 1993.³ Although PXA was classified as a WHO grade II tumor, “PXA with anaplastic features” composes 15%–50% of these lesions.^{4–7} The 2016 WHO classification system has divided PXA into 2 distinct entities based on histopathologic features: WHO grade II PXA and WHO grade III anaplastic PXA (APXA).^{8,9} The APXA is defined as the presence of ≥ 5 mitoses per 10 high-power fields. Only gross total resection may be performed for the patients with PXA, whereas attempted gross total resection and adjuvant therapies are required for the patients with APXA.^{5,10} Furthermore, APXA has been reported to have a worse prognosis than PXA, with 5-year overall survival of 57.1%.^{5,11} Therefore, preoperative differentiation between the 2 entities by MR imaging may aid in planning the treatment strategy and predicting prognosis.

APXA is associated with histopathologic features of malignancy, such as increased mitotic activity, necrosis, or endothelial

Received November 20, 2017; accepted after revision April 18, 2018.

From the Departments of Radiology (D.S., J.L., Z.X., D.C.) and Pathology (Y.Z.), First Affiliated Hospital of Fujian Medical University, Fuzhou, P.R. China; and Siemens Healthcare Ltd (Z.Z.), Shanghai, P.R. China

The first two authors contributed equally to this study.

This work was supported by the Leading Project of the Department of Science and Technology of Fujian Province (No. 2016Y0042).

Please address correspondence to Dairong Cao, MD, Department of Radiology, First Affiliated Hospital of Fujian Medical University, 20 Cha-Zhong Rd, Fuzhou, Fujian 350005, P.R. China; e-mail: dairongcao@163.com

Indicates open access to non-subscribers at www.ajnr.org

<http://dx.doi.org/10.3174/ajnr.A5701>

proliferation.^{12,13} Some studies have reported the characteristic MR imaging appearances of PXA^{14–20} but did not separate the imaging characteristics of APXA from PXA. Previously, only a few case reports or small case series were available regarding the MR imaging features of APXA, which demonstrated intense heterogeneous enhancement with severe peritumoral edema.^{20–26} Moreover, Moore et al¹⁴ reported a patient with APXA who underwent diffusion-weighted MR imaging showing diffusion restriction, indicating that DWI may be potentially useful for the characterization of APXA. To the best of our knowledge, conventional and advanced MR imaging for APXA have not been systematically reported. Therefore, the purpose of this study was to investigate the conventional and advanced MR imaging features of APXA and PXA to determine whether there are any differences in imaging characteristics between these 2 tumors.

MATERIALS AND METHODS

Study Population

This retrospective study was approved by the institutional review board, and the requirement of written informed consent was waived. We collected 19 consecutive patients who underwent preoperative MR imaging for a pathologically proved APXA ($n = 9$) or PXA ($n = 10$) in our hospital between January 2008 and November 2017. The MR imaging and clinical records of these patients were analyzed.

Histopathologic Diagnosis

All cases were reviewed on the basis of the histologic features by a neuropathologist (15 years of experience in neuropathology) according to the 2016 WHO classification of central nervous system tumors. The diagnostic criteria included tumors demonstrating a relatively solid growth pattern, composed of spindle-shaped, pleomorphic, and multinucleated cells, associated with both pale and bright eosinophilic granular bodies to be diagnosed as PXA. Anaplastic features, which included a mitotic index of ≥ 5 of 10 high-power fields with or without necrosis and endothelial proliferation, were diagnosed as APXA.

Preoperative MR Imaging Techniques

All patients underwent MR imaging on 3T scanners (Magnetom Verio or Magnetom Skyra; Siemens, Erlangen, Germany) or a 1.5T scanner (Signa TwinSpeed; GE Healthcare, Milwaukee, Wisconsin). The retrospective nature of this study resulted in variability in MR images and imaging protocols. Conventional MR imaging protocols included an axial T2-weighted sequence, nonenhanced axial and sagittal T1-weighted sequences, and 3 orthogonal plane contrast-enhanced T1-weighted sequences. An FOV of 22 cm², imaging matrix of 256 × 256, and slice thickness of 5 mm were uniformly applied in all sequences.

DWI was performed in 9 patients with PXA and 8 patients with APXA using an axial echo-planar sequence according to following technique parameters: TR/TE = 8200/102 ms, FOV = 22 × 22 cm, section thickness/gap = 5 mm/1 mm, diffusion gradient encoding = $b=0$, 1000 s/mm². The diffusion gradient was used in 3 orthogonal directions. ADC maps were automatically calculated using a monoexponential model.

Dynamic susceptibility contrast-enhanced perfusion-weighted im-

aging was available in 4 patients with PXA and 5 patients with APXA. DSC-PWI was performed with a T2*-weighted gradient recalled echo-planar imaging sequence during the intravenous power injection of 0.1 mmol/kg of gadopentetate dimeglumine or gadobenate dimeglumine at a flow rate of 5 mL/s. The parameters of DSC-PWI were as follows: TR/TE = 1000–1250/54 ms; FOV = 22 × 22 cm; section thickness/gap = 5 mm/1 mm. The CBV maps were generated with a single-compartment model and an automated arterial input function, as described in our previous study.²⁷

MR Imaging Analysis

All images were reviewed in consensus by 2 radiologists (readers 1 and 2 with 20 and 8 years of experience in neuroimaging, respectively) to make a factual comparison and minimize the confounding effects. The readers were blinded to tumor histology and recorded the following tumor characteristics: 1) tumor location (frontal, occipital, temporal, or parietal; superficial or deep); 2) tumor size (largest diameter, in centimeters); 3) the presence of cystic degeneration; 4) enhancement characteristics of the solid component (heterogeneous or homogeneous); 5) the presence and degree of peritumoral edema (largest diameter, in centimeters); 6) leptomeningeal contact; and 7) the presence of restricted diffusion, defined as high signal on DWI and corresponding low signal on ADC maps compared with contralateral normal brain parenchyma. Tumor size was defined as the largest diameter measured on contrast-enhanced T1WI. The peritumoral edema was defined as the nonenhanced, T2-hyperintense regions surrounding the enhancing tumors on contrast-enhanced T1WI. The tumor location was defined as the main lobe involvement when >1 lobe was involved.

When DWI or DSC-PWI examinations were available, another experienced radiologist (reader 3 with 4 years of experience in neuroimaging) blinded to tumor histopathology evaluated the ADC maps and CBV maps separately. The ADC values of tumor were calculated by placing an ROI inside the solid components of the tumor on the ADC maps. Three nonoverlapping ROIs (20–30 mm²) were manually placed inside the solid components of the tumor on the ADC maps where the tumor showed relatively low signal. The minimum ADC values were taken into account. In 2 tumors with smaller solid components or obvious hemorrhage, only 1 ROI could be placed on the enhancing portions of the tumor. The ROI placement was made from the contrast-enhancing solid components of the tumor, avoiding cystic, hemorrhagic, or apparent vascular structures that might influence the ADC values. To minimize variances of ADC values in an individual patient, we placed a single ROI inside the contralateral normal-appearing brain parenchyma on ADC maps. CBV measurements were performed with the same ROI as used for ADC measurements, and the maximum CBV values were considered. Tumor/parenchyma minimum relative ADC ratios ($rADC_{min}$) and maximum relative CBV ratios ($rCBV_{max}$) were calculated.

Statistical Analysis

The normality of all continuous parameters was initially assessed using the Kolmogorov-Smirnov test. The Fisher exact test was

Table 1: The demographic data and conventional MR imaging characteristics of PXA and APXA

	PXA (n = 10)	APXA (n = 9)	P Value
Clinical data			
Male sex (No.) (%)	6 (46.2%)	4 (44.4%)	.604
Mean age (yr)	32.8 ± 22.3	47.7 ± 11.7	.09
Location (No.)			
Frontal lobe	2	2	
Temporal lobe	5	3	
Occipital lobe	1		
Parietal lobe	2	3	
Superficial location (No.) (%)	9 (90%)	8 (88.9%)	.720
Conventional MR imaging			
Mean size (cm)	3.1 ± 1.1	4.7 ± 0.6	.001
Presence of cystic degeneration (No.) (%)	7 (70.0%)	8 (88.9%)	.497
Peritumoral edema (mean) (cm)	1.0 ± 0.9	2.3 ± 0.9	.008
Heterogeneous enhancement (No.) (%)	2 (20.0%)	8 (88.9%)	.01
Leptomeningeal contact (No.) (%)	9 (90%)	7 (77.8%)	.661

Table 2: Comparison of the PXA and APXA groups regarding the variables of interest^a

	PXA	APXA	P Value
rADC _{min} (n = 17)	1.5 ± 0.4	1.0 ± 0.2	.008
rCBV _{max} (n = 9)	1.6 ± 0.2	2.6 ± 0.8	.036

^a Data are mean ± SD.

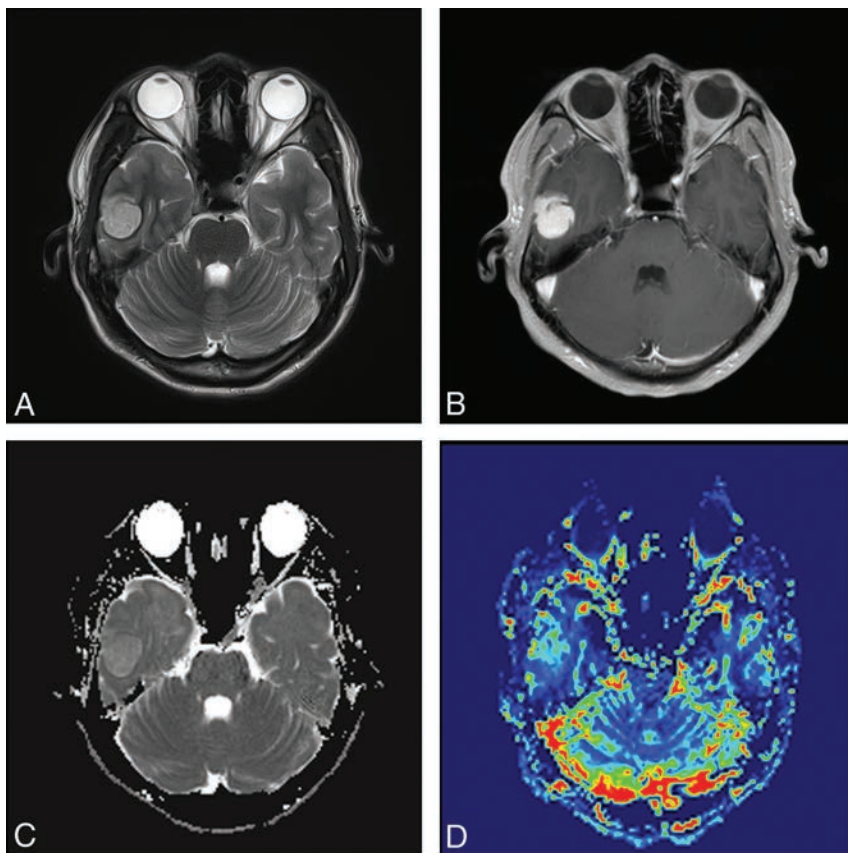


FIG 1. A 24-year-old male patient with pleomorphic astrocytoma. T2WI (A) and contrast-enhanced T1WI (B) show a homogeneous contrast-enhancing solid tumor without perilesional edema located in the temporal lobe. C, A correlative ADC map shows the tumor with an elevated ADC value (rADC_{min} = 1.5). D, A corresponding color CBV image shows significantly increased perfusion with the calculated rCBV_{max} of 1.6.

used to assess the differences in the categorical variables (age, sex, location, cystic degeneration, enhancement characteristics, leptomeningeal contact, and the presence of restricted diffusion) between the PXA and APXA groups. The Mann-Whitney *U* test was used to assess the differences in continuous variables (edema and size) between the PXA and APXA groups because of a lack of normality of the data. The Student *t* test was used to assess the differences for rCBV_{max} and rADC_{min} parameters between the 2 groups. Statistical analysis was performed with the Statistical Package for the Social Sciences (SPSS 22.0 Version for Windows; IBM, Armonk, New York). *P* values < .05 indicated statistical significance.

RESULTS

Demographic Data and Conventional MR Imaging

The demographic data and MR imaging features are summarized in Table 1. All 19 tumors were in the supratentorial region. Eight APXAs (8/9, 88.9%) and 9 PXAs (9/10, 90%) were superficial (on the surface of the brain parenchyma). There was no significance in the tumor location between PXA and APXA groups.

On the preoperative imaging, the lesion was significantly larger in patients with APXA than in those with PXA (4.7 ± 0.6 cm versus 3.1 ± 1.1 cm, *P* = .001). Peritumoral edema was observed in 7 PXA cases and 9 APXA cases, respectively. Eight patients with APXA (8/9, 88.9%) and 4 with PXA (4/10, 40.0%) had obvious

peritumoral edema (defined as >1 cm in diameter). The maximum diameter of peritumoral edema in the APXA group was significantly larger than that in the PXA group (*P* = .008). The presence of heterogeneous enhancement of solid portions was observed less frequently in patients with PXA than in those with APXA (2/10 versus 8/9, *P* = .01). Leptomeningeal contact was seen in 7 APXA cases and 9 PXA cases.

Advanced MR Imaging Findings

Table 2 summarizes the findings of 17 cases with DWI and 9 cases with DSC-PWI. Compared with contralateral normal brain parenchyma, relatively high signal intensity on DWI was more likely to be present in cases with APXA (5/8, 62.5%) than in those with PXA (1/9, 11.1%) (*P* = .027). Moreover, the rADC_{min} values of APXA were significantly lower than those of PXA (1.0 ± 0.2 versus 1.5 ± 0.4; *P* = .008). On CBV maps, the rCBV_{max} values of APXA were significantly higher than those of PXA (2.6 ± 0.8 versus 1.6 ± 0.2; *P* = .036). Representative cases are shown in Figs 1–3.

Table 3 summarizes the MR imaging findings of APXA previously reported in the literature.^{20–26,28–35}

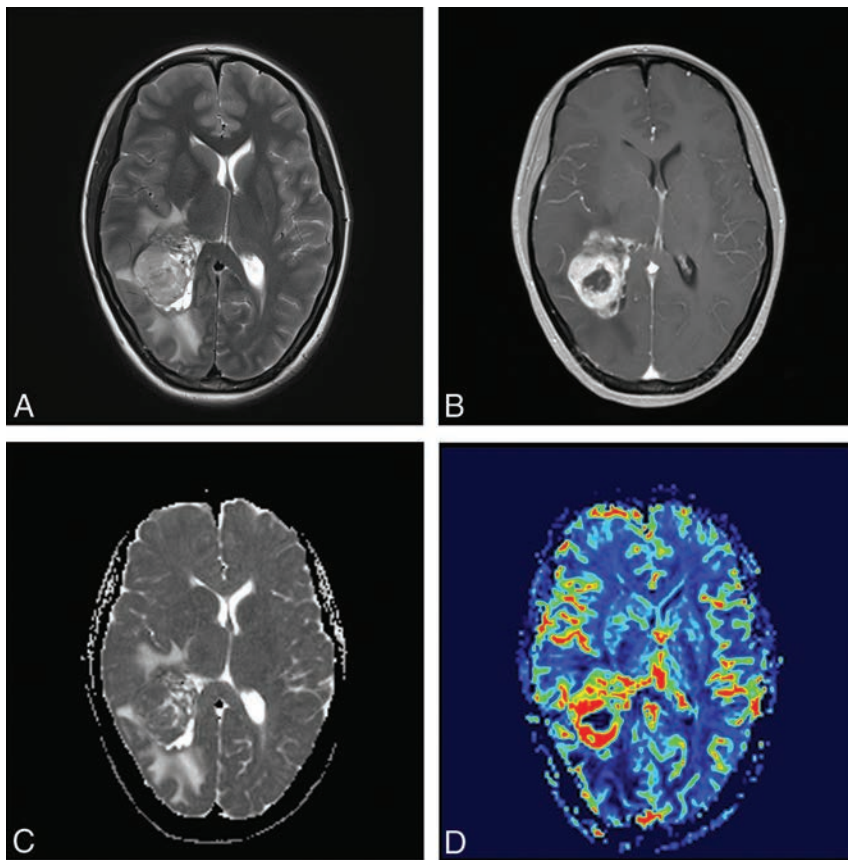


FIG 2. A 41-year-old female patient with anaplastic pleomorphic astrocytoma. T2WI (A) and contrast-enhanced TIWI (B) show a heterogeneous contrast-enhancing tumor with marked perilesional edema located in the occipital lobe. C, A correlative ADC map shows the lesion with a decreased ADC value ($rADC_{min} = 0.97$). D, A corresponding color CBV image shows significantly increased perfusion with a calculated $rCBV_{max}$ of 4.01.

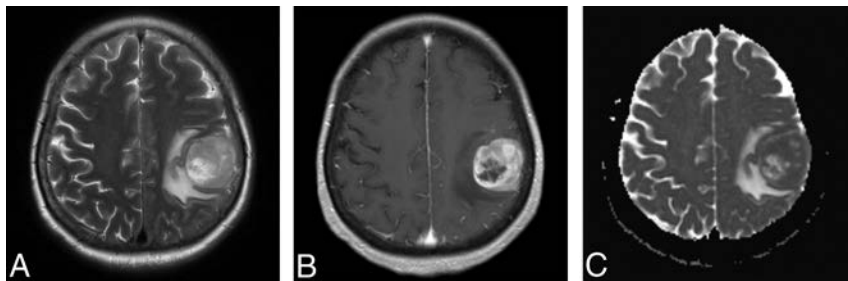


FIG 3. A 68-year-old female patient with anaplastic pleomorphic astrocytoma. T2WI (A) and contrast-enhanced TIWI (B) show a heterogeneous contrast-enhancing tumor with marked perilesional edema located in the parietal lobe. C, A correlative ADC map shows the lesion with diffusion restriction ($rADC_{min} = 0.92$).

DISCUSSION

Our results show that APXA had MR imaging features similar to those of other high-grade astrocytomas, namely more heterogeneous contrast enhancement, obvious peritumoral edema, lower $rADC_{min}$ ratio on DWI, and higher $rCBV_{max}$ ratio on DSC-PWI.

According to the 2016 WHO classification of the central nervous system, PXA is classified as a grade II astrocytoma histologically.⁸ Previous studies have found that PXAs may undergo spontaneous malignant transformation into high-grade gliomas across time without any treatment.^{12,22,36} In a study of the histologic evolution of the PXA, an abrupt transition from a typical PXA

without mitoses to a clearly high-grade tumor was found in a repeat biopsy during long follow-up, which was considered a secondary malignant change on a pre-existing PXA.³⁶ Thus, APXA (grade III astrocytoma) is more likely to be derived from a previous PXA with the development of anaplastic histologic features. In the present study, APXA accounted for 47.4% of the cases, which is much higher than the number previously reported by Giannini et al.⁷ However, the results reported by Hirose et al⁶ were that about 50% of PXAs showed anaplastic features, findings comparable with those in our study.

PXA most frequently occurred in children and young adults in our study, consistent with previous studies.^{1,5,37} In contrast, 6 of 9 patients with APXA were middle-aged adults (40–65 years of age) with a mean age of 47.7 years at their first presentation, which was discordant with previous studies.³⁷ It has been reported that high-grade astrocytomas, including anaplastic astrocytoma and glioblastoma, were more common in older adults with a median age of 56–64 years.^{38–40} However, most of the patients with APXA in our series were middle-aged adults and tended to be younger than those with other high-grade astrocytomas.

PXA is an overwhelming, superficial supratentorial tumor with a predilection for the temporal lobe. Previous studies reported that PXA occurred rarely in the cerebellum,³⁷ hypothalamus,⁴¹ quadrigeminal plate,⁴¹ or pineal gland.⁴² Similar to PXA, almost all APXA tumors in our series showed a superficial location in the cerebral hemispheres with involvement of the superficial cortex and leptomeninges. Both PXA and APXA are believed to develop from subpial astrocytes, which partly explains why these 2 tumors preferably arise from superficial cortical sites.² Our findings demonstrate

that a superficial location with leptomeningeal contact was a frequent feature of APXA and PXA. In addition, our results show that the common tumor location of PXA was the temporal lobe (50.0%), which is in keeping with findings in previous studies.^{16,17}

Conventional MR imaging can provide useful information regarding tumor size, contrast enhancement, peritumoral edema, necrosis, hemorrhage, and cystic degeneration, which are all helpful in characterizing tumor aggressiveness and evaluating tumor grading. In our study, we found that APXA had significantly

Table 3: Summary of MR imaging findings of APXA previously reported in the literature

No.	Author (Year)	Age (yr)/ Sex	Location	Size (cm)	Imaging Pattern	Enhancement	Peritumoral Edema	Well- Circumscribed
1	Tekkök and Sav (2004) ²²	13/M	Frontal	–	Solid-cystic	Heterogeneous/intense	Severe	–
2	Lubansu et al (2004) ²³	7/F	Temporal	6	Solid-cystic	Heterogeneous/intense	Severe	+
3	Chang et al (2006) ²⁴	4/F	Cerebellar vermis	–	Solid-cystic	Heterogeneous/intense	–	+
4	Nakajima et al (2006) ²⁵	31/F	Temporal	–	Solid	Heterogeneous/intense	–	+
5	Koga et al (2009) ²⁸	47/F	Frontal	6	Solid	Homogeneous/intense	Severe	+
6	Okazaki et al (2009) ²⁹	5/M	Frontal-temporal	–	Solid	Homogeneous/intense	–	+
7	Fu et al (2010) ²⁶	52/M	Ventricle	–	Cystic-solid	Heterogeneous/intense	–	+
8	Tsutsumi et al (2010) ³⁰	16/F	Temporal	6	Solid	Homogeneous/intense	–	+
9	Vu et al (2012) ³¹	50/M	Temporal	2.7	Solid-cystic	Heterogeneous/intense	Severe	+
10	Lim et al (2013) ²⁰	37/F	Corpus callosum	4	Cystic	–	Severe	+
11		60/F	Corpus callosum	4.8	Solid	Intense	Severe	+
12		53/F	Temporal	3.6	Solid	Intense	Severe	+
13	Montano et al (2013) ³²	22/M	Multicentric	–	Solid	Without enhancement	Mild	–
14	Benjamin et al (2015) ³³	65/M	Temporal	3.7	Cystic-solid	Heterogeneous/intense	–	+
15	Patibandla et al (2016) ²¹	35/M	Frontal	–	Solid	Heterogeneous/intense	Severe	–
16	Choudry et al (2016) ³⁴	55/M	Temporal	2.2	Solid	Heterogeneous/intense	Mild	+
17	Thara et al (2017) ³⁵	42/M	Temporal	8	Solid	Mild	Mild	+

Note:—+ indicates yes; –, no.

greater tumor size than PXA, which may be due to the relatively high proliferative potential of APXA. Previous case reports demonstrated that APXA showed intense heterogeneous enhancement and obvious peritumoral edema on conventional MR imaging.^{21,34} In our study, we also found that all except 1 APXA showed heterogeneous contrast enhancement with marked peritumoral edema. In contrast, only 2 PXA cases showed heterogeneous enhancement, and 3 cases had marked peritumoral edema. The enhancement pattern of APXA could be explained by the presence of necrosis, hemorrhage, and vascular proliferation within the tumor, which was observed in most APXAs by Rutkowski et al.¹¹ Additionally, our cohort showed results similar to those in a previous study for the frequency of the peritumoral edema.²⁰ In the study of Lim et al,²⁰ all PXAs with anaplastic features (4 cases) had severe perilesional edema, while only 1 of 18 PXAs presented with severe peritumoral edema, 6 cases had none, 8 cases had mild edema, and 3 cases had moderate edema. Our study demonstrated that the area of peritumoral edema in APXA was larger than that in PXA. Peritumoral edema was defined as nonenhancing, T2-hyperintense regions surrounding the enhancing tumors, which represented a heterogeneous mixture of infiltrative neoplastic cells and vasogenic edema in other high-grade astrocytomas.^{43,44} Despite appearing as a circumscribed tumor, most PXAs demonstrated infiltration into the surrounding brain.⁷ However, the pathology of peritumoral “edema” in APXA remains uncertain. Further pathologic investigations are required to explore whether the peritumoral edema surrounding the APXA tumor represents vasogenic edema or tumor infiltration.

DWI has been described as a useful tool for glioma grading using ADC values, which negatively correlate with cellularity and the Ki-67 labeling index in tumors.⁴⁵⁻⁴⁷ Only a few prior studies in the literature evaluated PXA and APXA using DWI.¹⁴ In a small group study of 11 children with PXA, Moore et al¹⁴ demonstrated that the mean ADC ratio of 6 PXAs, including 1 APXA, was 1.15, without statistical analysis. In the present study, we found that the signal intensity in the solid components of the APXA tended to be hyperintense relative to normal-appearing brain parenchyma on DWI. In addition, the signal intensity of APXA was significantly

higher than that of PXA on DWI. The rADC ratio of PXA and APXA in our study was 1.29 ± 0.44 , which was consistent with that in a recent study.¹⁴ To the best of our knowledge, the differences in ADC ratios between APXA and PXA have not been reported. Our study demonstrates that the rate of water diffusion of APXA, as reflected by the ADC ratio, was significantly lower than that of PXA. Compared with PXA, the association of lower ADC ratios in APXAs might be due to markedly high cellularity and a high nuclear/cytoplasmic ratio, which were also observed in other high grade astrocytomas. Therefore, our findings reveal that ADC could be a useful imaging parameter for assessing the differences between APXA and PXA based on distinct cell density and the nuclear/cytoplasmic ratio.

DSC-PWI has become an important tool in the preoperative characterization and grading of brain gliomas using rCBV values.⁴⁸⁻⁵¹ Although many studies have reported that rCBV parameters were useful in astrocytoma grading, most of these studies failed to group APXA as a high-grade glioma or even to consider it as a separate cohort.⁵¹⁻⁵⁴ To our knowledge, there are no studies assessing the differences in CBV values between APXA and PXA. Limited evidence suggested that the tumor vascularity of PXA was distinct from that in APXA. In a histopathologic study of PXA,⁶ 4 of 6 APXAs showed microvascular proliferation, while no PXA exhibited this phenomenon. We found that the rCBV_{max} values of APXA and PXA were 2.6 ± 0.8 and 1.6 ± 0.2 , respectively. The rCBV_{max} values of contrast-enhancing portions of APXA seemed to be higher than those of PXA. These preliminary findings may be explained by more microvascular proliferation in anaplastic lesions, resulting in an increase in the CBV value.⁶ However, the small number of patients did not allow making generalizations such as discrimination of APXA from PXA with DSC-PWI. Future investigations with emphasis on DSC-PWI of APXA and PXA may be of benefit.

In addition to the intrinsic limitations of a retrospective study, our study had several other limitations. First, the number of patients with advanced MR imaging remained limited; therefore, the conclusions should be interpreted with caution, especially for DSC-PWI. Future studies of larger cohorts with advanced MR

imaging are necessary to generalize these findings. Second, the patients with APXA seemed to be older than those with PXA, but the difference was not significant, possibly due to the small size of this study. Hence, the difference in age may affect the values of CBV and ADC. However, these parameters of the tumors were normalized by contralateral normal-appearing brain parenchyma to reduce intersubject variance including age and sex. Third, we only focused on imaging appearances and parameters, but there is a lack of a direct pathologic correlation. Therefore, we cannot state with certainty whether the imaging parameters represent true pathophysiologic information of the tumor. Thus, further prospective study with strict pathologic validation is recommended.

CONCLUSIONS

APXA can present with more aggressive conventional and advanced MR imaging features, mimicking high-grade astrocytoma at initial diagnosis, than PXA. Greater maximum tumor diameter, heterogeneous contrast enhancement, obvious peritumoral edema, and lower $rADC_{min}$ and higher $rCBV_{max}$ are more common features in APXA compared with PXA. DWI and DSC-PWI might be useful in the characterization and differentiation of APXA and PXA.

REFERENCES

- Rao AA, Laack NN, Giannini C, et al. **Pleomorphic xanthoastrocytoma in children and adolescents.** *Pediatr Blood Cancer* 2010;55:290–94 CrossRef Medline
- Kepes JJ, Rubinstein LJ, Eng LF. **Pleomorphic xanthoastrocytoma: a distinctive meningocerebral glioma of young subjects with relatively favorable prognosis—a study of 12 cases.** *Cancer* 1979;44:1839–52 Medline
- Kleihues P, Burger PC, Scheithauer BW. **The new WHO classification of brain tumours.** *Brain Pathol* 1993;3:255–68 CrossRef Medline
- Louis DN, Ohgaki H, Wiestler OD, et al. **The 2007 WHO classification of tumours of the central nervous system.** *Acta Neuropathol* 2007;114:97–109 CrossRef Medline
- Ida CM, Rodriguez FJ, Burger PC, et al. **Pleomorphic xanthoastrocytoma: natural history and long-term follow-up.** *Brain Pathol* 2015;25:575–86 CrossRef Medline
- Hirose T, Ishizawa K, Sugiyama K, et al. **Pleomorphic xanthoastrocytoma: a comparative pathological study between conventional and anaplastic types.** *Histopathology* 2008;52:183–93 Medline
- Giannini C, Scheithauer BW, Burger PC, et al. **Pleomorphic xanthoastrocytoma: what do we really know about it?** *Cancer* 1999;85:2033–45 Medline
- Louis DN, Perry A, Reifenberger G, et al. **The 2016 World Health Organization Classification of Tumors of the Central Nervous System: a summary.** *Acta Neuropathol* 2016;131:803–20 CrossRef Medline
- Wesseling P, Capper D. **WHO 2016 classification of gliomas.** *Neuropathol Appl Neurobiol* 2018;44:139–50 CrossRef Medline
- Marton E, Feletti A, Orvieto E, et al. **Malignant progression in pleomorphic xanthoastrocytoma: personal experience and review of the literature.** *J Neurol Sci* 2007;252:144–53 CrossRef Medline
- Rutkowski MJ, Oh T, Niflioglu GG, et al. **Pleomorphic xanthoastrocytoma with anaplastic features: retrospective case series.** *World Neurosurg* 2016;95:368–74 CrossRef Medline
- Kahramancetin N, Tihan T. **Aggressive behavior and anaplasia in pleomorphic xanthoastrocytoma: a plea for a revision of the current WHO classification.** *CNS Oncol* 2013;2:523–30 CrossRef Medline
- Tonse R, Gupta T, Epari S, et al. **Impact of WHO 2016 update of brain tumor classification, molecular markers and clinical outcomes in pleomorphic xanthoastrocytoma.** *J Neurooncol* 2018;136:343–50 CrossRef Medline
- Moore W, Mathis D, Gargan L, et al. **Pleomorphic xanthoastrocytoma of childhood: MR imaging and diffusion MR imaging features.** *AJNR Am J Neuroradiol* 2014;35:2192–96 CrossRef Medline
- Gonçalves VT, Reis F, Queiroz Lde S, et al. **Pleomorphic xanthoastrocytoma: magnetic resonance imaging findings in a series of cases with histopathological confirmation.** *Arq Neuropsiquiatr* 2013;71:35–39 CrossRef Medline
- Yu S, He L, Zhuang X, et al. **Pleomorphic xanthoastrocytoma: MR imaging findings in 19 patients.** *Acta Radiol* 2011;52:223–28 CrossRef Medline
- Crespo-Rodríguez AM, Smirniotopoulos JG, Rushing EJ. **MR and CT imaging of 24 pleomorphic xanthoastrocytomas (PXA) and a review of the literature.** *Neuroradiology* 2007;49:307–15 CrossRef Medline
- Bucciero A, De Caro M, De Stefano V, et al. **Pleomorphic xanthoastrocytoma: clinical, imaging and pathological features of four cases.** *Clin Neurol Neurosurg* 1997;99:40–45 CrossRef Medline
- Tien RD, Cardenas CA, Rajagopalan S. **Pleomorphic xanthoastrocytoma of the brain: MR findings in six patients.** *AJR Am J Roentgenol* 1992;159:1287–90 CrossRef Medline
- Lim S, Kim JH, Kim SA, et al. **Prognostic factors and therapeutic outcomes in 22 patients with pleomorphic xanthoastrocytoma.** *J Korean Neurosurg Soc* 2013;53:281–87 CrossRef Medline
- Patibandla MR, Nayak M, Purohit AK, et al. **Pleomorphic xanthoastrocytoma with anaplastic features: a rare case report and review of literature with reference to current management.** *Asian J Neurosurg* 2016;11:319 CrossRef
- Tekkök IH, Sav A. **Anaplastic pleomorphic xanthoastrocytomas: review of the literature with reference to malignancy potential.** *Pediatr Neurosurg* 2004;40:171–81 CrossRef Medline
- Lubansu A, Rorive S, David P, et al. **Cerebral anaplastic pleomorphic xanthoastrocytoma with meningeal dissemination at first presentation.** *Childs Nerv Syst* 2004;20:119–22 CrossRef Medline
- Chang HT, Latorre JG, Hahn S, et al. **Pediatric cerebellar pleomorphic xanthoastrocytoma with anaplastic features: a case of long-term survival after multimodality therapy.** *Childs Nerv Syst* 2006;22:609–13 CrossRef Medline
- Nakajima T, Kumabe T, Shamoto H, et al. **Malignant transformation of pleomorphic xanthoastrocytoma.** *Acta Neurochir (Wien)* 2006;148:67–71; discussion 71 CrossRef Medline
- Fu YJ, Miyahara H, Uzuka T, et al. **Intraventricular pleomorphic xanthoastrocytoma with anaplastic features.** *Neuropathology* 2010;30:443–48 CrossRef Medline
- Xing Z, Yang X, She D, et al. **Noninvasive assessment of IDH mutational status in World Health Organization grade II and III astrocytomas using DWI and DSC-PWI combined with conventional MR imaging.** *AJNR Am J Neuroradiol* 2017;38:1138–44 CrossRef Medline
- Koga T, Morita A, Maruyama K, et al. **Long-term control of disseminated pleomorphic xanthoastrocytoma with anaplastic features by means of stereotactic irradiation.** *Neuro Oncol* 2009;11:446–51 CrossRef Medline
- Okazaki T, Kageji T, Matsuzaki K, et al. **Primary anaplastic pleomorphic xanthoastrocytoma with widespread neuroaxis dissemination at diagnosis: a pediatric case report and review of the literature.** *J Neurooncol* 2009;94:431–37 CrossRef Medline
- Tsutsumi S, Abe Y, Yasumoto Y, et al. **Anaplastic pleomorphic xanthoastrocytoma with a component of anaplastic astrocytoma presenting as skull base tumor followed by downward extracranial extension: case report.** *Neurol Med Chir (Tokyo)* 2010;50:1108–12 CrossRef Medline
- Vu TM, Liubinas SV, Gonzales M, et al. **Malignant potential of pleomorphic xanthoastrocytoma.** *J Clin Neurosci* 2012;19:12–20 CrossRef Medline
- Montano N, Papacci F, Cioni B, et al. **Primary multicentric anaplastic pleomorphic xanthoastrocytoma with atypical features.** *J Clin Neurosci* 2013;20:1605–08 CrossRef Medline
- Benjamin C, Faustin A, Snuderl M, et al. **Anaplastic pleomorphic xanthoastrocytoma with spinal leptomeningeal spread at the time**

- of diagnosis in an adult. *J Clin Neurosci* 2015;22:1370–73 CrossRef Medline
34. Choudry UK, Khan SA, Qureshi A, et al. **Primary anaplastic pleomorphic xanthoastrocytoma in adults: case report and review of literature.** *Int J Surg Case Rep* 2016;27:183–88 CrossRef Medline
 35. Thara K, Sharma R, Thiagarajan G, et al. **Anaplastic pleomorphic xanthoastrocytoma in a case of neurofibromatosis type 1: a case report.** *J Clin Diagn Res* 2017;11:ED23–24 CrossRef Medline
 36. Wu X, Bandopadhyay P, Ng J, et al. **The evolution of the histology in pleomorphic xanthoastrocytomas in children: a study of 15 cases.** *Pathology* 2011;43:9–16 CrossRef Medline
 37. Perkins SM, Mitra N, Fei W, et al. **Patterns of care and outcomes of patients with pleomorphic xanthoastrocytoma: a SEER analysis.** *J Neurooncol* 2012;110:99–104 CrossRef Medline
 38. Ostrom QT, Gittleman H, Liao P, et al. **CBTRUS statistical report: primary brain and other central nervous system tumors diagnosed in the United States in 2010–2014.** *Neuro Oncol* 2017;19:v1–88 CrossRef Medline
 39. Thakkar JP, Dolecek TA, Horbinski C, et al. **Epidemiologic and molecular prognostic review of glioblastoma.** *Cancer Epidemiol Biomarkers Prev* 2014;23:1985–96 CrossRef Medline
 40. Rasmussen BK, Hansen S, Laursen RJ, et al. **Epidemiology of glioma: clinical characteristics, symptoms, and predictors of glioma patients grade I-IV in the Danish Neuro-Oncology Registry.** *J Neurooncol* 2017;135:571–79 CrossRef Medline
 41. Gallo P, Cecchi PC, Locatelli F, et al. **Pleomorphic xanthoastrocytoma: long-term results of surgical treatment and analysis of prognostic factors.** *Br J Neurosurg* 2013;27:759–64 CrossRef Medline
 42. Katayama K, Asano K, Shimamura N, et al. **Case of pleomorphic xanthoastrocytoma with anaplastic features in the pineal gland.** *Brain Tumor Pathol* 2013;30:242–46 CrossRef Medline
 43. Barajas RF Jr, Phillips JJ, Parvataneni R, et al. **Regional variation in histopathologic features of tumor specimens from treatment-naïve glioblastoma correlates with anatomic and physiologic MR imaging.** *Neuro Oncol* 2012;14:942–54 CrossRef Medline
 44. Konukoglu E, Clatz O, Bondiau PY, et al. **Extrapolating glioma invasion margin in brain magnetic resonance images: suggesting new irradiation margins.** *Med Image Anal* 2010;14:111–25 CrossRef Medline
 45. Sugahara T, Korogi Y, Kochi M, et al. **Usefulness of diffusion-weighted MRI with echo-planar technique in the evaluation of cellularity in gliomas.** *J Magn Reson Imaging* 1999;9:53–60 Medline
 46. Zeng Q, Dong F, Shi F, et al. **Apparent diffusion coefficient maps obtained from high b value diffusion-weighted imaging in the pre-operative evaluation of gliomas at 3T: comparison with standard b value diffusion-weighted imaging.** *Eur Radiol* 2017;27:5309–15 CrossRef Medline
 47. Higano S, Yun X, Kumabe T, et al. **Malignant astrocytic tumors: clinical importance of apparent diffusion coefficient in prediction of grade and prognosis.** *Radiology* 2006;241:839–46 CrossRef Medline
 48. Price SJ, Green HA, Dean AF, et al. **Correlation of MR relative cerebral blood volume measurements with cellular density and proliferation in high-grade gliomas: an image-guided biopsy study.** *AJNR Am J Neuroradiol* 2011;32:501–06 CrossRef Medline
 49. Sugahara T, Korogi Y, Kochi M, et al. **Correlation of MR imaging-determined cerebral blood volume maps with histologic and angiographic determination of vascularity of gliomas.** *AJR Am J Roentgenol* 1998;171:1479–86 CrossRef Medline
 50. Bisdas S, Kirkpatrick M, Giglio P, et al. **Cerebral blood volume measurements by perfusion-weighted MR imaging in gliomas: ready for prime time in predicting short-term outcome and recurrent disease?** *AJNR Am J Neuroradiol* 2009;30:681–88 CrossRef Medline
 51. Delgado AF, Delgado AF. **Discrimination between glioma grades II and III using dynamic susceptibility perfusion MRI: a meta-analysis.** *AJNR Am J Neuroradiol* 2017;38:1348–55 CrossRef Medline
 52. Law M, Yang S, Wang H, et al. **Glioma grading: sensitivity, specificity, and predictive values of perfusion MR imaging and proton MR spectroscopic imaging compared with conventional MR imaging.** *AJNR Am J Neuroradiol* 2003;24:1989–98 Medline
 53. Jain R, Griffith B, Alotaibi F, et al. **Glioma angiogenesis and perfusion imaging: understanding the relationship between tumor blood volume and leakiness with increasing glioma grade.** *AJNR Am J Neuroradiol* 2015;36:2030–35 CrossRef Medline
 54. Wang XC, Zhang H, Tan Y, et al. **Combined value of susceptibility-weighted and perfusion-weighted imaging in assessing WHO grade for brain astrocytomas.** *J Magn Reson Imaging* 2014;39:1569–74 CrossRef Medline

Application of 3D Fast Spin-Echo T1 Black-Blood Imaging in the Diagnosis and Prognostic Prediction of Patients with Leptomeningeal Carcinomatosis

J. Oh, S.H. Choi, E. Lee, D.J. Shin, S.W. Jo, R.-E. Yoo, K.M. Kang, T.J. Yun, J.-h. Kim, and C.-H. Sohn



ABSTRACT

BACKGROUND AND PURPOSE: Contrast-enhanced 3D fast spin-echo T1 black-blood imaging selectively suppresses the signal of blood flow and could provide a higher contrast-to-noise ratio compared with contrast-enhanced 3D ultrafast gradient recalled echo (contrast-enhanced gradient recalled echo) and 2D spin-echo T1WI (contrast-enhanced spin-echo). The purpose of our study was to evaluate whether black-blood imaging can improve the diagnostic accuracy for leptomeningeal carcinomatosis compared with contrast-enhanced gradient recalled-echo and contrast-enhanced spin-echo and, furthermore, to determine whether the grade of leptomeningeal carcinomatosis evaluated on black-blood imaging is a significant predictor of progression-free survival.

MATERIALS AND METHODS: Leptomeningeal carcinomatosis ($n = 78$) and healthy ($n = 31$) groups were enrolled. Contrast-enhanced gradient recalled-echo, contrast-enhanced spin-echo, and black-blood imaging were separately reviewed, and a diagnostic rating (positive, indeterminate, or negative) and grading of leptomeningeal carcinomatosis were assigned. The diagnostic accuracies of the 3 imaging sequences were compared in terms of leptomeningeal carcinomatosis detection. The Kaplan-Meier and the Cox proportional hazards model analyses were performed to determine the relationship between the leptomeningeal carcinomatosis grade evaluated on black-blood imaging and progression-free survival.

RESULTS: Black-blood imaging showed a significantly higher sensitivity (97.43%) than contrast-enhanced gradient recalled-echo (64.1%) and contrast-enhanced spin-echo (66.67%) ($P < .05$). In terms of specificities, we did not find any significant differences among contrast-enhanced gradient recalled-echo (90.32%), contrast-enhanced spin-echo (90.32%), and black-blood imaging (96.77%) ($P > .05$). A Cox proportional hazards model identified the time to metastasis, Karnofsky Performance Scale status, and a combination of the leptomeningeal carcinomatosis grade with a linear pattern as independent predictors of progression-free survival ($P < .05$).

CONCLUSIONS: Black-blood imaging can improve the diagnostic accuracy and predict progression-free survival in patients with leptomeningeal carcinomatosis.

ABBREVIATIONS: CE = contrast-enhanced; GRE = gradient recalled-echo; ICC = intraclass correlation coefficient; KPS = Karnofsky Performance Scale; LC = leptomeningeal carcinomatosis; PFS = progression-free survival; SE = spin-echo

Leptomeningeal carcinomatosis (LC) is a devastating complication of systemic cancer that occurs in approximately 5%–10% of patients with solid tumors and is most commonly observed in patients with breast cancer, lung cancer, or melanoma.¹

Recently, the incidence of LC has gradually started increasing as the diagnostic rate of primary cancer has increased and the outcome of primary cancer has improved due to effective antineoplastic treatments.^{2,3} However, the prognosis for patients with LC is extremely poor, and the median survival rate is 4–6 weeks if not treated, which can be increased to 4–6 months after active treatment with chemotherapy or radiation therapy.^{4,5} In addition,

Received February 18, 2018; accepted after revision May 23.

From the Department of Radiology (J.O., S.H.C., E.L., D.J.S., S.W.J., R.-E.Y., K.M.K., T.J.Y., J.-h.K., C.-H.S.), Seoul National University Hospital, Seoul, Korea; Department of Radiology (J.O., S.H.C., R.-E.Y., K.M.K., T.J.Y., J.-h.K., C.-H.S.), Seoul National University College of Medicine, Seoul, Korea; Institute of Radiation Medicine (S.H.C.), Seoul National University Medical Research Center, Seoul, Korea; and Center for Nanoparticle Research (S.H.C.), Institute for Basic Science, Seoul, Republic of Korea.

This study was supported by a grant from the Korea Healthcare Technology R&D Projects, Ministry for Health, Welfare & Family Affairs (HI16C1111); the Brain Research Program through the National Research Foundation of Korea funded by the Ministry of Science, ICT & Future Planning (2016M3C7A1914002); the Basic Science Research Program through the National Research Foundation of Korea

funded by the Ministry of Science, ICT & Future Planning (2017RIA2B2006526); Creative-Pioneering Researchers Program through Seoul National University; and Project Code (IBS-R006-D1).

Please address correspondences to Seung Hong Choi, MD, PhD, Department of Radiology, Seoul National University Hospital, 101 Daehak-ro, Jongno-gu, Seoul, 110-744, Republic of Korea; e-mail: verocay@snuh.org

Indicates open access to non-subscribers at www.ajnr.org

Indicates article with supplemental on-line tables.

<http://dx.doi.org/10.3174/ajnr.A5721>

proper treatment can prevent the deterioration of neurologic symptoms that impair the patient's quality of life.^{1,6} Therefore, early diagnosis and proper treatment of LC are the most important strategies to improve the overall survival and quality of life of patients with LC.

However, the diagnosis of LC is still a challenge. Identification of malignant cells by CSF cytology has been the diagnostic criterion standard, but the sensitivity of CSF cytology is limited. The initial cytology is falsely negative in up to 40%–50% of patients with pathologically proved LC, and this measure demonstrates a sensitivity of approximately 75% on repeat spinal tapping.^{7,8} With improved visualization of the subarachnoid space, MR imaging, especially contrast-enhanced (CE) T1-weighted imaging, is regarded as a reliable technique for confirming this diagnosis and for assessing the extent of the lesion and its response to therapy.^{9,10} However, LC is often missed on MR imaging because the leptomeninges is an anatomically thin membrane and subtle contrast enhancement is often mistaken for blood vessels by readers.

A recently introduced 3D fast spin-echo T1 black-blood imaging is one of the 3D spin-echo sequences that nullifies signals from moving flows^{11,12}; in other words, it selectively suppresses the signal of blood flow and provides a higher contrast-to-noise ratio. Several studies have demonstrated that black-blood imaging can improve the diagnostic accuracy of small brain parenchymal metastases due to its higher contrast-to-noise ratio.^{13,14} However, there are few studies that have explored the value of black-blood imaging in the detection of LC, and we hypothesized that black-blood imaging has a better diagnostic accuracy in detecting LC than CE 3D ultrafast gradient recalled-echo (CE GRE) and 2D spin-echo T1WI (CE SE).

Therefore, the purpose of our study was to evaluate whether black-blood imaging can improve the diagnostic accuracy for LC proved pathologically or clinically by comparing it with CE GRE and CE SE and, furthermore, to determine whether the grade of LC evaluated on black-blood imaging is a significant predictor of the patient's performance status and progression-free survival (PFS).

MATERIALS AND METHODS

Patients

This retrospective study was approved by the Seoul National University Hospital Institutional Review Board (SNUH IRB) with a waiver of informed consent. From January 2014 to October 2016, MR imaging was performed in 1758 consecutive patients (older than 18 years of age), including black-blood imaging, CE GRE, and CE SE. Among them, 78 patients met the following inclusion criteria: 1) having been diagnosed with LC and meeting the criteria below; 2) having contrast MR images of the brain, including black-blood imaging, CE GRE, and CE SE; and 3) having at least a 3-month follow-up if no progression. The exclusion criteria were as follows: 1) patients with prior intrathecal chemotherapy or whole-brain radiation therapy; and 2) patients with imaging studies from outside institutions or inadequate MR images for the analysis because of motion artifacts. The mean age of the patients was 56.5 years (age range, 19–87 years; 48 female and 30 male patients). The diagnoses were lung cancer ($n = 51$ patients), breast cancer ($n = 19$ patients), gastric cancer ($n = 5$ patients),

Table 1: Clinical characteristics

	LC+ ($n = 78$)	LC- ($n = 31$)
Age (yr)		
Mean	56.50 ± 13.61	64.03 ± 11.69
Sex (No.) (%)		
Male	30 (38.46%)	19 (61.29%)
Female	48 (61.54%)	12 (38.71%)
Primary cancer (No.) (%)		
Lung cancer	51 (65.38%)	28 (90.32%)
Breast cancer	19 (24.36%)	3 (9.68%)
Other	8 (10.26%)	0
Brain metastasis (No.) (%)		
Yes	60 (76.92%)	0
No	18 (23.08%)	31 (100%)
Extracranial metastasis (No.) (%)		
Yes	48 (61.54%)	1 (3.23%)
No	30 (38.46%)	30 (96.77%)
Neurologic symptom (No.) (%)		
Yes	73 (93.59%)	0
No	5 (6.41%)	31 (100%)
KPS		
Mean	52.56 ± 19.03	80.97 ± 3.01

Note:—LC + indicates patients with leptomeningeal carcinomatosis; LC -, patients without leptomeningeal carcinomatosis.

gallbladder cancer ($n = 1$ patient), cholangiocarcinoma ($n = 1$ patient), and osteosarcoma ($n = 1$ patient).

In addition, 31 patients without LC were also enrolled. We considered LC to be absent if there was no clinical evidence of LC with a follow-up of >12 months, in addition, negative cytology if CSF cytology was performed.¹⁵ The clinical criteria called for no new or progressive neurologic deficits for >12 months after the MR imaging. Only the negative CSF cytology criterion is not adequate because even three separate lumbar punctures can have a false negative rate of >10%.^{7,8}

Diagnosis of LC

The diagnosis was made in 1 of 2 ways: (1) a CSF cytology positive for malignant cells, which was repeated up to three times or (2) MRI scans showing LC on both initial and 2–3 month follow-up studies in patients with suspicious cytology (atypical cells) or biochemical test (elevated protein level and/or decreased glucose level in CSF).^{1,7,8,10,16–19} The various MR imaging findings used for the diagnosis included superficial sulcal/cisternal enhancement, sulcal/cisternal obliteration, multiple tiny superficial nodules along the sulci/cistern, enhancement of cranial nerves, and hydrocephalus.^{7,10} LC may grow in a linear pattern, creating a thin layer of cells spread diffusely over the brain surfaces, or in a nodular growth pattern, involving the leptomeninges in a multifocal skip pattern with intervening tumor-free areas.^{4,20}

MR Imaging Acquisition

In this study, MR imaging examinations were performed on 1 of three 3T MR imaging systems with 32-channel head coils, which included Verio (Siemens, Erlangen, Germany), Achieva dStream (Philips Healthcare, Best, the Netherlands), and Discovery MR750w (GE Healthcare, Milwaukee, Wisconsin) scanners. Each MR imaging scanning session included CE GRE, CE SE, and black-blood imaging, sequentially. CE T1WI was obtained after the intravenous administration (manual injection) of gadobutrol

(Gadovist; Bayer Schering Pharma, Berlin, Germany) at a dose of 0.1 mmol/kg of body weight.

The study was conducted in 63, 27, and 19 of 109 patients using the Verio, Achieva dStream, and Discovery MR750w scanners, respectively. The parameters used in the MR imaging examinations are summarized in On-line Table 1.

Image Analysis

A senior neuroradiologist (17 years of brain MR imaging experience) who was blinded to clinical information reviewed the images from each sequence individually and separately and assigned a diagnostic rating (positive, indeterminate, or negative) and a

Table 2: Results of the MR imaging readings in cases positive for LC (n = 78)

Findings	Imaging Technique		
	CE GRE	CE SE	Black-Blood Imaging
Positive	50	52	76
Indeterminate	7	5	0
Negative	21	21	2
Sensitivity (%)	64.1	66.67	97.43

Note:—Black-blood imaging indicates 3D fast SE T1 black-blood imaging.

grading of LC. We also scored leptomeningeal enhancement on MR imaging on a 0–5 scale. For each of the cerebral hemispheres, the presence of leptomeningeal enhancement was scored as 0 (absent), 1 (in 1 lobe), or 2 (>1 lobe). For the infratentorial area, it was scored as 0 (absent) or 1 (present).¹⁹ In addition, other imaging parameters were also collected, including the presence and number of brain metastases, the presence of hydrocephalus, the pattern of LC (linear or nodular), and the location of LC in the brain.

For the analysis of the interobserver agreement, 4 neuroradiologists (with 6, 8, 9, and 17 years of neuroimaging experience) who were blinded to clinical information analyzed 109 sets of MR images from each sequence individually and separately and assigned a diagnostic rating (positive, indeterminate, or negative) to each location of the cerebral hemispheres and a grading of LC.

Clinical Variables and Follow-Up

The patients' medical records were reviewed, and demographic and clinical data were collected, including age, sex, date of initial cancer diagnosis, date of LC diagnosis, Karnofsky Performance Scale (KPS) score at LC diagnosis, primary cancer histology, history of intrathecal chemotherapy or radiation to the brain, initial

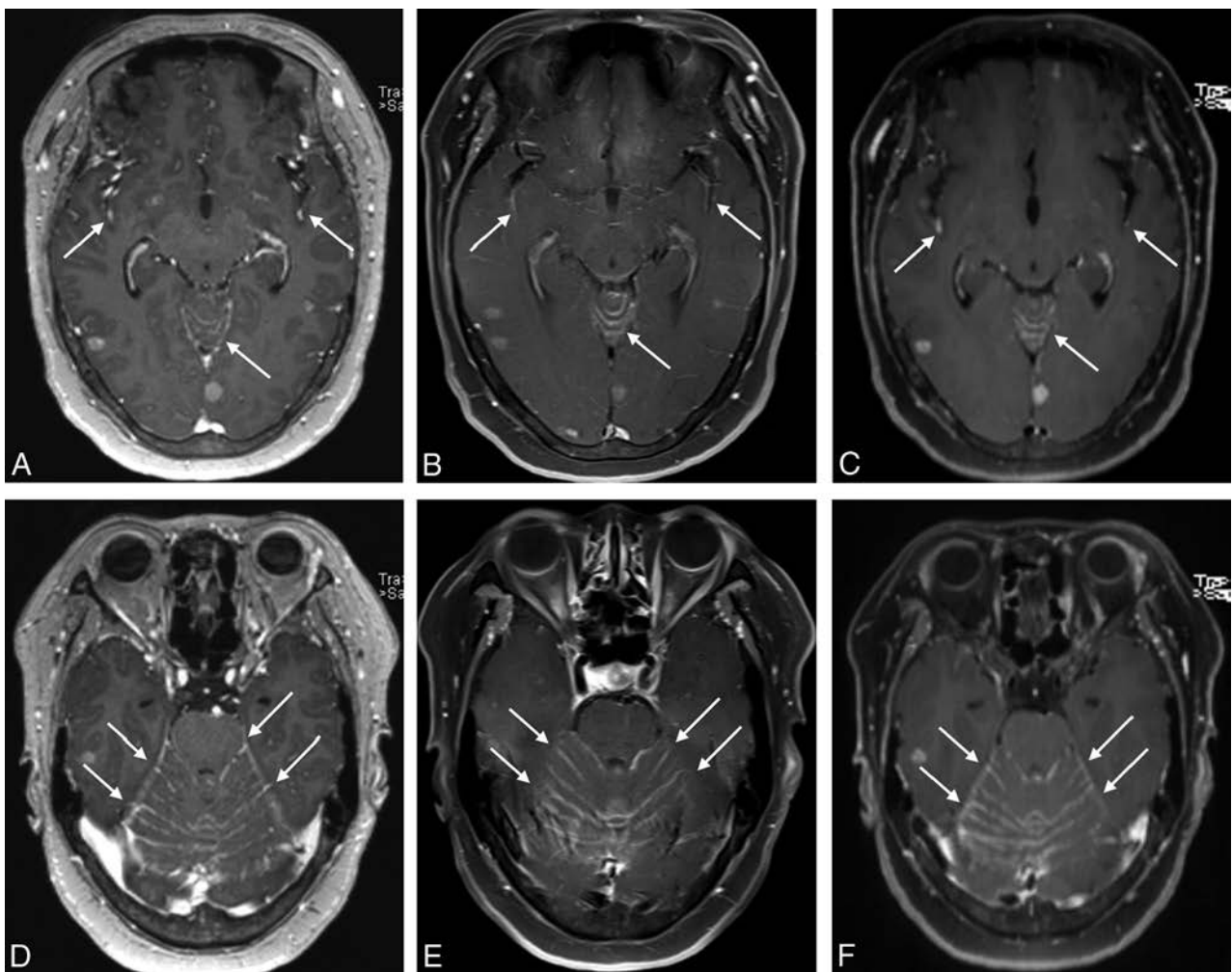


FIG 1. MR images of a 60-year-old female patient with lung cancer. On all contrast-enhanced 3D ultrafast GRE (A and D), SE T1WI (B and E), and black-blood imaging (C and F), leptomeningeal enhancement along the sulci of the bilateral cerebral hemispheres and cerebellar surface was observed (arrows).

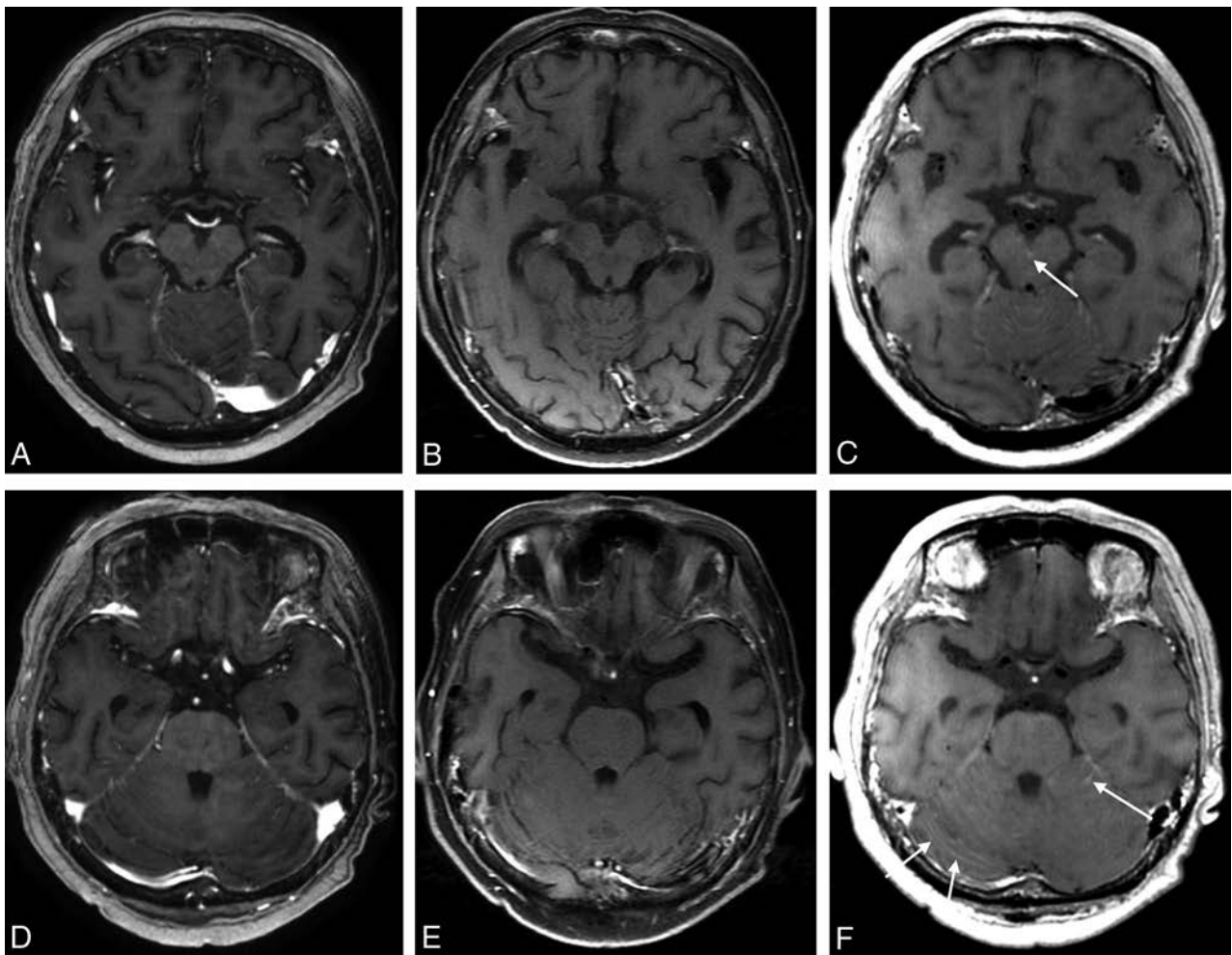


FIG 2. MR images of a 60-year-old female patient with lung cancer. The contrast-enhanced 3D ultrafast GRE (A and D) and SE TIWI (B and E) were negatively interpreted by all raters. On only the black-blood imaging (C and F) scans was leptomenigeal enhancement along the interpeduncular cistern (C, arrow) and bilateral cerebellar surface observed (F, arrows).

and subsequent treatment, and the date of last follow-up. The demographic and clinical information is summarized in Table 1.

For all enrolled patients with LC, treatment was performed properly as decided by an oncology team, and tumor progression was tracked at an outpatient clinic with follow-up MR imaging until death or March 2017 if the patient was still alive. Among the 78 patients with LC, 38 patients with lung cancer who underwent at least 1 follow-up MR imaging and had follow-up for at least 3 months if no progression were analyzed with the Kaplan-Meier and the Cox proportional hazards models. Tumor progression was designated as the time when the grade of LC evaluated on the MR imaging was elevated or when the size or number of the primary cancer or metastatic lesions increased. Progression-free survival was defined as the time span from the date of the brain MR imaging to the date of the documented progression or the last clinical follow-up.

Statistical Analysis

The data were checked with the Shapiro-Wilk test for normality and the Levene test for equality of variance. The sensitivity and specificity of the different MR images were calculated, and the Fisher exact test was performed. Additionally, the KPS scores were

compared between the groups with different grades using a Mann-Whitney *U* test. To perform the Kaplan-Meier analysis, we dichotomized each parameter regarding the cut-point, which was determined using the method of Contal and O'Quigley,²¹ which is based on the log-rank test statistic. For the 38 patients mentioned above, the Kaplan-Meier and the Cox proportional hazards model analyses were performed to determine the relationship between the LC grade evaluated on black-blood imaging and PFS. Additionally, the intraclass correlation coefficient (ICC) was used to assess interobserver agreement. A *P* value < .05 was considered a significant difference. All statistical analyses were performed using commercially dedicated software (MedCalc for Windows, Version 17.6, MedCalc Software, Mariakerke, Belgium; and SPSS 23 software for Windows, IBM, Armonk, New York).

RESULTS

Diagnostic Accuracy of the MR Images

Black-blood imaging (76 of 78 patients with LC, 97.43%) showed a significantly higher sensitivity than CE GRE (50 of 78, 64.1%) and CE SE (52 of 78, 66.67%) for the detection of LC (*P* < 0.001) (Table 2 and Figs 1 and 2). In terms of specificities, we did not find a significant difference among CE GRE (28 of 31 healthy patients,

90.32%), CE SE (28 of 31, 90.32%), and black-blood imaging (30 of 31, 96.77%) ($P > .05$) (Table 3). In addition, the Verio, Achieva dStream, and Discovery MR750w scanners did not show significantly different sensitivities or specificities for CE SE, CE GRE, or black-blood imaging ($P > .05$) (On-line Tables 2 and 3).

LC Grade and KPS

Among 78 patients with LC, only 3 patients (3.9%) had no clinical symptoms at diagnosis. The other 75 patients had neurologic symptoms at the time of diagnosis, and 38 patients (48.7%) had symptoms or signs referable to 1 compartment of the CNS (brain, cranial nerve, or spinal cord), whereas 37 patients (47.4%) had symptoms or signs referable to multiple levels of the neuraxis. Headache, altered mentality, nausea/vomiting, gait difficulty, leg weakness, diplopia, and facial palsy were the most common findings. There was no significant correlation between the presence of each symptom and the LC grade ($P > .05$). In addition, the patients with an LC grade of 5 based on the black-blood imaging had significantly lower KPS scores than the patients with LC grades of 0–4 ($P < .001$) (On-line Table 4).

Relationship between LC and PFS

For the 38 patients with lung cancer, the mean follow-up was 4.64 ± 4.48 months. Among them, 26 (68.4%) patients showed disease progression during the follow-up period. The LC grade evaluated on the follow-up MR imaging was elevated in 7 of the 26 patients (26.9%), the size or number of the primary cancer increased in 8 of the 26 patients (30.8%), and the size or number of the metastatic lesions increased in 11 of the 26 patients (42.3%). The median PFS of the patients was 4.17 months (95% CI, 3.10–6.17 months). The estimated 1-year PFS rate was 26.1%. Table 4 summarizes the results of the Kaplan-Meier analysis for PFS. The Kaplan-Meier analysis identified the time to metastasis (median PFS time, 12.27 versus 3.50 months; $P = .036$), KPS (median PFS

time, 11.63 versus 3.37 months; $P = .036$), and a combination of the LC grade and pattern (median PFS time, 4.87 versus 1.77 months; $P = .009$) as significant markers of PFS (Fig 3). Additionally, a Cox proportional hazards model identified a shorter time to metastasis (hazard ratio, 0.25; 95% confidence interval, 0.09–0.71; $P = .009$), a lower KPS (hazard ratio, 0.33; 95% CI, 0.12–0.89; $P = .029$), and a combined LC grade with a linear pattern (hazard ratio, 2.77; 95% CI, 1.08–7.08; $P = .034$) as separate independent predictors of PFS (On-line Table 5).

Interobserver Agreement

In terms of the interobserver agreements measured, black-blood imaging (0.9636; 95% CI, 0.9516–0.9734) revealed a slightly higher ICC than CE GRE (0.9626; 95% CI, 0.9502–0.9727) and CE SE (0.9342; 95% CI, 0.9124–0.9519) for assessing the grade of the LC (On-line Table 6). In addition, when assessing separately for the presence of LC in each location of cerebral hemispheres, black-blood imaging (range, 0.9017–0.9468) revealed a slightly higher ICC than CE GRE (range, 0.8710–0.9337) and CE SE (range, 0.8665–0.9275) for all locations of the cerebral hemispheres (On-line Table 7).

DISCUSSION

Our study demonstrates that black-blood imaging could improve the diagnostic accuracy for LC, especially for sensitivity, compared with CE GRE and CE SE and that it also has higher interobserver agreement. The grade of LC evaluated on the black-blood imaging showed significant associations with KPS scores. In addition, multivariate analysis using a Cox proportional hazards model revealed that the grade of LC evaluated on black-blood imaging is a significant predictor of PFS when combined with the LC enhancement pattern. On the basis of our study results, we believe that black-blood imaging could complement the low sensitivity of CSF cytology and provide a significant marker of PFS in patients with LC.

To date, several studies have compared the diagnostic accuracy of different MR images in detecting LC. Until now, the sensitivity of MR imaging to LC has been variably known from 20% to 71%.^{7,22–24} Singh et al²⁴ compared the sensitivity of 2D-FLAIR and CE T1-weighted SE in patients with cytologically confirmed LC, and the result was 34% in FLAIR and 66% in CE T1-weighted SE. A subsequent study by Singh et al¹⁵ showed that the sensitivity

Table 3: Results of the MR imaging readings for cases negative for LC (n = 31)

Findings	Imaging Technique		
	CE GRE	CE SE	Black-Blood Imaging
Positive	0	0	0
Indeterminate	3	3	1
Negative	28	28	30
Specificity (%)	90.32	90.32	96.77

Table 4: Kaplan-Meier analysis of the imaging and clinical parameters of PFS (n = 38)

Parameters	Threshold Values	Median Survival (mo) (95% CI)		P Value
		Above Threshold or Presence	Below Threshold or Absence	
Age (yr)	>60	33.47 (1.77–12.27)	4.57 (3.37–11.63)	.958
Sex		F 3.37 (1.37–4.73)	M 6.17 (3.47–12.27)	.100
Time to metastasis	≤229	12.27 (3.37–15.00)	3.50 (2.53–4.73)	.036
KPS	≤60	11.63 (3.67–13.57)	3.37 (1.37–4.73)	.036
Presence of brain metastasis		3.50 (3.00–4.97)	12.27 (4.57–15.88)	.275
No. of brain metastases	>4	3.47 (1.77–11.63)	4.73 (3.67–12.27)	.701
Presence of extracranial metastasis		3.47 (2.20–11.63)	4.57 (3.37–13.57)	.227
Presence of hydrocephalus		3.47 (2.57–5.37)	4.57 (3.10–6.17)	.607
LC grade		3.47 (1.13–4.97)	4.87 (3.67–12.27)	.449
Enhancement pattern		L 4.17 (2.20–6.17)	N 4.97 (3.00–15.00)	.279
Combination of LC grade and pattern		1.77 (1.07–3.50)	4.87 (3.47–12.27)	.009

Note:—F indicated female patients; M, male patients; L, indicates linear enhancement pattern; N, nodular enhancement pattern.

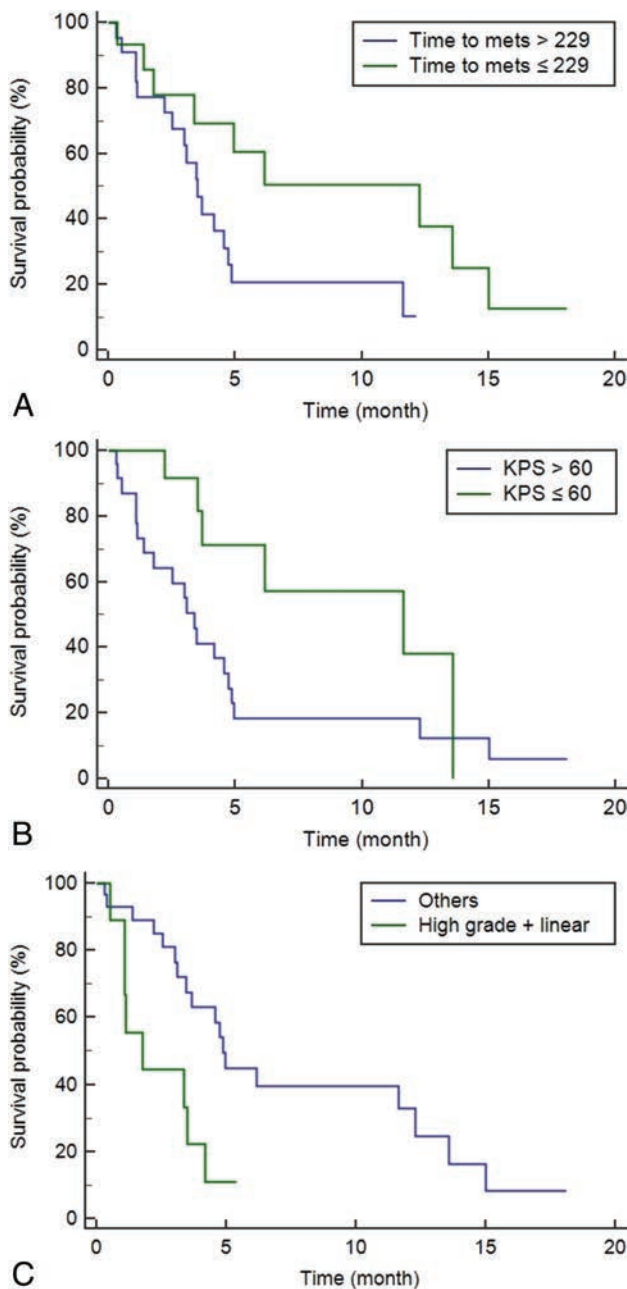


FIG 3. Kaplan-Meier curves showing a significant difference in the progression-free survival for the time to metastasis (A), Karnofsky Performance Scale (B), and a combination of the LC grade and pattern (C) with *P* values of .036, .036, and .009, respectively. When we compared the patients according to the cutoff values, the median PFS times were as follows: 12.27 months (95% CI, 3.37–15.00 months) versus 3.50 months (95% CI, 2.53–4.73 months; *P* = .036) in time to metastasis; 11.63 months (95% CI, 3.67–13.57 months) versus 3.37 months (95% CI, 1.37–4.73 months; *P* = .036) in KPS; and 4.87 months (95% CI, 3.47–1.27 months) versus 1.77 months (95% CI, 1.07–3.50 months; *P* = .009) in a combination of the LC grade and pattern, respectively.

and specificity of CE FLAIR for detecting LC were 41% and 88%, while those of CE T1-weighted MR imaging were 59% and 93%, respectively. LC diagnosis using contrast-enhanced MR imaging has relatively high specificity but still has low sensitivity.

A recently introduced black-blood imaging sequence is one of the 3D SE sequences that nullifies signals from moving flows, in other words, the signal of blood flow. Several studies have dem-

onstrated that black-blood imaging can improve the diagnostic accuracy of small brain parenchymal metastasis due to its higher contrast-to-noise ratio, compared with CE 3D ultrafast GRE and SE T1WI.^{13,14} This finding has theoretically been supported by several studies that demonstrated that lesions in CE 3D ultrafast GRE sequences are less enhanced by gadolinium than in SE-based sequences.^{11,25} In addition, a recent study comparing 2D-FLAIR, 2D-CE T1-weighted GRE, and black-blood imaging in the diagnosis of LC demonstrated that black-blood imaging showed a better detection rate of LC, regardless of the degree of the rater's experience.²⁶

Our study results were in good agreement with previous clinical studies, but our study differs from the previously published studies in some respects. First, we used clear inclusion criteria for those with LC and healthy patients. We only included pathologically or clinically proved patients with LC with a sufficient follow-up period. In addition, we considered LC absent if there was no clinical evidence of LC for a sufficient follow-up after MR imaging (>12 months). Second, we evaluated not only the diagnostic accuracy but also whether the grade of LC evaluated on black-blood imaging was a significant predictor of the patient's KPS scores and PFS. In our study, multivariate analysis showed that the grade of LC evaluated on black-blood imaging is a significant predictor of PFS when combined with the LC enhancement pattern. Therefore, the use of combination of the LC grade and pattern as prognostic biomarkers could improve the stratification of patients with LC at risk of progression and may allow modification of surveillance strategies for specific subgroups who are at high risk of progression. Early diagnosis and proper treatment of progression are the most important strategies for improving overall survival and preventing the deterioration of neurologic symptoms that impair the patient's quality of life. Third, we conducted an analysis of the interobserver agreement, and black-blood imaging was revealed to have a slightly higher ICC than the other sequences for all locations of the cerebral hemispheres, including the cranial nerves. Fourth, our results revealed that there was no significant difference in the diagnostic accuracy of black-blood imaging among the Verio, Achieva dStream, and Discovery MR750w scanners.

There were, however, several limitations in this study. First, this was a retrospective, single-center-based study with some potential bias. In addition, the sample size was rather small because we included only the patients with pathologically confirmed LC or definitive MR imaging findings of LC. Therefore, further studies with a larger number of cases should be performed. Second, unlike previously published studies, the MR imaging examinations were performed with different 3T MR imaging system vendors in this study (Siemens, GE Healthcare, and Philips Healthcare), and this feature may have influenced the overall study results. However, the sensitivity and specificity of each sequence showed no significant differences among the different vendors. Third, in this study, not all conditions of patients were pathologically confirmed. However, we included only patients with a definite sufficient follow-up period in this study. Fourth, our study did not include a postcontrast FLAIR sequence, which is also known to be sensitive to LC. Our hospital obtained black-blood imaging to better detect small metastases or LC in patients with

cancer but did not routinely obtain a postcontrast FLAIR image due to the limitation of scan time. Therefore, further study for the comparison with postcontrast FLAIR is warranted. Finally, in our study, each MR imaging scanning session included CE GRE, CE SE, and black-blood imaging, sequentially. Several studies have suggested that not only on the postcontrast scans performed at an early stage after administration of contrast medium but also on later images, contrast still is sufficient to obtain images of the tumor.^{27,28} In addition, a previous study suggested that imaging time delay did not have an effect on lesion conspicuity.²⁹ However, the scan time after contrast administration may cause some timing bias, so further study that randomizes the order of post-contrast sequences is warranted.

CONCLUSIONS

Black-blood imaging could improve the diagnostic accuracy for LC, especially in sensitivity, compared with CE GRE and CE SE, and it also has a higher interobserver agreement. In addition, a combination of the LC grade and pattern could be an independent predictor of PFS in patients with LC. Therefore, we believe that black-blood imaging is a clinically useful sequence that can play an important role in the early diagnosis as well as the prognosis prediction of patients with LC.

Disclosures: Seung Hong Choi—RELATED: Grant: governmental grants.* *Money paid to the institution.

REFERENCES

- Bruna J, González L, Miró J, et al; Neuro-Oncology Unit of the Institute of Biomedical Investigation of Bellvitge. **Leptomeningeal carcinomatosis: prognostic implications of clinical and cerebrospinal fluid features.** *Cancer* 2009;115:381–89 CrossRef Medline
- Chamberlain MC. **Neoplastic meningitis.** *Neurologist* 2006;12:179–87 CrossRef Medline
- Park JH, Kim YJ, Lee JO, et al. **Clinical outcomes of leptomeningeal metastasis in patients with non-small cell lung cancer in the modern chemotherapy era.** *Lung Cancer* 2012;76:387–92 CrossRef Medline
- Nakagawa H, Murasawa A, Kubo S, et al. **Diagnosis and treatment of patients with meningeal carcinomatosis.** *J Neurooncol* 1992;13:81–89 Medline
- Shapiro WR, Johanson CE, Boogerd W. **Treatment modalities for leptomeningeal metastases.** *Semin Oncol* 2008;36:S46–54 Medline
- Kaplan JG, DeSouza TG, Farkash A, et al. **Leptomeningeal metastases: comparison of clinical features and laboratory data of solid tumors, lymphomas and leukemias.** *J Neurooncol* 1990;9:225–29 CrossRef Medline
- Taillibert S, Laigle-Donadey F, Chodkiewicz C, et al. **Leptomeningeal metastases from solid malignancy: a review.** *J Neurooncol* 2005;75:85–99 CrossRef Medline
- Wasserstrom WR, Glass JP, Posner JB. **Diagnosis and treatment of leptomeningeal metastases from solid tumors: experience with 90 patients.** *Cancer* 1982;49:759–72 Medline
- Freilich RJ, Krol G, DeAngelis LM. **Neuroimaging and cerebrospinal fluid cytology in the diagnosis of leptomeningeal metastasis.** *Ann Neurol* 1995;38:51–57 CrossRef Medline
- Clarke JL, Perez HR, Jacks LM, et al. **Leptomeningeal metastases in the MRI era.** *Neurology* 2010;74:1449–54 CrossRef Medline
- Brant-Zawadzki M, Gillan GD, Nitz WR. **MP RAGE: a three-dimensional, T1-weighted, gradient-echo sequence—initial experience in the brain.** *Radiology* 1992;182:769–75 CrossRef Medline
- Qiao Y, Steinman DA, Qin Q, et al. **Intracranial arterial wall imaging using three-dimensional high isotropic resolution black blood MRI at 3.0 Tesla.** *J Magn Reson Imaging* 2011;34:22–30 CrossRef Medline
- Kato Y, Higano S, Tamura H, et al. **Usefulness of contrast-enhanced T1-weighted sampling perfection with application-optimized contrasts by using different flip angle evolutions in detection of small brain metastasis at 3T MR imaging: comparison with magnetization-prepared rapid acquisition of gradient echo imaging.** *AJNR Am J Neuroradiol* 2009;30:923–29 CrossRef Medline
- Park J, Kim EY. **Contrast-enhanced, three-dimensional, whole-brain, black-blood imaging: application to small brain metastases.** *Magn Reson Med* 2010;63:553–61 CrossRef Medline
- Singh SK, Leeds NE, Ginsberg LE. **MR imaging of leptomeningeal metastases: comparison of three sequences.** *AJNR Am J Neuroradiol* 2002;23:817–21 Medline
- Hyun JW, Jeong IH, Joung A, et al. **Leptomeningeal metastasis: clinical experience of 519 cases.** *Eur J Cancer* 2016;56:107–14 CrossRef Medline
- Kak M, Nanda R, Ramsdale EE, et al. **Treatment of leptomeningeal carcinomatosis: current challenges and future opportunities.** *J Clin Neurosci* 2015;22:632–37 CrossRef Medline
- Li YS, Jiang BY, Yang JJ, et al. **Leptomeningeal metastases in patients with NSCLC with EGFR mutations.** *J Thorac Oncol* 2016;11:1962–69 CrossRef Medline
- An YJ, Cho HR, Kim TM, et al. **An NMR metabolomics approach for the diagnosis of leptomeningeal carcinomatosis in lung adenocarcinoma cancer patients.** *Int J Cancer* 2015;136:162–71 CrossRef Medline
- Mack F, Baumert B, Schäfer N, et al. **Therapy of leptomeningeal metastasis in solid tumors.** *Cancer Treat Rev* 2016;43:83–91 CrossRef Medline
- Contal C, O'Quigley J. **An application of changepoint methods in studying the effect of age on survival in breast cancer.** *Computational Statistics & Data Analysis* 1999;30:253–70
- Davis P, Friedman N, Fry S, et al. **Leptomeningeal metastasis: MR imaging.** *Radiology* 1987;163:449–54 CrossRef Medline
- Chamberlain MC, Sandy AD, Press GA. **Leptomeningeal metastasis: a comparison of gadolinium-enhanced MR and contrast-enhanced CT of the brain.** *Neurology* 1990;40:435–38 CrossRef Medline
- Singh SK, Agris JM, Leeds NE, et al. **Intracranial leptomeningeal metastases: comparison of depiction at FLAIR and contrast-enhanced MR imaging.** *Radiology* 2000;217:50–53 CrossRef Medline
- Mugler JP 3rd, Brookeman JR. **Theoretical analysis of gadopentetate dimeglumine enhancement in T1-weighted imaging of the brain: comparison of two-dimensional spin-echo and three-dimensional gradient-echo sequences.** *J Magn Reson Imaging* 1993;3:761–69 CrossRef Medline
- Gil B, Hwang EJ, Lee S, et al. **Detection of leptomeningeal metastasis by contrast-enhanced 3D T1-SPACE: comparison with 2D FLAIR and contrast-enhanced 2D T1-weighted images.** *PLoS One* 2016;11:e0163081 CrossRef Medline
- Åkeson P, Nordström CH, Holtås S. **Time-dependency in brain lesion enhancement with gadodiamide injection.** *Acta Radiol* 1997;38:19–24 Medline
- Schörner W, Laniado M, Niendorf H, et al. **Time-dependent changes in image contrast in brain tumors after gadolinium-DTPA.** *AJNR Am J Neuroradiol* 1986;7:1013–20 Medline
- Jeon JY, Choi JW, Roh HG, et al. **Effect of imaging time in the magnetic resonance detection of intracerebral metastases using single dose gadobutrol.** *Korean J Radiol* 2014;15:145–50 CrossRef Medline

Comparative Study of MRI Biomarkers in the Substantia Nigra to Discriminate Idiopathic Parkinson Disease

N. Pyatigorskaya, B. Magnin, M. Mongin, L. Yahia-Cherif, R. Valabregue, D. Arnaldi, C. Eweczyk, C. Poupon, M. Vidailhet, and S. Lehéryc



ABSTRACT

BACKGROUND AND PURPOSE: Several new MR imaging techniques have shown promising results in patients with Parkinson disease; however, the comparative diagnostic values of these measures at the individual level remain unclear. Our aim was to compare the diagnostic value of MR imaging biomarkers of substantia nigra damage for distinguishing patients with Parkinson disease from healthy volunteers.

MATERIALS AND METHODS: Thirty-six patients and 20 healthy volunteers were prospectively included. The MR imaging protocol at 3T included 3D T2-weighted and T1-weighted neuromelanin-sensitive images, diffusion tensor images, and R2* mapping. T2* high-resolution images were also acquired at 7T to evaluate the dorsal nigral hyperintensity sign. Quantitative analysis was performed using ROIs in the substantia nigra drawn manually around the area of high signal intensity on neuromelanin-sensitive images and T2-weighted images. Visual analysis of the substantia nigra neuromelanin-sensitive signal intensity and the dorsolateral nigral hyperintensity on T2* images was performed.

RESULTS: There was a significant decrease in the neuromelanin-sensitive volume and signal intensity in patients with Parkinson disease. There was also a significant decrease in fractional anisotropy and an increase in mean, axial, and radial diffusivity in the neuromelanin-sensitive substantia nigra at 3T and a decrease in substantia nigra volume on T2* images. The combination of substantia nigra volume, signal intensity, and fractional anisotropy in the neuromelanin-sensitive substantia nigra allowed excellent diagnostic accuracy (0.93). Visual assessment of both substantia nigra dorsolateral hyperintensity and neuromelanin-sensitive images had good diagnostic accuracy (0.91 and 0.86, respectively).

CONCLUSIONS: The combination of neuromelanin signal and volume changes with fractional anisotropy measurements in the substantia nigra showed excellent diagnostic accuracy. Moreover, the high diagnostic accuracy of visual assessment of substantia nigra changes using dorsolateral hyperintensity analysis or neuromelanin-sensitive signal changes indicates that these techniques are promising for clinical practice.

ABBREVIATIONS: AD = axial diffusivity; DNH = dorsal nigral hyperintensity; FA = fractional anisotropy; ICC = intraclass correlation coefficient; HV = healthy volunteer; MD = mean diffusivity; NM = neuromelanin; PD = Parkinson disease; RD = radial diffusivity; ROC = receiver operating characteristic; SN = substantia nigra; UPDRS = Unified Parkinson's Disease Rating Scale

In Parkinson disease (PD), several MR imaging biomarkers have been successfully used to detect neurodegenerative changes in the substantia nigra (SN).¹⁻³ By means of DTI, decreased fractional anisotropy (FA)^{2,3} and modifications in axial (AD),⁴ radial (RD),² or mean (MD) diffusivity⁵ have been reported in the SN with

some variability across studies.⁵ In addition, increased iron content in the SN of patients with PD has been shown by R2* relaxometry^{2,3} or susceptibility imaging.⁶

In PD, dopaminergic neuronal loss occurs in the SN pars compacta,¹ and methods for specifically analyzing this region are of particular interest. Neuromelanin (NM), a by-product of dopamine that accumulates in dopaminergic neurons, has high signal intensity on T1-weighted spin-echo images due to its paramagnetic properties,^{7,8} and several studies have shown reduced NM

Received January 10, 2018; accepted after revision April 29.

From the Institut du Cerveau et de la Moelle épinière (N.P., B.M., M.M., L.Y.-C., R.V., D.A., M.V., S.L.), Centre de Neuroimagerie de Recherche, Paris, France; UMR S 1127, CNRS UMR 7225 (N.P., B.M., M.M., L.Y.-C., M.V., S.L.), Sorbonne University, Paris, France; Service de neuroradiologie (N.P., B.M., S.L.) and Département des Maladies du Système Nerveux (C.E., M.V.), Clinique des mouvements anormaux, Assistance Publique Hôpitaux de Paris, Hôpital Pitié-Salpêtrière, Paris, France; Clinical Neurology (D.A.), Department of Neuroscience, University of Genoa, Genoa, Italy; NeuroSpin (C.P.), Commissariat à l'Energie Atomique, Gif-Sur-Yvette, France; and Centre d'Investigation Clinique (D.A., M.V.), Hôpital Pitié-Salpêtrière, Paris, France.

Please address correspondence to Nadya Pyatigorskaya, MD, PhD, CENIR, ICM, Hôpital Pitié-Salpêtrière 47-83 Boulevard de l'Hôpital, 75651 Paris Cedex 13, France; e-mail: nadya.pyatigorskaya@gmail.com; @nadya.pya

Indicates open access to non-subscribers at www.ajnr.org

<http://dx.doi.org/10.3174/ajnr.A5702>

signal or volume in the SN in PD.^{9,10} Because NM accumulates in the substantia nigra pars compacta, NM MR imaging is a promising technique in PD.¹¹

Histologic studies in PD have shown that depletion of dopaminergic neurons is most pronounced in the caudal and lateral regions of the substantia nigra pars compacta, called nigrosome-1.¹² Signal changes in this area have been shown in PD using high-resolution T2*-weighted or susceptibility-weighted imaging at both 7T¹³ and 3T.¹⁴ The normal aspect of this dorsolateral region is a hyperintense, ovoid area within the hypointense SN. However, this hyperintensity, referred to as dorsal nigral hyperintensity (DNH), is lost in PD.^{13,14} Both NM-sensitive and DNH imaging may be useful in clinical practice.¹³⁻¹⁵

Although these MR imaging techniques have shown good results for differentiating patients from controls either separately^{16,17} or by using a combination of diffusion and iron imaging,³ the comparative diagnostic values of these measures at the individual level remain unclear and have not been tested yet. The aims of our study were to compare the diagnostic efficacy of DTI, R2*, NM-sensitive imaging, and DNH and to determine the best combination of measures to detect specific SN alterations in PD.

MATERIALS AND METHODS

Subjects

Thirty-six patients were prospectively recruited from the Movement Disorders Clinic at Pitié-Salpêtrière Hospital between April 2010 and September 2012. The inclusion criteria were clinical diagnosis of idiopathic PD (according to UK Parkinson's Disease Brain Bank criteria), no or minimal cognitive disturbances (Mini-Mental State Examination score = >24), age younger than 75 years, and complete MR imaging examination on both 3T and 7T scanners. Patients were compared with 20 healthy volunteers (HVs) with no medical history of any neurologic disorders, having normal clinical examination findings, and matched for age and sex. All subjects gave written informed consent, and the local ethics committee approved the study (CPP Paris VI, RCB: 2009-A00922-55).

Clinical and Neurologic Examination

Motor disability was evaluated using the Unified Parkinson's Disease Rating Scale, Part III (UPDRS-III) in the "ON" (peak effect of dopaminergic treatment) and "OFF" (12-hour dopaminergic treatment withdrawal) conditions and the Hoehn and Yahr staging.

MR Imaging Acquisition

Acquisitions were performed using 3T Trio and 7T Magnetom (Siemens, Erlangen, Germany) scanners and a 12-channel (3T) or an 8-channel (7T) head coil for signal reception for all subjects. The 3T protocol included high-resolution anatomic 3D T1WI, T2WI, NM-sensitive spin-echo T1WI, DTI, and R2* mapping. The 3D T1WI was acquired using a sagittal MPRAGE acquisition (TI, 900 ms; TR/TE/flip angle, 2300 ms/4.18 ms/9°; 1 average; voxel size, 1 × 1 × 1 mm³). NM-sensitive images were acquired using 2D axial turbo spin-echo T1WI (TR/TE/flip angle, 900 ms/15 ms/180°; 3 averages; voxel size, 0.4 × 0.4 × 3 mm³). DTI parameters were TR/TE/flip angle, 14,000 ms/101 ms/90°; b-value, 1500 s/mm²; voxel size, 1.7 × 1.7 × 1.7 mm³; 60 diffusion

gradient directions. R2* mapping was computed using a gradient echo-planar imaging sequence with 6 TEs (range, 24–94 ms); TR/flip angle, 9000 ms/90°; voxel size, 2 × 2 × 2 mm³. The 7T image acquisition included 3D T2*WI coronal images with TR/TE/flip angle, 2180 ms/29.9 ms/65°; FOV, 192 mm²; voxel size, 0.5 × 0.5 × 0.5 mm³; 40 slices.

Image Analysis

ROIs. SN segmentations at 3T were performed by 2 examiners using FreeSurfer software (<http://surfer.nmr.mgh.harvard.edu>) and at 7T by 1 trained examiner using ITK-SNAP 1.6 software (www.itksnap.org).¹⁸ To evaluate the accuracy of segmentation at 7T, a second examiner performed segmentations in the last 10 selected subjects. The concordance between the segmentations was good (Dice similarity coefficient = 0.87).

For NM images, contours of the SN were manually drawn around the area of high signal intensity twice by each blinded rater. The concordance between the segmentations was good (Dice similarity coefficient = 0.8). This 3T NM ROI primarily corresponded to the substantia nigra pars compacta.¹⁹ For 3T T2WI and 7T T2*WI, the SN was defined as the area of hypointensity ventral to the red nucleus and dorsal to the cerebral peduncle, primarily corresponding to the SN pars reticulata (Fig 1).¹⁹ The SN was separated from the subthalamic nucleus by a small notch on its lateral and anterior borders. The subthalamic nucleus was also segmented to avoid any error. All examiners were blinded to the subject's clinical status.

Quantitative Analysis. The volumes of NM-based ROIs were calculated using in-house Matlab algorithms (MathWorks, Natick, Massachusetts). The signal ratio was calculated by normalizing the mean signal of the SN in each slice to the signal in the background region, which was manually traced, including the tegmentum and superior cerebellar peduncles, as previously described.⁹ The interrater agreement was calculated, and the results were averaged across the raters and segmentations. DTI and R2* measures in the SN were calculated using both 3T NM and 3T T2WI ROIs. The DTI, NM-sensitive, and T2WI were coregistered to the 3D T1WI volume using the SPM coregister function (<http://www.fil.ion.ucl.ac.uk/spm/software/spm12>). DTI preprocessing was performed using the FMRIB Software Library, Version 5.0 (FSL; <http://www.fmrib.ox.ac.uk/fsl>). Motion and eddy currents were corrected using the eddy_correct function in FSL. Echo-planar deformations were corrected using field maps. FA and diffusivity maps were computed with the DTIFit (http://fsl.fmrib.ox.ac.uk/fsl/fsl-4.1.9/fdt/fdt_dtifit.html) function for the entire volume. Noise filtering was applied. The mean value of each measure was computed in the SN ROIs. For R2* calculation, all images were realigned, normalized, and coregistered. R2* maps were calculated by fitting the data to the logarithmic signal decay over all 6 TEs. The mean R2* value was calculated over each ROI.

Blind Visual Analysis. Two raters visually analyzed the SN signal intensity in the NM-sensitive images and the presence of DNH. To assess intra- and interobserver reproducibility, each reading was performed twice at a 4-week interval. There was no time limit for visual evaluations. For conflicting cases, agreement between raters was reached.

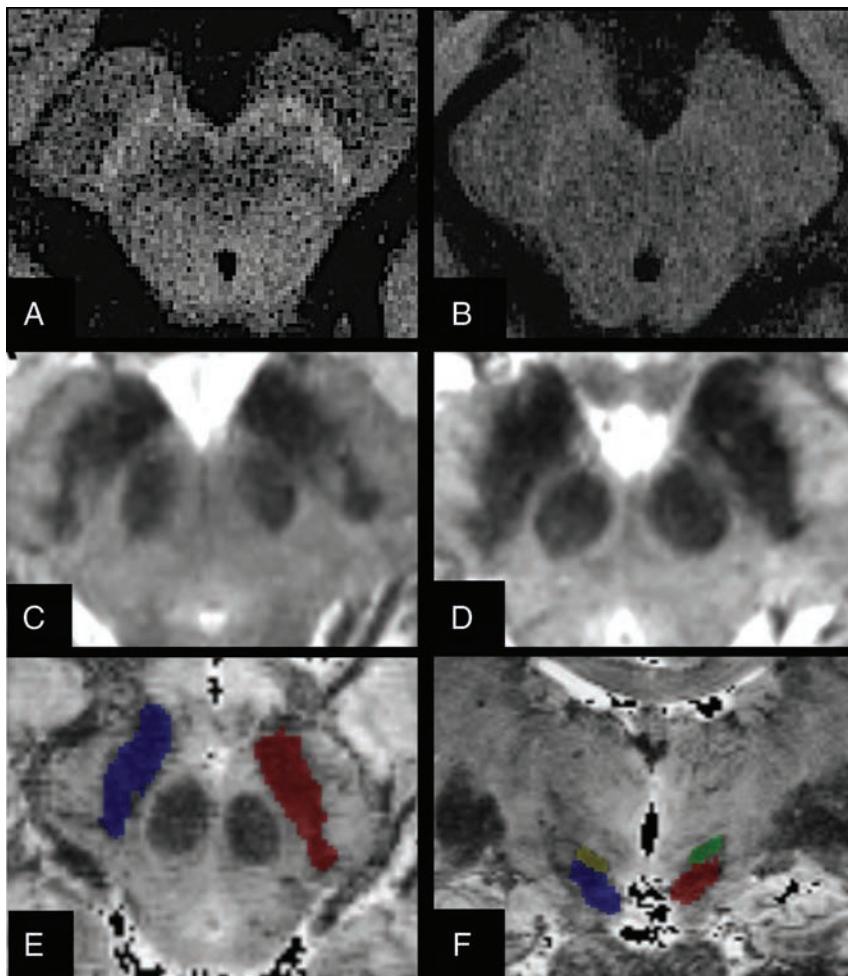


FIG 1. Segmentation of ROIs. Axial brain stem slices in a healthy volunteer (A) and a patient with Parkinson disease (B) show reduction of the neuromelanin signal intensity in the substantia nigra of the patient. Axial T2*WI 7T slices show dorsal nigral hyperintensity in a HV (C), which is absent in the patient with PD (D). T2WI axial (E) and coronal (F) images of the SN in a HV show T2-based segmentation of the SN.

NM-sensitive images were classified according to a 2-point scale, as follows: 1, a normal aspect of the SN with high signal intensity bilaterally and no volume loss, indicating a healthy subject; or 2, an abnormal aspect with reduced signal or volume of the SN unilaterally or bilaterally, indicating a subject with pathology.

The DNH sign was categorized using a 2-point scale: 1, normal; or 2, pathologic. We used 2 classification methods: 1) Unilateral or bilateral absence of DNH was considered pathologic,²⁰ and 2) only bilateral DNH absence was considered pathologic.¹⁴

Statistical Analysis

Statistical analysis was performed using Matlab (MathWorks). Intra- and interrater intraclass correlations (ICCs) were calculated for quantitative data. Group differences were determined using a 1-way MANOVA. Preliminary assumptions of homogeneity of variance were assessed by the Levene test. Between-group differences were estimated using Pillai's Trace (<http://www.statisticshowto.com/pillais-trace/>). Follow-up univariate ANOVA was performed for measures; differences were considered significant at $P < .05$. The diagnostic threshold value was calculated using receiver operating characteristic (ROC) curve analysis, and the sen-

sitivity and specificity of cutoff points were estimated using the Youden index. The inter- and intrarater agreement for qualitative measurements was estimated using the Cohen κ coefficient. The sensitivity, specificity, positive predictive value, and negative predictive value were calculated. Diagnostic accuracy between 0.9 and 1 was considered "excellent"; between 0.80 and 0.90, "good"; and between 0.70 and 0.80, "fair." The best combination of variables for disease prediction was determined using a logistic regression model. Associations between clinical measures and MR imaging measurements were studied regarding PD. Age and sex were controlled by partial correlations followed by a multiple comparisons permutation approach. An approximate multivariate permutation test was conducted, and the sampling distribution was built to calculate the corrected P value as the proportion of the observed significant correlation coefficient value.²¹

RESULTS

Population Characterization

Thirty-six patients with PD (mean age, 60.1 ± 10.1 years; 27 men) and 20 HVs (mean age, 60.8 ± 8.3 years; 12 men, $P = .2$) were analyzed. The mean duration of disease was 9.1 ± 3.6 years, the mean UPDRS-III-ON was 14.8 ± 8.8 , the mean UPDRS-III-OFF was 28.3 ± 9.6 , and the mean Hoehn and Yahr scale score was 1.9 ± 0.6 . The mean UPDRS-OFF score for the HV group was $0.8 \pm$

1.0 . The mean Mini-Mental State Examination score was 27.9 ± 1.8 in PD and 28.8 ± 1.1 in HV, $P = .03$. The mean Mattis score was 137 ± 5.2 in PD and 140 ± 2.6 in HV, $P = .009$.

Quantitative MR Imaging Data Analysis

MANOVA preliminary assumptions revealed homogeneity of variance (Levene test). The between-group differences for all measures in the SN were statistically significant [$F(12,43) = 5.387$, $P < .001$; partial $\eta^2 = 0.601$, Pillai's Trace].

The analysis was followed up by univariate ANOVAs for each SN metric.

NM-Sensitive Volume. The average NM-sensitive volume was lower in patients with PD than in HVs ($F = 24.85$, $P < .001$, Table 1 and Fig 2A).

ROC analysis showed good discrimination between patients with PD and HVs (Fig 3A and Table 2). Interrater (ICC = 0.86; 95% CI, 0.78–0.91; $P < .001$) and intrarater (reader 1: ICC = 0.81; 95% CI, 0.65–0.87; $P < .001$; reader 2: ICC = 0.84; 95% CI, 0.75–0.90; $P < .001$) agreements were good.

Table 1: Quantitative measurements in the SN^a

Side	PD	HV
3T NM ROI		
Volume		
L	184.41 ± 68.84	261.45 ± 47.68 ^b
R	176.91 ± 62.89	258.89 ± 46.62 ^b
Mean LR	180.66 ± 63.63	260.17 ± 42.87 ^b
Signal		
L	106.74 ± 2.64	110.21 ± 2.55 ^b
R	106.61 ± 3.32	110.46 ± 2.82 ^b
Mean LR	110.56 ± 2.62	110.33 ± 2.40 ^b
FA		
L	0.32 ± 0.04	0.34 ± 0.04 ^c
R	0.31 ± 0.04	0.33 ± 0.04
Mean LR	0.31 ± 0.03	0.33 ± 0.04 ^c
AD		
L	0.68 ± 0.09	0.59 ± 0.10 ^d
R	0.70 ± 0.08	0.62 ± 0.10 ^c
Mean LR	0.69 ± 0.08	0.60 ± 0.10 ^c
RD		
L	0.44 ± 0.06	0.38 ± 0.07 ^d
R	0.46 ± 0.06	0.40 ± 0.07 ^c
Mean LR	0.45 ± 0.06	0.39 ± 0.07 ^c
MD		
L	0.52 ± 0.07	0.45 ± 0.08 ^d
R	0.54 ± 0.06	0.48 ± 0.08 ^c
Mean LR	0.53 ± 0.11	0.46 ± 0.08 ^c
R2*		
L	35.91 ± 4.95	36.66 ± 2.84
R	36.10 ± 6.64	36.54 ± 2.80
Mean LR	35.65 ± 6.46	36.60 ± 2.64
3T T2 ROI		
FA		
L	0.39 ± 0.06	0.42 ± 0.06
R	0.37 ± 0.06	0.40 ± 0.05
Mean LR	0.38 ± 0.06	0.40 ± 0.05
AD		
L	0.50 ± 0.09	0.45 ± 0.10
R	0.53 ± 0.10	0.49 ± 0.11
Mean LR	0.52 ± 0.09	0.47 ± 0.10
RD		
L	0.30 ± 0.06	0.26 ± 0.10 ^c
R	0.33 ± 0.06	0.29 ± 0.06 ^c
Mean LR	0.32 ± 0.06	0.28 ± 0.0 ^c
MD		
L	0.37 ± 0.07	0.32 ± 0.07 ^c
R	0.40 ± 0.07	0.35 ± 0.08 ^c
Mean LR	0.38 ± 0.07	0.34 ± 0.08 ^c
R2*		
L	28.47 ± 4.17	30.21 ± 3.23
R	28.91 ± 3.98	29.93 ± 2.87
Mean LR	28.69 ± 3.97	30.07 ± 2.88
7T T2*WI ROI		
T2WI volume		
L	459.75 ± 120.74	541.14 ± 118.80 ^c
R	468.11 ± 130.00	523.01 ± 121.85 ^c
Mean LR	463.93 ± 122.83	532.07 ± 118.33 ^c

Note:—L indicates left; R, right; LR, average of left and right.

^aQuantitative measurements in the substantia nigra (mean and SD) are presented.

^bSignificant differences between patients with PD and HVs are indicated using $P < .001$.

^cSignificant differences between patients with PD and HVs are indicated using $P < .05$.

^dSignificant differences between patients with PD and HVs are indicated using $P < .005$.

NM-Sensitive Signal. The average NM-sensitive signal in patients with PD was lower than in that in HVs ($F = 27.39, P < .001$; Table 1 and Fig 2B). ROC analysis showed good discrimination between

patients with PD and HVs (Fig 3A and Table 2). Interrater agreement was excellent (ICC = 0.91; 95% CI, 0.86–0.94; $P < .001$), and intrarater agreement was good (reader 1: ICC = 0.8; 95% CI, 0.69–0.87; reader 2: ICC = 0.86; 95% CI, 0.77,0.91; $P < .001$).

DTI Parameters. For the DTI parameters, in the 3T NM SN ROI, patients with PD showed an increased average MD ($F = 11.47, P = .001$), AD ($F = 11.23, P = .001$), and RD ($F = 11.1, P = .002$) and a reduced FA ($F = 4.46, P = .04$). In the 3D T2WI SN ROI, an increase in RD ($F = 6.55, P = .01$) and MD ($F = 5.23, P = .03$) was observed, with no significant differences in FA or AD (Table 1 and Fig 2C). ROC analysis showed fair discrimination between patients with PD and HVs for all parameters (Table 2 and Fig 3A).

R2*. There was no difference between patients with PD and HVs for R2* in either 3T NM or 3T T2WI ROIs.

7T T2*WI SN Volume. Patients with PD exhibited lower 7T T2*WI SN volumes than the HV group ($F = 4.06, P = .05$) (Table 1 and Fig 2D). ROC analysis showed good discrimination between patients with PD and HVs (Fig 3A and Table 2), with a higher area under the curve for the NM-sensitive volume than for the 7T T2* volume. Interrater agreement for volume measurements was excellent (ICC = 0.9927; 95% CI, 0.9864–0.9961).

Best Variable Combinations. A logistic regression model was used to determine the best variable combinations optimizing disease prediction. The logistic regression model was statistically significant [$\chi^2(77) = 47.66, P < .001$], explaining 78% (Nagelkerke R²) of the variance and correctly classifying 93% of the cases. Among predictor variables, 3 were statistically significant (signal, volume, and FA in the 3T NM ROI), and the combination of these variables improved sensitivity (91.7%), specificity (95%), and the area under the curve (95.6; 95% CI, 0.903–1). While we considered only the combination of the signal and volume in the 3T NM ROI, 89% of cases were correctly classified (area under the curve = 0.89; 95% CI, 0.8–0.98).

Qualitative Visual Analysis

NM-Sensitive Images. The 2 raters discriminated the patients with PD and the HV group with good accuracy (Table 2). There was strong intrarater agreement for rater 1 (Cohen $\kappa = 0.823$; 95% CI, 0.674–0.972; $P < .001$) and rater 2 ($\kappa = 0.830$; 95% CI, 0.688–0.971; $P < .001$). Good interrater agreement was also found ($\kappa = 0.815$; 95% CI, 0.632–0.897; $P < .001$).

7T T2-weighted Images. The 2 raters discriminated between the PD and HV subjects with good accuracy by both methods 1 and 2 (Table 2). There was good intrarater ($\kappa = 0.834$; 95% CI, 0.806–0.862; $P < .001$) and interrater ($\kappa = 0.834$; 95% CI, 0.806–0.862; $P < .001$) agreement.

Correlation between MR Imaging Data and Clinical Changes

For the 3T NM ROI, RD and MD in both hemispheres correlated positively with the UPDRS-OFF score (RD: $r = 0.4, P = .007$; MD: $r = 0.4, P = .009$), whereas FA correlated negatively with disease duration for the 3T T2WI ROI ($r = -0.37, P = .015$). Regarding

the 7T T2*WI ROI, the SN volume bilaterally correlated positively with disease duration ($r = 0.47, P = .018$). No other significant correlations were found for the quantitative data.

DISCUSSION

We found that NM imaging and DTI measures in the SN at 3T, as well as the SN volume using T2* images at 7T, were significantly

different between patients with PD and HVs. The NM-based volume and signal had good diagnostic accuracy for separating patients with PD from HV subjects. DTI measures alone showed fair diagnostic accuracy, and their combination with NM imaging measures allowed excellent diagnostic performance. In addition, visual measures (DNH rating and NM visual assessment) also accurately distinguished patients with PD from the HV group.

The sensitivity was better with the DNH rating, whereas the specificity was better with NM visual assessment.

Histologic studies have shown that neurodegeneration of the SN pars compacta is associated with a reduced number of pigmented neurons and a decrease in NM in the remaining neurons.^{22,23} In line with these findings, NM-sensitive MR imaging showed a decrease in both the size and signal intensity of the SN area. These observations are in agreement with previous studies and confirmed that NM imaging is sensitive and specific for detecting nigrostriatal damage in PD.^{9,10,17,24} The combination of volume and signal loss slightly increased the diagnostic accuracy.¹⁰

In our study, we found a significant increase in diffusivity and a decrease in FA in the 3T NM ROI in patients with PD, which is congruent with previous studies reporting FA reduction²⁻⁴ and increases in RD² and MD.⁵ These changes may be explained by cell loss- and microstructural damage-induced changes in cell morphology and density and the destruction of diffusion barriers.^{24,25} In the 3T T2WI of the SN, we observed only slight modifications in

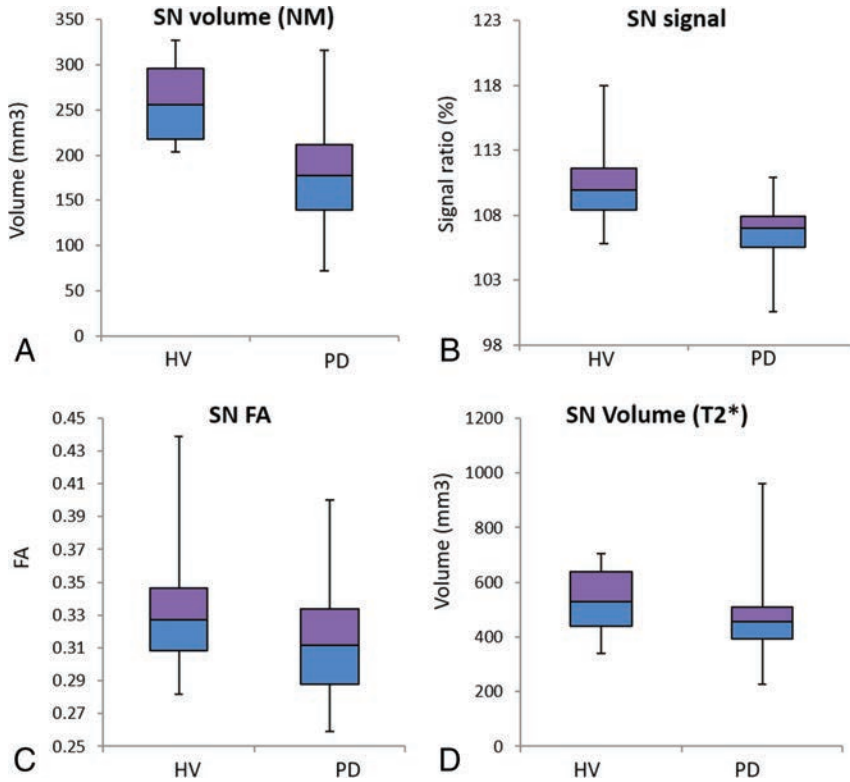


FIG 2. Boxplot of the 3T NM SN volume (cubic millimeters) (A) and signal intensity ratio (B) (calculated by normalizing the mean signal of the SN in each slice to the signal in the background region), the 3T NM FA (C), and the 7T T2*WI SN volume (D) shows a reduction in all measures in patients with PD compared with HVs.

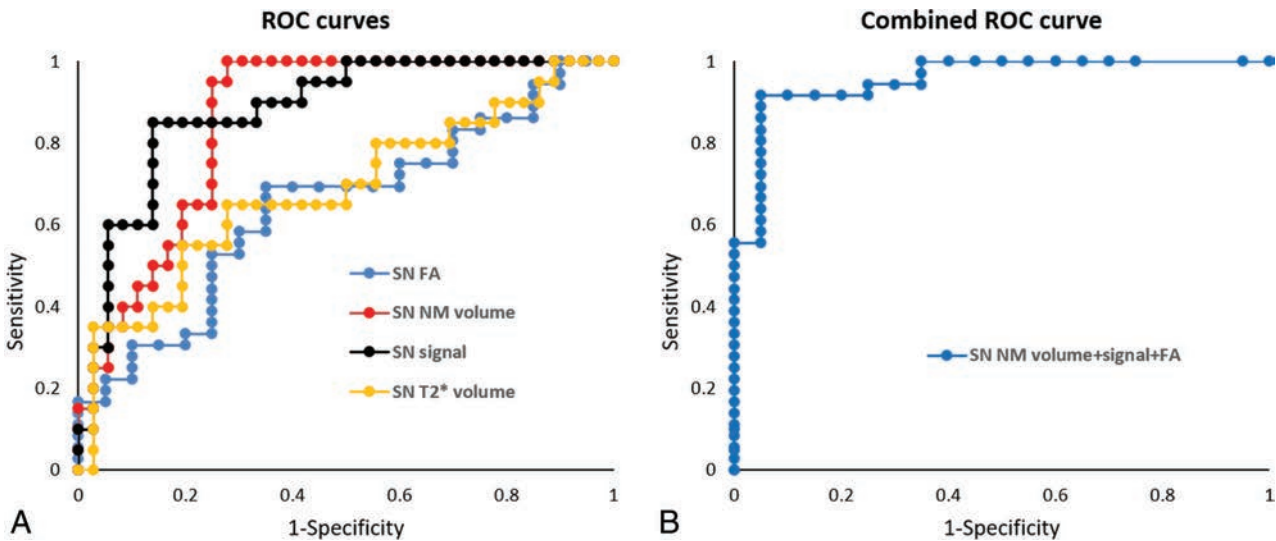


FIG 3. Receiver operating characteristic curves of the 3T NM volume, the 3T NM signal intensity ratio, the 3T NM FA, the 7T T2* volume (A), and the combination of the first 3 biomarkers for differentiating patients with PD from HVs (B).

Table 2: Diagnostic accuracy of quantitative and qualitative (visual) assessments

	Sensitivity	Specificity	PPV	NPV	AUC (95% CI)	Diagnostic Accuracy	Cutoff
Quantitative measurements							
3T NM signal	0.88	0.8	0.88	0.8	0.88 (0.79–0.97)	0.86	110.35
Volume	1	0.72	0.86	1	0.86 (0.76–0.95)	0.89	200.02
7T T2*WI volume	0.65	0.72	0.82	0.54	0.69 (0.53–0.84)	0.68	498.70
Diffusion measures							
FA 3T NM	0.75	0.53	0.75	0.55	0.68 (0.54–0.82)	0.68	0.33
3T T2WI	0.65	0.70	0.8	0.52	0.64 (0.5–0.79)	0.66	0.37
AD 3T NM	0.7	0.65	0.78	0.54	0.73 (0.59–0.87)	0.68	0.64
3T T2WI	0.61	0.75	0.81	0.52	0.65 (0.49–0.80)	0.66	0.5
RD 3T NM	0.64	0.75	0.82	0.54	0.72 (0.58–0.86)	0.67	0.43
3T T2WI	0.72	0.6	0.76	0.55	0.68 (0.52–0.83)	0.67	0.29
MD 3T NM	0.67	0.75	0.83	0.56	0.72 (0.58–0.87)	0.7	0.51
3T T2WI	0.64	0.75	0.82	0.54	0.67 (0.53–0.82)	0.67	0.38
Combined measurements							
NM signal and volume + FA (3T NM)	0.92	0.95	0.97	0.86	0.96 (0.9–1)	0.93	4.4
Qualitative evaluation							
NM at 3T	0.83	0.9	0.94	0.9	–	0.86	–
DNH at 7T							
Method 1	0.97	0.8	0.9	0.94	–	0.91	–
Method 2	0.94	0.85	0.92	0.9	–	0.91	–

Note:—AUC indicates area under the curve; NPV, negative predictive value; PPV, positive predictive value.

RD and MD. This finding is in line with a recent article that reported PD-related DTI changes in the 3T NM ROI, corresponding to the substantia nigra pars compacta, but not in the 3T T2WI of the SN.¹⁹ The diagnostic accuracy of DTI for predicting PD varies across studies, from very low to very high,^{4,26} and this was improved using free water models or kurtosis.^{27,28} Some studies have shown that a combination of FA and R2* improves discrimination.^{2,3} Here, we show that the diagnostic accuracy of DTI measures in the NM SN increased when combined with the NM signal and volume changes, though this was not the case for the 3T T2WI of the SN.

Quantitative measures are often challenging in clinical practice. First, DTI results largely differ among studies.^{2,3,19} Second, SN volume on NM-sensitive images is variable across studies, ranging from 128 to 370 mm³ in HVs and from 96 to 215 mm³ in PD.^{7,10,15,17,24} These differences may be related to the scanner type, magnetic field strength, sequence parameters, image-processing methods, partial volume effect on 2D imaging, or ROI selection methods.²⁹ Within this context, qualitative measurements such as visual assessment of NM-sensitive images or DNH appear interesting.

Visual evaluation of NM signal changes was efficient for distinguishing patients from HVs, with a diagnostic accuracy comparable with that of quantitative measurements. Furthermore, visual analysis of SN signal changes was fast and did not require any postprocessing algorithm. Therefore, visual reading of NM-sensitive images might be of interest for the diagnosis of idiopathic PD in clinical practice, as suggested previously.¹⁵

We found excellent diagnostic accuracy of DNH loss at 7T for PD characterization, which is in agreement with previous studies at 7T^{13,30} and 3T,^{14,31} supporting the use of this technique in a clinical setting.³² Both approaches of visual analysis of DNH, based on the uni- or bilateral presence of DNH loss, resulted in equivalent overall correct classification.

Despite the good diagnostic accuracy of both DNH loss and NM-sensitive visual assessment, further comparison of these 2 sequences in clinical practice is needed.

There was no significant increase in R2* in PD; such increases have been observed in many, but not all,³³ previous studies.^{2,3} A possible explanation for the lack of R2* changes is that R2* may decrease with disease progression.³⁴ Although iron accumulation leads to an increase in R2*, neuronal degeneration and gliosis induce a decrease in R2 relaxation rates within the tissue.³⁵

We found reduced T2*WI SN volume in PD at 7T, in line with previous studies.³⁶ Indeed, only 1 study at 7T reported an increase in SN volume in patients with PD.³⁰ These conflicting results may be due to differences in sequence parameters or patient populations. Further analysis is needed to clarify this issue.

In the 3T NM ROI, the UPDRS score correlated with MD and RD, and the disease duration correlated with FA and T2* volume. Overall, correlations between DTI measures and clinical variables are inconsistent across studies.^{2,3,19} Longitudinal studies and the use of more complex diffusion models, such as free water diffusion, may help enhance our understanding of this relationship.²⁸ No correlation between the signal/volume loss and the UPDRS, disease duration, or Hoehn and Yahr scale was observed, in line with most previous studies.¹⁷ Nonetheless, 1 study did report a correlation with the Hoehn and Yahr scale,²⁴ and another, with the UPDRS.⁹ There were no correlations between NM changes and age or sex, consistent with some previous studies.^{9,24} The lack of an age effect in our study may be explained by the relatively small age range of the subjects.

This study has several limitations. First, visual assessment is rater-dependent. However, both inter- and intrarater reproducibility were good. Manual segmentation is also dependent on the rater's reproducibility. However, Dice coefficients and the ICC were high (≥ 0.8), suggesting good accuracy of measurements. Second, the use of the 2D NM-sensitive sequences might have biased the volume measurements because of partial volume effects. Regardless, the results for NM-based volumes in the current study were comparable with those of previous studies.¹⁷ Moreover, ROC analysis allowed correct classification of the patients with PD and the HV group. Third, quantification of the NM signal in the SN required normalization with the background signal.

To avoid the influence of potential inhomogeneity, the background ROI was large and based on several regions in each slice. Fourth, the mean disease duration in our sample was long. Accordingly, markers for PD neurodegeneration need to be tested in the early stages of PD. Finally, the DNH evaluation was performed at 7T, which is not used in clinical practice, though previous studies have shown that 7T results are similar to those of 3T.³¹

CONCLUSIONS

The combination of signal, volume, and FA measurements on NM-sensitive images allowed excellent diagnostic accuracy. Moreover, excellent accuracy of the visual assessment of DNH loss and NM-based signal changes in the SN confirmed that these techniques are promising for clinical practice. A follow-up study of signal intensity changes in the SN with disease progression will help determine whether this marker could be used to track the neurodegenerative process in neuroprotective trials.

Disclosures: Nadya Pyatigorskaya—RELATED: Grant: ANR Nucleipark, DHOS-Institut Nationale de la santé et de la recherche médicale, France Parkinson, Ecole des NeuroSciences de Paris, Fondation pour la Recherche Médicale, and the Investissements d'Avenir (grant numbers IAIHU-06, Paris Institute of Neurosciences, ANR-II-INBS-0006), and Fondation d'Entreprise, Comments: noncommercial grants received by the institution for funding of the research*. Marie Mongin—RELATED: Grant: Fondation pour la Recherche Médicale. Marie Vidailhet—UNRELATED: Grant: Merz, Comments: unrestricted research grant*; Travel/Accommodations/Meeting Expenses Unrelated to activities listed: EAN, MDS, Comments: travel expenses for faculty at the MDS and EAN. Stéphane Lehericy—RELATED: Grant: Investissements d'Avenir (grant numbers ANR-10-IAIHU-06 and ANR-II-INBS-0006) and Fondation d'Entreprise, Agence nationale pour la recherche, DHOS-Institut Nationale de la santé et de la recherche médicale, France Parkinson, Ecole des NeuroSciences de Paris, Fondation pour la Recherche Médicale, Comments: academic grants*; UNRELATED: Grants/Grants Pending: Servier, Pfizer, Biogen, Comments: research grants*; Payment for Lectures Including Service on Speakers Bureaus: Pileje, Lundbeck, Roche, Comments: lectures; Travel/Accommodations/Meeting Expenses Unrelated to activities listed: Siemens, GE Healthcare, Comments: visit to facilities. *Money paid to the institution.

REFERENCES

- Fearnley JM, Lees AJ. Ageing and Parkinson's disease: substantia nigra regional selectivity. *Brain* 1991;114(Pt 5):2283–301 CrossRef Medline
- Du G, Lewis MM, Styner M, et al. Combined R2* and diffusion tensor imaging changes in the substantia nigra in Parkinson's disease. *Mov Disord* 2011;26:1627–32 CrossRef Medline
- Péran P, Cherubini A, Assogna F, et al. Magnetic resonance imaging markers of Parkinson's disease nigrostriatal signature. *Brain* 2010;133:3423–33 CrossRef Medline
- Vaillancourt DE, Spraker MB, Prodoehl J, et al. High-resolution diffusion tensor imaging in the substantia nigra of de novo Parkinson disease. *Neurology* 2009;72:1378–84 CrossRef Medline
- Schwarz ST, Abaei M, Gontu V, et al. Diffusion tensor imaging of nigral degeneration in Parkinson's disease: a region-of-interest and voxel-based study at 3 T and systematic review with meta-analysis. *Neuroimage Clin* 2013;3:481–88 CrossRef Medline
- Barbosa JH, Santos AC, Tumas V, et al. Quantifying brain iron deposition in patients with Parkinson's disease using quantitative susceptibility mapping, R2 and R2*. *Magn Reson Imaging* 2015;33:559–65 CrossRef Medline
- Sasaki M, Shibata E, Tohyama K, et al. Neuromelanin magnetic resonance imaging of locus ceruleus and substantia nigra in Parkinson's disease. *Neuroreport* 2006;17:1215–18 CrossRef Medline
- Naidich TP, Duvernoy HM. *Duvernoy's Atlas of the Human Brain Stem and Cerebellum: High-Field MRI, Surface Anatomy, Internal Structure, Vascularization and 3D Sectional Anatomy*. New York: Springer-Verlag; 2009
- Schwarz ST, Rittman T, Gontu V, et al. T1-weighted MRI shows stage-dependent substantia nigra signal loss in Parkinson's disease. *Mov Disord* 2011;26:1633–38 CrossRef Medline
- Reimão S, Pita Lobo P, Neutel D, et al. Substantia nigra neuromelanin magnetic resonance imaging in de novo Parkinson's disease patients. *Eur J Neurol* 2015;22:540–46 CrossRef Medline
- Haber SN. The primate basal ganglia: parallel and integrative networks. *J Chem Neuroanat* 2003;26:317–30 CrossRef Medline
- Jellinger KA. Neuropathology of sporadic Parkinson's disease: evaluation and changes of concepts. *Mov Disord* 2012;27:8–30 CrossRef Medline
- Blaziejewska AI, Schwarz ST, Pitiot A, et al. Visualization of nigrosome 1 and its loss in PD: pathoanatomical correlation and in vivo 7 T MRI. *Neurology* 2013;81:534–40 CrossRef Medline
- Reiter E, Mueller C, Pinter B, et al. Dorsolateral nigral hyperintensity on 3.0T susceptibility-weighted imaging in neurodegenerative Parkinsonism. *Mov Disord* 2015;30:1068–76 CrossRef Medline
- Reimão S, Pita Lobo P, Neutel D, et al. Quantitative analysis versus visual assessment of neuromelanin MR imaging for the diagnosis of Parkinson's disease. *J Parkinsons Dis* 2015;5:561–67 CrossRef Medline
- Ohtsuka C, Sasaki M, Konno K, et al. Differentiation of early-stage parkinsonisms using neuromelanin-sensitive magnetic resonance imaging. *Parkinsonism Relat Disord* 2014;20:755–60 CrossRef Medline
- Castellanos G, Fernández-Seara MA, Lorenzo-Betancor O, et al. Automated neuromelanin imaging as a diagnostic biomarker for Parkinson's disease. *Mov Disord* 2015;30:945–52 CrossRef Medline
- Yushkevich PA, Piven J, Hazlett HC, et al. User-guided 3D active contour segmentation of anatomical structures: significantly improved efficiency and reliability. *Neuroimage* 2006;31:1116–28 CrossRef Medline
- Langley J, Huddleston DE, Merritt M, et al. Diffusion tensor imaging of the substantia nigra in Parkinson's disease revisited. *Hum Brain Mapp* 2016;37:2547–56 CrossRef Medline
- Schwarz ST, Afzal M, Morgan PS, et al. The 'swallow tail' appearance of the healthy nigrosome: a new accurate test of Parkinson's disease—a case-control and retrospective cross-sectional MRI study at 3T. *PLoS One* 2014;9:e93814 CrossRef Medline
- Nichols TE, Holmes AP. Nonparametric permutation tests for functional neuroimaging: a primer with examples. *Hum Brain Mapp* 2002;15:1–25 CrossRef Medline
- Braak H, Del Tredici K, Rüb U, et al. Staging of brain pathology related to sporadic Parkinson's disease. *Neurobiol Aging* 2003;24:197–211 CrossRef Medline
- Kastner A, Hirsch EC, Lejeune O, et al. Is the vulnerability of neurons in the substantia nigra of patients with Parkinson's disease related to their neuromelanin content? *J Neurochem* 1992;59:1080–89 CrossRef Medline
- Kashihara K, Shinya T, Higaki F. Neuromelanin magnetic resonance imaging of nigral volume loss in patients with Parkinson's disease. *J Clin Neurosci* 2011;18:1093–96 CrossRef Medline
- Kempster PA, Gibb WR, Stern GM, et al. Asymmetry of substantia nigra neuronal loss in Parkinson's disease and its relevance to the mechanism of levodopa related motor fluctuations. *J Neurol Neurosurg Psychiatry* 1989;52:72–76 CrossRef Medline
- Menke RA, Scholz J, Miller KL, et al. MRI characteristics of the substantia nigra in Parkinson's disease: a combined quantitative T1 and DTI study. *Neuroimage* 2009;47:435–41 CrossRef Medline
- Wang JJ, Lin WY, Lu CS, et al. Parkinson disease: diagnostic utility of diffusion kurtosis imaging. *Radiology* 2011;261:210–17 CrossRef Medline
- Ofori E, Pasternak O, Planetta PJ, et al. Increased free water in the substantia nigra of Parkinson's disease: a single-site and multi-site study. *Neurobiol Aging* 2015;36:1097–104 CrossRef Medline
- Tosk JM, Holshouser BA, Aloia RC, et al. Effects of the interaction between ferric iron and L-dopa melanin on T1 and T2 relaxation

- times determined by magnetic resonance imaging. *Magn Reson Med* 1992;26:40–45 CrossRef Medline
30. Kwon DH, Kim JM, Oh SH, et al. **Seven-Tesla magnetic resonance images of the substantia nigra in Parkinson disease.** *Ann Neurol* 2012;71:267–77 CrossRef Medline
31. Cosottini M, Frosini D, Pesaresi I, et al. **Comparison of 3T and 7T susceptibility-weighted angiography of the substantia nigra in diagnosing Parkinson disease.** *AJNR Am J Neuroradiol* 2015;36:461–66 CrossRef Medline
32. Mahlknecht P, Krismer F, Poewe W, et al. **Meta-analysis of dorsolateral nigral hyperintensity on magnetic resonance imaging as a marker for Parkinson's disease.** *Mov Disord* 2017;32:619–23 CrossRef Medline
33. Michaeli S, Oz G, Sorce DJ, et al. **Assessment of brain iron and neuronal integrity in patients with Parkinson's disease using novel MRI contrasts.** *Mov Disord* 2007;22:334–40 CrossRef Medline
34. Esterhammer R, Seppi K, Reiter E, et al. **Potential of diffusion tensor imaging and relaxometry for the detection of specific pathological alterations in Parkinson's Disease (PD).** *PLoS One* 2015;10:e0145493 CrossRef Medline
35. Schwarz J, Weis S, Kraft E, et al. **Signal changes on MRI and increases in reactive microgliosis, astrogliosis, and iron in the putamen of two patients with multiple system atrophy.** *J Neurol Neurosurg Psychiatry* 1996;60:98–101 CrossRef Medline
36. Pujol J, Junqué C, Vendrell P, et al. **Reduction of the substantia nigra width and motor decline in aging and Parkinson's disease.** *Arch Neurol* 1992;49:1119–22 CrossRef Medline

Detection and Characteristics of Temporal Encephaloceles in Patients with Refractory Epilepsy

Z.M. Campbell, J.M. Hyer, S. Lauzon, L. Bonilha, M.V. Spampinato, and M. Yazdani

ABSTRACT

BACKGROUND AND PURPOSE: Temporal encephaloceles are increasingly visualized during neuroimaging assessment of individuals with refractory temporal lobe epilepsy, and their identification could indicate an intracranial abnormality that may be related to a potential seizure focus. Careful review by an experienced neuroradiologist may yield improved detection of TEs, and other clinical, neurophysiologic, and radiologic findings may predict their presence.

MATERIALS AND METHODS: Data were reviewed retrospectively in patients at our institution who were presented at a multidisciplinary conference for refractory epilepsy between January 1, 2010, and December 31, 2016. Clinical, neurophysiologic, and imaging data were collected. An expert neuroradiologist reviewed the latest MR imaging of the brain in patients for whom one was available, noting the presence or absence of temporal encephaloceles as well as other associated imaging characteristics.

RESULTS: A total of 434 patients were reviewed, 16 of whom were excluded due to unavailable or poor-quality MR imaging. Seven patients had temporal encephaloceles reported on initial imaging, while 52 patients had temporal encephaloceles identified on expert review. MR imaging findings were more often initially normal in patients with temporal encephaloceles ($P < .001$), and detection of temporal encephaloceles was increased in patients in whom 3T MR imaging was performed ($P < .001$), the T2 sampling perfection with application-optimized contrasts by using different flip angle evolutions sequence was used ($P < .001$), or the presence of radiologic findings suggestive of idiopathic intracranial hypertension was noted. Seizure onset by scalp electroencephalogram among patients with temporal encephaloceles was significantly more likely to be temporal compared with patients without temporal encephaloceles ($P < .001$). A significant correlation between intracranial electroencephalogram seizure onset and patients with temporal encephaloceles compared with patients without temporal encephaloceles was not observed, though there was a trend toward temporal-onset seizures in patients with temporal encephaloceles ($P = .06$).

CONCLUSIONS: Careful review of MR imaging in patients with refractory temporal lobe epilepsy by a board-certified neuroradiologist with special attention paid to a high-resolution T2 sequence can increase the detection of subtle temporal encephaloceles, and certain clinical and neurophysiologic findings should raise the suspicion for their presence.

ABBREVIATIONS: EEG = electroencephalogram; RTLE = refractory temporal lobe epilepsy; SPACE = sampling perfection with application-optimized contrasts by using different flip angle evolutions; TE = temporal encephalocele

Temporal encephaloceles (TEs) are herniations of the brain parenchyma through the dura mater and skull that involve the temporal lobe, typically the anteroinferior aspect.¹ Although spontaneous TEs are thought to be rare, the true prevalence is likely higher than recognized.²⁻⁴ Nevertheless, the

true prevalence of small TEs remains largely unknown because they could be easily overlooked on standard imaging techniques. The literature has predominantly focused on CSF leaks in TEs, and only 27 cases of temporal lobe epilepsy involving encephaloceles were published before 2015.⁵⁻¹² Since that time, a recent increase in cases of TEs in patients with refractory epilepsy has been observed.¹³⁻¹⁷ The prevalence of TEs among the largest case series has been 2%–4% of drug-resistant patients referred for epilepsy surgery evaluation, and TEs have been present in nearly 10% of patients with refractory temporal lobe epilepsy (RTLE), which have also accounted for 10% of surgical resections at some institutions.^{15,16} Furthermore, it has been previously reported that 16%–31% of pa-

Received February 19, 2018; accepted after revision May 1.

From the Departments of Neurology (Z.M.C., L.B.), Radiology and Radiologic Science (M.Y., M.V.S.), Neuroradiology, and Public Health Sciences (J.M.H., S.L.), Medical University of South Carolina, Charleston, South Carolina.

Please address correspondence to Zeke Campbell, MD, Medical University of South Carolina, 96 Jonathan Lucas St, Charleston, SC 29425; e-mail: campbeze@musc.edu

<http://dx.doi.org/10.3174/ajnr.A5704>

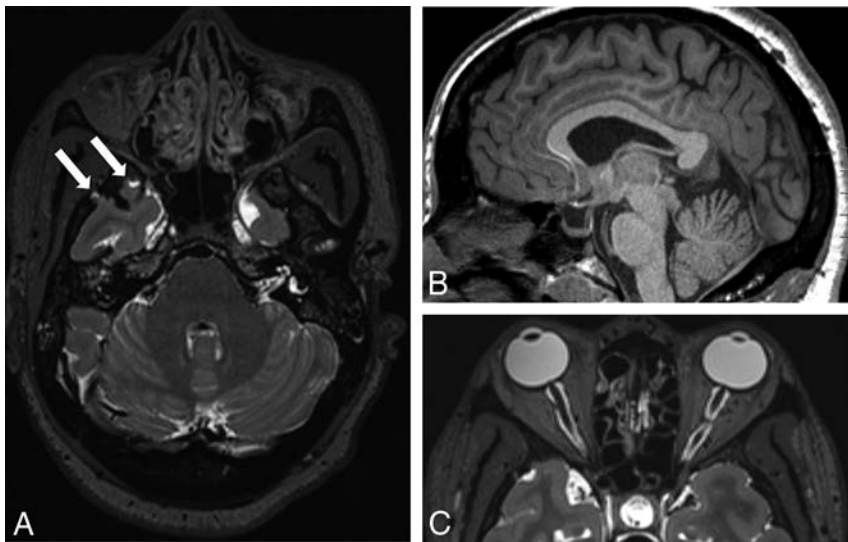


FIG 1. A 43-year-old woman with refractory epilepsy, right temporal onset based on ictal scalp EEG. A, Axial T2 SPACE image shows right anterior temporal encephaloceles (white arrows). A partially empty sella turcica (B) and flattening of the globe at the insertion of the optic nerves (C) are also noted.

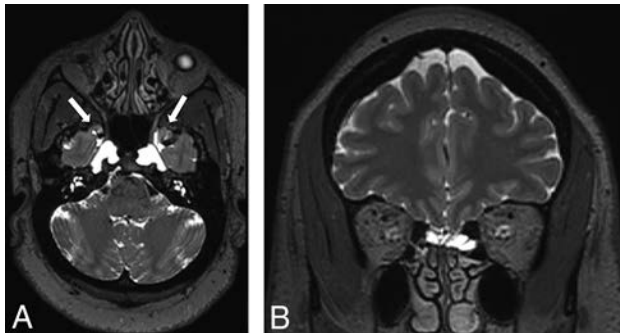


FIG 2. A 50-year-old woman with refractory epilepsy, left temporal onset based on ictal scalp EEG. A, Axial T2 SPACE image shows bilateral anterior temporal encephaloceles (white arrows) and enlarged Meckel caves. B, Coronal T2 SPACE image shows a cribriform plate meningocele.

tients with RTLE do not have a clearly identified lesion on routine MR imaging,^{18,19} and TEs have been observed more frequently in patients with RTLE who had previously normal MR imaging findings.¹⁶

Despite the increasing awareness of TEs in patients with refractory epilepsy, the rate at which TEs are overlooked in patients with RTLE remains unknown. We hypothesized that a substantial number of patients with RTLE have TEs that were not being reported on initial MR imaging interpretation and that careful review with special attention to a high-resolution T2 sequence may result in improved detection. We also suspected that other clinical, neurophysiologic, and radiologic factors would be associated with the presence of TEs and may provide radiologists and epileptologists with a greater index of suspicion so that careful scrutiny for TEs could be performed.

MATERIALS AND METHODS

The study was approved by the Medical University of South Carolina institutional review board and was compliant with the Health Insur-

ance Portability and Accountability Act. Informed consent was waived due to the retrospective nature of the study.

Patients

We retrospectively reviewed clinical, neurophysiologic, and imaging data on 434 patients (18–74 years of age at the time of presentation) presented at our multidisciplinary conference for refractory epilepsy between January 1, 2010, and December 31, 2016. Sixteen patients were excluded due to unavailable or poor-quality MR imaging of the brain for review. Patients were stratified into groups according to ictal seizure onset. MR imaging was reviewed for all patients by a board-certified neuroradiologist to assess the presence or absence of TEs. Neuroimaging in all patients was further assessed for findings suggestive of chronically elevated intracranial pressure.

MR Imaging Protocol

All patients underwent MR imaging on either a 1.5 Avanto or Aera or 3T Skyra or Verio (Siemens, Erlangen, Germany) system according to a protocol optimized for patients with epilepsy. The 3T epilepsy protocol was updated in the second half of 2013 to include sagittal T2 FLAIR (TI, 1800 ms; TE, 387 ms; TR, 5000 ms) and sagittal T2 (TE, 408 ms; TR, 3200 ms) sampling perfection with application-optimized contrasts by using different flip angle evolutions (SPACE; Siemens) sequences of the whole brain with section thickness of 0.9 mm and voxel size of $0.9 \times 0.9 \times 0.9$ mm, which were subsequently reconstructed in axial and coronal planes.

Image Analysis

Imaging was reviewed by a single reader (M.Y.), a board-certified neuroradiologist with 3 years of experience, who was blinded to the clinical history and radiology report at the time of imaging review. All MRIs had been initially read by a group of board-certified neuroradiologists with an experience range of 1–12 years. MR imaging of 418 patients was retrospectively reviewed with particular attention paid to the anterior temporal lobes. The number, size, and location of osseous dural defects of the middle cranial fossa with unequivocal extension of brain parenchyma into the defect (Fig 1A) were recorded. In addition, the presence or absence of an empty or partially empty sella, enlarged Meckel cave, cribriform plate meningocele, and optic nerve protrusion into the globes was documented (Figs 1 and 2). The height of the pituitary gland was classified into 5 categories using the system of Yuh et al.²⁰ We considered categories III (moderate concavity of the superior pituitary) and IV (severe concavity of the superior pituitary) as a partially empty sella and category V (enlarged sella without visible pituitary) as an empty sella. The width of the Meckel cave was measured on a coronal T2-weighted sequence and was considered enlarged if >7 mm.²¹

Comparison of clinical, radiologic, and neurophysiologic data of patients with-versus-without temporal encephaloceles^a

	Total	TEs (n = 52)	Without TEs (n = 366)	P
Demographics				
Age (yr)	43.3 ± 13.5	43.3 ± 12.1	36.4 ± 13.4	<.001
BMI	28.7 (24.1–35.4)	36.9 (30.0–40.7)	27.7 (23.9–33.7)	<.001 ^b
Age at onset (yr)	15.0 (6.0–29.0)	35.0 (29.0–45.0)	14.0 (5.0–22.0)	<.001 ^b
Years with epilepsy	16.0 (7.0–27.0)	4.5 (2.0–9.5)	17.0 (9.0–28.0)	<.001 ^b
Male	176 (42.1%)	9 (17.3%)	167 (45.6%)	<.001
Radiologic findings				
Normal initial MRI	157 (37.6%)	31 (59.6%)	126 (34.7%)	<.001
MRI magnet = 3T	341 (81.8%)	50 (96.2%)	291 (79.7%)	.002 ^c
SPACE was used	175 (41.9%)	37 (71.2%)	138 (37.7%)	<.001
Abnormal Meckel cave	11 (2.6%)	5 (9.6%)	6 (1.6%)	<.001
Abnormal sella turcica	98 (23.4%)	48 (92.3%)	50 (13.7%)	<.001
Papilledema, yes	9 (2.2%)	6 (11.5%)	3 (0.8%)	<.001 ^c
Seizure localization				
Seizures				<.001 ^c
Temporal	223 (57.6%)	46 (90.2%)	177 (52.7%)	
Nonlocalizable	102 (26.4%)	5 (9.8%)	97 (28.9%)	
Nontemporal	62 (16.0%)	0 (0.0%)	62 (16.0%)	
icEEG				.06 ^c
No seizures	1 (1.9%)	1 (2.5%)	0 (0.0%)	
Temporal	34 (63.0%)	7 (87.5%)	27 (58.7%)	
Nontemporal	11 (20.4%)	0 (0.0%)	11 (23.9%)	
Nonlocalizable	7 (13.0%)	0 (0.0%)	7 (15.2%)	
Temp + extratemp	1 (1.9%)	0 (0.0%)	1 (2.2%)	

Note:—icEEG indicates intracranial EEG; BMI, body mass index; temp, temporal; extratemp, extratemporal.
^a Results of the analysis are presented as mean ± SD for continuous variables and No. (%) for categorical variables unless otherwise noted. To assess statistical associations, we conducted a *t* test for continuous variables and a χ^2 test for categorical variables unless otherwise noted.
^b Descriptive statistics are presented as median (25th, 75th percentiles) and were tested using a Wilcoxon rank sum test.
^c Test conducted was a Fisher exact test.

Seizure Localization

Seizure onset was determined from neurophysiologic data and was based on interpretations of the ictal scalp electroencephalogram (EEG) and intracranial EEG. Three hundred eighty-seven patients had available ictal scalp EEGs. Fifty-five patients had intracranial monitoring, one of whom did not have seizures recorded. Patients were categorized by a board-certified epileptologist (Z.M.C.) on the basis of seizure onset as temporal (defining laterality when present), nontemporal (ie, either generalized or extratemporal onset), or nonlocalizable. Patients were only classified as having nonlocalizable onset if none of the recorded seizures could be clearly localized. One patient with an intracranial EEG was found to have independent temporal and extratemporal (nontemporal) seizure onset.

Statistical Analysis

All demographic and radiologic findings are presented as mean ± SD for continuous variables or as median (25th percentile, 75th percentile) for non-normally distributed variables and *n* (%) for categorical variables. To assess their statistical association with TEs, we conducted a *t* test for continuous variables and a χ^2 test for categorical variables. Wilcoxon rank sum tests and Fisher exact tests were used when appropriate. The McNemar test was used to assess the relationship between retrospective review and initial determination of TEs. All analyses were conducted using SAS, Version 9.4 (SAS Institute, Cary, North Carolina). Statistical significance was assessed at $\alpha = .05$.

RESULTS

Identification of Temporal Encephaloceles

Among the 418 patients with refractory epilepsy who had MR imaging available, 52 (12.5%) were found to have TEs on retrospective review, while only 7 (1.7%) had TEs identified on initial interpretation. Among the 52 patients with TEs, 19 TEs were unilateral (10 with left only, 9 with right only) and 33 TEs (63.5%) were bilateral. A total of 192 TEs (95 on the right and 97 on the left) were identified. There was an overall agreement of 89.2% between the retrospective reviewer and the initial interpretation. However, only 13.5% of patients were eventually discovered to have at least 1 TE on initial review (*P* < .001). All 7 TEs detected on initial interpretation were on scans that included a T2 SPACE sequence. There was no statistically significant difference between the size of TEs detected on the initial interpretation and TEs only detected on retrospective review.

Clinical Characteristics, Radiologic Findings, and Seizure Localization

Demographic, radiologic, and neurophysiologic data are summarized in the

Table. Comparisons of clinical characteristics between subgroups with or without TEs differed significantly in regard to age, sex, body mass index, age at epilepsy onset, and years with epilepsy. MR imaging findings were more often initially normal in patients with TEs (*P* < .001), and a strong association was noted among patients with TEs for whom MR imaging was acquired using a 3T magnet (*P* = .002) and a T2 SPACE sequence (*P* < .001). The presence of an enlarged Meckel cave (*P* < .001), an empty or partially empty sella (*P* < .001), or findings suggestive of papilledema (*P* < .001) was also significantly associated with the presence of TEs. There was no significant difference found between laterality (unilateral TE percentage versus bilateral TE percentage) and an enlarged Meckel cave (10.5% versus 9.1%, *P* = 1.00), an empty or partially empty sella (89.5% versus 93.9%, *P* = .62), or papilledema (5.3% versus 15.2%, *P* = .40). Ictal scalp EEG was significantly more likely to localize seizure onset as temporal in patients with TEs (*P* < .001). Among the 54 patients who underwent intracranial monitoring, localization of seizure onset did not achieve statistical significance (*P* = .06), though all patients with TEs for whom seizures were recorded during intracranial monitoring had seizures localized as temporal-onset.

DISCUSSION

Our study, which represents the largest cohort of patients with TEs and refractory epilepsy to date, to our knowledge, demonstrates that the detection of TEs in patients with refractory epi-

lepsy increased significantly after retrospective review with the explicit intent of assessing the MR imaging for the presence or absence of TEs. The use of 3T MR imaging and T2 SPACE sequences was correlated with improved detection of TEs, and their presence was accompanied by findings commonly associated with idiopathic intracranial hypertension. Detection of small TEs was greatly expedited by reviewing the axial and sagittal T2 SPACE sequences. Patients with TEs were more likely to have temporal-onset seizures on scalp EEG, and although statistical significance for patients with intracranial EEG was not achieved due to a lack of power for this comparison, all patients with TEs for whom seizures were recorded had seizures localized as temporal-onset.

Although the prevalence of TEs in patients referred to tertiary centers for epilepsy has been reported as 2%–4%,^{15,16} we found that 12.5% of patients referred to our refractory epilepsy conference were diagnosed with TEs after careful systematic review of MR imaging with special attention paid to the anterior temporal lobes. We found that TEs were often overlooked on initial review and that patients with TEs were likely to have prior imaging findings that were normal, similar to findings in other smaller studies.^{15,16} Saavalainen et al¹⁵ found that 17 of 23 patients with TEs required repeat MR imaging, while 4 were diagnosed only after re-evaluation by an experienced neuroradiologist. However, this appears to be an underestimate because our cohort determined that only 13.5% of patients with TEs were diagnosed on initial review. As expected, there was a significant association between the detection of TEs and the use of 3T MR imaging and SPACE sequences. The recent technologic improvements in imaging capabilities have been regarded by some as the most likely reason for the increased detection of TEs in patients with epilepsy.²² However, the increased awareness of TEs in patients with epilepsy among radiologists and epileptologists has also likely facilitated improved detection.

We also detected associations among a variety of clinical factors. In keeping with findings of authors in prior studies,^{8,23,24} we noted a strong correlation between an elevated body mass index and the presence of TEs, which some have assumed to be a consequence of idiopathic intracranial hypertension, though most patients in these prior studies were evaluated for CSF leak. Most TEs associated with seizures affect the greater wing of the sphenoid bone and are thus located along the medial aspect of the temporal lobe,^{1,15,24} which, due to its higher epileptogenicity, has led some to conclude that the TEs in this location are more likely to become epileptogenic, particularly because the absence of a CSF leak may obfuscate their detection for many years. This supposition is also supported by the older age of onset between our 2 groups, and prior literature supports epilepsy onset beyond the third decade of life in patients with TEs.¹⁶ The shorter duration of epilepsy at the time of evaluation in patients with TEs is particularly striking, and whether an association with TEs may represent a more aggressive form of epilepsy is curious, though more studies with other clinical measures of refractoriness would be needed to determine whether TEs are truly associated with more aggressive temporal lobe epilepsy. We also noted a tendency of patients with TEs to be female, an association that has also been strongly observed among patients with idiopathic intracranial hypertension.²⁵

The presence of TEs on review was significantly more com-

mon in patients with seizures of temporal onset on ictal scalp EEG, and none of the 52 patients identified were found to have extratemporal- or generalized-onset seizures on ictal scalp EEG. This proclivity of patients with TEs to have coexistent temporal lobe epilepsy has been observed in smaller studies¹⁶ and suggests that even if TEs are not structurally epileptogenic, the presence of TEs may at least represent a surrogate marker for a propensity toward temporal lobe epilepsy and thus may be of localizing value. While some patients with TEs had seizures that were poorly localized on ictal scalp EEG, it is unclear whether these patients simply had temporal-onset seizures that were not clearly localized or whether some proportion of these poorly localized seizures is nontemporal in origin. Although the localizing data from ictal intracranial EEG did not achieve statistical significance, there appeared to be a trend toward patients with TEs having temporal-onset seizures, and all patients with TEs in whom seizures were detected were found to have temporal-onset seizures. However, these results were limited by the sample size. Larger intracranial studies are required to further evaluate the localizing value of TEs and to determine to what extent TEs may be epileptogenic. While there are little data available to determine whether or how much TEs constitute epileptogenic lesions, the literature has supported good clinical outcomes in cases in which surgical resection was performed.^{5,7,13,19} Panov et al¹³ performed intraoperative electrocorticography in 6 patients, all of whom were found to have interictal epileptiform activity emanating from the TEs.

Additionally, seizures were found in 2 patients, both of whom had involvement of the area around the TEs at seizure onset, though there was synchronous or near-rapid spread to the hippocampus. Large case series have reported bilateral TEs in 14%–30% of patients with TEs and epilepsy,^{15,16} compared with 63.5% of patients in our study. It is conceivable that many patients may have bilateral TEs that may be overlooked without careful scrutiny and without an available high-resolution T2 sequence. We suspect that the presence of bilateral as opposed to unilateral TEs may be more likely to be associated with radiologic findings suggestive of idiopathic intracranial hypertension, and although not significant between these groups, these comparisons were insufficiently powered and may require further study with larger sample sizes. While the presence of bilateral TEs does appear to be a relatively common phenomenon among patients with TEs, Saavalainen et al¹⁵ also found that 3 of 5 patients with bilateral TEs who underwent epilepsy surgery were seizure-free at follow-up; this finding suggests that not all TEs are likely epileptogenic. We suspect that while not all TEs are likely epileptogenic, their relatively common presence in patients with RTLE (along with their scarcity among patients with extratemporal or generalized epilepsy) suggests that a subset of TEs may lie within or contribute to the epileptogenic zone. However, the scope of our present study was limited to examining the presence of TEs and associated factors, while other studies may provide more insight as to their epileptogenicity.

This study has several limitations. Due to its retrospective nature, no healthy control group was available, though patients with nontemporal seizures were used for comparison. Additionally, the use of an expert MR imaging reviewer is susceptible to rater-dependent bias. This could be mitigated by multiple-expert re-

view, with assessment to ensure appropriate interrater agreement; however, the development of guidelines may be necessary to facilitate a consensus among reviewers regarding what constitutes clinically relevant TEs in patients with epilepsy. Other than 1 patient who had a lumbar puncture with an elevated opening pressure, the remainder of patients with TEs included in the study did not undergo lumbar puncture to evaluate idiopathic intracranial hypertension. The association between idiopathic intracranial hypertension, TE, and temporal lobe epilepsy will require investigation in future studies. The localization of seizures was limited by the absence of seizures on intracranial EEGs in many patients, and larger studies with more patients undergoing intracranial monitoring should be able to confirm or refute our findings on the basis of the localizing data from ictal scalp EEG. Further studies to determine the frequency of TEs in the general population, the epileptogenicity of TEs, and outcomes of various treatment modalities are needed to better understand the relevance of and necessary approach to TEs.

CONCLUSIONS

Careful inspection of MR imaging with special attention paid to the high-resolution T2 sequence (T2 SPACE in our study) in patients with RTLE by a board-certified neuroradiologist can increase the detection of subtle TEs, which may be a source of focal refractory seizures. Certain clinical and neurophysiologic findings should raise suspicion for the presence of TEs, though further studies are necessary to determine their epileptogenicity and response to individual therapies.

Disclosures: Leonardo Bonilha—UNRELATED: Consultancy: Philips Healthcare*; Grants/Grants Pending: National Institutes of Health, American Heart Association.* M. Vittoria Spampinato—UNRELATED: Grants/Grants Pending: Bracco*. *Money paid to the institution.

REFERENCES

- Wind JJ, Caputy AJ, Roberti F. **Spontaneous encephaloceles of the temporal lobe.** *Neurosurg Focus* 2008;25:E11 CrossRef Medline
- Alonso RC, de la Peña MJ, Caicoya AG, et al. **Spontaneous skull base meningoencephaloceles and cerebrospinal fluid fistulas.** *RadioGraphics* 2013;33:553–70 CrossRef Medline
- Lloyd KM, DelGaudio JM, Hudgins PA. **Imaging of skull base cerebrospinal fluid leaks in adults.** *Radiology* 2008;248:725–36 CrossRef Medline
- Schuknecht B, Simmen D, Briner HR, et al. **Nontraumatic skull base defects with spontaneous CSF rhinorrhea and arachnoid herniation: imaging findings and correlation with endoscopic sinus surgery in 27 patients.** *AJNR Am J Neuroradiol* 2008;29:542–49 CrossRef Medline
- Abou-Hamden A, Lau M, Fabinyi G, et al. **Small temporal pole encephaloceles: a treatable cause of “lesion negative” temporal lobe epilepsy.** *Epilepsia* 2010;51:2199–202 CrossRef Medline
- Aquilina K, Clarke DF, Wheless JW, et al. **Microencephaloceles: another dual pathology of intractable temporal lobe epilepsy in childhood.** *J Neurosurg Pediatr* 2010;5:360–64 CrossRef Medline
- Byrne RW, Smith AP, Roh D, et al. **Occult middle fossa encephaloceles in patients with temporal lobe epilepsy.** *World Neurosurg* 2010;73:541–46 CrossRef Medline
- Carlson ML, Copeland WR 3rd, Driscoll CL, et al. **Temporal bone encephalocele and cerebrospinal fluid fistula repair utilizing the middle cranial fossa or combined mastoid-middle cranial fossa approach.** *J Neurosurg* 2013;119:1314–22 CrossRef Medline
- Gasparini S, Ferlazzo E, Villani F, et al. **Refractory epilepsy and encephalocele: lesionectomy or tailored surgery?** *Seizure* 2014;23:583–84 CrossRef Medline
- Giulioni M, Licchetta L, Bisulli F, et al. **Tailored surgery for drug-resistant epilepsy due to temporal pole encephalocele and microdysgenesis.** *Seizure* 2014;23:164–66 CrossRef Medline
- Giulioni M, Marucci G, Martinoni M, et al. **Seizure outcome in surgically treated drug-resistant mesial temporal lobe epilepsy based on the recent histopathological classifications.** *J Neurosurg* 2013;119:37–47 CrossRef Medline
- Kamiya K, Mori H, Kunimatsu A, et al. **Two cases of spontaneous temporal encephalocele.** *J Neuroradiol* 2012;39:360–63 CrossRef Medline
- Panov F, Li Y, Chang EF, et al. **Epilepsy with temporal encephalocele: characteristics of electrocorticography and surgical outcome.** *Epilepsia* 2016;57:e33–38 CrossRef Medline
- Morone PJ, Sweeney AD, Carlson ML, et al. **Temporal lobe encephaloceles: a potentially curable cause of seizures.** *Otol Neurotol* 2015;36:1439–42 CrossRef Medline
- Saavalainen T, Jutila L, Mervaala E, et al. **Temporal anteroinferior encephalocele: an underrecognized etiology of temporal lobe epilepsy?** *Neurology* 2015;85:1467–74 CrossRef Medline
- Toledano R, Jiménez-Huete A, Campo P, et al. **Small temporal pole encephalocele: a hidden cause of “normal” MRI temporal lobe epilepsy.** *Epilepsia* 2016;57:841–51 CrossRef Medline
- Shimada S, Kunii N, Kawai K, et al. **Spontaneous temporal pole encephalocele presenting with epilepsy: report of two cases.** *World Neurosurg* 2015;84:867.e6 CrossRef Medline
- Bien CG, Szinay M, Wagner J, et al. **Characteristics and surgical outcomes of patients with refractory magnetic resonance imaging-negative epilepsies.** *Arch Neurol* 2009;66:1491–99 CrossRef Medline
- Nguyen DK, Mbacou MT, Nguyen DB, et al. **Prevalence of nonlesional focal epilepsy in an adult epilepsy clinic.** *Can J Neurol Sci* 2013;40:198–202 CrossRef Medline
- Yuh WT, Zhu M, Taoka T, et al. **MR imaging of pituitary morphology in idiopathic intracranial hypertension.** *J Magn Reson Imaging* 2000;12:808–13 Medline
- Aaron GP, Illing E, Lambertsen Z, et al. **Enlargement of Meckel’s cave in patients with spontaneous cerebrospinal fluid leaks.** *Int Forum Allergy Rhinol* 2017;7:421–24 CrossRef Medline
- Van Gompel J, Miller J. **How epileptogenic are temporal encephaloceles?** *Neurology* 2015;85:1440–41 CrossRef Medline
- Brainard L, Chen DA, Aziz KM, et al. **Association of benign intracranial hypertension and spontaneous encephalocele with cerebrospinal fluid leak.** *Otol Neurotol* 2012;33:1621–24 CrossRef Medline
- Stucken EZ, Selesnick SH, Brown KD. **The role of obesity in spontaneous temporal bone encephaloceles and CSF leak.** *Otol Neurotol* 2012;33:1412–17 CrossRef Medline
- Durcan FJ, Corbett JJ, Wall M. **The incidence of pseudotumor cerebri: population studies in Iowa and Louisiana.** *Arch Neurol* 1988;45:875–77 CrossRef Medline

Morphology-Specific Discrimination between MS White Matter Lesions and Benign White Matter Hyperintensities Using Ultra-High-Field MRI

Z. Hosseini, J. Matusinec, D.A. Rudko, J. Liu, B.Y.M. Kwan, F. Salehi, M. Sharma, M. Kremenchutzky, R.S. Menon, and M. Drangova



ABSTRACT

BACKGROUND AND PURPOSE: Recently published North American Imaging in Multiple Sclerosis guidelines call for derivation of a specific radiologic definition of MS WM lesions and mimics. The purpose of this study was to use SWI and magnetization-prepared FLAIR images for sensitive differentiation of MS from benign WM lesions using the morphologic characteristics of WM lesions.

MATERIALS AND METHODS: Seventeen patients with relapsing-remitting MS and 18 healthy control subjects were enrolled retrospectively. For each subject, FLAIR and multiecho gradient-echo images were acquired using 7T MR imaging. Optimized postprocessing was used to generate single-slice SWI of cerebral veins. SWI/FLAIR images were registered, and 3 trained readers performed lesion assessment. Morphology, location of lesions, and the time required for assessment were recorded. Analyses were performed on 3 different pools: 1) lesions of >3 mm, 2) nonconfluent lesions of >3 mm, and 3) nonconfluent lesions of >3 mm with no or a single central vein.

RESULTS: The SWI/FLAIR acquisition and processing protocol enabled effective assessment of central veins and hypointense rims in WM lesions. Assessment of nonconfluent lesions with ≥ 1 central vein enabled the most specific and sensitive differentiation of patients with MS from controls. A threshold of 67% perivenous WM lesions separated patients with MS from controls with a sensitivity of 94% and specificity of 100%. Lesion assessment took an average of 12 minutes 10 seconds and 4 minutes 33 seconds for patients with MS and control subjects, respectively.

CONCLUSIONS: Nonconfluent lesions of >3 mm with ≥ 1 central vein were the most sensitive and specific differentiators between patients with MS and control subjects.

ABBREVIATIONS: CVS = central vein sign; EDSS = Expanded Disability Status Scale; HC = healthy control; IEV-SWI = inter-echo variance susceptibility-weighted imaging; LL = lesions of >3 mm; MP-FLAIR = magnetization-prepared FLAIR; NC = nonconfluent lesions of >3 mm; %PVWML = percentage of total perivenous white matter lesion count; RRMS = relapsing-remitting multiple sclerosis; SV = nonconfluent lesions of >3 mm with a single central vein; WML = white matter lesions

Multiple sclerosis is an autoimmune disease that affects the central nervous system. While the use of conventional MR imaging to detect WM lesions (WML) can support and supplement the McDonald criteria for the diagnosis of MS based on

dissemination in time and space,¹ using more advanced imaging biomarkers may enable diagnosis based on a single time point assessment. Such early diagnosis of MS could improve patient outcome because it would enable earlier application of disease-modifying therapies.²⁻⁵

The MS WML are detectable on T2-weighted FLAIR images, with superior diagnostic value over conventional T2-weighted imaging.⁶ However, the presence of nonspecific WML, which increase with age and with certain risk factors, confounds a confirmatory diagnosis of MS. A number of studies have proposed perivenous WM lesion count (herein referenced as a percentage of total perivenous white matter lesion count [%PVWML]), as de-

Received March 2, 2018; accepted after revision May 5.

From the Biomedical Engineering Graduate Program (Z.H., R.S.M., M.D.); Imaging Research Laboratories (Z.H., J.L., R.S.M., M.D.), Roberts Research Institute; Departments of Medicine (J.M.), Medical Imaging (B.Y.M.K., F.S., M.S.), and Medical Biophysics (R.S.M., M.D.), Schulich School of Medicine and Dentistry; Western University, London, Ontario, Canada; Department of Neurology and Neurosurgery (D.A.R.), McConnell Brain Imaging Centre, Montreal Neurological Institute, and Department of Biomedical Engineering (D.A.R.), McGill University, Montreal, Quebec, Canada; and Department of Clinical Neurological Sciences (M.S., M.K.), Western University and London Health Sciences Centre, London, Ontario, Canada.

This work was supported by the Canadian Institutes for Health Research Foundation grant 353372 and Natural Sciences and Engineering Council grant 401947-2011.

Paper previously presented at: Joint Annual Meeting of the International Society for Magnetic Resonance in Medicine and the European Society for Magnetic Resonance in Medicine and Biology, June 16–21, 2018; Paris, France. The title of the abstract was "Validation of a Radiological Definition for Central Vessel Sign using 7T FLAIR and SWI."

Please address correspondence to Maria Drangova, MD, Roberts Research Institute, 1151 Richmond St N, London, ON, Canada, N6A 5B7; e-mail: mdrangova@robarts.ca

Indicates open access to non-subscribers at www.ajnr.org

Indicates article with supplemental on-line photo.

<http://dx.doi.org/10.3174/ajnr.A5705>

ected by SWI or T2*-weighted magnitude images, as a promising imaging biomarker for differentiation of MS lesions from other white matter lesions.⁷⁻¹¹ SWI offers a definite advantage over T2*-weighted magnitude images because it enables visualization of veins of various sizes throughout the brain, even in the infratentorial region.¹² The lack of a cohesive practice in evaluating perivenous lesions has led to some uncertainty in evaluating %PVWML as an imaging biomarker. The recently published consensus statement by the North American Imaging in Multiple Sclerosis committee promotes a more controlled evaluation of the perivenous lesions¹³ by suggesting several exclusion criteria in defining the central vein sign (CVS); specifically, the exclusion of lesions that are <3 mm in diameter in any plane, are confluent, have multiple distinct veins, or have poor visibility. Additionally, the consensus statement calls for the investigation of a standard radiologic definition of the CVS.

Initial study of the radiologic definition of the CVS may benefit from high-field MR imaging, as in other neurologic applications.¹⁴⁻¹⁷ While advantageous due to the associated higher SNR, imaging at a high field also presents challenges.¹⁸ Susceptibility artifacts near the air-tissue interfaces are amplified at higher fields, rendering information in the phase image unusable in extreme cases. These effects can result in subtle phase artifacts, which may have a vessel-like appearance on SWI¹⁹ and lead to inaccurate %PVWML values. Previous work presented the inter-echo variance SWI (IEV-SWI) approach, which preserves the information in the phase by processing individual receive-coil complex image data separately.¹⁹ For accurate WM lesion identification at 7T, it is also advantageous to collect 3D-FLAIR images with efficient fluid suppression and T2 contrast, accomplished through the addition of magnetization-prepared pulses to the conventional FLAIR sequence (MP-FLAIR).¹⁸ Performing the study at 7T simultaneously evaluates the IEV-SWI approach under more challenging conditions than 3T, while providing a clinical baseline for further applications at both 7T and 3T.

In this study, we have performed a thorough evaluation of features included in the North American Imaging in Multiple Sclerosis consensus statement. Using IEV-SWI and MP-FLAIR images acquired at 7T, we sought to identify morphologic characteristics of WML to enable the sensitive and specific differentiation of clinically definite MS WML from benign WML in controls.

MATERIALS AND METHODS

Study Design and Patient Population

The study was approved by the University of Western Ontario Institutional Research Ethics Board. Written informed consent was obtained from each subject. Seventeen patients with relapsing-remitting MS (RRMS) and 18 age- and sex-matched healthy control (HC) subjects were selected from a larger study population²⁰; there was no overlap between the subject matter of the 2 studies, and subjects were selected on the basis of the availability of raw MR imaging data. Control subjects had no known neurologic conditions, but WML were found incidentally. Clinical data, including Expanded Disability Status Scale (EDSS) scores, were collected for all subjects with RRMS.

Imaging Protocol

Imaging was performed on a 7T MR imaging system (Agilent Technologies, Santa Clara, California) using a 23-channel transmit/receive head coil. A 3D flow-compensated 6-echo gradient-echo dataset was acquired in the axial orientation from each subject with the following parameters: imaging resolution, $0.5 \times 0.5 \times 1.25 \text{ mm}^3$ (with no zero padding); acquisition matrix, $380 \times 340 \times 102$; TR/TEs, 40/3.77, 7.86, 12.15, 16.64, 21.33, 26.22 ms; flip angle, 13°; generalized autocalibrating partially parallel acquisition acceleration factor, 2; total imaging time, 15 minutes 55 seconds. B1+ mapping and shimming were performed before each scan using the method of Curtis et al.²¹ Accompanying MP-FLAIR images (for hyperintense lesion identification) were also collected, as described previously.¹⁸ The MP-FLAIR images were acquired in the sagittal orientation with 1.0-mm^3 isotropic voxels; TR/TE, 2000/242.8 ms; total imaging time, 13 minutes 52 seconds.

Image Processing and Registration

Susceptibility-weighted images were generated from the complex channel data of the multiecho gradient-recalled-echo acquisition using the channel-by-channel IEV-SWI pipeline.¹⁹ Processing was performed off-line using parallel computing on a system with 16 cores using Matlab software (R2014a; MathWorks, Natick, Massachusetts).

IEV-SWI and MP-FLAIR images were registered using FSL tools (<http://www.fmrib.ox.ac.uk/fsl>)²²⁻²⁵; the IEV-SWIs were viewed as single-slice images.

White Matter Lesion Assessment

A neuroradiologist (M.S.) with 9 years of experience in MR imaging of neurodegenerative and demyelinating disorders performed WM lesion assessment. To enable intrareader variability assessment, M.S. repeated the lesion counting 1 month after the initial evaluation. For interreader variability assessment, 2 radiology residents (F.S., year 4, and B.Y.M.K., year 5) performed the same evaluations.

For each subject, the registered pair of IEV-SWI and MP-FLAIR images was randomized by a nonreader. Images were then imported into OsiriX Imaging Software (Version 5.8.1; <http://www.osirix-viewer.com>)²⁶ for viewing. Readers could view coregistered coronal, axial, and sagittal views of IEV-SWI and MP-FLAIR images. White matter lesions were defined as abnormal hyperintensities on MP-FLAIR images. Veins were defined as hypointensities on IEV-SWI extending over several voxels either in or through the axial plane of the images.

In line with the hypergeometric model validated previously to accelerate radiologic WM lesion assessment,¹⁵ readers were asked to identify the 10 largest lesions for each subject based on the MP-FLAIR images. They were then asked to assess morphologic information for each lesion (outlined below). For subjects with <10 lesions, readers recorded information for all lesions identified on the MP-FLAIR images.

Assessment Metrics

The following assessments were incorporated into tabular form to enable easy recording of the observations (ie, the possible re-

sponses were outlined in this form to control the range of variation in the responses).

Lesion location was recorded as being in 1 of 4 brain regions: infratentorial, juxtacortical (within 1 voxel from the cortex) periventricular (within 1 voxel of the ventricles), or subcortical/deep (between the ventricles and the cortex). Preliminary lesion size assessment was performed using digital calipers. If the lesion length along the longest axis was <3 mm, this was noted and the area was not measured. For lesions of >3 mm, the Closed Polygon tool of OsiriX was used to measure the area of the lesion on its largest axial cross-section.

The readers recorded the presence or absence of central veins within the lesions on the basis of the registered IEV-SWI. If central veins were present, the number of distinct veins was recorded. The presence or absence of an iron rim around the lesions and the time required to assess each dataset were also recorded. Data from subjects with <3 lesions were eliminated before analysis.

For each HC and subject with RRMS, %PVWML was calculated for each of the 3 readers, R_i , and each of the subjects, S_k ; this was subsequently averaged over all readers to give the average %PVWML for the subject (Average %PVWML $_{S_k}$).

Location-specific (loc $_j$) %PVWML was also calculated separately for each reader and subsequently averaged over all subjects to give the reader-specific %PVWML at each location (Average %PVWML $_{R_i,loc_j}$) for the HC and RRMS groups. The location-specific %PVWML was also averaged over the readers (Average %PVWML $_{loc_j,S_k}$) for the HC and RRMS groups.

These metrics were calculated for 3 different lesions pools: large lesions of >3 mm (LL pool), nonconfluent lesions of >3 mm (NC pool), and nonconfluent lesions of >3 mm with a single central vein (SV pool), where the NC and SV pools are subsets of the LL pool.

Statistics

Statistical analysis was performed using GraphPad Prism, Version 7.0a (GraphPad Software, San Diego, California). Average lesion size in each anatomic region was compared between the RRMS and HC groups using multiple-measures 2-way ANOVA (with a Tukey correction for multiple comparisons). Lesion size differences in each of the 4 regions within the RRMS group were compared using the nonparametric paired Friedman test. The average time taken by each reader to complete the review of each dataset was compared between RRMS and HC groups using the Mann-Whitney U test.

Average %PVWML $_{R_i,loc_j}$ was used to assess inter- and intrareader agreement using Bland-Altman analysis; in this analysis, the individual assessments were treated as independent observations. Average %PVWML $_{loc_j,S_k}$ and Average %PVWML $_{S_k}$ were used to calculate the sensitivity and specificity of location-specific %PVWML and average %PVWML over the brain volume, respectively, as means of differentiating MS from non-MS WML using the area under the receiver operating characteristic curve analysis.

The correlation between Average %PVWML $_{S_k}$ and the average lesion size and percentage confluency (number of confluent lesions divided by the total number of lesions for each subject) was evaluated. Additionally, the correlation between EDSS and Average

Table 1: Demographic and clinical data^a

	Control Subjects	Patients with RRMS
No. of subjects	18	17
No. of women	15	11
No. of men	3	7
Age (yr) ^b	37.4 ± 5.8 (26–46)	39.4 ± 5.4 (26–46)
EDSS	NA	2.2 ± 1.6 (0–6)
EDSS to scan time gap (days)	NA	297 ± 49

Note:—NA indicates not applicable.

^a Data are mean ± SD. Data in parentheses represent range.

^b $P = .23$, not significant, t test following the D'Agostino-Pearson Omnibus normality test.

%PVWML $_{S_k}$ was evaluated. All correlation analyses were performed using the Spearman correlation test.

For all statistical analyses, $P < .05$ was considered as significant.

RESULTS

Clinical and demographic information, including the EDSS, is provided in Table 1. The mean age and sex distribution of RRMS and HC cohorts was not statistically different.

Visualization of Perivenous Lesions

For all subjects, IEV-SWI was successfully registered to the MP-FLAIR images. Examples are shown for 3 different patients with RRMS and 3 different HC subjects in On-line Figs 1 and 2, respectively. Figure 1 shows examples of perivenous lesions in different regions of the brains of patients with RRMS. Regardless of lesion location and size, the IEV-SWI approach reliably identified veins of various sizes colocalized with lesions. In 3 of the examples presented in Fig 1, a hypointense rim is evident (around the lesion in the periventricular white matter and the lesion in the subcortical region). Figure 2 shows 2 representative WM lesion examples in each of the brain regions in HC subjects; no infratentorial lesions were found in HCs.

White Matter Lesion Assessment

During the 4 reviewing sessions, the readers identified 626 lesions in the 17 patients with RRMS: 13 infratentorial (range $_{readers}$, 3–4; median $_{readers}$, 3 per reader per session), 86 juxtacortical (range $_{readers}$, 18–29; median $_{readers}$, 20), 190 periventricular (range $_{readers}$, 37–55; median $_{readers}$, 49), and 337 subcortical (range $_{readers}$, 66–96; median $_{readers}$, 88). A total of 169 lesions were identified in the HC group: 9 juxtacortical (range $_{readers}$, 0–5; median $_{readers}$, 2), 7 periventricular (range $_{readers}$, 1–4; median $_{readers}$, 1), and 153 subcortical (range $_{readers}$, 31–48; median $_{readers}$, 37).

For each region, the mean lesion size was significantly larger in the RRMS than HC group ($P < .001$) (the infratentorial region was excluded from this analysis). Mean RRMS lesion sizes were also different among brain regions ($P < .001$), with periventricular lesions being the largest (average, 43.6 mm³), followed by subcortical lesions (average, 29.7 mm³), juxtacortical lesions (average, 23.5 mm³), and infratentorial lesions (average, 18.1 mm³).

The average image-assessment times, including area measurements, for the RRMS and control subjects were 12 minutes 10 seconds ± 3 minutes 47 seconds and 4 minutes 33 seconds ± 2 minutes 5 seconds, respectively ($P < .001$).

Diagnostic Value of %PVWML

The results of Bland-Altman analysis are presented in Table 2 for the 3 lesion pools analyzed. Overall, agreement among the readers improved when confluent lesions were removed (NC pool). While the inter- and intrareader agreement was degraded for the SV pool, the agreement of the data collected from the first reader with reader 2 and reader 3 is consistently lower across all lesion pools compared with the agreement of reader 2 and reader 3; thus, reader 1 is, to some degree, an outlier. This observation may lend support to the role of readers' experience in the level of consistency of the results of radiologic assessments.

Table 3 summarizes the location-specific %PVWML and the average %PVWML. The difference in %PVWML between the RRMS and HC groups is significant ($P < .001$). Figure 3 presents

the average %PVWML results over the brain volume for the 3 lesion pools. Many of the MS WML classified as perivenous have multiple distinct veins within them, the removal of which results in a spread of the MS data (Fig 3C). Meanwhile, the HC plots do not change from B to C. Meanwhile, the spread of data in A–C indicates that most of HC WML are nonconfluent.

Table 4 summarizes the sensitivity and specificity for %PVWML calculated for lesions belonging to each brain region. Separation of RRMS and HC groups based on the infratentorial lesions results in poor sensitivity (29% for the LL pool). The LL and NC pools, on average, demonstrated high sensitivity (94%) and specificity (100%). The sensitivity and specificity results for Average %PVWML_p are presented in Fig 4. This, together with the Bland-Altman results, suggests that the removal of confluent lesions

reduces the bias among different readers. Overall sensitivity was lower in the SV pool (77%). Cutoff thresholds of 30% perivenous white matter lesion and 67% perivenous white matter lesion allow differentiation of patients with RRMS and HCs with a sensitivity of 94% and a specificity of 100% in both the LL and NC pools, respectively.

Significant correlation was found between %PVWML and both average lesion size ($r = 0.6$, $P = .02$) and percentage confluency ($r = 0.7$, $P = .003$). No correlation was observed between EDSS scores and %PVWML ($r = 0.04$, $P = .88$).

DISCUSSION

In this study, we identified morphologic characteristics of WML and associated cerebral venous vasculature from registered MP-FLAIR¹⁸ and IEV-SWI.¹⁹ Through simultaneous visualization of WML and veins, data demonstrated that with a threshold of >67% perivenous nonconfluent WML of >3 mm in length, the RRMS group can be differentiated from HCs with a sensitivity of 94% and a specificity of 100%.

This study used high-field (7T) acquisitions and a custom image postprocessing protocol to assess the global and morphologic characteristics of WML in

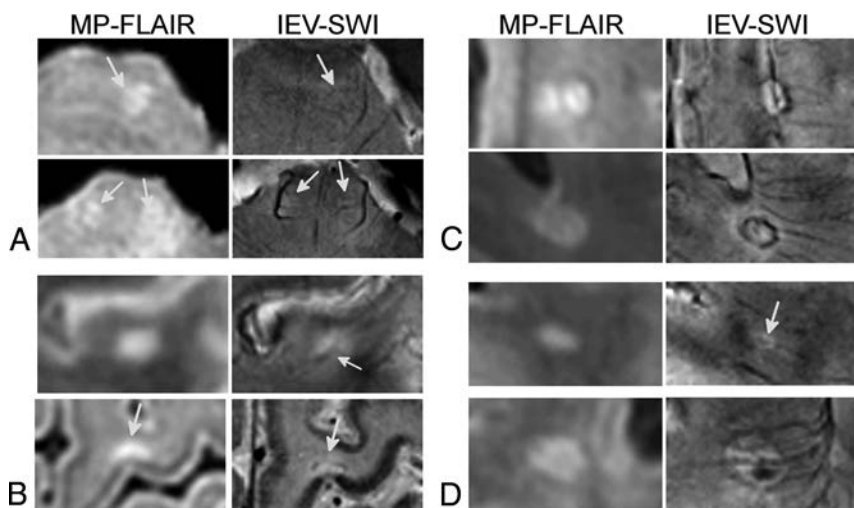


FIG 1. Magnified lesion views taken from axial slices of patients with RRMS enrolled in our study. CVS lesions are shown for each brain region: infratentorial (A), juxtacortical (B), periventricular (C), and subcortical lesions (D). For the lesions in the periventricular and subcortical regions, a hypointense rim is observed around the lesion on the IEV-SWI. Arrows point to select lesions and the central vessels running through them. Magnified panels range from 3.0 to 4.0 cm.

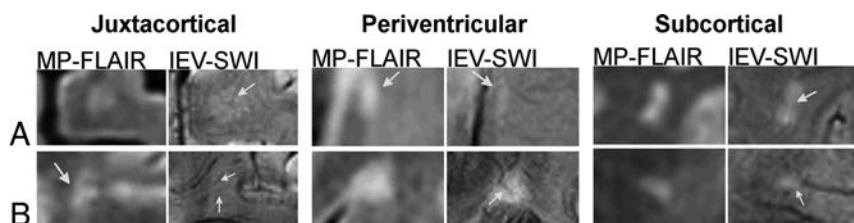


FIG 2. Examples of juxtacortical, periventricular, and subcortical lesions for HC participants. Arrows identify central veins running through the body of WML. IEV-SWI allows the visualization of CVS submillimeter vessels enabling accurate definition of %PVWML. Magnified panels range from 2.0 to 3.0 cm.

Table 2: Results of Bland-Altman test for reader agreement

	LL Lesion Pool		NC Lesion Pool		SV Lesion Pool	
	Bias ± SD	95% LoA	Bias ± SD	95% LoA	Bias ± SD	95% LoA
R1, R2	4.4 ± 8.5	−12.3:21.1	4.0 ± 10.1	−23.7:15.7	−12.7 ± 20.6	−53:27.7
R1, R3 (1)	16.4 ± 9.8	−2.9:35.6	−12.5 ± 3.3	−19.0:−6.0	−22.3 ± 12.6	−47:2.4
R1, R3 (2)	1.9 ± 6.7	−11.3:15.1	−12.7 ± 3.1	−18.7:−6.6	−22.9 ± 11.6	−45.6:−0.2
R2, R3 (1)	12 ± 11.5	−10.5:34.5	−8.5 ± 7.6	−23.4:6.3	−9.6 ± 8.6	−26.4:7.2
R2, R3 (2)	2.4 ± 11.1	−24.2:19.3	−8.7 ± 7.8	−23.8:6.5	−10.3 ± 9.4	−28.6:8.1
R3 (1), R3 (2)	−14.5 ± 3.8	−21.9:−7.1	−0.1 ± 0.2	−0.6:0.3	−0.6 ± 1.1	−2.8:1.5

Note:—R1 indicates reader 1; R2, reader 2; R3 (1), reader 3, first assessment; R3 (2) reader 3, second assessment; LoA, limits of agreement.

Table 3: Location-specific and averaged %PVWML (averaged over the 3 readers) are presented for each of the lesion pools^a

	RRMS		HC	
	At Each Location ^b	Average ^c	At Each Location ^b	Average ^c
LL lesion pool				
Average %PVWML _{infra}	10 ± 18	55 ± 14	0 ± 0	5 ± 6
Average %PVWML _{juxta}	59 ± 31		3 ± 8	
Average %PVWML _{peri}	68 ± 35		4 ± 10	
Average %PVWML _{subcort}	82 ± 16		12 ± 17	
NC lesion pool				
Average %PVWML _{infra}	3 ± 8	91 ± 15	0 ± 0	18 ± 23
Average %PVWML _{juxta}	50 ± 34		3 ± 8	
Average %PVWML _{peri}	47 ± 31		1 ± 6	
Average %PVWML _{subcort}	84 ± 17		16 ± 21	
SV lesion pool				
Average %PVWML _{infra}	2 ± 6	76 ± 24	0 ± 0	17 ± 23
Average %PVWML _{juxta}	52 ± 39		3 ± 8	
Average %PVWML _{peri}	20 ± 23		0 ± 0	
Average %PVWML _{subcort}	78 ± 22		16 ± 21	

Note:—infra indicates infratentorial; juxta, juxtacortical; peri, periventricular; subcort, subcortical.

^a All differences between RRMS and HC statistics were significant ($P < .001$). Data are mean ± SD.

^b Average %PVWML_{loc,j,k}.

^c Average %PVWML_{S_k}.

patients with MS and healthy controls. Previous studies have examined longitudinal changes in the volume of central veins²⁷ using 7T SWI/FLAIR images; this study did not perform the assessment of %PVWML in anatomically distinct brain regions. Furthermore, our study demonstrates that the IEV-SWI method enabled generation of venography images in the infratentorial region of the brain, where 7T phase data can often be corrupted. Readers in this study did not report corrupted phase information affecting %PVWML assessment in the infratentorial brain. The poor sensitivity of the infratentorial lesions (Table 4) must be interpreted while considering other known factors, such as the inclusion criteria of Fazekas et al.²⁸

The proposed %PVWML threshold (67%) is higher than the threshold of >40% previously reported¹⁵ and used

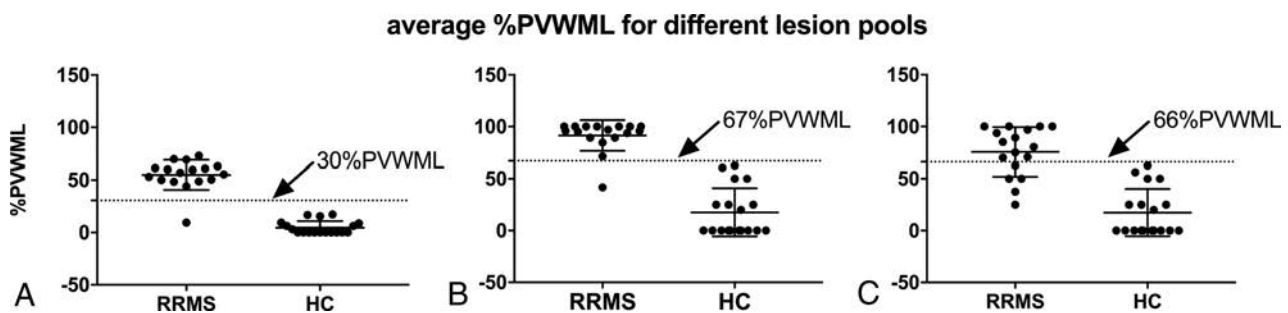


FIG 3. Average %PVWML_p presented for the RRMS and HC groups in the LL lesion pool (A), NC lesion pool (B), and SV lesion pool (C). A large number of WML with central veins are observed to have multiple central veins. The removal of lesions with multiple central veins results in a wider spread in the data. This yields a reduced diagnostic value of %PVWML for the NC lesion pool (C). The average %PVWML is found to be significantly different between the RRMS and HC groups for all lesion pools as per the Mann-Whitney U test ($P < .001$).

Table 4: Summary of ROC analysis for 3 lesion pools

	LL Lesion Pool	NC Lesion Pool	SV Lesion Pool
Infratentorial region			
Threshold; sensitivity, 95% CI	>13%; 29%, 10%–56%	>13%; 12%, 2%–36%	>13%; 6%, 0%–29%
Specificity, 95% CI	100%, 82%–100%	100%, 82%–100%	100%, 82%–100%
AUC	0.65	0.56	0.53
Juxtacortical region			
Threshold; sensitivity, 95% CI	>19%; 82%, 57%–96%	>7%; 82%, 57%–96%	>29%; 65%, 38%–86%
Specificity, 95% CI	89%, 65%–99%	89%, 65%–99%	100%, 82%–100%
AUC	0.93	0.89	0.86
Periventricular region			
Threshold; sensitivity, 95% CI	>13%; 88%, 64%–99%	>13%; 82%, 57%–96%	>13%; 53%, 28%–77%
Specificity, 95% CI	83%, 59%–96%	94%, 73%–100%	100%, 82%–100%
AUC	0.93	0.90	0.77
Subcortical region			
Threshold; sensitivity, 95% CI	>51%; 94%, 71%–100%	>61%; 94%, 71%–100%	>61%; 82%, 57%–96%
Specificity, 95% CI	100%, 82%–100%	100%, 82%–100%	100%, 82%–100%
AUC	0.99	0.99	0.96
Averaged results (over brain volume)			
Threshold; sensitivity, 95% CI	>30%; 94%, 71%–100%	>67%; 94%, 71%–100%	>66%; 77%, 50%–93%
Specificity, 95% CI	100%, 82%–100%	100%, 82%–100%	100%, 82%–100%
AUC	0.99	0.99	0.95

Note:—AUC indicates area under the receiver operating characteristic curve.

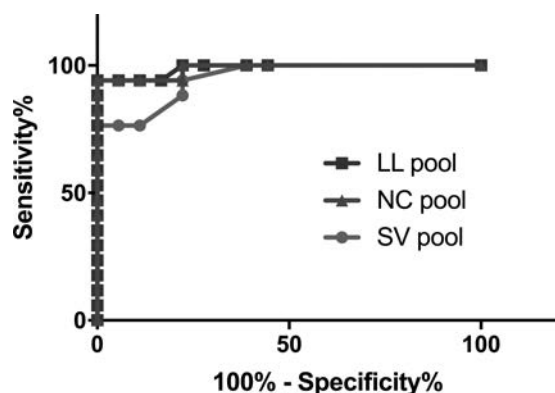


FIG 4. The diagnostic accuracy of the Average %PVWML_p, as analyzed by the receiver operating characteristic test, presented for the pool of all the lesions of >3 mm (LL pool), the pool of nonconfluent lesions of >3 mm (NC pool), and the pool of nonconfluent lesions of >3 mm with a single central vessel (SV pool).

in the literature.¹⁰ This difference can be attributed to the quality of IEV-SWI venography images, which enabled the visualization of submillimeter-sized veins and a proportionally higher %PVWML in both groups. The study also demonstrated the possibility of visualizing hypointense rims around MS lesions. Such hypointense rims have previously been attributed to iron-laden macrophages²⁹ and may be an imaging biomarker for MS. Based on the results of this study, it may be concluded that hypointense rims are not seen in benign lesions and may be used as radiologic signs to differentiate benign and MS WML; the study of a larger cohort may further validate this finding.

The control cohort in our study was selected from a pool of age-matched, self-reported healthy individuals, with no known neurologic disorders. Incidental findings of WML in these individuals (63 lesions of >3 mm and range of 0–17 lesions in each HC subject) may be indicative of undocumented risk factors, such as small-vessel disease. Incidental findings of white matter hyperintensities have been reported previously,³⁰ even in young healthy cohorts.³¹ Morphologic characterization of benign WML (eg, number, size, dominant location with respect to venous network, and so forth) may further enable the validation of the radiologic definition of MS lesions and mimicking WML by allowing identification and elimination of non-disease-contributing lesions.

Strong inter- and intrareader agreement was observed (Table 2), particularly when confluent lesions were not included in the analysis. Agreement among readers was reduced when lesions with multiple central veins were excluded. This change can be explained by the spread of data in the HC plot from Fig 3A to B and the lack of change from Fig 3B to C, which suggest that nonconfluent benign lesions are likely to have a single vessel. On the other hand, the spread of the data of patients with RRMS (Fig 3C) suggests that the morphology of most MS (confluent and nonconfluent WML) WML includes multiple veins.

A consequence of using channel-by-channel SWI processing is the added calculation time and large storage needed for the individual channel data; these added challenges were mitigated in this study by taking advantage of the noniterative nature of IEV-SWI and parallel computing on a network of processors. Visualization of lesions and corresponding venograms on 2 separate datasets

may have added uncertainty to the readings performed in this study. In a previous study using the FLAIR* approach,³² a T2*-weighted image was multiplied by a FLAIR image on a pixel-by-pixel basis; this step facilitated assessment of colocalized WML with vessels. Adopting the approach of superposition of FLAIR and SWI would allow simultaneous assessment of the IEV-SWI information and the MP-FLAIR images but requires precise registration and re-sampling. Neurodegenerative disorders mimicking MS may exhibit benign WML with unique morphologic characteristics. The proposed radiologic definition for CVS is strictly for separating MS WML from benign WML. The guidelines of the North American Imaging in Multiple Sclerosis criteria should be investigated further for other mimics of MS. While this study was performed at 7T, the radiologic definitions of CVS defined here are expected to hold at 3T, but the threshold to separate patients with RRMS and HC may need to be validated through further investigation.

CONCLUSIONS

Based on the investigation of the North American Imaging in Multiple Sclerosis consensus criteria, we have identified a sensitive and specific radiologic definition for CVS: Our work suggests that %PVWML, as calculated for nonconfluent lesions of >3 mm in length with ≥1 central vein observed on 7T MP-FLAIR and IEV-SWI, can be used as a sensitive and specific discriminator of patients with RRMS from control subjects with benign WML.

REFERENCES

- Polman CH, Reingold SC, Banwell B, et al. **Diagnostic criteria for multiple sclerosis: 2010 revisions to the McDonald criteria.** *Ann Neurol* 2011;69:292–302 CrossRef Medline
- Freedman MS, Comi G, De Stefano N, et al. **Moving toward earlier treatment of multiple sclerosis: findings from a decade of clinical trials and implications for clinical practice.** *Mult Scler Relat Disord* 2014;3:147–55 CrossRef Medline
- Miller AE, Wolinsky JS, Kappos L, et al; TOPIC Study Group. **Oral teriflunomide for patients with a first clinical episode suggestive of multiple sclerosis (TOPIC): a randomised, double-blind, placebo-controlled, phase 3 trial.** *Lancet Neurol* 2014;13:977–86 CrossRef Medline
- Comi G, De Stefano N, Freedman MS, et al. **Comparison of two dosing frequencies of subcutaneous interferon beta-1a in patients with a first clinical demyelinating event suggestive of multiple sclerosis (REFLEX): a phase 3 randomised controlled trial.** *Lancet Neurol* 2012;11:33–41 CrossRef Medline
- Kappos L, Freedman MS, Polman CH, et al; BENEFIT Study Group. **Effect of early versus delayed interferon beta-1b treatment on disability after a first clinical event suggestive of multiple sclerosis: a 3-year follow-up analysis of the BENEFIT study.** *Lancet* 2007;370:389–97 CrossRef Medline
- Hannoun S, Heidelberg D, Hourani R, et al; Imaging Working Group of the Observatoire Français de la Sclérose en Plaques. **Diagnostic value of 3DFLAIR in clinical practice for the detection of infratentorial lesions in multiple sclerosis in regard to dual echo T2 sequences.** *Eur J Radiol* 2018;102:146–51 CrossRef Medline
- Tan L, van Schijndel RA, Pouwels PJ, et al. **MR venography of multiple sclerosis.** *AJNR Am J Neuroradiol* 2000;21:1039–42 Medline
- Grabner G, Dal-Bianco A, Schernthaner M, et al. **Analysis of multiple sclerosis lesions using a fusion of 3.0 T FLAIR and 7.0 T SWI phase: FLAIR SWI.** *J Magn Reson Imaging* 2011;33:543–49 CrossRef Medline
- Kau T, Taschwer M, Deutschmann H, et al. **The “central vein sign”:**

- is there a place for susceptibility weighted imaging in possible multiple sclerosis? *Eur Radiol* 2013;23:1956–62 CrossRef Medline
10. Mistry N, Dixon J, Tallantyre E, et al. **Central veins in brain lesions visualized with high-field magnetic resonance imaging: a pathologically specific diagnostic biomarker for inflammatory demyelination in the brain.** *JAMA Neurol* 2013;70:623–28 CrossRef Medline
 11. Cortese R, Magnolay L, Tur C, et al. **Value of the central vein sign at 3T to differentiate MS from seropositive NMOSD.** *Neurology* 2018; 90:e1183–90 CrossRef Medline
 12. Cai M, Zhang XF, Qiao HH, et al. **Susceptibility-weighted imaging of the venous networks around the brain stem.** *Neuroradiology* 2015; 57:163–69 CrossRef Medline
 13. Sati P, Oh J, Constable RT, et al; NAIMS Cooperative. **The central vein sign and its clinical evaluation for the diagnosis of multiple sclerosis: a consensus statement from the North American Imaging in Multiple Sclerosis Cooperative.** *Nat Rev Neurol* 2016;12:714–22 CrossRef Medline
 14. Springer E, Dymerska B, Cardoso PL, et al. **Comparison of routine brain imaging at 3 T and 7 T.** *Invest Radiol* 2016;51:469–82 CrossRef Medline
 15. Tallantyre EC, Dixon JE, Donaldson I, et al. **Ultra-high-field imaging distinguishes MS lesions from asymptomatic white matter lesions.** *Neurology* 2011;76:534–39 CrossRef Medline
 16. Zwanenburg JJ, Hendrikse J, Visser F, et al. **Fluid attenuated inversion recovery (FLAIR) MRI at 7.0 Tesla: comparison with 1.5 and 3.0 Tesla.** *Eur Radiol* 2010;20:915–22 CrossRef Medline
 17. Tallantyre EC, Morgan PS, Dixon JE, et al. **A comparison of 3T and 7T in the detection of small parenchymal veins within MS lesions.** *Invest Radiol* 2009;44:491–94 CrossRef Medline
 18. Visser F, Zwanenburg JJ, Hoogduin JM, et al. **High-resolution magnetization-prepared 3D-FLAIR imaging at 7.0 Tesla.** *Magn Reson Med* 2010;64:194–202 CrossRef Medline
 19. Hosseini Z, Liu J, Solovey I, et al. **Susceptibility-weighted imaging using inter-echo-variance channel combination for improved contrast at 7 Tesla.** *J Magn Reson Imaging* 2017;45:1113–24 CrossRef Medline
 20. Rudko DA, Solovey I, Gati JS, et al. **Multiple sclerosis: improved identification of disease-relevant changes in gray and white matter by using susceptibility-based MR imaging.** *Radiology* 2014;272: 851–64 CrossRef Medline
 21. Curtis AT, Gilbert KM, Klassen LM, et al. **Slice-by-slice B1+ shimming at 7 T.** *Magn Reson Med* 2012;68:1109–16 CrossRef Medline
 22. Jenkinson M, Beckmann CF, Behrens TE, et al. **FSL.** *Neuroimage* 2012;62:782–90 CrossRef Medline
 23. Smith SM. **Fast robust automated brain extraction.** *Hum Brain Mapp* 2002;17:143–55 CrossRef Medline
 24. Jenkinson M, Bannister P, Brady M, et al. **Improved optimization for the robust and accurate linear registration and motion correction of brain images.** *Neuroimage* 2002;17:825–41 CrossRef Medline
 25. Zhang Y, Brady M, Smith S. **Segmentation of brain MR images through a hidden Markov random field model and the expectation-maximization algorithm.** *IEEE Trans Med Imaging* 2001;20:45–57 Medline
 26. Rosset A, Spadola L, Ratib O. **OsiriX: an open-source software for navigating in multidimensional DICOM images.** *J Digit Imaging* 2004;17:205–16 CrossRef Medline
 27. Dal-Bianco A, Hametner S, Grabner G, et al. **Veins in plaques of multiple sclerosis patients: a longitudinal magnetic resonance imaging study at 7 Tesla.** *Eur Radiol* 2015;25:2913–20 CrossRef Medline
 28. Fazekas F, Offenbacher H, Fuchs S, et al. **Criteria for an increased specificity of MRI interpretation in elderly subjects with suspected multiple sclerosis.** *Neurology* 1988;38:1822–25 CrossRef Medline
 29. Dal-Bianco A, Grabner G, Kronnerwetter C, et al. **Slow expansion of multiple sclerosis iron rim lesions: pathology and 7 T magnetic resonance imaging.** *Acta Neuropathol* 2017;133:25–42 CrossRef Medline
 30. Labate A, Gambardella A, Aguglia U, et al. **Temporal lobe abnormalities on brain MRI in healthy volunteers; a prospective case-control study.** *Neurology* 2010;74:553–57 CrossRef Medline
 31. Vernooij MW, Ikram MA, Tanghe HL, et al. **Incidental findings on brain MRI in the general population.** *N Engl J Med* 2007;357: 1821–28 CrossRef Medline
 32. Sati P, George IC, Shea CD, et al. **FLAIR*: a combined MR contrast technique for visualizing white matter lesions and parenchymal veins.** *Radiology* 2012;265:926–32 CrossRef Medline

Impact of Focal White Matter Damage on Localized Subcortical Gray Matter Atrophy in Multiple Sclerosis: A 5-Year Study

 T.A. Fuchs,  K. Carolus,  R.H.B. Benedict,  N. Bergsland,  D. Ramasamy,  D. Jakimovski,  B. Weinstock-Guttman,  A. Kuceyeski,  R. Zivadinov, and  M.G. Dwyer



ABSTRACT

BACKGROUND AND PURPOSE: It is unclear to what extent subcortical gray matter atrophy is a primary process as opposed to a result of focal white matter damage. Correlations between WM damage and atrophy of subcortical gray matter have been observed but may be partly attributable to indirect relationships between co-occurring processes arising from a common cause. Our aim was to cross-sectionally and longitudinally characterize the unique impact of focal WM damage on the atrophy of connected subcortical gray matter regions, beyond what is explainable by global disease progression.

MATERIALS AND METHODS: One hundred seventy-six individuals with MS and 47 healthy controls underwent MR imaging at baseline and 5 years later. Atrophy and lesion-based disruption of connected WM tracts were evaluated for 14 subcortical gray matter regions. Hierarchic regressions were applied, predicting regional atrophy from focal WM disruption, controlling for age, sex, disease duration, whole-brain volume, and T2-lesion volume.

RESULTS: When we controlled for whole-brain volume and T2-lesion volume, WM tract disruption explained little additional variance of subcortical gray matter atrophy and was a significant predictor for only 3 of 14 regions cross-sectionally ($\Delta R^2 = 0.004$) and 5 regions longitudinally ($\Delta R^2 = 0.016$). WM tract disruption was a significant predictor for even fewer regions when correcting for multiple comparisons.

CONCLUSIONS: WM tract disruption accounts for a small percentage of atrophy in connected subcortical gray matter when controlling for overall disease burden and is not the primary driver in most cases.

ABBREVIATIONS: HC = healthy controls; NeMo = Network Modification; SGM = subcortical gray matter; T2LV = T2-lesion volume; WBV = whole-brain volume

It has recently become clear that gray matter pathology is a critical component of MS, relating strongly to both disability and cognition.¹ In particular, atrophy of subcortical GM (SGM) occurs from early phases of the disease² and continues throughout.³ Despite its importance, the precise cause of SGM atrophy has not been fully established. On one hand, direct mechanisms for GM

atrophy, GM lesions, microglial activation, and lymphocyte infiltration have been observed.^{1,4,5} On the other hand, it has also been proposed that GM atrophy in MS results from anterograde and retrograde cell death due to new white matter lesions in tracts extending to connected GM.^{6,7} In support of the second hypothesis, such anterograde and retrograde cell death has been observed in postmortem biopsies and various biologic mechanisms are thought to contribute.^{8,9} Additionally, spatial relationships between WM damage and GM atrophy have been observed cross-sectionally in MS with T1-lesion probability maps, T2-lesion probability maps, and DTI.^{6,10-13}

These studies established a clear association between WM damage and SGM atrophy, but it remains unclear to what extent this relationship is directly causal as opposed to both proceeding independently from a common cause (Fig 1). WM damage and atrophy would still be highly correlated even if they progressed separately but at an overall pace determined by shared underlying disease factors. It is therefore important to somehow control for overall disease burden when assessing these relationships. Unfor-

Received March 19, 2018; accepted after revision May 18.

From the Department of Neurology (T.F., K.C., N.B., D.R., D.J., R.Z., M.G.D.), Buffalo Neuroimaging Analysis Center, and MR Imaging Clinical Translational Research Center (R.Z.), Jacobs School of Medicine and Biomedical Sciences, University at Buffalo, State University of New York, Buffalo, New York; Department of Neurology (T.F., R.H.B.B., N.B., D.R., D.J., B.W.G., M.G.D.), Jacobs Multiple Sclerosis Center, Jacobs School of Medicine and Biomedical Sciences, University at Buffalo, State University of New York, Buffalo, New York; and Department of Radiology (A.K.), Weill Cornell Medicine, Feil Family Brain and Mind Research Institute, New York, New York.

Please address correspondence to Michael Dwyer, PhD, Buffalo Neuroimaging Analysis Center, MRI Clinical Translational Research Center, Jacobs School of Medicine and Biomedical Sciences, University at Buffalo, State University of New York, 100 High St, Buffalo, NY 14203; e-mail: mgdwyer@buffalo.edu

 Indicates article with supplemental on-line tables.

<http://dx.doi.org/10.3174/ajnr.A5720>

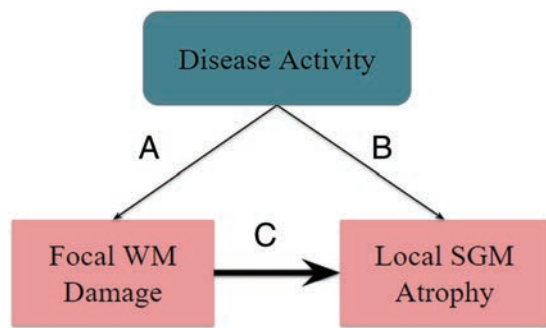


FIG 1. If WM damage in connected tracts is a primary driver of local SGM atrophy, then pathology represented by (C) ought to explain local SGM atrophy, beyond what is otherwise predicted by whole-brain atrophy and overall lesion growth (A and B) alone. On the other hand, if SGM atrophy largely progresses from independent pathology, we would still expect it to be correlated with overall lesion growth due to shared underlying overall disease activity (via A and B) but we would not expect (C) to explain any additional variance in atrophy. We therefore controlled for overall progression of disease-related pathology (A and B) in our analysis to determine the independent contribution of (C).

unately, the best indicators of overall disease burden are likely atrophy and lesion accrual themselves. However, if there is a true causal relationship, then the specific location of lesions should have direct influence on the specific location of SGM atrophy. SGM regions with greater lesion burden in connected WM tracts would be expected to have greater atrophy, even after controlling for whole-brain atrophy and total lesion volume.

In addition, longitudinal rather than cross-sectional investigation can better elucidate the temporal relationship between WM damage and SGM atrophy. Although most previous analyses have been cross-sectional, the relationship has been observed longitudinally in a few studies.^{10,14} However, these analyses did not control for overall disease burden or for specific connections affected by localized WM damage. Therefore, our understanding of atrophy and lesion accrual might be improved by longitudinal analysis with reference to precise lesion location while controlling for whole-brain atrophy and total lesion burden.

Therefore, we aimed to characterize the extent to which new lesions in connected WM tracts contribute to atrophy of specific SGM regions across 5 years. We additionally replicated cross-sectional findings.^{6,13} We applied the Network Modification (NeMo) tool,¹⁵ to quantify tract-based disruptions caused by new focal WM lesions while avoiding the issues associated with tractography through lesions.¹⁶ For this work, we chose to use the word “disruption” rather than “disconnection” to refer to this lesion-based WM tract damage because WM tract streamlines that pass through lesions may not necessarily be fully disconnected. We also quantified global atrophy and lesion burden to control for overall MR imaging-visible disease progression in our analyses, to determine the extent to which new focal WM damage contributes to SGM atrophy beyond what would be observed as a result of indirectly related co-occurring processes arising from a common cause. We also performed an analysis to separately account for both T1WI and T2-FLAIR lesions.

MATERIALS AND METHODS

Subjects

One hundred seventy-six individuals with MS or clinically isolated syndrome and 47 healthy controls (HC) were enrolled retrospectively from a larger 5-year longitudinal cardiovascular, environmental, and genetics study.^{17,18} All individuals diagnosed with clinically isolated syndrome at baseline converted to MS by follow-up 5 years later. Disease course and disease duration were determined by clinical assessments. Subjects were at least 18 years of age and free from a known history of additional neurologic diseases, psychiatric disorders, or substance abuse, and all met the safety criteria for MR imaging examination. The study was approved by the institutional ethics review board, and all subjects provided written informed consent.

MR Image Acquisition

MR imaging data were obtained at baseline and again at follow-up 5 years later. All MR imaging data described in the aforementioned analysis were available for each participant included in the study. These data were obtained on a 3T Signa Excite HD 12.0 TwinSpeed 8-channel scanner (GE Healthcare, Milwaukee, Wisconsin) and included structural 3D T1-weighted inversion recovery fast-spoiled gradient-recalled (voxel size = $1.0 \times 1.0 \times 1.5$, TR = 5.9 ms, TE = 2.8 ms, TI = 900 ms) images and 2D T2-FLAIR images (voxel size = $1.0 \times 1.0 \times 3.0$ mm, TR = 8500 ms, TE = 120 ms, TI = 2100 ms).

Image Processing and Analysis

T2-FLAIR and T1WI lesion masks were obtained using a previously described semiautomated edge-detection contouring/thresholding technique, and T2-lesion volume (T2LV) was quantified.¹⁹ MR imaging analysts were blinded to the subjects’ physical and neurologic statuses. N4 bias field correction was applied to all images. High-resolution 3D T1-weighted images were preprocessed using a lesion-filling tool to minimize the impact of T1 hypointensities.²⁰ SIENAX (<http://fsl.fmrib.ox.ac.uk/fsl/fslwiki/SIENAX>) was then applied (Version 2.6) to calculate whole-brain volume (WBV).²¹ SGM volumes were assessed using the FMRIB Integrated Registration and Segmentation Tool (FIRST; <http://fsl.fmrib.ox.ac.uk/fsl/fslwiki/FIRST>) to segment the same images.²² SGM and whole-brain volumes were normalized using the SIENAX head-size scaling factor. Volumetric data were collected for the left and right thalamus, caudate, putamen, globus pallidus, hippocampus, amygdala, and accumbens. Two-time-point percentage volume change was calculated for each SGM region before use of these measures in longitudinal regression analysis. As well, 2-time-point percentage WBV change was estimated with SIENAX.²³

Network Modification Tool

High-resolution T1WI was nonlinearly normalized into Montreal Neurological Institute space using Advanced Normalization Tools (<https://sourceforge.net/projects/advants/>).²⁴ These transforms were applied to the corresponding lesion masks with nearest-neighbor interpolation. Aligned lesion masks were processed by means of NeMo, using methods that have been previously published.²⁵ In short, the percentage disruption obtained

for each SGM region is proportional, representing the percentage of normative data base–derived connected tract streamlines that pass through the given lesion mask and are therefore considered disrupted. The percentage disruption is determined probabilistically using control tractograms in the NeMo-provided normative data base. Additional details regarding NeMo are publicly available.¹⁵ This tool was applied to determine the percentage tract disruption caused by T2-FLAIR lesions as well as T1WI black hole lesions.

For the primary analyses, tract streamlines traveling through T2-FLAIR lesions were considered disrupted. For a secondary exploratory analysis, tract streamlines traveling through T1WI black hole lesions were considered disrupted, whereas tract streamlines traveling only through non-black hole T2-FLAIR lesions were considered half-disrupted. Although this weighting is arbitrary, we have chosen to consider this additional method of quantifying WM tract disruption because T1WI black hole lesions are likely to represent more severe neuropathology than lesions observed on T2 FLAIR alone.²⁶ Our intention here was to determine whether lesional WM tract damage of greater severity has an increased impact on longitudinal GM atrophy.

The percentage WM tract disruption was evaluated for all SGM regions. Change in percentage disruption was calculated by subtracting baseline from follow-up values. This step resulted in an absolute change, in which a positive value indicated increased disruption caused by lesions.

Statistical Analysis

Independent-sample *t* tests and the Fisher exact test were applied to compare the MS group with HC regarding age, sex, and race (due to differential MS progression and incidence by race). We applied ANCOVAs, controlling for age and sex, to examine group differences in percentage atrophy of each SGM region under investigation. HC were used only for comparison of longitudinal atrophy (not for comparison of lesion-based tract disruption). One-sample *t* tests were used to determine whether the change in percentage tract disruption of connected WM was statistically significant for each SGM region. All longitudinal percentage changes were annualized before analysis.

To replicate results in previous cross-sectional studies,^{6,10-13} we applied preliminary hierarchic regressions to associate cross-sectional predictor variables with cross-sectional SGM volumes at follow-up for each SGM region under investigation. In model 1, age, sex, and disease duration were included as predictors. In model 2, we added percentage disruption of WM tracts connected to the SGM region while retaining variables from model 1.

Our central hypothesis was that increases in focal WM damage would predict increased SGM atrophy in connected regions, beyond what could be explained by a general progression of MS-related pathology if WM damage is a primary driver of SGM atrophy. To evaluate this cross-sectionally, we used hierarchic regressions to control for overall disease burden and to better elucidate specific interrelationships between focal WM damage and SGM atrophy beyond what would be expected if these were only indirectly related co-occurring processes arising from a common cause. In model 1, we predicted SGM region volume from T2LV, WBV, age, sex, and disease duration. Next, in model 2, we

Table 1: Demographic and clinical characteristics of study participants

	MS (n = 176)	HC (n = 47)	P
Age at baseline (mean) (yr)	46.95 ± 11.247	45.96 ± 14.47	.616
Female/male; % female	130:46; 73.9	34:13; 72.3	.853
Disease duration (mean) (yr)	15.16 ± 9.87	–	–
CIS (No.) (%)	16, 9.1	–	–
RRMS (No.) (%)	114, 64.8	–	–
PPMS (No.) (%)	7, 4.0	–	–
SPMS (No.) (%)	39, 22.2	–	–
EDSS (median) (IQR)	2.5, 1.5–4.5	–	–
White (No.) (%)	167, 94.9	43, 91.5	.480
Hispanic/Latino (No.) (%)	3, 1.7	0, 0.0	–
Black/African American (No.) (%)	3, 1.7	3, 6.4	.110
Asian (No.) (%)	1, 0.6	1, 2.1	.378

Note:—CIS indicates clinically isolated syndrome; IQR, interquartile range; RRMS, relapsing-remitting MS; EDSS, Expanded Disability Status Scale; –, not applicable/not evaluable; PPMS, primary-progressive MS; SPMS, secondary-progressive MS.

added disruption of connected WM tracts while retaining variables from model 1. In the case of a specific, locally causative relationship between connected WM damage and SGM atrophy, we would expect a significant increase in *R*² when including this additional information in model 2.

Next, we extended this analysis longitudinally using similar hierarchic regressions with single derived percentage change outcome variables. In model 1, regional atrophy of >5 years was predicted using baseline age, sex, disease duration, change in T2LV (Δ T2LV), change in WBV (Δ WBV), and baseline disruption of WM tracts connected to the SGM region. Then, in model 2, longitudinal change in the disruption of connected WM tracts (Δ tract disruption) was also included, while retaining predictors from model 1. Because we would expect a causal relationship to be temporally related, if WM damage directly contributes to SGM atrophy, then we would expect new WM damage to explain a significant portion of new SGM atrophy across 5 years.

*R*² values were adjusted for the number of predictors included in each model. Model fit and changes in *R*² between models were considered significant on the basis of *F* tests at *P* < .05. T2LV and localized tract disruption data were cube-root-transformed for normality before analyses. These analyses were performed using tract-disruption data generated on the basis of T2-FLAIR lesions. To determine the value of more pathologically specific lesion assessment, we repeated the longitudinal hierarchic regression analysis using the combination T2-FLAIR and T1WI black hole approach described above.

All *P* values reported for the hierarchic regression models were corrected for multiple comparisons using the Holm-Bonferroni test correction.

RESULTS

Study Participant Characteristics

At baseline, participants were 47.0 ± 11.2 years of age with a disease duration of 15.2 ± 9.9 years. One hundred thirty-eight (78.4%) were using disease-modifying therapies. Mean follow-up time was 5.5 ± 0.7 years. Subjects with MS did not significantly differ from HC regarding age, sex, or race (Table 1).

Table 2: Annualized atrophy and change in tract disruption^a

	% Atrophy, MS	% Atrophy, HC	P (ANCOVA)	Δ Tract Disruption, MS	P (1-Sample)
Left thalamus	-1.22 ± 1.01	-0.78 ± 0.77	.006 ^b	0.0051 ± 0.0236	.005 ^b
Right thalamus	-1.06 ± 0.93	-0.81 ± 0.80	.090	0.0052 ± 0.0204	.001 ^b
Left caudate	-0.92 ± 1.33	-0.29 ± 2.10	.011 ^b	0.0224 ± 0.0614	<.001 ^b
Right caudate	-0.73 ± 1.58	-0.15 ± 2.11	.04 ^b	0.0285 ± 0.0652	<.001 ^b
Left putamen	-1.13 ± 1.46	-0.72 ± 1.01	.065	0.0115 ± 0.0307	<.001 ^b
Right putamen	-0.98 ± 1.67	-0.68 ± 0.85	.245	0.0119 ± 0.0318	<.000 ^b
Left globus pallidus	-1.90 ± 2.36	-0.72 ± 1.31	.001 ^b	0.0030 ± 0.0165	.017 ^b
Right globus pallidus	-1.85 ± 1.93	-0.60 ± 1.11	<.001 ^b	0.0019 ± 0.0113	.029 ^b
Left hippocampus	-1.27 ± 1.75	-0.69 ± 1.21	.040 ^b	0.0015 ± 0.0095	.032 ^b
Right hippocampus	-0.99 ± 1.80	-0.63 ± 1.52	.232	0.0047 ± 0.0162	<.00 ^b
Left amygdala	-1.87 ± 3.03	-0.55 ± 2.11	.005 ^b	0.0014 ± 0.0088	.040 ^b
Right amygdala	-2.03 ± 3.22	-0.51 ± 2.99	.003 ^b	0.0025 ± 0.0114	.004 ^b
Left accumbens	-1.57 ± 4.76	-0.58 ± 3.29	.203	0.0011 ± 0.0079	.073
Right accumbens	-1.52 ± 5.10	0.20 ± 5.21	.051	0.0021 ± 0.0090	.002 ^b

Note:—Δ Tract Disruption indicates longitudinal change in the disruption of connected WM tracts.

^a Data are means unless otherwise indicated.

^b Significant.

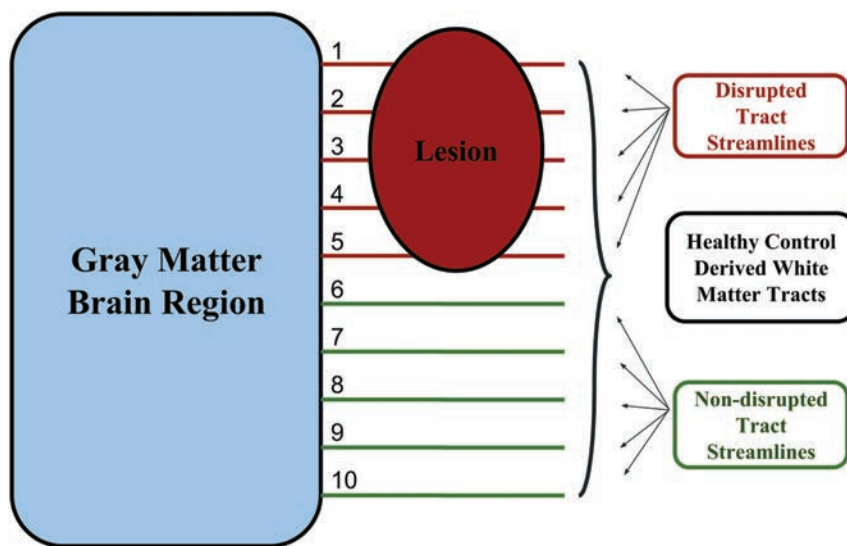


FIG 2. The Network Modification tool measures the proportion of disrupted WM tracts connected to a given GM region. An individual WM abnormality mask is referenced with respect to a data base of HC tractograms to probabilistically determine the proportion of connected tract streamlines that pass through a WM abnormality and are therefore considered disrupted.

Atrophy and WM Tract Disruption

The mean annualized ΔT2LV in subjects with MS was 0.58 ± 5.1 mL, and the percentage tract disruption increased significantly in 13 of 14 regions studied. The mean annualized whole-brain volume loss in our study participants with MS and HC was $-0.61\% \pm 0.38\%$ and $-0.52\% \pm 0.05\%$ ($P = .11$), respectively. Subjects with MS exhibited significantly greater atrophy for most SGM regions under investigation. Further information is provided in Table 2 and Fig 3.

Preliminary Analysis

The preliminary linear regression, model 1 (age, sex, and disease duration) was significant for 12 of 14 SGM regions included in our analyses (all regions except the left globus pallidus and right amygdala). When regional percentage tract disruption was added to the model, the explained variance increased significantly for 13 of 14 regions. This increased explained variance remained significant for 13 of 14 regions after controlling for multiple corrections. Average

ΔR^2 across all regions was 0.165. Detailed results are presented On-line Table 1.

Cross-Sectional Analysis Controlling for T2LV and WBV

In our primary cross-sectional analysis, T2LV and WBV were included in addition to age, sex, and disease duration in models 1 and 2. In contrast to the preliminary analysis, tract disruption explained significant additional variance for only 3 of 14 SGM regions when controlling for overall disease burden: left caudate, right amygdala, and left accumbens (On-line Table 2). This increased explained variance did not remain significant for any SGM region after controlling for multiple corrections. The average ΔR^2 across all regions was 0.004.

Longitudinal Analysis Controlling for T2LV and WBV

The model 1 regression, predicting regional annualized SGM atrophy from age, sex, disease duration, ΔWBV, ΔT2LV, and baseline tract disruption, was significant for 13 of 14 regions (all regions except the right amygdala). In model 2, the addition of Δ tract disruption resulted in a significant increase in the total explained variance for 5 of 14 regions: left putamen, right putamen, left globus pallidus, right amygdala, and left accumbens. This increased explained variance remained significant for only 1 of 14 regions (right putamen) after controlling for multiple corrections. Average ΔR^2 across all regions was 0.016. Detailed information regarding model R^2 values is provided in Table 3.

Separate Analysis of T2 FLAIR and T1WI Black Hole Lesions

In the supplementary longitudinal analysis based on both T2-FLAIR and T1WI black hole lesions, results were very similar to those observed in the models accounting for only T2-FLAIR lesions (average ΔR^2 across all regions was 0.016). See On-line Table 3 for additional details.

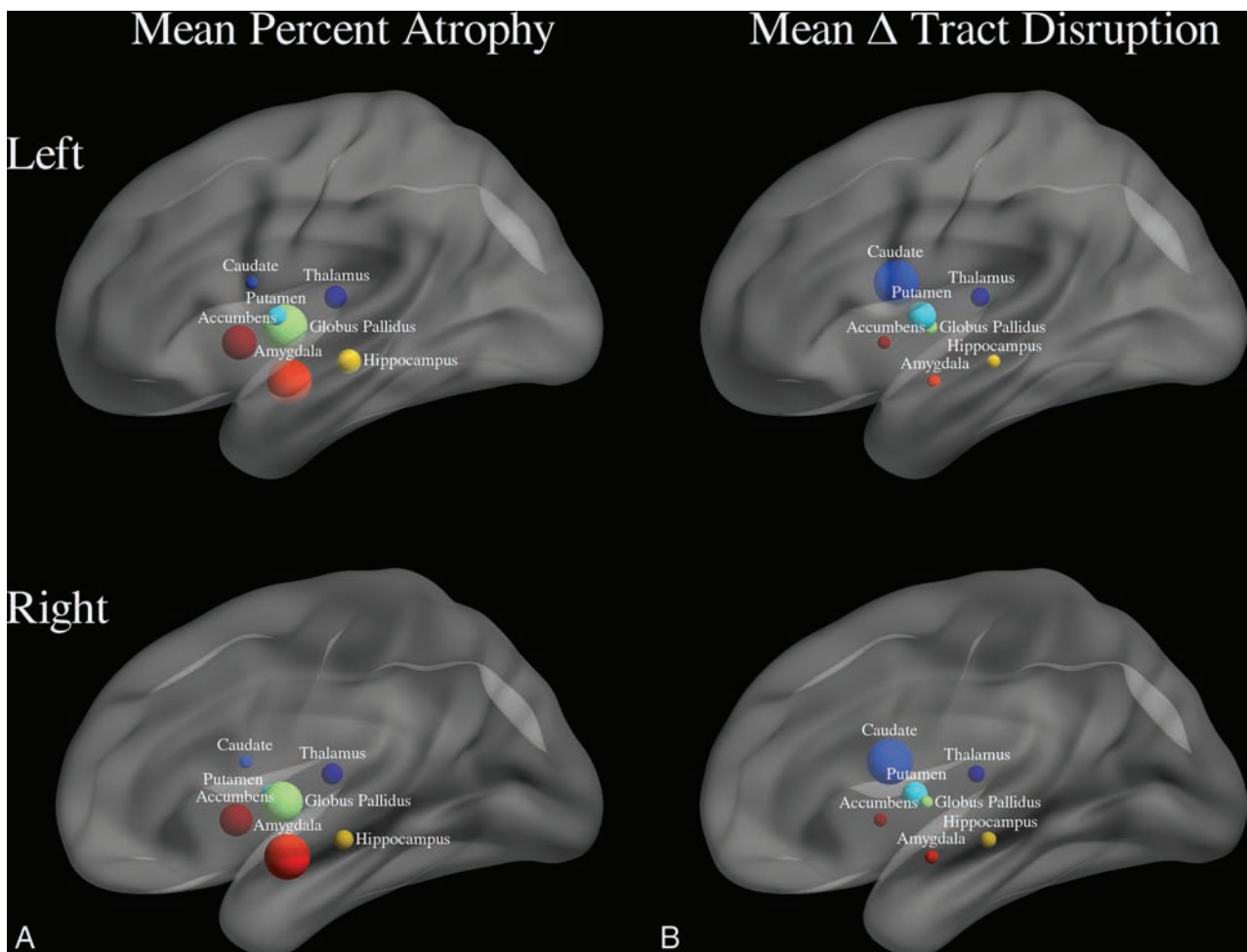


FIG 3. Mean annualized atrophy (A) and change in WM tract disruption (B) for each SGM region across 5 years. Each sphere represents an SGM region. The size of each sphere is proportional to the magnitude of longitudinal atrophy and increased disruption of connected WM tracts.

Table 3: Longitudinal analysis controlling for T2LV and WBV^a

Region	Model 1			Model 2			Change		
	R ²	P	P ^b	R ²	P	P ^b	ΔR ²	P	P ^b
Left thalamus	0.156	.000	.000	0.160	.000	.000	0.004	.181	.984
Right thalamus	0.141	.000	.000	0.147	.000	.000	0.006	.137	.984
Left caudate	0.067	.007	.028	0.074	.005	.020	0.007	.135	.984
Right caudate	0.084	.002	.014	0.092	.001	.008	0.008	.123	.984
Left putamen	0.146	.000	.000	0.164	.000	.000	0.018	.034	.340
Right putamen	0.055	.016	.036	0.130	.000	.000	0.075	.000	.000
Left globus pallidus	0.140	.000	.000	0.164	.000	.000	0.024	.017	.187
Right globus pallidus	0.152	.000	.000	0.161	.000	.000	0.009	.101	.909
Left hippocampus	0.102	.000	.000	0.097	.001	.008	-0.005	.729	1.00
Right hippocampus	0.098	.0001	.000	0.094	.001	.008	0.004	.590	1.00
Left amygdala	0.059	.012	.036	0.062	.012	.024	0.003	.207	.984
Right amygdala	-0.013	.711	.711	0.028	.106	.106	0.041	.005	.065
Left accumbens	0.070	.005	.025	0.104	.008	.024	0.034	.008	.096
Right accumbens	0.084	.002	.014	0.086	.002	.010	0.002	.240	.984

Note:—ΔWBV indicates change in whole-brain volume; ΔT2LV, change in T2 lesion volume.

^a Hierarchic regression analyses predicting regional SGM 5-year atrophy. Predictors included in each model are as follows: model 1, age, sex, disease duration, ΔWBV, ΔT2LV, baseline tract disruption; model 2, age, sex, disease duration, ΔWBV, ΔT2LV, baseline tract disruption, longitudinal change in disruption of connected WM tracts.

^b Holm-Bonferroni-corrected *P* values. All *P* values are significant.

DISCUSSION

We aimed to characterize the extent to which focal WM damage in MS contributes to atrophy in connected SGM regions, beyond what would be expected as a result of indirectly related co-occurring processes arising from a common cause. Previous cross-sectional studies indicated a moderate correlation between WM damage and SGM volume, establishing a relationship between WM damage and GM atrophy.^{6,10-13} That relationship was also observed longitudinally. However, overall disease burden and the location of WM damage relative to GM were not accounted for in

tional studies indicated a moderate correlation between WM damage and SGM volume, establishing a relationship between WM damage and GM atrophy.^{6,10-13} That relationship was also observed longitudinally. However, overall disease burden and the location of WM damage relative to GM were not accounted for in

these longitudinal analyses.^{12,14} Our analyses, controlling for global disease burden and accounting for lesion location along connected WM tracts, builds on this previous work to explore the specific causal relationship between focal WM damage and SGM atrophy.

We have confirmed earlier cross-sectional findings. In our models predicting regional SGM volumes, disruption of connected WM tracts explained significant added variance for 13 of 14 regions. Thus, we consistently observed an association between the degree to which connected WM tracts were disrupted by T2-FLAIR lesions and regional SGM volume. However, in subsequent analysis controlling for overall disease burden, the relationship between focal WM damage and connected SGM volume was substantially blunted: A significant relationship remained for only 3 of 14 regions (left caudate, right amygdala, and left accumbens), and the additional variance explained was an order of magnitude smaller. This added explained variance was nonsignificant for all SGM regions after controlling for multiple comparisons. The location of lesions in MS is highly heterogeneous in general and in our current population. Therefore, if lesions in connected tracts were truly the principal driver of SGM atrophy, we would expect information about their specific location to provide substantial additional explanatory value beyond whole-brain lesion volume or atrophy. Therefore, we believe that although anterograde and retrograde degeneration does play an important role, the magnitude of associations commonly observed between WM disruptions and SGM atrophy may, in large part, reflect the progression of parallel but indirectly related pathology.

We then extended our analysis longitudinally to better characterize the temporal relationship between new focal WM damage and SGM atrophy in connected regions. We observed a significant correlation between Δ tract disruption and regional atrophy for only 5 of 14 regions (left putamen, right putamen, left globus pallidus, right amygdala, and left accumbens) when controlling for age, sex, disease duration, Δ WBV, and Δ T2LV. This increase in explained variance remained statistically significant for only 1 SGM region (right putamen) after controlling for multiple comparisons. Furthermore, the absolute changes in explanatory power that we observed were small, on average 1.6% of a total 11.2% explained variance. This total explained variance is in accordance with a previous study.¹⁴ This also suggests that although important, direct disruption of connected WM tracts is not necessarily the primary driver of SGM atrophy.

Although our findings show that the relationship varies among SGM regions, the effect of new focal WM damage on SGM atrophy is weaker and less consistent than we expected. For many SGM regions, it seems likely that other pathologic mechanisms are more important drivers of the SGM atrophy in MS. There are a number of reasons why GM atrophy may occur independent of WM damage. Both cortical and deep gray matter lesions have been extensively documented in MS and may have a direct impact on local tissue volume.^{1,10} Microglial activation has also been observed in cortical tissue and SGM and may contribute to direct pathology.^{1,4} In addition, GM atrophy may be caused by local B-cell infiltration—for example, leptomeningeal enhancement has been shown to be related to cortical atrophy.^{4,27} Finally, thalamic atrophy in MS has been shown to vary according to the

distance from CSF and may arise from CSF-mediated immune cytotoxic factors.²⁸

Participants in this study were evaluated at only 2 time points 5 years apart. The simultaneous analysis of new lesions and increased atrophy may not be the best for measuring this relationship if there is a lag between incident lesions and atrophy. In future studies, annual imaging following individual new lesion incidence would be better suited for understanding the exact timeline of the impact of WM tract disruption on the atrophy of connected GM regions. These analyses may also allow a better account of resolving lesions. However, we observed similar results in our cross-sectional analysis. Also notable is that WM tract disruption data used for this study were derived from lesion masks using NeMo rather than via direct diffusion tractography. This finding is advantageous to avoid the issue of invalid streamlines due to lesions but increases the reliance on normative data. In our analysis, we attempted to account for the degree of WM damage by weighting disruption caused by T1WI black hole lesions more strongly than disruption caused by T2-FLAIR lesions. Nonetheless, this weighting was partly arbitrary and resulted in only a coarse estimate of actual tract damage. Future studies might better quantify the degree of WM tract damage using local magnetization transfer ratio or DTI tissue metrics. Another potential limitation associated with the use of the NeMo tool is that the tractogram data base is derived from a population of HC who are younger than the cohort under investigation. This difference may bias results. However, the NeMo tool determines the level of WM tract disruption caused by lesions probabilistically by taking the mean effect across all 73 HC tractograms. We believe that this processing step, in addition to the co-registration of the tractograms to the Montreal Neurological Institute space, helps mitigate this potential bias.

Average disease duration at baseline for our study participants was long, >15 years. Although potentially a strength, it is possible that substantial atrophy may have already occurred in early-affected SGM. However, we found significant longitudinal changes in tract disruption and atrophy for nearly all SGM regions. Therefore, the observed lack of significant associations is unlikely due to waning progression of either factor.

Taken as a whole, the current study emphasizes the need for continued investigation of primary pathologic factors in GM in MS and lends further credence to the idea that GM atrophy is at least partially independent from WM lesions. Hence, it is likely that SGM atrophy should be considered independently in imaging assessments of disease progression or clinical trials.²⁹

CONCLUSIONS

Focal WM damage in connected tracts explains only a small amount of unique additive variance in cross-sectional and longitudinal atrophy of some connected SGM regions. These findings point toward independent mechanisms related to SGM atrophy and support the use of SGM metrics as additional end points in clinical trials.

Disclosures: Ralph H.B. Benedict—UNRELATED: Consultancy: Novartis, Roche, Sanofi, Takeda Pharmaceutical Company; Grants/Grants Pending: Biogen, Mallinckrodt, Genzyme, Genentech*; Payment for Lectures Including Service on Speakers Bureaus: EMD Serono; Royalties: Psychological Assessment Resources. Bianca Wein-

stock-Guttman—UNRELATED: Board Membership: Biogen, TEVA Neuroscience, Novartis, Celgene, Sanofi Genzyme, EMD Serono; Consultancy: Biogen, TEVA Neuroscience, Novartis, Celgene, Sanofi Genzyme, EMD Serono; Grants/Grants Pending: Biogen, TEVA Neuroscience, EMD Serono*; Payment for Lectures Including Service on Speakers Bureaus: Biogen, TEVA Neuroscience, Genentech. Robert Zivadinov—UNRELATED: Consultancy: Celgene, Sanofi Genzyme, Novartis; Grants/Grants Pending: Celgene, Sanofi Genzyme, Novartis, IMS Health, Protebms*; Payment for Lectures Including Service on Speakers Bureaus: Sanofi Genzyme, Novartis, EMD Serono. Michael Dwyer—UNRELATED: Consultancy: Claret Medical, EMD Serono; Grants/Grants Pending: Novartis*. *Money paid to the institution.

REFERENCES

- Geurts JJ, Barkhof F. **Grey matter pathology in multiple sclerosis.** *Lancet Neurol* 2008;7:841–51 CrossRef Medline
- Audoain B, Zaaoui W, Reuter F, et al. **Atrophy mainly affects the limbic system and the deep grey matter at the first stage of multiple sclerosis.** *J Neurol Neurosurg Psychiatry* 2010;81:690–95 CrossRef Medline
- Zivadinov R, Uher T, Hagemeyer J, et al. **A serial 10-year follow-up study of brain atrophy and disability progression in RRMS patients.** *Mult Scler* 2016;22:1709–18 CrossRef Medline
- Absinta M, Vuolo L, Rao A, et al. **Gadolinium-based MRI characterization of leptomeningeal inflammation in multiple sclerosis.** *Neurology* 2015;85:18–28 CrossRef Medline
- Minagar A, Barnett MH, Benedict RH, et al. **The thalamus and multiple sclerosis: modern views on pathologic, imaging, and clinical aspects.** *Neurology* 2013;80:210–19 CrossRef Medline
- Kuceyeski AF, Vargas W, Dayan M, et al. **Modeling the relationship among gray matter atrophy, abnormalities in connecting white matter, and cognitive performance in early multiple sclerosis.** *AJNR Am J Neuroradiol* 2015;36:702–09 CrossRef Medline
- Calabrese M, Magliozzi R, Ciccarelli O, et al. **Exploring the origins of grey matter damage in multiple sclerosis.** *Nat Rev Neurosci* 2015;16:147–58 CrossRef Medline
- Dziedzic T, Metz I, Dallenga T, et al. **Wallerian degeneration: a major component of early axonal pathology in multiple sclerosis.** *Brain Pathol* 2010;20:976–85 CrossRef Medline
- Vargas ME, Barres BA. **Why is Wallerian degeneration in the CNS so slow?** *Annu Rev Neurosci* 2007;30:153–79 CrossRef Medline
- Mühlau M, Buck D, Förtscher A, et al. **White-matter lesions drive deep gray-matter atrophy in early multiple sclerosis: support from structural MRI.** *Mult Scler* 2013;19:1485–92 CrossRef Medline
- Sepulcre J, Goñi J, Masdeu JC, et al. **Contribution of white matter lesions to gray matter atrophy in multiple sclerosis: evidence from voxel-based analysis of T1 lesions in the visual pathway.** *Arch Neurol* 2009;66:173–79 CrossRef Medline
- Sepulcre J, Sastre-Garriga J, Cercignani M, et al. **Regional gray matter atrophy in early primary progressive multiple sclerosis: a voxel-based morphometry study.** *Arch Neurol* 2006;63:1175–80 CrossRef Medline
- Henry RG, Shieh M, Amirbekian B, et al. **Connecting white matter injury and thalamic atrophy in clinically isolated syndromes.** *J Neurol Sci* 2009;282:61–66 CrossRef Medline
- Chard DT, Brex PA, Ciccarelli O, et al. **The longitudinal relation between brain lesion load and atrophy in multiple sclerosis: a 14 year follow up study.** *J Neurol Neurosurg Psychiatry* 2003;74:1551–54 CrossRef Medline
- Kuceyeski A, Maruta J, Relkin N, et al. **The Network Modification (NeMo) tool: elucidating the effect of white matter integrity changes on cortical and subcortical structural connectivity.** *Brain Connect* 2013;3:451–63 CrossRef Medline
- Reich DS, Ozturk A, Calabresi PA, et al. **Automated vs. conventional tractography in multiple sclerosis: variability and correlation with disability.** *Neuroimage* 2010;49:3047–56 CrossRef Medline
- Kappus N, Weinstock-Guttman B, Hagemeyer J, et al. **Cardiovascular risk factors are associated with increased lesion burden and brain atrophy in multiple sclerosis.** *J Neurol Neurosurg Psychiatry* 2016;87:181–87 CrossRef Medline
- Zivadinov R, Ramasamy DP, Benedict RR, et al. **Cerebral microbleeds in multiple sclerosis evaluated on susceptibility-weighted images and quantitative susceptibility maps: a case-control study.** *Radiology* 2016;281:884–95 CrossRef Medline
- Zivadinov R, Rudick RA, De Masi R, et al. **Effects of IV methylprednisolone on brain atrophy in relapsing-remitting MS.** *Neurology* 2001;57:1239–47 CrossRef Medline
- Gelineau-Morel R, Tomassini V, Jenkinson M, et al. **The effect of hypointense white matter lesions on automated gray matter segmentation in multiple sclerosis.** *Hum Brain Mapp* 2012;33:2802–14 CrossRef Medline
- Smith SM, Zhang Y, Jenkinson M, et al. **Accurate, robust, and automated longitudinal and cross-sectional brain change analysis.** *Neuroimage* 2002;17:479–89 CrossRef Medline
- Patenaude B, Smith S, Kennedy D, et al. **A Bayesian model of shape and appearance for subcortical brain.** *Neuroimage* 2011;56:907–22
- Smith SM, De Stefano N, Jenkinson M, et al. **Normalized accurate measurement of longitudinal brain change.** *J Comput Assist Tomogr* 2001;25:466–75 CrossRef Medline
- Avants BB, Tustison NJ, Song G, et al. **A reproducible evaluation of ANTs similarity metric performance in brain image registration.** *Neuroimage* 2011;54:2033–44 CrossRef Medline
- Fuchs T, Dwyer M, Kuceyeski A, et al. **White matter tract network disruption explains reduced conscientiousness in multiple sclerosis.** *Hum Brain Mapp* 2018 May 8. [Epub ahead of print] CrossRef Medline
- Van Waesberghe JH, Kamphorst W, De Groot CJA, et al. **Axonal loss in multiple sclerosis lesions: magnetic resonance imaging insights into substrates of disability.** *Ann Neurol* 1999;46:747–54 Medline
- Zurawski J, Lassmann H, Bakshi R. **Use of magnetic resonance imaging to visualize leptomeningeal inflammation in patients with multiple sclerosis: a review.** *JAMA Neurol* 2017;74:100–09 CrossRef Medline
- Louapre C, Govindarajan ST, Gianni C, et al. **Heterogeneous pathological processes account for thalamic degeneration in multiple sclerosis: insights from 7 T imaging.** *Mult Scler* 2017 Aug 1. [Epub ahead of print] CrossRef Medline
- Kappos L, De Stefano N, Freedman MS, et al. **Inclusion of brain volume loss in a revised measure of “no evidence of disease activity” (NEDA-4) in relapsing-remitting multiple sclerosis.** *Mult Scler* 2016;22:1297–305 CrossRef Medline

Primary Angioplasty without Stenting for Symptomatic, High-Grade Intracranial Stenosis with Poor Circulation

Y. Wang, Y. Ma, P. Gao, Y. Chen, B. Yang, and L. Jiao



ABSTRACT

BACKGROUND AND PURPOSE: Although the Stenting versus Aggressive Medical Management for Preventing Recurrent Stroke in Intracranial Stenosis (SAMMPRIS) study demonstrated a high incidence of perioperative complications for Intracranial Atherosclerotic disease (ICAD) treatments with stent placement, some studies have shown that submaximal angioplasty with an undersized balloon limits the risks of perioperative complications, suggesting that intervention may remain an alternative option for ICAD if perioperative complications are minimized. We sought to evaluate clinical and angiographic outcomes after primary angioplasty without stent placement in patients with symptomatic, high-grade intracranial stenosis and poor antegrade flow who were refractory to medical therapy.

MATERIALS AND METHODS: All cases with high-grade, symptomatic intracranial stenosis and poor antegrade flow treated with intracranial angioplasty without stent placement at Xuanwu Hospital, Capital Medical University, from January 2010 to December 2016, were retrospectively reviewed. The main outcomes included the changes in antegrade flow and residual stenosis and any stroke or death within 1 month. We also evaluated functional outcomes, stroke, and restenosis in patients on follow-up.

RESULTS: Thirty-five patients (mean age, 64.3 years) were included, and the mean follow-up time was 9.7 months. The average preprocedural stenosis was 88.4%. The immediate, average postprocedure stenosis rate was 25.3%, and the average postprocedural stenosis rate at last angiographic follow-up was 34.7%. The primary end point of major stroke or death at 30 days was observed in 1 patient (1/35, 2.9%), and no patient had intraprocedural complications. The incidence of stroke or death at the last follow-up was 2.9%, which was superior to the results of the medical and stent-placement arms of the SAMMPRIS study. Severe restenosis was observed in 3 (3/25, 12%) patients but without any symptoms.

CONCLUSIONS: In this retrospective series, primary balloon angioplasty was an effective treatment option for symptomatic intracranial stenosis with a high risk of stroke.

ABBREVIATION: SAMMPRIS = Stenting versus Aggressive Medical Management for Preventing Recurrent Stroke in Intracranial Stenosis

The results of the Stenting versus Aggressive Medical Management for Preventing Recurrent Stroke in Intracranial Stenosis (SAMMPRIS) study showed a 5.8% 30-day stroke or death rate in the medical treatment arm compared with 14.7% in the stent arm.¹ Therefore, the optimal treatment for symptomatic intracranial stenosis remains unclear. Many experts continue to question whether certain population subsets might still benefit from endovascular therapy for treatment of severe intracranial stenosis. There is clearly still room for great improvement in the

management of these patients because the projected stroke or death rate at 1 year has approached 12.2%, even in the medical arm of the SAMMPRIS study. Thus, for patients at the highest risk of stroke, a more permissive role for primary angioplasty, especially in situations in which stent navigation is technically challenging, has been advocated.²

Compared with stent-placement angioplasty, primary angioplasty may have some advantages: First, the stent system is difficult to advance if the target artery is too tortuous and may cause injury to atherosclerotic plaques, such as increasing the risk of the snowplowing effect and the “cheese grater” effect. Several recent reports have suggested there are advantages of primary angioplasty without stent placement for the treatment of intracranial stenosis in selected patients.³

In this retrospective review of cases from our single center, we analyzed high-risk patients with stroke treated with primary bal-

Received January 11, 2018; accepted after revision May 7.

From the Department of Neurosurgery, Xuanwu Hospital, Capital Medical University, Beijing, China.

Please address correspondence to Liqun Jiao, MD, PhD, Xuanwu Hospital, Capital Medical University, Beijing 100053, China; e-mail: Liqunjiao@sina.cn

 Indicates article with supplemental on-line table.

<http://dx.doi.org/10.3174/ajnr.A5708>

loon angioplasty without stent placement to compare the outcomes of these patients with those of the medical and stent placement treatment arms of the SAMMPRIS study as well as with other published series.

MATERIALS AND METHODS

Patient Selection

Patient selection included all patients who underwent primary intracranial balloon angioplasty at Xuanwu Hospital, Capital Medical University, from January 2010 to December 2016. This trial was performed in line with the requirements of the ethics committee, and all patients gave their signed informed consent before the procedure.

All patients underwent DSA to confirm stenosis, and their angiographic characteristics were evaluated. The degree of stenosis was measured by digital subtraction angiography according to the criteria of the Warfarin-Aspirin Symptomatic Intracranial Disease method.⁴ Endovascular therapy was considered after discussion by an expert team on neurovascular diseases, including a neuroradiologist, neurologist, and neurosurgeon. For patients with complicated angiographic features, such as extremely eccentric lesions or lesions close to perforators, angioplasty with stent placement was considered unsuitable or dangerous, and only primary angioplasty without a stent was suggested. The 35 patients who underwent primary angioplasty had high-grade, angiographic stenosis (>70%) and poor antegrade flow with ischemic symptoms in the territory of the same vascular distribution, and their angiographic characteristics met at least 1 of the following conditions: a lesion of >10 mm in length, extremely eccentric, or near perforators. The Thrombolysis in Cerebral Infarction grading system was used to evaluate the antegrade blood flow according to digital subtraction angiography. The assessment of neuroimaging was performed by an independent neurologist who was blinded to the clinical outcomes of the patients. Patients were excluded if they had acute infarcts within 2 weeks or nonatherosclerotic lesions confirmed by high-resolution MR imaging.

Periprocedural Management

The procedures were performed by an experienced neurointerventionist at our center. General anesthesia was induced in all patients. After vascular access was achieved, intravenous heparin was administered via a bolus of 75 U/kg followed by a half dose 1 hour later. The guiding catheter was advanced into the cervical vertebral or internal carotid artery as high as the vessel tortuosity allowed. A 0.014-inch guidewire would be carefully manipulated across the lesion, and the balloon catheter was then used to navigate the microwire. When it was difficult for the microwire to reach the safety zone, usually a microcatheter was also used if the target artery was too tortuous or there was very severe stenosis. The microcatheter would be exchanged for the balloon catheter after it crossed the stenotic lesion. In the exchange procedure, the tip of the microwire was shaped into a U and placed in a straight portion of a distal artery to avoid the possibility of a wire perforation during the procedure. Angioplasty was performed using a balloon approximately not greater than 70% of the size of the normal vessel diameter. A Gateway balloon (Stryker, Kalamazoo, Michigan) or a Maverick balloon (Boston Scientific, Natick, Massachusetts) was

chosen as the device during the procedure as the surgeons' experience dictated. The length of the lesion should have been covered totally by the chosen balloon, and the balloon should have been positioned precisely under the guidance of the roadmap.

The balloon was inflated as slowly as possible during the procedure, usually, 1 atm per 10 seconds to reach the nominal pressure, and was kept inflated for at least 60 seconds. In addition, the balloon was slowly deflated by 1 atm per 30 seconds. With a normal pressure of 6 atm as given in the balloon catheter instructions, this procedure accounted for no more than 5–8 minutes of flow cessation per case.

All procedures were performed with the patient under general anesthesia using a standard transfemoral access. Stenosis <50% after angioplasty was acceptable. Usually, a single procedure of balloon inflation angioplasty was performed. If residual stenosis was >50% or the phenomenon of elastic recoil was distinct, repeat angioplasty would be performed with a higher inflation pressure or with a larger balloon within the range of 80% of the diameter of the distal normal artery.

A noncontrast head CT was performed to ensure that potential hemorrhage did not occur after the procedure. A glycoprotein IIb/IIIa inhibitor was routinely administered for 12 hours (tirofiban, weight-based dose) after exclusion of hemorrhage by the CT scan. A weight-based dose of low-molecular-weight heparin was given to all patients every 12 hours subcutaneously for 3 days, and patients were monitored closely until discharge. Preoperative and postoperative images of 2 sample cases are presented in the case presentation.

Periprocedural Medical Management

All patients received aspirin (100 mg/day) and clopidogrel (75 mg/day) for at least 5 days before the intervention. The dual-antiplatelet therapy was maintained for 90 days after the procedure. Risk factor control was suggested to achieve the following: systolic blood pressure of <140 mm Hg (or <130 mm Hg in patients with diabetes mellitus), low-density lipoprotein of <70 mg/dL (1.81 mmol/L) or a decrease by 50%, smoking cessation, and lifestyle modifications to reduce obesity and sedentary states.

Clinical and Imaging Assessment

All patients were systematically assessed independently by an expert team including a senior neurologist and a senior neurosurgeon. Neurologic status was evaluated using the NIHSS, Barthel Index (BI), and mRS on admission and within 1 week before discharging postoperatively. The follow-up evaluation of neurologic status was also performed at 90 days and at 6 and 12 months postoperatively in the outpatient department. The patients' characteristics and risk factors are presented in the Table.

Pre- and postoperative head MR imaging were performed for all patients to evaluate ischemic lesions using T1, T2, and DWI series. MR imaging was assessed independently by an experienced neuroradiologist.

Follow-Up Policy

All data were collected from clinical records, operation records, and medical imaging systems. We mainly evaluated the degree of stenosis and the changes in antegrade flow pre-/posttreatment

Patient and lesion characteristics

Characteristic (N = 35)	No. (%)
Mean age (yr)	63.43 ± 5.41
Male	74.3%
Risk factors	
Diabetes mellitus	9 (25.7%)
Hypertension	22 (62.8%)
Hyperlipidemia	14 (40%)
Atrial fibrillation	2 (5.7%)
Coronary artery disease	7 (20%)
Lesion location	
Basilar artery	16
Supraclinoid ICA	2
M1 segment of MCA	5
M2 segment of MCA	4
Vertebral artery	2
Vertebrobasilar junction	6

and the adverse events related to the interventional therapy to clarify its safety. To appraise its long-term efficacy, we also assessed the patients' functional status, recurrence of stroke, rate of restenosis, and reinterventions for the lesion. A modified Rankin Scale score of 0–2 was defined as good functional status. Follow-up imaging by digital subtraction angiography and/or MRA or CTA was performed to assess the rate of restenosis (restenosis was defined as >50%), and head MR imaging was used to look for recurrent ischemic lesions 6 months after the intervention. Re-treatment was considered when the patient had recurrent ischemic symptoms and >50% restenosis occurred.

Illustrative Cases

Example 1. A 65-year-old man had intermittent vertigo for 3 months, left-sided weakness, and slurred speech. Even with aggressive medical therapy including aspirin (100 mg/day) and clopidogrel (75 mg/day) plus a statin for 3 months, he still had vertigo. MR imaging revealed a pons infarction, and DSA demonstrated severe stenosis of the proximal basilar artery. High Resolution Magnetic Resonance Imaging revealed the site of the stenosis. Regarding the angiographic characteristics of the lesion, the length of the lesion was approximately 11 mm and included the site of the vertebrobasilar junction, and the right AICA was very close to the stenotic lesion. He underwent primary angioplasty for the vertebrobasilar junction stenosis, and the postoperative period was uneventful. The immediate DSA after angioplasty demonstrated that antegrade blood flow was markedly improved, and 2-day postoperative MR imaging showed no fresh infarction in the territory of the posterior circulation. The 14-month follow-up by DSA and MR imaging demonstrated no obvious restenosis and no recurrent infarction. All images are shown in Fig 1.

Example 2. A 63-year-old man had paroxysmal dizziness, numbness of the right hand, and weakness of the lower limb. MR imaging revealed a subacute cerebral infarction involving the left frontal area. DSA identified severe stenosis of the left middle cerebral artery (1 branch of M2), and HRMRI revealed high-grade focal stenosis within the M2 segment of the left MCA. He underwent primary angioplasty of the left MCA. Postoperative DSA showed the lumen obviously improved, and MR imaging indicated no fresh infarction. The 9-month follow-up DSA indicated no obvious restenosis. He was referred to our institution where he under-

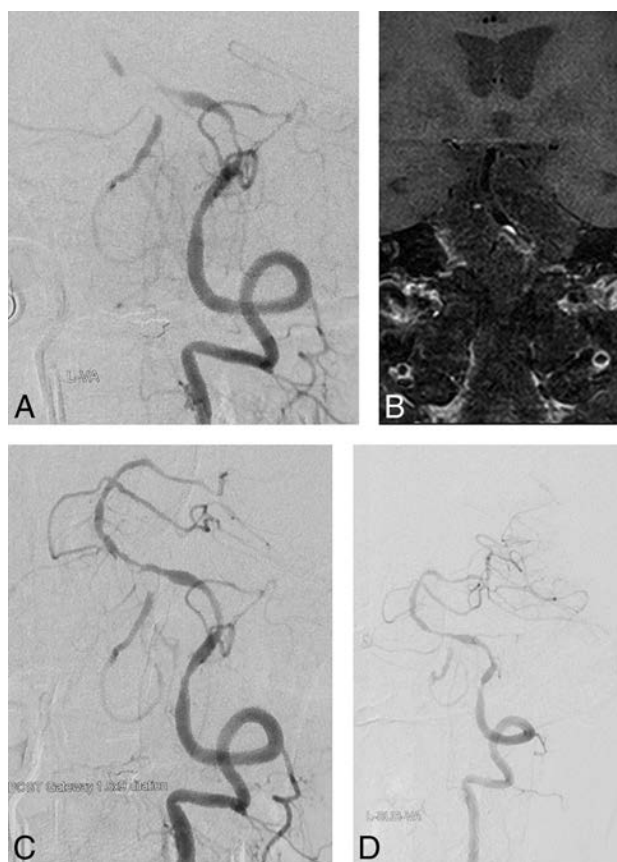


FIG 1. A 65-year-old man with symptomatic severe basilar artery stenosis, refractory to medical therapy (case 1). *A*, Angiogram of the left vertebral artery reveals severe stenosis of the vertebrobasilar junction (angiographic characteristic: TIC1 1). *B*, High-resolution MR imaging confirms the atherosclerotic lesion and shows the eccentric plaque located at the vertebrobasilar junction and the surface of the plaque enhancement. *C*, Immediate angiogram after primary angioplasty with a 1.5- to 9-mm Gateway balloon; antegrade flow improved and reached TIC1 grade 2b. *D*, Angiogram of the left vertebral artery at 14-month follow-up reveals no severe restenosis, and antegrade flow reaches TIC1 grade 3.

went angiography and subsequent angioplasty. All images are shown in Fig 2.

RESULTS

Patients and Intervention Procedures

Thirty-five patients (26 men, 9 women; mean age, 63.43 ± 5.41 years; range, 56–74 years) with symptomatic intracranial stenosis were treated by primary balloon angioplasty from January 2010 to December 2016, with a mean of 10.6 months of follow-up. Patients who were treated in the acute period (2 weeks from onset) were not included in this study. Most ($n=33$) of the included patients (94.3%) presented with ischemic strokes, and the other 2 patients presented with TIAs (5.7%). The time interval from the onset of the last symptom to interventional treatment was 35.6 days (range, 15–69 days). The most common risk factor for intracranial stenosis in the study population was hypertension (62.8%). Other risk factors were as follows: hyperlipidemia (40%), diabetes mellitus (25.7%), coronary artery disease (20%), and atrial fibrillation (5.7%). The clinical features of all patients in our study are listed in the Table. The anatomic location of the stenotic lesion in each case is shown in the On-line Table.

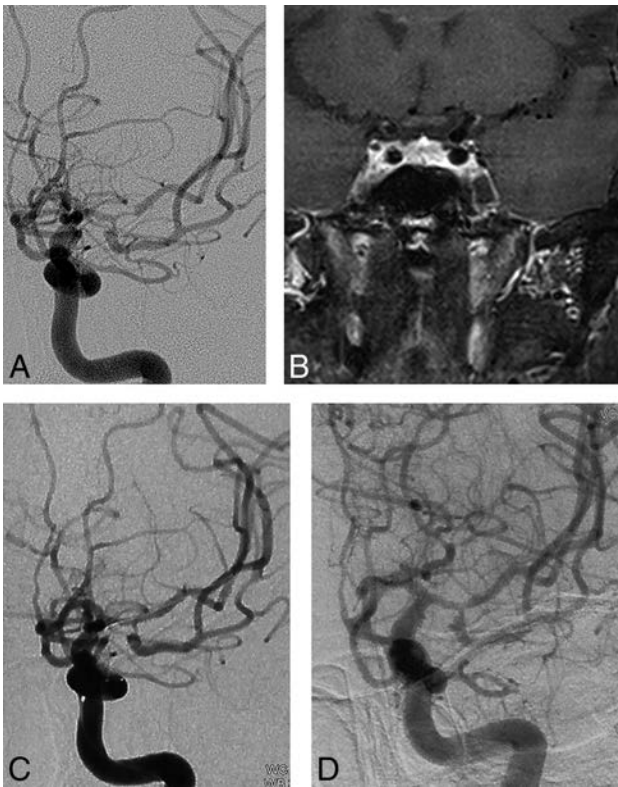


FIG 2. A 63-year-old man with symptomatic MCA severe stenosis. (case 26). *A*, Angiogram of the left internal carotid artery reveals severe stenosis of the left middle cerebral artery (M2 segment) (angiographic characteristic: TIC1 2a). *B*, High-resolution MR imaging confirms the atherosclerotic lesion and shows the plaque located at the M2 branch. *C*, Immediate angiogram after primary angioplasty with a 2- to 9-mm Gateway balloon reveals that antegrade flow improved and reached TIC1 grade 2b. *D*, Angiogram of the left vertebral artery at 6-month follow-up demonstrates no severe restenosis, and antegrade flow reached TIC1 grade 3.

In our series, coronary balloon catheters (Maverick) for intracranial angioplasty were used in 2 patients, and Gateway balloon catheters were used in 33 patients. Each balloon catheter was strictly selected to be no larger than 70% of the normal diameter of the parent vessel. The balloon catheters were dilated slowly to reach the nominal pressure following the manufacturer's instructions. No vessel rupture or wire perforations occurred during the procedures. No stent angioplasty was needed to maintain the patency of the lesions during the procedure.

The average preprocedural stenosis was 82.7% (range, 71%–94%), and the average immediate postprocedural stenosis was 31.2% (range, 23%–46%).

Retreatment was required in only 1 (1/35, 2.9%) patient during the perioperative period, secondary to acute basilar artery thrombosis 5 days after the procedure. Acute recanalization of the basilar artery was then performed, and the patient recovered well. The primary end point of major stroke or death at 30 days was observed in only this patient (2.9%), and no intraprocedural complication occurred.

The mean follow-up was 17.6 months (range, 6–42 months) for 33 patients. Of these 33 patients, 31 (93.9%) had good nerve function status (mRS, 0–2). Two patients had recurrent ischemic

stroke, including one with ipsilateral lacunar infarction (MCA stenosis, 6 months after the interventional therapy) and one with a brain stem infarction (basilar artery stenosis, 14 months after the interventional therapy). The rate of recurrence of ischemic stroke beyond 30 days was 3.0% at 1 year (1/33 of the followed patients), and the combined rates of major stroke and death within 30 days and the ipsilateral ischemic stroke rate beyond 30 days at 1 year were 6%.

Follow-up imaging data were available in 25 patients, of whom 3 (12%) had restenosis without any symptoms. Of the 33 patients followed, 25 patients underwent some type of radiographic follow-up performed using either conventional angiography, CTA, or MRA. Twenty patients underwent DSA as a primary method of follow-up, 3 patients underwent CTA, and 2 patients underwent MRA as their primary method of follow-up, with an average follow-up interval of 16.3 months (range, 6–38 months). Severe restenosis was observed in 3 (3/25, 12%) patients, but no symptoms were observed. Retreatment was not performed for these 3 patients because no further symptoms occurred.

DISCUSSION

Good collateral compensation is seen as a protective factor to reduce the risk of stroke in patients with symptomatic intracranial stenosis, and adequate antegrade flow is associated with favorable outcomes and a lower recurrence of stroke.⁵ Thus, patients with severe intracranial stenosis and poor antegrade blood flow are at high risk of ischemic stroke, and any effort to increase antegrade flow and improve lumen augmentation should reduce the risk of ischemic stroke. Our findings may cause renewed interest in primary balloon angioplasty in this specific patient population with severe stenosis and poor antegrade flow. We report the outcomes of 35 consecutive patients with symptomatic intracranial artery stenosis with poor antegrade circulation who underwent primary angioplasty in this study.

In our case series the 30-day stroke or death rate was 2.9%. The combined stroke or death rate within 1 year beyond 30 days was 6%, and 93.9% of the available follow-up patients had a good functional status (mRS, 0–2). Because our case series was retrospective, it is difficult to perform direct comparisons with the SAMMPRIS study. However, the results within 30 days in our study were better than those reported in the stent-placement group of the SAMMPRIS study (2.9% versus 14.7%), and the 1-year results in our study were still better than the results in the stent-placement group of the SAMMPRIS study (6% versus 19.7%).⁶

In the SAMMPRIS study, most of the adverse events occurred in the perioperative period, and some perioperative complications were related to the procedure of deploying or manipulating the stent system, such as perforator ischemia, stent thrombosis, and wire perforation. A reappraisal of primary angioplasty without stents has recently been conducted.⁷ There are several potential benefits to primary balloon angioplasty over stent placement in the intracranial circulation. Tortuous anatomy may cause technical challenges in stent navigation and increase procedural risks. Theoretically, the technique of submaximal angioplasty without stents could result in adequate lumen augmentation for a symptomatic stenotic lesion. This technique could significantly avoid

the danger of arterial injury by the stent system, perforator snow plowing occlusion, and distal embolization. It also may reduce the risk of severe intracerebral hemorrhage caused by hyperperfusion syndrome due to the gradual recovery of the vessel lumen.⁸

Different intracranial stenosis locations have various perioperative complications due to their anatomic features, especially the MCA and basilar artery because these 2 locations involve a perforator-rich zone. In our series, most of these lesions were in the basilar artery, and the subgroup with lesions in the basilar artery had the lowest risk of stroke during medical therapy in SAMMPRIS. However, even the 2-year primary end point of the basilar artery subgroup in SAMMPRIS was 10% for the medical therapy arm,⁹ which means that these patients still suffered from recurrent stroke, which suggests that intervention may remain an alternative option if perioperative complications are minimized. In our experience, patients with higher grade stenosis and poor antegrade flow are most likely to benefit from flow augmentation by primary angioplasty.

As some literature has mentioned, one of the design flaws of SAMMPRIS was that the time interval between qualifying symptoms and intervention was too short.¹⁰ In our case series, the time interval from onset of the last symptom to interventional treatment was 35.6 days. The good results of the Wingspan Stent System Post Market Surveillance Study (WEAVETM Trial) also prolonged the time interval, which hints that the longer interval may be a protective factor for the intervention.

Our series demonstrates the feasibility and relative safety of primary balloon angioplasty and supports the incorporation of this technique into future trials that seek to identify high-risk population subsets that might benefit from angioplasty in conjunction with aggressive medical therapy for high-grade, symptomatic intracranial atherosclerosis. Our results suggest that primary balloon angioplasty is safer than stent angioplasty in some specific situations.

The contemporary literature includes several reports of primary balloon angioplasty for intracranial atherosclerosis that use a wide variety of balloons, mostly marketed for coronary use, that have reported a success rate and risk profile that are largely comparable with those of stent placement. A recent multi-institutional retrospective review reported a 92% success rate for primary balloon angioplasty and a 3-month stroke or death rate of 8.5% in a series of 74 patients. Either Gateway or Maverick balloon catheters were used in all cases, and the mean pretreatment stenosis rate was 79% \pm 14%.¹¹ One of the largest multicenter studies to compare primary angioplasty with stent placement for symptomatic intracranial stenosis showed no difference in survival at a 2-year follow-up. The 30-day rate of major stroke or death was 8.4% in the angioplasty group (8/95) versus 9.2% in the stent-placement group (9/98).¹²

In our series of 35 patients treated during the past 6 years at a single institution, we found a 2.9% rate of major stroke or death at 1 month, which is comparable with rates in the existing literature on this topic. The 1-year stroke or death rate in our series was 6%, which was comparable with the 1-year stroke or death rate in the medical arm of the SAMMPRIS study. This raises the question of whether angioplasty confers an up-front risk with a protective payoff from stroke as follow-up time increases. Therefore, further

studies regarding the long-term durability of this treatment method are needed.

In our series, a submaximal angioplasty technique with slow inflation was used. No rescue stent placement was necessary because there was no plaque disruption or obvious dissection.

As we continue to add to the collective experience with primary balloon angioplasty for intracranial stenosis, it will be important to study whether certain patient populations or lesions with particular angiographic characteristics are more favorable to interventional treatment.

The senior author routinely administers a glycoprotein IIb/IIIa inhibitor (eg, eptifibatid [Integrilin]) intraprocedurally. It is possible that the use of this agent may decrease the rate of acute thrombus formation. This effect may be especially pertinent in patients who exhibit some degree of resistance to aspirin, clopidogrel, or both because some studies have shown that this population is at a higher risk of thromboembolic complications from neurointerventions.¹³ This practice is not standardized, and no studies have documented the impact of glycoprotein IIb/IIIa inhibitor use at the time of angioplasty on patient outcomes. Thus, there is a concern regarding increased hemorrhage rates in patients receiving these agents; however, none of the patients in our series experienced a hemorrhage as a result of the procedure.

Primary angioplasty has 2 main disadvantages: iatrogenic arterial dissection and elastic recoil. If arterial occlusion occurs due to dissection or significant residual stenosis, stent placement angioplasty is an effective remedial measure.

For the endovascular therapy of intracranial stenosis, the most important factor is to reduce any perioperative complications. According to our experience, submaximal primary angioplasty may offer a safe treatment alternative to best medical therapy in complex intracranial arterial stenosis. The strict selection of patients is also important. Patients with severe stenosis combined with poor antegrade flow are at a high risk of recurrent stroke if treated with only medical therapy; therefore, it is worth trying an additional interventional therapy for those patients refractory to medical therapy with poor antegrade flow. While it has been suggested that lesion length, degree of stenosis, and anatomic location might also affect endovascular outcomes, the role that these factors play remains largely unknown. If we use the classification of Mori et al¹⁴ for intracranial stenosis lesions, type A lesions (\leq 5 mm in length, concentric plaque) correspond to better clinical outcomes compared with the other 2 types of lesions.

Measuring vessel stenosis is a gross simplification for endovascular therapy. In our study, we took into account antegrade flow by means of the TIC1 classification. Assessment of angiographic features may be valuable for screening out the subset of patients who are at a higher risk for recurrent stroke due to inadequate flow from an atherosclerotic stenotic lesion. Further prospective studies considering this evaluation for intracranial artery stenosis should be performed to identify which patients are best suited for revascularization.

Due to the inevitable restrictions in this retrospective study, there are still many deficiencies, such as a small sample and the absence of a valid comparison arm. A well-designed randomized controlled study is necessary to verify the safety and efficacy of this treatment for the selected patient group.

CONCLUSIONS

In our retrospective series, primary angioplasty was found to have a certain value with a relatively acceptable result for symptomatic patients with intracranial stenosis with a high risk of stroke. Further studies may elucidate specific clinical factors, anatomic sites, or patterns of stenosis that make a patient particularly amenable to balloon angioplasty.

Based on our preliminary results, compared with the results of the stent placement arm in the SAMMPRIS study, primary angioplasty for ICAD in the selected patients was a feasible and safe option with a favorable result. The positive effects of primary angioplasty were maintained with a mean of 10.6 months follow-up among the successfully followed patients in our series. In our experience, for patients with symptomatic intracranial stenosis refractory to aggressive medical therapy and for those with poor antegrade circulation, primary angioplasty without a stent should be the first neurointerventional therapy tried before considering stent angioplasty. A prospective randomized controlled trial will be conducted to verify the safety and efficacy of this interventional technique.

REFERENCES

1. Chimowitz MI, Lynn MJ, Derdeyn CP, et al; SAMMPRIS Trial Investigators. **Stenting versus aggressive medical therapy for intracranial arterial stenosis.** *N Engl J Med* 2011;365:993–1003 CrossRef Medline
2. Qureshi AI, Al-Senani FM, Husain S, et al. **Intracranial angioplasty and stent placement after stenting and aggressive medical management for preventing recurrent stroke in intracranial stenosis (SAMMPRIS) trial: present state and future considerations.** *J Neuroimaging* 2012;22:1–13 CrossRef Medline
3. Karanam LSP, Sharma M, Alurkar A, et al. **Balloon angioplasty for intracranial atherosclerotic disease: a multicenter study.** *J Vasc Interv Neurol* 2017;9:29–34
4. Samuels OB, Joseph GJ, Lynn MJ, et al. **A standardized method for measuring intracranial arterial stenosis.** *AJNR Am J Neuroradiol* 2000;21:643–46
5. Lau AY, Wong EH, Wong A, et al. **Significance of good collateral compensation in symptomatic intracranial atherosclerosis.** *Cerebrovasc Dis* 2012;33:517–24 CrossRef Medline
6. Derdeyn CP, Chimowitz MI, Lynn MJ, et al. **Aggressive medical treatment with or without stenting in high-risk patients with intracranial artery stenosis (SAMMPRIS): the final results of a randomised trial.** *Lancet* 2014;383:333–41
7. Siddiq F, Vazquez G, Memon MZ, et al. **Comparison of primary angioplasty with stent placement for treating symptomatic intracranial atherosclerotic diseases: a multicenter study.** *Stroke* 2008;39:2505–10 CrossRef Medline
8. Dumont TM, Sonig A, Mokin M, et al. **Submaximal angioplasty for symptomatic intracranial atherosclerosis: a prospective Phase I study.** *J Neurosurg* 2016;125:964–71 CrossRef Medline
9. Derdeyn CP, Chimowitz MI, Lynn MJ, et al; Stenting and Aggressive Medical Management for Preventing Recurrent Stroke in Intracranial Stenosis Trial Investigators. **Aggressive medical treatment with or without stenting in high-risk patients with intracranial artery stenosis (SAMMPRIS): the final results of a randomised trial.** *Lancet* 2014;383:333–41 CrossRef Medline
10. Abou-Chebl A, Steinmetz H. **Critique of “Stenting versus aggressive medical therapy for intracranial arterial stenosis” by Chimowitz, et al New England Journal of Medicine.** *Stroke* 2012;43:616–20 CrossRef Medline
11. Nguyen TN, Zaidat OO, Gupta R, et al. **Balloon angioplasty for intracranial atherosclerotic disease: periprocedural risks and short-term outcomes in a multicenter study.** *Stroke* 2011;42:107–11 CrossRef Medline
12. Khan M, Naqvi I, Bansari A, et al. **Intracranial atherosclerotic disease.** *Stroke Res Treat* 2011;2011:282845 CrossRef Medline
13. Ryu DS, Hong CK, Sim YS, et al. **Anti-platelet drug resistance in the prediction of thromboembolic complications after neurointervention.** *J Korean Neurosurg Soc* 2010;48:319–24 CrossRef Medline
14. Mori T, Fukuoka M, Kazita K, et al. **Follow-up study after intracranial percutaneous transluminal cerebral balloon angioplasty.** *AJNR Am J Neuroradiol* 1998;19:1525–33 Medline

Preoperative Mapping of the Supplementary Motor Area in Patients with Brain Tumor Using Resting-State fMRI with Seed-Based Analysis

J. Wongsripuemtet, A.E. Tyan, A. Carass, S. Agarwal, S.K. Gujar, J.J. Pillai, and H.I. Sair



ABSTRACT

BACKGROUND AND PURPOSE: The supplementary motor area can be a critical region in the preoperative planning of patients undergoing brain tumor resection because it plays a role in both language and motor function. While primary motor regions have been successfully identified using resting-state fMRI, there is variability in the literature regarding the identification of the supplementary motor area for preoperative planning. The purpose of our study was to compare resting-state fMRI to task-based fMRI for localization of the supplementary motor area in a large cohort of patients with brain tumors presenting for preoperative brain mapping.

MATERIALS AND METHODS: Sixty-six patients with brain tumors were evaluated with resting-state fMRI using seed-based analysis of hand and orofacial motor regions. Rates of supplementary motor area localization were compared with those in healthy controls and with localization results by task-based fMRI.

RESULTS: Localization of the supplementary motor area using hand motor seed regions was more effective than seeding using orofacial motor regions for both patients with brain tumor (95.5% versus 34.8%, $P < .001$) and controls (95.2% versus 45.2%, $P < .001$). Bilateral hand motor seeding was superior to unilateral hand motor seeding in patients with brain tumor for either side (95.5% versus 75.8%/75.8% for right/left, $P < .001$). No difference was found in the ability to identify the supplementary motor area between patients with brain tumors and controls.

CONCLUSIONS: In addition to task-based fMRI, seed-based analysis of resting-state fMRI represents an equally effective method for supplementary motor area localization in patients with brain tumors, with the best results obtained with bilateral hand motor region seeding.

ABBREVIATIONS: DCS = direct cortical stimulation; rs-fMRI = resting-state fMRI; SMA = supplementary motor area; tb-fMRI = task-based fMRI

Precise brain function localization is critical for neurosurgical procedures in which lesions are near the eloquent cortex. While direct cortical stimulation (DCS) is the criterion standard for assessing brain function, preoperative noninvasive functional brain imaging can aid in operative planning and decrease operative time.¹⁻⁴ Task-based fMRI (tb-fMRI), a noninvasive technique for examining brain function, demonstrates good correlation with DCS for identification of eloquent brain regions, particularly in areas of sensorimotor and language representation.^{5,6}

Thus, fMRI is a valuable clinical tool for preoperative brain function localization.

There are, however, limitations to tb-fMRI, including dedicated hardware and software, trained personnel to administer tasks, designing a suitable task to interrogate a specific brain function, and, most important, patient cooperation, which may be difficult for subsets of patients with cognitive impairment or advanced neurologic disease. Resting-state fMRI (rs-fMRI) can address some of these limitations.⁷ Instead of limiting interrogation to a specific brain function interrogated by a particular task, multiple brain networks can be assessed with a single rs-fMRI acquisition. Because no specific task needs to be performed, rs-fMRI can be more readily applied in patients with neurologic deficits or cognitive disturbance and in young children. Finally, intrinsic brain networks have been shown to be present even during sleep or anesthesia, opening the possibility of using this technique in patients who otherwise may not be able to tolerate MR imaging.^{8,9}

The sensorimotor network has been well-studied using rs-fMRI in the preoperative setting,¹⁰ with good agreement of

Received January 26, 2018; accepted after revision May 8.

From the Russell H. Morgan Department of Radiology and Radiological Sciences (J.W., A.E.T., S.A., S.K.G., J.J.P., H.I.S.) and Department of Neurosurgery (J.J.P.), Johns Hopkins University School of Medicine, Baltimore, Maryland; Department of Radiology (J.W.), Siriraj Hospital, Mahidol University, Bangkok, Thailand; and Department of Computer Science and Department of Electrical and Computer Engineering (A.C.), Johns Hopkins University, Baltimore, Maryland.

Please address correspondence to Haris Sair, MD, Russell H. Morgan Department of Radiology and Radiological Science, 600 N Wolfe St, Phipps B-100, Baltimore, MD 21287; hsair1@jhmi.edu; @hsairmd

<http://dx.doi.org/10.3174/ajnr.A5709>

rs-fMRI with both tb-fMRI¹¹ and DCS.¹² While the sensorimotor network proper is readily characterized in these studies, there is, however, variability in depiction of the supplementary motor area (SMA) in these studies; in the study of Kokkonen et al,¹¹ the SMA was not reliably demonstrated in all subjects. In clinical tb-fMRI, often there are specific requests to localize the SMA due to adjacent lesions.

Many postoperative brain tumor studies have shown that the degree of neurologic deficit after tumor resection correlates with the extent of resection of SMA regions.^{9,13} Findings of transient contralateral weakness and transient speech deficits, including mutism (in the case of SMA resection in the dominant hemisphere) after resection or manipulation are well-established in the neurosurgical literature.¹⁴

To date, there are limited studies specifically evaluating the feasibility of rs-fMRI for SMA localization in patients with brain tumors. Vassal et al¹⁵ recently published a study characterizing the pre- and postoperative SMA in 6 patients with brain tumors. With small numbers of subjects however, the effects of intersubject variability are limited; indeed, while early reports of rs-fMRI for preoperative language localization showed promise in a small number of subjects,¹⁶ 2 subsequent independent analyses with larger sample sizes demonstrated a wide range of accuracy across subjects.^{3,17} We therefore aimed to evaluate the utility of rs-fMRI using seed-based analysis in localizing the SMA in a larger cohort of patients with brain tumors. We hypothesized that the SMA can be readily identified using rs-fMRI in patients with brain tumors and is comparable with tb-fMRI.

MATERIALS AND METHODS

Subjects

In this institutional review board–approved retrospective study, 113 patients with brain lesions who underwent preoperative functional MR imaging between May 2012 and June 2016 were identified using the Johns Hopkins Hospital radiology information system. Forty-one patients were excluded due to lack of hand motor tb-fMRI and rs-fMRI performed during the same scanning session. Two patients were excluded due to artifacts. Four patients were excluded due to diagnoses other than brain tumors. After exclusion, data from 66 patients were used for analysis.

Additionally, 21 healthy subjects from the Kirby 21 Multi-Modal Reproducibility Study dataset (F.M. Kirby Center, Kennedy Krieger Institute, Baltimore, Maryland) were included in the study for comparison.¹⁸

Handedness

A laterality index for patients was calculated using the Edinburgh Handedness Inventory questionnaire.¹⁹

Lesion Characterization

Tumor location for each patient was determined from structural MR imaging. The World Health Organization histologic grade was recorded. Lesion volume (in cubic millimeters) was calculated by manual ROI drawing on T2 fluid-attenuated inversion recovery images using the Medical Image Processing, Analysis and Visualization application.²⁰

Image Acquisition

A 3T Trio Tim system (Siemens, Erlanger, Germany) was used with a 12-channel head coil. Structural images included a 3D T1 sequence (TR = 2300 ms, TI = 900 ms, TE = 3.5 ms, flip angle = 9°, FOV = 24 cm, acquisition matrix = 256 × 256 × 176, slice thickness = 1 mm) and a 2D T2 FLAIR sequence (TR = 9310 ms, TI = 2500 ms, TE = 116 ms, flip angle = 141°, FOV = 24 cm, acquisition matrix = 320 × 240 × 50, slice thickness = 3 mm).

2D gradient-echo-planar imaging was used for blood oxygen level–dependent functional imaging (TR = 2000 ms, TE = 30 ms, flip angle = 90°, FOV = 24 cm, acquisition matrix = 64 × 64 × 33, slice thickness = 4 mm, slice gap = 1 mm, interleaved acquisition).

Given brain shifts due to mass lesions, tb-fMRI was performed in the brain tumor patient group to improve localization of the SMA. All patients underwent bilateral sequential finger-tapping tasks, and 50/66 patients additionally underwent a tongue motor task involving repetitive vertical tongue movements because their lesions were more in proximity to the ventral motor region. A block design of a 30-second alternation of task and rest was used for both tasks with 90 volumes acquired.

One hundred eighty volumes were acquired for rs-fMRI (~6 minutes). All patients were instructed to not move, keep their eyes closed, and not to think of anything during the acquisition.

Imaging details for the Kennedy Krieger Institute dataset are previously described.¹⁸

Image Analysis and Processing

fMRI was analyzed using Statistical Parametric Mapping (SPM; (<http://www.fil.ion.ucl.ac.uk/spm/software/spm12>)) as well as custom Matlab (MathWorks, Natick, Massachusetts) scripts.

Both tb-fMRI and rs-fMRI underwent slice-timing correction, motion-correction, coregistration to the T1-weighted images, normalization to the Montreal Neurological Institute-152 template, and spatial smoothing using a 6-mm full width at half maximum Gaussian kernel. For rs-fMRI, additional processing included tagging of outlier volumes based on large shifts in global average signal using the ArtRepair toolbox (<http://cibsr.stanford.edu/tools/human-brain-project/artrepair-software.html>) in SPM²¹ after motion correction, linear detrending, physiologic nuisance regression using CompCor,²² bandpass filtering (0.01–0.1 Hz) after normalization, and finally removal of outlier volumes tagged by ArtRepair (“scrubbing”).

Standard general linear model analysis was used for tb-fMRI with the canonical hemodynamic response function convolved with a boxcar function. No derivatives, global intensity normalization, or confound matrix was used. A 128-second high-pass filter was used. An autoregressive model was used to account for temporal autocorrelations. A design matrix was constructed to detect activation during the active task state compared with rest. SPM T-contrast maps were generated without clustering or multiple comparison correction as is customary for single-subject clinical data at our institution.

Rs-fMRI seed to whole brain voxel analysis was performed to generate the motor network. We placed 10-mm cubic ROIs consistently across subjects in the hand motor and orofacial motor regions of the brain as described below. After extraction of the

mean time-varying signal across time within the ROI, this time course was used to generate Pearson correlation coefficients with time courses of every other voxel, generating a 3D correlation coefficient map across the entire brain:

1) Hand motor functional areas in bilateral brain hemispheres of each subject were determined by identifying the middle of the hand knob (Ω -shaped) of the primary motor cortex within the precentral gyri.

2) Bilateral orofacial motor functional areas were identified in the inferolateral part of the precentral gyrus, superior to the Sylvian fissures, and below the imaginary line from the intersection of the inferior frontal sulcus and precentral sulcus on the sagittal view.

The anatomic coordinates were placed by a neuroradiologist with 3 years of experience following subspecialty training and supervised by a neuroradiologist with 6 years of experience, including in functional brain imaging.

SMA Positive-Connectivity Evaluation

For each patient, 6 whole-brain correlation maps were generated with ROIs in the following areas: 1) the left hand motor region, 2) the right hand motor region, 3) the left orofacial region, 4) the right orofacial region, 5) bilateral hand motor regions, and 6) bilateral orofacial regions. Final correlation maps were registered to the anatomic image to identify areas of functional connectivity with the SMA region. The SMA was defined as the area in the medial portion of the superior frontal gyrus in front of the primary motor cortex and superior to the cingulate sulcus. Its anterior boundary was defined by a line passing perpendicularly through the rostrum of the corpus callosum.²³ Identification of the SMA was evaluated by 2 neuroradiologists with specific expertise in fMRI with consensus. Tb-fMRI was used to localize the SMA for confirmation in the patient group.

Statistical Analysis

The number of cases (as well as the percentage of total cases) in which the SMA was identified from rs-fMRI was recorded and reported for each of the 6 ROI schemes. Considering the dependent design, we used the McNemar χ^2 test to assess differences in positive SMA identification when the ROI went from single to bilateral regions. All analysis was performed in R statistical and computing software (Version 3.2.4; <http://www.r-project.org>).

RESULTS

Subjects

Of the 66 patients, 38 were men and 28 were women, ranging from 18 to 75 years of age (mean, 40.8 ± 14.6 years). For the 21 healthy control subjects, there were 11 men and 10 women, from 25 to 61 years of age (mean, 31.8 ± 9.2 years).

Handedness

By means of the laterality index cutoff points of ± 0.2 (less than -0.2 = left-handedness, >0.2 = right-handedness, and -0.2 – 0.2 = ambidexterity), in the patient group, the laterality index ranged from -0.72 to 1 (mean = 0.696). Sixty-three patients

demonstrated right-handedness, and 3 patients demonstrated left-handedness.

For control patients, on the basis of the Kirby 21 Multi-Modal Reproducibility Study data base, 19 demonstrated right-handedness and 2 subjects demonstrated left-handedness. No laterality index information was available from this dataset.

Lesions

Of 66 patients, 46 had tumors in the left hemisphere (24 involving the left frontal lobe); 18, in the right hemisphere (12 involving the right frontal lobe); 1, in both frontal lobes; and 1 had multiple lesions throughout both hemispheres. In 7 patients, there was direct tumor involvement of the expected region of the SMA (4 on the left and 3 on the right side); in 3 patients, there was involvement of the primary motor cortex.

Fifty-three percent (35/66) of tumors were low-grade gliomas (6 diffuse astrocytomas, 1 fibrillary astrocytoma, 26 oligodendrogliomas, and 2 that had not been histologically confirmed but appeared to be low-grade gliomas on imaging). Forty-two percent (28/66) of the lesions were high-grade gliomas (9 infiltrative astrocytomas, 8 anaplastic astrocytomas, 3 anaplastic oligoastrocytomas, and 8 glioblastomas). The remaining patients were diagnosed with myeloid sarcoma, metastatic melanoma, or metastatic adenocarcinoma. The tumor sizes ranged from 8.4×10^2 to 1.6×10^5 mm³ (mean = $4.3 \times 10^4 \pm 3.7 \times 10^4$ mm³).

The demographics of subjects, location, histopathology, and World Health Organization grading of the lesions are listed in Table 1.

SMA Identification

In both the control and patient groups, the SMA was identified more frequently using seeding location from hand motor areas than from orofacial areas, with use of bilateral ROIs superior to the unilateral right or left motor ROI (Figure and Table 2).

In the patients with brain tumors, the SMA was identified in 50/66 (75.8%) using the left hand motor ROI, 50/66 (75.8%) using the right hand motor ROI, 63/66 (95.5%) using the bilateral hand motor ROIs, 18/66 (27.3%) using the left orofacial ROI, 17/66 (25.8%) using the right orofacial ROI, and 23/66 (34.8%) using the bilateral orofacial ROIs (Table 3). A significant difference was seen between using bilateral hand motor ROIs versus either unilateral hand motor ROI ($P < .001$). In addition, a significant difference was seen between using bilateral hand motor ROIs versus bilateral orofacial ROIs ($P < .001$) (Table 3).

In the control group, the SMA was identified in 34/42 (81.0%) scans using the left hand motor ROI, 38/42 (90.5%) scans using the right hand motor ROI, 40/42 (95.2%) scans using the bilateral hand motor ROIs, 9/42 (21.4%) scans using the left orofacial ROI, 14/42 (33%) scans using the right orofacial ROI, and 19/42 (45.2%) scans using the bilateral orofacial ROIs. While no significant difference was found between unilateral and bilateral ROIs for either hand or orofacial motor ROIs after multiple-comparison correction, there was a significant difference between bilateral hand motor ROIs versus bilateral orofacial ROIs (Table 4).

There was no statistically significant difference in the percentage of positive SMA identification between the group of patients with brain tumor and healthy control subjects (Table 5).

Table 1: Demographic and clinical characteristics of patients and controls

Characteristic	Patients with Brain Tumor (n = 66)	Control Subjects (n = 21)
Age (range) (mean) (yr)	18–75 (40.8 ± 14.6)	25–61 (31.8 ± 9.24)
Sex (No.)		
Male	38	11
Female	28	10
Tumor size (mean) (mm ³)	8.4 × 10 ² to 1.6 × 10 ⁵ (4.3 × 10 ⁴ ± 3.7 × 10 ⁴)	–
Pathology (No.)		–
Diffuse astrocytoma	6	
Fibrillary astrocytoma	1	
Infiltrative astrocytoma	9	
Anaplastic astrocytoma	8	
Glioblastoma	8	
Oligodendroglioma	26	
Anaplastic oligoastrocytoma	3	
Myeloid sarcoma	1	
Metastatic melanoma	1	
Metastatic adenocarcinoma	1	
No pathologic report (low-grade tumor by imaging)	2	
WHO classification (No.)		
Grade I	0	
Grade II	33	
Grade III	20	
Grade IV	8	
Tumor location (No.)		
Right hemisphere	18	
Frontal	12 (3 SMA, 1 PMC)	
Parietal	1	
Temporal	1	
Insular	2	
Frontoparietal	1	
Frontotemporal	1	
Left hemisphere	46	
Frontal	24 (4 SMA, 2 PMC)	
Parietal	3	
Temporal	11	
Insular	4	
Frontoparietal	2	
Frontotemporal	1	
Parietotemporal	1	
Bilateral hemisphere	1	
Multiple lesions	1	

Note:—PMC indicates primary motor cortex.

DISCUSSION

There are operative challenges for brain tumors near the SMA, a functional brain region that is not uniformly anatomically bound according to well-established landmarks in contrast to the primary motor cortex. Resection of the SMA, an area primarily involved in voluntary motor movement,²⁴ can result in motor and language deficits.²⁵ The degree of neurologic deficit corresponds to the extent of resection: Aphasia without motor impairment was seen with anterior SMA resection, likely extending into language-related regions termed “pre-SMA”; and manipulation extending to the posterior SMA was correlated with contralateral paresis, with a small percentage of cases having permanent deficits.¹³ Because of these potential deficits, tb-fMRI has been used to help localize the SMA for operative planning, supplemented with DCS if necessary, though the SMA is often difficult to localize even with DCS.

A recent study using seed-based rs-fMRI was able to demonstrate the SMA in patients with gliomas using seeds placed in the

hand motor region.²⁶ We extended the investigation in a larger cohort of subjects by comparing the accuracy of SMA detection in patients with brain lesions with controls and used different sites of ROI placement, because the hand motor region may not always be feasible for ROI placement depending on the volume and distribution of brain lesions. We demonstrate that the SMA can be identified in both patients with brain tumor and healthy controls using rs-fMRI with seed-based analysis. In a recent study comparing tb-fMRI primary hand motor activation with rs-fMRI using the task-based activation as the seed region for seed-based analysis, the authors reported that the SMA could be identified from the rs-fMRI but not from the tb-fMRI.²⁷ In our study, the seed location was blinded to tb-fMRI, thus representing a possible scenario in which rs-fMRI may be used in isolation without tb-fMRI activation maps.

Between the patients with brain tumor and healthy controls, there was no statistical difference in the rates of SMA detection with the use of hand motor seeding for rs-fMRI. Within the larger cohort of patients with brain tumor, the detection rate of SMA activation was significantly higher when selecting the hand motor region as the seeding area instead of the orofacial motor region. This result indicates stronger correlation between hand motor areas and the SMA compared with the orofacial motor areas. This difference may be due to the variable connectivity of the dorsal-versus-ventral motor systems; indeed, when independent component analysis

is performed, these 2 systems routinely are separated into different components with current acquisition and analysis methods. Underlying differences in dynamic connectivity may drive this phenomenon, with the ventral motor system demonstrating higher homotopic connectivity compared with the dorsal motor system.²⁸ In addition, our study demonstrated higher rates of SMA detection when using seeds from the bilateral hand motor areas compared with the unilateral hand motor areas, conceivably also due to potential differences in dynamic connectivity between the homotopic regions, which, when averaged, result in improved detection of the SMA. While the SMA is known to lateralize with lateralizing tasks, signal from the unilateral ROIs may be less robust to demonstrate the SMA with the standard methods used in our study. Further studies may investigate whether incorporating dynamic connectivity can improve SMA detection, as well as determine whether the SMA may be lateralized

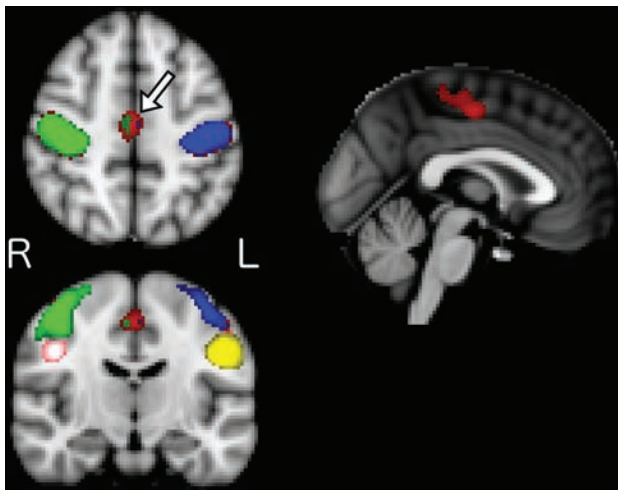


FIGURE. Mean group correlation maps across different seed locations for patients with brain tumor (bilateral hand motor seed in red, left hand motor in blue, right hand motor in green, left tongue motor in yellow, and right tongue motor in pink; please note that left and right denote the cerebral hemisphere of the seeds and thus represent contralateral functional regions). The greatest correlation in the supplementary motor area (arrow on the axial image) is seen with bilateral hand motor seeds. To a much lesser extent in this group visualization, left hand and right hand motor seeds demonstrate correlation in the SMA; however, neither tongue motor seed does so. R indicates right; L, left.

Table 2: Number of cases with identifiable SMA by seeding areas

ROI	Patient		Control	
	+SMA (No.) (%)	-SMA (No.) (%)	+SMA (No.) (%)	-SMA (No.) (%)
Hand (right)	50 (75.8)	16 (24.2)	38 (90.5)	4 (9.5)
Hand (left)	50 (75.8)	16 (24.2)	34 (81.0)	8 (19.0)
Hand (both)	63 (95.5)	3 (4.5)	40 (95.2)	2 (4.8)
Orofacial (right)	17 (25.8)	49 (74.2)	14 (33.3)	28 (66.7)
Orofacial (left)	18 (27.3)	48 (72.7)	9 (21.4)	33 (78.6)
Orofacial (both)	23 (34.8)	43 (65.2)	19 (45.2)	23 (54.8)

Note:—+SMA indicates that the SMA was identified; -SMA, the SMA was not identified.

Table 3: Identifiable SMA percentages compared across ROIs in patients with brain tumor

Target Group	Percentage Identified (95% CI)	Reference Group		P Value ^a
		Percentage Identified (95% CI)	P	
Hand		Hand (both)		
Hand (right)	75.8 (63.4–85.1)	95.5 (86.4–98.8)		<.001 ^b
Hand (left)	75.8 (63.4–85.1)	95.5 (86.4–98.8)		<.001 ^b
Orofacial		Orofacial (both)		
Orofacial (right)	25.8 (16.1–38.2)	34.8 (23.8–47.7)		.074
Orofacial (left)	27.3 (17.4–39.8)	34.8 (23.8–47.7)		.041
Hand (both)	95.5 (86.4–98.8)	34.8 (23.8–47.7)		<.001 ^b

^a From the McNemar χ^2 test.

^b Significant.

using unilateral ROIs with improved scanning, processing, and analysis methods.

Regarding various rs-fMRI techniques, prior studies have demonstrated high correspondence in overall connectivity results between seed-based analysis and independent component analysis methods.²⁹ Seed-based analysis requires a priori selection of ROIs, which can be somewhat challenging and may slightly differ

Table 4: Identifiable SMA percentages compared across ROIs in the control group

Target Group	Percentage Identified (95% CI)	Reference Group		P Value ^a
		Percentage Identified (95% CI)	P	
Hand		Hand (both)		
Hand (right)	90.5 (76.4–96.9)	95.2 (82.6–99.2)		.480
Hand (left)	81.0 (65.4–90.8)	95.2 (82.6–99.2)		.041
Orofacial		Orofacial (both)		
Orofacial (right)	33.3 (20.0–49.6)	45.2 (30.2–61.2)		.074
Orofacial (left)	21.4 (10.8–37.2)	45.2 (30.2–61.2)		.004 ^b
Hand (both)	95.2 (82.6–99.2)	45.2 (30.2–61.2)		<.001 ^b

^a From the McNemar χ^2 test.

^b Significant.

Table 5: Number of cases with identifiable SMA across ROIs, control vs brain tumor group

	SMA Identified (No.) (%)		P Value ^a
	Control	Brain Tumor	
Total	42 (100.0)	66 (100.0)	
Hand (right)	38 (90.5)	50 (75.8)	.055
Hand (left)	34 (81.0)	50 (75.8)	.527
Hand (both)	40 (95.2)	63 (95.5)	1.000
Orofacial (right)	14 (33.3)	17 (25.8)	.513
Orofacial (left)	9 (21.4)	18 (27.3)	.649
Orofacial (both)	19 (45.2)	23 (34.8)	.315

^a Fisher exact test.

between study protocols. In particular, brain shifts or gyral expansion in patients with large brain tumors may cause a large amount of distortion that precludes accurate placement of seed ROIs. Independent component analysis overcomes this specific problem; however, identification of specific network subcomponents may be limited due to the number of targeted independent component analysis components. This may be the limiting factor in another study in which the SMA was inconsistently found using independent component analysis, which was thought to be due to network fragmentation related to independent component analysis order.¹¹ Our approach demonstrates that despite possible mass effect, the SMA can be readily identified in nearly all patients using well-known anatomic landmarks that are not in the immediate vicinity of the area of interest. The question of SMA localization for operative planning is relevant when tumors are within or adjacent to the expected location of the SMA. Therefore, in most cases, the primary motor cortex may still be effectively used for ROI placement as shown in this study.

There are several limitations to our study, one being that findings were not compared directly with the criterion standard of direct cortical stimulation. However, SMA evaluation using DCS is more challenging compared with evaluation of the primary motor regions; indeed, at our institution, neurosurgical requests for primary motor function localization using fMRI are far less common compared with requests for SMA localization, due to the difficulty of obtaining accurate results for the latter using DCS. For identification of the SMA, no independent assessment was performed between the 2 neuroradiologists, and consensus evaluation was used. In addition, no quantitative analysis was performed; while there have been attempts to standardize thresholding of fMRI (eg, using a percentage of the maximum local

signal),³⁰ there are no current established standards. Our qualitative method, however, actually represents a more real-world scenario, in which localization and thresholding of the SMA in tb-fMRI are performed using clinical judgment. Finally, the images of the patients with brain tumor were acquired on different scanners than for the healthy controls, potentially introducing scanner variability as a confounder in our results.

CONCLUSIONS

We demonstrate that rs-fMRI can be reliably used to identify the SMA in most patients with brain tumors, to the same degree as subjects with no brain lesions. We also demonstrate that the use of bilateral hand motor regions for seed placement is superior in identifying the SMA compared with unilateral hand motor or orofacial motor region seeding.

Disclosures: Jay J. Pillai—UNRELATED: Royalties: Springer Science & Business Media, Elsevier, Comments: royalty for books.

REFERENCES

- Ojemann G, Ojemann J, Lettich E, et al. **Cortical language localization in left, dominant hemisphere: an electrical stimulation mapping investigation in 117 patients. 1989.** *J Neurosurg* 2008;108:411–21 CrossRef Medline
- Matthews PM, Honey GD, Bullmore ET. **Applications of fMRI in translational medicine and clinical practice.** *Nat Rev Neurosci* 2006;7:732–44 CrossRef Medline
- Sair HI, Yahyavi-Firouz-Abadi N, Calhoun VD, et al. **Presurgical brain mapping of the language network in patients with brain tumors using resting-state fMRI: Comparison with task fMRI.** *Hum Brain Mapp* 2016;37:913–23 CrossRef Medline
- Schneider FC, Pailler M, Faillenot I, et al. **Presurgical assessment of the sensorimotor cortex using resting-state fMRI.** *AJNR Am J Neuroradiol* 2016;37:101–07 CrossRef Medline
- Branco P, Seixas D, Deprez S, et al. **Resting-state functional magnetic resonance imaging for language preoperative planning.** *Front Hum Neurosci* 2016;10:11 CrossRef Medline
- Bizzi A, Blasi V, Falini A, et al. **Presurgical functional MR imaging of language and motor functions: validation with intraoperative electrocortical mapping.** *Radiology* 2008;248:579–89 CrossRef Medline
- Biswal B, Yetkin FZ, Haughton VM, et al. **Functional connectivity in the motor cortex of resting human brain using echo-planar MRI.** *Magn Reson Med* 1995;34:537–41 CrossRef Medline
- Palanca BJ, Mitra A, Larson-Prior L, et al. **Resting-state functional magnetic resonance imaging correlates of sevoflurane-induced unconsciousness.** *Anesthesiology* 2015;123:346–56 CrossRef Medline
- Sämman PG, Wehrle R, Hoehn D, et al. **Development of the brain's default mode network from wakefulness to slow wave sleep.** *Cereb Cortex* 2011;21:2082–93 CrossRef Medline
- Dierker D, Roland JL, Kamran M, et al. **Resting-state functional magnetic resonance imaging in presurgical functional mapping: sensorimotor localization.** *Neuroimaging Clin N Am* 2017;27:621–33 CrossRef Medline
- Kokkonen SM, Nikkinen J, Remes J, et al. **Preoperative localization of the sensorimotor area using independent component analysis of resting-state fMRI.** *Magn Reson Imaging* 2009;27:733–40 CrossRef Medline
- Liu H, Buckner RL, Talukdar T, et al. **Task-free presurgical mapping using functional magnetic resonance imaging intrinsic activity.** *J Neurosurg* 2009;111:746–54 CrossRef Medline
- Fontaine D, Capelle L, Duffau H. **Somatotopy of the supplementary motor area: evidence from correlation of the extent of surgical resection with the clinical patterns of deficit.** *Neurosurgery* 2002;50:297–303, discussion 303–05 Medline
- Russell SM, Kelly PJ. **Incidence and clinical evolution of postoperative deficits after volumetric stereotactic resection of glial neoplasms involving the supplementary motor area.** *Neurosurgery* 2003;52:506–16; discussion 515–16 CrossRef Medline
- Vassal M, Charroud C, Deverduin J, et al. **Recovery of functional connectivity of the sensorimotor network after surgery for diffuse low-grade gliomas involving the supplementary motor area.** *J Neurosurg* 2017;126:1181–90 CrossRef Medline
- Mitchell TJ, Hacker CD, Breshears JD, et al. **A novel data-driven approach to preoperative mapping of functional cortex using resting-state functional magnetic resonance imaging.** *Neurosurgery* 2013;73:969–82, discussion 982–83 CrossRef Medline
- Cochereau J, Deverduin J, Herbet G, et al. **Comparison between resting state fMRI networks and responsive cortical stimulations in glioma patients.** *Hum Brain Mapp* 2016;37:3721–32 CrossRef Medline
- Landman BA, Huang AJ, Gifford A, et al. **Multi-parametric neuroimaging reproducibility: a 3-T resource study.** *Neuroimage* 2011;54:2854–66 CrossRef Medline
- Oldfield RC. **The assessment and analysis of handedness: the Edinburgh inventory.** *Neuropsychologia* 1971;9:97–113 CrossRef Medline
- McAuliffe MJ, Lalonde FM, McGarry D, et al. **Medical image processing, analysis and visualization in clinical research.** In: *Proceedings of the IEEE Symposium on Computer-Based Medical Systems*, Bethesda, Maryland. July 26–27, 2001:381–86
- Mazaika PK, Fumiko H, Glover GH, et al. **Methods and software for fMRI analysis for clinical subjects.** In: *Proceedings of the Annual Meeting of the Organization for Human Brain Mapping*, San Francisco, California; June 15, 2009
- Behzadi Y, Restom K, Liau J, et al. **A component based noise correction method (CompCor) for BOLD and perfusion based fMRI.** *Neuroimage* 2007;37:90–101 CrossRef Medline
- Chauvel PY, Rey M, Buser P, et al. **What stimulation of the supplementary motor area in humans tells about its functional organization.** *Adv Neurol* 1996;70:199–209 Medline
- Fried I. **Electrical stimulation of the supplementary sensorimotor area.** *Adv Neurol* 1996;70:177–85 Medline
- Ibe Y, Tosaka M, Horiguchi K, et al. **Resection extent of the supplementary motor area and post-operative neurological deficits in glioma surgery.** *Br J Neurosurg* 2016;30:323–29 CrossRef Medline
- Qiu TM, Yan CG, Tang WJ, et al. **Localizing hand motor area using resting-state fMRI: validated with direct cortical stimulation.** *Acta Neurochir (Wien)* 2014;156:2295–302 CrossRef Medline
- Hou BL, Bhatia S, Carpenter JS. **Quantitative comparisons on hand motor functional areas determined by resting state and task BOLD fMRI and anatomical MRI for pre-surgical planning of patients with brain tumors.** *Neuroimage Clin* 2016;11:378–87 CrossRef Medline
- Syed MF, Lindquist M, Pillai JJ, et al. **Dynamic functional connectivity states between the dorsal and ventral sensorimotor networks revealed by dynamic conditional correlation analysis of resting state functional magnetic resonance imaging.** *Brain Connect* 2017;7:635–42 CrossRef Medline
- Rosazza C, Minati L, Ghielmetti F, et al. **Functional connectivity during resting-state functional MR imaging: study of the correspondence between independent component analysis and region-of-interest-based methods.** *AJNR Am J Neuroradiol* 2012;33:180–87 CrossRef Medline
- Voyvodic JT. **Reproducibility of single-subject fMRI language mapping with AMPLE normalization.** *J Magn Reson Imaging* 2012;36:569–80 CrossRef Medline

Application of Reduced-FOV Diffusion-Weighted Imaging in Evaluation of Normal Pituitary Glands and Pituitary Macroadenomas

M. Wang, H. Liu, X. Wei, C. Liu, T. Liang, X. Zhang, C. Jin, X. Li, Q. Sun, H. Jiang, and J. Yang



ABSTRACT

BACKGROUND AND PURPOSE: FOV optimized and constrained undistorted single-shot imaging provides relatively high-resolution images with few artifacts. This study evaluated the image quality and value of FOV optimized and constrained undistorted single-shot DWI in the evaluation of normal pituitary glands and pituitary macroadenomas.

MATERIALS AND METHODS: Subjects with normal pituitary glands and patients with pituitary macroadenomas underwent FOV optimized and constrained undistorted single-shot and EPI DWI. Two neuroradiologists graded the image quality based on visualization of the pituitary stalk, pituitary gland, and pituitary macroadenoma. Intra- and interobserver agreements were assessed by κ statistics. Image quality and ADCs were compared between the 2 methods by the paired Wilcoxon signed rank test and *t* test. Differences in ADC between normal pituitary glands and macroadenomas were analyzed by the independent-samples *t* test.

RESULTS: Twenty-eight subjects with normal pituitary glands and 16 patients with macroadenomas were enrolled. Intra- and interobserver agreements for image-quality assessment were moderate to substantial. Relative to EPI DWI, FOV optimized and constrained undistorted single-shot DWI exhibited obviously better image quality both in normal pituitary glands and macroadenomas. There was no significant difference in ADCs of macroadenomas between the 2 methods. Macroadenomas with soft consistency ($0.75 \pm 0.14 \times 10^{-3} \text{ mm}^2/\text{s}$) had significantly lower mean ADC than normal pituitary glands ($1.18 \pm 0.19 \times 10^{-3} \text{ mm}^2/\text{s}$; $P < .001$).

CONCLUSIONS: FOV optimized and constrained undistorted single-shot DWI helps acquire high-resolution images of normal pituitary glands and pituitary macroadenomas with relatively few susceptibility artifacts in a clinically feasible scan time. This sequence might be helpful for evaluating the consistency of pituitary macroadenomas.

ABBREVIATION: FOCUS = FOV optimized and constrained undistorted single-shot

Diffusion-weighted imaging can not only help detect pituitary apoplexy and differentiate pituitary mass lesions but can also help assess the consistency of pituitary macroadenomas, evaluate the diffusivity of normal pituitary glands, and predict the success of surgical treatment.¹⁻⁵ It contributes to deciding the best surgical strategy and reducing postoperative complications. The most

widely used DWI technique is EPI DWI, which has limitations such as low spatial resolution, strong susceptibility artifacts, and distortion due to eddy currents, especially in the sellar region.⁶ Consequently, this sequence has limited application and can provide valuable information only for large tumors. Previous studies have attempted to use various diffusion sequences, such as line scan,⁷ readout segmentation of long variable echo trains,⁸ BLADE (Siemens, Erlangen, Germany), and PROPELLER,^{5,9-11} to overcome issues related to artifacts and image degradation and to analyze the diffusivities of tumors. However, at present, there is only experiential knowledge regarding the relationship between normal pituitary glands and pituitary adenomas, which shows that pituitary adenomas are often soft and white in contrast to the more firm, orange-yellow anterior pituitary

Received August 31, 2017; accepted after revision April 13, 2018.

From the Department of Diagnostic Radiology (M.M.W., H.L., X.C.W., C.C.L., T.L., X.H.Z., C.J., X.J.L., Q.L.S., H.X.J., J.Y.), the First Affiliated Hospital, and Department of Biomedical Engineering (H.L., T.L., Q.L.S., H.X.J., J.Y.), the Key Laboratory of Biomedical Information Engineering of the Ministry of Education, School of Life Science and Technology, Xi'an Jiaotong University, Xi'an, China.

This work was supported by a grant from the National Natural Science Foundation of China (No. 81171317, 81471631, 81771810), the National Key Research and Development Program of China (2016YFC0100300), the 2011 New Century Excellent Talent Support Plan from the Ministry of Education of China (NCET-11-0438), and the Clinical Research Award of the First Affiliated Hospital of Xi'an Jiaotong University (XJTUIAF-CRF-2015-004).

Please address correspondence to Jian Yang, PhD, Department of Diagnostic Radiology, the First Affiliated Hospital, Xi'an Jiaotong University, Xi'an, Shaanxi, China; e-mail: yj1118@mail.xjtu.edu.cn

Indicates open access to non-subscribers at www.ajnr.org

Indicates article with supplemental on-line table.

Indicates article with supplemental on-line photo.

<http://dx.doi.org/10.3174/ajnr.A5735>

tissue.¹² Because of inadequate image quality in the sellar region, the diffusion characteristics of these 2 tissues have not been fully elucidated.

Recently, FOV optimized and constrained undistorted single-shot (FOCUS; GE Healthcare, Milwaukee, Wisconsin) DWI has been reported to have superior performance in the evaluation of the spine,¹³ neck tumors,¹⁴ pancreas,¹⁵ breast,¹⁶ and prostate.¹⁷ This improved small-FOV sequence uses a 90° 2D spatially selective radiofrequency pulse and a 180° refocusing pulse. The 2D radiofrequency pulse excites only a limited extent of tissue along the phase-encoding direction in the target slice, resulting in a multislice and restrained FOV excitation without introducing aliasing artifacts. This technique not only enables a reduced number of *k*-space lines in the phase-encoding direction but also provides a higher resolution for a fixed scan time. Additionally, the reduced FOV decreases the readout duration needed for imaging to reduce off-resonance-induced artifacts.^{13,18} To the best of our knowledge, the application of FOCUS DWI for the evaluation of normal pituitary glands and pituitary macroadenomas has not been reported to date. The purpose of this study was to evaluate the image quality and value of FOCUS DWI in the evaluation of normal pituitary glands and pituitary macroadenomas.

MATERIALS AND METHODS

This study was conducted with approval from the involved institutional review boards of the First Affiliated Hospital of Xi'an Jiaotong University.

Subjects

Between December 2016 and January 2018, subjects with normal pituitary glands and patients with preoperative pituitary macroadenomas were enrolled in this study. All participants were imaged by FOCUS and EPI DWI in succession. Subjects in the normal pituitary gland group who underwent brain MR imaging examinations for the evaluation of headache or dizziness were eligible for inclusion if they met the following conditions: 1) at least 20 years of age; 2) no abnormalities of the pituitary gland on conventional MR imaging and DWI sequences; 3) no history of pituitary, sellar, or hypothalamus diseases; 4) no history of endocrine medication; 5) no suspected or diagnosed hormonal imbalance within 1 year; and 6) no history of central nervous system tumor, skull trauma, operation, radiation, or chemotherapy. The exclusion criteria were as follows: 1) breast diseases, 2) lung cancer, and 3) artifacts caused by oral implants. Patients with pituitary macroadenomas were enrolled in accordance with the following criteria: 1) lesion size >10 mm on MR images, and 2) diagnosis confirmed by pathologic and immunohistochemical examination. Patients with any preoperative treatment were excluded, as were subjects with incomplete MR imaging data.

MR Imaging

All MR images were acquired using a 3T system (Discovery 750w; GE Healthcare) with a 24-channel head coil. Pituitary MR imaging was performed using the following routine sequences: sagittal and coronal T1WI (TR/TE = 400 ms/minimum, FOV = 20 cm,

Table 1: Imaging parameters for DWI sequences

	FOCUS DWI	EPI DWI
TR (ms)	2200	2200
TE (ms)	Minimum	Minimum
B-value (s/mm ²)	0, 500	0, 500
Diffusion directions	All	All
Frequency-encoding direction	S/I	S/I
FOV (cm)	16 × 4.8	24 × 24
Matrix size	128 × 38	160 × 160
NEX for B ₀	4	4
NEX for b=500	12	12
Slice thickness (mm)	2.0	2.0
Intersection gap (mm)	0	0
Spatial resolution (mm ³)	1.25 × 1.26 × 2	1.5 × 1.5 × 2
Acquisition time (min:s)	01:30	01:30

Note:—S/I indicates superior/inferior.

slice thickness = 2 mm without intersection gap) and sagittal and coronal T2WI (TR/TE = 3880/128 ms, FOV = 18 cm, slice thickness = 2 mm without intersection gap). In 12 patients, enhanced coronal T1WI was acquired after injection of 0.2 mmol/kg of contrast medium (Gd-DTPA, Magnevist; Bayer HealthCare Pharmaceuticals, Wayne, New Jersey). Before Gd-DTPA administration, FOCUS and EPI DWI were acquired in the coronal plane. Image-acquisition parameters are presented in Table 1.

Image Analysis

Assessment of Image Quality. The MR images were anonymized and reviewed with the same window widths and levels on the same workstation. Two experienced neuroradiologists independently reviewed coronal images (*b* = 500 s/mm²) acquired using FOCUS and EPI sequences and evaluated their image quality with reference to coronal T1WI. On the basis of the degrees of susceptibility artifacts and spatial distortion as well as the quality of anatomic details displayed, image quality was scored from 0 to 4 for normal pituitary glands and 0 to 5 for pituitary macroadenomas (Table 2). Two months after initial review, the MR images were reviewed again by one of the observers.

Measurement of ADC Values. All image analyses for ADC mapping were performed on the ADW4.6 workstation (GE Healthcare). For ADC calculation, ROIs were drawn on MR images (*b* = 500 s/mm²) by one of the observers and cross-referenced with the anatomic structures on T1WI. In the normal pituitary gland group, ROIs (10–15 mm²) were placed on the anterior lobe of the pituitary gland. In the macroadenoma group, ROIs (20–30 mm²) were placed on regions with a solid appearance, taking care to avoid cysts, hemorrhages, blood vessels, and areas with visible image distortion/signal loss. To minimize bias, we measured each area 3 times and calculated the average ADCs.

Statistical Analysis

Statistical analysis was performed using SPSS 18.0 (IBM, Armonk, New York). The Wilcoxon signed rank test and χ^2 test were performed to compare the age and sex between the normal pituitary gland and macroadenoma groups. Intra- and interobserver agreements were assessed using κ statistics, with the level of agreement indicated as follows: poor, κ = 0.00–0.20; slight, κ = 0.21–0.40; moderate, κ = 0.41–0.60; substantial, κ = 0.61–0.80; and almost perfect, κ = 0.81–1.00. Disagreements regarding imaging find-

ings were resolved by discussion and agreement. The paired Wilcoxon signed rank test and *t* test were used for comparison of image quality and ADCs between FOCUS and EPI DWI. Differences in ADCs between normal pituitary glands and macroadenomas were analyzed using the independent-samples *t* test. *P* < .05 was considered statistically significant.

RESULTS

Of 56 participants (34 subjects in the normal pituitary gland group and 22 patients in the macroadenoma group) reviewed, 28 subjects with normal pituitary glands (11 men and 17 women; age range, 22–79 years; median age, 40 years) and 16 patients with macroadenomas (8 men and 8 women; age range, 20–73 years; median age, 48 years) were included. In the normal pituitary

gland group, 6 subjects were excluded with breast diseases (*n* = 1), lung cancer (*n* = 3), and artifacts caused by oral implants (*n* = 2). Six patients in the macroadenoma group with preoperative treatment (*n* = 4) and incomplete MR imaging data (*n* = 2) were also excluded. There were no significant differences in age (*P* = .15) and sex (*P* = .49) between the 2 groups. Among the 16 patients, 13 had nonfunctional macroadenomas, 2 had prolactin-producing macroadenomas, and 1 patient had a growth-hormone-producing macroadenoma. All tumors were amenable to resection with the direct endoscopic transsphenoidal technique, and an operation of nonfunctional macroadenomas was undergone due to compression symptoms. With H&E staining of the specimens, the extracellular matrix (mainly composed of collagen) of each tumor was found to account for <5% of the entire area of stained tissue; consequently, all macroadenomas were considered of soft consistency.

Table 2: Evaluation indexes of DWI

Score	Criteria
Normal pituitary gland	
0	Pronounced artifacts; pituitary stalk and gland cannot be recognized
1	Considerable artifacts; the stalk is visible, but the gland cannot be recognized
2	Pituitary stalk and gland are visible, with moderate-to-obvious image distortion and/or most of the pituitary gland (>50%) exhibiting signal loss
3	Pituitary stalk and gland are distinctly visible, with mild image distortion and/or <50% of the pituitary gland exhibiting signal loss
4	Visualization of pituitary stalk and gland is as clear as that on T1WI
Pituitary macroadenoma	
0	Pronounced artifacts; adenoma cannot be recognized
1	Considerable artifacts; adenoma is visible, with or without most of the adenoma (>50%) exhibiting signal loss
2	Adenoma is visible, with obvious image distortion and with or without nearly half of the adenoma (25%–50%) exhibiting signal loss
3	Adenoma is distinctly visible; moderate image distortion, with or without <25% of the adenoma exhibiting signal loss
4	Adenoma is distinctly visible, with only mild image distortion
5	Visualization of adenoma is as clear as that on T1WI

Comparison of Image Quality between FOCUS and EPI DWI

The intraobserver agreement for image quality was substantial for both normal pituitary glands ($\kappa = 0.79, P < .001$) and pituitary macroadenomas ($\kappa = 0.74, P < .001$). The interobserver agreement was moderate to substantial for both normal pituitary glands ($\kappa = 0.61, P < .001$) and pituitary macroadenomas ($\kappa = 0.57, P < .001$).

The image-quality scores of the 2 sequences are presented in Figs 1 and 2. Images acquired using the FOCUS sequence showed no or minimal degrees of artifacts and distortion, a finding significantly better than the performance of EPI in both normal pituitary glands (median score: 3 versus 2; *P* < .001) and macroadenomas (median score: 4 versus 3; *P* < .001).

Measurement of ADC in Normal Pituitary Glands and Pituitary Macroadenomas

While FOCUS DWI provided images without obvious distortion in 24 subjects with normal pituitary glands and all patients, images acquired by EPI DWI failed ADC measurement in 25 subjects in the normal pituitary gland group and 1 patient in the macroadenoma group because of unidentifiable anatomic structures caused by severe image degradation and artifacts. In FOCUS DWI, the mean ADC of the anterior lobe of normal pituitary glands was $1.18 \pm 0.19 \times 10^{-3} \text{ mm}^2/\text{s}$ (range, 0.83×10^{-3} to $1.49 \times 10^{-3} \text{ mm}^2/\text{s}$). In pituitary macroadenomas, ADCs measured in FOCUS and EPI DWI were $0.75 \pm$

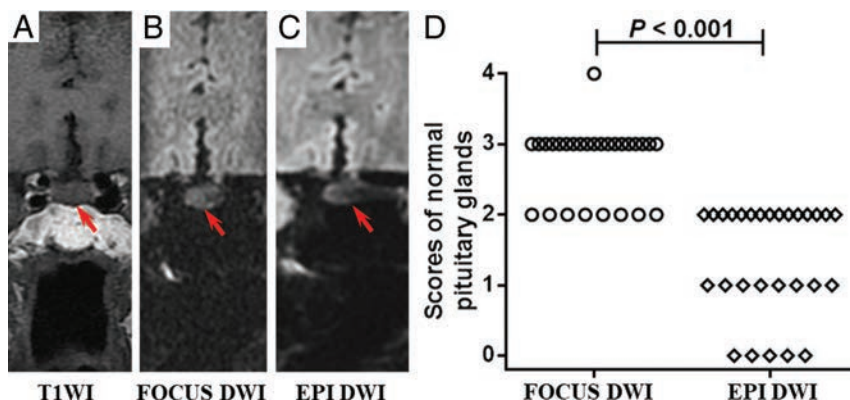


FIG 1. A–C, Images of a 68-year-old woman with dizziness for 1 week. The pituitary gland has a score of 3 for FOCUS DWI and 2 for EPI DWI, respectively (red arrow indicates the pituitary gland). The mean ADC value of the FOCUS DWI measurement is $1.19 \times 10^{-3} \text{ mm}^2/\text{s}$. D, The image-quality scores of normal pituitary glands between the 2 methods are statistically significant (*P* < .001). The number of subjects for each score in FOCUS and EPI DWI sequences is shown in the On-line Table.

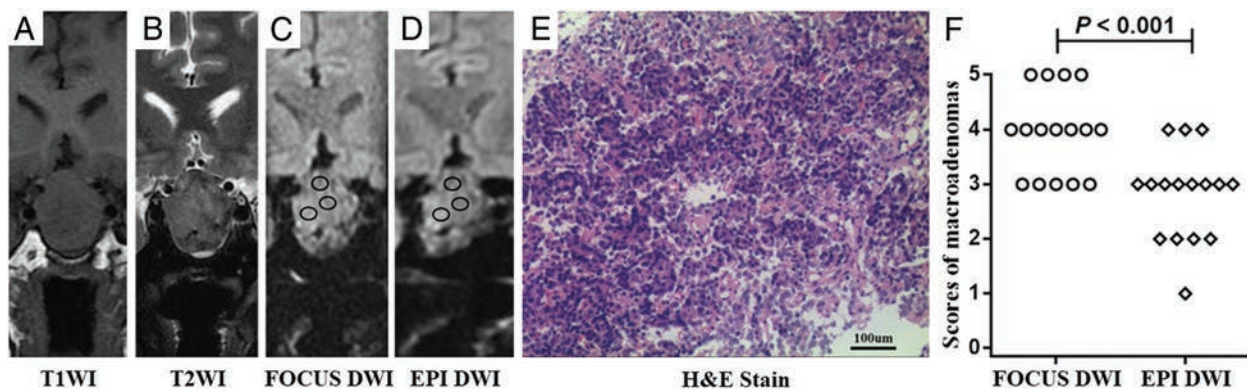


FIG 2. A–D, Images of a 51-year-old man with immunohistochemical staining–proved nonfunctional adenoma. The scores of the macroadenoma in FOCUS and EPI DWI are 4 and 3, respectively (black circles indicate the ROIs of ADC measurements). The mean ADC values of the FOCUS and EPI DWI measurements are $0.66 \times 10^{-3} \text{ mm}^2/\text{s}$ and $0.80 \times 10^{-3} \text{ mm}^2/\text{s}$, respectively. E, A specimen of the mass at histologic examination (H&E stain; original magnification, $\times 200$) shows plenty of small cells (blue) with scant fibrous stroma (deep pink). F, The image-quality scores of macroadenomas between 2 methods are statistically significant ($P < .001$). The number of patients for each score in FOCUS and EPI DWI sequences is shown in the On-line Table.

$0.14 \times 10^{-3} \text{ mm}^2/\text{s}$ (range, 0.54×10^{-3} to $0.99 \times 10^{-3} \text{ mm}^2/\text{s}$) and $0.77 \pm 0.18 \times 10^{-3} \text{ mm}^2/\text{s}$ (range, 0.53×10^{-3} to $1.11 \times 10^{-3} \text{ mm}^2/\text{s}$), respectively. There was no significant difference in mean tumor ADC between the 2 methods ($P = .45$). The ADC measurements of the 2 methods based on individuals are shown in the On-line Figure. Furthermore, in the FOCUS DWI, the mean ADC of the pituitary macroadenomas ($0.75 \pm 0.14 \times 10^{-3} \text{ mm}^2/\text{s}$) was significantly lower than that of the anterior lobe of the normal pituitary glands ($1.18 \pm 0.19 \times 10^{-3} \text{ mm}^2/\text{s}$; $P < .001$).

DISCUSSION

This study demonstrated that FOCUS DWI enables acquisition of high-resolution images of both normal pituitary glands and pituitary macroadenomas with fewer artifacts and less distortion than EPI DWI. In terms of quantitative findings, although both imaging sequences provided generally comparable ADCs of macroadenomas, the diffusivity distribution of macroadenomas with soft consistency was lower than that of the anterior lobe of normal pituitary glands in the present study population.

Conventional single-shot EPI is the most commonly used DWI technique in routine clinical practice. However, because of its vulnerability to the off-resonance effect, it has a severely limited capability for imaging the sellar region. Because the pituitary gland is surrounded by the sphenoid sinus and cavernous sinuses, the presence of a series of air-tissue interfaces in this area alters the local magnetic field, resulting in B_0 -related artifacts.^{3,11} The presence of heterogeneities finally leads to signal pile-up and image distortion and renders small lesions and normal structures unrecognizable, especially in case of structures located near the skull base.¹¹ Taking all these factors into account, the present study used semiquantitative indexes for qualitative assessment, which proved to be highly feasible and exhibited good repeatability. In the present study, EPI DWI showed greater degrees of obvious artifacts, geometric distortion, and signal loss than FOCUS DWI. All these factors serve to severely degrade the quality of overall visualization of anatomic structures and abnormalities, thus decreasing the accuracy of ADC measurement as well as the value of

an auxiliary diagnosis. Both imaging protocols in the present study used the same TRs, b-values, slice thicknesses, and NEX, but not the same FOV. This is because a FOV of 24 cm for EPI DWI can include all tissues along the phase-encoding direction, which aims to avoid aliasing artifacts. For FOCUS DWI, there are 2 reasons for us to choose 16 cm instead of 24 cm in the frequency-encoding direction. First, a smaller FOV is achievable for FOCUS but not for EPI, which makes higher spatial resolution easier. Second, it takes fewer steps to encode a smaller FOV, and this would further benefit the image-distortion control. As a result, only FOCUS DWI demonstrated the ability to acquire images of high spatial resolution and less distortion, while maintaining a clinically feasible scan time.

On DWI, differences in signal intensity and contrast between different tissues depend on the b-values. To date, no study has suggested the optimal b-value for evaluation of the normal pituitary gland and pituitary diseases. It is common knowledge that MR signal intensity and the SNR of DWI decrease with an increase in b-values.¹⁹ Previous pituitary studies mainly used a b-value of 1000 s/mm^2 and a slice thickness ranging from 3 to 6 mm, with varying degrees of intersection gap.^{3,7,10,20} After a careful trade-off among imaging parameters such as b-value, slice thickness, and spatial resolution, we finally chose a b-value of 500 s/mm^2 for FOCUS DWI in the present study.

Among the DWI techniques that can reduce the susceptibility artifacts of the sellar region, the scanning time for FOCUS DWI (1 minute 30 seconds) is shorter than those for line scan (1 minute 57 seconds to 3 minutes 15 seconds)⁷ and the readout segmentation of long variable echo trains (3 minutes 28 seconds)⁸ in similar slice thicknesses and/or in-plane resolutions. For the advanced 3D diffusion-sensitized driven-equilibrium turbo field-echo sequence (5 minutes 22 seconds)⁴ and BLADE/PROPELLER (5 minutes 51 seconds),¹¹ a relatively long acquisition time is needed to significantly reduce and even remove the susceptibility-related signal loss and image distortion. Their scanning time is >3 times longer than that of FOCUS DWI. Thus, FOCUS DWI can acquire high-quality images in a relatively short time, which not only

boosts patient throughput but also minimizes the possibility of patient motion during scanning.

The mean ADC of the anterior lobe of the normal pituitary glands in the present study ($1.18 \pm 0.19 \times 10^{-3} \text{ mm}^2/\text{s}$) is in agreement with the values reported by Hiwatashi et al.⁴ As speculated by these authors, lack of myelination and hypervascularity might contribute to diffusivity. Despite the resolution of FOCUS DWI ($1.25 \times 1.26 \times 2 \text{ mm}^3$) being slightly higher than that reported for diffusion-sensitized driven-equilibrium turbo field echo imaging ($1.5 \times 1.5 \times 1.5 \text{ mm}^3$),⁴ it is still difficult to evaluate the diffusivity of the posterior lobe of the pituitary gland. In addition, in the present study, the difference between average ADC values of the 2 sequences in the soft macroadenoma group was not significant. This finding is consistent with the results reported by studies on the spinal cord,²¹ prostate cancer,¹⁷ and the pancreas.¹⁵ In contrast, some studies on breast cancer have found that the lower ADC of reduced-FOV DWI relative to that of EPI DWI is attributable to the decreased partial volume effect between tumors and surrounding healthy tissues.^{16,22} In case of macroadenomas accompanied by severe displacement and compression of the normal pituitary glands, both sequences would measure the same bulk tumor, and regardless of resolution, the bulk tumor would be presumed to have the same mean ADC. When individual values were examined, the ADC measurements of the 2 DWI sequences were also consistent. Furthermore, the present diffusion results revealed that the ADC of soft pituitary macroadenomas ($0.75 \pm 0.14 \times 10^{-3} \text{ mm}^2/\text{s}$) was significantly lower than that of the anterior lobe of normal pituitary glands ($1.18 \pm 0.19 \times 10^{-3} \text{ mm}^2/\text{s}$). To our knowledge, only 1 study to date has evaluated both pituitary adenomas and pituitary glands simultaneously; the authors reported no significant difference in ADC between pituitary adenomas and the unaffected anterior lobe of the pituitary glands.²³ This discrepancy could be because the authors focused only on differences between different functional adenomas and pituitary glands, without considering tumor consistency. The present study included surgically and pathologically confirmed macroadenomas with soft consistency. Possible explanations for the low ADC of soft macroadenomas include an increase in cellularity, reduction in extracellular space, and the presence of cytoplasmic content with a relatively high nucleus-to-cytoplasm ratio.²⁴ Besides, a pathologic study has proved that tumor cells form irregular sheets or masses and contain larger and more uniform nuclei than normal pituitary tissues.²⁵ Moreover, low expression levels of laminin, fibronectin, reticulin, and type IV collagen in adenomatous pituitary tissues might also contribute to the low ADC.^{3,26} Our results appeared to be discordant with the study of Boxerman et al,³ who found that macrocystic and macrohemorrhagic macroadenomas and solid tumors with higher ADC were more likely to be successfully managed with an operation. This might be due to the differences in the proportion of tumor components in different study populations.

Because an endoscopic transsphenoidal technique is applied as a minimally invasive surgical method for resection of pituitary adenomas, tumor consistency is one of the most important parameters influencing the success of this approach.³ Soft pituitary macroadenomas account for most pituitary adenomas and are always associated with a low incidence of complications (CSF rhi-

norrhea and hormonal deficiency).^{3,12} Resection of macroadenomas requires removal of the inferior or posterior portions first.¹² Improved anatomic depiction of the sellar region with FOCUS DWI is most notable in regions near the skull base. Superior image quality is the fundamental basis of accurate disease assessment. Combined with the relationship of diffusivity between soft pituitary macroadenomas and normal pituitary glands, the FOCUS sequence provides a new perspective for evaluation of tumor consistency. It might help surgeons prepare detailed surgical strategies and decrease the rates of postoperative pain and discomfort.

This study has several limitations. First, the sample size was relatively small. Because we focused on only comparative qualitative and quantitative analysis of the 2 methods, we did not consider the functional variation of macroadenomas. Second, because pituitary macroadenomas with firm consistency occur in 4%–15% of patients,^{3,9} we encountered very few such cases. However, these patients were excluded because preoperative treatment might have induced fibrotic changes in tumors. Future studies would ideally comparatively evaluate the ADCs of adenomas of different consistencies and normal pituitary glands to achieve better results.

CONCLUSIONS

Relative to conventional single-shot EPI DWI, FOCUS DWI can acquire images of normal pituitary glands and pituitary macroadenomas with higher resolution and fewer susceptibility artifacts in a clinically feasible scan time. The FOCUS technique enables evaluation of the diffusivity of normal pituitary glands, which might serve as a reference for evaluating the consistency of macroadenomas in the future.

REFERENCES

1. Lomban E, Bonneville F, Karachi C, et al. **Massive stroke in a patient with pituitary apoplexy, cervical carotid artery stenosis and hypotension.** *J Neuroradiol* 2006;33:259–62 CrossRef Medline
2. Takayasu T, Yamasaki F, Tominaga A, et al. **A pituitary abscess showing high signal intensity on diffusion-weighted imaging.** *Neurosurg Rev* 2006;29:246–48 CrossRef Medline
3. Boxerman JL, Rogg JM, Donahue JE, et al. **Preoperative MRI evaluation of pituitary macroadenoma: imaging features predictive of successful transsphenoidal surgery.** *AJR Am J Roentgenol* 2010;195:720–28 CrossRef Medline
4. Hiwatashi A, Yoshiura T, Togao O, et al. **Evaluation of diffusivity in the anterior lobe of the pituitary gland: 3D turbo field echo with diffusion-sensitized driven-equilibrium preparation.** *AJNR Am J Neuroradiol* 2014;35:95–98 CrossRef Medline
5. Mahmoud OM, Tominaga A, Amatya VJ, et al. **Role of PROPELLER diffusion weighted imaging and apparent diffusion coefficient in the diagnosis of sellar and parasellar lesions.** *Eur J Radiol* 2010;74:420–27 CrossRef Medline
6. Le Bihan D, Poupon C, Amadon A, et al. **Artifacts and pitfalls in diffusion MRI.** *J Magn Reson Imaging* 2006;24:478–88 CrossRef Medline
7. Suzuki C, Maeda M, Hori K, et al. **Apparent diffusion coefficient of pituitary macroadenoma evaluated with line-scan diffusion-weighted imaging.** *J Neuroradiol* 2007;34:228–35 CrossRef Medline
8. Wei XE, Li WB, Li MH, et al. **Detection of brain lesions at the skull base using diffusion-weighted imaging with readout-segmented echo-planar imaging and generalized autocalibrating partially parallel acquisitions.** *Neurol India* 2011;59:839–43 CrossRef Medline
9. Yiping L, Ji X, Daoying G, et al. **Prediction of the consistency of**

- pituitary adenoma: a comparative study on diffusion-weighted imaging and pathological results. *J Neuroradiol* 2016;43:186–94 CrossRef Medline
10. Mahmoud OM, Tominaga A, Amatya VJ, et al. **Role of PROPELLER diffusion-weighted imaging and apparent diffusion coefficient in the evaluation of pituitary adenomas.** *Eur J Radiol* 2011;80:412–17 CrossRef Medline
 11. Yiping L, Hui L, Kun Z, et al. **Diffusion-weighted imaging of the sellar region: a comparison study of BLADE and single-shot echo planar imaging sequences.** *Eur J Radiol* 2014;83:1239–44 CrossRef Medline
 12. Theodoros D, Patel M, Ruzevick J, et al. **Pituitary adenomas: historical perspective, surgical management and future directions.** *CNS Oncol* 2015;4:411–29 CrossRef Medline
 13. Saritas EU, Cunningham CH, Lee JH, et al. **DWI of the spinal cord with reduced FOV single-shot EPI.** *Magn Reson Med* 2008;60:468–73 CrossRef Medline
 14. Vidiri A, Minosse S, Piludu F, et al. **Feasibility study of reduced field of view diffusion-weighted magnetic resonance imaging in head and neck tumors.** *Acta Radiol* 2017;58:292–300 CrossRef Medline
 15. Ma C, Li YJ, Pan CS, et al. **High resolution diffusion weighted magnetic resonance imaging of the pancreas using reduced field of view single-shot echo-planar imaging at 3 T.** *Magn Reson Imaging* 2014;32:125–31 CrossRef Medline
 16. Dong H, Li Y, Li H, et al. **Study of the reduced field-of-view diffusion-weighted imaging of the breast.** *Clin Breast Cancer* 2014;14:265–71 CrossRef Medline
 17. Korn N, Kurhanewicz J, Banerjee S, et al. **Reduced-FOV excitation decreases susceptibility artifact in diffusion-weighted MRI with endorectal coil for prostate cancer detection.** *Magn Reson Imaging* 2015;33:56–62 CrossRef Medline
 18. Riffel P, Michaely HJ, Morelli JN, et al. **Zoomed EPI-DWI of the head and neck with two-dimensional, spatially-selective radiofrequency excitation pulses.** *Eur Radiol* 2014;24:2507–12 CrossRef Medline
 19. Pereira FP, Martins G, Figueiredo E, et al. **Assessment of breast lesions with diffusion-weighted MRI: comparing the use of different b values.** *AJR Am J Roentgenol* 2009;193:1030–35 CrossRef Medline
 20. Mohamed FF, Abouhashem S. **Diagnostic value of apparent diffusion coefficient (ADC) in assessment of pituitary macroadenoma consistency.** *The Egyptian Journal of Radiology and Nuclear Medicine* 2013;44:617–24 CrossRef
 21. Zaharchuk G, Saritas EU, Andre JB, et al. **Reduced field-of-view diffusion imaging of the human spinal cord: comparison with conventional single-shot echo-planar imaging.** *AJNR Am J Neuroradiol* 2011;32:813–20 CrossRef Medline
 22. Singer L, Wilmes LJ, Saritas EU, et al. **High-resolution diffusion-weighted magnetic resonance imaging in patients with locally advanced breast cancer.** *Acad Radiol* 2012;19:526–34 CrossRef Medline
 23. Hiwatashi A, Togao O, Yamashita K, et al. **Evaluation of diffusivity in pituitary adenoma: 3D turbo field echo with diffusion-sensitized driven-equilibrium preparation.** *British J Radiol* 2016;89:20150755 CrossRef Medline
 24. Pierallini A, Caramia F, Falcone C, et al. **Pituitary macroadenomas: preoperative evaluation of consistency with diffusion-weighted MR imaging—initial experience.** *Radiology* 2006;239:223–31 CrossRef Medline
 25. Noh S, Kim SH, Cho NH, et al. **Rapid reticulin fiber staining method is helpful for the diagnosis of pituitary adenoma in frozen section.** *Endocr Pathol* 2015;26:178–84 CrossRef Medline
 26. Jarzembowski J, Lloyd R, McKeever P. **Type IV collagen immunostaining is a simple, reliable diagnostic tool for distinguishing between adenomatous and normal pituitary glands.** *Arch Pathol Lab Med* 2007;131:931–35 Medline

Reversible Dilatation of the Superior Ophthalmic Vein in Intubated Patients

S.A. Nabavizadeh, S.H. Sundararajan, J.E. Schmitt, and L.A. Loevner

ABSTRACT

BACKGROUND AND PURPOSE: Superior ophthalmic vein enlargement has typically been associated with increased intracranial or orbital pressure. This study evaluates the incidence of superior ophthalmic vein enlargement in intubated patients without pre-existing intracranial or intraorbital pathologies.

MATERIALS AND METHODS: Two cohorts (patients with trauma and epilepsy patients undergoing stereotactic intracranial lead placement) who underwent CT while intubated and shortly following extubation and a cohort of 30 outpatients with a history of headache and normal head CT findings (healthy controls) were included. The superior ophthalmic vein diameter was measured on all scans.

RESULTS: Seventy patients intubated for trauma and 45 patients with intraoperative CT were included ($n = 115$). While intubated, 66% of the total sample had at least unilateral superior ophthalmic vein dilation of >2.5 mm and 48% had bilateral dilation. Fifty-seven percent of patients with trauma and 84% of intraoperative patients with dilated superior ophthalmic veins showed reversal of mean superior ophthalmic vein dilation to <2.5 mm on postextubation CT. The mean superior ophthalmic vein diameter decreased an average of 1.2 mm following extubation. Changes in superior ophthalmic vein diameter between intubated and extubated states were statistically significant ($P < .001$). Differences between the control group and the extubated subjects were not statistically significant ($P = .21$).

CONCLUSIONS: Bilateral dilation of the superior ophthalmic vein is common in intubated patients and usually reverses following extubation. In the appropriate clinical setting, this knowledge will prevent misinterpretation of prominent superior ophthalmic veins as automatically indicative of an underlying pathology.

ABBREVIATION: SOV = superior ophthalmic vein

Superior ophthalmic veins (SOVs) are routinely detected in high-resolution head CT obtained for a variety of indications. This important orbital venous drainage pathway is located superior to the optic nerve and medially in the anterior part of the orbit, courses between the heads of the superior and lateral rectus muscles, and ultimately exits the orbit via the superior orbital fissure to enter the anterior part of the cavernous sinus.¹ SOV enlargement is associated with a variety of pathologic entities. For example, lack of intravenous valves contributes to unilateral SOV enlargement in carotid cavernous fistula, Graves orbitopathy, orbital pseudotumor and Tolosa-Hunt syndrome, parasellar and cavernous sinus tumors, orbital varices, arteriovenous malforma-

tions, orbital hematoma, and other orbital infectious or inflammatory etiologies.²⁻⁵ Bilateral superior ophthalmic vein enlargement has been reported in patients with diffuse cerebral swelling and increased intracranial pressure.^{4,6,7} Given such associations, SOV enlargement often raises concerns for an underlying pathologic state. However, in our clinical radiology practice, we have empirically observed reversible SOV enlargement in intubated patients (Fig 1). The aim of the current study was to determine the incidence and reversibility of SOV enlargement in 2 cohorts evaluated by CT during and after intubation. We hypothesized that intubation contributes to reversible bilateral enlargement of the SOV.

MATERIALS AND METHODS

Patient Population

The study was performed with approval of the institutional review board and was compliant with guidelines of the Health Insurance Portability and Accountability Act. A radiology information system key word search using MONTAGE Search and Analytics software (Montage Healthcare Solutions, Philadelphia, Pennsylvania)

Received December 16, 2017; accepted after revision April 13, 2018.

From the Department of Neuroradiology, Hospital of the University of Pennsylvania, Philadelphia, Pennsylvania.

Please address correspondence to S. Ali Nabavizadeh, MD, Hospital of the University of Pennsylvania, 3400 Spruce St, Philadelphia, PA 19104; e-mail: seyedali.nabavizadeh@uphs.upenn.edu

<http://dx.doi.org/10.3174/ajnr.A5699>

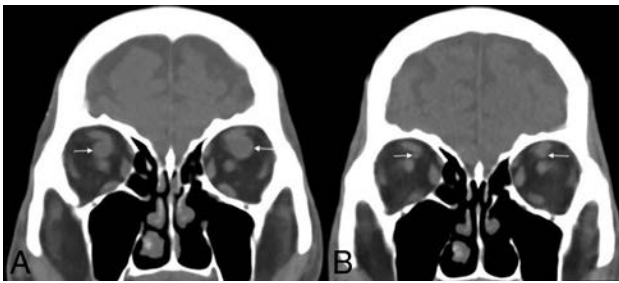


FIG 1. A 75-year-old man presenting to the emergency department as a trauma alert after experiencing a fall. No intracranial hemorrhage or acute intracranial abnormality was found. The patient was intubated for airway protection secondary to aspiration. The right SOV diameter was 7.9 mm and the left SOV diameter was 10 mm on initial head CT (A, arrows). On 2-week follow-up CT following extubation, the SOV diameter significantly decreased bilaterally (B, arrows).

nia) was performed on all CT examinations of the brain between July 2010 and July 2016 to find 2 cohorts of intubated patients. The first cohort consisted of patients with epilepsy with intraoperative CT scans for stereotactic placement of subdural or depth electrodes. Search terms included “intraoperative,” “depth electrodes,” and “subdural electrodes.” All intraoperative imaging was acquired during positive pressure ventilation. These patients with epilepsy did not have any intracranial mass effect, and all underwent a follow-up CT within 1 week of the operation to monitor the electrode placement.

The second cohort consisted of emergency department patients with trauma without intracranial hemorrhage or acute intracranial abnormality. Search terms included “fall,” “MVC,” and “trauma.” This included patients who had fallen, were involved in motor vehicle collisions, or other types of trauma. Airway maintenance in this emergency department cohort was established with or without positive pressure ventilation. The included patients also had head CT imaging performed following intubation and within 4 weeks following extubation. The reason for the follow-up CT in patients with trauma ranged from altered mental status to fall or headache. Patients who had any structural intracranial pathology (eg, intracranial hemorrhage, cerebral edema, or mass effect) that would contribute to elevated intracranial or intraorbital pressure were excluded from the study. Finally, a third cohort was included. These included patients who had head CT as a work-up for their headache and normal CT examination findings. Search terms included “headache,” “CT,” and “normal.”

CT and Image Analysis

All CT was performed without contrast administration. In the intraoperative cohort, the SOV transverse diameter was recorded on coronal reformations of 1-mm-section axial images acquired on our institutional portable CT scanner (CereTom, 8-slice; NeuroLogica, Danvers, Massachusetts). The transverse diameter of the emergency department cohort was recorded on coronal reformations of 1-mm-section axial source images acquired on our institutional emergency department CT scanners (Somatom Definition Edge, 128-slice, and Somatom Definition Flash, 128-slice; Siemens, Erlangen, Germany). Dilated SOVs were considered to be ≥ 2.5 mm based on prior studies of mean SOV diameter

ranging from 1.7 to 2.2 mm with SD ± 1.2 mm^{8,9} and also another study that demonstrated this threshold is associated with increased intracranial pressure.⁷ SOV diameter was recorded in all patients, posterior to the globe of the eye where the SOV crossed the inferior aspect of superior rectus muscle, by a neuroradiology fellow (S.H.S.). To assess interrater reliability of measurements, a board-certified neuroradiology attending with 5 years of experience (S.A.N.) measured the SOV diameter in a random subset of 10 subjects from each cohort ($n = 20$).

Statistical Analysis

Data were imported into the R statistical environment (Version 3.2.4; <http://www.r-project.org/>) for analysis.¹⁰ First, descriptive statistics were calculated. Interrater reliability was assessed via intraclass correlations. Data were then visualized to assess normality. We first tested differences between intubated and extubated states in our intraoperative and trauma groups.

Because the normality assumptions required for parametric statistics were not met in these data, Wilcoxon (paired) signed rank tests were performed to test differences with the intubation state. Left, right, and mean SOV diameters were tested. To ensure that cohort differences (ie, intraoperative versus trauma) did not confound the results, we repeated our analysis with each cohort separately. The effect of the intubation state on the number of subjects with SOV diameters above a threshold of 2.5 mm was assessed via the McNemar test for the trauma and intraoperative groups separately. The Bonferroni correction on 12 statistical tests was used to adjust for multiple testing.

To provide an alternate baseline for SOV diameter, we also compared our trauma and intraoperative cohorts with a third group consisting of outpatient healthy controls. Three-way Kruskal Wallis tests (outpatient, intraoperative, and trauma) were performed to identify group differences in SOV caliber, with post hoc pair-wise comparisons performed via the Dunn test.

RESULTS

A total of 145 patients were included in our study (30 patients in the control group, 45 patients in the intraoperative cohort, 70 patients in the emergency department trauma cohort). In the control group, there were 23 women and 7 men (mean age, 54.78 ± 17.7 years; range, 24–93 years). Within the intraoperative cohort, 24 patients were men and 21 patients were women (mean age, 56.1 ± 16.2 years; range, 21–84 years). In the emergency department trauma cohort, 48 patients were men and 22 patients were women (mean age, 58.1 ± 21.7 years; range, 21–87 years).

Initial imaging following intubation showed that 55 of the 115 patients in the experimental cohorts (48%) demonstrated dilation of the bilateral SOVs to ≥ 2.5 mm. Sixty percent of patients in the intraoperative cohort (27/45) and 40% of patients in the emergency department trauma cohort (28/70) had bilateral SOV dilation. Sixty-six percent of patients (76/115) demonstrated at least unilateral dilation of the superior ophthalmic veins when intubated. Of the 58% (67/115) of patients with dilated mean SOVs during intubation, 47/67 (70%) demonstrated reversal of average SOV dilation below 2.5 mm on postextubation CT. Differences in mean SOV dilation between intubated and extubated

states were statistically significant for the combined sample cohort (McNemar $\chi^2 = 42.18$, $df = 1$, $P < .001$) as well as when examining the intraoperative ($\chi^2 = 25.03$, $df = 1$, $P < .001$) and trauma cohorts ($\chi^2 = 15.43$, $df = 1$, $P < .001$) separately.

SOV diameter decreased for most subjects following extubation (Fig 2); for example, mean SOV diameter decreased in 88% of subjects (102/115). When considering group means, SOV caliber decreases following extubation ranged from 0.90 to 1.14 mm (Table). Reductions in mean, left, and right SOV diameters were all statistically significant ($P < .001$). These differences remained significant when examining the trauma and intraoperative subgroups separately ($P < .001$). The intraclass correlation for inter-rater reliability was 0.93.

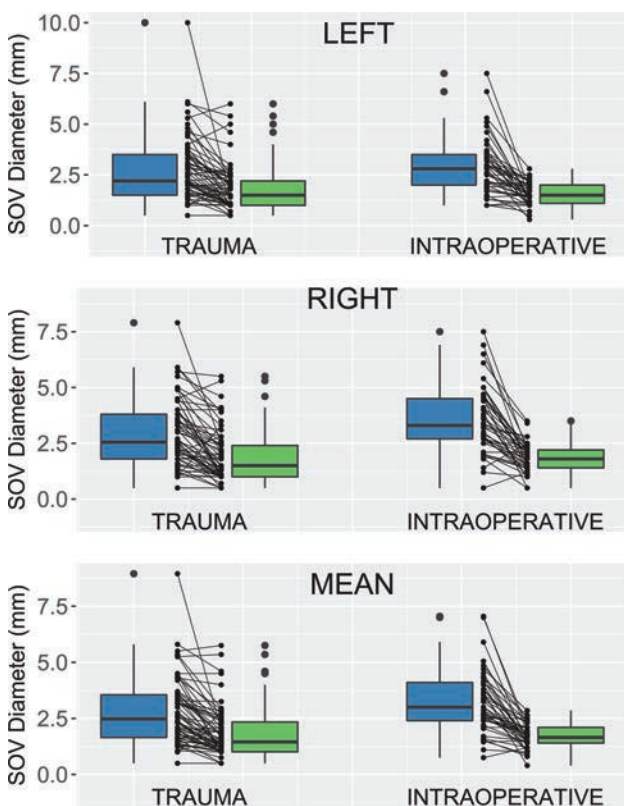


FIG 2. SOV diameter during and after intubation for both emergency department trauma and intraoperative cohorts. Both paired boxplots and dotplots are provided. In each cohort, boxplots on the left represent patients while intubated, with boxplots on the right showing SOV values following extubation. Left, right, and mean (average) SOV diameters are shown separately.

Differences in SOV caliber before and after intubation

Cohort (No.)	SOV	Mean (SD)		Mean Difference (99% CI)	P Value
		Intubated	Extubated		
Intraoperative (45)	Right	3.56 (1.51)	1.82 (0.66)	1.74 (1.31–2.17)	<.001 ^a
	Left	2.91 (1.41)	1.53 (0.54)	1.36 (0.95–1.79)	<.001
Trauma (70)	Right	2.88 (1.48)	1.86 (1.16)	1.02 (0.74–1.30)	<.001
	Left	2.68 (1.59)	1.78 (1.11)	0.90 (0.5–1.21)	<.001
Control (30)	Right	–	1.88 (0.51)	–	≤.001 ^b
	Left	–	1.83 (0.49)	–	<.001

^a Bonferroni-corrected Wilcoxon paired signed rank tests between intubated and extubated states.

^b Three-way Kruskal-Wallis test between controls and intubated cohorts. Post hoc pair-wise comparisons between controls and the experimental groups were also statistically significant ($P < .001$). Comparisons with extubated patients were not statistically significant.

Mean SOV diameter in the outpatient control group was 1.86 ± 0.46 mm. SOV diameter in the controls was comparable with that in the extubated experimental cohorts (Table), with only 3/30 (10%) having a mean SOV of >2.5 mm. Differences between the control group and the extubated subjects were not statistically significant for left ($P = .11$), right ($P = .30$), or average SOV diameter ($P = .21$). However, there were statistically significant group differences between mean SOV diameters in controls and the intubated cohorts (Kruskal-Wallis $\chi^2 = 22.3121$, $df = 2$, $P < .001$). Post hoc comparisons demonstrated that the mean SOV diameter in the control group was significantly lower than that in both intubated trauma ($z = 3.27$, $P = .005$) and intraoperative ($z = 4.72$, $P < .001$) cohorts.

DISCUSSION

The current study provides evidence of a strong association between intubation state and SOV diameter in 2 different groups of patients without intracranial mass or increased intracranial pressure. The result of our study is concordant with prior cerebral angiography studies that have shown that the SOV is more frequently visualized in intubated patients.^{11–13} Ricker et al¹² demonstrated that the SOV was visualized on 43% of cerebral angiograms obtained for intubated patients compared with only 22% on nonintubated patients. In a study of 452 patients, Servo¹⁴ showed that intubation increased the visualization of the SOV. However, this finding was only observed in patients with normal flow direction from the facial vein to the cavernous sinus, but not in patients with reversed flow. In addition, Servo showed statistically significant differences on SOV visualization based on middle cerebral and uncal vein drainage either normally draining into the cavernous sinus or bypassing direct drainage via normal-variant collateral pathways.¹⁴

The effect of the direction of flow in the facial vein has also been studied using 3D TOF MR angiography.¹⁵ Besides the effect of anatomic variations in the venous system, another proposed mechanism for increased visualization of the SOV in intubated patients in cerebral angiography is facilitated accumulation of contrast in the nasal mucosa.^{11,13} The above angiographic studies have been performed in patients with intracranial pathologies ranging from intracranial mass lesions and hydrocephalus to other pathologies that could increase the intracranial pressure. In addition, the diameter of the SOV was not measured in these studies. Our study is the first of its kind to investigate the effect of intubation on SOV using cross-sectional imaging in patients without intracranial mass or increased intracranial pressure, to our knowledge.

Our findings suggest that bilateral SOV dilation is common in intubated patients and that it is usually reversible following extubation. All patients in the intraoperative cohort received positive pressure ventilation (compared with the emergency department trauma cohort in which patients may or may not have received positive pressure ventilation). Positive pressure ventilation intubation might contribute to significantly

larger and more frequent changes in SOV diameter in this cohort, perhaps because of accentuated intrathoracic pressure mediating venous backflow into the head and neck. In addition, there are other factors that could contribute to changes in SOV diameter such as the state of hydration and blood pressure at the time of imaging and the effect of sedative-anesthetic medications. Nevertheless, the purpose of this study was not necessarily to surmise the mechanism by which this process occurs. Rather, it was to demonstrate that with intubation, it is certainly possible for prominence of the SOVs to be attributable to intubation status rather than immediately indicative of an underlying abnormality. In the appropriate clinical setting, awareness of this entity may help prevent misinterpretation of prominent SOVs as automatically indicative of an underlying pathology.

Another observation is that the diameter of the SOV in some patients in both the intraoperative and trauma cohorts stayed the same or even slightly increased. We believe that this finding could be due to dilated SOVs as a normal variation as suggested by prior studies^{8,9} or it could be the result of additional factors that were not measured in this retrospective study, such as the state of hydration and blood pressure at the time of imaging and the effect of sedative-anesthetic medications.

This study has some limitations. The lack of CT-evident intracranial or intraorbital findings was used as the criteria for delineating lack of elevated intracranial and intraorbital pressure, respectively. The standard for measurement of elevated intracranial pressure—lumbar puncture or intraventricular catheter results—was not logistically feasible for this study. Additionally, although it was known that positive pressure ventilation was used in all intraoperative cases and intermittently in our emergency department trauma cohort, exact numeric data regarding pressure settings were not available in the medical record because such data are not frequently recorded by the anesthesiologists during their routine documentation. In addition, given the retrospective nature of the study, reliable data about the state of hydration and blood pressure at the time of imaging could not be obtained. Finally, dedicated vascular imaging was not generally available; therefore, it was not possible to correlate our findings with vascular anatomy, including venous anatomic variations in the face, skull base, and brain. Future prospective studies could incorporate some of this information to better understand the causes of SOV dilation.

CONCLUSIONS

Bilateral dilation of the SOV is common in intubated patients and usually reverses following extubation. In the appropriate clinical setting, knowledge of this entity will prevent misinterpretation of prominent SOVs as automatically indicative of an underlying pathology.

REFERENCES

1. Rhoton AL. *Cranial Anatomy and Surgical Approaches*. Philadelphia: Lippincott Williams & Wilkins; 2003
2. Wei R, Cai J, Ma X, et al. **Imaging diagnosis of enlarged superior ophthalmic vein**. *Zhonghua Yan Ke Za Zhi* 2002;38:402–04 Medline
3. Peyster RG, Savino PJ, Hoover ED, et al. **Differential diagnosis of the enlarged superior ophthalmic vein**. *J Comput Assist Tomogr* 1984;8:103–07 CrossRef Medline
4. Servo A, Jääskinen J. **The superior ophthalmic vein and tumours of the sellar area**. *Acta Neurochir (Wien)* 1983;68:195–202 CrossRef Medline
5. Adam CR, Shields CL, Gutman J, et al. **Dilated superior ophthalmic vein: clinical and radiographic features of 113 cases**. *Ophthalmic Plast Reconstr Surg* 2018;34:68–73 CrossRef Medline
6. Khanna RK, Pham CJ, Malik GM, et al. **Bilateral superior ophthalmic vein enlargement associated with diffuse cerebral swelling: report of 11 cases**. *J Neurosurg* 1997;86:893–97 CrossRef Medline
7. Lirng JF, Fuh JL, Wu ZA, et al. **Diameter of the superior ophthalmic vein in relation to intracranial pressure**. *AJNR Am J Neuroradiol* 2003;24:700–03 Medline
8. Reis CV, Gonzalez FL, Zabramski JM, et al. **Anatomy of the superior ophthalmic vein approach for direct endovascular access to vascular lesions of the orbit and cavernous sinus**. *Neurosurgery* 2009;64(5 Suppl 2):318–23; discussion 323 CrossRef Medline
9. Tsutsumi S, Nakamura M, Tabuchi T, et al. **The superior ophthalmic vein: delineation with high-resolution magnetic resonance imaging**. *Surg Radiol Anat* 2015;37:75–80 CrossRef Medline
10. R Core Team. The R Project for Statistical Computing. <https://www.R-project.org/>. Accessed November 1, 2017
11. Hacker H, Porrero M. **Demonstration and significance of the ophthalmic vein in carotid angiography** [in German]. *Fortschr Geb Rontgenstr Nuklearmed* 1969;110:656–63 CrossRef Medline
12. Ricker H, Reiner I, Nadjmi M. **Significance of the superior ophthalmic vein in the phlebogram** [in German]. *Radiologe* 1972;12:414–16 Medline
13. Bradac GB, Simon RS, Leonhardt W. **The ophthalmic vein in the carotid angiogram**. *Neuroradiology* 1974;8:39–47 CrossRef Medline
14. Servo A. **Visualization of the superior ophthalmic vein on carotid angiography**. *Neuroradiology* 1982;23:141–6 Medline
15. Uchino A, Egashira R, Nomiya K, et al. **Visualization of the superior ophthalmic veins by 3 Tesla 3D-TOF-MR angiography**. *Neuroradiol J* 2008;21:619–22 CrossRef Medline

Prognostic Implications of Gadolinium Enhancement of Skull Base Chordomas

E. Lin, T. Scognamiglio, Y. Zhao, T.H. Schwartz, and C.D. Phillips

ABSTRACT

BACKGROUND AND PURPOSE: Skull base chordomas often demonstrate variable MR imaging characteristics, and there has been limited prior research investigating the potential clinical relevance of this variability. The purpose of this retrospective study was to assess the prognostic implications of signal intensity on standard imaging techniques for the biologic behavior of skull base chordomas.

MATERIALS AND METHODS: Medical records were retrospectively reviewed for 22 patients with pathologically confirmed skull base chordomas. Clinical data were recorded, including the degree of surgical resection, the presence or absence of radiation therapy, and time to progression/recurrence of the tumor or time without progression/recurrence of the tumor following initial treatment. Pretreatment imaging was reviewed for the presence or absence of enhancement and the T2 signal characteristics. Tumor-to-brain stem signal intensity ratios on T2, precontrast T1, and postcontrast T1 spin-echo sequences were also calculated. Statistical analysis was then performed to assess correlations between imaging characteristics and tumor progression/recurrence.

RESULTS: Progression/recurrence of skull base chordomas was seen following surgical resection in 11 of 14 (78.6%) patients with enhancing tumors and in zero of 8 patients with nonenhancing tumors. There was a statistically significant correlation between skull base chordoma enhancement and subsequent tumor progression/recurrence ($P < .001$), which remained significant after controlling for differences in treatment strategy ($P < .001$). There was also a correlation between postcontrast T1 signal intensity (as measured by postcontrast T1 tumor-to-brain stem signal intensity ratios) and recurrence/progression ($P = .02$). While T2 signal intensity was higher in patients without tumor progression (median tumor-to-brain stem signal intensity ratios on T2 = 2.27) than in those with progression (median tumor-to-brain stem signal intensity ratios on T2 = 1.78), this association was not significant ($P = .12$).

CONCLUSIONS: Enhancement of skull base chordomas is a risk factor for tumor progression/recurrence following surgical resection.

ABBREVIATIONS: BSS = brain stem signal; R_{post} = ratio of tumor-to-brain stem postcontrast T1 signal intensity; R_{pre} = ratio of tumor-to-brain stem precontrast T1 signal intensity; R_{T2} = ratio of tumor-to-brain stem T2 signal intensity; TS = tumor signal

Chordomas are tumors derived from undifferentiated notochordal remnants residing throughout the axial skeleton.¹⁻³ Chordomas are relatively rare tumors, accounting for approximately 1%–4% of primary bone tumors, with an incidence of approximately 0.08 per 100,000.^{4,5} Current treatment strategies for chordomas typically consist of surgical resection and adjuvant radiation therapy, with proton beam therapy favored over tradi-

tional photon therapy. Although chordomas are considered low-grade neoplasms on a histologic basis, most chordomas will recur or progress, regardless of initial treatment strategies.^{4,6,7} The typically insidious clinical course, large tumor burden at the time of diagnosis, and locally aggressive nature of chordomas all pose clinical management difficulties.^{4,8,9} Metastases have also been reported in 7%–14% of cases, most commonly to the lung.^{10,11} Skull base chordomas, which account for approximately 32% of chordomas, are particularly difficult to treat given their proximity to cranial nerves, the brain stem, and skull base vasculature, and this anatomic site presents more pronounced challenges to gross total resection and radiation therapy.⁴

A variety of prognostic factors has been reported for skull base chordomas, including the degree of surgical resection, tumor size, preoperative Karnofsky Performance Status, type of adjuvant radiation therapy, prior surgical and radiation history, and

Received December 13, 2017; accepted after revision May 11, 2018.

From the Departments of Radiology (E.L., C.D.P.), Pathology (T.S.), Healthcare Policy and Research (Y.Z.), and Neurological Surgery (T.H.S.), New York-Presbyterian Hospital/Weill Cornell Medical Center, New York, New York.

Paper previously presented at: Annual Meeting of the American Society of Head and Neck Radiology, September 16–20, 2017; Las Vegas, Nevada.

Please address correspondence to Eaton Lin, MD, New York-Presbyterian Hospital Weill Cornell Medical Center, Department of Radiology, 525 East 68th St, New York, NY 10065; e-mail: eal9007@med.cornell.edu

<http://dx.doi.org/10.3174/ajnr.A5714>

tumor pathology.^{7,12-23} Three pathologic subtypes have been identified—conventional, chondroid, and dedifferentiated—with conventional chordomas the most common and dedifferentiated chordomas the least common and having the least favorable prognosis.^{12,20,22,24} Other factors, such as age and sex, have demonstrated variable associations with outcome.^{14,18,20-22,25-29} However, there is a paucity of research investigating the correlation between imaging features for skull base chordomas and prognosis, or the lack thereof.

The current radiology literature on chordomas has focused mostly on imaging to distinguish chordomas from other differential considerations.³⁰⁻³² On MR imaging examinations, chordomas classically have been described as demonstrating T2 hyperintensity with enhancement on postcontrast imaging. Investigations into diffusion-weighted MR imaging characteristics have shown low ADC values for chordomas, particularly when compared with chondrosarcomas, which may otherwise have similar imaging characteristics.³³ However, chordomas are also known to have marked variability in T2 signal and degree of enhancement.³³⁻³⁵ While some studies have posited a correlation between MR imaging characteristics and histologic grade, analyses with larger samples have failed to demonstrate a statistically significant correlation between imaging features and chordoma histology.^{33,34,36}

Aside from its standard use as a diagnostic tool, MR imaging has demonstrated prognostic utility for many entities, with extensive literature supporting the use of signal intensity measurements in predicting prognosis for a variety of tumors.³⁷⁻⁴⁰ However, prior radiology literature addressing skull base chordomas has focused largely on identifying diagnostic imaging features, with only 1 recent study investigating the use of imaging as a prognostic tool.³⁶ In this study, we present findings suggesting that enhancement characteristics of skull base chordomas may be predictive of the clinical course.

MATERIALS AND METHODS

Overview

A retrospective study was performed after approval by the institutional review board, with patient privacy protected in accordance with the requirements of the Health Insurance Portability and Accountability Act. Medical records were reviewed for patients with pathologically confirmed skull base chordomas treated at our institution between May 2003 and July 2016. Patients were included in the study only if the following were available for review: pretreatment MR imaging examination, posttreatment MR imaging examinations (remote from the immediate postoperative imaging), operative reports, and pathologic specimens. Using these inclusion and exclusion criteria, we identified a group of 22 patients for this study.

Pathology

All pathologic specimens were re-analyzed by a neuropathologist with expertise in head and neck tumors, and the diagnosis of chordoma was confirmed in all 22 cases. Classic histopathologic features, including cords and nests of epithelial cells with variable atypia and the presence of physaliphorous cells embedded within an abundant myxoid matrix, were observed in all cases, in addition to an infiltrative growth pattern. Pathologic diagnosis was

also confirmed with positive immunohistochemical staining for pan-cytokeratin and epithelial membrane antigen in all cases. Of the 22 cases of chordoma, 8 had chondroid features, 1 was a dedifferentiated subtype, and the remaining 13 cases were the conventional type.

Clinical Data

Clinical data for these 22 patients were obtained from electronic medical records, with documentation of the degree of surgical resection, the presence or absence of radiation therapy, and time to progression/recurrence or time without progression/recurrence. The degree of surgical resection was categorized as gross total or subtotal on the basis of surgical and radiologic assessments documented in operative reports and immediate postoperative imaging. Nine patients had gross total resections, while 13 had subtotal resections. Sixteen of the 22 patients had adjuvant radiation therapy. Clinical and radiologic follow-up was available for all patients, with a median follow-up time of 28.5 months (range, 2–115 months). Progression and recurrence were defined by imaging assessments, with all except 1 case of progression/recurrence also having pathologic confirmation of chordoma on repeat resection.

Imaging

MR imaging examinations were performed on either 1.5T or 3T magnets. The available pretreatment MR imaging sequences were variable: Twenty patients had postcontrast spin-echo T1 imaging, 18 patients had postcontrast spoiled gradient-echo T1 imaging, 8 patients had precontrast spin-echo T1 imaging, 9 patients had diffusion-weighted imaging, and 12 patients had precontrast spin-echo T2 imaging performed with their available pretreatment MR imaging examinations. Pre- and postcontrast spin-echo T1 imaging was obtained with TRs ranging from 466.7 to 650.0 ms and TEs ranging from 7.9 to 16.5 ms. Precontrast spin-echo T2 imaging was performed with TRs ranging from 3000.0 to 4483.3 ms and TEs ranging from 72.0 to 95.0 ms. Diffusion-weighted imaging was not analyzed, given the relatively small number of patients for whom this sequence was available on pretreatment imaging.

For all 22 patients, the presence or absence of tumor enhancement on pretreatment imaging as a dichotomous variable was documented. Subsequently, pretreatment tumor signal intensity on T2 and pre- and postcontrast spin-echo T1 imaging were assessed in patients with available imaging. For the 2 patients without pretreatment postcontrast spin-echo T1 imaging, pretreatment postcontrast T1 spoiled gradient-echo images were available for assessing the presence or absence of tumor enhancement, but postcontrast T1 signal intensity was not measured. By means of the institutional PACS, signal-intensity measurements were made within ROIs selected in each patient's tumor. ROIs were selected on 3 different axial planes for all except 1 patient, for whom 2 axial planes were used due to constraints from smaller tumor size. To account for differences in imaging technique and image noise, we selected a control region within the brain stem on each of these axial images, and a similar technique was used to measure signal intensity in this region of the brain stem. ROIs were selected by drawing the largest possible elliptic area within the tumor or brain

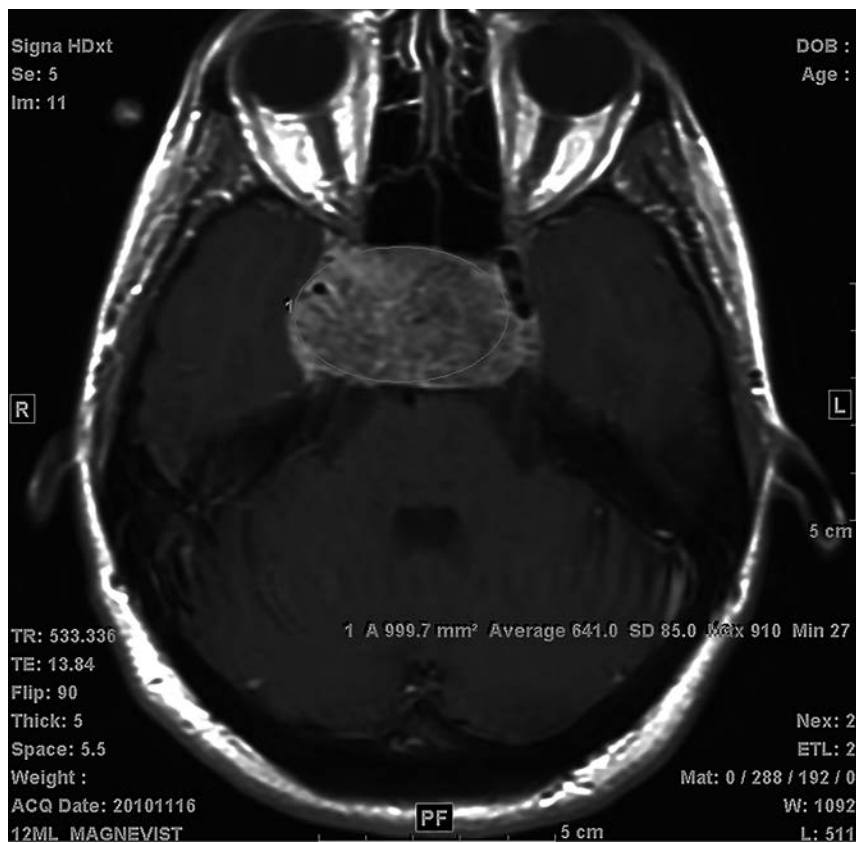


FIG 1. Example of an ROI selection. The largest possible elliptic ROI was drawn within the boundaries of the tumor or brain stem on axial images for average signal intensity measurements.

stem without incorporating adjacent structures (Fig 1). All ROI signal measurements were performed by a board-certified neuro-radiologist with 3 years of experience, blinded to clinical information. Subsequently, measurements in each patient were averaged to obtain the mean tumor precontrast T1, postcontrast T1, and T2 signal (TS_{pre} , TS_{post} , and TS_{T2} , respectively) and mean brain stem precontrast T1, postcontrast T1, and T2 signal (BSS_{pre} , BSS_{post} , and BSS_{T2} , respectively). The ratios of tumor signal to brain stem signal were then calculated for T1 precontrast ($R_{pre} = TS_{pre}/BSS_{pre}$), T1 postcontrast ($R_{post} = TS_{post}/BSS_{post}$), and T2 ($R_{T2} = TS_{T2}/BSS_{T2}$) imaging.

Statistical Analysis

Initial statistical analysis was performed with binary categorization of tumor enhancement (present or absent) and tumor recurrence/progression (present or absent). The Fisher exact test was used to analyze the association between tumor enhancement and recurrence/progression. To mitigate bias relating to differential follow-up time (ie, those with more follow-up time have more opportunity to have recurrence/progression), we also repeated the Fisher exact test in a cohort of 16 patients who were followed up for ≤ 50 months. We re-analyzed the association between tumor enhancement and tumor recurrence/progression, adjusting for treatment strategy (surgical resection alone or surgical resection and radiation therapy).

Ordinal and continuous values for tumor signal and time to tumor recurrence/progression were subsequently analyzed. The association between enhancement and time to recurrence/

progression was analyzed using a *t* test. A Wilcoxon rank sum test was used to evaluate whether the groups of patients with and without tumor recurrence/progression had statistically significant differences in R_{post} and R_{T2} . R_{post} was then divided into 3 categories ($R_{post} < 1.1$, $R_{post} = 1.1-1.5$, and $R_{post} > 1.5$), and respective Kaplan-Meier curves were plotted, with a log-rank test used to assess the overall difference between the degree of enhancement and time without recurrence/progression.

The association between pathologic subtype and the presence or absence of enhancement was analyzed using the Fisher exact test, while the association between subtype and degree of enhancement (as defined by R_{post}) was analyzed using both the *t* test and the Wilcoxon signed rank test. The Fisher exact test was also used to analyze the association between pathologic subtype and the presence or absence of progression/recurrence, while a Cox model was used to analyze the association between subtype and time to recurrence.

RESULTS

Of the 22 patients with skull base chordomas in this sample, 14 patients had enhancing tumors and 8 patients had nonenhancing tumors (Fig 2). Eleven (78.6%) of the 14 patients with enhancing tumors had recurrence or progression of tumor, while zero of 8 patients with nonenhancing tumors had recurrence or progression. The association between tumor enhancement and tumor recurrence/progression was statistically significant ($P < .001$), and the statistical significance remained after restricting the cohort to patients with ≤ 50 months of follow-up time to mitigate bias related to differential follow-up time ($P = .001$).

All patients in the sample underwent surgical resection for their skull base chordomas, but 6 of the 22 patients did not undergo adjuvant radiation therapy, 4 of whom had enhancing tumors and 2 of whom had nonenhancing tumors. Given findings in prior studies demonstrating statistically significant correlations between treatment strategies and recurrence/progression of tumor, statistical analysis was also performed adjusting for treatment strategy, which still demonstrated a statistically significant association between enhancement and tumor recurrence ($P < .001$).

The degree of enhancement, as assessed by R_{post} calculations, was higher among patients with recurrence/progression (median $R_{post} = 1.42$) than in patients without recurrence/progression (median $R_{post} = 1.05$), with the Wilcoxon rank sum test demonstrating a statistically significant association ($P = .003$). Based on a *t* test, there was also a statistically significant correlation between the presence or absence of enhancement and time to recurrence

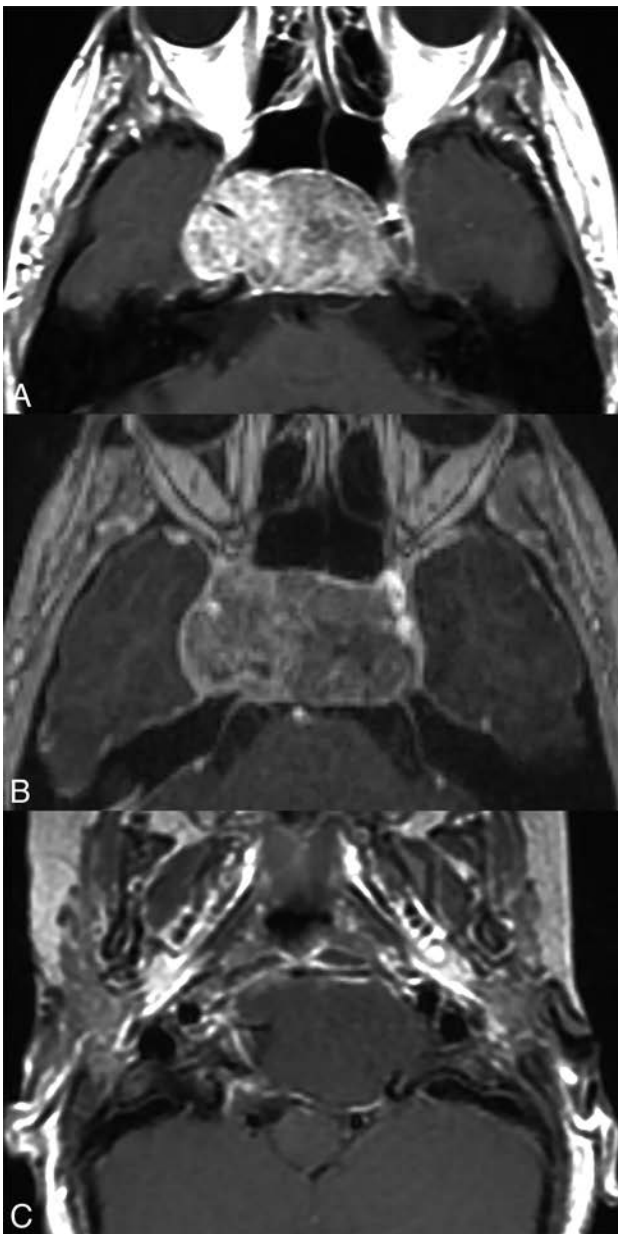


FIG 2. Axial postcontrast T1 images of pathologically proved chordomas, demonstrating a range of enhancement characteristics. Patient 1 (A) had an avidly enhancing chordoma, treated with near-gross total resection and proton beam radiation therapy. Twenty-four-month follow-up (not shown) demonstrated significant progression of tumor, treated with re-resection, but with further progression of tumor 10 months later. Patient 2 (B) had a heterogeneously enhancing chordoma, treated with near-gross total resection and proton beam radiation therapy. There was progression of the tumor at 29-month follow-up (not shown). Patient 3 (C) had a nonenhancing chordoma, treated with near-gross total resection and proton beam radiation therapy. As of 52-month follow-up (not shown), there has been no evidence of tumor progression.

($P = .02$). However, there was no statistically significant correlation between the degree of tumor enhancement and time to recurrence/progression ($P = .30$).

Finally, there was higher average tumor T2 signal in patients without recurrence/progression (median $R_{T2} = 2.27$) than in patients with recurrence/progression (median $R_{T2} = 1.78$), but this association was not statistically significant ($P = .12$).

Given prior literature reporting a correlation between chordoma subtype and prognosis,^{20,22,24} pathologic subtypes were also documented for each patient. Of the 22 chordomas, 8 were chondroid, 1 was dedifferentiated, and 13 were conventional. There was neither a statistically significant association between chordoma subtype and enhancement ($P = 1.0$) nor a significant association between subtype and degree of enhancement ($P = .81$ using a *t* test, $P = .78$ using the Wilcoxon signed rank test). While prior literature has shown a relationship between subtype and prognosis, this sample demonstrated no statistically significant association between chordoma subtype and time to recurrence/progression ($P = .18$).

DISCUSSION

Among the 22 patients in this study, there was a statistically significant correlation between the presence of skull base chordoma enhancement and future tumor progression/recurrence ($P < .001$). This correlation remained statistically significant after restricting the cohort to a 50-month follow-up period to mitigate differential follow-up time bias ($P = .001$) and demonstrated statistical significance after controlling for differences in treatment strategy ($P < .001$). While categorization of the chordomas into enhancing and nonenhancing tumors is somewhat subjective, there was also a statistically significant correlation between the intensity of postcontrast T1 signal and recurrence/progression ($P = .02$). This relationship between chordoma enhancement and future tumor progression/recurrence was also not attributable to previously reported associations between chordoma subtype and prognosis because there was no statistically significant association between subtype and degree of enhancement ($P = .81$). While average tumor T2 signal intensity was higher in patients without tumor progression than those with progression, this association was not statistically significant ($P = .12$).

There were several limitations to this study, the foremost being the small sample size. The relative rarity of skull base chordomas limited acquisition of additional patients in a single-center study; a multicenter study would have offered the possibility of an increased sample size but with concomitant limitations from greater heterogeneity in treatment, follow-up, and imaging inherent in any multicenter study.

There were also variations in imaging and treatment that were inherent in a 13-year retrospective study, due to expected changes in MR imaging magnets, imaging parameters, and treatment approaches during such a lengthy timeframe. Notably, proton beam therapy was less frequently used for patients presenting in the earlier part of the study timeframe. The statistical analysis did not control for differences in timeframe; thus, this omission introduced potential bias from any changes in treatment approaches during this period.

Along with the differences in adjuvant radiation therapy, there were also variations in residual tumor volume for patients without gross total resection. The degree of surgical resection is known to affect prognosis and the probability of recurrence for patients with chordomas,^{17,20} so controlling for this variable would have been ideal. However, variable availability and detail of posttreatment medical records precluded correlation with residual tumor volume.

Given the small sample size of patients and the variable pretreatment imaging acquired for this sample, compromises also had to be made with the study design. For example, assessments of enhancement would ideally be based on differential signal between pre- and postcontrast T1 imaging. However, most patients in this sample were referred for treatment from outside institutions, and the only available pretreatment MR imaging examination for many of these patients was an abbreviated institutional surgical planning MR imaging protocol, which lacks precontrast T1 imaging. Only 8 patients in the sample had precontrast T1 imaging available for signal intensity measurement, requiring an analysis that did not factor in variations in precontrast T1 signal. For patients in the sample with precontrast T1 imaging, the SD for intrinsic T1 signal ratio was relatively low (0.10), suggesting that postcontrast T1 signal was a relatively accurate measure of enhancement; nonetheless, the exclusion of this factor is a limitation, particularly given the known propensity for T1 shortening associated with intratumoral hemorrhage and mucous pools in chordomas. For the 14 patients without institutional pretreatment precontrast T1 spin-echo imaging, there were limitations in distinguishing intrinsic T1 shortening and true enhancement. For 9 of these 14 patients, outside imaging was available for review to confirm true enhancement. However, for 5 patients, the presence or absence of enhancement was determined partly on the basis of outside imaging reports from studies with precontrast T1 imaging; this feature is certainly less than ideal. For 4 of these 5 patients, there was either residual or recurrent tumor, with institutional posttreatment MR imaging demonstrating enhancement characteristics corresponding to those stated in outside pretreatment MR imaging studies, slightly mitigating this limitation.

CONCLUSIONS

Despite several limitations in this retrospective study, the findings suggest that nonenhancing or minimally enhancing chordomas have a better prognosis than those that show more avid enhancement on pretreatment imaging. There was also a difference in median T2 signal between patients with and without tumor recurrence/progression, but this difference did not demonstrate statistical significance; however, it is certainly possible that a larger sample may demonstrate a significant association between T2 signal and prognosis. Further investigations with a larger sample size are warranted to confirm the prognostic value of skull base chordoma imaging characteristics.

Disclosures: Theodore H. Schwartz—UNRELATED: Consultancy: elliquence; Stock/Stock Options: Visionsense.

REFERENCES

- Vujovic S, Henderson S, Presneau N, et al. **Brachyury, a crucial regulator of notochordal development, is a novel biomarker for chordomas.** *J Pathol* 2006;209:157–65 CrossRef Medline
- Salisbury JR, Deverell MH, Cookson MJ, et al. **Three-dimensional reconstruction of human embryonic notochords: clue to the pathogenesis of chordoma.** *J Pathol* 1993;171:59–62 CrossRef Medline
- Choi KS, Cohn MJ, Harfe BD. **Identification of nucleus pulposus precursor cells and notochordal remnants in the mouse: implications for disk degeneration and chordoma formation.** *Dev Dyn* 2008;237:3953–58 CrossRef Medline
- McMaster ML, Goldstein AM, Bromley CM, et al. **Chordoma: incidence and survival patterns in the United States, 1973–1995.** *Cancer Causes Control* 2001;12:1–11 CrossRef Medline
- Healey JH, Lane JM. **Chordoma: a critical review of diagnosis and treatment.** *Orthop Clin North Am* 1989;20:417–26 Medline
- Chambers KJ, Lin DT, Meier J, et al. **Incidence and survival patterns of cranial chordoma in the United States.** *Laryngoscope* 2014;124:1097–102 CrossRef Medline
- Tzortzidis F, Elahi F, Wright D, et al. **Patient outcome at long-term follow-up after aggressive microsurgical resection of cranial base chordomas.** *Neurosurgery* 2006;59:230–37 CrossRef Medline
- Bergh P, Kindblom LG, Gunterberg B, et al. **Prognostic factors in chordoma of the sacrum and mobile spine: a study of 39 patients.** *Cancer* 2000;88:2122–34 Medline
- Chugh R, Tawbi H, Lucas DR, et al. **Chordoma: the nonsarcoma primary bone tumor.** *Oncologist* 2007;12:1344–50 CrossRef Medline
- Young VA, Curtis KM, Temple HT, et al. **Characteristics and patterns of metastatic disease from chordoma.** *Sarcoma* 2015;2015:517657 CrossRef Medline
- Heffelfinger MJ, Dahlin DC, MacCarty CS, et al. **Chordomas and cartilaginous tumors at the skull base.** *Cancer* 1973;32:410–20 Medline
- Rosenberg AE, Brown GA, Bhan AK, et al. **Chondroid chordoma: a variant of chordoma—a morphologic and immunohistochemical study.** *Am J Clin Pathol* 1994;101:36–41 CrossRef Medline
- Safwat A, Nielsen OS, Jurik AG, et al. **A retrospective clinicopathological study of 37 patients with chordoma: a Danish national series.** *Sarcoma* 1997;1:161–65 CrossRef Medline
- Benk V, Liebsch NJ, Munzenrider JE, et al. **Base of skull and cervical spine chordomas in children treated by high-dose irradiation.** *Int J Radiat Oncol Biol Phys* 1995;31:577–81 CrossRef Medline
- Berven S, Zurakowski D, Mankin HJ, et al. **Clinical outcome in chordoma: utility of flow cytometry in DNA determination.** *Spine (Phila Pa 1976)* 2002;27:374–79 CrossRef Medline
- Borba LA, Colli B, Al-Mefty O. **Skull base chordomas.** *Neurosurgery Quarterly* 2001;11:124–39 CrossRef
- Colli B, Al-Mefty O. **Chordomas of the craniocervical junction: follow-up review and prognostic factors.** *J Neurosurg* 2001;95:933–43 CrossRef Medline
- Crockard HA, Steel T, Plowman N, et al. **A multidisciplinary approach to skull base chordomas.** *J Neurosurg* 2001;95:175–83 CrossRef Medline
- Kaneko Y, Sato Y, Iwaki T, et al. **Chordoma in early childhood: a clinicopathological study.** *Neurosurgery* 1991;29:442–46 CrossRef Medline
- Wu Z, Zhang JT, Zhang LW, et al. **Prognostic factors for long-term outcome of patients with surgical resection of skull base chordomas: 106 case review in one institution.** *Neurosurg Rev* 2010;33:451–56 CrossRef Medline
- Bohman LE, Koch M, Bailey RL, et al. **Skull base chordoma and chondrosarcoma: influence of clinical and demographic factors on prognosis—a SEER analysis.** *World Neurosurg* 2014;82:806–14 CrossRef Medline
- Zou MX, Lv GH, Zhang QS, et al. **Prognostic factors in skull base chordoma: a systematic literature review and meta-analysis.** *World Neurosurg* 2018;109:307–27 CrossRef Medline
- Zhai Y, Bai J, Gao H, et al. **Clinical features and prognostic factors of children and adolescents with clival chordomas.** *World Neurosurg* 2017;98:323–28 CrossRef Medline
- Jian BJ, Bloch OG, Yang I, et al. **Adjuvant radiation therapy and chondroid chordoma subtype are associated with a lower tumor recurrence rate of cranial chordoma.** *J Neurooncol* 2010;98:101–08 CrossRef Medline
- Mitchell A, Scheithauer BW, Unni KK, et al. **Chordoma and chondroid neoplasms of the sphenoid-occiput: an immunohistochemical study of 41 cases with prognostic and nosologic implications.** *Cancer* 1993;72:2943–49 Medline
- Dorfman HD, Czerniak B. **Bone cancers.** *Cancer* 1995;75(1 Suppl):203–10 Medline
- Forsyth PA, Cascino TL, Shaw EG, et al. **Intracranial chordomas: a**

- clinicopathological and prognostic study of 51 cases. *J Neurosurg* 1993;78:741–47 CrossRef Medline
28. Soo MY. **Chordoma: review of clinicoradiological features and factors affecting survival.** *Australas Radiol* 2001;45:427–34 CrossRef Medline
 29. Thieblemont C, Biron P, Rocher F, et al. **Prognostic factors in chordoma: role of postoperative radiotherapy.** *Eur J Cancer* 1995; 31A:2255–59 CrossRef Medline
 30. Lang N, Su MY, Xing X, et al. **Morphological and dynamic contrast enhanced MR imaging features for the differentiation of chordoma and giant cell tumors in the axial skeleton.** *J Magn Reson Imaging* 2017;45:1068–75 CrossRef Medline
 31. Si MJ, Wang CS, Ding XY, et al. **Differentiation of primary chordoma, giant cell tumor and schwannoma of the sacrum by CT and MRI.** *Eur J Radiol* 2013;82:2309–15 CrossRef Medline
 32. Tsuji T, Chiba K, Watanabe K, et al. **Differentiation of spinal giant cell tumors from chordomas by using a scoring system.** *Eur J Orthop Surg Traumatol* 2016;26:779–84 CrossRef Medline
 33. Yeom KW, Lober RM, Mobley BC, et al. **Diffusion-weighted MRI: distinction of skull base chordoma from chondrosarcoma.** *AJNR Am J Neuroradiol* 2013;34:1056–61 CrossRef Medline
 34. Pamir MN, Ozduman K. **Analysis of radiological features relative to histopathology in 42 skull-base chordomas and chondrosarcomas.** *Eur J Radiol* 2006;58:461–70 CrossRef Medline
 35. Erdem E, Angtuaco EC, Van Hemert R, et al. **Comprehensive review of intracranial chordoma.** *Radiographics* 2003;23:995–1009 CrossRef Medline
 36. Tian K, Wang L, Ma J, et al. **MR imaging grading system for skull base chordoma.** *AJNR Am J Neuroradiol* 2017;38:1206–11 CrossRef Medline
 37. Pope WB, Sayre J, Perlina A, et al. **MR imaging correlates of survival in patients with high-grade gliomas.** *AJNR Am J Neuroradiol* 2005; 26:2466–74 Medline
 38. Hilario A, Sepulveda JM, Perez-Nuñez A, et al. **A prognostic model based on preoperative MRI predicts overall survival in patients with diffuse gliomas.** *AJNR Am J Neuroradiol* 2014;35:1096–102 CrossRef Medline
 39. Valles FE, Perez-Valles CL, Regalado S, et al. **Combined diffusion and perfusion MR imaging as biomarkers of prognosis in immunocompetent patients with primary central nervous system lymphoma.** *AJNR Am J Neuroradiol* 2013;34:35–40 CrossRef Medline
 40. Pope WB, Lai A, Mehta R, et al. **Apparent diffusion coefficient histogram analysis stratifies progression-free survival in newly diagnosed bevacizumab-treated glioblastoma.** *AJNR Am J Neuroradiol* 2011;32:882–89 CrossRef Medline

Ultrafast Brain MRI Can Be Used for Indications beyond Shunted Hydrocephalus in Pediatric Patients

A. Tekes, S.S. Senglaub, E.S. Ahn, T.A.G.M. Huisman, and E.M. Jackson

ABSTRACT

BACKGROUND AND PURPOSE: Evaluation of shunted hydrocephalus is the most common indication for ultrafast brain MRI. Radiation-/sedation-free imaging capabilities make this protocol more desirable over CT and standard brain MRI. We hypothesized that ultrafast brain MRI can be used for selected indications beyond shunted hydrocephalus without adverse outcomes.

MATERIALS AND METHODS: Ultrafast brain MRI was performed with axial, sagittal, and coronal HASTE. The radiology information system was used to identify pediatric patients (0–18 years of age) who underwent ultrafast brain MRI between March 2014 and May 2016. A retrospective chart review was completed to identify indications other than shunted hydrocephalus, such as ventriculomegaly, macrocephaly, or intracranial cyst. All ultrafast brain MRIs were evaluated by a certified neuroradiologist and a neurosurgeon. Ultrafast brain MRI was deemed of sufficient diagnostic value for these indications if no further standard brain MRI was required for the study indication or if additional imaging was performed for an alternate indication.

RESULTS: The radiology information system identified 800 patients who had undergone an ultrafast brain MRI during the study period. One hundred twenty-two of these patients had ventriculomegaly, macrocephaly, or intracranial cyst as the study indication. Twenty-one of the 122 patients were excluded due to insufficient follow-up. Of the remaining 101 patients, only 5 had a standard brain MRI for the same indication, with no additional clinically significant information identified on those studies.

CONCLUSIONS: These results suggest that ultrafast brain MRI is sufficient to evaluate ventriculomegaly, macrocephaly, or intracranial cyst. Ultrafast brain MRI is radiation- and sedation-free; therefore, we recommend its use as the primary screening neuroimaging study for these indications.

ABBREVIATION: UFB-MRI = ultrafast brain MRI

Ultrafast brain MRI (UFB-MRI) has been used for evaluation of shunted hydrocephalus since 2002 per published data in PubMed.¹ Lack of ionizing radiation made UFB-MRI a preferred technique for evaluation of pediatric shunted hydrocephalus, given the longer survival rates and concerns for cumulative radiation doses in these children.^{2–4} In addition, UFB-MRI does not require sedation or general anesthesia due to the short imaging time. Adverse outcomes of general anesthesia in young children⁵ make standard brain MRI protocols less desirable. In addition, the

short total acquisition time of UFB-MRI improves patient throughput/work flow and consequently may improve overall health care costs.^{6,7} Initially, the published literature focused on the use of UFB-MRI in patients with shunted hydrocephalus.^{1,3,8,9} Later, modified fast protocols were proposed, such as for brain trauma.^{10,11} Although the use of UFB-MRI for indications other than hydrocephalus has been proposed in prior publications,^{12,13} validation for those indications has not been published.

UFB-MRI demonstrates fluid-containing structures well against the brain parenchyma and calvaria. We hypothesized that UFB-MRI can be used beyond shunted hydrocephalus for indications such as ventriculomegaly (Figs 1–3), macrocephaly (Fig 4), or intracranial cyst (Fig 5) without adverse outcomes.

MATERIALS AND METHODS

The radiology information system was used to identify pediatric patients (0–18 years of age) who underwent UFB-MRI between March 2014 and May 2016. A retrospective chart review was com-

Received March 29, 2018; accepted after revision May 18.

From the Department of Radiology (A.T., T.A.G.M.H.), Division of Pediatric Radiology and Pediatric Neuroradiology, and Department of Neurosurgery (S.S.S., E.S.A., E.M.J.), Division of Pediatric Neurosurgery, Johns Hopkins University School of Medicine, Baltimore, Maryland.

Please address correspondence to Aylin Tekes, MD, Division of Pediatric Radiology, The Russell H. Morgan Department of Radiology and Radiological Science, Johns Hopkins School of Medicine, Charlotte R. Bloomberg Children's Center, Sheikh Zayed Tower, Room 4174, 1800 Orleans St, Baltimore, MD 21287-0842; e-mail: atekes1@jhmi.edu

<http://dx.doi.org/10.3174/ajnr.A5724>

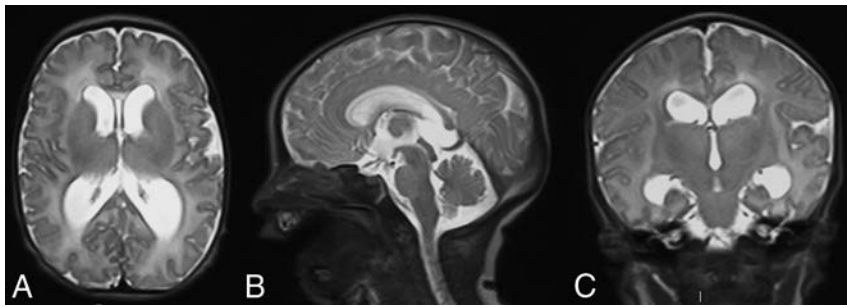


FIG 1. UFB-MRI performed in axial (A), sagittal (B), and coronal (C) planes with HASTE in a 1-day-old male infant with natural sleep. The study indication was a prenatal diagnosis of ventriculomegaly. Note the mild enlargement of the supratentorial ventricles and normal size of the fourth ventricle. There were no clinical signs of increased intracranial pressure. Although the cerebral aqueduct patency evaluation was limited in this study, the patient was followed with UFB-MRI. No additional standard MRI was deemed clinically necessary (Fig 2).

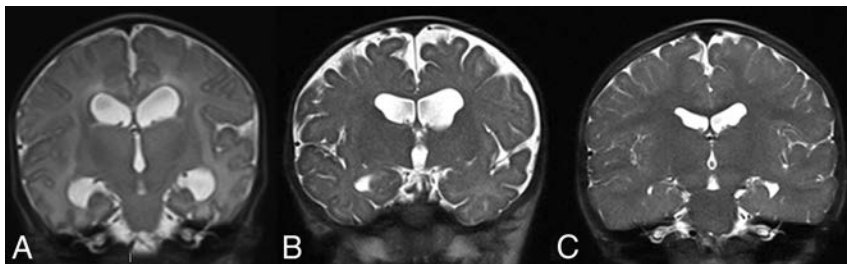


FIG 2. Coronal HASTE of the same patient as in Fig 1 obtained at day of life 1 (A), 5 months of age (B), and 2 years of age (C). Imaging demonstrates normalization of the ventricular size across time. High-quality diagnostic images were obtained without exposure to radiation or sedation/analgesia. Ventricular size and extra-axial spaces are easily seen in all UFB-MRIs. This case shows the value of UFB-MRI in follow-up examinations in children with ventriculomegaly.



FIG 3. A 10-year-old girl incidentally found to have hydrocephalus. In this imaging, she is 6 months status post third ventriculostomy. A, Sagittal HASTE in the midline shows lateral ventriculomegaly. Note the CSF flow artifacts/signal loss through the ventriculostomy site (arrow) at the floor of the third ventricle. B, Sagittal CISS at the same plane shows similar findings (arrow) with higher spatial resolution.

pleted in these cases to identify the following indications: ventriculomegaly, macrocephaly, or intracranial cyst. UFB-MRI was performed with axial, sagittal, and coronal HASTE (TR, 3000 ms; TE, 90–120 ms; slice thickness, 4 mm) using the head coils on 1.5T and 3T scanners (Siemens, Erlangen, Germany).

All UFB-MRIs were evaluated by a pediatric neuroradiologist and a pediatric neurosurgeon. Each MRI was evaluated for diagnostic quality to assess the ventricular size and extra-axial CSF spaces, and patients were categorized with the following diagnoses: ventriculomegaly/hydrocephalus, intracranial cysts, and macrocephaly. Inclusion criteria were as follows:

1) No follow-up standard brain MRI required after the UFB-MRI for the indicated diagnosis.

2) If clinical presentation, neurologic examination and UFB-MRI were diagnostic for patient discharge from pediatric neurosurgery.

3) Cases that required additional standard MRI were reviewed to assess whether additional imaging contributed to the indicated diagnosis.

4) All cases followed up clinically or radiographically for at least 6 months, unless discharged from care.

Ventriculomegaly diagnosis included etiologies of congenital or acquired origin (eg, secondary to intraventricular hemorrhage, post traumatic injury, or follow-up of ventriculomegaly secondary to tumor) or idiopathic origin. Intracranial cysts were defined as arachnoid, intraventricular, leptomeningeal, choroid plexus, or germinolytic. For postoperative tumor cases, UFB-MRI did not replace standard contrast-enhanced postoperative MRI.

RESULTS

The radiology information system identified 800 patients who had UFB-MRI during the study period. Of these 800 patients, 122 met the study criteria based on their imaging diagnosis. Twenty-one of the 122 did not meet the follow-up criteria either

due to moving out of state without adequate follow-up, not presenting for their scheduled clinical appointments, or having less than 6 months imaging/clinical follow-up.

We used the presence of additional MRI following UFB-MRI as a surrogate for insufficiency of UFB-MRI. Five patients had a standard brain MRI completed after UFB-MRI for the same indication. However, UFB-MRI was still deemed diagnostic for the indicated purposes in these cases: 1) A patient with ventriculomegaly was also noted to have a Chiari I malformation. He had an endoscopic third ventriculostomy based on the UFB-MRI and then had standard brain and spine MRI under anesthesia following his operation to further assess the Chiari I malformation. 2) A patient with ventriculomegaly had a routine follow-up study that included CISS imaging months later to assess aqueductal stenosis, though no significant additional diagnostic information was obtained. 3 and 4) Two patients with hydrocephalus were treated with endoscopic third ventriculostomy; they had endoscopic third ventriculostomy protocol brain MRIs (including CISS and cine) postoperatively as part of routine postoperative protocol. 5) A patient with an intracranial cyst underwent a standard brain MRI on long-term follow-up after an operation for cyst fenestration, including CISS imaging.

Fourteen other patients underwent standard brain MRI following UFB-MRI; however, the UFB-MRI was sufficient for the indicated diagnosis because the standard MRI was performed for an alternate diagnosis: Eleven of the 14 were patients with ventriculomegaly. The indication for the standard MRI was vascular

malformation ($n = 3$), postoperative tumor ($n = 6$), and myelomeningocele (entire neuroaxis MRI, $n = 2$); 3 of the 14 had intracranial cysts: All 3 had preoperative navigation studies. No adverse outcomes were noted in these 14 patients during the study period related to imaging.

There were 65 males and 57 females, 0.003–17.63 years of age (average, 3.21 ± 4.40 years; median, 1.12 years). Ninety-seven of 122 (79.5%) patients were 5 years of age or younger, 79/122 (64.8%) were 1 year of age or younger, and 57/122 (46.7%) were younger than 1 year of age (Table). Ventriculomegaly was seen in 84/122 (44 males and 40 females): Sixty-five of 84 (77.3%) were 5 years of age or younger, 57/84 (67.9%) were 1 year of age or younger, and 41/84 (48.8%) were younger than 1 year of age. Macrocephaly was seen in 18/122 (13 males and 5 females): Eighteen of 18 (100%) patients were 5 years of age or younger, 14/18 (77.8%) were 1 year of age or younger, and 9/18 (50%) were younger than 1 year of age. Intracranial cysts were seen in 20/122 (8 males and 12 females): Fourteen of 20 (70%) were 5 years of age or younger, 8/20 (40%) were 1 year of age or younger, and 7/20 (35%) were younger than 1 year of age.

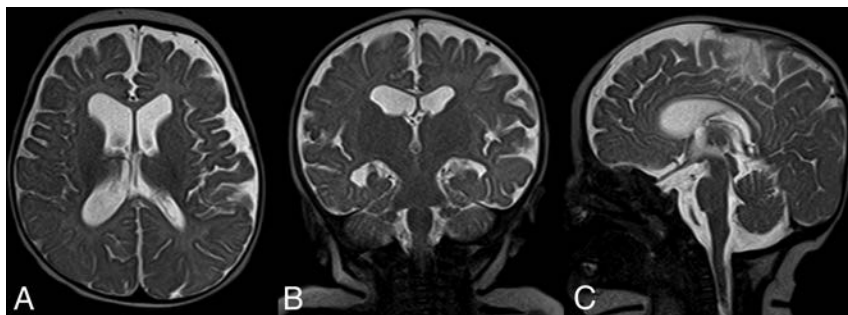


FIG 4. A 3-month-old child with macrocephaly and head circumference increase from the 50th to >95th percentile with normal neurologic developmental milestones. UFB-MRI was performed with axial (A), coronal (B), and sagittal (C) HASTE. Note mild supratentorial ventriculomegaly and prominence of the frontoparietal extra-axial CSF spaces confirming benign enlargement of the extra-axial CSF spaces.

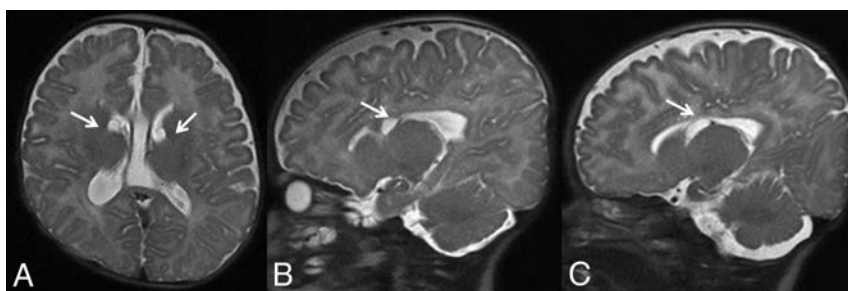


FIG 5. A 2-month-old boy with a prenatal diagnosis of intracranial cysts. Axial (A), right (B), and left (C) parasagittal HASTE shows simple-appearing cysts at the caudothalamic notches (arrows) without other abnormalities. Note the normal ventricular size. Follow-up MRI at 6 months of age showed resolution of these cysts.

DISCUSSION

UFB-MRI has proved safe and effective for imaging of shunted hydrocephalus.^{1,3,8,9} Ventriculomegaly, intracranial cysts, and macrocephaly, which often require imaging for diagnosis and management, are frequent referrals to the pediatric neurosurgery clinic in young children. Eighty percent of our cohort was 5 years of age or younger; 65%, 1 year of age or younger; and 47%, younger than 1 year of age. Our data demonstrate the young age of children for these diagnoses, further supporting the value of UFB-MRI to eliminate anesthesia/sedation for standard brain MRI or the risk of ionizing radiation. Rather than subjecting young children to radiation with head CT or anesthesia with a standard protocol brain MRI, we explored the utility of this radiation-free, anesthesia-/sedation-free UFB-MRI in indications beyond shunted hydrocephalus.

In our institution, UFB-MRI includes triplanar HASTE, which is a T2-weighted sequence. Acquisition time is short and relatively less motion-sensitive. In addition, the single-slice acquisition allows interrupting the image acquisition during moments of patient movement. Therefore, for this study, we only included patients in which assessment of CSF-containing spaces/structures was the primary objective, such as ventriculomegaly, intracranial cyst, or macrocephaly.

We did not have to exclude any UFB-MRI due to motion artifacts because it, in part, relies on our triplanar (axial, coronal, and sagittal) imaging. In case there was motion in 1 imaging plane, at least 1 other imaging plane proved to be free of motion artifacts, providing the required information. In all patients, UFB-MRI was deemed sufficient for diagnosis or follow-up of ventriculomegaly, intracranial cyst, or macrocephaly with adequate clinical/neurologic follow-up. In 5 patients where standard brain MRI was performed, all imaging was performed to further evaluate with advanced MRI sequences like CISS or CSF flow studies—information from these sequences would also not be obtained from head CT or conventional brain MRI sequences. We used clinical care/follow-up as our criterion standard rather than comparing UFB-MRI with standard brain MRI or head CT to avoid anesthesia/sedation or radiation.

In the past decade, “modified” fast brain MRI protocols have emerged, es-

Patient age and sex distribution per diagnosis

	Total	Male	Female	Age Range (yr)	Age (Mean) (yr)	Age (SD) (yr)	Age (Median) (yr)	5 Years of Age or Younger	1 Year of Age or Younger	Younger than 1 Year of Age
Ventriculomegaly	84	44	40	0.003–17.63	3.28	4.64	1.05	65/84 (77%)	57/84 (68%)	41/84 (49%)
Macrocephaly	18	13	5	0.2–4.42	1.26	1.09	0.98	18/18 (100%)	14/18 (78%)	9/18 (50%)
Cyst	20	8	12	0.3–17.47	4.72	4.68	4.84	14/20 (70%)	8/20 (40%)	7/20 (35%)

pecially in children with traumatic brain injuries.^{10,11} Guided by medical indications, each hospital sets their neuroimaging protocols based on their resources, such as scanner availability, staffing, and other urgent indications. Most of the modified protocols have diffusion-weighted imaging to look for ischemic injury and susceptibility-weighted imaging to look for hemorrhagic injuries. Although additional sequences are necessary for these indications, a UFB-MRI protocol with HASTE without any other added sequences is sufficient in patients with ventriculomegaly, intracranial cysts, and macrocephaly because CSF-containing structures are the primary area of concern.

UFB-MRI is “quick” and does not require sedation or anesthesia. Still, incorporating this technique into a routine MRI schedule 24 hours a day, 7 days a week, may be challenging. Work flow changes require a coordinated effort between pediatric neuroradiology and the provider’s department as well as support of the radiology department administration.¹⁴ Tekes et al¹⁵ previously published information on how to incorporate UFB-MRI into clinical routine following lean six sigma methodology; however, each institution may need to work on a work flow that best fits their internal resources. Variable practices were noted, depending on the resources and provider team’s preferences and experience. In urgent cases in which UFB-MRI is not possible, head CT does remain an alternative, but to minimize the radiation in these cases, optimized low-dose pediatric head CT protocols should be used.¹⁶

We recognize the limitations of UFB-MRI, especially in the assessment of parenchymal diseases with a wide range of etiologies, including but not limited to myelination, cortical development, brain tumors, ischemia/stroke, and intracranial hemorrhages.^{8,12,17} Thus, UFB-MRI should not be used as a “quick scan” to evaluate these diseases.

We are proposing specific additional indications for UFB-MRI beyond the most commonly used and published indication, shunted hydrocephalus, and we used stringent inclusion criteria in our patient population (requiring either discharge from medical care for the stated indication or at least 6 months of clinical and/or imaging follow-up). Because we practice in a quaternary care children’s center where we receive out-of-state and international patients, some loss to follow-up is inevitable. Some patients not meeting the stringent inclusion criteria does not reflect on the utility of the UFB-MRI.

CONCLUSIONS

Our data validate using UFB-MRI for indications like ventriculomegaly, macrocephaly, and intracranial cysts without impacting diagnostic accuracy in children. The elimination of radiation and sedation/anesthesia is magnified in its impact on patient safety due to the young age of the patient population typically presenting for evaluation of these diagnoses.

Disclosures: Thierry A.G.M. Huisman—UNRELATED: Board Membership: editorial board of the *American Journal of Neuroradiology*.

REFERENCES

1. Penzkofer AK, Pfluger T, Pochmann Y, et al. **MR imaging of the brain in pediatric patients: diagnostic value of HASTE sequences.** *AJR Am J Roentgenol* 2002;179:509–14 CrossRef Medline
2. Forbes KP, Pipe JG, Karis JP, et al. **Brain imaging in the unsedated pediatric patient: comparison of periodically rotated overlapping parallel lines with enhanced reconstruction and single-shot fast spin-echo sequences.** *AJNR Am J Neuroradiol* 2003;24:794–98 Medline
3. Ashley WW Jr, McKinstry RC, Leonard JR, et al. **Use of rapid-sequence magnetic resonance imaging for evaluation of hydrocephalus in children.** *J Neurosurg* 2005;103(2 Suppl):124–30 CrossRef Medline7
4. Brenner DJ, Hall EJ. **Computed tomography: an increasing source of radiation exposure.** *N Engl J Med* 2007;357:2277–84 CrossRef Medline
5. Malviya S, Voepel-Lewis T, Prochaska G, et al. **Prolonged recovery and delayed side effects of sedation for diagnostic imaging studies in children.** *Pediatrics* 2000;105:E42 CrossRef Medline
6. Vanderby SA, Babyn PS, Carter MW, et al. **Effect of anesthesia and sedation on pediatric MR imaging patient flow.** *Radiology* 2010;256:229–37 CrossRef Medline
7. Simon TD, Riva-Cambrin J, Srivastava R, et al; Hydrocephalus Clinical Research Network. **Hospital care for children with hydrocephalus in the United States: utilization, charges, comorbidities, and deaths.** *J Neurosurg Pediatr* 2008;1:131–37 CrossRef Medline
8. Sugahara T, Korogi Y, Hirai T, et al. **Comparison of HASTE and segmented-HASTE sequences with a T2-weighted fast spin-echo sequence in the screening evaluation of the brain.** *AJR Am J Roentgenol* 1997;169:1401–10 CrossRef Medline
9. Iskandar BJ, Sansone JM, Medow J, et al. **The use of quick-brain magnetic resonance imaging in the evaluation of shunt-treated hydrocephalus.** *J Neurosurg* 2004;101(2 Suppl):147–51 Medline
10. Roguski M, Morel B, Sweeney M, et al. **Magnetic resonance imaging as an alternative to computed tomography in select patients with traumatic brain injury: a retrospective comparison.** *J Neurosurg Pediatr* 2015;15:529–34 CrossRef Medline
11. Ryan ME, Jaju A, Ciolino JD, et al. **Rapid MRI evaluation of acute intracranial hemorrhage in pediatric head trauma.** *Neuroradiology* 2016;58:793–99 CrossRef Medline
12. Singh RK, Smith JT, Wilkinson ID, et al. **Ultrafast MR imaging in pediatric neuroradiology.** *Acta Radiol* 2003;44:550–57 Medline
13. Missios S, Quebada PB, Forero JA, et al. **Quick-brain magnetic resonance imaging for nonhydrocephalus indications.** *J Neurosurg Pediatr* 2008;2:438–44 CrossRef Medline
14. Durand DJ, Kohli MD. **Advanced practice quality improvement project: how to influence physician radiologic imaging ordering behavior.** *J Am Coll Radiol* 2014;11(12 Pt A):1155–59 CrossRef Medline
15. Tekes A, Jackson EM, Ogborn J, et al. **How to reduce head CT orders in children with hydrocephalus using the lean six sigma methodology: experience at a major quaternary care academic children’s center.** *AJNR Am J Neuroradiol* 2016;37:990–96 CrossRef Medline
16. Pindrik J, Huisman TA, Mahesh M, et al. **Analysis of limited-sequence head computed tomography for children with shunted hydrocephalus: potential to reduce diagnostic radiation exposure.** *J Neurosurg Pediatr* 2013;12:491–500 CrossRef Medline
17. Rozovsky K, Ventureyra EC, Miller E. **Fast-brain MRI in children is quick, without sedation, and radiation-free, but beware of limitations.** *J Clinical Neurosci* 2013;20:400–05 CrossRef Medline

Neurodevelopmental Correlates of Fetal Motor Behavior Assessed Using Cine MR Imaging

T.T.A. Hayat, M. Martinez-Biarge, V. Kyriakopoulou, J.V. Hajnal, and M.A. Rutherford



ABSTRACT

BACKGROUND AND PURPOSE: Fetal motor behavior is widely used as a clinical indicator for healthy development; however, our understanding of its potential as a marker for neurologic integrity is underdeveloped. MR imaging allows complete views of the whole fetus, which, combined with brain imaging, may improve the characterization of this relationship. This study aimed to combine an analysis of fetal motor behavior, brain MR imaging, and postnatal outcome, to provide insight into neurodevelopmental correlates of motor behavior.

MATERIALS AND METHODS: Cine MR imaging was used to acquire sequences of fetal motor behavior in subjects with normal and abnormal findings on conventional brain MR imaging between 18 weeks' gestation and term. General movement sequences were analyzed using established criteria. Brain MR imaging was reported by an expert fetal neuroradiologist. Subjects were followed for up to 4 years postnatally with standard postnatal assessments.

RESULTS: Nineteen of 21 fetuses with normal brain MR imaging findings showed normal general movements, compared with 14 of 22 of the fetuses with abnormal brain MR imaging findings, which, when classified by severity of the malformation, showed a significant relationship with postnatal outcome ($P = .021$). There was a significant relationship among neurodevelopmental outcome, general movement quality, and MR imaging of the brain ($P = .020$).

CONCLUSIONS: The findings from this study demonstrate that a combined structural and functional imaging approach to the fetus will improve the characterization of early neurologic integrity, with the potential to inform postnatal outcome. This also lays the groundwork for further in vivo research as advanced imaging techniques are developed to study fetal neurologic development.

ABBREVIATION: GM = general movements

Motor impairment is common to many neuropathologic conditions at early stages of development. The assessment of motor function constitutes an important component of the neurologic examination in early infancy, with numerous studies demonstrating that deviations in posture, tone, reflexes, and gross

and fine motor behavior correlate strongly with neuropathology.^{1,2} Observations of spontaneous motor behavior in the full-term and preterm infant have demonstrated that deviations in their quality occur in the presence of supraspinal CNS lesions.³ The pattern of movements most frequently observed is termed "general movements" (GM), which are characterized by a global sequence of movements of variable speed, amplitude, direction, and fluency.⁴ Disruptions in the GM pattern are characterized by changes in the quality of movements, which are qualitatively described as monotonous and cramped movements, among others.⁵ The GM analysis approach has been extended to the fetus using sonographic imaging; pathologic conditions in the fetus have been associated with a variety of deviant GM patterns.^{6,7} There is evidence to suggest that postnatal GM assessment is predictive of neurologic impairment, ranging from cerebral palsy to cognitive impairment.^{8,9}

Sonography has been used for capturing fetal motor behavior at a relatively high temporal resolution. However, the FOV is lim-

Received January 31, 2018; accepted after revision April 11.

From the Centre for the Developing Brain (T.T.A.H., V.K., J.V.H., M.A.R.), Perinatal Imaging and Health, Imaging Sciences & Biomedical Engineering Division, King's College London, London, UK; and Department of Paediatrics (M.M.-B.), Hammer-smith Hospital, Imperial College London, London, UK.

This study was supported by a Medical Research Council PhD studentship.

Please address correspondence Tayyib T.A. Hayat, MRCP, PhD, Centre for the Developing Brain, Perinatal Imaging and Health, Imaging Sciences & Biomedical Engineering Division, King's College London, 1st Floor South Wing, St Thomas' Hospital, London SE1 7EH, United Kingdom; e-mail: tayyib.hayat@nhs.net; @DrTayyib

Indicates open access to non-subscribers at www.ajnr.org

Indicates article with supplemental on-line table.

Indicates article with supplemental on-line video.

<http://dx.doi.org/10.3174/ajnr.A5694>

ited; this limitation results in only a partial view of the fetus beyond the gestational age of 20 weeks, thus preventing accurate GM assessment later in pregnancy. Relatively more recently, MR imaging has been explored as a method for observing gross motor activity in the fetus; MR imaging–based studies are taking advantage of the improved global view of the fetus, particularly as it approaches full-term.^{10–12} By means of cine MRI, in an earlier study by our group, changes in fetal motor behavior across gestation were characterized in relation to the volume of available intrauterine space.¹²

In this study, we sought to test the hypothesis that the assessment of the quality of fetal motor behavior using cine MRI is associated with the presence of neurologic abnormalities demonstrated on conventional clinical MR imaging of the brain and is predictive of postnatal neurodevelopmental outcome.

MATERIALS AND METHODS

Ethics approval was obtained before the start of the study, and written consent was obtained in all subjects. MR images were acquired at the Robert Steiner MRI Unit, Hammersmith Hospital, between October 2007 and February 2010. Subjects were either recruited prospectively as healthy volunteers or referred to the unit following a routine ultrasound requiring further characterization. All subjects had standard clinical MR imaging brain sequences obtained, which were reported by an expert fetal neuroradiologist (M.A.R.).

Cine Image Acquisition

All imaging examinations were performed on a 1.5T Achieva scanner (Philips Healthcare, Best, the Netherlands) using a 5-channel phased array cardiac coil. Sequence parameters were flip angle, 60°; FOV, 50 cm²; TR/TE, 3.2/1.59 ms; voxel size, 2.2 × 2.2 mm; slice thickness, 30–40 mm; partial Fourier, 62.5%; sensitivity encoding factor, 2; specific absorption rate, 2 W/kg; slice acquisition time, 0.303 seconds; temporal resolution, 3.3 frames per second. Patients were scanned in a lateral tilt position to avoid inferior vena cava compression by the uteroplacental unit, without any sedation. Mothers were not given any specific advice about eating and drinking. All examinations were performed in the morning between 9 AM and 1 PM; no other variable was controlled. Total MR imaging examination time was approximately 60 minutes, including all other clinical and research sequences.

Qualitative Analysis of Fetal Motor Behavior

The assessment of the quality of motor behavior was based on the criteria for analysis of general movements.^{3,5,13} This motor sequence was selected due to the capability of visualizing the whole fetus with cine MRI, the need for a noninteractive assessment tool, and the established predictive validity of GM analysis in both fetal and ex utero subjects.^{7,14} General movements are defined as a spontaneously generated variable sequence of movements in which there is generalized involvement of the limbs, head, and trunk; the sequence can last from a few seconds to several minutes. The assessment of the quality of GM focuses on 3 main components: fluency—movements should have a smooth appearance and be free from rigidity; variability—a difference in the pattern of movements from one GM to the next; and com-

plexity—movements should involve most of the body. GM sequences that fulfill all the above criteria are deemed normal (see On-line Videos 1–3 for examples of normal and 4–6 for examples of abnormal fetal GM).

All GM assessment was performed by 2 raters (T.T.A.H. and M.M.-B.) who had undergone formal training in GM assessment in preterm infants and healthy and unhealthy neonates and were blinded to findings on brain MR imaging. A consensus decision was made on cases in which the individual raters made different assessments.

Assessment of Postnatal Neurologic Outcome

Outcome data were obtained in the form of postnatal neurologic assessment using the Bayley Scales of Infant Development¹⁵ or the Griffiths Mental Development Scales.¹⁶ Assessments were performed by pediatricians experienced with these methods. Other outcomes such as postnatal death, termination of pregnancy, or intrauterine death were also recorded. The aim was to follow the subjects at 12 and 24 months postnatally.

Statistical Analysis

Statistical analysis was performed using GraphPad Prism software, Version 7.0 (GraphPad Software, San Diego, California). Relationships among GM, structural malformations and neurodevelopmental outcome, GM analysis, and brain MR imaging were analyzed using χ^2 and Fisher Exact tests. In the group with abnormal brain imaging findings, a further classification and analysis were made on the basis of the severity of malformation, with subjects with isolated ventriculomegaly classified as “mild,” and the others, as “severe.” Interrater variability was calculated after a training period using all datasets and was tested using the Cohen κ statistic. *P* values < .05 were considered significant.

RESULTS

Fetal general movements were assessed in 43 pregnancies (median gestational age, 25 weeks; range, 20–36 weeks); the interrater variability was 0.764 (Cohen κ). The median number of GM sequences assessed per fetus was 3 (range, 1–7). Four subjects were lost to follow-up, all of whom were in the subgroup that had normal brain imaging findings and normal GM. The On-line Table summarizes the unhealthy cases, including the findings from the clinical brain images, the movement analysis, and the outcome assessment.

Analysis of the Cohort with Normal Brain MR Imaging Findings

Twenty-one subjects were included in this cohort (median gestational age, 25 weeks; range, 20–34 weeks), of which 18 were healthy volunteers. The median postnatal follow up was 22 months (range, 1–47 months); 4 subjects were lost to follow-up. Fifteen subjects had a normal outcome, of whom 13 had normal GM. Two subjects had abnormal outcomes (neonatal death associated with premature birth at a gestational age of 26 weeks; mild language delay at 25 months), and both showed normal GM. There was no association between GM and outcome (*P* = .583, Fisher exact test).

Analysis of the Cohort with Abnormal Brain MR Imaging Findings

Twenty-two subjects were included in this cohort (median gestational age, 25 weeks; range, 21–36 weeks), all of whom were referred following abnormal ultrasound findings. The median postnatal follow-up was 24 months (range, 12–31 months; On-line Table); none were lost to follow-up. Six pregnancies were terminated, of which 3 showed abnormal GM. Seven subjects had abnormal outcomes, of whom 4 showed abnormal GM. Nine subjects had normal outcomes, of whom 3 showed abnormal GM. There was no association between GM and outcome ($P = .607$, Fisher exact test); subjects were further classified into mild and severe groups based on brain malformations, for which a significant relationship was drawn between GM and outcome ($P = .021$, χ^2 test).

Association with Postnatal Neurodevelopmental Outcome

There was a significant relationship between MR imaging and postnatal outcome ($P = .004$, Fisher exact test) and among the 3 variables for both cohorts combined: GM assessment, postnatal outcome, and MR imaging brain findings ($P = .020$, χ^2 test); if the classification combined normal and mild malformations into a single group, the relationship remained positive ($P = .022$, χ^2 test).

DISCUSSION

The assessment of GM was originally devised to study the motor function of neonates and preterm infants as a marker of neurologic integrity in a range of conditions.^{3-5,17,18} The presence of GM is stable from its emergence in the first trimester to 3–5 months postterm, which has led to the investigation of fetal GM with ultrasound.⁶ Use of MR imaging was a natural progression and allowed a more detailed view of the fetus, particularly in late gestation.¹²

This study has shown that cine MRI can capture fetal general movements across a wide range of gestational ages and can be used to identify findings of normal and abnormal sequences that are consistent with the GM definitions for premature infants and neonates. A positive association was found among postnatal outcome, structural MR imaging, and GM analysis and suggests that fetal motor assessment may reflect pathologic deviations in CNS development. The data did not reach significance for demonstrating a relationship between GM and outcome in each cohort when classified by structural brain imaging.

The use of brain MR imaging to assess neurologic integrity in the fetus has a caveat: Several studies have shown that structural malformations are associated with a variable clinical outcome.¹⁹⁻²¹ The likely explanation is the capacity for plasticity in the early CNS, which allows a range of normal or mildly abnormal outcomes, despite malformations or insults. Evidence for this has emerged from studies that report neurodevelopmental outcomes after several years of follow-up and which demonstrate a high proportion of neurologically normal outcomes despite structural malformations.²²⁻²⁵ Thus, a longer period of follow-up in the present study may allow brain maturation and emergence of the likely long-term neurodevelopmental status for these subjects against which in utero GM assessment could be assessed. On the contrary, other studies with long-term follow-up

have shown the emergence of autism and related disorders in individuals with a distribution of incidental CNS lesions similar to those in controls.²⁶

There are certain limitations when using cine MRI: In particular, the frame rate generated with the sequence is approximately 3 frames per second, compared with a video, which can be up to 30 frames per second, similar to ultrasound. In a previous study,¹² we showed that important information pertaining to fetal movement and its complexity was not lost. Also due to the practicalities of MR imaging as an imaging technique, there are limitations on the maximum duration of cine sequence acquisition, which include patient tolerability, limitations due to the specific absorption rate, and the need to acquire other clinical and research data. Given the limitations of ultrasound in the latter half of gestation, further exploration of the role of motor behavioral analysis as 1 element of a complete MR imaging–based fetal neurologic assessment would be justified.

Spontaneous fetal movements are generally considered a barrier to effective MR imaging acquisition due to motion corruption of static brain images. However, as with all ex utero age groups, useful clinical information regarding the integrity of the neuraxis is contained in motor output. This study is limited by its relatively small size and heterogeneous group of neurologic malformations; therefore, the study may not be sufficiently powered to elucidate a positive association. The subgroup with abnormal findings is also very variable in the severity of malformations, and the high representation of ventriculomegaly cases in particular is associated with milder outcomes, some of which require a longer duration of follow-up.²⁰ The potential for a mild, if not normal, outcome in the ventriculomegaly subjects may be reflected in the positive relationship between GM and outcome when the group with abnormal findings was further subdivided on the basis of the severity of malformations. This finding is important and suggests that GM analysis has the potential to serve as a biomarker of CNS integrity and add to the assessment provided by brain structure.

There is still a need to improve the understanding of fetal movement and to further explore classifying motor output into normal and pathologic. Further studies may better demonstrate their association with the underlying neurologic integrity, allowing motor patterns to represent a relevant biomarker when combined with emerging functional and structural imaging techniques such as fMRI and tractography.^{27,28} Last, a detailed characterization of motor patterns, with a model of the role of intrauterine constraints,^{11,29} will help develop a comprehensive understanding of the maturation of sensorimotor networks, which, from studies in preterm infants, have been shown to undergo important developmental trajectories early in life and which are likely affected by the physical environment.³⁰

CONCLUSIONS

This study has provided exploratory data on the use of general movements as a framework for analyzing fetal motor behavior using cine MRI in both neurologically healthy and unhealthy fetuses. Future studies could expand the cohort to include larger homogeneous groups of pathologic conditions and to continue long-term monitoring of subjects to establish the predictive value of fetal GM analysis as a marker of neurologic integrity. This ex-

pansion may provide a foundation for a framework for the in utero clinical assessment of motor behavior as an adjunct to current approaches and provide a functional marker that could be related to data gathered using advanced imaging techniques that are currently undergoing development.

Disclosures: Joseph V. Hajnal—RELATED: Grant: Medical Research Council, Comments: research grant to support technical and clinical studies focused on MRI of fetuses*; Other: Philips Healthcare, Comments: research support governed by a collaborative research agreement to facilitate advanced use of MRI equipment*; UNRELATED: Grants/Grants Pending: European Research Council, Comments: grant support including for technical development of methods for imaging fetuses.* Mary A. Rutherford—RELATED: Grant: Medical Research Council, Comments: research grant to support technical and clinical studies focused on MRI of fetuses; UNRELATED: Grants/Grants Pending: European Research Council, Comments: grant support including for technical development of methods for imaging fetuses. *Money paid to the institution.

REFERENCES

- Saint-Anne Dargassies S. **Value of assessing clinical neuropathology at birth.** *Proc R Soc Med* 1971;64:468–71 Medline
- Dubowitz L, Ricciw D, Mercuri E. **The Dubowitz neurological examination of the full-term newborn.** *Ment Retard Dev Disabil Res Rev* 2005;11:52–60 CrossRef Medline
- Prechtl HF, Einspieler C, Cioni G, et al. **An early marker for neurological deficits after perinatal brain lesions.** *Lancet* 1997;349:1361–63 CrossRef Medline
- Guzzetta A, Mercuri E, Rapisardi G, et al. **General movements detect early signs of hemiplegia in term infants with neonatal cerebral infarction.** *Neuropediatrics* 2003;34:61–66 CrossRef Medline
- Ferrari F, Cioni G, Prechtl HF. **Qualitative changes of general movements in preterm infants with brain lesions.** *Early Hum Dev* 1990;23:193–231 CrossRef Medline
- de Vries JL, Fong BF. **Changes in fetal motility as a result of congenital disorders: an overview.** *Ultrasound Obstet Gynecol* 2007;29:590–99 CrossRef Medline
- Rosier-van Dunné FM, van Wezel-Meijler G, Bakker MP, et al. **Fetal general movements and brain sonography in a population at risk for preterm birth.** *Early Hum Dev* 2010;86:107–11 CrossRef Medline
- Ferrari F, Cioni G, Einspieler C, et al. **Cramped synchronized general movements in preterm infants as an early marker for cerebral palsy.** *Arch Pediatr Adolesc Med* 2002;156:460–67 CrossRef Medline
- Einspieler C, Bos AF, Libertus ME, et al. **The general movement assessment helps us to identify preterm infants at risk for cognitive dysfunction.** *Front Psychol* 2016;7:406 CrossRef Medline
- Shen SH, Guo WY, Hung JH. **Two-dimensional fast imaging employing steady-state acquisition (FIESTA) cine acquisition of fetal non-central nervous system abnormalities.** *J Magn Reson Imaging* 2007;26:672–77 CrossRef Medline
- Verbruggen SW, Loo JH, Hayat TTA, et al. **Modeling the biomechanics of fetal movements.** *Biomech Model Mechanobiol* 2016;15:995–1004 CrossRef Medline
- Hayat TTA, Nihat A, Martinez-Biarge M, et al. **Optimization and initial experience of a multisection balanced steady-state free precession cine sequence for the assessment of fetal behavior in utero.** *AJNR Am J Neuroradiol* 2011;32:331–38 CrossRef Medline
- Einspieler C, Prechtl HF. **Prechtl's assessment of general movements: a diagnostic tool for the functional assessment of the young nervous system.** *Ment Retard Dev Disabil Res Rev* 2005;11:61–67 CrossRef Medline
- Burger M, Louw QA. **The predictive validity of general movements: a systematic review.** *Eur J Paediatr Neurol* 2009;13:408–20 CrossRef Medline
- Bayley N. *Bayley Scales of Infant and Toddler Development.* San Antonio: Psychological Corporation; 2006
- Griffiths R. *The Griffiths Mental Development Scales from Birth to 2 Years, Manual, 1996 Revision.* Henley, UK: Association for Research in Infant and Child Development Test Agency; 1996
- van Iersel PA, Bakker SC, Jonker AJ, et al. **Quality of general movements in term infants with asphyxia.** *Early Hum Dev* 2009;85:7–12 CrossRef Medline
- Hadders-Algra M, Mavinkurve-Groothuis AM, Groen SE, et al. **Quality of general movements and the development of minor neurological dysfunction at toddler and school age.** *Clin Rehabil* 2004;18:287–99 CrossRef Medline
- Poretti A, Limperopoulos C, Roulet-Perez E, et al. **Outcome of severe unilateral cerebellar hypoplasia.** *Dev Med Child Neurol* 2010;52:718–24 CrossRef Medline
- Gaglioti P, Danelon D, Bontempo S, et al. **Fetal cerebral ventriculomegaly: outcome in 176 cases.** *Ultrasound Obstet Gynecol* 2005;25:372–77 CrossRef Medline
- Chervenak FA, Duncan C, Ment LR, et al. **Outcome of fetal ventriculomegaly.** *Lancet* 1984;2:179–81
- Tarui T, Limperopoulos C, Sullivan NR, et al. **Long-term developmental outcome of children with a fetal diagnosis of isolated inferior vermian hypoplasia.** *Arch Dis Child Fetal Neonatal Ed* 2014;99:F54–58 CrossRef Medline
- Bar-Yosef O, Barzilay E, Dorembus S, et al. **Neurodevelopmental outcome of isolated ventriculomegaly: a prospective cohort study.** *Prenat Diagn* 2017;37:764–68 CrossRef Medline
- Letouzey M, Chadie A, Brasseur-Daudruy M, et al. **Severe apparently isolated fetal ventriculomegaly and neurodevelopmental outcome.** *Prenat Diagn* 2017;37:820–26 CrossRef Medline
- Cooper S, Katorza E, Berkenstadt M, et al. **Prenatal abnormal width of the cavum septum pellucidum: MRI features and neurodevelopmental outcome.** *J Matern Fetal Neonatal Med* 2017 Aug 16. [Epub ahead of print] CrossRef Medline
- Monterrey JC, Philips J, Cleveland S, et al. **Incidental brain MRI findings in an autism twin study.** *Autism Res* 2017;10:113–20 CrossRef Medline
- Seshamani S, Blazejewska AI, Mckown S, et al. **Detecting default mode networks in utero by integrated 4D fMRI reconstruction and analysis.** *Hum Brain Mapp* 2016;37:4158–78 CrossRef Medline
- Marami B, Mohseni Salehi SS, Afacan O, et al. **Temporal slice registration and robust diffusion-tensor reconstruction for improved fetal brain structural connectivity analysis.** *Neuroimage* 2017;156:475–88 CrossRef Medline
- Verbruggen SW, Oyen ML, Phillips ATM, et al. **Function and failure of the fetal membrane: modelling the mechanics of the chorion and amnion.** *PLoS One* 2017;12:e0171588 CrossRef Medline
- Allievi AG, Arichi T, Tumor N, et al. **Maturation of sensori-motor functional responses in the preterm brain.** *Cereb Cortex* 2016;26:402–13 CrossRef Medline

Thalamocortical Connections and Executive Function in Pediatric Temporal and Frontal Lobe Epilepsy

N. Law, M.L. Smith, and E. Widjaja



ABSTRACT

BACKGROUND AND PURPOSE: Largely accepted in the literature is the role the interconnections between the thalamus and cortex play in generalized epilepsy. However, thalamocortical involvement is less understood in focal epilepsy in terms of the effect of seizures on thalamocortical circuitry in the developing brain and subsequent cognitive outcome. We investigated thalamocortical pathway microstructure in pediatric frontal lobe epilepsy and temporal lobe epilepsy and examined the associations between pathway microstructure and measures of executive function.

MATERIALS AND METHODS: We examined thalamocortical connections in 24 children with frontal lobe epilepsy, 17 patients with temporal lobe epilepsy, and 25 healthy children using DTI. We investigated several executive function measures in patients and controls, which were distilled into latent executive function components to compare among groups, and the associations between measures of thalamocortical microstructure and executive function.

RESULTS: We found no differences in thalamocortical pathway microstructure between the groups, but aspects of executive function (mental flexibility/inhibition/shifting) were impaired in the frontal lobe epilepsy group compared with controls. In patients with frontal lobe epilepsy, younger age at seizure onset and a greater number of antiepileptic drugs were associated with DTI indices indicative of damaged/less developed thalamocortical pathways. In patients with temporal lobe epilepsy, poorer performance on all measures of executive function was associated with DTI indices reflective of damaged/less developed pathways.

CONCLUSIONS: Our results give insight into vulnerable neural networks in pediatric focal epilepsy and suggest thalamocortical pathway damage as a potential mechanism of executive function impairment in temporal lobe epilepsy but not frontal lobe epilepsy. Identifying structure-function relations can help inform how we measure functional and cognitive/behavioral outcomes in these populations.

ABBREVIATIONS: AEDs = antiepileptic drugs; CPT3 = Conners' Continuous Performance Task, 3rd ed; D-KEFS = Delis-Kaplan Executive Function System; EF = executive function; FLE = frontal lobe epilepsy; HC = healthy controls; KMO = Kaiser-Meyer-Olkin Measure of Sampling Adequacy; MANOVA = multivariate analysis of variance; MD = mean diffusivity; PCA = principal components analysis; RD = radial diffusivity; TLE = temporal lobe epilepsy

Structural and functional alterations of the brain, extending beyond the region of epileptogenic focus, may result from seizure-induced cellular changes in epilepsy.¹ Thalamocortical connections are involved in the generation and propagation of

typical spike and wave seizures in generalized epilepsy.² In idiopathic generalized epilepsy, abnormal thalamocortical reciprocal connections underlie epileptogenic activity via large-scale synchronization of thalamocortical loops³ or via thalamic propagation to cortical networks,⁴ with the thalamus acting as an extension of the cortical epileptic network during seizures.⁵ Thalamocortical connections have been investigated in adults with juvenile myoclonic epilepsy⁶ and idiopathic generalized epilepsy.⁷ Reduced white matter integrity of the anterior thalamus and prefrontal cortex was found in adults with juvenile myoclonic epilepsy compared with healthy controls (HC).⁶ In contrast, functional but not structural differences were found for thalamofrontal pathways in adults with idiopathic generalized epilepsy versus controls.⁷

Thalamocortical connections have been implicated in wakefulness/arousal and attention/executive function (EF), among other functions. Damage to these connections has been docu-

Received October 9, 2017; accepted after revision April 11, 2018.

From the Department of Psychology (N.L., M.L.S.), University of Toronto, Toronto, Ontario, Canada; and Department of Psychology (N.L., M.L.S.), Program in Neurosciences and Mental Health (N.L., M.L.S.), Diagnostic Imaging (E.W.), and Division of Neurology (E.W.), Hospital for Sick Children, Toronto, Ontario, Canada.

This research was conducted with the support of EpLink – The Epilepsy Research Program of the Ontario Brain Institute (OBI). The OBI is an independent nonprofit corporation, funded partially by the Ontario government. The opinions, results and conclusions are those of the authors and no endorsement by the Ontario Brain Institute is intended or should be inferred.

Please address correspondence to Elysa Widjaja, MD, 555 University Ave, Toronto, ON, Canada, M5G 1X8; e-mail: elysa.widjaja@sickkids.ca

Indicates article with supplemental on-line tables.

<http://dx.doi.org/10.3174/ajnr.A5691>

mented in children with cerebellar brain tumors and developmental dyslexia and has been linked with working memory deficits⁸ and reading ability,⁹ respectively. It is not surprising then that structural and functional alterations in these pathways have been proposed to underlie functional deficits in generalized epilepsy.¹⁰ Impairments in attention/EF have been documented in generalized epilepsy,¹⁰ which, in turn, have been associated with disruption of thalamic and frontal circuits.¹¹ However, thalamocortical involvement is less understood in focal epilepsy.

Children with frontal lobe epilepsy (FLE) have deficits in EF, including planning and impulse control,¹² verbal fluency, and mental flexibility.¹³ There is also evidence of EF impairment in children with temporal lobe epilepsy (TLE),¹⁴ though EF deficits may be more pronounced in FLE.^{12,15-17} It is possible that a common neural substrate—thalamocortical connections—could be affected in FLE and to a lesser extent in TLE, and this compromise, in turn, may influence EF.

Widespread reduced functional and structural connectivity has been documented in children with FLE, such as reduced frontal network connectivity,¹⁸ and multilobar white matter abnormalities, including frontal connections.¹⁹ Reduced connectivity within the frontal network was related to performance in EF in children with FLE.¹⁸ Cognitively impaired children with FLE showed the greatest white matter compromise compared with cognitively unimpaired children with FLE and HC.²⁰ Several studies have documented structural abnormalities in association fibers such as the superior longitudinal fasciculus, inferior fronto-occipital fasciculus, uncinate fasciculus, cingulum, forceps minor, and corpus callosum in patients with focal epilepsy.²¹⁻²⁴ Abnormality in the uncinate fasciculus has been shown to correlate with EF in patients with TLE.²⁵ Additionally, abnormal association fibers have been shown to correlate with EF in other neurologic disorders.^{26,27} For the current study, we chose to examine connections between the thalamus and ipsilateral frontal lobe for the following reasons: 1) Thalamocortical fibers have been implicated in both adult and pediatric generalized epilepsy, 2) less is known about the role of thalamocortical pathways in focal epilepsy, and 3) thalamocortical connections and their microstructure have been previously linked to aspects of EF in other pediatric populations.⁸

We examined thalamocortical pathways in children with FLE, TLE, and HC; measures of EF; and the associations between pathway microstructure and EF to determine whether thalamocortical pathways are a potential mechanism of EF deficits in focal epilepsy. We hypothesized that altered thalamocortical microstructure would be observed in both FLE and TLE, with patients with FLE showing the greatest compromise to the pathways. Furthermore, multiple components of EF would be impaired in children with FLE compared with those with TLE and HC. Last, measures of thalamocortical microstructure would be correlated with EF.

MATERIALS AND METHODS

Participants

Participants included 24 children with FLE, 17 with TLE, and 25 HC. All patients had nonlesional etiology, and epileptogenic focus was defined on the basis of ictal video electroencephalography. The protocol for this study was approved by the Research Ethics Board, and informed consent was obtained. Table 1 contains de-

Table 1: Demographic and medical variables for the HC, FLE, and TLE groups

	FLE (n = 24)	TLE (n = 17)	HC (n = 25)
Sex (male/female)	10:14	8:9	14:11
Age (yr)			
Mean (SD)	13.10 (3.21)	14.54 (2.65)	13.95 (3.20)
Range	6.96–16.96	10.11–19.08	6.97–18.76
Handedness (right/left)	20/4	16/1	22/3
Age at seizure onset (yr)			
Mean (SD)	7.79 (4.01)	8.75 (3.76)	–
Range	1.00–14.40	1.30–15.00	–
Duration of epilepsy (yr)			
Mean (SD)	5.20 (2.93)	4.90 (3.62)	–
Range	1.70–12.00	.33–12.00	–
No. of AEDs			
Mean (SD)	2.00 (.659)	1.94 (.748)	–
Range	1–3	1–3	–
Laterality of epileptogenic focus			
Left	13	10	–
Right	9	4	–
Bilateral	2	3	–
Region of epileptogenic focus (TLE)			
Mesial	–	3	–
Lateral	–	12	–
Both mesial and lateral	–	2	–
Region of epileptogenic focus (FLE)			
Prefrontal	2	–	–
Inferior frontal	1	–	–
Frontal-central	9	–	–
Supplementary motor area	3	–	–
Unable to localize precisely	9	–	–

mographic and medical variables. There were no differences among the groups for sex [$\chi^2_{(2)} = 1.026, P = .599$], age at study [$F(2,63) = 1.138, P = .327$], and handedness [$\chi^2_{(2)} = 1.087, P = .581$]. The epilepsy groups were comparable for age at seizure onset [$F(1,39) = 0.572, P = .454$], duration of epilepsy [$F(1,39) = 0.084, P = .774$], laterality of epileptogenic focus [$\chi^2_{(2)} = 1.359, P = .507$], and number of antiepileptic drugs (AEDs) [$F(1,39) = 0.071, P = .791$].

Neuroimaging Protocol

MR imaging was performed on an Achieva 3T scanner (Philips Healthcare, Best, the Netherlands) using an 8-channel phased array head coil in all patients and controls. The imaging consisted of axial and coronal FLAIR, proton-density/T2, volumetric T1, and DTI (TR/TE = 10,000/60 ms, slice thickness = 2 mm, FOV = 22 cm, matrix = 112 × 112, NEX = 1, sensitivity encoding = 1, $b = 1000 \text{ s/mm}^2$, 32 noncollinear directions). The DTI indices and maps (eg, eigenvectors, fractional anisotropy, mean diffusivity [MD], axial diffusivity, and radial diffusivity [RD]) were calculated using the FMRIB Software Library (FSL; <http://www.fmrib.ox.ac.uk/fsl>)²⁸ to serve as a basis for probabilistic tractography.

ROI Placement and Standardization for DTI Tractography

To provide a standardized protocol for ROI placement, we drew all ROIs on axial sections of the zero diffusion-weighted (b_0) images of 10 randomly selected HC. The following 4 ROIs were

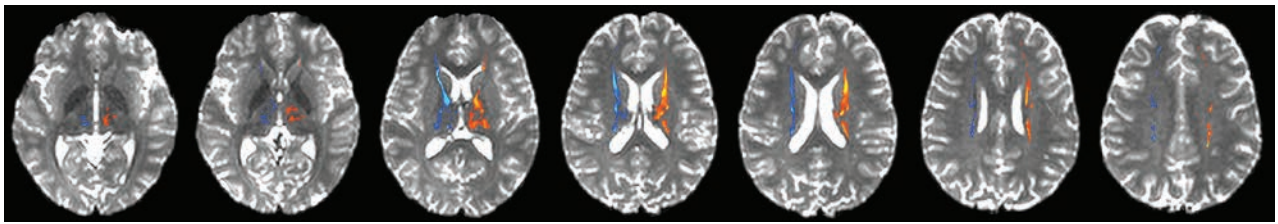


FIG 1. Thalamocortical pathways connecting the thalamus with the frontal cortex in a healthy brain. The left thalamocortical pathway is depicted in red/yellow, and the right thalamocortical pathway is depicted in dark/light blue. Axial sections are presented as the tracts progress dorsally from the thalamus to the frontal lobe (left to right).

produced for all 10 individuals using FSL²⁹: left and right frontal hemispheric white matter (ie, the frontal lobe was masked in its entirety for each hemisphere) and left and right thalamus (ie, masks were placed over the entirety of the thalamus of each hemisphere). The 10 sets of individually delineated ROIs were then combined into a single composite volume and registered to a brain template using Automated Image Registration³⁰ to produce template ROIs. The resultant template ROIs were registered onto each participant's b0 images using Automated Image Registration.³⁰ ROIs were brought into the native space for each participant, visually examined, and, if necessary, manually refined so that they covered only the appropriate region.

DTI Probabilistic Tractography and Pathway Segmentation

Using the FMRIB Diffusion Toolbox (<http://fsl.fmrib.ox.ac.uk/fsl/fslwiki/FDT>),²⁹ we completed probabilistic tractography to delineate bilateral thalamocortical white matter pathways connecting the left or right thalamus with the ipsilateral frontal cortex and to examine the microstructure of pathways. Within each hemisphere, to delineate the thalamocortical pathway, we used the thalamus ROI as the seed point and the ipsilateral frontal hemisphere ROI as the waypoint. The threshold was set to 10% for all pathways and was edited, as appropriate, to eliminate erroneous streamlines. Means and SDs for DTI indices were calculated for each pathway.

Measures of EF

Delis-Kaplan Executive Function System. The Verbal Fluency, Color-Word Interference, and Sorting subtests of the Delis-Kaplan Executive Function System (D-KEFS)³¹ measured generative naming, cognitive efficiency, response inhibition, mental flexibility, and planning/problem solving (see On-line Table 1 for test descriptions). Raw scores were converted to norm-referenced scaled scores before statistical analysis.

Conners' Continuous Performance Task, 3rd ed. We used the Conners' Continuous Performance Task, 3rd ed (CPT3),³² a computer-based task, to measure sustained attention. Omission errors (ie, failure to respond to target letters, a measure of inattention) T-scores were obtained and converted to scaled scores before analysis.

Statistics/Analytic Approach

The FLE and TLE groups were divided into 4 groups: left FLE ($n = 13$), right FLE ($n = 9$), left TLE ($n = 10$), and right TLE ($n = 4$),

and group means were compared with HC ($n = 25$) using multivariate analysis of variance (MANOVA). All participants with bilateral seizure focus were omitted from these analyses ($n = 5$). We performed 2 MANOVAs on DTI indices for the left and right thalamocortical pathways separately, with group as the between-subject variable. Planned tests of simple effects were used to examine the a priori hypothesis that the FLE group would show compromise in white matter microstructure within the thalamocortical pathways relative to the TLE and HC groups.

Next, we used principal component analysis (PCA) to reduce our measures of EF into component factors that represented underlying/latent EFs across our entire sample. As part of a data-quality examination process, we used the Kaiser-Meyer-Olkin Measure of Sampling Adequacy (KMO) and the Bartlett Test of Sphericity to determine the suitability of our data for being entered into PCA for factor/structure detection. A varimax rotation was used. The factor solution was based on those components with eigenvalues of >1.0 and the interpretability of the components (eg, loadings of $>.45$ and/or the highest loadings on each component). Any components identified from the PCA were considered for subsequent analyses of EF differences among the groups.

Third, a MANOVA was performed using the EF components extracted from PCA, with group as a between-subject variable. We used mean regression factor scores (residuals extracted) from the PCA to compare group differences in the EF components; a constant (ie, 10) was added to the regression factor scores to eliminate negative values before MANOVA. For interpretability, composite scores for each significant factor were calculated and compared between the groups (eg, FLE versus controls and TLE versus controls) using MANOVA. A Bonferroni correction was used in all analyses.

Last, correlation analyses investigated associations between DTI indices and EF component scores, age at seizure onset, duration of epilepsy, and the number of AEDs.

RESULTS

Delineation of Thalamocortical Pathways and Examination of Microstructure

Left and right thalamocortical pathways were produced (Fig 1). Regardless of group, pathways were qualitatively identical (ie, they began and ended within similar neuroanatomic locations). On-line Table 2 contains means and SDs for each pathway measure and all multivariate and between-subject effects. The

Table 2: Factor structure and factor loadings (> .45 and/or highest loading) after varimax rotation of 6 measures of EF in the FLE, TLE, and HC groups (n = 55)

EF Measure	EF1	EF2
D-KEFS Verbal Fluency Test: Letter Fluency	–	.596
D-KEFS Verbal Fluency Test: Category Switching	–	.450
D-KEFS Color-Word Interference Test: Inhibition	.850	–
D-KEFS Color-Word Interference Test: Inhibition/Switching	.912	–
D-KEFS Sorting Test: Confirmed Correct Sorts	–	.824
CPT3 omission errors	–	.783

Note:—EF1 indicates executive function component factor 1; EF2, executive function component factor 2.

MANOVA yielded no significant effect of group for the left or right thalamocortical pathways.

EF Components

PCA extracted 2 latent components that were independent of each other and reflected independent aspects of EF. The KMO and Bartlett test validated that structure detection was appropriate for our data [KMO = 0.742; $\chi^2_{(15)} = 88.25, P < .001$]. The component loadings for our 6 measures of EF are provided in Table 2. Together, these 2 components accounted for approximately 64% of the variance. The first component (EF1) explained 32.5% of the variance in the data and reflected a mental flexibility/inhibition/shifting dimension. Measures that loaded highly on this component included the D-KEFS Color-Word subtests. The highest loadings on the second component (EF2), explaining 31.2% of the variance, reflected an attention/cognitive efficiency/problem-solving component of EF. Specifically, the CPT3 Omission Errors and D-KEFS Verbal Fluency and Sorting subtests were included in this dimension.

Group Differences in EF

When regression factor scores from the PCA were compared, we found group differences across both EF components ($\lambda = 0.584, F = 7.861, P < .001$): EF1 [$F(2,52) = 11.44, P < .001, \eta^2 = 0.306$] and EF2 [$F(2,52) = 3.426, P = .04, \eta^2 = 0.116$]. For EF1, the FLE group had scores significantly below HC and the TLE group ($P < .001$ and $P = .007$, respectively). For EF2, the FLE group had scores significantly below HC ($P = .04$). No differences in EF component scores were found between the HC and TLE groups. For increased interpretability, composite factor scores were compared among the groups, yielding similar results as seen above (Fig 2).

When the FLE and TLE groups were divided on the basis of left-versus-right epileptogenic focus, we found group differences in the composite factor scores for both EF components ($\lambda = 0.511, F = 4.692, P < .001$): EF1 [$F(4,48) = 7.218, P < .001$] and EF2 [$F(4,48) = 7.173, P < .001$]. The left and right FLE groups had scores significantly below those of HC on both EF1 ($P = .001$) and EF2 ($P < .001$ and $P = .009$, respectively) (Fig 3). Furthermore, the left FLE group had scores significantly below those of left TLE group ($P = .044$). No differences in EF composite factor scores were found between the HC and TLE groups.

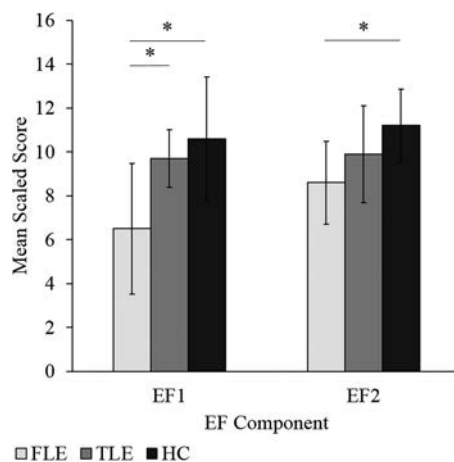


FIG 2. Mean composite EF factor scores for the FLE, TLE, and HC groups. Error bars represent SDs. The asterisk indicates a significant group difference (FLE < HC and FLE < TLE for EF1 and FLE < HC for EF2) at the $P < .05$ level. EF1 represents a mental flexibility/inhibition/switching component, while EF2 represents an attention/cognitive efficiency/problem-solving component.

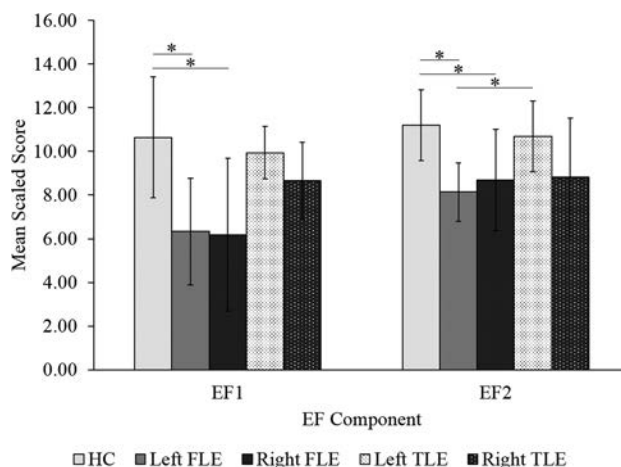


FIG 3. Mean composite EF scores for the left and right FLE, left and right TLE, and HC groups. Error bars represent SDs. The asterisk indicates a significant group difference (EF1: left FLE < HC and right FLE < HC; EF2: left FLE < HC, right FLE < HC, left FLE < left TLE) at the $P < .05$ level. EF1 represents a mental flexibility/inhibition/switching component, while EF2 represents an attention/cognitive efficiency/problem-solving component.

EF and Thalamocortical Microstructure

No correlations were found between EF1 or EF2 and the thalamocortical DTI indices for FLE group and HC. In the TLE group, EF1 was correlated with left thalamocortical RD ($r = -.559, P = .047$), while EF2 was correlated with left thalamocortical MD ($r = -.611, P = .026$) and RD ($r = -.620, P = .024$), and with right thalamocortical RD ($r = -.566, P = .044$).

Age of Seizure Onset, Number of AEDs, Duration of Epilepsy, and Thalamocortical Microstructure

In the FLE group, younger age at seizure onset was associated with lower fractional anisotropy and higher MD and RD of the thalamocortical pathways (left: $r = 0.431, P = .035; r = -.412, P = .045; r = -.487, P = .016$, respectively; and right: $r = 0.407, P = .049; r = -.530, P = .008; r = -.528, P = .008$, respectively).

In the FLE group, a greater number of AEDs was correlated

with higher MD ($r = 0.491, P = .015$) and RD ($r = 0.448, P = .028$) of the right thalamocortical pathway. In the TLE group, there were no significant correlations between age of seizure onset or number of AEDs and measures of thalamocortical pathway microstructure. No correlations were found between the duration of epilepsy and any of the DTI indices for either group.

DISCUSSION

To our knowledge, the current study was the first to examine the white matter microstructure of circumscribed thalamocortical pathways in pediatric focal epilepsy using DTI. The investigation of structure-function relations in pediatric focal epilepsy gives insight into the impact of seizures on thalamocortical circuitry in the developing brain and consequently potential impairment in frontally mediated EF.

We found no differences in DTI indices of either the left or right thalamocortical pathway among children with left FLE, right FLE, left TLE, right TLE, and HC. These findings were somewhat surprising, given previous evidence of reduced frontal lobe connectivity in children with FLE.^{18–20} Our analyses were limited to connections between the thalamus and ipsilateral frontal cortex. Seizures may spread from the frontal or temporal lobe via white matter primarily to other lobes in the ipsilateral or contralateral hemisphere, rather than the thalamus. The current study did not examine structural measures of other frontal pathways and therefore may be missing areas that are injured in FLE or TLE. Furthermore, the thalamus is not the generator of seizures in FLE or TLE, which could, in part, explain the findings that the thalamocortical pathway was not significantly impaired in children with FLE or TLE. He et al³³ found that thalamocortical functional connectivity to the parietal/occipital and temporal lobes was abnormal, but not thalamocortical connectivity to the frontal lobe in adults with TLE. Similarly, structural measures of thalamocortical architecture were documented to be no different between adults with idiopathic generalized epilepsy and healthy controls.⁷

Earlier age at FLE onset was associated with lower fractional anisotropy and higher MD and RD of the left and right thalamocortical pathways, implying that frontal lobe seizures early in life have a detrimental impact on thalamocortical connections. Specifically, FLE could interfere with normal development of thalamocortical pathways and, in turn, potentially affect function. We did not find associations between thalamocortical microstructure and the duration of epilepsy for either epilepsy group, suggesting that it may be the severity/extent of the epileptogenic activity, or early age at seizure onset, or both, not the cumulative time of epilepsy, which influence abnormal structure. These findings were like those in previous studies documenting a significant correlation between DTI measures and age of seizure onset but not duration of epilepsy.^{18,34}

A greater number of AEDs in the FLE group was correlated with higher MD and RD of the right thalamocortical pathway. A higher number of AEDs may reflect greater seizure severity, which, in turn, may be associated with damaged or less developed white matter. Alternatively, it is possible that AEDs themselves may injure or impede developing white matter.³⁵ However, it is difficult to tease apart the effects of seizure severity from the un-

derlying contribution of AEDs on white matter development in this study.

Two latent components of EF were extracted from our data, reflecting the mental flexibility/inhibition/shifting dimension (EF1) and the attention/cognitive efficiency/problem-solving dimension (EF2). Children with left or right FLE had scores significantly below those of HC for EF1 and EF2. Our findings are in line with previous research in that difficulties with planning and impulse control,^{12,13,15} mental flexibility/set-shifting,^{13,17} attention,¹⁶ and verbal fluency¹³ have been documented in children with FLE relative to HC. Although difficulties with aspects of EF have been reported in TLE relative to controls,¹⁴ we did not observe differences in EF between TLE and HC, likely due to the relatively small sample sizes. Previous studies have revealed impairment in concept formation,¹⁷ mental flexibility/set-shifting,^{17,36} and attention/concentration³⁶ in children with FLE compared with TLE. Congruently, we documented poorer performance on tasks that loaded onto EF2 (attention/cognitive efficiency/problem solving) for the FLE group compared with the TLE group; this difference was found only for children with left epileptogenic focus. The lack of a difference between the FLE and TLE groups for EF1 suggests that there may be a minimal or comparable impact of frontal and temporal lobe seizures on brain regions important for mental flexibility/inhibition/shifting (EF1); the same may not be true for brain regions that underlie cognitive efficiency and problem solving (EF2), which is why we observed EF2 to be impacted in FLE.

Significant correlations between measures of thalamocortical microstructure and EF component scores emerged only for the TLE group. Specifically, higher scores on EF1 (the mental flexibility/inhibition/shifting) were correlated with lower RD of the left thalamocortical pathway. Furthermore, higher scores on EF2 (the attention/cognitive efficiency/problem solving) were associated with lower RD of the left and right thalamocortical pathways as well as lower MD of the left thalamocortical pathway. These findings suggest that greater insult or damage to the pathways (or less developed pathways) is associated with poorer scores on the EF1 in TLE. We expected to observe these findings for the FLE group because reduced connectivity within the frontal network has been related to performance on tasks of EF in children with FLE.¹⁸ Furthermore, cognitively impaired children with FLE showed the greatest white matter compromise throughout the brain, including decreased frontal lobe connectivity compared with cognitively unimpaired children with FLE and healthy controls.²⁰ It is possible that an abnormal frontal lobe, and not solely thalamocortical pathways, is sufficient to cause EF impairment in FLE. However, for children with TLE, abnormal thalamocortical microstructure may be contributing to EF difficulties in the absence of overt frontal abnormality.

Limitations of the current study include the relatively small sample size, especially when considering whether laterality of seizure focus impacted both thalamocortical microstructure and EF outcomes. Furthermore, the reliability and validity of our PCA were limited by a relatively small overall sample size and, in turn, moderate-to-low participants-to-variables ratio (eg, 9:1).³⁷ However, relatively high communalities (>0.65) were found for all but 1 of our items, and many of our variables loaded strongly (ie, >0.7) and cleanly (ie, no cross-loadings; cutoff was loadings of

>0.45) onto each factor (Table 2). Considering these findings, we are confident that our PCA findings can be considered valid.

Additionally, we acknowledge that several identified thalamocortical pathways exist (eg, the pulvinar and lateral geniculate nucleus of the thalamus and parietal-occipital cortex; ventral posterolateral, ventral posteromedial, and lateral posterior nuclei of the thalamus and somatosensory cortex). However, in terms of thalamofrontal connections, other than the anterior nuclei of the thalamus being linked with the prefrontal cortex,⁶ no other thalamic nuclei have been structurally associated with the frontal cortex using DTI tractography in children with epilepsy. We chose not to segment the thalamus to investigate specific connections between its nuclei and the frontal lobe for several reasons: Aside from small cell sizes across our groups, our FLE sample was a heterogeneous group in terms of the region of frontal epileptogenic focus (Table 1). It is possible that in choosing to delineate all possible connections between the thalamus and ipsilateral frontal lobe, we may be including fibers such as the anterior and posterior thalamic radiations; however, any fibers from the thalamus that fell outside the frontal lobe were not included in our analyses. Furthermore, we believed that the focus of initial investigations should be on examining “whole” thalamocortical connections—that is, all the potential connections between the thalamus and frontal lobe that met the specified threshold for connectivity. As a result, our study provides a basis for thalamocortical (ie, frontal) connectivity in the developing (and epileptogenic) brain.

Once these connections are identified in the developing brain, examined structurally, and linked to broad aspects of EF, then future research can begin to tease apart the microstructure of thalamocortical connections as they relate to function. For example, subdividing the thalamus into nuclei and investigating the corresponding cortical connections should be considered (eg, anterior or posterior thalamic radiations); contrasting these pathways in FLE and TLE may reveal microstructural differences. Additionally, the medial-dorsal nucleus of the thalamus has been implicated in the initiation and spread of seizures in TLE (thought to be related to reciprocal connections between the midline thalamus and the hippocampus, entorhinal cortex, amygdala, and the olfactory cortex complex).³⁸ We did not include specific assessment of the thalamic medial dorsal nucleus because our patient population included children with FLE and TLE, and most of those with TLE had neocortical (or lateral) TLE rather than mesial TLE. Future research could include assessment of the connectivity between the medial dorsal thalamic nucleus and the hippocampus, entorhinal cortex, and amygdala in children with mesial TLE.

Last, although we investigated several EF tasks, further research is necessary to examine such functions as emotion regulation, planning, and organization in pediatric focal epilepsy populations and the potential impact of thalamocortical pathways on these aspects of EF. Because poorer performance on measures of EF was associated with thalamocortical microstructure in the TLE group, future research should investigate architectural differences in medial-versus-lateral TLE and implications on EF.

CONCLUSIONS

Our results suggest that in pediatric FLE, alterations to thalamocortical pathways at the structural level may not be sufficient to

produce a functional deficit; the frontal cortex itself as well as other frontal-extrafrontal connections may play a significant role in EF impairment. Results from this study also give insight into potential mechanisms of EF impairment in pediatric TLE, in that thalamocortical pathway microstructure is associated with EF in children with TLE. Therefore, TLE may have a significant impact on extratemporal regions, including the frontal lobe and its connections. Identifying vulnerable neural systems in pediatric focal epilepsy and the relation of these systems and neurocognitive outcome will influence how we measure functional and cognitive/behavioral outcome in this population.

Disclosures: Elysa Widjaja—UNRELATED: Grants/Grants Pending: Canadian Institutes of Health Research.* *Money paid to the institution.

REFERENCES

1. Cavazos JE, Jones SM, Cross DJ. **Sprouting and synaptic reorganization in the subiculum and CA1 region of the hippocampus in acute and chronic models of partial-onset epilepsy.** *Neuroscience* 2004; 126:677–88 CrossRef Medline
2. Zhang CH, Sha Z, Mundahl J, et al. **Thalamocortical relationship in epileptic patients with generalized spike and wave discharges: a multimodal neuroimaging study.** *Neuroimage Clin* 2015;9:117–27 CrossRef Medline
3. Meeren HK, Pijn JP, Van Luijtelaar EL, et al. **Cortical focus drives widespread corticothalamic networks during spontaneous absence seizures in rats.** *J Neurosci* 2002;22:1480–95 CrossRef Medline
4. Castro-Alamancos MA. **Neocortical synchronized oscillations induced by thalamic disinhibition in vivo.** *J Neurosci* 1999;19:RC27 CrossRef Medline
5. Guye M, Regis J, Tamura M, et al. **The role of corticothalamic coupling in human temporal lobe epilepsy.** *Brain* 2006;129(Pt 7):1917–28 CrossRef
6. Deppe M, Kellinghaus C, Duning T, et al. **Nerve fiber impairment of anterior thalamocortical circuitry in juvenile myoclonic epilepsy.** *Neurology* 2008;71:1981–85 CrossRef Medline
7. McGill ML, Devinsky O, Wang X, et al. **Functional neuroimaging abnormalities in idiopathic generalized epilepsy.** *Neuroimage Clin* 2014;6:455–62 CrossRef Medline
8. Law N, Smith ML, Greenberg M, et al. **Executive function in paediatric medulloblastoma: the role of cerebrocerebellar connections.** *J Neuropsychol* 2017;11:174–200 CrossRef Medline
9. Fan Q, Davis N, Anderson AW, et al. **Thalamo-cortical connectivity: what can diffusion tractography tell us about reading difficulties in children?** *Brain Connect* 2014;4:428–39 CrossRef Medline
10. O’Muircheartaigh J, Vollmar C, Barker GJ, et al. **Abnormal thalamocortical structural and functional connectivity in juvenile myoclonic epilepsy.** *Brain* 2012;135:3635–44 CrossRef Medline
11. Alexander GE, Crutcher MD. **Functional architecture of basal ganglia circuits: neural substrates of parallel processing.** *Trends Neurosci* 1990;13:266–71 CrossRef Medline
12. Hernandez MT, Sauerwein HC, Jambaqué I, et al. **Deficits in executive functions and motor coordination in children with frontal lobe epilepsy.** *Neuropsychologia* 2002;40:384–400 CrossRef Medline
13. Luton LM, Burns TG, DeFilippis N. **Frontal lobe epilepsy in children and adolescents: a preliminary neuropsychological assessment of executive function.** *Arch Clin Neuropsychol* 2010;25:762–70 CrossRef Medline
14. Rzezak P, Fuentes D, Guimarães CA, et al. **Frontal lobe dysfunction in children with temporal lobe epilepsy.** *Pediatr Neurol* 2007;37: 176–85 CrossRef Medline
15. Culhane-Shelburne K, Chapieski L, Hiscock M, et al. **Executive functions in children with frontal and temporal lobe epilepsy.** *J Int Neuropsychol Soc* 2002;8:623–32 Medline
16. Hernandez MT, Sauerwein HC, Jambaqué I, et al. **Attention, mem-**

- ory, and behavioral adjustment in children with frontal lobe epilepsy. *Epilepsy Behav* 2003;4:522–36 CrossRef Medline
17. Longo CA, Kerr EN, Smith ML. **Executive functioning in children with intractable frontal lobe or temporal lobe epilepsy.** *Epilepsy Behav* 2013;26:102–08 CrossRef Medline
 18. Widjaja E, Zamyadi M, Raybaud C, et al. **Abnormal functional network connectivity among resting-state networks in children with frontal lobe epilepsy.** *AJNR Am J Neuroradiol* 2013;34:2386–92 CrossRef Medline
 19. Widjaja E, Kis A, Go C, et al. **Bilateral white matter abnormality in children with frontal lobe epilepsy.** *Epilepsy Res* 2014;108:289–94 CrossRef Medline
 20. Braakman HM, Vaessen MJ, Jansen JF, et al. **Frontal lobe connectivity and cognitive impairment in pediatric frontal lobe epilepsy.** *Epilepsia* 2013;54:446–54 CrossRef Medline
 21. Holt RL, Provenzale JM, Veerapandiyam A, et al. **Structural connectivity of the frontal lobe in children with drug-resistant partial epilepsy.** *Epilepsy Behav* 2011;21:65–70 CrossRef Medline
 22. Campos BM, Coan AC, Beltramini GC, et al. **White matter abnormalities associate with type and localization of focal epileptogenic lesions.** *Epilepsia* 2015;56:125–32 CrossRef Medline
 23. Liu Z, Xu Y, An J, et al. **Altered brain white matter integrity in temporal lobe epilepsy: a TBSS study.** *J Neuroimaging* 2015;25:460–64 CrossRef Medline
 24. Paldino MJ, Hedges K, Zhang W. **Independent contribution of individual white matter pathways to language function in pediatric epilepsy patients.** *Neuroimage Clin* 2014;6:327–32 CrossRef Medline
 25. Diao L, Yu H, Zheng J, et al. **Abnormalities of the uncinate fasciculus correlate with executive dysfunction in patients with left temporal lobe epilepsy.** *Magn Reson Imaging* 2015;33:544–50 CrossRef Medline
 26. Koini M, Rombouts SA, Veer IM, et al. **White matter microstructure of patients with neurofibromatosis type 1 and its relation to inhibitory control.** *Brain Imaging Behav* 2017;11:1731–40 CrossRef Medline
 27. Treit S, Chen Z, Rasmussen C, et al. **White matter correlates of cognitive inhibition during development: a diffusion tensor imaging study.** *Neuroscience* 2014;276:87–97 CrossRef Medline
 28. Woolrich MW, Jbabdi S, Patenaude B, et al. **Bayesian analysis of neuroimaging data in FSL.** *Neuroimage* 2009;45:S173–86 CrossRef Medline
 29. Behrens TE, Johansen-Berg H, Woolrich MW, et al. **Non-invasive mapping of connections between human thalamus and cortex using diffusion imaging.** *Nat Neurosci* 2003;6:750–57 CrossRef Medline
 30. Woods RP, Grafton ST, Holmes CJ, et al. **Automated image registration, I: general methods and intrasubject, intramodality validation.** *J Comput Assist Tomogr* 1998;22:139–52 CrossRef Medline
 31. Delis DC, Kaplan E, Kramer JH. *Delis-Kaplan Executive Function System (D-KEFS)*. San Antonio: The Psychological Corporation; 2001
 32. Conners KC. *Conners' Continuous Performance Test*. 3rd ed. Toronto: Multi-Health Systems; 2014
 33. He X, Doucet GE, Sperling M, et al. **Reduced thalamocortical functional connectivity in temporal lobe epilepsy.** *Epilepsia* 2015;56:1571–79 CrossRef Medline
 34. Riley JD, Franklin DL, Choi V, et al. **Altered white matter integrity in temporal lobe epilepsy: association with cognitive and clinical profiles.** *Epilepsia* 2010;51:536–45 CrossRef Medline
 35. Kaushal S, Tamer Z, Opoku F, et al. **Anticonvulsant drug-induced cell death in the developing white matter of the rodent brain.** *Epilepsia* 2016;57:727–34 CrossRef Medline
 36. Riccio CA, Pliego JA, Cohen MJ, et al. **Executive function performance for children with epilepsy localized to the frontal or temporal lobes.** *Appl Neuropsychol Child* 2015;4:277–84 CrossRef Medline
 37. Osborne JW, Costello AB. **Sample size and subject to item ratio in principal components analysis.** *Practical Assessment, Research, & Evaluation* 2004;9:1–9
 38. Bertram EH. **Extratemporal lobe circuits in temporal lobe epilepsy.** *Epilepsy Behav* 2014;38:13–18 CrossRef Medline

Assessing Corticospinal Tract Asymmetry in Unilateral Polymicrogyria

O. Foesleitner, K.-H. Nennung, T. Traub-Weidinger, M. Feucht, S. Bonelli, T. Czech, C. Dorfer, D. Prayer, and G. Kasprian



ABSTRACT

BACKGROUND AND PURPOSE: Asymmetry of the corticospinal tract in congenital lesions is a good prognostic marker for preserved motor function after hemispherectomy. This study aimed to assess this marker and provide a clinically feasible approach in selected cases of unilateral polymicrogyria.

MATERIALS AND METHODS: Corticospinal tract asymmetry of 9 patients with unilateral polymicrogyria substantially affecting the central region was retrospectively assessed on axial T1WI and DTI. Volumes of the brain stem and thalamus and DTI parameters of the internal capsule were measured. Two neuroradiologists independently rated the right-left asymmetry at 4 levels along the corticospinal tract. DTI tractography was used to determine the motor cortex within polymicrogyria, with task-based functional MR imaging available in 3/9 cases.

RESULTS: Visual assessment of the brain stem asymmetry showed excellent correlation with quantitative measures on both T1WI and color-coded DTI maps ($P = .007$ and $P = .023$). Interrater reliability regarding structural and DTI-based corticospinal tract asymmetry was best at the midbrain (Cohen $\kappa = 0.77$, $P = .018$). Three patients underwent functional hemispherectomy with postsurgical stable motor function, all showing marked corticospinal tract asymmetry preoperatively. Following the DTI-based corticospinal tract trajectories allowed identifying the presumed primary motor region within the dysplastic cortex in 9/9 patients, confirmed by functional MR imaging in 3/3 cases.

CONCLUSIONS: Visual assessment of corticospinal tract asymmetry in unilateral polymicrogyria involving the motor cortex is most reliable with T1WI and color-coded DTI maps at the level of the midbrain. Pronounced asymmetry predicts preserved motor function after hemispherectomy. DTI-based tractography can be used as a guidance tool to the motor cortex within polymicrogyria.

ABBREVIATIONS: AD = axial diffusivity; CST = corticospinal tract; FA = fractional anisotropy; PMG = polymicrogyria; RD = radial diffusivity

Polymicrogyria (PMG) is a cortical malformation due to abnormal postmigrational development, which is morphologically characterized by an excess of small gyri.¹ Depending on the localization and the extent of cortical involvement, clinical man-

ifestations range from selective impairment of higher cognitive functions to severe epilepsy with intractable seizures. Epilepsy surgery is a delicate matter in these patients. Complete resection of the epileptogenic zone is a strong prognostic factor for surgical success² and supports extensive surgery. However, there is often preserved function in the polymicrogyric cortex,³⁻⁵ with the risk of postoperative de novo deficits.

Küpper et al⁶ recently formulated “rules” for the prediction of preserved grasping ability after hemispherectomy, stating that “marked asymmetry of the brain stem and, more specifically, marked asymmetry of the corticospinal tract (CST) within the brain stem, predict preservation of grasping ability in patients who can grasp preoperatively.” This conclusion is based on observations in a large but heterogeneous cohort of different pre-, peri-, and postnatally acquired lesions not specifically focusing on PMG.

Due to the extreme divergence from normal anatomy, charac-

Received February 18, 2018; accepted May 2.

From the Departments of Biomedical Imaging and Image-Guided Therapy (O.F., K.-H.N., T.T.-W., D.P., G.K.), Pediatrics and Adolescent Medicine (M.F.), Neurology (S.B.), and Neurosurgery (T.C., C.D.), Medical University of Vienna, Vienna, Austria.

Paper previously presented as a poster at: Annual Meeting of the European Congress of Radiology, March 1–5, 2017, Vienna, Austria; Annual Meeting of the German and Austrian Societies of Neuroradiology, October 5–8, 2016, Cologne/Germany; and Annual Meeting of the European Conference of Epileptology, September 11–15, 2016, Prague, Czech Republic.

Please address correspondence to Gregor Kasprian, MD, Department of Biomedical Imaging and Image-Guided Therapy, Medical University of Vienna, Waehringer Guertel 18–20, 1090 Vienna, Austria; e-mail: gregor.kasprian@meduniwien.ac.at



Indicates article with supplemental on-line table.



Indicates article with supplemental on-line photos.

<http://dx.doi.org/10.3174/ajnr.A5715>

teristic landmarks for the identification of the central sulcus cannot be used in PMG. Thus, structural imaging alone fails to localize the preserved motor function within the dysplastic cortex. Shown to be concordant with intraoperative cortical mapping,^{3,7} fMRI serves as a noninvasive criterion standard for localizing the motor area. Because PMG is typically symptomatic in early childhood,⁸ the results of preoperative task-based fMRI studies in these young uncooperative patients are frequently vague and often degraded by severe motion artifacts.

By measuring the anisotropic motion of water, diffusion tensor imaging can provide imaging correlates of the fiber architecture of the human brain.⁹ Tractography visualizes these fiber tracts by combining voxel-based anisotropy values, constructing continuous fiber bundles. The accuracy and reliability of DTI-based tractography in the visualization of the corticospinal tract has been confirmed by intraoperative correlation, mainly in brain tumor surgery.¹⁰ To the best of our knowledge, the use of DTI as a neuroradiologic tool to localize preserved motor function within PMG has not been investigated.

This study had the following objectives: 1) propose a clinically feasible imaging approach to assess CST asymmetry in unilateral polymicrogyria, 2) check diffusion-based tractography as guidance to the presumed motor area within the dysplastic cortex, and 3) investigate whether the “rule” of CST asymmetry as a good prognostic factor for postsurgical motor function preservation specifically applies to cases of unilateral PMG involving the central region.

MATERIALS AND METHODS

The retrospective data analysis was approved by the Ethics Committee of the Medical University of Vienna (1139/2012).

Inclusion criteria for this single-center retrospective study were existing presurgical MR imaging examinations performed between 2008 and 2017 with dedicated epilepsy imaging protocols, including a T1-weighted isovoxel sequence (1-mm³ voxel size) and a DTI sequence (16 or 32 gradient encoding directions, b-values of 0 and 700 s/mm², 2- to 3-mm slice thickness) from 3T (patients 1–3) or 1.5T scanners (patients 4–9). All patients were diagnosed with PMG substantially (>two-thirds of the motor cortex) involving the primary motor cortex of 1 hemisphere. Patients with a malformation in the contralateral hemisphere or any other structural alteration along the CST or a prior neurosurgical procedure were excluded.

In a retrospective chart review, 9 cases of unilateral PMG involving the central region (6 right-hemispheric) were identified (for anatomic images see On-line Fig 1). The median age at MR imaging was 7 years (range, 3–34 years). Patient characteristics are outlined in the On-line Table.

Brain stem volume was obtained by manual segmentation of the left and right halves on axial T1WI from below the mammillary bodies to the obex as anatomic landmarks to ensure intersubject comparability using ITK-SNAP (www.itksnap.org; On-line Fig 3).¹¹ We determined the midline considering the central canal, the anterior median fissure, and the posterior median sulcus. Anatomic correctness was further checked by visual inspection of the segmented volume in the sagittal and coronal planes and as 3D volume. The ratio of contralesional-to-ipsilesional brain stem

volumes quantifying asymmetry was then calculated (brain stem volume ratio):

$$\frac{(\text{Contralesional} - \text{Ipsilesional Volume})}{(\text{Contralesional} + \text{Ipsilesional Volume})}$$

Diffusion tensor images were quantitatively analyzed by manually drawing ROIs on axial planes (DSIStudio; Johns Hopkins University, Baltimore, Maryland). Diffusion parameters of the posterior limb (being the normal anatomic location of the CST) and of the whole internal capsule were measured. Fractional anisotropy (FA), ADC, axial diffusivity (AD), radial diffusivity (RD) of the full axial area of the brain stem, and the normal anatomic location of the CST only were obtained from 1 axial slice below the mammillary bodies (On-line Fig 2). A DTI-based CST asymmetry ratio was then calculated with a score of zero indicating symmetry:

$$\frac{(\text{Contralesional} - \text{Ipsilesional Value})}{(\text{Contralesional} + \text{Ipsilesional Value})}$$

Two experienced academic neuroradiologists (G.K. and D.P., with 5 and 30 years of experience) blinded to clinical data independently assessed the asymmetry of the CST on 4 levels (internal capsule, cerebral crus, medulla, and spine) and the thalamus. Asymmetry was rated as 0 (no asymmetry), 1 (mild), 2 (moderate), or 3 (severe) and summed into an asymmetry index ranging from 0 to 15. A positive and high asymmetry index indicated a pronounced asymmetry and a smaller CST ipsilateral to the lesional hemisphere. Next to the structural images, the readers were shown the color-coded diffusion tensor images on the level of the midbrain (1 slice below the mammillary bodies, corresponding to the quantitative measurement). The simultaneous assessment of structural and diffusion tensor images aimed to reflect the true clinical setting.

Task-based fMRI data acquired at 3T were available in 3 patients (1.8 × 1.8 × 4.0 mm slice thickness, 128 × 128 matrix, TE = 35 ms, TR = 3000 ms, flip angle = 90°). The motor task consisted of alternating blocks of activation (finger tapping, ankle flexion and extension) and visual stimulation, each lasting 30 seconds with a total time of 5 minutes. Due to severe paresis, patient 1 could only move both hands simultaneously. fMRI data were preprocessed on SPM12 software (<http://www.fil.ion.ucl.ac.uk/spm/software/spm12>). Functional images were coregistered with the original T1WI, realigned and smoothed with a Gaussian kernel of 8-mm full width at half maximum, and motion-corrected with standard parameters.

Deterministic tractography of the CST was performed by manually drawing ROIs on axial slices into the internal capsule and lateral to the lateral ventricle (DTIStudio). In patients in whom functional imaging was available, fiber tracking was performed first and then compared with the fMRI activation map by measuring the Euclidean distance from the center of the blood oxygen level-dependent cluster to the presumed motor area indicated by DTI.

The results of clinical neurologic examinations were retrieved from the medical charts. An experienced neurologist or neuroepidemiologist systematically performed all examinations. Hand motor strength was graded according to the Medical Research Coun-

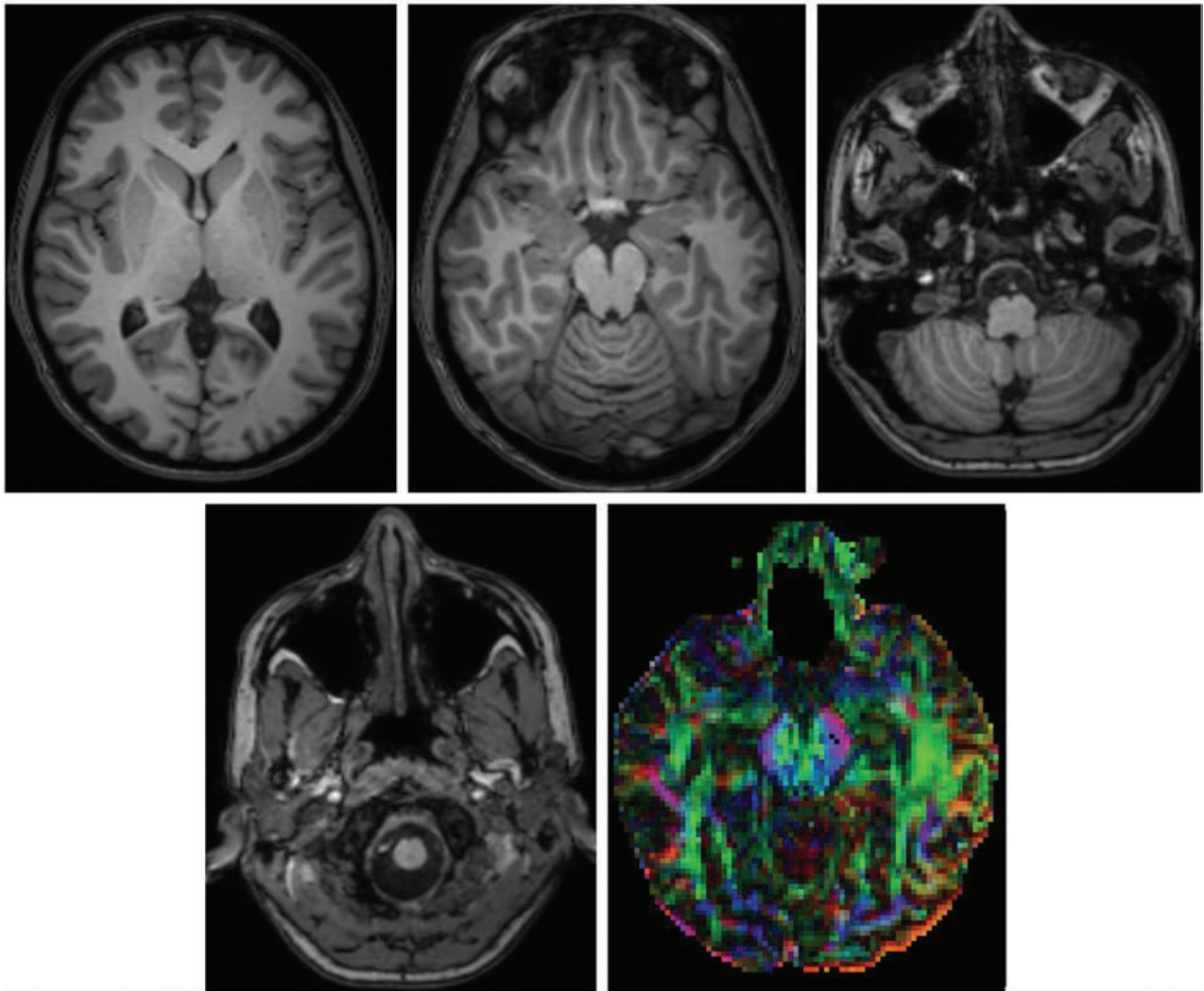


FIG 1. CST characterization in patient 3: T1WI at different levels of the corticospinal tract (internal capsule, cerebral crus, medulla, spine), color-coded FA color map (brain stem). Asymmetry was altogether rated as no/mild asymmetry.

cil scale¹² and, together with fine motor skills, was categorized as “minimal” or “distinct” impairment.

Imaging and clinical values were correlated with bivariate analyses and the Pearson coefficient (SPSS, Version 22.0; IBM, Armonk, New York), while the interrater reliability was calculated using the Cohen coefficient. The threshold of significance was set at $<.05$.

RESULTS

Figures 1 and 2 show structural and functional imaging in patient 3. Another example of structural and functional imaging for patient 1 can be found in On-line Figs 4 and 5.

Structural Asymmetry

The mean left-right asymmetry ratio of the manually segmented brain stem was 0.1 ± 0.05 (range, 0.03–0.17). The mean left-right asymmetry ratio of the anterior parts of the brain stem (as the normal location of the CST) was 0.14 ± 0.06 (range, 0.07–.22).

The visual assessment of the CST at 4 different levels plus the thalamus resulted in a median asymmetry index of 9 (range, 1–12) for 1 rater and 7 (range, 3–11) for the second rater.

Interrater reliability in the assessment of CST asymmetry was most robust at the level of the cerebral crus. Excellent congruence was reached by categorizing the asymmetry degree into no/minimal asymmetry or moderate/severe asymmetry (Cohen $\kappa = 1.0$, $P = .003$). The other levels of assessment did not result in significant agreement (Cohen $\kappa = 0.21$ –0.6; $P > .05$).

Visual assessment of the brain stem asymmetry showed an excellent correlation with manual brain stem volumetry ($P = .007$).

Clinical hand motor impairment correlated with the visual assessment of the structural CST asymmetry at the internal capsule ($P = .001$), cerebral crus ($P = .014$), and the overall structural asymmetry index ($P = .002$). The structural CST asymmetry assessed at the level of the thalamus, medulla, and spine did not correlate significantly with the clinical hand motor function ($P > .05$).

Diffusion Tensor–Based Asymmetry

The mean ratio of FA values in the internal capsule was 0.05 ± 0.05 (range, 0.0–0.16). The mean ratio of FA values in only the posterior limb of the internal capsule was 0.08 ± 0.05 (range, 0.02–0.18).

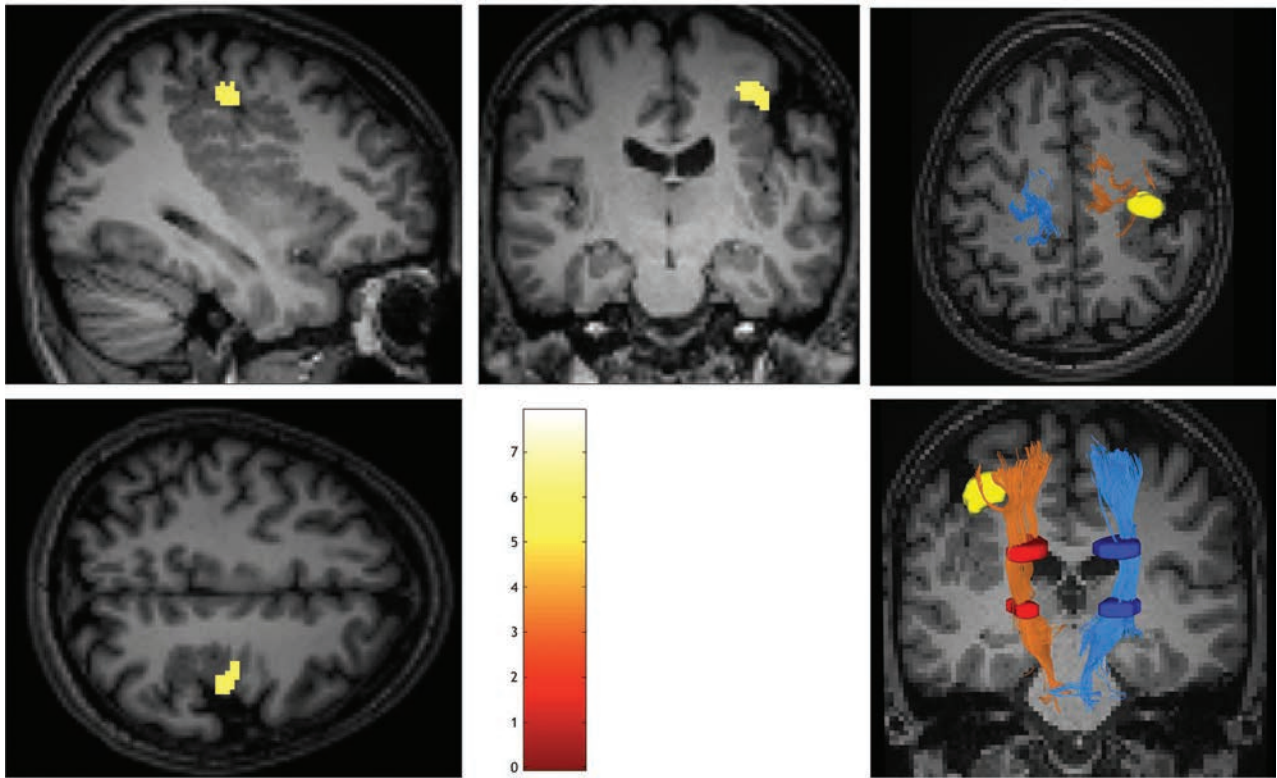


FIG 2. fMRI activation map (hand motor task, family-wise error of $<.05$, 6-voxel minimum cluster size) and DTI tractography of the CST in patient 3.

Mean ratios of DTI parameters in the brain stem taken from 1 axial slice (below the mammillary bodies) were as follows (Online Fig 2): mean FA = 0.05 ± 0.06 (range, -0.01 – 0.2), mean ADC = -0.02 ± 0.07 (range, -0.15 – 0.06), mean AD = 0.01 ± 0.03 (range, -0.04 – 0.6), mean RD = -0.05 ± 0.09 (range, -0.21 – 0.05). Mean ratios of diffusion tensor parameters in only the anterior half of the brain stem measured at 1 axial slice were as follows: mean FA = 0.01 ± 0.09 (range, 0.0 – 0.26); mean ADC = -0.09 ± 0.06 (range, -0.17 – 0.01); mean AD = -0.03 ± 0.07 (range, -0.11 – 0.1); and mean RD = -0.16 ± 0.07 (range, -0.25 to -0.07).

Diffusion tensor parameters measured at the anterior part of the brain stem correlated well with the visually assessed diffusion asymmetry at the same height ($P = .023$). Diffusion measures from the whole manually segmented brain stem did not correlate with the raters' asymmetry index.

Visual rating of color-coded DTI maps of the brain stem resulted in a mean asymmetry score of 2 ± 0.87 (range, 1–3) in 1 rater and 1.9 ± 1.3 (range, 0–3) in the second rater. By using a simplified asymmetry rating of only 2 instead of 4 categories (no/minimal or moderate/severe asymmetry) an excellent interrater reliability could be achieved (Cohen $\kappa = 1.0$, $P = .003$) as opposed to no significant interrater reliability using all 4 categories ($P > .05$).

The visual asymmetry rating of the color-coded FA diffusion tensor maps at the level of the brain stem correlated with hand motor function ($P = .018$). Quantitative diffusion tensor measures did not correlate significantly with clinical hand motor function.

Motor Cortex

Task-based functional imaging showed highly significant task-related activation within the polymicrogyric cortex in 3/3 cases ($P < .05$, family-wise error correction; minimum cluster size, 6 voxels). Patients were 19, 26, and 34 years of age at the fMRI scan.

Tractography successfully determined the corticospinal tract bilaterally in 9/9 patients and led to the primary motor cortex with a mean distance of 9 mm to the fMRI motor activation in 3/3 cases (range, 0–17.9 mm).

Clinical Motor Function

Two patients showed minimal hand function impairment (full muscle strength, minimal impairment of fine motor skills), while 7/9 patients had moderate-to-severe motor function deficits.

Three patients underwent functional hemispherectomy. Preoperatively, hand motor strength was rated Medical Research Council grade 4 in all 3 cases, with moderate-to-severe deficits in fine-motor skills in the contralateral extremity. Ipsilateral hand motor function was graded as normal. After the operation, these 3 patients were seizure-free (2-year follow-up) with no de novo motor deficits. On presurgical imaging, all 3 patients showed marked asymmetry of the CST on visual inspection (anatomic and/or diffusion tensor images) and in asymmetry quantification.

DISCUSSION

This series of unilateral polymicrogyria affecting the central region further supports the good prognostic value of CST asymmetry for postoperative motor function preservation. We showed that asymmetry of the CST can be reliably assessed with visual

inspection of T1WI and diffusion tensor images, showing the most robust assessment at the level of the cerebral crus using a dichotomous asymmetry scale (no/minimal or moderate/severe asymmetry). Quantitative measures of the CST using brain stem volumetry and diffusion tensor parameters (FA, ADC, AD, RD) significantly correlated with the visual inspection–based asymmetry assessment. Additionally, this study proposed tractography as a guidance tool to the preserved motor area not identifiable on structural images due to the extreme divergence from normal anatomy. Proving the concept of abnormal axonal wiring in brain malformations,¹³ presurgical structural and tractographic visualization of the asymmetric CST indicated significantly altered structural motor connectivity in the motor cortex involving PMG.

Küpper et al⁶ recently defined “rules” for the prediction of postoperative hand motor function after hemispherectomy in a large cohort of pre-, peri-, and postnatally acquired lesions using manual brain stem segmentation, probabilistic tractography, and visual inspection of axial FA color maps by 1 reader. They found that in patients with preoperatively normal hand function and in patients with postnatally acquired lesions or progressive diseases, “complete loss of grasping ability must be expected.” Similarly, CST asymmetry was shown to be a good prognostic factor for preserved motor function after hemidisconnection. In their cohort, they included 16 cases of PMG not explicitly located in the central region, with T1WI being available in 15 and DTI performed in 6 cases. Our series of a highly selective population of unilateral PMG involving the central region confirms these “rules.” Furthermore, our study adds a clinically feasible imaging approach in the preoperative setting by showing the reliability of visual inspection by experienced neuroradiologists as opposed to also reliable but demanding quantitative analyses not practical in clinical routine (manual brain stem volumetry, DTI parameters).

Three of our patients underwent functional hemispherectomy with postoperative seizure freedom and no deterioration of motor function. This result proves the concept of potential motor function preservation in prenatally acquired lesions due to reorganization.⁶ Both our raters, independently and blinded to clinical data, assessed the CST asymmetry as moderate/severe in these 3 patients. This could have served as helpful prognostic information in the preoperative setting. Early-onset childhood epilepsy is often medically refractory and results in widespread brain dysfunction.¹⁴ An epilepsy operation in patients with PMG has recently been shown to be significantly better than medical treatment alone.¹⁵ Mühlebner et al¹⁴ found 5/7 patients with PMG seizure-free after a disconnective operation at our center and extended surgery to be a positive predictive marker for seizure freedom. In adequately selected patients, an operation can achieve seizure freedom in 67% of cases.¹⁵

However, with possible function preserved within the to-be-resected or disconnected brain tissue, the risk of de novo deficits must be weighed against the benefits of potential postoperative seizure freedom. Despite the associated substantial derangement of the affected cortical anatomy and the severely disrupted neuronal layering, PMG is known to have functionally relevant sensorimotor and visual representations.¹⁶ This observation is well-documented in smaller series^{4,5,17,18} by fMRI, transcranial magnetic stimulation,⁵ and magnetoencephalography.¹⁹

PMG can potentially affect any supratentorial brain region except for the striatum, hippocampus, and gyrus rectus.²⁰ It is more commonly found bilaterally, most frequently involving the posterior aspect of the Sylvian fissure and the frontal or parietal lobes. Although summarized as 1 pathology, the molecular and developmental etiology of PMG can vary substantially. Generally, typical unilateral PMG is today seen as a result of abnormal post-migrational development and therefore a developmental disorder that occurs relatively late in corticogenesis.¹ Thus, preserved function is rather common in PMG compared with other malformations of cortical development, which lead to abnormal corticogenesis at much earlier time points and consequently more frequently cause functional cortical reorganization.³ This is confirmed by our series in which structural and diffusion tensor–based asymmetry of the CST was closely correlated with hand motor impairment.

Most interesting, unilateral PMG typically does not macroscopically affect the subcortical and deep white matter.²⁰ This finding is in line with that in our series using deterministic tractography as a robust measure of grossly preserved sensorimotor structural connectivity in the region of PMG. Thus, DTI tractography can potentially help to identify preserved motor function within the dysplastic motor cortex, giving additional information in the setting of preoperative evaluation. Functional MR imaging is often not feasible in these pediatric and intellectually disabled patients or is only feasible using passive movements in sedation.²¹

In pre- or perinatal cortical lesions, preservation of ipsilateral corticospinal projections is associated with favorable functional outcome.²² Neurophysiologic studies suggest that neurons in a damaged sensorimotor cortex fail to maintain their contralateral spinal terminations, while projections from the healthy contralateral primary motor cortex increase.²² Asymmetry of the CST in early acquired lesions (ie, pre- or perinatal) is thus a good prognostic factor because it indicates structural and functional reorganization into the ipsilateral sensorimotor cortex.

Limitations

The observations of this study are based on a retrospective analysis of a relatively small population. Given the strict inclusion criteria (unilateral PMG involving the central region) and the rarity of the disease, however, this is the largest series addressing the defined aims so far. We deliberately wanted to focus on unilateral PMG affecting the central region because this has not specifically been the focus before but is of high clinical relevance in specialized centers. This study intended to elaborate an imaging approach robust and feasible for clinical routine in the preoperative work-up of patients with PMG, thus concentrating on the radiologic perspective. Only 3 patients underwent an epilepsy operation, but all had marked asymmetry of the CST preoperatively and did not show clinical de novo deficits postoperatively. Given the limited statistical power, evaluating the prognostic value of structural and tensor-based asymmetry of the CST on postoperative motor function is beyond the scope of this study, but it has been convincingly shown in a large population of pre- or perinatal lesions.⁶

CONCLUSIONS

Visual assessment of structural and diffusion tensor images of the corticospinal tract (especially at the cerebral crus) is a reliable and clinically feasible imaging approach in the preoperative work-up of patients with unilateral PMG affecting the central region. In noncompliant patients, DTI-based tractography is a useful alternative to task-based fMRI and helps in the anatomic localization of the primary motor cortex. Moreover, this study confirmed the assumption of CST asymmetry as a good prognostic factor for postoperative hand motor function in this highly selected population. Finally, it adds to the concept of preserved ipsilateral corticospinal connectivity as a plasticity mechanism in early unilateral hemispheric brain lesions.

ACKNOWLEDGMENTS

The authors thank Dr Gudrun Groeppel for her participation in the data acquisition.

Disclosures: Gregor Kasprian—UNRELATED: Consulting Fee or Honorarium: Shire, Comments: honorarium for a lecture held on November 2017; Payment for Lectures Including Service on Speakers Bureaus: Shire, Comments: honorarium for a lecture on neuroimaging in Fabry disease; Travel/Accommodations/Meeting Expenses Unrelated to Activities Listed: Philips Healthcare Europe, Comments: flight to Amsterdam for a Pediatric User Meeting in Eindhoven, Holland, February 2018.

REFERENCES

1. Barkovich AJ, Guerrini R, Kuzniecky RI, et al. **A developmental and genetic classification for malformations of cortical development: update 2012.** *Brain* 2012;135:1348–69 CrossRef Medline
2. Hader WJ, Mackay M, Otsubo H, et al. **Cortical dysplastic lesions in children with intractable epilepsy: role of complete resection.** *J Neurosurg* 2004;100:110–17 Medline
3. Janszky J, Ebner A, Kruse B, et al. **Functional organization of the brain with malformations of cortical development.** *Ann Neurol* 2003;53:759–67 CrossRef Medline
4. Nikolova S, Bartha R, Parrent AG, et al. **Functional MRI of neuronal activation in epilepsy patients with malformations of cortical development.** *Epilepsy Res* 2015;116:1–7 CrossRef Medline
5. Zsoter A, Pieper T, Kudernatsch M, et al. **Predicting hand function after hemispherotomy: TMS versus fMRI in hemispheric polymicrogyria.** *Epilepsia* 2012;53:e98–101 CrossRef Medline
6. Küpper H, Kudernatsch M, Pieper T, et al. **Predicting hand function after hemidisconnection.** *Brain* 2016;139:2456–68 CrossRef Medline
7. Yetkin FZ, Mueller WM, Morris GL, et al. **Functional MR activation correlated with intraoperative cortical mapping.** *AJNR Am J Neuroradiol* 1997;18:1311–15 Medline
8. Caraballo RH, Cersósimo RO, Fortini PS, et al. **Congenital hemiparesis, unilateral polymicrogyria and epilepsy with or without status epilepticus during sleep: a study of 66 patients with long-term follow-up.** *Epileptic Disord* 2013;15:417–27 CrossRef Medline
9. Le Bihan D, Mangin JF, Poupon C, et al. **Diffusion tensor imaging: concepts and applications.** *J Magn Reson Imaging* 2001;13:534–46 CrossRef Medline
10. Stadlbauer A, Buchfelder M, Salomonowitz E, et al. **Fiber density mapping of gliomas: histopathologic evaluation of a diffusion-tensor imaging data processing method.** *Radiology* 2010;257:846–53 CrossRef Medline
11. Yushkevich PA, Piven J, Hazlett HC, et al. **User-guided 3D active contour segmentation of anatomical structures: significantly improved efficiency and reliability.** *Neuroimage* 2006;31:1116–28 CrossRef Medline
12. John J. **Grading of muscle power: comparison of MRC and analogue scales by physiotherapists: Medical Research Council.** *Int J Rehabil Res* 1984;7:173–81 CrossRef Medline
13. Besseling RM, Jansen JF, de Louw AJ, et al. **Abnormal profiles of local functional connectivity proximal to focal cortical dysplasias.** *PLoS One* 2016;11:e0166022 CrossRef Medline
14. Mühlebner A, Gröppel G, Dressler A, et al. **Epilepsy surgery in children and adolescents with malformations of cortical development: outcome and impact of the new ILAE classification on focal cortical dysplasia.** *Epilepsy Res* 2014;108:1652–61 CrossRef Medline
15. Cossu M, Pelliccia V, Gozzo F, et al. **Surgical treatment of polymicrogyria-related epilepsy.** *Epilepsia* 2016;57:2001–10 CrossRef Medline
16. Barkovich AJ, Gressens P, Evrard P. **Formation, maturation, and disorders of brain neocortex.** *AJNR Am J Neuroradiol* 1992;13:423–46 Medline
17. Burneo JG, Bartha R, Gati J, et al. **4-T fMRI of the motor and sensory cortices in patients with polymicrogyria and epilepsy.** *Clin Neurol Neurosurg* 2014;122:29–33 CrossRef Medline
18. Araujo D, de Araujo DB, Pontes-Neto OM, et al. **Language and motor FMRI activation in polymicrogyric cortex.** *Epilepsia* 2006;47:589–92 CrossRef Medline
19. Burneo JG, Kuzniecky RI, Bebin M, et al. **Cortical reorganization in malformations of cortical development: a magnetoencephalographic study.** *Neurology* 2004;63:1818–24 CrossRef Medline
20. Barkovich AJ. **Current concepts of polymicrogyria.** *Neuroradiology* 2010;52:479–87 CrossRef Medline
21. Ogg RJ, Laningham FH, Clarke D, et al. **Passive range of motion functional magnetic resonance imaging localizing sensorimotor cortex in sedated children.** *J Neurosurg Pediatr* 2009;4:317–22 CrossRef Medline
22. Eyre JA. **Corticospinal tract development and its plasticity after perinatal injury.** *Neurosci Biobehav Rev* 2007;31:1136–49 CrossRef Medline

Arterial Spin-Labeling in Children with Brain Tumor: A Meta-Analysis

 A.F. Delgado,  F. De Luca,  P. Hanagandi,  D. van Westen, and  A.F. Delgado



ABSTRACT

BACKGROUND: The value of arterial spin-labeling in a pediatric population has not been assessed in a meta-analysis.

PURPOSE: Our aim was to assess the diagnostic accuracy of arterial spin-labeling–derived cerebral blood flow to discriminate low- and high-grade tumors.

DATA SOURCES: MEDLINE, EMBASE, the Web of Science Core Collection, and the Cochrane Library were used.

STUDY SELECTION: Pediatric patients with arterial spin-labeling MR imaging with verified neuropathologic diagnoses were included.

DATA ANALYSIS: Relative CBF and absolute CBF and tumor grade were extracted, including sequence-specific information. Mean differences in CBF between low- and high-grade tumors were calculated. Study quality was assessed.

DATA SYNTHESIS: Data were aggregated using the bivariate summary receiver operating characteristic curve model. Heterogeneity was explored with meta-regression and subgroup analyses. The study protocol was published at PROSPERO (CRD42017075055). Eight studies encompassing 286 pediatric patients were included. The mean differences in absolute CBF were 29.62 mL/min/100 g (95% CI, 10.43–48.82 mL/min/100 g), $I^2 = 74$, $P = .002$, and 1.34 mL/min/100 g (95% CI, 0.95–1.74 mL/min/100 g), $P < .001$, $I^2 = 38$ for relative CBF. Pooled sensitivity for relative CBF ranged from 0.75 to 0.90, and specificity, from 0.77 to 0.92 with an area under curve = 0.92. Meta-regression showed no moderating effect of sequence parameters TE, TR, acquisition time, or ROI method.

LIMITATIONS: Included tumor types, analysis method, and original data varied among included studies.

CONCLUSIONS: Arterial spin-labeling–derived CBF measures showed high diagnostic accuracy for discriminating low- and high-grade tumors in pediatric patients with brain tumors. The relative CBF showed less variation among studies than the absolute CBF.

ABBREVIATIONS: aCBF = absolute CBF; ASL = arterial spin-labeling; HGT = high-grade tumor; LGT = low-grade tumor; rCBF = relative CBF; QUADAS-2 = Quality Assessment of Diagnostic Accuracy Studies; WHO = World Health Organization

Brain tumors are the second most common tumor affecting children up to 19 years of age.¹ Preoperative radiologic assessment strives to describe the grade (ie, high- versus low-grade), location, and type of the lesion to guide therapeutic decisions. The

spatial location of the lesions differs from that in adults, with pediatric tumors commonly located infratentorially, including the brain stem, which renders surgical resection more difficult.² Location in eloquent areas might delay an operation when the risk of postoperative deficit is weighed against potential longer overall survival, or it may even hamper an operation. Thus, presurgical grading into low- or high-grade tumor, respectively, is of clinical importance for therapeutic and surgical decisions.

In adults, the traditional differentiation between low-grade tumors (LGTs) and high-grade tumors (HGTs), based on the absence or presence of contrast enhancement alone, has proved too simplistic.^{3,4} Previous reports have described the utility of gado-

Received January 22, 2018; accepted after revision May 18.

From the Departments of Clinical Neuroscience (Anna F.D.) and Neuroradiology (P.H.), Karolinska Institute, Stockholm, Sweden; Faculty of Medicine and Surgery (F.D.L.), School of Medicine and Health Sciences, University “G. d’Annunzio,” Chieti, Italy; Faculty of Medicine (D.v.W.), Clinical Sciences, Lund University, Sweden; and Department of Surgical Sciences (Alberto F.D.), Uppsala University, Uppsala, Sweden.

Anna F.D. received time from the Department of Neuroradiology at Karolinska University Hospital for conducting the study. Karolinska University Hospital has a research agreement with Philips Healthcare on stroke assessment unrelated to this work.

Please address correspondence to Anna Falk Delgado, MD, PhD, Clinical Neuroscience, Karolinska Institute, Stockholm, Sweden, Neuroradiology Department, Karolinska University Hospital, 17176 Solna, Sweden; e-mail: anna.falk-delgado@sll.se

 Indicates article with supplemental on-line tables.

 Indicates article with supplemental on-line photos.

<http://dx.doi.org/10.3174/ajnr.A5727>

linium-based perfusion MR imaging for differentiation of low- and high-grade tumors in adults.^{5,6} However, children are more susceptible to repeat gadolinium-based contrast agent injection with reportedly increased signal intensity in the dentate nucleus.⁷ A further concern is the nonlinear correlation between contrast enhancement and tumor grade in children, in which grade I tumors (pilocytic astrocytomas) can show vivid enhancement despite the low tumor grade.^{8,9}

As an alternative to contrast-enhanced MR perfusion, arterial spin-labeling (ASL) is based on magnetic labeling of water molecules as an endogenous contrast agent. ASL, which provides absolute estimates of CBF, has been proved a valuable tool for adult patients with brain tumors for discriminating LGT and HGT.¹⁰⁻¹⁶ However, adults and children have divergent tumor types, and the diagnostic value of ASL in pediatric brain tumors has not been fully investigated, to our knowledge.

The value of ASL for cerebral blood flow measurement in pediatric patients with brain tumors has only recently received attention, and reports have shown mainly promising results.¹⁷ Yet, there is no consensus on the clinical role of ASL, partly due to technical differences, including parameter settings, postprocessing schemes, and analysis methods, in hitherto published studies. A meta-analysis would contribute to the body of evidence on the value of ASL in pediatric brain tumors by evaluating data from different centers using a variety of techniques and elucidating the influence of different aspects of its diagnostic accuracy for discrimination of LGT and HGT. The primary aim of this study was to aggregate the body of evidence on ASL in pediatric patients with brain tumors and to assess the diagnostic accuracy of ASL-derived CBF measures to discriminate LGTs and HGTs. In addition, we investigated to what extent variability in the technique and difficulties rendering stable measurements that have previously hampered its wide clinical introduction¹⁸ influence the validity of CBF measurements using ASL.

MATERIALS AND METHODS

This meta-analysis was performed according to the Cochrane Handbook for Diagnostic Test Accuracy Reviews¹⁹ and is reported according to the Preferred Reporting Items for Systematic Reviews and Meta-Analyses 2009 guidelines.²⁰ The study design also adhered to current recommendations for diagnostic test accuracy meta-analyses,²¹ and the study protocol was prospectively registered at PROSPERO (CRD42017075055; <https://www.crd.york.ac.uk/PROSPERO/>).

Eligibility Criteria

Eligible studies reported ASL data for a pediatric cohort of patients (younger than 18 years of age) with brain tumors. Inclusion criteria were the following: 1) Preoperative MR imaging was performed, including ASL, and 2) postoperative tumor diagnosis was established by histopathology. Further inclusion criteria were that CBF measurements from ASL had been stratified for tumor grade. All ASL techniques were considered eligible for inclusion. Studies presenting data on both absolute and relative CBF were considered for inclusion. Studies reporting recurrent tumors, longitudinal follow-up, adults, or single case reports were excluded. The previously classified diffuse intrinsic pontine gliomas were ex-

cluded for 2 reasons: 1) Current World Health Organization (WHO) 2016 guidelines that differ from those in 2007 and recognize diffuse midline gliomas as grade IV, and 2) errors in tissue sampling or lack of neuropathologic information in included studies due to the eloquent location.

Search Strategy and Selection Criteria

A literature search strategy was developed by a researcher with 9 years' experience in meta-analysis along with a librarian with 5 years' experience in conducting systematic searches (On-line Fig 1). The electronic search was performed at the Karolinska Institutet University Library, including the following databases: MEDLINE (Ovid), Embase.com, the Web of Science Core Collection, and the Cochrane Library (Wiley). The MeSH-terms identified for searching MEDLINE (Ovid) were adapted in accordance with the corresponding vocabulary in EMBASE (On-line Tables 6–9). Each search concept was complemented with relevant free-text terms like “brain tumor,” “choroid plexus neoplasm,” “astrocytoma,” “arterial spin labeling” and “ASL.” The free-text terms were, if appropriate, truncated and/or combined with proximity operators. Conference abstracts were excluded. No language restriction was applied. Data bases were searched from inception until January 8, 2018. Retrieved hits were assessed for inclusion independently by 2 researchers with 9 years' and 1 year's experience in meta-analyses, respectively, and were checked for congruency. Incongruencies in the data extraction were solved through discussion until a consensus was reached or by consulting a third researcher with 4 years' experience in meta-analysis.

Data Items and Extraction

Data from each eligible study were extracted independently by 2 researchers onto preformed sheets developed for this study. They extracted the following parameters: mean and maximum absolute (aCBF) or relative CBF (rCBF)—that is, the ratio of signal intensity in the lesion over signal intensity in the contralateral normal-appearing cortical gray matter, for example, in the cerebellum or the temporal lobe, in LGT and HGT. In addition, the number of patients, patient age, WHO classification, general anesthesia (yes/no), study first author, year of publication, study region origin, MR imaging scanner model and manufacturer, number of channels in the head coil used, field strength Tesla, ASL technique (pseudocontinuous or pulsed), TR, TE, number of partitions, flip angle, postlabeling delay (milliseconds), postprocessing, acquisition time, ROI technique, and reference region were extracted. Any incongruencies in the data extraction were solved as mentioned above.

Bias Assessment

Risk of bias in the individual studies was assessed by the revised Quality Assessment of Diagnostic Accuracy Studies (QUADAS-2) tool.²² One author with 9 years of experience adapted the QUADAS-2 template to fit the assessment of studies included and added relevant questions for each item. Two researchers independently performed a risk of bias assessment based on the published articles and supplementary material if available. Each item in the QUADAS-2 tool was scored as either “low,” “high,” or “indeterminate” risk of bias for each of the individual studies or applica-

		Risk of bias				Applicability concerns		
		Patient Selection	Index Test	Reference Standard	Flow and Timing	Patient Selection	Index Test	Reference Standard
Dangouloff-Ros	2016	+	+	+	?	+	+	+
Dangouloff-Ros	2015	+	+	?	?	+	+	+
Hales	2013	?	-	?	?	+	?	?
Liu	2015	?	-	?	?	+	?	-
Kikuchi	2017	+	-	?	?	+	+	+
Morana	2017	+	-	?	?	+	-	+
Vidyasagar	2016	?	-	?	?	+	-	?
Yeom	2014	+	+	?	?	+	+	+

+ indicates low risk
 - indicates high risk
 ? indicates unclear risk

FIG 1. Risk of bias. Patient selection: it is low if consecutive or reported in years of inclusion together with clear inclusion criteria. Unclear if no mention of consecutive series of patients. High if a nonconsecutive series was reported. Index test: low if ASL was interpreted blinded. Unclear if no information on blinding but a predefined cutoff was specified for a positive test. High if an exploratory cutoff was used and no information on blinding was given. Reference standard: low if reported on a blinded evaluation and WHO adherence. Unclear if no information on blinding was given. High if reported on an unblinded evaluation. Flow and timing: low if <30 days between ASL and histopathology. Unclear if not reported. High if reported after >6 months. Applicability concerns. Patient selection: low if mixed tumor types. Unclear if tumor types were not reported or only 1 tumor type was reported. High if other comparisons than between high- and low-grade were given. Index test: low if presented as relative CBF from 3D pseudocontinuous ASL. Unclear if CBF was not normalized but pseudocontinuous ASL was used. High if perfusion metrics other than CBF were presented or if pulsed ASL was used. Reference standard: low if tumors were classified according to WHO 2007 or later. Unclear if WHO was used but the year was unspecified. High if no report on the histopathologic diagnosis classification system.

bility concerns of studies regarding the main outcome of this meta-analysis.

Statistical Analysis

The sensitivity and specificity of aCBF/rCBF to discriminate LGT and HGT in the studies were used to calculate the true-positive, true-negative, false-positive, and false-negative counts. In studies reporting individual patient data, aCBF and rCBF from each individual were used to calculate the receiver operating characteristic and contingency (2 × 2) table data, including the optimal cutoff.

The mean difference in aCBF/rCBF and its corresponding 95% confidence interval between LGT and HGT was presented using the inverse variance statistical method with the random-effects analysis model for the effects measure in RevMan (<http://community.cochrane.org/help/tools-and-software/revman-5>).²³

The univariate measures of sensitivity and specificity for aCBF and rCBF to discriminate LGT from HGT were calculated for eligible studies.²⁴ To take into account the inverse relationship between sensitivity and specificity in diagnostic-accuracy studies, we applied a bivariate approach using the restricted maximum likelihood estimation method. The bivariate summary receiver operating characteristic curve described the overall diagnostic performance of ASL to differentiate LGT and HGT, with a corresponding 95% confidence interval for sensitivity and specificity.²⁴

Heterogeneity was explored by bivariate meta-regression. Statistical analyses were prespecified and analyzed in RevMan²³ and in R statistical and computing software (<http://www.r-project.org>),²⁵ implementing the mada²⁴ and pROC packages.²⁶

RESULTS

Search Results

The systematic search yielded 105 hits before deduplication. Sixty-one hits remained after removing duplicates and were screened for inclusion in the meta-analysis. Thirty-nine articles were excluded after title and abstract assessment, with 22 articles remaining for full-text evaluation. After full-text evaluation, 14 studies were excluded for the following reasons: 12 having no pediatric cohort, 1 review article, and 1 having no quantitative data available. Eight studies including 286 patients were included in the meta-analysis.^{17,27-33} The study selection is presented in the On-line Figure 1.

Study Characteristics

Study characteristics of 8 included studies are presented in On-line Table 1, with ASL sequences and study specifications in On-line Tables 2–5. Most (6 of 8 studies) included studies used 3D-pseudocontinuous ASL.^{17,27-29,32,33}

Two studies used pulsed ASL.^{30,31} Four of 8 studies used 1.5T, with the remaining using 3T. Risk of bias within studies as assessed by the QUADAS-2 tool, which showed a general low or indeterminate risk of bias (Fig 1). High risk of bias was attributed to undefined blinding procedures when analyzing the ASL data and applying the exploratory cutoff determination in 5 of 8 studies.^{28-31,33} High risk of applicability concern was found in 3 studies²⁹⁻³¹: One study did not report a clear description of the reference standard,²⁹ and 2 studies applied pulsed ASL^{30,31} as well as a unique (for the meta-analysis cohort) postprocessing method of vascular crushing.³¹ Applicability concerns were taken into account in the subgroup analyses by stepwise exclusion.

Mean Difference in CBF between Low- and High-Grade Tumors

The mean difference in aCBF showed a significantly higher CBF in HGT compared with LGT; the mean difference for aCBF was 29.62 mL/min/100 g (95% CI, 10.43–48.82 mL/min/100 g). The test for overall effect (*Z*) was 3.03 (*P* = .002), and for rCBF, 1.34 mL/min/100 g (95% CI, 0.95–1.74 mL/min/100 g) (*P* < .001), depicted in Tables 1 and 2. Reported or calculated optimal cutoffs for the discrimination of low- and high-grade tumors are pre-

Table 1: Absolute CBF in low- and high-grade tumors with associated results from meta-analysis of mean data^a

Study	High-Grade Tumors			Low-Grade Tumors			Weight	Mean Difference, IV, Random-Effects, 95% CI (aCBF)
	Mean aCBF	SD	Total (No.)	Mean aCBF	SD	Total (No.)		
Dangouloff-Ros et al, 2015 ²⁷	239	94.75	2	81.14	33.92	7	1.90%	157.86 (24.16–291.56)
Dangouloff-Ros et al, 2016 ¹⁷	80.12	47.31	65	31.6	10.39	52	24.20%	48.52 (36.68–60.36)
Hales et al, 2013 ²⁸	111.5	2.12	2	80.33	29.66	6	18.80%	31.17 (7.26–55.08)
Kikuchi et al, 2017 ³³	46.33	22.89	7	19.89	21.33	11	20.10%	26.44 (5.31–47.57)
Liu et al, 2015 ²⁹	53.52	17.4	6	47.32	14.74	6	21.50%	6.20 (–12.05–24.45)
Morana et al, 2017 ³⁰	0	0	0	0	0	0		Not estimable
Vidyasagar et al, 2016 ³¹	68.75	31.77	4	51.3	42.87	19	13.50%	17.45 (–19.17–54.07)
Yeom et al, 2014 ³²	0	0	0	0	0	0		Not estimable
Total (95% CI)			86			101	100%	29.62 (10.43–48.82)

Note:—IV indicates inverse variance.

^a Heterogeneity: $\tau^2 = 360.34$, $\chi^2 = 19.31$, $df = 5$ ($P = .002$); $I^2 = 46\%$; Test for overall effect: $Z = 3.03$ ($P = .002$).

Table 2: Relative CBF in low- and high-grade tumors with associated results from meta-analysis of mean data^a

Study	High-Grade Tumors			Low-Grade Tumors			Weight	Mean Difference, IV, Random-Effects, 95% CI (rCBF)
	Mean rCBF	SD	Total (No.)	Mean rCBF	SD	Total (No.)		
Dangouloff-Ros et al, 2015 ²⁷	3.4	0.99	2	0.9	0.26	7	7.10%	2.50 (1.11–3.89)
Dangouloff-Ros et al, 2016 ¹⁷	1.74	1.45	65	0.68	0.24	52	37.50%	1.06 (0.70–1.42)
Hales et al, 2013 ²⁸	0	0	0	0	0	0		Not estimable
Kikuchi et al, 2017 ³³	1.76	0.95	7	0.69	0.81	11	15.40%	1.07 (0.22–1.92)
Liu et al, 2015 ²⁹	0	0	0	0	0	0		Not estimable
Morana et al, 2017 ³⁰	2.08	0.98	14	0.81	0.56	12	23.90%	1.27 (0.67–1.87)
Yeom et al, 2014 ³²	2.98	1.9	21	1.12	0.36	32	16.20%	1.86 (1.04–2.68)
Total (95% CI)			109			114	100%	1.34 (0.95–1.74)

Note:—IV indicates inverse variance.

^a Heterogeneity: $\tau^2 = 0.13$, $\chi^2 = 9.28$, $df = 5$ ($P = .10$); $I^2 = 46\%$; Test for overall effect: $Z = 5.94$ ($P < .00001$).

sented in Table 1. Heterogeneity regarding the results was lower for relative CBF compared with absolute CBF.

Summary Receiver Operating Characteristics

Absolute CBF. Distributions of the sensitivity and specificity for aCBF ranged between 0.69 and 0.92 for sensitivity and from 0.63 to 0.93 for specificity.^{17,27–29,33}

The bivariate summary receiver operating characteristic curve described an area under the curve of 0.90. Excluding pilocytic astrocytomas and the subgroup of posterior fossa tumors in the study by Dangouloff-Ros et al 2016¹⁷ only slightly affected the diagnostic performance (area under curve = 0.88). Excluding 1 study with a high risk of applicability concern of the reference standard in QUADAS-2 did not lower the overall diagnostic performance to discriminate low- and high-grade tumors (area under curve = 0.92).²⁹ Bivariate meta-regression found no moderating effect on the outcome (sensitivity or specificity) by TE, TR, acquisition time, or ROI method (maximum or mean CBF) ($P > .05$).

Relative CBF. rCBF univariate measures of sensitivity and specificity are presented in On-line Fig 2 and ranged between 0.75 to 0.94 for sensitivity and from 0.79 to 0.92 for the specificity. The bivariate summary receiver characteristics curve depicted in Fig 2 described the area under the curve to discriminate LGT and HGT by rCBF as 0.92. In sensitivity analysis, excluding pilocytic astrocytomas and the subgroup of posterior fossa tumors in the study by Dangouloff-Ros et al 2016¹⁷ did not increase the diagnostic performance (area under curve = 0.91). Excluding 1 study that used pulsed ASL³⁰ did not increase the diagnostic performance (area under curve = 0.88). In agreement with the subgroup anal-

ysis of pulsed-ASL or 3D-pseudocontinuous had no moderating effect on the outcome (sensitivity or specificity) in bivariate meta-regression ($P > .05$). Furthermore, bivariate meta-regression found no moderating effect on the outcome by TE, TR, or acquisition time ($P > .05$).

DISCUSSION

This meta-analysis found an aggregated high diagnostic accuracy for cerebral blood flow measurements derived from ASL MR imaging to discriminate LGT and HGT in pediatric patients. Preoperative indications of tumor grade can be important when considering different treatment strategies, clinical decisions related to the timing of treatment, surgical strategies, and prognosis and in longitudinal follow-up of patients.

Factors that might potentially affect the results were analyzed to gain an understanding of the diagnostic potential of ASL, depending on technical properties and patient-specific factors. Both the sensitivity and specificity of ASL-derived CBF measurements were taken into account in evaluating the overall summary receiver operating characteristic curve and when exploring the role for potential moderators of the effect size.

This report is in accordance with a previous meta-analysis evaluating ASL in an adult population that reported the standardized mean differences in CBF between LGT and HGT,¹⁰ even though pediatric brain tumors have different biologic properties though similar histology.³⁴

Our results show that the diagnostic accuracy to discriminate brain tumor grades in children is similar to previous reports evaluating perfusion MR using gadolinium injection in a pediatric cohort.³⁵

SROC curve (bivariate model) for rCBF in low-grade and high-grade tumors

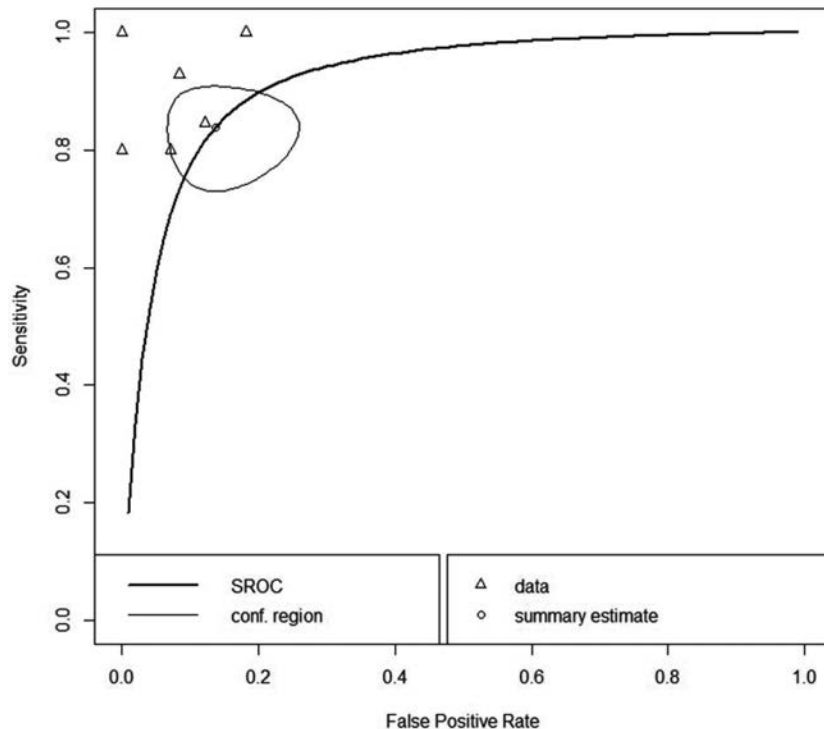


FIG 2. Summary of the receiver operating characteristic curve (bivariate model) for the discrimination of low- and high-grade tumors by relative CBF. The curved line describes the variation in sensitivity and false-positive rate (1-specificity) across the data depicted by *open triangles* and the *open circle*, indicating the summary estimate surrounded by the confidence region illustrated by the *thinner black line*. The area under the curve was 0.92. SROC indicates summary receiver operating characteristic; conf, confidence.

The use of ASL seems justified in children due to its noninvasive nature, with lack of contrast agent injection and lack of radiation exposure. Pediatric patients subject to MR imaging and not having an intravenous line might thus be investigated with brain MR imaging rendering both morphologic and physiologic data on perfusion without gadolinium-based contrast agent injection.

The ASL technique has been available for >2 decades without being introduced in full in the clinic.³⁶⁻⁴¹ This study, including original studies published between 2013 and 2017, provides evidence that ASL is approaching an introduction in clinical practice for the evaluation of pediatric brain tumors. There have been concerns raised that ASL would be an immature and unreliable perfusion technique regarding low signal-to-noise ratio,^{42,43} the influence of physiologic fluctuations on the blood flow,⁴³ and the effects of anesthesia.⁴⁴

Although absolute CBF is desirable, ASL-derived CBF shows high variation among subjects due to global physiologic factors such as hematocrit, sex, age, and cardiovascular disease.⁴⁵⁻⁴⁷ In addition, ASL-derived CBF measurements can be variable when the pulse sequences and postprocessing algorithms are not standardized.⁴⁸ Due to the variability of the tumors in individual studies in this meta-analysis, estimated and reported cutoffs for the discrimination of low- and high-grade tumors varied among studies even when data acquisition was similar (3D pseudocontinuous arterial spin/labeling). However, the cutoff for relative CBF varied less than that for absolute CBF. For studies reporting

relative CBF in intra-axial brain tumors, cutoffs were more similar.

The impact of age on measurements has not been fully accounted for in the included studies nor has a standardized measurement been used across studies. Representative measurement of tumor blood flow might be hampered by partial volume effects in ASL.

Our study shows that slight parameter changes between study protocols did not have a moderating effect on the diagnostic accuracy. Most included studies applied the 3D-pseudocontinuous ASL technique. Pseudocontinuous ASL has a high repeatability among scanners, and examinations are in accordance with findings in previous reports.^{18,49} Although not immediately evident in our study, the 3D technique has been shown to be superior to 2D.⁵⁰

Future research in this field should be directed toward the evaluation of other indications when a noninvasive evaluation of blood flow could give important clinical information and possibly also continue to extend the method to calculate cerebral blood volume, mean transit time,⁵¹ and permeability.⁵²⁻⁵⁴ An additional advantage of ASL could be the possibility of quantitative measured perfusion. Furthermore, the impact of CBF measurement on overall survival and longitudinal follow-up should be evaluated.

We strove to diminish the influence of publication bias by also searching for gray literature in scientific data bases. Second, the number of included studies is quite small, in part reflecting the difficulty in evaluating pediatric patients with rare diseases and new techniques. However, the included studies comprised 286 patients from several different centers in the world. Included articles mainly used the 2007 WHO brain tumor classification. One measure that was used to adapt to the 2016 classification of brain tumors was to exclude midline gliomas located in the pons. This decision was supported by the lack of a histologic sample from some of these patients due to the eloquent location of these tumors.

CONCLUSIONS

Available data on the applicability of ASL in children with brain tumors indicate a high diagnostic accuracy to discriminate low- and high-grade tumors. Relative CBF showed less variation between studies compared with absolute CBF.

ACKNOWLEDGMENTS

We thank Klas Moberg, Librarian at the Karolinska Institute Library, for planning and conducting the search.

Disclosures: Anna Falk Delgado—RELATED: Other: Department of Neuroradiology Karolinska University Hospital; UNRELATED: Grants/Grants Pending: EU-financed unrelated research project*. *Money paid to the institution.

REFERENCES

1. Patel S, Bhatnagar A, Wear C, et al. **Are pediatric brain tumors on the rise in the USA? Significant incidence and survival findings from the SEER database analysis.** *Childs Nerv Syst* 2014;30:147–54 CrossRef Medline
2. Spennato P, Nicosia G, Quaglietta L, et al. **Posterior fossa tumors in infants and neonates.** *Childs Nerv Syst* 2015;31:1751–72 CrossRef Medline
3. Pallud J, Capelle L, Taillandier L, et al. **Prognostic significance of imaging contrast enhancement for WHO grade II gliomas.** *Neuro Oncol* 2009;11:176–82 CrossRef Medline
4. Hu J, Wu W, Zhu B, et al. **Cerebral glioma grading using Bayesian network with features extracted from multiple modalities of magnetic resonance imaging.** *PLoS One* 2016;11:e0153369 CrossRef Medline
5. Santarosa C, Castellano A, Conte GM, et al. **Dynamic contrast-enhanced and dynamic susceptibility contrast perfusion MR imaging for glioma grading: preliminary comparison of vessel compartment and permeability parameters using hotspot and histogram analysis.** *Eur J Radiol* 2016;85:1147–56 CrossRef Medline
6. Young R, Babb J, Law M, et al. **Comparison of region-of-interest analysis with three different histogram analysis methods in the determination of perfusion metrics in patients with brain gliomas.** *J Magn Reson Imaging* 2007;26:1053–63 CrossRef Medline
7. Flood TF, Stence NV, Maloney JA, et al. **Pediatric brain: repeated exposure to linear gadolinium-based contrast material is associated with increased signal intensity at unenhanced T1-weighted MR imaging.** *Radiology* 2017;282:222–28 CrossRef Medline
8. de Fatima Vasco Aragao M, Law M, Batista de Almeida D, et al. **Comparison of perfusion, diffusion, and MR spectroscopy between low-grade enhancing pilocytic astrocytomas and high-grade astrocytomas.** *AJNR Am J Neuroradiol* 2014;35:1495–502 CrossRef Medline
9. Alkonyi B, Nowak J, Gnekow AK, et al. **Differential imaging characteristics and dissemination potential of pilomyxoid astrocytomas versus pilocytic astrocytomas.** *Neuroradiology* 2015;57:625–38 CrossRef Medline
10. Kong L, Chen H, Yang Y, et al. **A meta-analysis of arterial spin labeling perfusion values for the prediction of glioma grade.** *Clin Radiol* 2017;72:255–61 CrossRef Medline
11. Zeng Q, Jiang B, Shi F, et al. **3D pseudocontinuous arterial spin-labeling imaging in the preoperative evaluation of gliomas.** *AJNR Am J Neuroradiol* 2017;38:1876–83 CrossRef Medline
12. Haller S, Zaharchuk G, Thomas DL, et al. **Arterial spin labeling perfusion of the brain: emerging clinical applications.** *Radiology* 2016; 281:337–56 CrossRef Medline
13. Warmuth C, Gunther M, Zimmer C. **Quantification of blood flow in brain tumors: comparison of arterial spin labeling and dynamic susceptibility-weighted contrast-enhanced MR imaging.** *Radiology* 2003;228:523–32 CrossRef Medline
14. Chawla S, Wang S, Wolf RL, et al. **Arterial spin-labeling and MR spectroscopy in the differentiation of gliomas.** *AJNR Am J Neuroradiol* 2007;28:1683–89 CrossRef Medline
15. Kim HS, Kim SY. **A prospective study on the added value of pulsed arterial spin-labeling and apparent diffusion coefficients in the grading of gliomas.** *AJNR Am J Neuroradiol* 2007;28:1693–99 CrossRef Medline
16. Noguchi T, Yoshiura T, Hiwatashi A, et al. **Perfusion imaging of brain tumors using arterial spin-labeling: correlation with histopathologic vascular density.** *AJNR Am J Neuroradiol* 2008;29: 688–93 CrossRef Medline
17. Dangouloff-Ros V, Deroulers C, Foissac F, et al. **Arterial spin labeling to predict brain tumor grading in children: correlations between histopathologic vascular density and perfusion MR imaging.** *Radiology* 2016;281:553–66 CrossRef Medline
18. Gevers S, van Osch MJ, Bokkers RP, et al. **Intra- and multicenter reproducibility of pulsed, continuous and pseudo-continuous arterial spin labeling methods for measuring cerebral perfusion.** *J Cereb Blood Flow Metab* 2011;31:1706–15 CrossRef Medline
19. Leeflang MM, Deeks JJ, Takwoingi Y, et al. **Cochrane Diagnostic Test Accuracy Reviews.** *Syst Rev* 2013;2:82 CrossRef Medline
20. Moher D, Liberati A, Tetzlaff J, et al; PRISMA Group. **Preferred Reporting Items for Systematic Reviews and Meta-Analyses: the PRISMA statement.** *PLoS Med* 2009;16:e1000097 CrossRef Medline
21. McGrath TA, Alabousi M, Skidmore B, et al. **Recommendations for reporting of systematic reviews and meta-analyses of diagnostic test accuracy: a systematic review.** *Syst Rev* 2017;6:194 CrossRef Medline
22. Whiting PF, Rutjes AW, Westwood ME, et al; QUADAS-2 Group. **QUADAS-2: a revised tool for the quality assessment of diagnostic accuracy studies.** *Ann Intern Med* 2011;155:529–36 CrossRef Medline
23. Review. Version RevMan 5.3. Copenhagen: The Nordic Cochrane Centre, The Cochrane Collaboration, 2014. <http://community.cochrane.org/help/tools-and-software/revman-5/revman-5-download>. Accessed 2 May 2017
24. Doebler P, Holling H. **Meta-Analysis of diagnostic accuracy studies with mada.** <https://cran.r-project.org/web/packages/mada/vignettes/mada.pdf>. Accessed 16 Sept 2016
25. R Development Core Team (2010). **R: A Language and Environment for Statistical Computing.** Vienna, Austria: R Foundation for Statistical Computing. <http://www.R-project.org>. Accessed: 19 April 2017
26. Robin X, Turck N, Hainard A, et al. **pROC: an open-source package for R and S+ to analyze and compare ROC curves.** *BMC Bioinformatics* 2011;12:77 CrossRef Medline
27. Dangouloff-Ros V, Grevent D, Pagès M, et al. **Choroid plexus neoplasms: toward a distinction between carcinoma and papilloma using arterial spin-labeling.** *AJNR Am J Neuroradiol* 2015;36: 1786–90 CrossRef Medline
28. Hales PW, Phipps KP, Kaur R, et al. **A two-stage model for in vivo assessment of brain tumor perfusion and abnormal vascular structure using arterial spin labeling.** *PLoS One* 2013;8:e75717 CrossRef Medline
29. Liu HL, Chang TT, Yan FX, et al. **Assessment of vessel permeability by combining dynamic contrast-enhanced and arterial spin labeling MRI.** *NMR Biomed* 2015;28:642–49 CrossRef Medline
30. Morana G, Piccardo A, Tortora D, et al. **Grading and outcome prediction of pediatric diffuse astrocytic tumors with diffusion and arterial spin labeling perfusion MRI in comparison with 18F-DOPA PET.** *Eur J Nucl Med Mol Imaging* 2017;44:2084–93 CrossRef Medline
31. Vidyasagar R, Abernethy L, Pizer B, et al. **Quantitative measurement of blood flow in paediatric brain tumours: a comparative study of dynamic susceptibility contrast and multi time-point arterial spin labelled MRI.** *Br J Radiol* 2016;89:20150624 CrossRef Medline
32. Yeom KW, Mitchell LA, Lober RM, et al. **Arterial spin-labeled perfusion of pediatric brain tumors.** *AJNR Am J Neuroradiol* 2014;35: 395–401 CrossRef Medline
33. Kikuchi K, Hiwatashi A, Togao O, et al. **Correlation between arterial spin-labeling perfusion and histopathological vascular density of pediatric intracranial tumors.** *J Neurooncol* 2017;135:561–69 CrossRef Medline
34. Louis DN, Perry A, Reifenberger G, et al. **The 2016 World Health Organization Classification of Tumors of the Central Nervous System: a summary.** *Acta Neuropathol* 2016;131:803–20 CrossRef Medline
35. Dallery F, Bouzerar R, Michel D, et al. **Perfusion magnetic resonance imaging in pediatric brain tumors.** *Neuroradiology* 2017;59:1143–53 CrossRef Medline
36. Alsop DC, Detre JA. **Reduced transit-time sensitivity in noninvasive magnetic resonance imaging of human cerebral blood flow.** *J Cereb Blood Flow Metab* 1996;16:1236–49 CrossRef Medline
37. Alsop DC, Detre JA. **Multisection cerebral blood flow MR imaging**

- with continuous arterial spin labeling. *Radiology* 1998;208:410–16 CrossRef Medline
38. Detre JA, Alsop DC. **Perfusion magnetic resonance imaging with continuous arterial spin labeling: methods and clinical applications in the central nervous system.** *Eur J Radiol* 1999;30:115–24 CrossRef Medline
 39. Detre JA, Zhang W, Roberts DA, et al. **Tissue specific perfusion imaging using arterial spin labeling.** *NMR Biomed* 1994;7:75–82 CrossRef Medline
 40. Silva AC, Zhang W, Williams DS, et al. **Multi-slice MRI of rat brain perfusion during amphetamine stimulation using arterial spin labeling.** *Magn Reson Med* 1995;33:209–14 CrossRef Medline
 41. Williams DS, Detre JA, Leigh JS, et al. **Magnetic resonance imaging of perfusion using spin inversion of arterial water.** *Proc Natl Acad Sci U S A* 1992;89:212–16 CrossRef Medline
 42. Spann SM, Kazimierski KS, Aigner CS, et al. **Spatio-temporal TGV denoising for ASL perfusion imaging.** *Neuroimage* 2017;157:81–96 CrossRef Medline
 43. Chen Y, Wang DJ, Detre JA. **Test-retest reliability of arterial spin labeling with common labeling strategies.** *J Magn Reson Imaging* 2011;33:940–49 CrossRef Medline
 44. Venkatraghavan L, Poulanc J, Bharadwaj S, et al. **Noninvasive measurement of cerebral blood flow under anesthesia using arterial spin labeling MRI: a pilot study.** *J Neurosurg Anesthesiol* 2016;28:331–36 CrossRef Medline
 45. Ibaraki M, Shinohara Y, Nakamura K, et al. **Interindividual variations of cerebral blood flow, oxygen delivery, and metabolism in relation to hemoglobin concentration measured by positron emission tomography in humans.** *J Cereb Blood Flow Metab* 2010;30:1296–305 CrossRef Medline
 46. Henriksen OM, Kruuse C, Olesen J, et al. **Sources of variability of resting cerebral blood flow in healthy subjects: a study using ¹³³Xe SPECT measurements.** *J Cereb Blood Flow Metab* 2013;33:787–92 CrossRef Medline
 47. Xu F, Li W, Liu P, et al. **Accounting for the role of hematocrit in between-subject variations of MRI-derived baseline cerebral hemodynamic parameters and functional BOLD responses.** *Hum Brain Mapp* 2018;39:344–53 CrossRef Medline
 48. Alsop DC, Detre JA, Golay X, et al. **Recommended implementation of arterial spin-labeled perfusion MRI for clinical applications: a consensus of the ISMRM perfusion study group and the European consortium for ASL in dementia.** *Magn Reson Med* 2015;73:102–16 CrossRef Medline
 49. Wu B, Lou X, Wu X, et al. **Intra- and interscanner reliability and reproducibility of 3D whole-brain pseudo-continuous arterial spin-labeling MR perfusion at 3T.** *J Magn Reson Imaging* 2014;39:402–09 CrossRef Medline
 50. Kilroy E, Apostolova L, Liu C, et al. **Reliability of two-dimensional and three-dimensional pseudo-continuous arterial spin labeling perfusion MRI in elderly populations: comparison with 15O-water positron emission tomography.** *J Magn Reson Imaging* 2014;39:931–39 CrossRef Medline
 51. van Westen D, Petersen ET, Wirestam R, et al. **Correlation between arterial blood volume obtained by arterial spin labelling and cerebral blood volume in intracranial tumours.** *MAGMA* 2011;24:211–23 CrossRef Medline
 52. Bibic A, Knutsson L, Schmidt A, et al. **Measurement of vascular water transport in human subjects using time-resolved pulsed arterial spin labelling.** *NMR Biomed* 2015;28:1059–68 CrossRef Medline
 53. Hales PW, Clark CA. **Combined arterial spin labeling and diffusion-weighted imaging for noninvasive estimation of capillary volume fraction and permeability-surface product in the human brain.** *J Cereb Blood Flow Metab* 2013;33:67–75 CrossRef Medline
 54. Wang J, Fernández-Seara MA, Wang S, et al. **When perfusion meets diffusion: in vivo measurement of water permeability in human brain.** *J Cereb Blood Flow Metab* 2007;27:839–49 CrossRef Medline

The Bone Does Not Predict the Brain in Sturge-Weber Syndrome

R.R. Warne, O.M. Carney, G. Wang, D. Bhattacharya, W.K. Chong, S.E. Aylett, and K. Mankad



ABSTRACT

BACKGROUND AND PURPOSE: It has been hypothesized that skull marrow signal alteration may represent an early disease manifestation of Sturge-Weber syndrome before development of its intracranial manifestations. We alternatively hypothesized that intraosseous changes are associated with the overlying port-wine stain rather than the intracranial stigmata of Sturge-Weber syndrome and hence are not a predictor of brain involvement.

MATERIALS AND METHODS: MR imaging of children presenting with port-wine stain and/or Sturge-Weber syndrome between 1998 and 2017 was evaluated by 2 pediatric neuroradiologists for marrow signal abnormality and pial angioma and other Sturge-Weber syndrome features: ocular hemangioma, atrophy, and white matter changes (advanced myelination). Groups were divided into port-wine stain–only (without intracranial Sturge-Weber syndrome features) and Sturge-Weber syndrome (the presence of cerebral pial angioma). The χ^2 test was performed to evaluate the association between port-wine stain and bone marrow changes and between osseous change and pial angioma.

RESULTS: We reviewed 139 cases: 40 with port-wine stain–only and 99 with Sturge-Weber syndrome with pial angioma. Fifteen of 99 cases of Sturge-Weber syndrome had no port-wine stain. In the port-wine stain–only cohort, 78% had ipsilateral bony changes and 17% had no intraosseous changes. In the Sturge-Weber syndrome cohort, 84/99 had associated port-wine stain, 91% ($P < .01$) had bony changes ipsilateral to the port-wine stain or had no bone changes in the absence of port-wine stain, and 77% ($P = .27$) had bony changes ipsilateral to a cerebral pial angioma. Eighty percent of patients with Sturge-Weber syndrome who lacked a port-wine stain also lacked marrow changes. Five patients with bilateral port-wine stain and bilateral marrow changes had only a unilateral pial angioma.

CONCLUSIONS: Intraosseous marrow changes are strongly associated with facial port-wine stain; no significant association was found between pial angioma and bone marrow changes.

ABBREVIATIONS: PWS = port-wine stain; SWS = Sturge Weber syndrome

Port-wine stain (PWS) or the synonymous term “port-wine birthmark” is a common vascular anomaly affecting 0.3% of neonates, and it usually presents as an isolated finding.¹ For this article, the term “PWS” will be used. A small proportion of PWSs are associated with leptomeningeal angiomatosis and ocular hemangioma, the classic triad of Sturge-Weber syndrome (SWS). Typical features of SWS with gadolinium contrast on MR imaging include enhancing pial angioma, cortical/subcortical atrophy

with calcification, and ocular choroidal enhancement. There are other neuroradiologic features that have been reported in association with SWS, including advanced or accelerated myelination,² prominent transmedullary and cortical veins,^{3,4} and glomus angioma (Fig 1).⁵ For this study, the term “glomus angioma” refers to a venous angioma involving the choroid plexus.

Accelerated or advanced myelination relates to the decreased parenchymal signal on T2WI sequences in the subcortical white matter, which is variably speculated to relate to either calcification, altered myelination states, and/or cerebral blood oxygenation effect.² A combination of these mechanisms is likely.

Posterior chamber choroidal hemangiomas may lead to glaucoma by fluid hypersecretion⁶ and may also lead to visual impairment by exudative retinal detachment and macular edema. Choroidal hemangiomas are usually <6 mm in thickness⁷ and can be seen in up to 70% of cases of SWS.⁸ Approximately 50% of patients with SWS have ocular changes ipsilateral to the PWS.⁹

It has been hypothesized that osseous intramedullary signal

Received March 1, 2018; accepted after revision May 18.

From the Department of Paediatric Neuroradiology (R.R.W., O.M.C., D.B., W.K.C., K.M.), Great Ormond Street Hospital for Children, NHS Foundation Trust, London, UK; Neurosciences (S.E.A.), Great Ormond Street Hospital for Children and Developmental Neurosciences University College London, NHS Foundation Trust, London UK; Department of Biostatistics (G.W.), University of Sydney School of Public Health, Sydney, New South Wales, Australia 2006.

Please address correspondence to Kshitij Mankad, MBBS, FRCR, Great Ormond Street Hospital for Children, NHS Foundation Trust, Paediatric Neuroradiology, Great Ormond St, London WC1N3JH UK; e-mail: Kshitij.Mankad@gosh.nhs.uk; @Richie_Warne

<http://dx.doi.org/10.3174/ajnr.A5722>

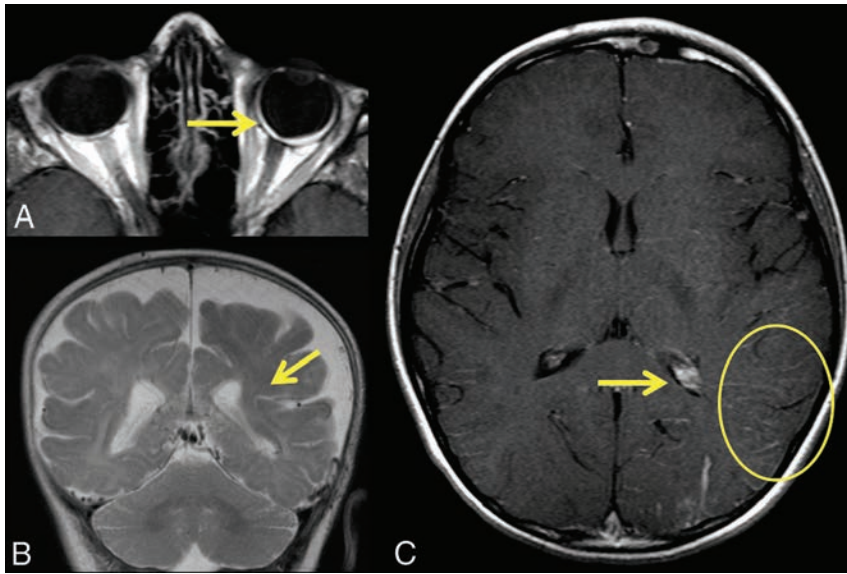


FIG 1. Associated findings of SWS. A 4-month-old boy with SWS. A, Postcontrast T1WI of the orbits shows a left ocular choroidal hemangioma (clinically confirmed). B, Coronal T2WI of the brain reveals volume loss of the left hemisphere with associated accelerated myelination (arrow). C, Postcontrast axial T1WI of the brain shows an enlarged and enhancing left glomus angioma (arrow) and prominent transmedullary veins (circle).

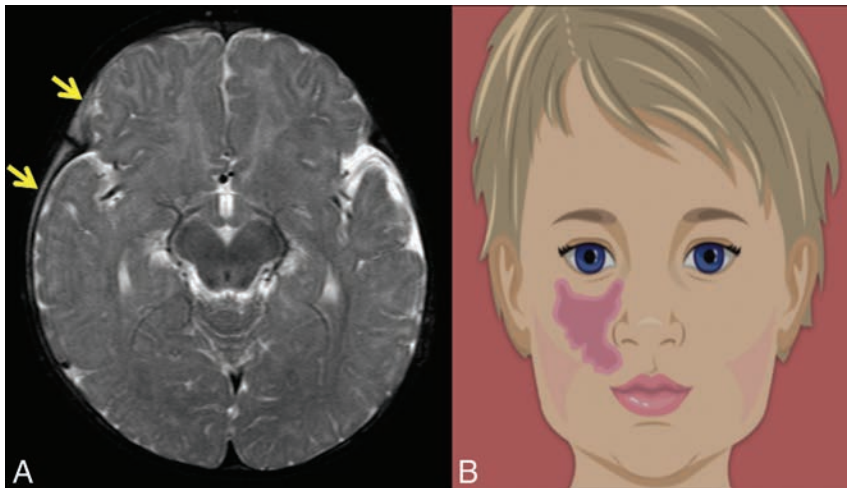


FIG 2. Calvarial bone marrow abnormality. A 6-month-old boy with right PWS only. A, Axial T2-weighted STIR shows high-signal abnormality in the right calvaria (arrows). B, Graphic of a child with right-sided PWS. Reproduced with permission from Scio21/Bigstock.com.

alteration within the skull may represent early disease manifestation of SWS before the development of its intracranial manifestations.¹⁰ The purpose of our study was to explore and challenge this previously published hypothesis from analysis of a large cohort of children presenting with SWS and/or PWS. We therefore alternatively hypothesized that the osseous changes relate to the overlying PWS (Fig 2) rather than intracranial stigmata of SWS and hence are not a predictor of SWS.

MATERIALS AND METHODS

This project was approved by the institutional research board (reference number 2045). The cohort for the study comprised all patients referred to the department of neuroradiology at a tertiary children's hospital between 1998 and 2017 for imaging assessment of suspected

SWS. The criterion for referral was clinical or dermatologic: the presence of a facial PWS or clinical suspicion of SWS in those patients in whom a PWS was absent.

All patients had ≥ 1 MR imaging brain scan, including gadolinium-enhanced T1WI sequences. A standardized protocol using a 1.5T scanner (Symphony or Avanto; Siemens, Erlangen, Germany) or a 3T Magnetom Prisma scanner (Siemens) was used for imaging performed at our center.

If the patients were younger than 24 months of age, the protocol included the following: axial dual-echo STIR inversion recovery with T1-weighted axial, coronal, sagittal postgadolinium, and DWI sequences. For patients older than 24 months of age, the axial dual-echo STIR was replaced by an axial T2WI and FLAIR.

Of note, 56 scans (40% of the imaging) had been obtained at the patient's local radiology department, and the imaging was transferred electronically for a second opinion to our institution. Each study was evaluated for the presence of calvarial marrow change, marrow or dural thickening or enhancement, and stigmata of SWS intracranial findings, including cerebral pial angioma, choroidal hemangioma, glomus angioma, transmedullary and prominent cortical veins, and accelerated myelination. Cortical calcification and mineralization were not routinely recorded because not all studies had dedicated sequences. However, if the study had a recent CT or a susceptibility-weighted MR imaging sequence that confirmed calcification, it was noted. The essential criterion in the PWS-only group was the presence of a facial PWS and the absence of any intracranial findings (cerebral changes or pial angioma).

The inclusion criterion of the SWS group was the presence of a pial angioma.

The clinical notes were reviewed following the imaging analysis to obtain the neurologic and ophthalmologic details; when possible, clinical photography records were reviewed to determine the side of the PWS distribution.

Patients were excluded from analysis if the site of the PWS was not available as per clinical records or their imaging was unavailable, they did not have a contrast scan, or they had a crossover syndrome (eg, Klippel-Trenaunay syndrome).

Statistics

χ^2 and Fischer exact tests were used to evaluate the association between PWS and intraosseous change and, in addition in the SWS

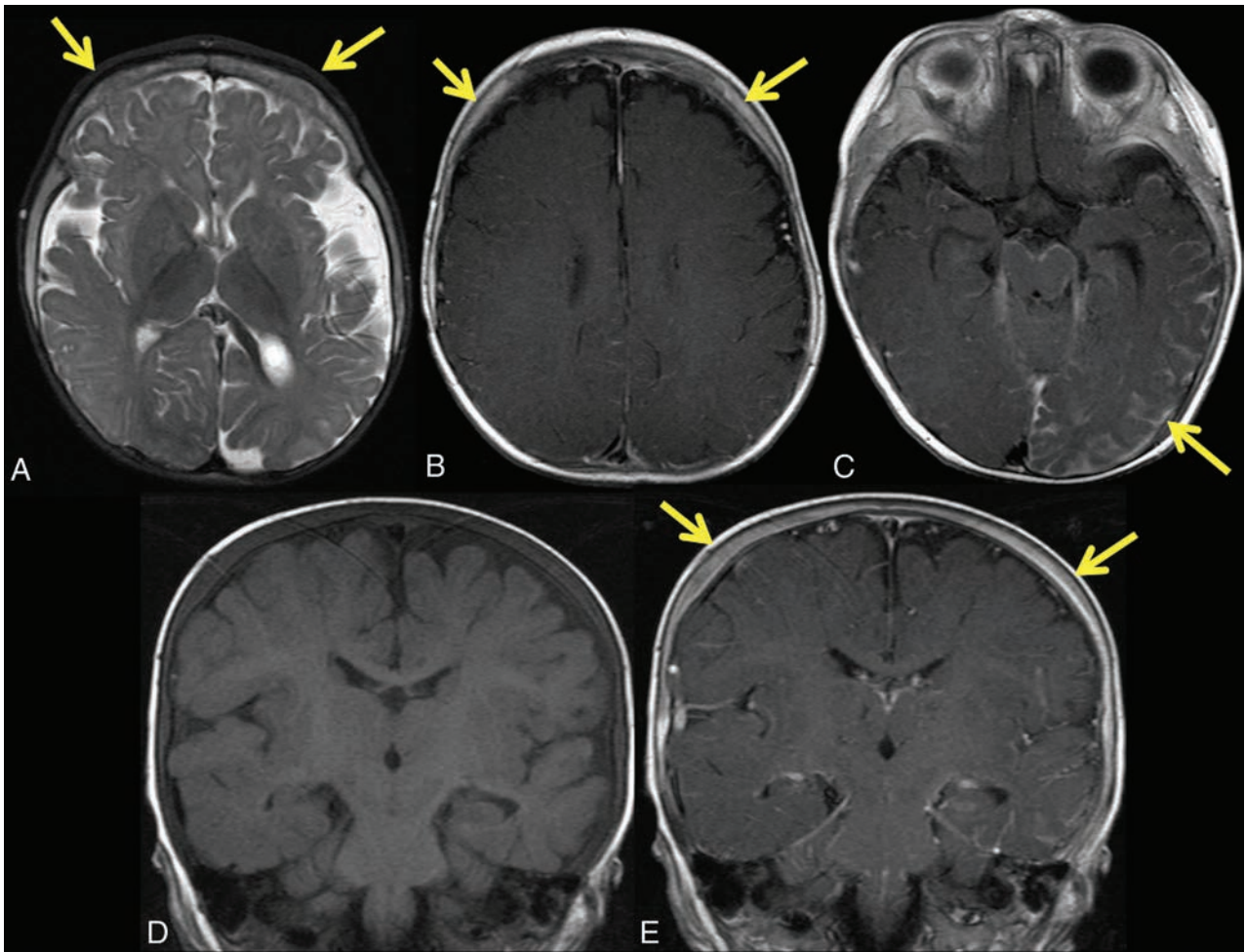


FIG 3. Bilateral PWS with bilateral calvarial marrow abnormality. An 8-month-old boy with SWS. Axial T2-weighted-STIR (A) and axial T1-weighted postcontrast (B) images reveal a bilateral marrow T2 high-signal calvarial abnormality and enhancement. C, Axial T1WI postcontrast shows a left-sided temporo-occipital pial angioma. Coronal T1-weighted precontrast (D) and postcontrast (E) imaging show bilateral marrow and dural enhancement.

Intraosseous signal abnormality versus same-sided PWS

PWS	Intraosseous Signal Abnormality	
	Present	Absent
Present	109	10
Absent	3	12

group, the association between the intraosseous change and the pial angioma.

RESULTS

In total, 139 cases were included (40 patients with PWS only and 99 patients with SWS).

PWS-Only Group

The PWS-only group ($n = 40$) comprised an even distribution of 20 male and 20 female patients, with ages ranging from 10 weeks to 13.5 years (mean, 2.4 years).

PWS and Intraosseous Change Relationship

Of the 40 patients in the PWS-only group, 31 (78%) had concordant bone marrow changes ipsilateral to the PWS. Seven patients (18%) had absent bone marrow changes, with the remaining 2

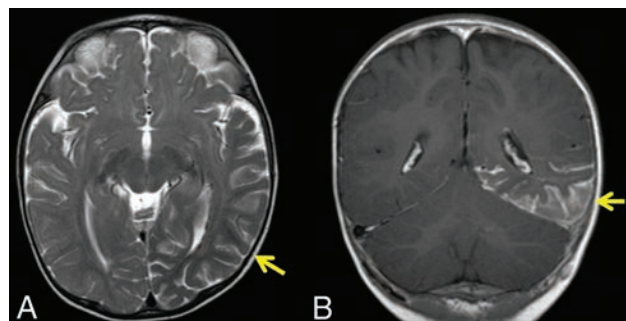


FIG 4. SWS with absent PWS. An 8-month-old girl with SWS. A, Axial T2-weighted STIR shows left temporo-occipital calvarial thinning with no bone marrow abnormality. B, Axial postcontrast T1WI shows a corresponding thick enhancing left hemispheric pial angioma.

cases revealing bilateral changes from a unilateral PWS. All 31 concordant intraosseous changes had associated intraosseous/dural enhancement and/or thickening noted.

SWS Group

The SWS group ($n = 99$) included 45 male and 54 female patients, ranging from 1 day to 14.5 years of age (mean, 2.4 years). Of the 99 patients with SWS, 84 had associated PWS.

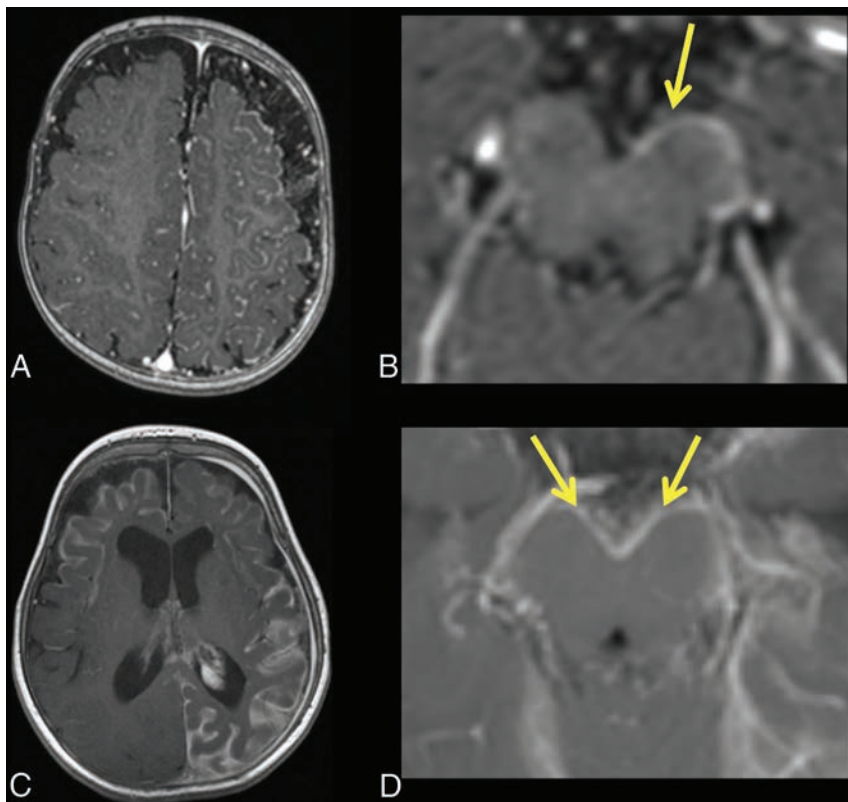


FIG 5. The interpeduncular cistern sign. *Upper panel*, a 9-month-old boy with SWS. *A and B*, Postcontrast axial T1WI shows a left-sided unilateral pial angioma and a zoomed-in view of the interpeduncular cistern confirming the unilaterality (*arrow*). *Lower panel*, a 10-month-old girl with SWS. *C and D*, Bilateral pial angiomas with a zoomed-in view confirming the bilaterality (*arrows*), positive for the “warning sign of Warne-Mankad.”

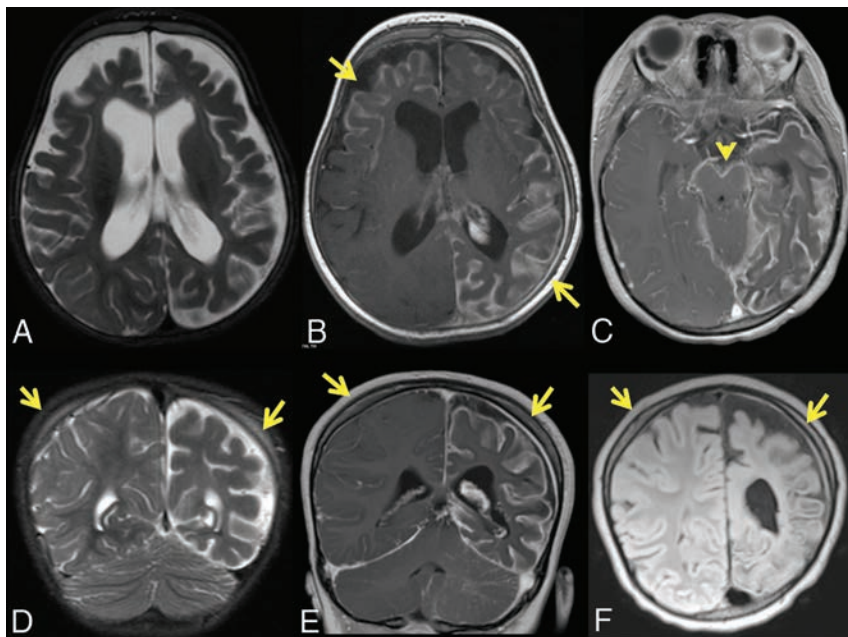


FIG 6. “Warning sign of Warne-Mankad.” Bilateral interpeduncular cistern enhancement. A 10-month-old girl with SWS and bilateral PWS. *A*, Axial T2-weighted STIR shows bilateral hemispheric volume loss. *B*, Axial postcontrast T1WI shows a right-frontal and left-hemispheric pial angioma with the warning sign confirming the bilateral interpeduncular cistern enhancement (*C*). Coronal T2-weighted STIR (*D*) shows bilateral calvarial high signal and marrow enhancement (*E*). Coronal postcontrast FLAIR image (*F*) shows bilateral marrow enhancement and left-sided dural thickening.

PWS and Intraosseous Change Relationship in the SWS Group

Of the 99 patients in the SWS group, 90 (91%, $P < .01$) had concordant intraosseous changes ipsilateral to the PWS (Fig 3) or absent if they did not have a PWS (Table). Of the 84 patients with PWS, 78 (93%) had concordance between the PWS and intraosseous change, with 76 of these having associated intraosseous/dural enhancement or thickening (Fig 3).

Pial Angioma Side and Intraosseous Change Relationship

The association between the side of the pial angioma and marrow change was also documented. All 99 patients in the SWS group had a pial angioma; 76 of the 99 (77%) ($P > .05$) cases were concordant with the pial angioma and intraosseous change side. Of note, 12/15 (80%) patients with SWS who lacked a PWS also lacked marrow signal changes (Fig 4), while the remaining 3 cases revealed bony changes ipsilateral to the leptomeningeal angioma. In 6 of the 76 patients (8%) with concordant pial angioma and intraosseous change, the pial angioma was distant from the marrow abnormality.

Additional Observation

Five patients with bilateral PWS and bilateral marrow changes only had a unilateral pial angioma rendering further support to our hypothesis.

Associated SWS Imaging Features

In the PWS-only group, 0/40 had an associated SWS imaging feature. In the SWS group, 36/99 (36%) had accelerated myelination.

Intraosseous/Dural Enhancement and/or Thickening

In the PWS-only group, 31/40 had intraosseous/dural enhancement and/or thickening. Eighty-five of 99 patients with SWS had intraosseous/dural enhancement or thickening.

Ocular Hemangioma

In the PWS-only group, 9 of the 40 (23%) patients had ocular choroidal enhancements, all of which were ipsilateral to the PWS. Eight of these were ipsilateral to the bone marrow abnormality; the other

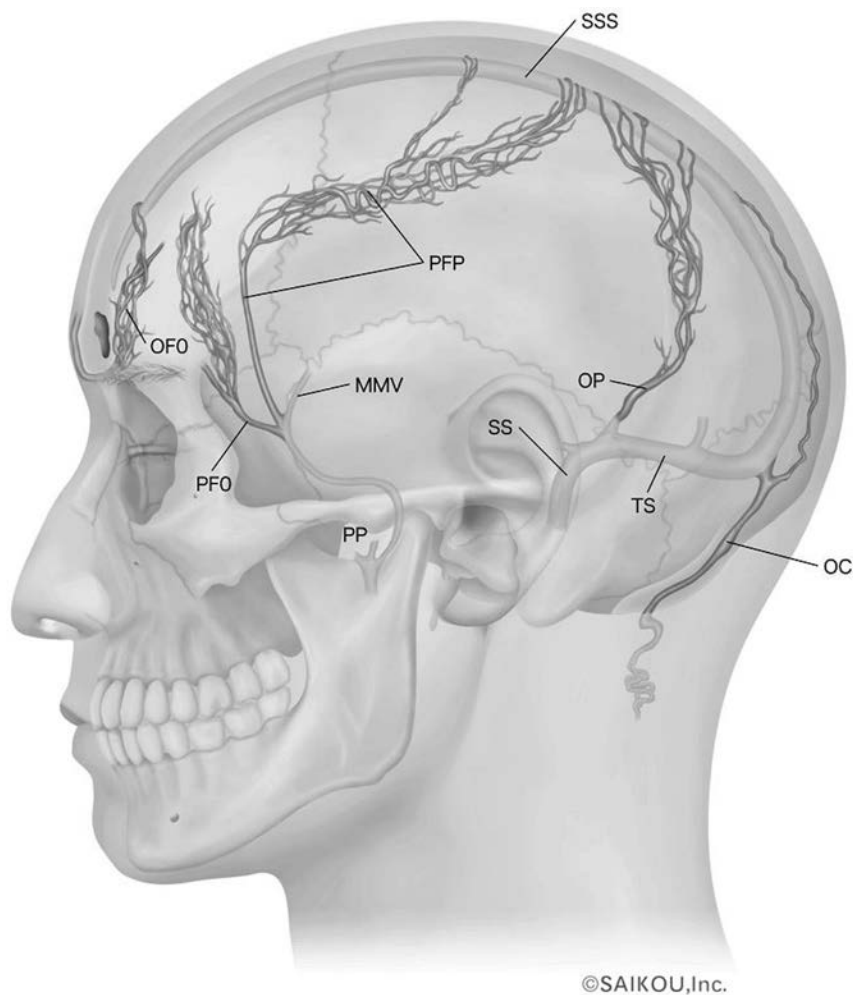


FIG 7. Schematic illustration of the major calvarial diploic venous channel routes over the skull. Reproduced with permission from Springer Nature (Tsutsumi et al¹⁶). MMV indicates middle meningeal vein; OC, occipitocervical route; OFO, orbital part of the fronto-orbital route; OP, occipitoparietal route; PFO, pterional part of the fronto-orbital route; PFP, pteriofrontoparietal route; PP, pterygoid plexus; SS, sigmoid sinus; SSS, superior sagittal sinus; TS, transverse sinus.

one had absent bone marrow change. In the SWS group, 58 of the 99 (59%) patients had ocular choroidal enhancement. Three of these had an absent PWS. The remaining 55 patients had ocular enhancement ipsilateral to the PWS and pial angioma side. Of the absent-PWS SWS group, 3/15 had a choroidal hemangioma.

Glomus Angioma

In the PWS-only group, 0/40 had glomus angioma. In the SWS group, 80/99 (81%) had glomus angioma.

Atrophy

In the PWS-only group, 0/40 had atrophy. In the SWS group, 63/99 (64%) had atrophy. Eight patients had associated cortical calcification (gradient dataset or on CT when available).

Prominent Transmedullary Veins

In the PWS-only group, 0/40 had prominent transmedullary veins. In the SWS group, 78/99 (79%) had prominent transmedullary veins.

Unusual Pial Angioma Imaging Appearances

Interpeduncular Cistern Location. Twelve of 99 patients had an interpeduncular cistern (posterior fossa) location for the pial angioma. Most interesting, of those 12, three of the 4 patients with a unilateral PWS had a pial angioma, which did not cross the midline (Fig 5A, -B), while the remaining 8 patients had bilateral PWS with interpeduncular cistern enhancement crossing the midline (Fig 5C, -D). We called this type of W-shaped enhancement the “warning sign of Warne-Mankad” after this phenomenon and propose this as a review area for subtle pial angiomas as well as a predictor of bilateralism.

DISCUSSION

About SWS

Sturge-Weber syndrome is a rare congenital neurovascular disorder (estimated at 1:50,000) characterized by the triad of facial capillary malformation (port-wine stain), ocular choroidal hemangioma, and leptomeningeal (pial) angioma. SWS and nonsyndromic PWS are caused by somatic activating mutations in the *GNAQ* gene located on chromosome 19q21, affecting early fetal vascular development.¹¹ A recent study¹² suggested that the strongest predictor of SWS is based on a classification of PWS considering the vascular embryologic distribution. The best predictor of adverse outcomes is a PWS involving any part of the forehead, delineated at its inferior border by a line joining the outer canthus of the eye to the top of the ear, including the upper eyelid.

The Roach classification has been used to classify patients with SWS into 3 groups¹³: type 1, facial PWS and leptomeningeal angioma (classic); type 2, facial PWS alone; and type 3, isolated leptomeningeal angioma.

Other authors have however considered the diagnosis of SWS to apply only when there is a typical contrast-enhancing leptomeningeal angioma.¹⁴

Our SWS group had 25% of patients with bilateral pial angiomas (Fig 6); the rest were unilateral. The typically associated imaging findings within this group were glomus angioma (81%), prominent transmedullary veins (79%), atrophy (64%), accelerated myelination (36%), and cortical calcification (8%). The relatively low yield of cortical/subcortical calcification was most likely due to the lack of calcium-specific imaging.

A lesser known finding in SWS is the intraosseous signal abnormality, previously described as related to the pial angioma and

AJNR Am J Neuroradiol 39:1543–49 Aug 2018 www.ajnr.org 1547

hence an early predictor of brain involvement when other findings are absent.

The calvaria is a site for diffuse hematopoietic marrow activity with the vascular supply of marrow largely from nutrient arteries and an extensively anastomosing venous plexus. Birthmarks and vascular lesions are known to have adjacent skeletal marrow changes.¹⁵ We hypothesize that the facial PWS drains into the calvarial diploic system and, in particular, the pteriofrontoparietal and fronto-orbital pathways¹⁶ (Fig 7); this feature would then result in the intraosseous signal change.

The cases in this study were age-matched for normal signal because in the infant and young child, red marrow comprises 40% water, 40% fat, and 20% protein. There are changes in these constituents with age, with an increase in fat and decrease in water and protein in the adult.¹⁷

Both PWS-only and SWS groups were similarly matched in a nearly equal male/female distribution with similar mean ages and ranges. The comparison of nearly equally matched patient demographics between these 2 groups is a study strength, especially compared with the previous literature.¹⁰

This is a cross-sectional study in which 139 subjects had PWS and/or diagnosed SWS. Of the 139 cases, 114 had both port-wine stain and marrow edema. Of these 114 cases, 5 had PWS on the opposite side of marrow edema, while 109 had PWS and marrow edema on the same side.

On the basis of the calculation using a total of 139 patients who had PWS and/or diagnosed SWS, we detected a statistically significant association between marrow edema and PWS with a relative risk of 4.58 (95% CI, 1.67–12.7; $P < .05$). This association is present regardless of the marrow edema and PWS being on the same side or opposite each other.

We performed a subgroup analysis by excluding the 5 patients who had PWS on the opposite side of the marrow edema. We detected a statistically significant association between marrow edema and same-sided PWS. The relative risk was 4.58 (95% CI, 1.66–12.6; $P < .05$).

In other words, in patients with PWS or diagnosed SWS, marrow edema and PWS are 4.6 times more likely to be coexistent than not. This supports our hypothesis that the bone marrow change is not reflective of developing a pial angioma but corresponds to the skin change. There was no statistically significant association identified between the intraosseous bone marrow change and pial angioma (95% CI, 0.49–3.9; $P > .05$).

Most interesting, an ocular choroidal hemangioma being seen in patients without a pial angioma suggests further that it may also relate more strongly to the presence of PWS.

For this study, choroidal enhancement has been described as choroidal hemangioma. We note however that there is controversy in the published literature as to the exact nature of the ocular lesion, and some authors have described it as a choroidal capillary malformation.¹⁸ Our analysis revealed that 23% of the PWS-only and 59% of the SWS group had this finding. Our study, therefore, shows that the ocular findings can be seen with isolated PWS and in association with SWS.

Similarities with Meningioangiomas

Of the 15 cases of SWS with absent PWS, 14 had a thick pial angioma that filled the adjacent subarachnoid space and are similar to previously published case reports.¹⁹ These appearances are not typical for a SWS pial angioma but similar to some of the imaging descriptions of meningioangiomas.²⁰

About PWS

PWSs are low-flow malformations of dermal capillaries and post-capillary venules, present at birth, that do not regress with time. With age, they grow in proportion to the patient's size and become thicker and darker in adulthood.

Role of Imaging and Contrast

MR imaging should be performed with contrast T1-weighted imaging to visualize the leptomeningeal angioma and to determine its extent and laterality. Associated findings of ocular choroidal hemangioma, glomus angioma, and prominent draining veins are also better visualized on a contrast scan. Contrast-enhanced FLAIR has also been shown to improve the conspicuity of leptomeningeal angioma.²¹ If an unenhanced study in the neonate without contrast has been performed, a repeat study at 1 year of age to exclude the pial angioma should be performed.

CONCLUSIONS

Bone marrow changes are strongly associated with the presence of facial port-wine stain. No significant association was found between the presence or development of a pial angioma and bone marrow changes. On the basis of our imaging findings, we conclude that the calvarial intraosseous marrow abnormality is related to the cutaneous PWS and is not a predictor of intracranial SWS.

Disclosures: Sarah E. Aylett—UNRELATED: Board Membership: EXIST 3 Advisory Board, Comments: 2016, organized by Novartis in relation to the everolimus trial; Payment for Manuscript Preparation: Payment for writing the article with a co-author; Comments: "Tuberous Sclerosis Complex: From Child to Adult," published January 1, 2016, in *Key Opinions in Medicine* (Wiley).

REFERENCES

1. Kanada KN, Merin MR, Munden A, et al. **A prospective study of cutaneous findings in newborns in the United States: correlation with race, ethnicity, and gestational status using updated classification and nomenclature.** *J Pediatr* 2012;161:240–45 CrossRef Medline
2. Lin DD, Barker PB, Kraut MA, et al. **Early characteristics of Sturge-Weber syndrome shown by perfusion MR imaging and proton MR spectroscopic imaging.** *AJNR Am J Neuroradiol* 2003;24:1912–15 Medline
3. Mittal S, Wu Z, Neelavalli J, et al. **Susceptibility-weighted imaging: technical aspects and clinical applications, Part 2.** *AJNR Am J Neuroradiol* 2009;30:232–52 CrossRef Medline
4. Adams ME, Aylett SE, Squier W, et al. **A spectrum of unusual neuroimaging findings in patients with suspected Sturge-Weber syndrome.** *AJNR Am J Neuroradiol* 2009;30:276–81 CrossRef Medline
5. Smirniotopoulos JG. **Neuroimaging of phakomatoses: Sturge-Weber syndrome, tuberous sclerosis, von Hippel-Lindau syndrome.** *Neuroimaging Clin N Am* 2004;14:171–83, vii CrossRef Medline
6. Sharan S, Swamy B, Taranath DA, et al. **Port-wine vascular malformations and glaucoma risk in Sturge-Weber syndrome.** *J AAPOS* 2009;13:374–78 CrossRef Medline

7. Singh AD, Kaiser PK, Sears JE. **Choroidal hemangioma.** *Ophthalmol Clin North Am* 2005;18:151–61, ix CrossRef Medline
8. Arora KS, Quigley HA, Comi AM, et al. **Increased choroidal thickness in patients with Sturge-Weber syndrome.** *JAMA Ophthalmol* 2013;131:1216–19 CrossRef Medline
9. Mantelli F, Bruscolini A, La Cava M, et al. **Ocular manifestations of Sturge-Weber syndrome: pathogenesis, diagnosis, and management.** *Clin Ophthalmol* 2016;10:871–78 CrossRef Medline
10. Whitehead MT, Vezina G. **Osseous intramedullary signal alteration and enhancement in Sturge-Weber syndrome: an early diagnostic clue.** *Neuroradiology* 2015;57:395–400 CrossRef Medline
11. Shirley MD, Tang H, Gallione CJ, et al. **Sturge-Weber syndrome and port-wine stains caused by somatic mutation in GNAQ.** *N Engl J Med* 2013;368:1971–79 CrossRef Medline
12. Waelchli R, Aylett SE, Robinson K, et al. **New vascular classification of port-wine stains: improving prediction of Sturge-Weber risk.** *Br J Dermatol* 2014;171:861–67 CrossRef Medline
13. Roach ES. **Neurocutaneous syndromes.** *Pediatr Clin North Am* 1992;39:591–620 CrossRef Medline
14. Comi AM. **Presentation, diagnosis, pathophysiology, and treatment of the neurological features of Sturge-Weber syndrome.** *Neurologist* 2011;17:179–84 CrossRef Medline
15. Boyd JB, Mulliken JB, Kaban LB, et al. **Skeletal changes associated with vascular malformations.** *Plast Reconstr Surg* 1984;74:789–97 CrossRef Medline
16. Tsutsumi S, Nakamura M, Tabuchi T, et al. **Calvarial diploic venous channels: an anatomic study using high-resolution magnetic resonance imaging.** *Surg Radiol Anat* 2013;35:935–41 CrossRef Medline
17. Chan BY, Gill KG, Rebsamen SL, et al. **MR imaging of pediatric bone marrow.** *Radiographics* 2016;36:1911–30 CrossRef Medline
18. Sullivan TJ, Clarke MP, Morin JD. **The ocular manifestations of the Sturge-Weber syndrome.** *J Pediatr Ophthalmol Strabismus* 1992;29:349–56 Medline
19. Siri L, Giordano L, Accorsi P, et al. **Clinical features of Sturge-Weber syndrome without facial nevus: five novel cases.** *Eur J Paediatr Neurol* 2013;17:91–96 CrossRef Medline
20. Nascimento FA, Kiehl TR, Tai PC, et al. **Meningioangiomas: a disease with many radiological faces.** *Can J Neurol Sci* 2016;43:847–49 CrossRef Medline
21. Lee EK, Lee EJ, Kim S, et al. **Importance of contrast-enhanced fluid-attenuated inversion recovery magnetic resonance imaging in various intracranial pathologic conditions.** *Korean J Radiol* 2016;17:127–41 CrossRef Medline

Detection of the Stellate and Thoracic Sympathetic Chain Ganglia with High-Resolution 3D-CISS MR Imaging

A. Chaudhry, A. Kamali, D.A. Herzka, K.C. Wang, J.A. Carrino, and A.M. Blitz

ABSTRACT

BACKGROUND AND PURPOSE: Despite the importance of the sympathetic nervous system in homeostasis and its putative role in various disease states, little is known regarding our ability to image the sympathetic chain and sympathetic chain ganglia, perhaps owing to their small size. In this retrospective study, we sought to evaluate the normal anatomy of the sympathetic chain ganglia and assess the detectability of the sympathetic chain and sympathetic chain ganglia on high-resolution 3D-CISS images.

MATERIALS AND METHODS: This study included 29 patients who underwent 3D-CISS MR imaging of the thoracic spine for reasons unrelated to abnormalities of the sympathetic nervous system. Patients with a prior spinal operation or visible spinal pathology were excluded. The sympathetic chain ganglia were evaluated using noncontrast 3D-CISS MR imaging. Statistical analyses included *t* tests and measures of central tendency. The Cohen κ statistic was calculated to evaluate interrater reliability.

RESULTS: The stellate ganglion and thoracic chain ganglia were identified in all subjects except at the T10–T11 and T11–T12 levels. The stellate ganglion was found inferomedial to the subclavian artery and anterior and inferior to the transverse process of C7 in all subjects. Thoracic sympathetic chain ganglia were identified ventral to the costovertebral junction in all subjects from T2 to T10. There was strong interobserver agreement for the detection of the sympathetic chain ganglia with $\kappa > 0.80$. The size, shape, and location of these structures corresponded with gross anatomic and surgical observations.

CONCLUSIONS: The thoracic sympathetic chain ganglia can be identified on precontrast 3D-CISS MR imaging. This technique may aid in the initial evaluation of stellate ganglion and/or sympathetic chain ganglia size and signal change for comparison in future studies.

ABBREVIATION: SCG = sympathetic chain ganglia

The autonomic nervous system is composed of a sympathetic component, responsible for the “fight or flight” response, and a parasympathetic portion, known for “rest and digest” functions. The sympathetic component differs in structure from the remainder of the peripheral nervous system. The sympathetic chain is generally divided into 2 nerve trunks that extend the entire length of the vertebral column along its lateral aspect.^{1–3} The stellate ganglion provides sympathetic supply to the head, neck, and up-

per limbs, while the sympathetic chain ganglia (SCG) provide key innervations to the thoracic viscera, including the heart.^{1–5} The stellate ganglion receives nerve fibers from the C6, C7, and T1 nerve roots with occasional contributions from T2, T3, and T4. The thoracic sympathetic chain receives nerve fibers from nuclei located within the lateral gray horn of the T2–T8 spinal segment that leave the spinal cord in the anterior rootlets of thoracic nerves, then traverse the white communicating rami, to enter the sympathetic trunk, synapsing onto their target postganglionic neurons in the paravertebral thoracic sympathetic ganglia. The postganglionic fibers traveling to the upper limb originate from the middle cervical ganglion, the stellate ganglion, and the upper thoracic ganglia; join the thoracic nerves through the gray rami communicantes; and then enter the brachial plexus and travel along different nerves to their end targets.^{6,7}

Stellate ganglion and SCG blocks are performed for various conditions, including complex regional pain syndrome, postherpetic neuralgia, herpes zoster, causalgia, or intractable angina.¹ An SCG block can also be performed to treat patients with vaso-

Received March 19, 2017; accepted after revision April 19, 2018.

From the Departments of Neuroradiology (A.C., A.K.) and Radiology and Radiologic Sciences (A.M.B.), Johns Hopkins University School of Medicine, Baltimore, Maryland; Department of Biomedical Engineering (D.A.H.), Johns Hopkins University, Baltimore, Maryland; Department of Diagnostic Radiology and Nuclear Medicine (K.C.W.), University of Maryland, School of Medicine, Baltimore, Maryland; Imaging Service (K.C.W.), Baltimore VA Medical Center, Baltimore, Maryland; and Department of Radiology and Imaging (J.A.C.), Weill Cornell Medical College, Hospital for Special Surgery, New York, New York.

Please address correspondence to Ari M. Blitz, MD, Department of Radiology and Radiologic Sciences, Johns Hopkins University School of Medicine, 600 North Wolfe St, Phipps B-100, Baltimore, MD 21287; e-mail: ablitz1@jhmi.edu

<http://dx.doi.org/10.3174/ajnr.A5698>

spasm (eg, primary or secondary Raynaud phenomenon), phantom pain, cardiac arrhythmias (including long QT syndromes), and primary hyperhidrosis.¹⁻⁵ Patients are generally referred for SCG block due to persistence of symptoms (pain, vasospasm, hyperhidrosis, and so forth) despite medical management.^{4,8-10} An SCG block is routinely performed in the clinical setting with sonography, fluoroscopy, or CT used to provide anatomic landmark guidance. However, the SCG itself is never directly visualized before the procedure.¹⁰ Although the efficacy of interventions is well-established, a considerable proportion of patients do not see improvement and/or resolution of symptoms (eg, continued pain in up to 27.2%–33% in patients treated with SCG radiofrequency ablation for complex regional pain syndrome and recurrence of symptoms within 7 weeks in >66% of cases).¹¹ The reasons for the lack of short-term and long-term treatment benefit are not well-understood. Authors have suggested several possibilities, including incomplete SCG block secondary to anatomic variation.^{2,11-14} In other words, it is possible that in some failed cases, the SCG was not directly and/or incompletely targeted because the structure itself was not actually visualized and was in a location variant from the commonly described one.

The peripheral components of the sympathetic nervous system have not been previously well-characterized on cross-sectional imaging, to our knowledge. There are only 2 small case series that identified the sympathetic chain ganglia on T1-weighted MR imaging,^{2,12} primarily identifying the location of only the stellate ganglion.

The 3D-CISS refocused gradient-echo MR imaging sequence is a high-spatial-resolution technique performed to evaluate intracranial and spinal nerves.¹⁵⁻²⁰ 3D-CISS MR imaging generates images with contrast ideally proportional to the ratio of T2/T1 relaxation time, generating what appear to be heavily T2-weighted images.¹⁸ In our experience, 3D-CISS MR imaging before intravenous contrast administration provides visualization in vivo of the sympathetic chain ganglia within the paravertebral fat. In this retrospective observational study, we aimed to evaluate the normal anatomy of the stellate ganglion and thoracic sympathetic chain ganglia and assess the detectability of each of the thoracic sympathetic chain ganglia on noncontrast CISS images.

MATERIALS AND METHODS

Study Group

This observational study was approved by the Johns Hopkins University institutional review board, and informed consent was waived in this Health Insurance Portability and Accountability Act-compliant retrospective study. Initially, 29 subjects underwent high-resolution CISS clinical MR imaging for the evaluation of either back pain or CSF leak. Subjects with other spine pathology, including 2 spinal tumors and 3 cases of prior spinal operations, were excluded from the study. Subjects were included in the study if the entire thoracic spine, including the thoracic inlet, was imaged. Studies were evaluated for image quality, and 1 scan with images degraded by motion artifacts was excluded. On the initial review of images, the SCG was noted to enhance uniformly on postcontrast images and became indistinct from surrounding tissue. Therefore, only precontrast CISS images were used to collect data on the SCG; 6 scans with only postcontrast images were ex-

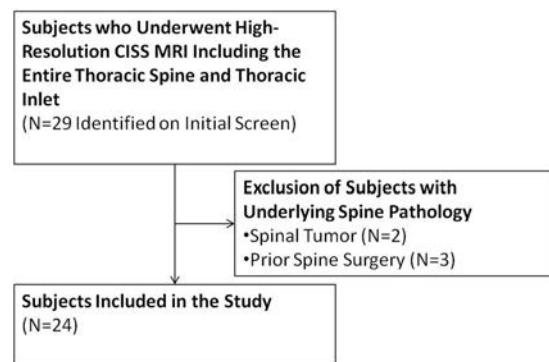


FIG 1. Flow diagram of included subjects. Of the 29 subjects screened, 24 were included in this study.

cluded from the study for this reason. Only the first valid examination was included for each subject when multiple examinations had been performed. Ultimately, 24 examinations of 24 subjects were included for evaluation (Fig 1).

Imaging Protocol

The scans were obtained at 3T field strength with 0.6-mm isotropic image resolution. Typical imaging parameters were the following: TR/TE, 5.11/2.26 ms; 0.6-mm isotropic voxels; flip angle range, 25°–45°; FOV, 380 × 80 mm (read × phase encode); 320 × 80 acquisition matrix. Twenty-four subjects (10 men, 14 women) met the inclusion criteria.

Study Design

From the cohort of 24 patients who met the inclusion criteria, 480 normal thoracic sympathetic chain ganglia and 48 stellate ganglia were evaluated. Quantitative image analysis was performed by 2 independent readers blinded to each other's interpretation. The first reader, reader A, is a fellowship-trained radiologist with >6 years of experience. The second reader, reader B, is a first-year neuroradiology fellow. The detectability of the sympathetic chain ganglia was evaluated using precontrast enhanced 3D-CISS MR imaging. The expected location of the SCG was extrapolated from anatomy and surgical literature.^{6,7} Both readers were credentialed neuroradiologists and had reviewed the anatomic literature before this study, to reach a consensus regarding the expected location of the sympathetic chain ganglia. A training or washout period was not attempted due to the limited number of subjects who met the inclusion criteria. The stellate ganglion is most commonly located anterior to the C7 vertebra transverse process, below the subclavian artery, superior to the first rib.^{6,7} The thoracic SCG are located at the costovertebral junction anterior to the head of the ribs.^{6,7} Confirmation of stellate ganglion and the SCG was made, ensuring connection of the SCG with spinal nerves and interconnection within the SCG chain on multiplanar (sagittal and coronal) reconstructions. The stellate ganglion is not entirely spheric or ellipsoid. Therefore, a calculation of volume using the largest diameter in each 3D plane would be misleading. Instead, the authors opted to quantify size consistent with reports in the anatomic literature.^{6,7,21-26} The largest 2 axial dimensions of the ganglion were recorded (in millimeters), and surface area was subsequently obtained. Both readers were aware of the study objectives,

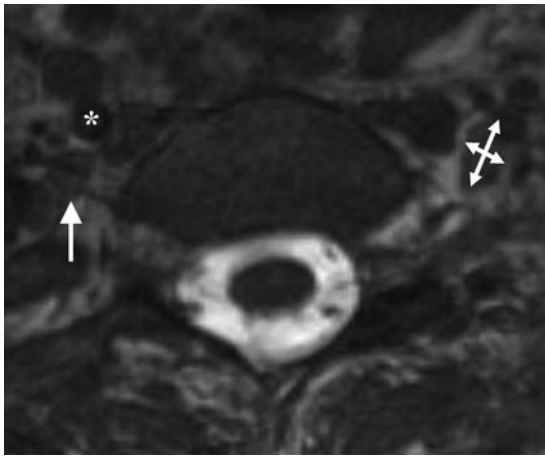


FIG 2. Axial oblique reformatted 3D-CISS MR imaging at C7 demonstrates the stellate ganglion (arrow) posterior to the subclavian artery (asterisk). The technique of measurement is demonstrated on the patient's left (double-sided arrows). The stellate ganglion was found inferior and anterior to the transverse process of C7 in all patients.

both reviewed the studies at different locations and times, and both were blinded to subjects' clinical data.

Statistical Analysis

Statistical analysis was performed using MedCalc for Windows, Version 12.5 (MedCalc Software, Mariakerke, Belgium). After controlling for subject sex, we performed measures of central tendency (mean, median) and a paired *t* test to assess differences between the mean sizes of the left and right SCG and to discern whether there was a difference in the observed size of the SCG between the right and left sympathetic chains. Additionally, a κ test was performed to evaluate interrater reliability.

RESULTS

In our cohort of 10 men and 14 women (mean age, 51.7 years), the stellate ganglion and thoracic chain ganglia were successfully identified in all subjects except at the T10–T11 and T11–T12 levels. The subjects enrolled in the study tolerated the MR imaging procedure well, and there were no acute complications during or immediately after this study.

Precontrast CISS demonstrated the stellate ganglion and SCG to be isointense relative to gray matter noted in the spinal cord. The stellate ganglion (Fig 2) and thoracic SCG (Figs 3 and 4) were present in all subjects in the expected location. The stellate ganglion (also referred to as T1 in anatomic texts⁶) was the largest of the sympathetic chain ganglia, with mean sizes of 36.62 ± 9.63 mm² on the right and 36.90 ± 8.9 mm² on the left. These size estimates were concordant with an anatomic study performed by Zhang et al.⁷ The next 2 largest SCG were at T2 (13.70 ± 5.94 mm² on the right and 13.56 ± 5.25 mm² on left) and T3 (10.23 ± 2.85 mm² on the right and 10.21 ± 2.42 mm² on the left, Fig 3). The size of the SCG decreased in a craniocaudal direction from the stellate ganglia to the thoracolumbar junction (Fig 5). The T4–to T10–thoracic chain ganglia ranged from 4.1 to 19.35 mm². Table 1 summarizes the mean size and SD of the thoracic SCG. The 2-tailed *P* value demonstrated no significant difference between the mean values of the right and left sympathetic chain

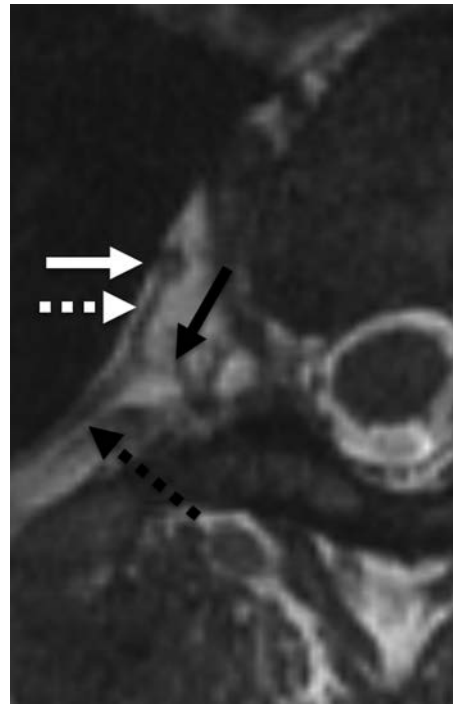


FIG 3. Axial oblique CISS MR imaging through the thoracic spine illustrates the sympathetic ganglion (white arrow), rami communicantes (dashed white arrow), and the ventral ramus (black arrow) and intercostal nerve (dashed black arrow).

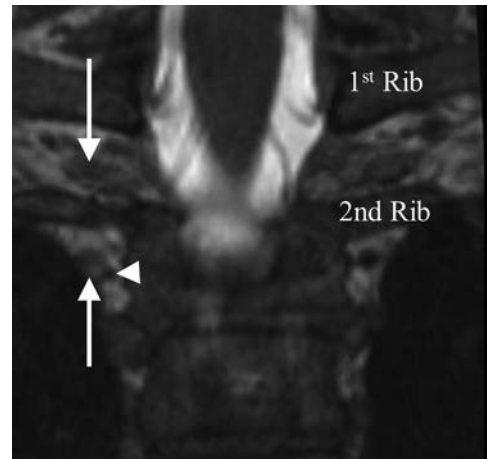


FIG 4. Coronal reformatted CISS through the upper thoracic region demonstrates the relationship of the second thoracic SCG (down arrow) with respect to the first and second ribs. The third SCG (up arrow) is seen just lateral to a venous flow void (arrowhead). The relationship of the SCG to adjacent venous structures is variable.

ganglia with a *P* = .82 (95% CI, –0.108 to 0.088). There was strong interobserver agreement for detection of the SCG with $\kappa > 0.8$.

DISCUSSION

Isotropic or near-isotropic high-resolution 3D-CISS imaging provides the capability of visualizing structures not typically seen with standard spine MR imaging techniques. Our study shows that stellate and thoracic sympathetic chain ganglia can be readily characterized on precontrast 3D-CISS MR imaging. Our results demonstrate the stellate ganglia to be the largest of the SCG with a

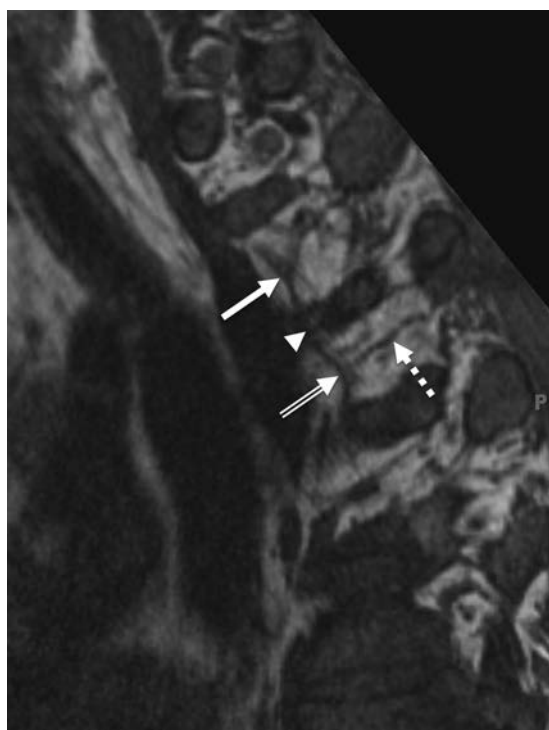


FIG 5. Sagittal oblique CISS through the paravertebral region oriented so that anterior is to the left of the image. The connection of the sympathetic chain ganglia (*solid and open arrows*) via the sympathetic chain (*arrowhead*) is visible. The rami communicantes (*dashed arrow*) are seen in continuity extending posteriorly toward the neural foramina.

Table 1: Summary of the mean size and SD of the thoracic SCG

SCG	Mean (mm ²)	SD (mm ²)
Stellate ganglion	36.76	9.27
T2	13.64	5.60
T3	10.22	2.64
T4	9.24	1.50
T5	8.80	1.07
T6	8.32	0.83
T7	8.05	0.75
T8	7.85	0.80
T9	7.60	0.84
T10	7.33	0.86

gradual decrease in size of the SCG at subsequent levels. Additionally, the stellate ganglia were noted to be the most lateral in location, with gradual medialization of the sympathetic chain trunk, with lower thoracic levels situated most medially. These findings are consistent with gross anatomic studies.^{6,7,21-26} Prior studies have reported the size of the stellate ganglia, which vary ranging from 10 to 250 mm² (Table 2). The SCG size observed in our cohort, 35 mm², falls within the range reported by Hogan and Erickson,³ Moore,²⁴ Kiray et al,²⁵ Zhang et al,⁷ and Marcer et al.²⁶

No prior systematic study identifies and characterizes the sympathetic chain ganglia using 3D-CISS technique. Two small case series previously reported by Hogan and Erickson³ and Slappendel et al¹² have attempted to identify the stellate ganglion using MR imaging (with cohorts of 10 and 8 subjects, respectively). Both studies used T1-weighted imaging to demonstrate the stellate ganglion; however, these studies did not demonstrate the remainder of the thoracic sympathetic chain ganglia.

Table 2: Size of the stellate ganglion reported by prior studies

Author (Year of Publication)	Length (mm)	Width (mm)	Height (mm)
Anatomic/surgical specimen			
Moore (1954) ²⁴	25	10	5
Kiray et al (2005) ²⁵	20.6	8.3	3.9
Zhang et al (2009) ⁷	19.3	6.3	
Marcer et al (2012) ²⁶	18.5	8.17	4.5
MRI-based measurement			
Hogan and Erickson (1992) ³	10 (in largest dimension)		

Abnormalities of the SCG have been implicated in various conditions, including primary hyperhidrosis, reflex sympathetic dystrophy, Raynaud phenomenon, and so forth. Multiple interventional^{1,2,4,5,8-14} and surgical²⁴⁻³³ studies have reported resolution of clinical symptoms following SCG ablation, nerve block, or surgical resection of the sympathetic chain. However, none of these studies document pre- or postprocedure in vivo visualization of the SCG. The results of this pilot study show that 3D-CISS MR imaging is a safe and feasible technique that can reliably characterize the SCG. The knowledge derived from our study delineates the precise location of stellate ganglion and thoracic SCG.

There are several limitations of our study. This is a retrospective study and thus has disadvantages that are inherent to the design, including selection bias. Our cohort included only those patients who underwent high-resolution imaging for back pain or CSF leak, a population that may not be representative of the normally distributed population. Sample size is another limitation of the study, which may result in under- or overestimation of the mean size of the SCG at various levels. However, because our data appear to be congruent with the anatomic literature, the degree of variance between our results and the overall population may not be large. “Experimenter effect” is another potential limitation of this study. Because both readers were aware of the aim and design of this study, the measurement and final consensus of imaging characteristics could have been biased. Thus, our findings should be confirmed with a larger normally distributed patient cohort free of the aforementioned limitations.

CONCLUSIONS

The thoracic sympathetic chain ganglia can be readily seen and well-characterized on precontrast 3D-CISS MR imaging. This technique can aid in the initial evaluation of potential stellate and/or SCG pathology and allow posttreatment follow-up.

Disclosures: Kenneth Wang—RELATED: Grant: Radiological Society of North America, Comments: Fellowship Training Grant No. FT0904.* John Carrino—UNRELATED: Board Membership: Carestream Health, Halyard Health, GE Healthcare, Comments: medical advisory boards; Consultancy: Pfizer, Globus Medical, Comments: clinical trials. Ari Blitz—UNRELATED: Consultancy: Guerbet, Comments: medical-legal consulting and medical advisory; Grants/Grants Pending: R21 NS096497, U01DC013778, and grant for hydrocephalus research from Aesculap USA (Center Valley, PA).* *Money paid to the institution.

REFERENCES

- Kim YU, Cheong Y, Kong YG, et al. **The prolongation of pulse transit time after a stellate ganglion block: an objective indicator of successful block.** *Pain Res Manag* 2015;20:305–08 CrossRef Medline
- Elias M. **Cervical sympathetic and stellate ganglion blocks.** *Pain Physician* 2000;3:294–304 Medline
- Hogan QH, Erickson SJ. **MR imaging of the stellate ganglion: nor-**

- mal appearance. *AJR Am J Roentgenol* 1992;158:655–59 CrossRef Medline
4. Wong W. **Spinal nerve blocks.** In: Williams AL, Murtagh FR, eds. *Handbook of Diagnostic and Therapeutic Spine Procedures.* St Louis: Mosby; 2002:20–40
 5. Erickson SJ, Hogan QH. **CT-guided injection of the stellate ganglion: description of technique and efficacy of sympathetic blockade.** *Radiology* 1993;188:707–09 CrossRef Medline
 6. Kommuru H, Jothi S, Bapuji P, et al. **Thoracic part of sympathetic chain and its branching pattern variations in South Indian cadavers.** *J Clin Diagn Res* 2014;8:AC09–12 CrossRef Medline
 7. Zhang B, Li Z, Yang X, et al. **Anatomic variations of the upper thoracic sympathetic chain.** *Clin Anat* 2009;22:595–600 CrossRef Medline
 8. Shibata Y, Fujiwara Y, Komatsu T. **A new approach of ultrasound-guided stellate ganglion block.** *Anesth Analg* 2007;105:550–51 CrossRef Medline
 9. Malmqvist EL, Bengtsson M, Sörensen J. **Efficacy of stellate ganglion block: a clinical study with bupivacaine.** *Reg Anesth* 1992;17:340–47 Medline
 10. Feigl GC, Rosmarin W, Stelzl A, et al. **Comparison of different injectate volumes for stellate ganglion block: an anatomic and radiologic study.** *Reg Anesth Pain Med* 2007;32:203–08 Medline
 11. Kastler A, Aubry S, Sailey N, et al. **CT-guided stellate ganglion blockade vs. radiofrequency neurolysis in the management of refractory type I complex regional pain syndrome of the upper limb.** *Eur Radiol* 2013;23:1316–22 CrossRef Medline
 12. Slappendel F, Thijssen H, Crul BJ, et al. **The stellate ganglion in magnetic resonance imaging: a quantification of anatomic variability.** *Anesthesiology* 1995;83:424–26 CrossRef Medline
 13. Prithvi RP. **Stellate ganglion block.** In: Waldman SD, Steven D, eds. *Pain Management.* 2nd ed. Philadelphia: Saunders; 2011:1103–15
 14. Price DD, Long S, Wilsey B, et al. **Analysis of peak magnitude and duration of analgesia produced by local anesthetics injected into sympathetic ganglia of complex regional pain syndrome patients.** *Clin J Pain* 1998;14:216–26 CrossRef Medline
 15. Blitz AM, Choudhri AF, Chonka ZD, et al. **Anatomic considerations, nomenclature, and advanced cross-sectional imaging techniques for visualization of the cranial nerve segments by MR imaging.** *Neuroimaging Clin N Am* 2014;24:1–15 CrossRef Medline
 16. Blitz AM, Macedo LL, Chonka ZD, et al. **High-resolution CISS MR imaging with and without contrast for evaluation of the upper cranial nerves: segmental anatomy and selected pathologic conditions of the cisternal through extraforaminal segments.** *Neuroimaging Clin N Am* 2014;24:17–34 CrossRef Medline
 17. Soldatos T, Batra K, Blitz AM, et al. **Lower cranial nerves.** *Neuroimaging Clin N Am* 2014;24:35–47 CrossRef Medline
 18. Yagi A, Sato N, Taketomi A, et al. **Normal cranial nerves in the cavernous sinuses: contrast-enhanced three dimensional constructive interference in the steady state MR imaging.** *AJNR Am J Neuroradiol* 2005;26:946–50 Medline
 19. Yousry I, Moriggl B, Schmid UD, et al. **Trigeminal ganglion and its divisions: detailed anatomic MR imaging with contrast-enhanced 3D-constructive interferences in the steady state sequences.** *AJNR Am J Neuroradiol* 2005;26:1128–35 Medline
 20. Sheth S, Branstetter BF 4th, Escott EJ. **Appearance of normal cranial nerves on steady-state free precession MR images.** *Radiographics* 2009;29:1045–55 CrossRef Medline
 21. Haam S, Kim D, Hwang J, et al. **An anatomical study of the relationship between the sympathetic trunk and intercostal veins of the third and fourth intercostal spaces during thoracoscopy.** *Clin Anat* 2010;23:702–06 CrossRef Medline
 22. Singh B, Ramsaroop L, Partab P, et al. **Anatomical variations of the second thoracic ganglion.** *Surg Radiol Anat* 2005;27:119–22 Medline
 23. Chung IH, Oh CS, Koh KS, et al. **Anatomic variations of the T2 nerve root (including nerve of Kuntz) and their implications for sympathectomy.** *J Thorac Cardiovasc Surg* 2002;123:498–501 CrossRef Medline
 24. Moore DC. **Anatomy of the cervical and upper thoracic portions of the sympathetic nervous system.** In: *Stellate Ganglion Block: Techniques-Indications-Uses.* Springfield: Thomas; 1954:10–22
 25. Kiray A, Arman C, Naderi S, et al. **Surgical anatomy of the cervical sympathetic trunk.** *Clin Anat* 2005;18:179–85 CrossRef Medline
 26. Marcer N, Bergmann M, Klie A, et al. **An anatomical investigation of the cervicothoracic ganglion.** *Clin Anat* 2012;25:444–51 CrossRef Medline
 27. Kim DH, Hong JY, Hwang JJ, et al. **Topographical considerations under video-scope guidance in the T2, T4 levels sympathectomy surgery.** *Eur J Cardiothorac Surg* 2008;33:786–89 CrossRef Medline
 28. Lin TS, Chou MC. **Treatment of palmary hyperhidrosis using needlescopic T2 sympathetic block by clipping: analysis of 102 cases.** *Int Surg* 2004;89:198–201 Medline
 29. Inbar O, Levie D, Shwartz I, et al. **Thoracic sympathectomy and cardiopulmonary responses to exercise.** *Eur J Appl Physiol* 2008;104:79–86 CrossRef Medline
 30. Fiorelli A, D'Aponte A, Canonico R, et al. **T2–T2 sympathectomy versus sympathicotomy for essential palmary hyperhidrosis: comparison of effects on cardio-respiratory function.** *Eur J Cardiothorac Surg* 2012;42:454–61 CrossRef Medline
 31. Cerfolio RJ, De Campos JR, Bryant AS, et al. **The Society of Thoracic Surgeons expert consensus for surgical treatment of hyperhidrosis.** *Ann Thor Surg* 2011;91:1642–48 CrossRef Medline
 32. Holland LC, Navaratnarakah M, Taggart DP. **Does surgical sympathectomy improve clinical outcomes in patients with refractory angina pectoris?** *Interact Cardiovasc Thorac Surg* 2016;22:488–92 CrossRef Medline
 33. Coveliers H, Hoexum F, Rauwerda JA, et al. **Endoscopic thoracic sympathectomy for upper limb ischemia: a 16-year follow-up in a single center.** *Surgeon* 2016;14:265–69 CrossRef Medline

Zonally Magnified Oblique Multislice and Non-Zonally Magnified Oblique Multislice DWI of the Cervical Spinal Cord

M. Alizadeh, M.M. Poplawski, J. Fisher, R.J.T. Gorniak, A. Dresner, F.B. Mohamed, and A.E. Flanders

ABSTRACT

BACKGROUND AND PURPOSE: The zonally magnified oblique multislice EPI (ZOOM-EPI) diffusion-weighted sequence has been visually shown to provide superior MR diffusion image quality compared with the full-FOV single-shot EPI sequence (non-ZOOM-EPI) in the adult cervical spinal cord. The purpose of this study was to examine the diffusion tensor imaging indices in the normal human cervical spinal cord between ZOOMED and non-ZOOMED DTI acquisitions and determine whether DTI values are comparable between direct and indirect age-matched groups.

MATERIALS AND METHODS: Fifty-four subjects 23–58 years of age (9 direct age-matched and 45 indirect age-matched) were scanned using a 1.5T scanner. Diffusion tensor indices including fractional anisotropy, mean diffusivity, axial diffusivity, and radial diffusivity were generated from the DTI dataset. These DTI values were calculated for both ZOOM and non-ZOOM acquisitions and compared at each intervertebral disc level. The variability of the DTI values for ZOOM and non-ZOOM sequences was measured using a coefficient of variation within direct and indirect age-matched controls.

RESULTS: The mean diffusivity, axial diffusivity, and radial diffusivity values obtained along the cervical spinal cord in the age-matched controls showed a significant decrease using the ZOOM sequence ($P = .05$, $P = .002$, and $P < .001$). Mean fractional anisotropy showed a significant increase ($P = .04$) using the ZOOM sequence. The indirect age-matched controls showed a statistically significant increase in fractional anisotropy ($P = .03$) and a decrease in mean diffusivity ($P = .002$), axial diffusivity ($P < .001$), and radial diffusivity ($P = .002$) using the ZOOM sequence. Less variability has been shown in DTI using the ZOOM sequence compared with the non-ZOOM sequence in both direct and indirect age groups. The ZOOM sequence exhibited higher SNR ($\text{SNR}_{\text{ZOOM}} = 22.84 \pm 7.59$) compared with the non-ZOOM sequence ($\text{SNR}_{\text{non-ZOOM}} = 19.7 \pm 7.05$). However, when we used a 2-tailed *t* test assuming unequal variances, the ZOOM sequence did not demonstrate a statistically significant increase.

CONCLUSIONS: ZOOM DTI acquisition methods provide superior image quality and precision over non-ZOOM techniques and are recommended over conventional full-FOV single-shot EPI DTI for clinical applications in cervical spinal cord imaging.

ABBREVIATIONS: AD = axial diffusivity; CoV = coefficient of variation; FA = fractional anisotropy; MD = mean diffusivity; RD = radial diffusivity; ZOOM = zonally magnified oblique multislice

In recent years, techniques like diffusion tensor imaging of the spinal cord have become powerful quantitative tools that track the diffusion of water molecules throughout the length of the cord.¹ DTI has been used in past studies to investigate white matter and its axonal projections in the cord. However, it is difficult to

obtain distortion-free, high-resolution diffusion-weighted images of the spinal cord using single-shot EPI.¹ Long readout times and low bandwidths in the phase-encode direction of the standard single-shot EPI sequence increase the possibility of distortion in the resultant images.¹ Coherent macroscopic or bulk motion varies during each echo acquisition; this variation can give rise to ghosting artifacts in the final images. Motion adds additional phase to the spins, which will also challenge the phase requirements between transverse magnetization and radiofrequency pulses.^{1,2} Despite these challenges, single-shot EPI offers a short acquisition time that decreases the probability of motion-related artifacts, making this technique most appealing for clinical imaging of the spinal cord.³

Recently, reduced FOV imaging sequences have generated

Received February 18, 2018; accepted after revision April 26.

From the Department of Radiology (M.A., M.M.P., J.F., R.J.T.G., A.D., F.B.M., A.E.F.), Jefferson Integrated Magnetic Resonance Imaging Center, and Department of Neurosurgery (M.A.), Thomas Jefferson University, Philadelphia, Pennsylvania.

Please address correspondence to Adam E. Flanders, MD, 909 Walnut St, Jefferson Integrated Magnetic Resonance Imaging Center, Department of Radiology, Thomas Jefferson University, Philadelphia, PA 19107; e-mail: Adam.Flanders@jefferson.edu

<http://dx.doi.org/10.3174/ajnr.A5703>

valuable spinal cord imaging data. Diffusion-weighted imaging sequences like the zonally magnified oblique multislice (ZOOM) sequence have used this reduced FOV to acquire diffusion metrics in the spinal cord.^{3,4} The impetus was to create a ZOOM acquisition that could replace the standard full-FOV method for clinical use. This is predicated on the goal of keeping acquisition times as close to or less than those of conventional full-field DTI techniques, with superior results. Several reduced FOV diffusion-weighted sequences, including the ZOOM sequence and the inner FOV 2D radiofrequency excitation and overvolume suppression techniques, have been applied to obtain DTI of the spinal cord. It has been shown that in nearly all these instances, the reduced FOV EPI DTI method provides an increase in the signal-to-noise ratio compared with conventional full-FOV EPI techniques (non-ZOOM).^{3,5,6} Using these techniques, several researchers have been able to acquire more precise diffusion metrics using ZOOM DTI sequences. In 1 study, ZOOM DTI increased diagnostic confidence in 33% of clinical examinations in a sample size of 180 clinical scans.⁷ This cohort included a range of various pathologies such as demyelination, acute infarction, infection, and abnormal tissue growth.⁷ Other groups have used these techniques to investigate the healthy population, ranging from mapping of the optic nerve,⁸ assessing the pediatric spinal cord, and comparing of intrinsic artifacts among imaging techniques.⁹ In each use, the ZOOM DTI sequences have been shown useful for clinical application.

The purpose of this study was to perform a quantitative comparison of ZOOM and non-ZOOM DTI techniques in the adult cervical spinal cord. We hypothesized that due to the inherent capability of ZOOM to reduce susceptibility artifacts coupled with a higher SNR, the DTI metrics generated from ZOOM methods would be more precise. A direct age match compares data from the same subject scanned using both imaging sequences, while an indirect age match is a comparison of 2 different subjects whose ages match. In theory, a direct age match will reduce variation that may arise from natural anatomic and diffusive differences among participating subjects compared with indirect age-matched groups.

MATERIALS AND METHODS

Subject Recruitment

In this prospective monocenter study, 54 patients between 23 and 58 years of age (mean age, 38.09 ± 8.5 years; 26 men and 28 women) were recruited. Each of the patients was deemed healthy; with no clinical or imaging criteria of spinal cord pathology. Examinations were performed as part of clinical care for screening in trauma to exclude soft-tissue injuries. Nine of the recruited subjects underwent scans that implemented both acquisition techniques that were used for a direct age-matched comparison. In addition, an indirect age-matched group was created using a separate group of 22 subjects who were scanned using the non-ZOOM technique and who were later used to compare with the 23 subjects scanned using the ZOOM technique. The diffusion data of this study were compared using the 2 different methods. The study was approved by the institutional review board of Thomas Jefferson University Hospital. Informed consent was obtained from all patients.

Image Acquisition

All MR imaging scans were performed on the same magnet using an Achieva 1.5T scanner (Philips Healthcare, Best, Netherlands) with a 16-channel neurovascular array coil, including 8 head elements and 4 neck and 4 chest elements. Axial DTI covering the cervical spinal cord was acquired using either the ZOOM or non-ZOOM techniques in the same anatomic location prescribed for the T2-weighted images to cover the entire cervical spinal cord (C1 to C7–T1 levels). The non-ZOOM DTI scan parameters were the following: TR = 6176 ms, TE = 82 ms, number of signal averages = 8, FOV = 220×130 mm, matrix = 144×84 , number of slices = 36, slice thickness = 4 mm, voxel size = $1.53 \times 1.53 \times 4.0$ mm. The ZOOM scan parameters were the following: TR = 4950 ms, TE = 95 ms, number of signal averages = 4, FOV = 110×110 mm, matrix = 96×96 , number of slices = 32, slice thickness = 4 mm, voxel size = $1.15 \times 1.15 \times 4.0$ mm. Both sequences used 6 directions at $b=800$ s/mm². The acquisition time of each technique was kept under 5 minutes. The imaging acquisition time was deliberately minimized to make it as clinically practical as possible; therefore, neither gating nor anesthesia was used during scanning.

In both techniques, manual shim and fat saturation volume adjustments were also performed before data acquisition to confine the adjustment volume to the anatomy of interest as much as possible to limit residual distortions and chemical shift artifacts.

Image Processing

Initially, DTI volumes were corrected for motion-induced artifacts by aligning diffusion directional images to the reference image (B_0) based on the affine transformation technique. Next, DTI scalars, including fractional anisotropy (FA), mean diffusivity (MD), axial diffusivity (AD), and radial diffusivity (RD), were computed using a linear estimation of the tensor in DTI Fiber-Trak software (Philips Healthcare; <https://www.usa.philips.com/healthcare/product/HCNMRB617/dti-fibertrak-mr-software>). Global thresholding and smoothing techniques were applied to remove background, decrease the computational time, and minimize the effects of noise in the tensor calculation.

Manual ROI Definition

To obtain DTI metrics, we manually drew ROIs at each cervical intervertebral disc level on the generated FA map in the axial plane. These intervertebral disc levels included C1–C2, C2–C3, C3–C4, C4–C5, C5–C6, C6–C7, C7–T1. Each ROI was drawn within 1–2 voxels of the cord boundary to prevent partial volume effects from the nearby cord/CSF junction.³ Figure 1 shows the mean size of the ROIs at each intervertebral disc level in all subjects.

Statistics

On the basis of the definition of whole-cord ROIs, we performed statistical analysis between the non-ZOOM and ZOOM groups. A comprehensive data table was created containing information about DTI measures (Tables 1 and 2). Means and SDs of each measure for every subject along the cervical spinal cord were calculated. These measures then were compared between non-ZOOM and ZOOM subjects for both indirect and direct groups

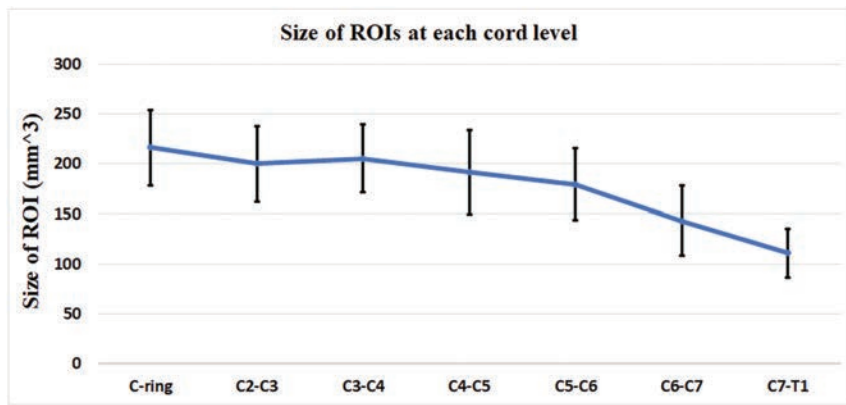


FIG 1. The size of ROIs manually drawn at each intervertebral disc level. The error bars represent the SDs.

Table 1: Comparison of non-ZOOM and ZOOM of averaged FA, MD, AD, and RD values along the cervical spinal cord levels and across direct age-matched subjects^a

	Non-ZOOM	ZOOM	Prob< t
FA	0.65 ± 0.042	0.74 ± 0.038	P = .04
MD	0.72 ± 0.038	0.50 ± 0.032	P = .005
AD	1.36 ± 0.086	0.99 ± 0.021	P = .002
RD	0.42 ± 0.041	0.24 ± 0.037	P < .001

Note:—Prob<|t| indicates the P value for 2-tailed test.

^a Data are means and SDs.

Table 2: Comparison of non-ZOOM and ZOOM of averaged FA, MD, AD, and RD values along the cervical spinal cord levels and across indirect age-matched subjects^a

	Non-ZOOM	ZOOM	Prob< t
FA	0.65 ± 0.067	0.76 ± 0.04	P = .03
MD	0.7 ± 0.038	0.49 ± 0.047	P = .002
AD	1.3 ± 0.06	1.02 ± 0.05	P < .001
RD	0.4 ± 0.06	0.23 ± 0.05	P = .002

^a Data are means and SDs.

on the basis of the standard least squares linear regression model and restricted maximum likelihood method (JMP Pro 13.0 software; SAS Institute, Cary, North Carolina). This model was constructed looking at group differences by assuming ROI level and group (non-ZOOM/ZOOM) composition as the fixed effects and subject as the random effect. A P value of .05 was used throughout to determine statistical significance.

Image-Quality Assessment

Image-quality assessments were performed on raw datasets for each sequence using the SNR. The signal intensities within manually drawn ROIs for each directional diffusion image were calculated and averaged ($\mu_{\text{DTI_cord}}$). Next, the SNR was computed for each sequence as follows: $\text{SNR}_{\text{DTI}} = \mu_{\text{DTI_cord}} / \sigma_{\text{air}}$.¹⁰ The SD of air was measured from a large area outside the cord and surrounding tissues.

RESULTS

The mean AD values of the whole cord along the entirety of the cervical spinal cord in the age-matched controls for the proposed sequences were the following: non-ZOOM = $1.36 \pm 0.086 \times 10^{-3} \text{mm}^2/\text{s}$ and ZOOM = $0.99 \pm 0.021 \times 10^{-3} \text{mm}^2/\text{s}$, which show a significant decrease using the ZOOM sequence ($P = .002$). The mean RD values were the following: non-ZOOM = $0.42 \pm$

$0.041 \times 10^{-3} \text{mm}^2/\text{s}$ and ZOOM = $0.24 \pm 0.037 \times 10^{-3} \text{mm}^2/\text{s}$. A statistically significant decrease was shown in RD ($P < .001$). The mean FA (non-ZOOM = 0.65 ± 0.042 and ZOOM = 0.74 ± 0.038) and MD (non-ZOOM = $0.72 \pm 0.038 \times 10^{-3} \text{mm}^2/\text{s}$ and ZOOM = $0.50 \pm 0.032 \times 10^{-3} \text{mm}^2/\text{s}$) showed a significant increase ($P = .04$) and decrease ($P = .05$), respectively, using the ZOOM sequence. Also, these parameters (ie, FA, MD, AD, and RD) were calculated and compared between proposed sequences in the indirect age-matched controls. Statistically significant increases in FA ($P = .03$) and decreases in MD ($P = .002$), AD ($P < .001$), and RD ($P = .002$) were shown (Tables 1 and 2).

Figures 2 and 3 represent the DTI indices as a function of intervertebral disc levels. In all cases, there is a clear difference between data acquired from the ZOOM and the non-ZOOM sequences. In both direct and indirect age-matched groups, the ZOOM sequence uniformly demonstrated an increase in mean FA values and a decrease in mean MD, AD, and RD values at each cervical intervertebral cord level compared with the non-ZOOM method.

Using the spinal cord mask, we calculated means and SDs of SNR_{ZOOM} and $\text{SNR}_{\text{non-ZOOM}}$. The ZOOM sequence exhibited higher SNR ($\text{SNR}_{\text{ZOOM}} = 22.84 \pm 7.59$) compared with the non-ZOOM sequence ($\text{SNR}_{\text{non-ZOOM}} = 19.7 \pm 7.05$). However, by means of a 2-tailed t test assuming unequal variances, the ZOOM sequence did not demonstrate a statistically significant increase. As seen in Figs 4 and 5, ZOOM DTI shows better definition of WM/GM, CSF, and CSF/cord edge.

Variability of ZOOM EPI versus Full-FOV Single-Shot EPI

The variability of the DTI values for ZOOM and non-ZOOM sequences was measured using the coefficient of variation (CoV) within direct and indirect age-matched controls. The CoV of the DTI values within direct age-matched subjects showed: FA ($\text{CoV}_{\text{ZOOM}} = 0.06 \pm 0.02$, $\text{CoV}_{\text{non-ZOOM}} = 0.1 \pm 0.01$), MD ($\text{CoV}_{\text{ZOOM}} = 0.14 \pm 0.05$, $\text{CoV}_{\text{non-ZOOM}} = 0.2 \pm 0.05$), AD ($\text{CoV}_{\text{ZOOM}} = 0.14 \pm 0.04$, $\text{CoV}_{\text{non-ZOOM}} = 0.24 \pm 0.13$), and RD ($\text{CoV}_{\text{ZOOM}} = 0.25 \pm 0.06$, $\text{CoV}_{\text{non-ZOOM}} = 0.31 \pm 0.09$). Less variability was shown in DTI using the ZOOM sequence compared with the non-ZOOM sequence. Similar results were shown in the indirect age group as follows: FA ($\text{CoV}_{\text{ZOOM}} = 0.06 \pm 0.01$, $\text{CoV}_{\text{non-ZOOM}} = 0.09 \pm 0.02$), MD ($\text{CoV}_{\text{ZOOM}} = 0.18 \pm 0.04$, $\text{CoV}_{\text{non-ZOOM}} = 0.19 \pm 0.04$), AD ($\text{CoV}_{\text{ZOOM}} = 0.16 \pm 0.03$, $\text{CoV}_{\text{non-ZOOM}} = 0.22 \pm 0.02$) and RD ($\text{CoV}_{\text{ZOOM}} = 0.28 \pm 0.05$, $\text{CoV}_{\text{non-ZOOM}} = 0.23 \pm 0.03$).

DISCUSSION

This report demonstrates that a ZOOM-EPI DTI sequence acquires more precise high-resolution cervical spinal cord diffusion images compared with the more common non-ZOOM DTI in the healthy adult cervical spinal cord. In the clinical setting, non-ZOOM is commonly used to generate DTI due to its rapid acqui-

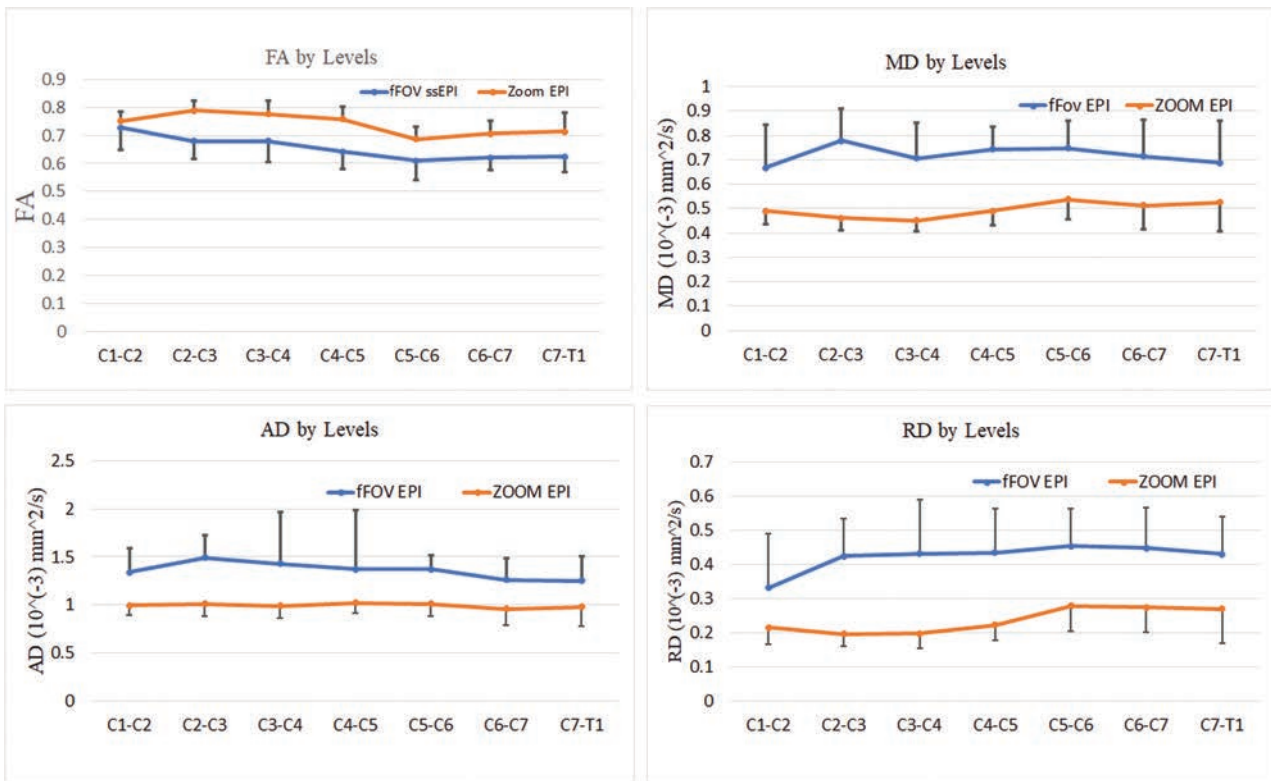


FIG 2. Averaged DTI parameters of ZOOM and non-ZOOM (full-FOV [fFOV] single-shot-EPI [ss-EPI]) sequences for the direct age-matched group as a function of intervertebral disc levels across all subjects. The error bars represent the SDs.

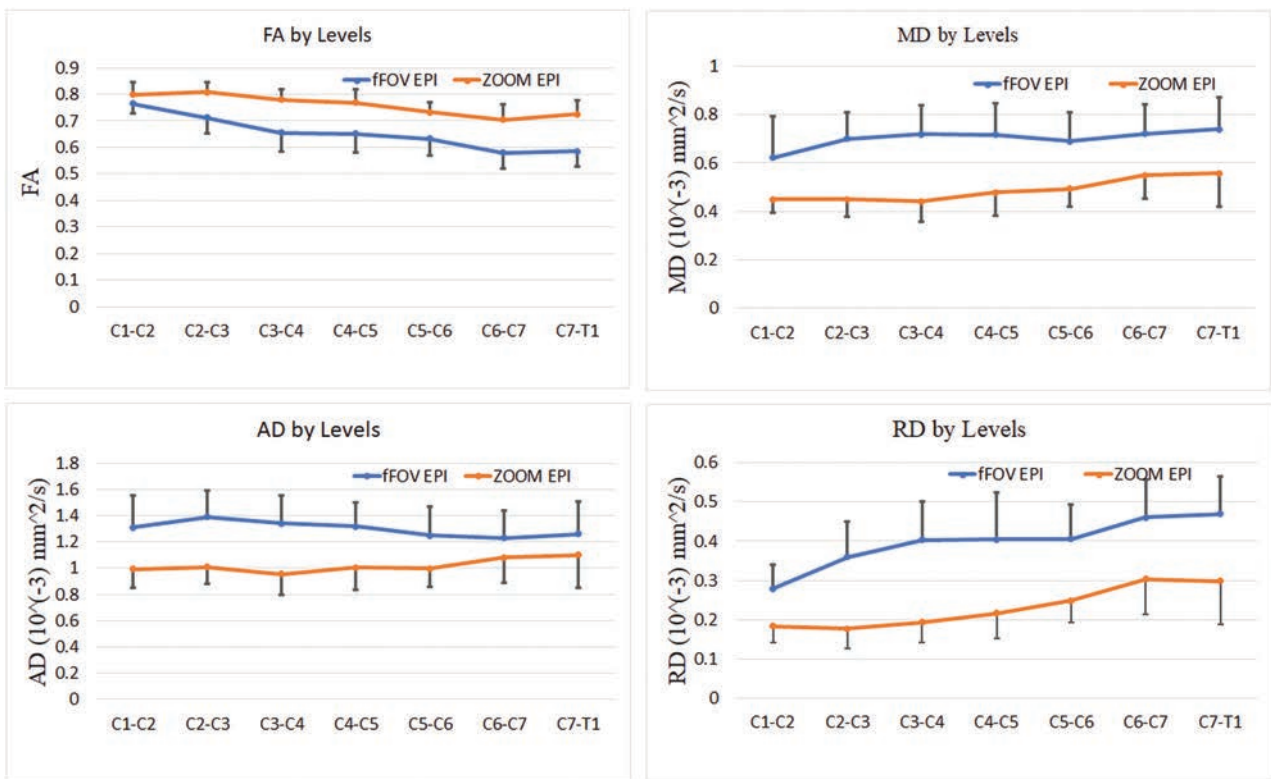


FIG 3. Averaged DTI indices of ZOOM EPI and non-ZOOM (full-FOV [fFOV] single-shot-EPI) sequences for the indirect age-matched group as a function of intervertebral disc levels across all subjects. The error bars represent the SDs.

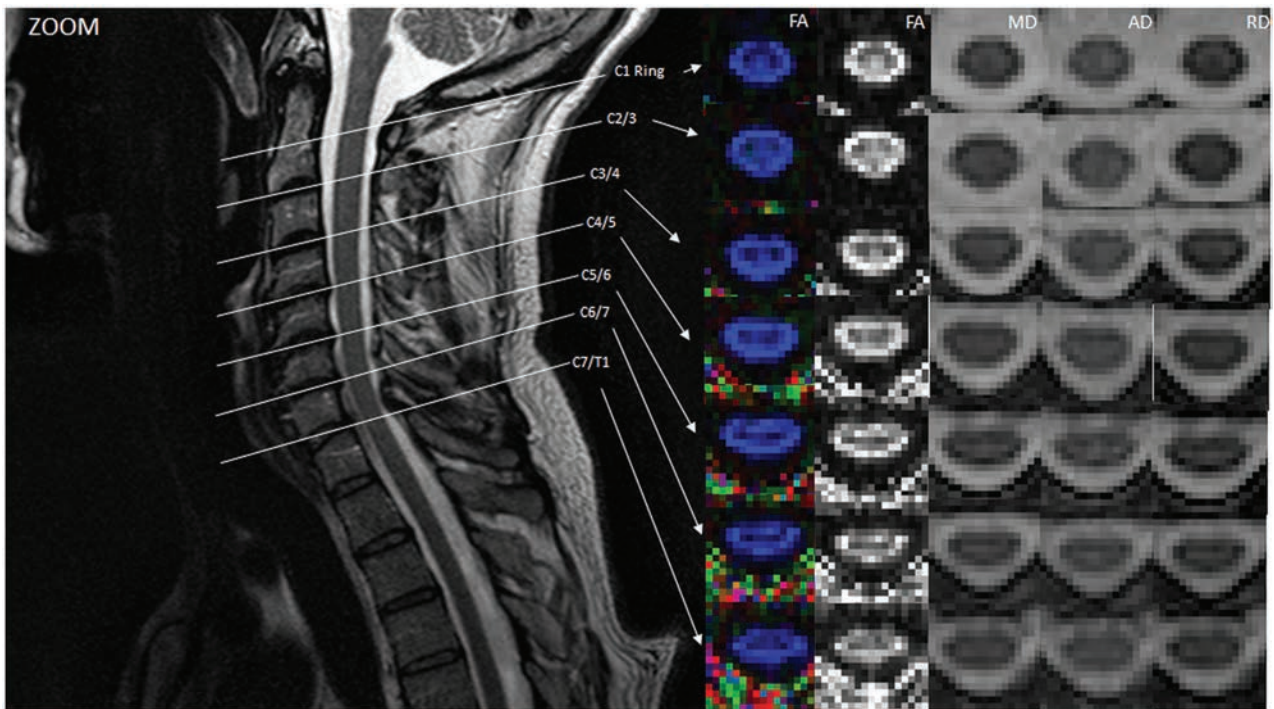


FIG 4. Illustration of DTI indices at different spinal cord levels localized by a T2-weighted image in ZOOM. Midsagittal T2-weighted image shows the location of the 7 axial diffusion tensor images that cover the entire length of the cervical spinal cord. Color and gray-scale FA maps are in the first and second columns. MD, AD, and RD maps at each location are also shown. Note that spatial resolution is improved and distortion is lower compared with the non-ZOOM acquisition (Fig 5). ssEPI indicates single-shot EPI.

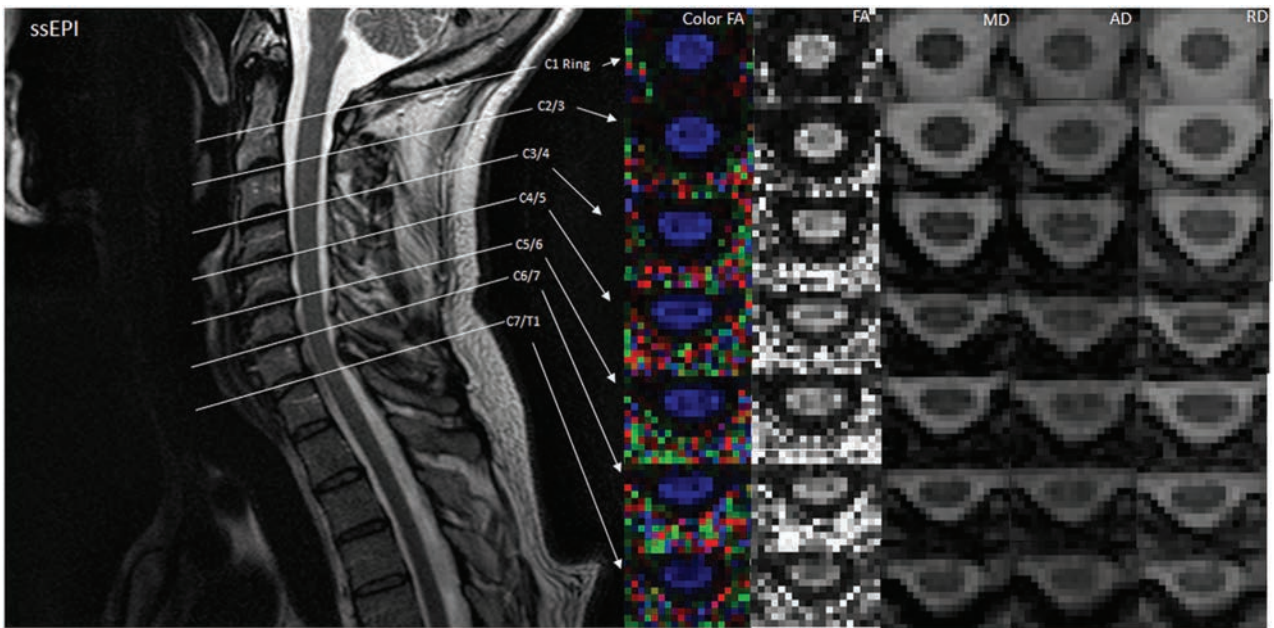


FIG 5. Illustration of DTI indices at different spinal cord levels localized by a T2-weighted image in non-ZOOM. Midsagittal T2-weighted image shows the location of the 7 axial diffusion tensor images that cover the entire length of the cervical spinal cord. Color and gray-scale FA maps are in the first and second columns. MD, AD, and RD maps at each location are also shown.

sition time coupled with a high SNR. These appealing variables result in a quick scan that is relatively insensitive to motion artifacts. However, due to the low pixel bandwidth of EPI along the phase-encoding direction, images are vulnerable to susceptibility artifacts such as chemical shift and geometric distortions.¹ Additionally, EPI generates poor in-plane spatial resolution.² These

disadvantages become especially apparent in smaller anatomic structures like the spinal cord. One way to reduce the probability of these susceptibility artifacts is to limit the FOV along the phase-encoding direction, the method that ZOOM-EPI implements.^{5,8}

In the direct age-matched group comparison, the mean FA

values were significantly higher using reduced-FOV ZOOM at each cervical level. MD, AD, and RD values were significantly lower at all cervical cord levels compared with the non-ZOOM method. The disparity of these DTI indices generated from these 2 imaging techniques is predominantly a product of the ability of ZOOM to accurately segment white matter from gray matter with artifact reduction. The higher SNR of ZOOM coupled with the manual ROI definition is the significant strengthening factor for the segmentation algorithms in the future.

One limitation of this study was the inability to compare all subjects using a direct age-matched comparison. This would have increased the sample size, allowing greater power to detect differences between the experimental groups and reduce intersubject variability. Although this was not the case, each analysis showed clear differences and patterns, supporting the conclusion that ZOOM offers superior results for DTI acquisitions in the cervical cord.

A major focal point for this study was to develop a protocol appropriate for clinical use. For clinical scans, one must minimize the scan time while maintaining an acceptable image quality. Thus, the number of gradient directions was kept low, resulting in an acquisition time of <5 minutes. For future examination of this sequence, additional gradient directions may be considered to further increase image quality with a slight increase in scan time. Past studies have used 15 gradient directions for 7 minutes and 30 seconds¹¹ and 20 gradient directions for 8:49 minutes.⁹ Despite the slight increase in scan time, these additional gradient directions have improved DTI metric estimations. Nonetheless, the ZOOM sequence for this study showed clear advantages over conventional single-shot EPI. This limitation could be overcome by imaging the spinal cord using parallel or multiband DTI techniques, which will allow faster imaging.

Several published spinal cord ZOOM studies have evaluated this technique in the thoracic spinal cord using a standard clinical 1.5T scanner. Future exploration of this ZOOM imaging technique will also focus on the general application in the thoracic spinal cord, the intrinsic capability for segmentation and analysis of white matter, and the generation of white matter fiber tracts using tractography. In this evaluation, the ROIs of the spinal cord were manually defined to encompass both gray and white matter in a cross-section of the entire cervical spinal cord. White matter is inherently more anisotropic due to the longitudinal organization of axonal tracts and myelin sheath architecture.¹² The natively higher resolution and improved SNR capability of ZOOM offer the best means to make this assessment. There are added benefits for ZOOM methods in improved tractography modeling.

The ZOOM technique as implemented on a Philips scanner is based on the technique known as inner volume imaging. Inner volume imaging limits the FOV to acquire the target structure while excluding any extraneous tissues. Like full-FOV, single-shot EPI ZOOM excites a volume using a 90° radiofrequency pulse followed by a 180° refocusing pulse. On the contrary, ZOOM uniquely applies this 180° refocusing pulse obliquely, effectively acquiring a reduced FOV volume of the pertinent tissue.

In general, previous studies have shown that DTI indices obtained using high-field scanners (3T) are statistically significantly

different from those generated by 1.5T scanners.^{13,14} These quantitative differences are largely a product of the increase in SNR that one can achieve on a 3T scanner. In prior studies investigating the effect of field strength on diffusion parameters, there was good agreement, showing a significant increase in FA and a significant decrease in MD. Our results of an increase in FA and a decrease in MD, AD, and RD are supported by other literature as well.^{6,15} However, our mean MD values were slightly reduced^{6,16,17} and may be due to the slight differences in scanner parameters.

CONCLUSIONS

The cervical spinal cord data obtained with the ZOOM imaging sequence provide more precise diffusion metrics, FA, MD, AD, and RD, with less variability compared with standard full-FOV single-shot EPI. These results suggest that ZOOM DTI is the preferred method for cervical spinal imaging.

REFERENCES

1. Zaharchuk G, Saritas EU, Andre JB, et al. **Reduced field-of-view diffusion imaging of the human spinal cord: comparison with conventional single-shot echo-planar imaging.** *AJNR Am J Neuroradiol* 2011;32:813–20 CrossRef Medline
2. Le Bihan D, Poupon C, Amadon A, et al. **Artifacts and pitfalls in diffusion MRI.** *J Magn Reson Imaging* 2006;24:478–88 CrossRef Medline
3. Saksena S, Middleton DM, Krisa L, et al. **Diffusion tensor imaging of the normal cervical and thoracic pediatric spinal cord.** *AJNR Am J Neuroradiol* 2016;37:2150–57 CrossRef Medline
4. Banerjee S, Nishimura DG, Shankaranarayanan A, et al. **Reduced field-of-view DWI with robust fat suppression and unrestricted slice coverage using tilted 2D RF excitation.** *Magn Reson Med* 2016;76:1668–76 CrossRef Medline
5. Thierfelder KM, Scherr MK, Notohamiprodjo M, et al. **Diffusion-weighted MRI of the prostate: advantages of zoomed EPI with parallel-transmit-accelerated 2D-selective excitation imaging.** *Eur Radiol* 2014;24:3233–41 CrossRef Medline
6. Samson RS, Lévy S, Schneider T, et al. **ZOOM or Non-ZOOM? Assessing spinal cord diffusion tensor imaging protocols for multicentre studies.** *PLoS One* 2016;11:e0155557 CrossRef Medline
7. Andre JB, Zaharchuk G, Saritas E, et al. **Clinical evaluation of reduced field-of-view diffusion-weighted imaging of the cervical and thoracic spine and spinal cord.** *AJNR Am J Neuroradiol* 2012;33:1860–66 CrossRef Medline
8. Wheeler-Kingshott CA, Hickman SJ, Parker GJ, et al. **Investigating cervical spinal cord structure using axial diffusion tensor imaging.** *Neuroimage* 2002;16:93–102 CrossRef Medline
9. Hodel J, Besson P, Outteryck O, et al. **Pulse-triggered DTI sequence with reduced FOV and coronal acquisition at 3T for the assessment of the cervical spinal cord in patients with myelitis.** *AJNR Am J Neuroradiol* 2013;34:676–82 CrossRef Medline
10. Polders DL, Leemans A, Hendrikse J, et al. **Signal to noise ratio and uncertainty in diffusion tensor imaging at 1.5, 3.0, and 7.0 Tesla.** *J Magn Reson Imaging* 2011;33:1456–63 CrossRef Medline
11. Bosma RL, Stroman PW. **Characterization of DTI indices in the cervical, thoracic, and lumbar spinal cord in healthy humans.** *Radiol Res Pract* 2012;2012:143705 CrossRef Medline
12. Wheeler-Kingshott CA, Parker GJ, Symms MR, et al. **ADC mapping of the human optic nerve: increased resolution, coverage, and reliability with CSF-suppressed ZOOM-EPI.** *Magn Reson Med* 2002;47:24–31 CrossRef Medline
13. Huisman TA, Loenneker T, Barta G, et al. **Quantitative diffusion tensor MR imaging of the brain: field strength related variance of**

- apparent diffusion coefficient (ADC) and fractional anisotropy (FA) scalars.** *Eur Radiol* 2006;16:1651–58 CrossRef Medline
14. Rossi C, Boss A, Lindig TM. **Diffusion tensor imaging of the spinal cord at 1.5 and 3.0 Tesla.** *Rofo* 2007;179:219–24 CrossRef Medline
 15. Yokohama T, Iwasaki M, Oura D, et al. **The reliability of reduced field-of-view DTI for highly accurate quantitative assessment of cervical spinal cord tracts.** *Magn Reson Med Sci* 2018 Mar 23. [Epub ahead of print] CrossRef Medline
 16. Dowell NG, Jenkins TM, Ciccarelli O, et al. **Contiguous-slice zonally oblique multislice (CO-ZOOM) diffusion tensor imaging: examples of in vivo spinal cord and optic nerve applications.** *J Magn Reson Imaging* 2009;29:454–60 CrossRef Medline
 17. Poplawski MM, Gorniak RJ, Dresner MA, et al. **Improved reliability of diffusion tensor imaging utilizing reduced field-of-view ZOOM-EPI in normal human cervical spinal cord.** In: *Proceedings of the Annual Meeting of the Radiological Society of North America, Chicago, Illinois. November 30–December 5, 2014*

C1 Posterior Arch Flare Point: A Useful Landmark for Fluoroscopically Guided C1–2 Puncture

M.E. Peckham, L.M. Shah, A.C. Tsai, E.P. Quigley III, J. Cramer, and T.A. Hutchins

ABSTRACT

BACKGROUND AND PURPOSE: The C1–2 intrathecal puncture is routinely performed when lumbar puncture is not feasible. Usage has steadily decreased in part because of the perceived high risk of injury to the cervical cord. Up to this point, vague fluoroscopic guidelines have been used, creating uncertainty about the actual needle location relative to the spinal cord. We present a novel osseous landmark to aid in C1–2 intrathecal puncture, corresponding to the posterior spinal cord margin on lateral fluoroscopic views. This landmark, which we have termed the “flare point,” represents the triangular “flaring” of the posterior C1 arch at its junction with the anterior arch.

MATERIALS AND METHODS: Cervical spine CT myelograms were reviewed. High-resolution axial images were reformatted into the sagittal plane, and maximum-intensity-projection images were created to simulate a lateral fluoroscopic view. Tangential lines were drawn along the superior cortices of the anterior and posterior C1 arches, with the point of intersection used to approximate the flare point. Chart review was performed for all C1–2 punctures using the flare point technique in the past 3 years.

RESULTS: Forty-two cervical myelograms were reviewed. The average flare point was 0.2 ± 0.5 mm posterior to the dorsal spinal cord margin. In 37/42 subjects, the flare point was localized posterior to the spinal cord. Targeting by means of the flare point was used in 16 C1–2 punctures without complications.

CONCLUSIONS: The C1 posterior arch flare point accurately approximates the dorsal spinal cord margin on myelography. Targeting between the flare point and the spinolaminar line, at the mid-C1–2 interspace, allows safe and optimal needle positioning.

ABBREVIATIONS: FP = flare point; PC-PD = posterior cord to the posterior dura; PC-SL = posterior cord to the spinolaminar line; SC = spinal cord; SL = spinolaminar line

The C1–2 intrathecal puncture technique is performed when routine lumbar puncture is contraindicated or not feasible for any of the following reasons: severe spinal stenosis, arachnoiditis, infection overlying the skin, extensive posterior bony fusion, extensive neoplastic involvement, or tethered cord/spinal dysraphism.¹ This technique was first described as an approach for cervical myelography in 1968, offering opacification above the level of a complete spinal block,^{2,3} and it first appeared in the neuroradiology literature in 1972.^{2,4} In recent years, this procedure has declined in use by many neuroradiologists, in part related to the perceived high risk of injury due to the proximity of

the needle to the spinal cord (SC).¹ There have been multiple reported cases of cervical cord puncture and injection of contrast into the SC, and a few cases of subarachnoid and subdural hemorrhage.^{5–12} These concerns, compounded by the frequency of myelography itself decreasing because of the superior contrast and spatial resolution of MR imaging, have led to this procedure being used sparingly. In fact, almost half of neuroradiology fellowship program directors responding to a 2009 survey reported that the C1–2 puncture technique had been performed at their institutions ≤ 5 times in the prior year.⁵ Although other novel techniques for collection of CSF, including atlanto-occipital and transforaminal lumbar puncture approaches, have been reported, they are not currently in widespread use.^{13–16}

The cervical puncture can be safely performed under image guidance using either fluoroscopy or CT/CT fluoroscopy. With the conventional technique, a 22- or 25-ga spinal needle is advanced into the posterior third of the spinal canal at the level of the C1–2 interspace from a lateral approach, with the patient in a prone, supine, or decubitus position.¹ The target is the posterior subarachnoid space, which has been found, on a prior myelo-

Received March 13, 2018; accepted after revision May 4.

From the Departments of Radiology and Imaging Sciences (M.E.P., L.M.S., A.T., E.P.Q., T.A.H.), University of Utah, Salt Lake City, Utah; and Department of Radiology (J.C.), University of Nebraska Medical Center, Omaha, Nebraska.

Please address correspondence to Miriam E. Peckham, MD, Departments of Radiology and Imaging Sciences, University of Utah Health Sciences Center, 30 North, 1900 East, #1A071, Salt Lake City, UT 84132-2140; e-mail: Miriam.Peckham@hsc.utah.edu; @Miriam_Peckham

<http://dx.doi.org/10.3174/ajnr.A5706>

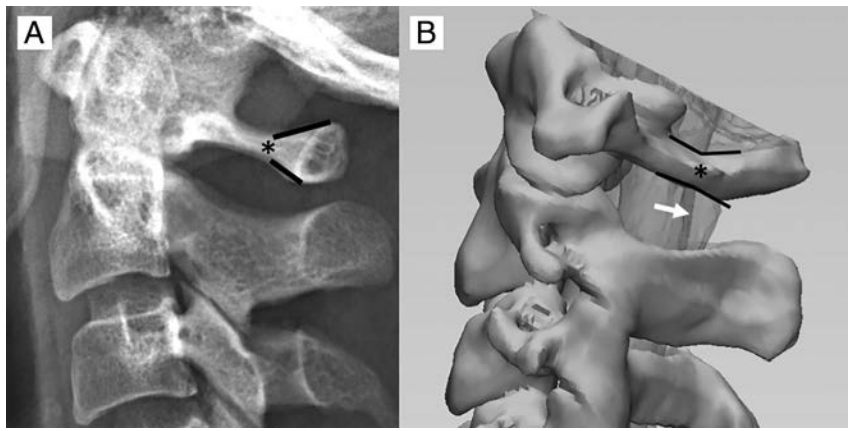


FIG 1. A, The C1 arch has a unique osseous morphology demonstrating triangular flaring of the posterior arch (black lines). We have termed the origin of this posterior osseous flaring the “flare point” (asterisk). B, 3D image derived from a CT myelogram demonstrates the relationship of the C1 flare point (asterisk) and the dorsal border of the cervical cord, with the flare point location closely approximating the posterior border of the cord (white arrow) on the lateral view.

graphic fluoroscopy study of 100 patients, to measure an average of 4.3 mm from the posterior dura to the dorsal aspect of the SC.¹⁷ The SC itself has been reported to measure between 9 and 12 mm in the anteroposterior dimension (average, 10.3 mm), and the anterior subarachnoid space measures less than the posterior subarachnoid space from the dural margin (2.6 mm on average).¹⁷

Another consideration with the conventional C1–2 puncture technique is dural tenting, which was noted on cadaveric studies with the passage of the spinal needle into the posterior subarachnoid space.³ The amount of dural tenting measured between 5 and 10 mm, and sometimes more, before the dura was penetrated.³ Dural tenting was present on all studied routes of approach (anterior, midplane, and posterior); but most interesting, when the needle was advanced via the posterior approach to the posterior one-third of the spinal canal, the SC was rotated by the tented dura but was not punctured by the needle.³ Based on these anatomic studies, penetration of the posterior one-third of the canal from a lateral approach, approximately 5 mm anterior to the spinolaminar line (SL), has been considered the standard technique.¹⁸

Although the posterior one-third of the spinal canal has been considered the safest approach, exact osseous landmarks correlating with the SC location have not been described in the literature, leading to some ambiguity in fluoroscopic targeting. We propose a novel osseous landmark on lateral views corresponding to the posterior SC margin, which we have termed the “flare point.” This osseous landmark is the triangular “flaring” of the posterior C1 arch at the transition of the lateral and posterior aspects of the arch (Fig 1). In the neurosurgical literature, this osseous transition has been described as a landmark for C1 lateral screw placement.¹⁹ The apex of the flare, the flare point (FP), is hypothesized to correspond with the posterior margin of the SC on lateral fluoroscopic views and has, up to this point, never been investigated, to our knowledge. In this study, we propose that the flare point is a reproducible osseous landmark that could approximate the position of the spinal cord to aid safe fluoroscopic needle placement during C1–2 puncture. We also report normative distances of the osseous canal and posterior subarachnoid space.

MATERIALS AND METHODS

This retrospective study was conducted under an institutional review board–approved protocol and informed consent was waived. Investigators were compliant with the Health Insurance Portability and Accountability Act.

Subjects

We searched our PACS for cervical CT myelograms obtained at our institution within the past 3 years (2015–2017), and the 50 most recent studies were chosen to obtain the necessary power. Only studies performed with high-resolution, 1-mm-thick, axial slices were included for reformatting purposes. Studies were excluded if there was inadequate opacification of the thecal sac hindering definite

delineation of the SC, surgical or congenital absence of the C1 posterior arch, presence of a subdural collection, or evidence of craniocervical osseous trauma that distorted normal anatomic relationships. Indications for the studies included contraindication for MR imaging, CSF leak, and degenerative disease with concern for stenosis.

Flare Point

The relative location of the C1 posterior arch triangular FP to the dorsal spinal cord border was determined in all cases by the following methods: 1) A maximum-intensity-projection image was generated for each cervical myelogram using sagittal reformats of high-resolution (1-mm-thick) axial images. An MIP thickness of 3.5 cm was used to simulate the appearance of the C1 arch projecting over the spinal canal on a lateral fluoroscopic view, with alignment adjustments performed to ensure that the bilateral posterior arches precisely overlapped. 2) Two lines were drawn to approximate the angle of the anterolateral and posterior arches—the first line tangential to the superior cortex of the anterolateral arch and the second line tangential to the superior cortex of the posterior arch. 3) The FP apex was determined at the point where these lines intersected. 4) The distance of the FP apex to the dorsal margin of the spinal cord was measured. If this line was anterior to the cord, negative measurement values were used, and if the line was posterior to the cord, positive measurement values were used (Fig 2). Measurements were performed by a neuroradiology fellow and neuroradiology attending physician.

Normative Distances

The following measurements were obtained on all studies: anteroposterior measurements of the osseous canal from the posterior C2 border to the SL as seen on fluoroscopy, anteroposterior measurements of the posterior SC border to the SL (PC-SL), and anteroposterior measurements of the posterior SC border to the posterior dura (PC-PD). Measurements of the posterior SC border to both the SL and the posterior dura were performed because the SL can be seen on fluoroscopy while the posterior dura cannot. This allowed comparison of the perceived space by

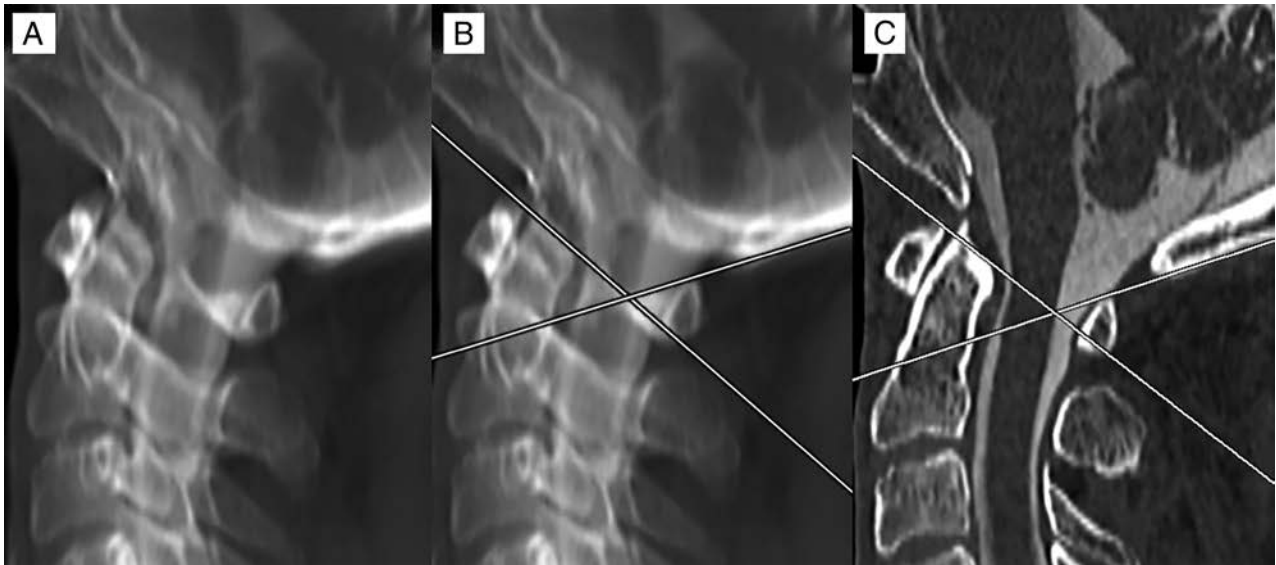


FIG 2. Method of measurement for the C1 posterior arch FP. An MIP image was created of a high-resolution sagittal reformatted cervical CT myelogram. Alignment adjustments were performed to overlap the bilateral posterior arches (A). Lines were drawn tangential to the superior cortex of the anterolateral and posterior arches. Where these lines overlapped was considered the FP (B). The MIP was then converted back to a 1-mm-thick section to evaluate the position of the FP from the dorsal spinal cord, which, in this case, showed direct correspondence, measuring 0 mm (C).



FIG 3. Measurements were performed on high-resolution sagittal cervical myelogram CT reformatted images. A line was drawn along the posterior margin of the SC (*short dashed white line*), with a second line approximating the SL (*long dashed white line*). The osseous canal was measured along the upper, mid, and lower aspects of the C1–2 interspace (*solid lines*) from the posterior margin of the dens to the SL. Additional measurements were performed between the posterior cord to the SL and the posterior cord to the posterior dura at the upper, mid, and lower aspects of the C1–2 interspace (not shown).

fluoroscopy and the actual size of the posterior subarachnoid space by CT. Measurements were performed at 3 levels: the upper C1–2 interspace, the mid-C1–2 interspace, and the lower C1–2 interspace (Fig 3).

Statistical Analysis

Power analysis was performed to determine an adequate number of subjects. Two-tailed *t* tests were performed to determine differences in the size of the posterior subarachnoid space between subjects with the FP falling posterior to the SC and subjects in whom the FP fell anterior to the dorsal SC margin. Intraclass correlation coefficient estimates and their 95% confidence intervals were calculated between 2 readers using a single-measure, absolute-agreement, 2-way mixed-effects model. Analyses were performed using SPSS, Version 25 (IBM, Armonk, New York).

Procedural Technique

Prior cervical imaging was reviewed for each patient for adequate subarachnoid space in the posterior spinal canal at C1–2, for position of the vertebral arteries, and for assessment of the C1 flare point with respect to the dorsal cord. Patients were positioned prone or supine with the neck neutral or slightly extended. A C-arm or biplane fluoroscopy was rotated to obtain a true lateral view centered at the C1–2 level. A metallic marker was used to localize a skin entry site midway between the spinolaminar line and flare point at the mid-C1–2 interspace. The overlying skin was prepped, draped, and anesthetized with 1% lidocaine via a 25-ga needle. A 22-ga Quincke needle (Halyard Health Global, Alpharetta, Georgia) was advanced toward the dorsal thecal sac under fluoroscopic guidance, with care taken to keep the needle tip from straying ventrally or dorsally. The needle depth was intermittently checked with anteroposterior fluoroscopy. When the needle reached the dura (approximated to be in line with the uncinat processes on an anteroposterior view), the bevel was rotated posteriorly to increase the likelihood of dural puncture. The needle was then advanced a few millimeters at a time under fluoroscopy, and the stylet was removed after each advancement until CSF return was noted. In our experience, it is common for the needle to reach the midline or just past midline on the antero-

Demographics and normative distances^a

Demographics/Distances	
Age (yr)	56 ± 15.5
Sex (F/M)	20:22
OC	
Upper ^b	18.3 ± 2.9
Mid	17.8 ± 3.0
Lower	17.0 ± 2.9
PC-SL	
Upper	4.3 ± 1.5
Mid	4.1 ± 1.2
Lower	3.7 ± 1.0
PC-PD	
Upper	3.7 ± 1.4
Mid	4.4 ± 1.6
Lower	3.4 ± 1.2
FP distance to cord	0.2 ± 0.5
PC-SL in subjects with anterior FP	
Upper	3.8 ± 1.9
Mid	3.6 ± 1.6
Lower	3.3 ± 1.3
PC-PD in subjects with anterior FP	
Upper	3.2 ± 1.7
Mid	3.7 ± 1.7
Lower	2.9 ± 1.3

Note:—OC indicates osseous canal.

^a Data are means and all measurements are in millimeters, unless otherwise stated.

^b Refers to the position in the C1–2 interspace.

posterior view due to substantial dural tenting before entering the subarachnoid space.

Clinical Follow-Up

A search was performed for all C1–2 punctures performed using the FP technique in the past 3 years. Procedural images were evaluated, and a chart review was performed to determine whether complications were noted in the postprocedural note and first follow-up clinical note in outpatients or the discharge summary in inpatients.

RESULTS

Subjects

Fifty subjects underwent CT cervical myelographic evaluation. Eight patients were excluded for the following reasons: Two had prior posterior C1 arch decompression, 2 had poor myelographic opacification, 2 had axial sections thicker than 1 mm, one had a C1 arch fracture, and one had a subdural collection. Forty-two cervical spine CT myelograms met all the criteria for evaluation (20 women; 56.0 ± 15.5 years of age) (Table), with most studies performed for CSF leak or evaluation of cervical stenosis when MR imaging was contraindicated. This exceeded the necessary subject size by power analysis (39 patients).

Flare Point

The FP was, on average, 0.2 ± 0.5 mm posterior to the dorsal margin of the spinal cord and corresponded exactly to the dorsal margin (0 mm) in 23/42 subjects. In the remaining subjects, the FP was within <1 mm of the dorsal spinal cord margin in 17/19, and in 2/19, the FP was >1 mm (1.5 and 2.2 mm, respectively) posterior to the dorsal spinal cord. In 5/42 subjects, the FP fell anterior to the dorsal spinal cord margin with distances ranging between 0.3 and 0.8 mm (Table and Fig 2). Readers had good

reliability with an intraclass correlation coefficient single measure of 0.72 (95% CI, 0.53–0.84; $P < .001$).

Normative Distances

The osseous canal was largest at the upper portion of the C1–2 interspace (18.3 ± 2.9 mm), with a slightly smaller dimension at the midportion of the interspace (17.8 ± 3.0 mm) and the smallest diameter at the lower portion of the interspace (17.0 ± 2.9 mm). The PC-SL distances ranged from 4.3 mm at the upper interspace to 3.7 mm at the lower one. The largest dimension of the PC-PD was in the midportion of the interspace (4.4 ± 1.6 mm), which exceeded or equaled the PC-SL in 26/42 subjects (Table). The ratio of the PC-SL to the osseous canal ranged between 0.22 and 0.24, and the ratio of the PC-PD to the osseous canal ranged between 0.20 and 0.26.

Clinical Follow-Up

Since 2015, sixteen C1–2 punctures have been performed on 15 subjects at our institution, University of Utah Health, using the FP method for fluoroscopic targeting. Indications for C1–2 puncture included suspected basilar meningitis, tethered cord, spinal block, arachnoiditis, meningitis in the setting of spina bifida, as well as encephalopathy, multiple sclerosis, back pain, and elevated intracranial pressure in subjects without a feasible access for lumbar puncture. Evaluation of postprocedure notes in all subjects, as well as follow-up clinic notes in outpatients and discharge summaries in inpatients, revealed no immediate or delayed procedural complications using this technique (17.9 days on average between notes, with a range of 2–45 days).

DISCUSSION

The practice of the C1–2 intrathecal puncture has steadily decreased in part because of its perceived high risk.^{1,5} However, this procedure demonstrates some advantages over other alternate routes of CSF collection, such as a lower theoretic risk of vascular injury than atlanto-occipital puncture. In the instances of spinal block, the C1–2 puncture may be the only option. Unlike transforaminal lumbar puncture, the C1–2 technique can be performed with the patient supine and can be performed in subjects with severe neuroforaminal narrowing who are not amenable to a transforaminal approach. We sought to determine whether the FP of the posterior C1 arch could be used as an osseous landmark to approximate the location of the dorsal spinal cord. Our results showed high accuracy of this landmark in approximating the dorsal spinal cord margin. This landmark was within 1 mm of the dorsal spinal cord margin in most of our subjects and rarely was located anterior to the dorsal margin of the cord. Because of a few instances in which the FP was anterior to the dorsal cord margin, targeting for cervical puncture should be placed midway between the FP and SL, not directly in line with the FP, to ensure that the needle does not contact the posterior SC margin (Fig 4).

Subjects in whom the FP fell anterior to the dorsal margin of the spinal cord had, on average, a smaller dorsal subarachnoid space using both PC-SL and PC-PD compared with those with the FP behind the cord ($P = .11$ for both parameters) (Table). Even in these few subjects, the FP never fell greater than 1 mm anterior to the spinal cord, demonstrating that the accuracy of this landmark

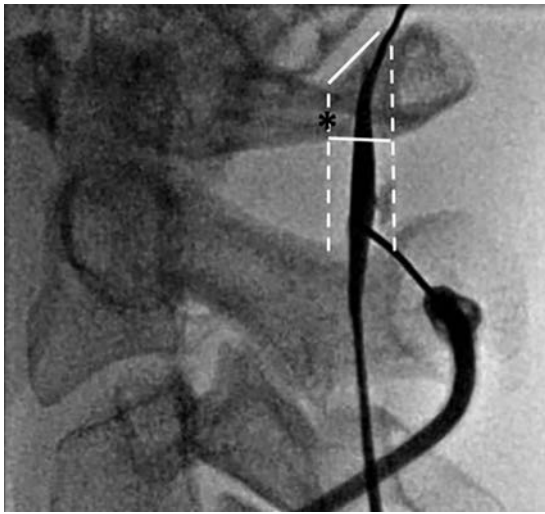


FIG 4. Intraprocedural fluoroscopic image demonstrating proper use of the flare point as an osseous landmark during a C1–2 puncture for a myelogram with the subject supine. The flare point (*asterisk*) is used to approximate the dorsal border of the spinal cord, and the needle is placed centrally between the dorsal cord border and the spinolaminar line (*white dashed lines*). Although the most capacious portion of the posterior subarachnoid space is in the mid-C1–2 interspace, successful puncture was performed in the slightly thinner lower portion of the interspace.

was maintained even in subjects with a smaller posterior subarachnoid space. We also found that the SL often underestimated the size of the posterior subarachnoid space at the mid-C1–2 interspace, with the dura extending up to 0.4 mm more posterior to the SL. The midportion of the C1–2 interspace was, overall, the largest portion of the posterior subarachnoid space, supporting targeting of this region.

The posterior subarachnoid space has frequently been thought to represent approximately one-third of the spinal canal, and this ratio has been historically recommended for targeting in C1–2 intrathecal puncture.^{1,18} In our study, we found the posterior subarachnoid space to be smaller than 33% (one-third), averaging between 22% and 23% of the total osseous canal when evaluating upper, mid, and lower portions of the C1–2 interspace. Only 4 subjects of 42 had a posterior subarachnoid space that measured at least 33% of the osseous canal, with the remaining 38 subjects demonstrating a smaller posterior subarachnoid space. One explanation for why overestimation of this space has not led to more complications could be the rotation of the spinal cord with dural tenting, which has been seen in postmortem studies.³ While studies have found no difference in the size of the posterior subarachnoid space between supine and prone positioning, flexion and extension can have an effect on the size of the posterior thecal sac, with a larger space for puncture on extension than in flexion.²⁰ Most interesting, 1 study reported increased complications with neck hyperextension.⁶ Thus, a neutral to slightly extended neck positioning is used at our institution.

Although the posterior one-third of the spinal canal has been found to be the safest and most capacious subarachnoid target for cervical puncture, an aberrant vertebral artery coursing in this location can present a rare cause for hemorrhage with few reported cases.^{11,21} A posterior coursing vertebral artery is a rare anomaly, which, in a study of 164 patients, was only found to

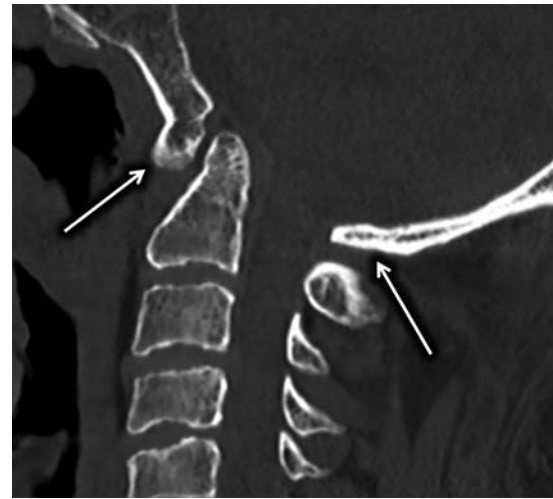


FIG 5. Sagittal CT of the cervical spine demonstrating congenital atlanto-occipital assimilation with 360° fusion of the C1 arch (*arrows*) resulting in complete absence of the FP.

occur 2% of the time.⁶ An even rarer anomaly is vertebral artery partial duplication or fenestration, which was seen in only 1% of 1685 angiograms.²² The risk of PICA injury is extremely rare because fewer than 1% have been reported to extend below the C1 level.^{1,23–25} Use of the FP cannot entirely exclude vascular injury in these rare anomalous cases, and vascular injury remains a very rare risk.

Magnification is inherent in fluoroscopic imaging, which can distort measurements.^{26,27} This contrasts with CT images, which are calibrated to a phantom.^{28,29} Thus, measurements between modalities can vary due to geometric distortion. Although normative distances on this study were acquired by CT myelography rather than fluoroscopy, the flare point technique itself does not depend on transposition of distances from one technique to another. Rather, this technique depends on determination of the midway point between the flare point and spinolaminar line. Because this technique uses relative ratios rather than exact measurements, the flare point can be used fluoroscopically even if there are geometric measurement differences with CT.

Limitations in the use of the FP include congenital anomalies of the posterior arch, specifically atlanto-occipital assimilation including both complete and incomplete forms (Fig 5). Other limitations include C1 arch fracture or surgical resection. Such conditions affect the morphology of the C1 posterior arch and therefore the FP approximation to the posterior SC, making it unreliable for fluoroscopic targeting. Study limitations include the retrospective design, small subject size, potential for inconsistencies in orientation of MIP reformats, and mild variations in patient positioning within the CT scanner.

CONCLUSIONS

The C1 posterior arch flare point accurately approximates the dorsal margin of the spinal cord on myelography and can be used to ensure a safe approach during C1–2 intrathecal puncture. Targeting midway between the flare point and the spinolaminar line, at the mid-C1–2 interspace, is recommended for safe and optimal needle positioning.

REFERENCES

1. Gibbs WN, Skalski MR, Kim PE, et al. **C1–2 puncture: a safe, efficacious, and potentially underused technique.** *Neurographics* 2017;7:1–8 CrossRef
2. Kelly DL Jr, Alexander E Jr. **Lateral cervical puncture for myelography: technical note.** *J Neurosurg* 1968;29:106–10 CrossRef Medline
3. Orrison WW, Eldevik OP, Sackett JF. **Lateral C1–2 puncture for cervical myelography, Part III: historical, anatomic, and technical considerations.** *Radiology* 1983;146:401–08 CrossRef Medline
4. Heinz ER. **Development of the C1–C2 puncture in neuroradiology: a historical note.** *AJNR Am J Neuroradiol* 2005;26:5–6 Medline
5. Yousem DM, Gujar SK. **Are C1–2 punctures for routine cervical myelography below the standard of care?** *AJNR Am J Neuroradiol* 2009;30:1360–63 CrossRef Medline
6. Katoh Y, Itoh T, Tsuji H, et al. **Complications of lateral C1–2 puncture myelography.** *Spine* 1990;15:1085–87 CrossRef Medline
7. Lin J, Olivero WC, McCluney KW. **Acute hydrocephalus following lateral C1–2 puncture: case illustration.** *J Neurosurg* 1999;90(2 Suppl):277 Medline
8. Müller-Vahl H, Vogelsang H. **Spinal cord injury caused by a lateral C1–2 puncture for cervical myelography.** *Eur J Radiol* 1986;6:160–62 Medline
9. Johansen JG, Orrison WW, Amundsen P. **Lateral C1–2 puncture for cervical myelography, part I: report of a complication.** *Radiology* 1983;146:391–93 CrossRef Medline
10. Mapstone TB, Rekeate HL, Shurin SB. **Quadriplegia secondary to hematoma after lateral C-1, C-2 puncture in a leukemic child.** *Neurosurgery* 1983;12:230–31 CrossRef Medline
11. Rogers LA. **Acute subdural hematoma and death following lateral cervical spinal puncture: case report.** *J Neurosurg* 1983;58:284–86 CrossRef Medline
12. Simon SL, Abrahams JM, Sean Grady M, et al. **Intramedullary injection of contrast into the cervical spinal cord during cervical myelography: a case report.** *Spine* 2002;27:E274–77 CrossRef Medline
13. Gong D, Yu H, Yuan X. **A new method of subarachnoid puncture for clinical diagnosis and treatment: lateral atlanto-occipital space puncture.** *J Neurosurg* 2017 Jul 28. [Epub ahead of print] CrossRef Medline
14. Geraci AP, Black K, Jin M, et al. **Transforaminal lumbar puncture for intrathecal nusinersen administration.** *Muscle Nerve* 2018 Jan 24. [Epub ahead of print] CrossRef Medline
15. Weaver JJ, Natarajan N, Shaw DW, et al. **Transforaminal intrathecal delivery of nusinersen using cone-beam computed tomography for children with spinal muscular atrophy and extensive surgical instrumentation: early results of technical success and safety.** *Pediatric Radiol* 2018;48:392–97 CrossRef Medline
16. Nascene DR, Ozutemiz C, Estby H, et al. **Transforaminal lumbar puncture: an alternative technique in patients with challenging access.** *AJNR Am J Neuroradiol* 2018;39:986–91 CrossRef Medline
17. Orrison WW, Sackett JF, Amundsen P. **Lateral C1–2 puncture for cervical myelography, Part II: recognition of improper injection of contrast material.** *Radiology* 1983;146:395–400 CrossRef Medline
18. Burt TB, Seeger JF, Carmody RF, et al. **Dural infolding during C1–2 myelography.** *Radiology* 1986;158:546–47 CrossRef Medline
19. Kim JH, Kwak DS, Han SH, et al. **Anatomic consideration of the C1 laminar arch for lateral mass screw fixation via the C1 lateral lamina: a landmark between the lateral and posterior lamina of the C1.** *J Korean Neurosurg Soc* 2013;54:25–29 CrossRef Medline
20. Bazylewicz MP, Berkowitz F, Sayah A. **3D T2 MR imaging-based measurements of the posterior cervical thecal sac in flexion and extension for cervical puncture.** *AJNR Am J Neuroradiol* 2016;37:579–83 CrossRef Medline
21. Robertson HJ, Smith RD. **Cervical myelography: survey of modes of practice and major complications.** *Radiology* 1990;174:79–83 CrossRef Medline
22. Kowada M, Yamaguchi K, Takahashi H. **Fenestration of the vertebral artery with a review of 23 cases in Japan.** *Radiology* 1972;103:343–46 CrossRef Medline
23. Brinjikji W, Cloft H, Kallmes DF. **Anatomy of the posterior inferior cerebellar artery: relevance for C1–C2 puncture procedures.** *Clin Anat* 2009;22:319–23 CrossRef Medline
24. Tokuda K, Miyasaka K, Abe H, et al. **Anomalous atlantoaxial portions of vertebral and posterior inferior cerebellar arteries.** *Neuroradiology* 1985;27:410–13 CrossRef Medline
25. Siclari F, Burger IM, Fasel JH, et al. **Developmental anatomy of the distal vertebral artery in relationship to variants of the posterior and lateral spinal arterial systems.** *AJNR Am J Neuroradiol* 2007;28:1185–90 CrossRef Medline
26. van der Maas R, de Jager B, Steinbuch M, et al. **Model-based geometric calibration for medical x-ray systems.** *Med Phys* 2015;42:6170–81 CrossRef Medline
27. Nickoloff EL. **AAPM/RSNA physics tutorial for residents: physics of flat-panel fluoroscopy systems—survey of modern fluoroscopy imaging: flat-panel detectors versus image intensifiers and more.** *Radiographics* 2011;31:591–602 CrossRef Medline
28. Xu Y, Yang S, Ma J, et al. **Simultaneous calibration phantom commission and geometry calibration in cone beam CT.** *Phys Med Biol* 2017;62:N375–90 CrossRef Medline
29. Yang H, Kang K, Xing Y. **Geometry calibration method for a cone-beam CT system.** *Med Phys* 2017;44:1692–706 CrossRef Medline

Clinical Utility of a Novel Ultrafast T2-Weighted Sequence for Spine Imaging

M.B. Keerthivasan, B. Winegar, J.L. Becker, A. Bilgin, M.I. Altbach, and M. Saranathan

ABSTRACT

BACKGROUND AND PURPOSE: TSE-based T2-weighted imaging of the spine has long scan times. This work proposes a fast imaging protocol using variable refocusing flip angles, optimized for blurring and specific absorption rate.

MATERIALS AND METHODS: A variable refocusing flip angle echo-train was optimized for the spine to improve the point spread function and minimize the specific absorption rate, yielding images with improved spatial resolution and SNR compared with the constant flip angle sequence. Data were acquired from 51 patients (35 lumbar, 16 whole-spine) using conventional TSE and the proposed sequence, with a single-shot variant for whole-spine. Noninferiority analysis was performed to evaluate the efficiency of the proposed technique.

RESULTS: The proposed multishot sequence resulted in a 2× shorter scan time with a >1.5× lower specific absorption rate. The variable flip angle sequence was noninferior to the conventional TSE ($P < .025$) for all image-quality and clinical criteria except signal-to-noise ratio for the lumbar spine protocol. However, mean image scores for the TSE-variable refocusing flip angle were ≥ 4.3 for all criteria, and concordance analysis showed high agreement (>90%) with the TSE, indicating clinical equivalence. The single-shot sequence resulted in 4× shorter whole-spine scans, and image scores were ≥ 4.4 for all criteria, attesting to its clinical utility.

CONCLUSIONS: We present a fast T2-weighted spine protocol using variable refocusing flip angles, including a single-shot variant. The sequences have better point spread function behavior than their constant flip angle counterparts and, being faster, should be less sensitive to patient motion, often seen in the longer TSE scans.

ABBREVIATIONS: ETL = echo-train length; SAR = specific absorption rate; VFA = variable refocusing flip angle

T2-weighted MR imaging protocols are routinely used in the clinic for spine imaging. T2WI sequences such as 2D fast spin-echo or turbo spin-echo have proved useful for the detection and diagnosis of osteomyelitis, stenosis, nerve root compression, disc characterization, and other pathology.^{1,2} A typical spine protocol includes sequences for T2WI, T1WI, and short-tau inversion recovery fat-suppressed T2 imaging, all with FSE/TSE readouts. While TSE/FSE with multiecho readout reduces scan times compared with conventional spin-echo sequences, the scan times are still on the order of 3–4 minutes, and these double or triple when

performing combination spine examinations (eg, thoracolumbar). This scan time is uncomfortable for patients with painful spine conditions and makes the imaging more vulnerable to motion artifacts. While approaches using parallel imaging³ have been explored to reduce scan times, the use of higher acceleration factors is limited by image-quality degradation arising from poor coil coverage. While the scan time of a multislice TSE sequence could also be reduced by increasing the echo-train length (ETL), the corresponding increase in the specific absorption rate (SAR) results in an increased minimum TR, which offsets any reduction in scan time. In addition, increased ETL exacerbates image blurring from T2 decay during the long echo-train.

Single-shot sequences such as single-shot fast spin-echo and HASTE have been used for lumbar spine myelography,⁴ cervical spine motion imaging,⁵ and functional imaging of the spine.⁶ However, these sequences are not preferred for routine T2WI because they have severe image blurring and SAR limitations arising from the long echo-trains, often addressed by scanning at a low spatial resolution.⁷

Various approaches have been proposed to minimize radio-

Received September 22, 2017; accepted after revision May 14, 2018.

From the Departments of Electrical and Computer Engineering (M.B.K., A.B.), Medical Imaging (M.B.K., B.W., J.L.B., M.I.A., M.S.), and Biomedical Engineering (A.B.) University of Arizona, Tucson, Arizona.

Paper previously presented, in part, at: Annual Meeting and Exhibition of the International Society for Magnetic Resonance in Medicine, April 22–28, 2017; Honolulu, Hawaii.

Please address correspondence to Manojkumar Saranathan, PhD, Department of Medical Imaging, University of Arizona, 1609 N Warren Ave, Tucson, AZ 85724; e-mail: manojksar@radiology.arizona.edu

<http://dx.doi.org/10.3174/ajnr.A5713>

frequency power deposition in TSE-based sequences.⁸⁻¹⁰ These approaches optimize the refocusing flip angle train to improve the imaging point spread function, leading to reduced T2 blurring and an improved signal-to-noise ratio and SAR performance. While the variable refocusing flip angle (VFA) technique has been successfully used for 3D TSE-based brain,^{11,12} knee,^{13,14} and spine¹⁵ imaging, its use in 2D imaging has been rather limited. Recently, VFA along with 2D single-shot TSE was used in abdominal and pelvic imaging¹⁶ with increased sharpness and significant reduction in scan times due to the reduced SAR compared with conventional single-shot TSE.

In this work, we propose a fast T2-weighted spine imaging protocol using a multishot turbo spin-echo sequence with variable refocusing flip angles (TSE-VFA) optimized for spatial resolution, SNR, and SAR. We also explore the use of a single-shot variant (HASTE-VFA) as a fast T2WI screening sequence for whole-spine protocols, in which the use of conventional TSE is prohibitively long.

MATERIALS AND METHODS

Pulse Sequence and Parameter Optimization

The vendor-supplied TSE and HASTE sequences were modified to incorporate the refocusing flip angle modulation scheme proposed by Busse et al,¹⁰ which parameterizes the refocusing flip angle train by using 4 control angles (α_{start} , α_{min} , α_{cent} , α_{end}). Following the approach of Loening et al,¹⁶ flip angles were optimized to maximize the SNR for the desired effective TE and minimize the SAR, with minimal spatial blurring. Numeric simulations were performed using Matlab (MathWorks, Natick, Massachusetts) to narrow the range of “optimal” refocusing flip angle values. For each possible value of the control angle vector (α_{start} , α_{min} , α_{cent} , α_{end}), T2 signal evolution from the turbo spin-echo pulse sequence was simulated using the Echo Phase Graph algorithm, assuming T1 and T2 values for the spine at 3T (T1 = 1060 ms, T2 = 69 ms), echo-train length = 56, and effective TE = 105 ms. The imaging point spread function was computed using the simulated signal. The peak and full width at half maximum value of the point spread function were measured because these are indicative of the SNR and resolution, respectively. Relative SAR was computed as the sum of squared refocusing flip angles divided by the echo-train length: $SAR_{rel} = \frac{\sum_{i=1}^{ETL} \alpha_i^2}{ETL}$, where α_i is flip angle of the *i*th refocusing pulse.

The optimal flip angles were chosen by using a 2-step search algorithm: 1) The search space was reduced by choosing control angles that maximize the point spread function on the basis of a preset threshold while maintaining the SNR at the effective TE. 2) Control angles that yield minimum SAR were chosen to generate the tailored refocusing flip angle train. This approach ensures adequate resolution and SNR for the VFA sequence compared with a constant flip angle train for the same echo-train length. To minimize motion-related signal dephasing at very low values of α_{min} ¹⁷, we chose a value of $\alpha_{min} = 45^\circ$. Due to the nonconvex nature of the search space, the resultant flip angle parameters are one of many possible optimal solutions.

Table 1: Scan parameters used for the conventional TSE and the proposed variable flip angle sequences

Parameters	Conventional		
	TSE	TSE-VFA	HASTE-VFA
Resolution (phase × freq) (mm ²)	0.81 × 0.73	0.81 × 0.73	1.25 × 1.0
Slice thickness (mm)	3	3	3
Refocusing flip angle	140°	$\alpha_{start} = 130^\circ$ $\alpha_{min} = 45^\circ$ $\alpha_{cent} = 110^\circ$ $\alpha_{end} = 45^\circ$	$\alpha_{start} = 130^\circ$ $\alpha_{min} = 50^\circ$ $\alpha_{cent} = 90^\circ$ $\alpha_{end} = 45^\circ$
Parallel imaging acceleration factor	2	2	1
ETL	21	56	160
TR (ms)	2800	3600	770
Scan time (min)	3 min 25 sec	1 min 28 sec	1 min 57 sec

Note:—freq indicates frequency.

Phantom and Volunteer Scanning

TSE-VFA and HASTE-VFA sequences were implemented and tested on a 3T Siemens Skyra scanner (Siemens, Erlangen, Germany). Phantom experiments were performed to study the blurring behavior and SNR of the proposed technique based on flip angle parameters chosen from simulations. Two nickel-doped agarose gel phantoms with T2 = 45 ms, T1 = 1000 ms and T2 = 80 ms, T1 = 1300 ms were imaged using the following sequences: a conventional TSE sequence at ETL = 21, TSE at ETL = 56, and TSE-VFA at ETL = 56. Data were acquired at an effective TE = 100 ms for all 3 sequences. The mean signal in the 2 phantoms was measured by drawing ROIs inside the object and in the background noise. The acquisition SNR was computed

as $SNR = \frac{Signal_{mean}}{Background_{SD}}$. In addition, SNR efficiency was calculated as $SNR_{eff} = \frac{SNR}{\sqrt{Scan Time}}$. The use of variable refocusing

flip angles can alter TSE image contrast. To ensure comparable contrast behavior of TSE-VFA, we also measured relative contrast between the 2 phantoms: $RelC = \frac{(Signal_1 - Signal_2)}{Signal_1}$. The SAR computed by the scanner was also recorded for the 3 sequences.

Because a complete sweep of the flip angle parameter space is not practical in vivo, the optimal flip angles obtained from simulations were validated using data acquired from volunteers. Sagittal lumbar spine data were acquired from 5 volunteers after informed consent, using the conventional TSE and TSE-VFA sequences with the parameters listed in Table 1.

Clinical Imaging

The optimized TSE-VFA sequence was added to the lumbar and cervical spine protocols as an addition to the routine T2WI TSE sequences. The HASTE-VFA sequence was added to the whole-spine protocol (covering the cervical, thoracic, and lumbar spine), which currently omits the T2WI TSE sequence due to long scan times (~9 minutes). This omission was possible due to the lower spatial resolution typically used in whole-spine screening protocols, which makes single-shot VFA with an adequate SNR viable. The effective TE was set to 108 ms for all the sequences, and images were acquired in the sagittal plane in accordance with the standard clinical protocol. The scan parameters for conventional

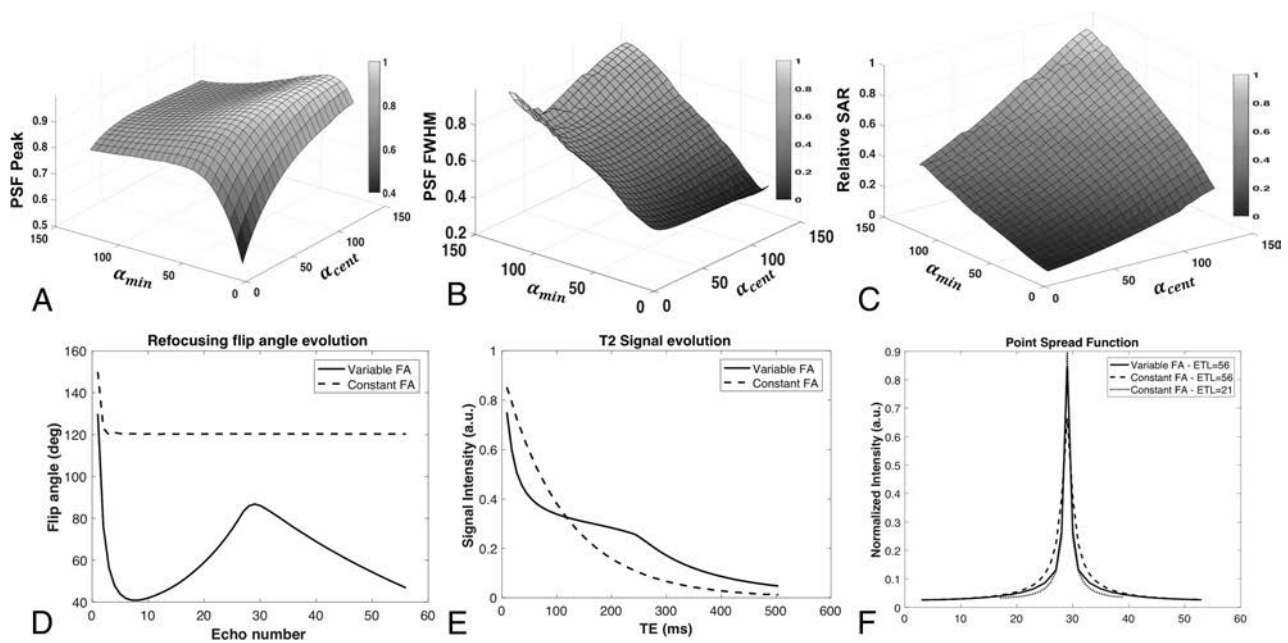


FIG 1. Surface plots of the peak and full width at half maximum (FWHM) of the simulated point spread function (PSF) as a function of α_{min} and α_{cent} are shown in A and B, respectively. C, The relative SAR as a function of the 2 control angles. Note that the computed PSF is maximized at higher values of α_{cent} , however, at the cost of increased SAR. D, The refocusing flip angle modulation scheme for a conventional fast spin-echo and the variable flip angle sequence along with the T2 signal evolution (E). Note that the VFA scheme stabilizes the signal evolution over the echo-train. The point spread functions for the constant and the variable flip angle echo-trains are compared in F. There is a considerable improvement in the PSF with the use of variable refocusing flip angles at longer echo-train lengths, resulting in better spatial resolution and less blurring. FA indicates flip angle; deg, degree; a.u., arbitrary units.

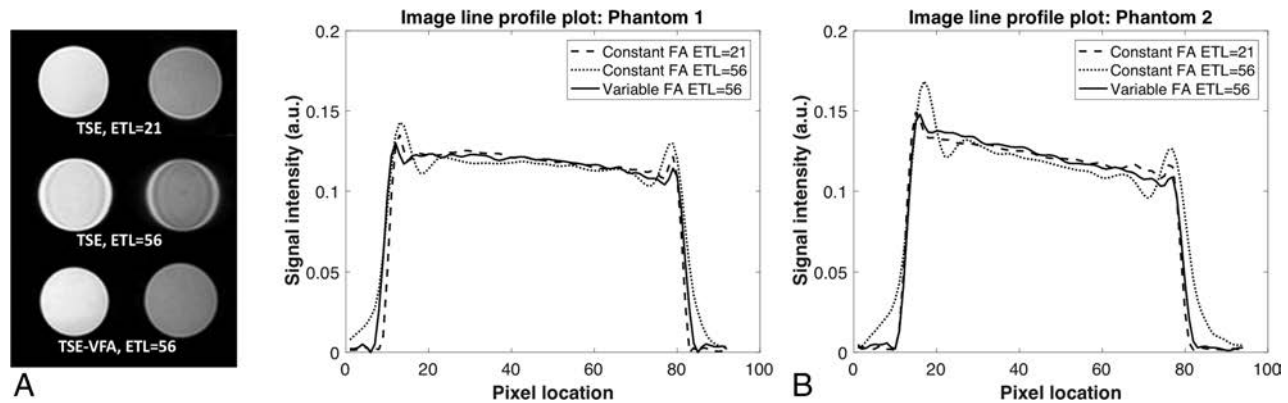


FIG 2. Phantom experiments comparing the resolution performance of TSE-VFA. Data were acquired on agarose gel phantoms (A) using the conventional TSE at ETL = 21, ETL = 56, and TSE-VFA at ETL = 56. B, Line plots across the 2 phantoms for the 3 sequences. Note the reduction in ringing when using TSE-VFA at the longer echo-train length of 56. FA indicates flip angle; a.u., arbitrary units.

TSE, TSE-VFA, and HASTE-VFA are shown in Table 1. As part of a prospective study, data were acquired from 51 patients (35 lumbar spine, 16 whole-spine) after written informed consent and in compliance with the institutional review board.

Image-Quality Assessment

Performance of the proposed VFA sequences was assessed independently by 2 neuroradiologists (2 and 12 years of experience) in a blinded fashion for both the volunteer and clinical data. To avoid recall bias, images from the 2 sequences were scored at least 2 weeks apart with random assignment of one or the other sequence for each patient in each reading session. Images were graded on a scale of 1–5 (1, nondiagnostic images; 2, severely limited; 3, limited; four, 1 or 2 suboptimal attributes but still

diagnostic; and 5, optimal image quality for diagnosis). Images were assessed on the basis of the following criteria: edge sharpness, motion, artifacts, and noise. Clinical utility of the sequences was assessed by quantifying the ability of the reader to interpret facet joints, endplates, nerve roots, spinal cord, and discs, also on a scale of 1–5. All levels of the spine were evaluated in terms of the image-quality metrics and the degree to which each structure could be interpreted. The lowest score was then applied for each of the anatomic structures.

Quantitative Analysis

An ROI analysis was performed on the volunteer and clinical lumbar spine data to quantitatively measure the SNR and relative contrast of the 2 sequences. ROIs were placed in the L3 vertebral

Table 2: Quantitative analysis of TSE and TSE-VFA using phantom data

Sequence	SNR	SNR	SNR Efficiency	SNR Efficiency	Relative Contrast	SAR	Scan Time (min)
	Phantom 1	Phantom 2	Phantom 1	Phantom 2			
Conventional TSE ETL = 21	469.76	248.56	261.38	138.30	0.47	0.24	3 min 13 sec
Conventional TSE ETL = 56	412.99	195.29	201.52	95.29	0.46	0.38	4 min 12 sec
TSE-VFA ETL = 56	423.54	216.12	338.02	172.48	0.46	0.17	1 min 34 sec

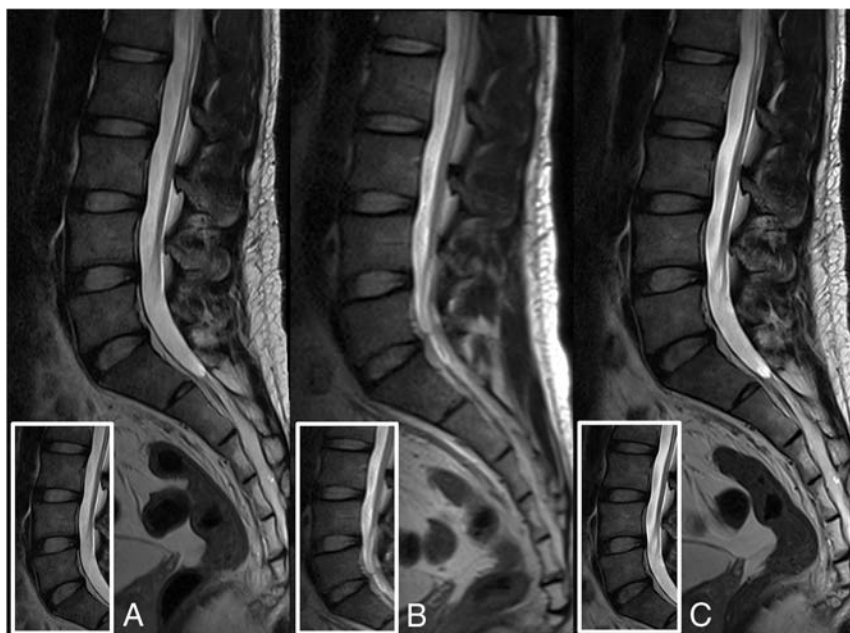


FIG 3. Images of the lumbar spine demonstrating better PSF behavior (reduced blurring) with variable flip angle TSE at ETL = 56 (A) compared with conventional TSE at the same ETL (B). C, Image acquired using the TSE sequence at ETL = 21. The TSE-VFA had a lower SAR value of 1.22 compared with the TSE at ETL = 21 (SAR = 1.665). Note that at the effective TE = 105 ms, the contrast between TSE-VFA and the T2-TSE sequence is comparable.

Table 3: Image-quality assessment scores for lumbar spine data of 5 volunteers

Scoring Criteria	Mean Score TSE	Mean Score TSE-VFA	Weighted Gwet AC1
Motion	4.9 ± 0.32	5 ± 0	0.97
Artifacts	5 ± 0	5 ± 0	1
Edge sharpness	5 ± 0	5 ± 0	1
SNR	5 ± 0	4.4 ± 0.52	0.93
Facet joints	5 ± 0	4.8 ± 0.42	1
Endplates	5 ± 0	5 ± 0	1
Nerve roots	5 ± 0	4.8 ± 0.42	1
Spinal cord	5 ± 0	5 ± 0	1
Discs	5 ± 0	5 ± 0	1

body and the L3–L4 disc to measure the mean signal intensity. The noise SD was measured from the background air region. The vertebral body SNR was calculated as $SNR = \frac{Signal_{mean}}{Noise_{stdev}}$, and the SNR efficiency was defined as SNR per unit scan time computed as $SNR_{eff} = \frac{SNR}{\sqrt{Scan\ Time}}$. The relative contrast between the disc and the vertebral body was calculated to quantify image contrast, defined as $Contrast_{vertebrae-disc} = \frac{Signal_{vertebrae} - Signal_{disc}}{Signal_{vertebrae}}$. A 2-tailed *t* test was performed to compare the mean SNR, relative contrast, and SAR from the 2 sequences for the 35 clinical scans.

Statistical Analysis

Noninferiority Analysis. Statistical analysis was performed using R statistical and computing software, Version 3.4.1 (<http://www.r-project.org/>).¹⁸ A noninferiority analysis between TSE-VFA and conventional TSE was performed using a 1-sided Wilcoxon signed rank test¹⁹ for the healthy volunteers and clinical patients. In this analysis, we sought to show the noninferiority of the proposed TSE-VFA compared with the conventional sequence—that is, the proposed technique does not significantly differ from the conventional method by testing the following hypothesis: $H_0: M_{VFA} - M_{TSE} \leq -\Delta$; $H_a: M_{VFA} - M_{TSE} > -\Delta$, where M_{TSE} and M_{VFA} are the median scores of the 2 sequences respectively, H_0 is the null hypothesis and H_a is the alternate hypothesis. The clinically acceptable range of differences is defined using the noninferiority margin Δ . In this context, the null hypothesis states that the median difference in image quality scores

between TSE and TSE-VFA is greater than a predetermined noninferiority margin Δ . The null hypothesis implies differences in the performance between the 2 sequences, and by rejecting the null at the significance level (α), we show noninferiority in the performance of TSE-VFA compared with TSE. The analysis was performed with a noninferiority margin of $\Delta = 0.5$ and significance level $\alpha = .025$. The noninferiority margin $\Delta = 0.5$ was chosen on the basis of preliminary data using recommendations from Ahn et al¹⁹ for noninferiority studies in radiology. To reduce type I error from multiple comparisons, we adjusted *P* values from the hypothesis test with the Bonferroni correction factor of 9. A *P* value $< \alpha$ results in the rejection of the null hypothesis and implies noninferiority of the proposed sequence compared with conventional TSE.

Agreement Analysis

To compare the clinical utility of the 2 sequences, we performed an agreement analysis^{20,21} using TSE as the non-reference standard for the 5 clinical criteria considered (ie, facet joints, endplates, nerve roots, spinal cord, and discs). A McNemar test of proportions was performed for each of the clinical criteria on the basis of the assumption that a score of ≥ 4 indicates diagnostic image quality. In accordance with FDA statistical guidelines,²¹ an overall percentage agreement and the positive percentage agreement were also computed to characterize the diagnostic agreement of the proposed TSE-VFA sequence with TSE.

Table 4: Quantitative analysis of lumbar spine data from volunteers and clinical subjects

	Sequence	Vertebral Body SNR	Vertebral Body SNR Efficiency	Vertebrae-Disc Relative Contrast	SAR
Healthy volunteers	TSE	36.08 ± 7.51	19.48 ± 4.05	0.47 ± 0.33	1.69 ± 0.14
	TSE-VFA	27.81 ± 4.33	22.94 ± 3.57	0.45 ± 0.32	1.31 ± 0.21
Clinical patients	TSE	55.45 ± 18.75	29.93 ± 10.12	0.13 ± 0.69	1.84 ± 0.61
	TSE-VFA	45.18 ± 14.96	37.27 ± 12.34	0.12 ± 0.7	1.37 ± 0.34

The Cohen κ statistic was initially used to assess interobserver reliability. However, it was observed that the statistic yielded low values for grading criteria that have a high percentage of agreement and are skewed in the score distribution. To overcome this so-called κ paradox,²² we instead used a weighted Gwet AC1 statistic to measure interobserver variability because it has been shown²³ to be more robust to skewed distributions. For HASTE-VFA, images were graded by the 2 observers and the Gwet AC1 was computed.

RESULTS

Figure 1 shows surface plots of the peak and full width at half maximum of the point spread function and SAR computed from the simulated TSE signal evolution as a function of α_{\min} and α_{cent} . For a fixed echo-train length and effective TE, a lower α_{\min} and higher α_{cent} results in better peak signal and resolution, with a very small increase in SAR. Figure 1 also illustrates a VFA scheme and compares the simulated T2 signal decay curves for the constant and proposed VFA echo-trains. From the point spread function plots in Fig 1F, the improvement in spatial resolution with VFA echo-trains can be clearly observed at longer ETLs, albeit with a slight reduction in signal compared with a short ETL constant flip angle sequence.

T2WI generated using the agarose gel phantoms is shown in Fig 2A. To visualize the spatial resolution differences between the acquisitions, a line profile through the 2 phantoms is shown in Fig 2B. The conventional TSE sequence with a constant flip angle exhibits ringing artifacts at long echo-train lengths as observed in the acquired images and the line plots. Table 2 shows the SNR and relative contrast values for the 3 different sequences along with the SAR value computed by the scanner. The proposed TSE-VFA has a 1.5 \times reduction in SAR compared with the short ETL conventional TSE sequence and 2.3 \times reduction compared with the long ETL variant. The proposed sequence can generate images with comparable contrast in a 2 \times shorter scan time. While prolongation of the echo-train and insufficient magnetization recovery lead to a slight loss in SNR, the reduction in scan time results in slightly improved SNR efficiency.

To verify the improvement in point spread function behavior in vivo, we acquired lumbar spine data from 5 healthy volunteers using both TSE and TSE-VFA with an ETL of 56. The conventional TSE sequence with a shorter ETL of 21 was also acquired as a reference. As seen in Fig 3, TSE-VFA has considerably reduced blurring compared with TSE with ETL = 56 and comparable image quality with TSE with ETL = 21. The TSE-VFA also had a 1.6 \times lower SAR, resulting in scan time reduction from 3.9 to 1.7 minutes. With a long ETL, conventional TSE has poor image quality and higher SAR, resulting in longer scan times (3 min 12 sec) compared with TSE-VFA.

Qualitative assessment of images from 5 healthy volunteers by neuroradiologists (Table 3) showed that TSE-VFA had comparable mean scores for all the different criteria except SNR. Table 4

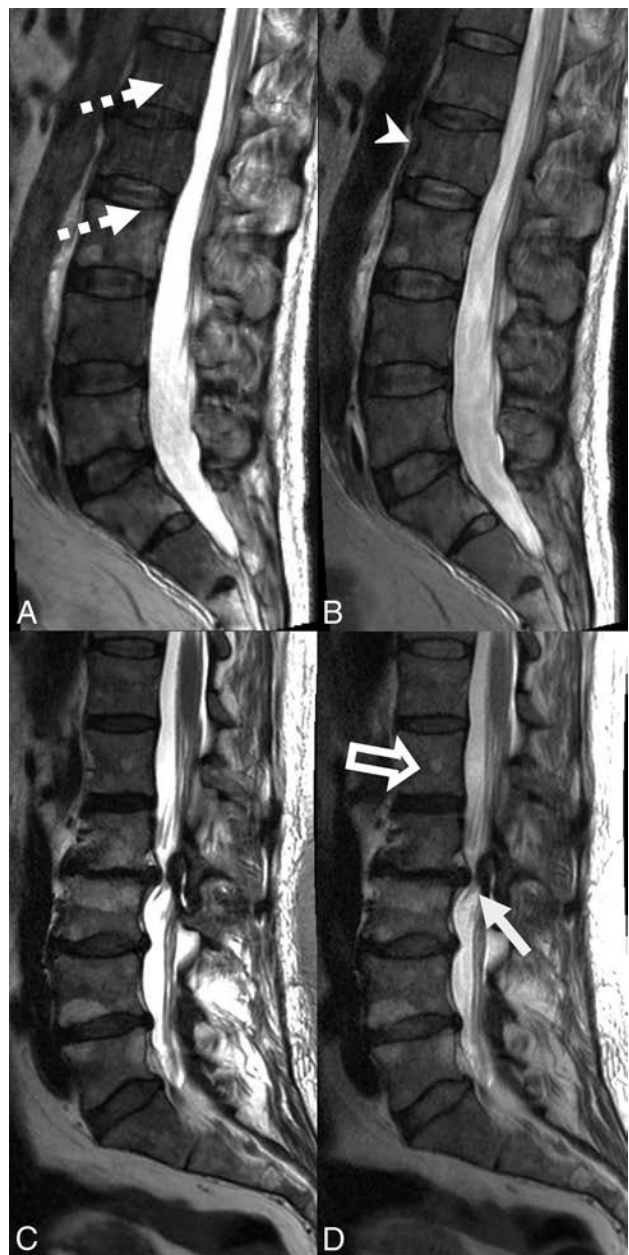


FIG 4. Sagittal T2WI TSE (A and C) and TSE-VFA (B and D) images of the lumbar spine for 2 subjects. A and B, The presence of multifocal osseous metastases with a pathologic fracture of L2 (arrowhead). The conventional TSE image (3 min 24 sec scan time) shows aliasing artifacts (dotted arrows) due to motion, which are absent in the TSE-VFA image (1 min 30 sec scan time). C and D, Images are from a patient with multilevel degenerative disc disease and a right subarticular disc protrusion abutting the right L3 nerve root at L2-L3 (white arrow). Note that the small hemangioma within the L1 vertebral body (open arrow) is well-resolved by the TSE-VFA (D). The TSE-VFA image for this subject received a score of 4 for the SNR and the CSF signal compared with a score of 5 for the TSE image.

Table 5: Image-quality assessment scores from 35 clinical lumbar spine cases

Scoring Criteria	Mean Score TSE	Mean Score TSE-VFA	P Value of Wilcoxon Test ^a	Weighted Gwet AC1
Motion	4.71 ± 0.59	4.83 ± 0.42	<.001	0.88
Artifacts	4.94 ± 0.23	4.76 ± 0.46	<.001	0.93
Edge sharpness	4.91 ± 0.33	4.79 ± 0.41	<.001	0.93
SNR	4.84 ± 0.40	4.36 ± 0.64 ^b	.371 ^b	0.84
Facet joints	4.83 ± 0.40	4.67 ± 0.50	<.001	0.86
Endplates	4.94 ± 0.23	4.83 ± 0.38	<.001	0.94
Nerve roots	4.76 ± 0.49	4.51 ± 0.58	<.001	0.78
Spinal cord	4.73 ± 0.51	4.47 ± 0.61	<.01	0.86
Discs	4.87 ± 0.44	4.80 ± 0.44	<.001	0.91

^a The null hypothesis states that the median difference in the image-quality scores between TSE and TSE-VFA is greater than the noninferiority margin Δ , and rejecting the null hypothesis shows noninferiority in performance.

^b Refers to lack of noninferiority between the TSE-VFA and TSE at a significance level of $P < .025$.

Table 6: Estimate of agreement in diagnostic quality between the conventional TSE and the proposed sequence

Clinical Diagnostic Criteria	Lumbar Spine	
	Overall Agreement (%)	Positive Agreement (%)
Facet joints	100	100
Endplates	100	100
Nerve roots	98.57	98.53
Spinal cord	97.14	97.06
Discs	100	100

shows mean values from the ROI analysis on the volunteer images. The proposed sequence generates T2WI with contrast comparable with that of conventional TSE at a lower SAR. However, TSE-VFA had slightly lower measured SNR, consistent with the qualitative scores and the phantom experiments.

Figure 4 shows representative examples of lumbar spine T2WI acquired from 2 subjects using TSE and TSE-VFA sequences. Figure 4A illustrates the presence of motion artifacts on a patient diagnosed with multifocal osseous metastases during the 3 min 24 sec TSE scan. On the other hand, TSE-VFA (1 min 30 sec scan time) generated images with comparable image quality and reduced motion artifacts. Figure 4C, -D shows images from a subject with multilevel degenerative disc disease. The shorter TSE-VFA sequence (D) has resolution comparable with that of the TSE but received a SNR score of 4, while TSE received a score of 5. Note a slight reduction in CSF signal due to insufficient recovery of the magnetization in TSE-VFA.

Table 5 summarizes the mean scores from the 2 observers for TSE and TSE-VFA for lumbar examinations. The median difference in scores between the 2 sequences for lumbar scans was significantly ($P < .025$) less than the noninferiority margin ($\Delta = 0.5$) for all criteria except SNR, implying noninferiority of TSE-VFA compared with conventional TSE. Note that our null hypothesis states that median difference in the image-quality scores between TSE and TSE-VFA is greater than Δ . The interobserver reliability AC1 scores between readers listed in Table 5 indicate a strong agreement between the 2 readers.

The clinical utility of the TSE-VFA spine protocols is further affirmed by the high positive percentage agreement (>80%) and overall agreement values shown in Table 6 for the lumbar spine. In addition, the McNemar test of proportions showed no significant difference ($P > .05$) between the conventional and the proposed sequences for the clinical criteria.

The SNR and relative contrast for the lumbar spine were mea-

sured for 35 clinical subjects as shown in Table 4. There was a difference in the mean SNR and relative contrast between clinical subjects and healthy volunteers for both TSE and TSE-VFA, presumably due to the hyperintense vertebral body signal caused by edema. There was no significant difference ($P = .32$) in the vertebrae-disc relative contrast between TSE-VFA and TSE. The proposed sequence had a significantly lower ($P < .001$) SAR compared with TSE. Note that the mean SAR for TSE was higher in clinical subjects than in healthy volunteers due to higher variability in patient weight. Furthermore, the TSE sequence had a significantly ($P = .006$) higher SNR than TSE-VFA.

Figure 5 illustrates the utility of the fast HASTE-VFA sequence in a whole-spine protocol acquired in <2 minutes. While HASTE-VFA has a slightly lower resolution (1.25×1.0 mm compared with TSE with 1.18×0.82 mm), it is about 4 times faster than the TSE, making it viable in a clinical setting and potentially more robust to patient motion. HASTE-VFA (Fig 5B) clearly depicts pathology while exhibiting reduced motion artifacts in the cervical spine section compared with the 9-minute STIR-TSE scan (Fig 5A).

Mean scores for whole-spine scans along with the Gwet AC1 for interobserver agreement are shown in Table 7. There is excellent interobserver agreement in the scores except for SNR, which shows a moderate concordance. The image scores follow a trend similar to that of the lumbar TSE-VFA scores.

DISCUSSION

We have demonstrated the use of variable refocusing flip angle TSE as a fast adjunct for routine spine imaging. Flip angle modulation reduced the blurring and SAR typically associated with long-ETL TSE sequences. The TSE-VFA sequence was roughly 2.3× faster than the conventional TSE sequence (1 min 28 sec versus 3 min 25 sec). The refocusing flip angles of the TSE-VFA sequence were optimized to maximize the spatial resolution and minimize SAR. Image scores were ≥ 4 for all the image quality and clinical criteria used and for all the clinical criteria considered; TSE-VFA was noninferior to TSE, attesting to the equivalence of the 2 sequences. While we have shown the clinical viability of TSE-VFA for sagittal T2WI, this technique can also be used as a fast alternative to the conventional TSE to generate T1WI and STIR contrasts in axial and sagittal planes. A spine protocol encompassing TSE-VFA for T1, T2, and STIR contrasts would reduce overall scan times.

We have also demonstrated the use of variable refocusing flip

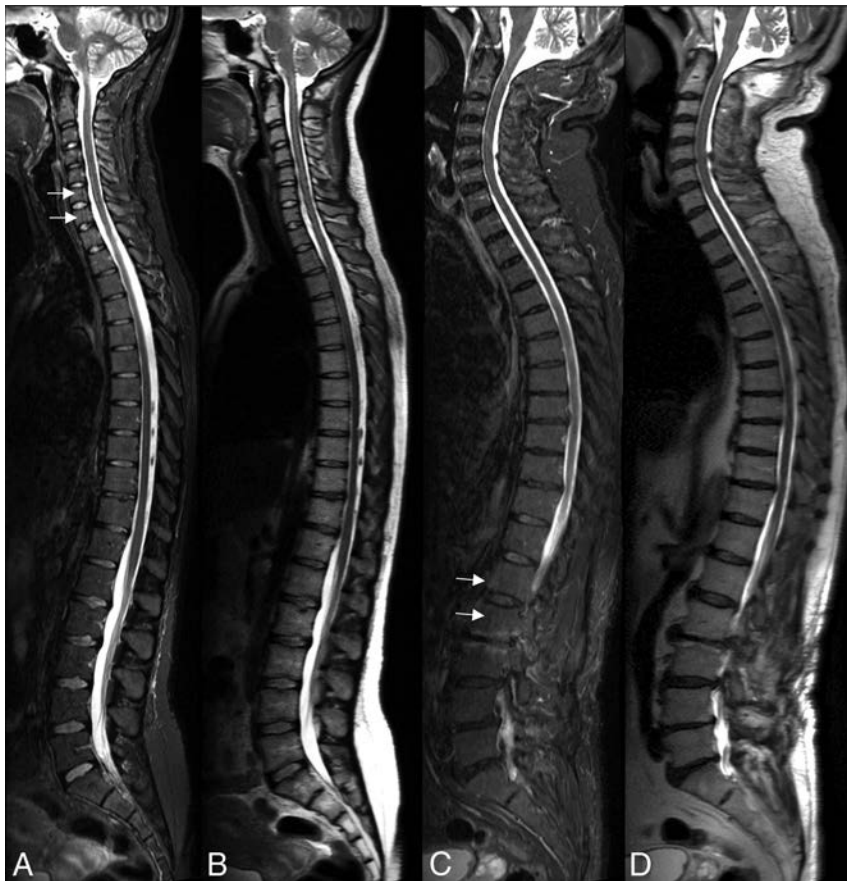


FIG 5. Sagittal STIR TSE (A and C) and sagittal HASTE-VFA (B and D) images of the whole spine for 2 subjects. A and B, Disc protrusions in the lower thoracic spine with several Schmorl nodes in the lumbar spine. C and D, Images from a subject with degenerative disc changes in the lumbar and the lower thoracic spine. Note the increased motion-related artifacts (arrows) with the 9 min 30 sec STIR TSE sequence (A and C) when compared to the single-shot sequence (B and D) with a 1 min 54 sec scan time.

Table 7: Image-quality assessment scores for the whole-spine cases

Scoring Criteria	Mean Score HASTE-VFA	Gwet AC1 Interobserver Reliability
Motion	4.66 ± 0.48	0.74
Artifacts	4.56 ± 0.50	0.65
Edge sharpness	4.78 ± 0.42	0.94
SNR	4.34 ± 0.75	0.39
Facet joints	4.69 ± 0.47	0.77
Endplates	4.91 ± 0.51	0.98
Nerve roots	4.47 ± 0.57	0.66
Spinal cord	4.72 ± 0.46	0.79
Discs	4.75 ± 0.44	0.91

angle single-shot sequences as a valuable addition for whole-spine imaging protocols (4× shorter scan time), whereas TSE sequences are prohibitively long. The HASTE-VFA sequence was added to the whole-spine protocol as a fast T2WI scan (1 min 54 sec), and its diagnostic value was confirmed by the excellent image-quality scores (clinical criteria had an average score of 4.71, and image quality metrics showed artifact behavior and SNR comparable with those in the lumbar spine). The HASTE-VFA protocol had a slightly lower resolution than the TSE-VFA (1.25 × 1 mm versus 0.81 × 0.73 mm) to minimize image blurring

and maintain SNR, and this limits its use for high-resolution lumbar spine imaging. We are exploring the use of optimal radio-frequency pulses to further reduce echo-spacing and enable higher resolution single-shot T2 imaging.

While the mean motion score of TSE-VFA was noninferior to TSE for the clinical subjects (Table 5), presumably due to the relative lack of patient motion in lumbar spine imaging, we observed a trend toward significance when we eliminated 9 subjects with motion scores of 5 on both sequences (4.43 for TSE-VFA versus 4.04 for TSE, $P < .1$). This suggests that TSE-VFA could be a good alternative to conventional TSE in patients who cannot tolerate long scans or for cervical spine imaging, in which motion artifacts are common from swallowing.

One possible limitation of the proposed VFA technique is the slight reduction in CSF signal due to insufficient magnetization recovery. This needs to be studied further in a larger clinical study, even though our study showed no detrimental effects from this phenomenon and subtle changes in CSF signal in the spine were adequately visualized in the VFA sequences due to the inherent contrast between CSF and other structures such as the spinal cord and intervertebral discs.

In TSE-VFA sequences, spatial resolution is limited by the available SNR, resulting in slightly lower SNRs for the same resolution as conventional TSE. This feature is indicated both by the slightly lower qualitative SNR scores compared with the TSE sequence (4.36 versus 4.84) and quantitative SNR measurements (45.18 versus 55.45). However, SNR efficiency is slightly higher for TSE-VFA (37.27 versus 29.93) due to the reduced scan time. Preliminary studies on volunteers indicate that the use of anterior coil arrays, atypical in spine imaging, in addition to the posterior coil array would improve SNR and enable comparable spatial resolution between TSE-VFA and TSE. We are currently exploring the feasibility of this clinically.

In this study, the TSE-VFA protocol parameters obtained from numeric simulations have been validated using phantoms and healthy volunteers and then tested on clinical patients. In the patient data, we did see our VFA protocol perform comparably with the conventional TSE, indicating that we are not far off from the volunteer and phantom optimal values. However, an analysis on a larger cohort of clinical patients is necessary to study the optimality of the proposed protocol and its clinical diagnostic utility.

VFA sequences have also been shown¹⁷ to be sensitive to motion, a feature determined by the choice of the flip angle parameters. While low values of α_{\min} can enable longer echo-trains, they can cause signal dephasing in the presence of substantial motion.

VFA-based sequences are also sensitive to B_1 field homogeneities²⁴ because B_1 variations cause changes in the refocusing flip angle that could lead to SNR loss in very large patients. We used α_{\min} values of 45°–50°, which were a good compromise between blurring and motion sensitivity.

CONCLUSIONS

We have developed fast T2WI spine protocols using variable refocusing flip angles, including a single-shot variant. VFA-based sequences have better point spread function behavior than their constant flip angle counterparts and are less sensitive to patient motion, often observed in longer TSE scans. These features enable the use of VFA sequences as an adjunct or replacement in clinical spine protocols, especially for pediatric 3T spine imaging where TSE scans are highly SAR limited.

ACKNOWLEDGMENTS

The authors thank Dr Srinivasan Vedantham for helping with the statistical analysis and interpretation of the results.

Disclosures: Manojkumar Saranathan—UNRELATED: Consultancy: ABC Medical Education.

REFERENCES

- Perry J, Haughton V, Anderson PA, et al. **The value of T2 relaxation times to characterize lumbar intervertebral disks: preliminary results.** *AJNR Am J Neuroradiol* 2006;27:337–42 Medline
- Stankiewicz JM, Neema M, Alsop DC, et al. **Spinal cord lesions and clinical status in multiple sclerosis: a 1.5T and 3T MRI study.** *J Neurol Sci* 2009;279:99–105 CrossRef Medline
- Fruehwald-Pallamar J, Szomolanyi P, Fakhrai N, et al. **Parallel imaging of the cervical spine at 3T: optimized trade-off between speed and image quality.** *AJNR Am J Neuroradiol* 2012;33:1867–74 CrossRef Medline
- O'Connell MJ, Ryan M, Powell T, et al. **The value of routine MR myelography at MRI of the lumbar spine.** *Acta Radiol* 2003;44:665–72 Medline
- Duerinckx AJ, Yu WD, El-Saden S, et al. **MR imaging of cervical spine motion with HASTE.** *Magn Reson Imaging* 1999;17:371–81 CrossRef Medline
- Xie C, Kong K, Guan J, et al. **SSFSE sequence functional MRI of the human cervical spinal cord with complex finger tapping.** *Eur J Radiol* 2009;70:1–6 CrossRef Medline
- Greenspan SL, Mathews VP, Caldemeyer KS, et al. **FLAIR and HASTE imaging in neurologic diseases.** *Magn Reson Imaging Clin N Am* 1998;6:53–65 Medline
- Hennig J, Scheffler K. **Hyperechoes.** *Magn Reson Med* 2001;46:6–12 CrossRef Medline
- Hennig J, Weigel M, Scheffler K. **Multiecho sequences with variable refocusing flip angles: optimization of signal behavior using smooth transitions between pseudo steady states (TRAPS).** *Magn Reson Med* 2003;49:527–35 CrossRef Medline
- Busse RF, Hariharan H, Vu A, et al. **Fast spin echo sequences with very long echo trains: design of variable refocusing flip angle schedules and generation of clinical T2 contrast.** *Magn Reson Med* 2006;55:1030–37 CrossRef Medline
- Busse RF, Brau A, Vu A, et al. **Effects of refocusing flip angle modulation and view ordering in 3D fast spin echo.** *Magn Reson Med* 2008;60:640–49 CrossRef Medline
- Mugler JP 3rd. **Optimized three-dimensional fast-spin-echo MRI.** *J Magn Reson Imaging* 2014;39:745–67 CrossRef Medline
- Kijowski R, Davis KW, Woods MA, et al. **Knee joint: comprehensive assessment with 3D isotropic resolution fast spin-echo MR imaging—diagnostic performance compared with that of conventional MR imaging at 3.0 T.** *Radiology* 2009;252:486–95 CrossRef Medline
- Li CQ, Chen W, Rosenberg JK, et al. **Optimizing isotropic three-dimensional fast spin-echo methods for imaging the knee.** *J Magn Reson Imaging* 2014;39:1417–25 CrossRef Medline
- Lee S, Jee WH, Jung JY, et al. **MRI of the lumbar spine: comparison of 3D isotropic turbo spin-echo SPACE sequence versus conventional 2D sequences at 3.0 T.** *Acta Radiol* 2015;56:174–81 CrossRef Medline
- Loening AM, Saranathan M, Ruangwattanapaisarn N, et al. **Increased speed and image quality in single-shot fast spin echo imaging via variable refocusing flip angles.** *J Magn Reson Imaging* 2015;42:1747–58 CrossRef Medline
- Litwiller DV, Holmes JH, Saranathan M, et al. **Sensitivity of modulated refocusing flip angle single-shot fast spin echo to impulsive cardiac-like motion.** In: *Proceedings of the Annual Meeting of the International Society for Magnetic Resonance in Medicine and the European Society for Magnetic Resonance in Medicine*, Milan, Italy. May 10–16, 2014
- R Core Team. *R: A Language and Environment for Statistical Computing.* Vienna: R Foundation for Statistical Computing; 2013
- Ahn S, Park SH, Lee KH. **How to demonstrate similarity by using noninferiority and equivalence statistical testing in radiology research.** *Radiology* 2013;267:328–38 CrossRef Medline
- Langenbucher J, Labouvie E, Morgenstern J. **Measuring diagnostic agreement.** *J Consult Clin Psychol* 1996;64:1285–89 CrossRef Medline
- Food Drug Administration Center for Devices and Radiological Health. **Statistical Guidance on Reporting Results from Studies Evaluating Diagnostic Tests, Document 1620, Maryland, 2007.** <https://www.fda.gov/downloads/MedicalDevices/DeviceRegulationandGuidance/GuidanceDocument/ucm071287.pdf>. Accessed July 23, 2017
- Cicchetti DV, Feinstein AR. **High agreement but low kappa, II: resolving the paradoxes.** *J Clin Epidemiol* 1990;43:551–58 CrossRef Medline
- Wongpakaran N, Wongpakaran T, Wedding D, et al. **A comparison of Cohen's Kappa and Gwet's AC1 when calculating inter-rater reliability coefficients: a study conducted with personality disorder samples.** *BMC Med Res Methodol* 2013;13:61 CrossRef Medline
- Madhuranthakam AJ, Busse RF, Brittain JH, et al. **Sensitivity of low flip angle SSFSE of the abdomen to cardiac motion.** In: *Proceedings of the Joint Annual Meeting of the International Society for Magnetic Resonance in Medicine and European Society for Magnetic Resonance in Medicine and Biology*, Berlin, Germany. May 19–25, 2007

Radiation-Induced Myelitis: Initial and Follow-Up MRI and Clinical Features in Patients at a Single Tertiary Care Institution during 20 Years

M. Khan, P. Ambady, D. Kimbrough, T. Shoemaker, S. Terezakis, J. Blakeley, S.D. Newsome, and I. Izbudak

ABSTRACT

SUMMARY: Myelitis is a rare complication of radiation exposure to the spinal cord and is often a diagnosis of exclusion. A retrospective review of clinical records and serial imaging was performed to identify subjects with documented myelitis and a history of prior radiation. Eleven patients fulfilled the inclusion criteria. All patients had longitudinally extensive cord involvement with homogeneous precontrast T1 hyperintense signal in the adjacent vertebrae, corresponding to the radiation field. T2 signal abnormalities involving the central two-thirds of the cord were seen in 6/11 patients (55%). The degree of cord expansion and contrast enhancement was variable but was seen in 6 (54%) and 5 (45%) patients, respectively. On follow-up, 2 patients developed cord atrophy, while complete resolution was noted in 1. Clinical improvement was noted in 5 patients, with symptom progression in 2 patients. Our results suggest that radiation myelitis is neither universally progressive nor permanent, and some radiographic and clinical improvement may occur.

ABBREVIATION: RM = radiation myelitis

Radiation myelitis (RM) is a rare-but-dreaded complication of radiation exposure to the spinal cord. This feared complication often limits volume, dose per fraction, and field of radiation therapy.¹ Most centers limit the total dose to the cord to <45 Gy in 1.8- to 2-Gy fractions to minimize this risk.²⁻⁶ Diagnosis of delayed RM is difficult and often a diagnosis of exclusion. More common causes of transverse myelitis (partial and/or longitudinally extensive), including demyelinating diseases (multiple sclerosis, neuromyelitis optica), rheumatoid diseases (lupus, Sjögren syndrome), and infectious etiologies (viral, bacterial), as well as primary and metastatic tumors, should be considered. Occasionally, paraneoplastic syndromes can also present with myelitis.⁷ Although very rare, ruling out recurrent or metastatic tumors is a major concern in the context of a prior history of malignancies.⁸⁻¹⁰ However, it is important to keep RM in the differential

diagnosis, especially when patients have a history of prior radiation therapy. Prompt diagnosis of RM is difficult because symptoms can vary, and onset (latent period) can range from a few months to several years following radiation exposure.^{11,12}

Contrast-enhanced MR imaging is frequently used as a diagnostic tool to help develop a differential diagnosis. Frequently described MR imaging characteristics of RM include spinal cord expansion, atrophy, hyperintense signal changes on T2-weighted images, and contrast enhancement.¹³⁻¹⁹ However, these imaging findings are nonspecific and can vary depending on the timing of MR imaging with respect to radiation exposure.^{14,19} This study aims to describe the clinical features and MR imaging characteristics of delayed radiation-induced myelitis at our institution in past 2 decades.

Case Series

The institutional review board at Johns Hopkins Hospital approved this retrospective study and waived patient informed consent. A radiology departmental data base of MR imaging spine studies conducted between 1993 and 2013 was searched using the keywords “myelitis” and “radiation.” A neuro-oncologist (P.A.) and a neuroimmunologist (D.K.), both in their second year of their respective fellowships, reviewed clinical records and identified patients with a history of radiation therapy and neurologic symptoms localized to the spinal cord as the reason for spine imaging. Two neuroradiologists (I.I. and M.K.) with 10 years of experience independently reviewed all relevant MR imaging findings.

The MR imaging examinations were performed with either 1.5T or 3T magnets from different manufacturers: 1.5 Intera

Received March 11, 2018; accepted March 16.

From the Brain Cancer Program (P.A., J.B., S.T.), Department of Radiation Oncology (S.T.), Sidney Kimmel Comprehensive Cancer Center at Johns Hopkins; Division of Neuroimmunology and Neuroinfectious Diseases, Department of Neurology (D.K., T.S., S.D.N.); and Division of Neuroradiology, Russell H. Morgan Department of Radiology (M.K., I.I.), Johns Hopkins University School of Medicine, Baltimore, Maryland; Neuro-Oncology Branch (P.A.), National Cancer Institute, Bethesda, Maryland; and Blood Brain Barrier and Neuro-Oncology Program (P.A.), Oregon Health and Science University, Portland, Oregon.

Majid Khan and Prakash Ambady contributed equally to this work.

Please address correspondence to Izlem Izbudak, MD, Department of Radiology, Johns Hopkins Hospital, Phipps B112, 600 N Wolfe St, Baltimore, MD 21287; e-mail: iizbudal@jhmi.edu

<http://dx.doi.org/10.3174/ajnr.A5671>

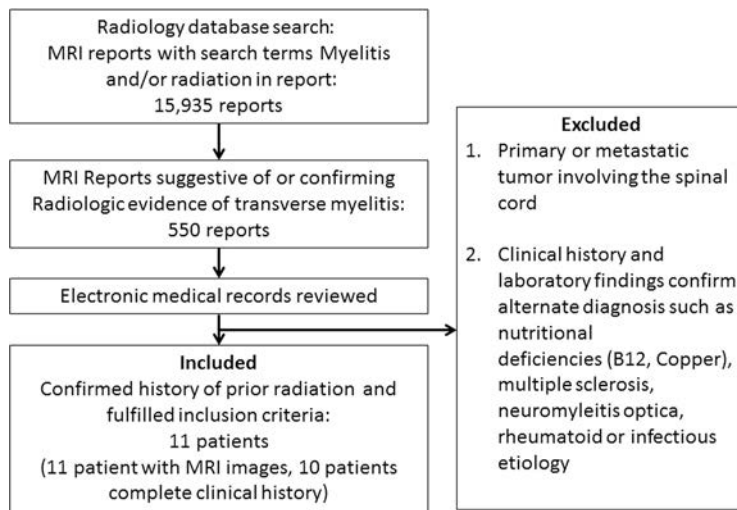


FIG 1. Study schema describes the method used to identify the patients in this series. It also highlights the rarity of the occurrence of radiation myelitis.

Table 1: Clinical course of myelopathy

Symptoms at presentation ^a	Paresthesia lower limbs: 6/10 (60%) Pain (back and legs): 5/10 (50%) Lower extremity motor weakness: 7/10 (70%) Urinary incontinence: 4/10 (40%) Bowel incontinence: 2/10 (20%)
Treatment received	Steroids: 9 Ivlg: 1 Hyperbaric oxygen: 2 Plasmapheresis: 2 Bevacizumab (Avastin): 1
Mean duration of clinical follow-up (mo)	22 (range: 4–162)
Clinical course on follow-up (available in 7 patients)	Improved with some sequelae: 5 Progressive: 2 Resolved: 0

Note:—Ivlg indicates intravenous immunoglobulin.

^a Detailed clinical examination was not available for 1 patient. Hence, only 10 patients were included for evaluation of the clinical course.

Table 2: Demographics of 11 subjects included in the study

Attributes	Median (Range)
Sex	6 males, 5 females
Median age (yr)	33 (11–60)
Primary malignancy (No. of patients)	1) Recurrent Hodgkin lymphoma: 5 2) Hodgkin lymphoma: 1 3) Gastric carcinoma: 1 4) Acute lymphocytic lymphoma: 1 5) Brain stem glioma: 1 6) Medulloblastoma: 1 7) Recurrent multiple myeloma: 1
Median time to symptom onset from RT (mo)	17 (2–194)
Median delay in diagnosis from symptom onset (mo)	6 (0–14)

Note:—RT indicates radiation therapy.

(Philips Healthcare, Best, the Netherlands), 1.5T Signa (GE Healthcare, Milwaukee, Wisconsin), Aera 1.5T, and Skyra 3T (Siemens, Erlangen, Germany), with routine spine MR imaging including sagittal T1-weighted and sagittal STIR imaging. Axial and sagittal T1-weighted images after intravenous gadolinium contrast administration (0.1 mL/kg) were also acquired. The scan

parameters were almost identical between different 1.5 T and 3T scanners.

The inclusion criterion for the study was only patients with cord signal changes in the field of radiation with pertinent neurologic symptoms attributed to the involved spinal segments. There was no restriction to the age at presentation or duration since radiation exposure occurred. Exclusion criteria were patients with a documented clinical diagnosis of neurologic symptomatology such as primary or metastatic spinal tumors, patients having undergone radiation for spinal cord tumors, multiple sclerosis, neuromyelitis optica, rheumatoid diseases, infectious etiologies, and/or vitamin B12/copper deficiency (Fig 1).

Eleven patients fulfilled the criteria

for final analysis. One patient included only in the imaging review was referred to our institution for a second opinion, and only a single brief clinical note was available, with symptom onset and clinical follow-up not available for this patient. Therefore, we did not include this patient in the analysis of clinical symptoms (Table 1). Six males and 5 females (mean age, 33 years; range, 11–60 years) were identified (Table 2). CSF analysis findings were non-specific, and cytology was negative for malignancies in all.

All 11 patients received radiation therapy for malignancies not directly involving the spine, with segments of the spinal cord developing myelitis included within the radiation field. Details of individual cases are summarized in Table 3. Six (55%) patients had prior chemotherapy. The median time from radiation therapy to symptom onset (latent period) was 17 months (range, 2–194 months). We noted a further median delay of 6 months (range, 0–14 months) from symptom onset to confirmation of clinical diagnosis. Sixty percent of patients reported lower leg paresthesia, 70% reported lower extremity motor weakness, and 50% reported back pain with radiculopathy at presentation. Four patients reported urinary and 2 reported bowel incontinence at presentation. Steroids were the most frequent therapy given at presentation. Among 7 patients with clinical follow-up data (mean follow-up, 22 months; range, 4–162 months), 5 reported some improvement in clinical symptoms, while 2 were noted to have progressive symptoms (wheelchair-bound).

The mean duration from symptom onset to the first MR imaging was around 6 months (range, 0–41 months). Imaging findings summarized in Table 4 revealed that all 11 patients had at least 1 MR imaging that demonstrated cervical and/or thoracic cord lesions in a longitudinally extensive pattern (Fig 2), with T1 hyperintensity in the adjacent vertebrae included in the field of radiation (Fig 1A). T2 signal abnormalities predominantly involved the central cord on axial images. Involvement of the central two-thirds of the axial cord was noted in 4, the central and posterior cord was involved in 1, and the entire circumference of the axial cord was involved in 5 patients at their initial MR imaging (Fig 3). Cord expansion was seen in 6 patients, with promi-

Table 3: Patient demographics and oncology treatment history

Patient	Age (yr)	Cancer Type	Prior Chemotherapy	Prior Chemotherapy Regimen	Adjuvant Chemotherapy
1	33	Recurrent Hodgkin lymphoma	Yes	ABVD	ICE followed by cyclophosphamide (Cytoxan) and busulfan Autologous bone marrow transplant
2	32	Recurrent Hodgkin lymphoma	Yes	CHOP/ABVD	Ara-C, vincristine, cisplatin Danazol
3	11	Brain stem medulloblastoma	No	–	Vincristine, VP-16, carboplatin CCNU, cisplatin
4	60	Recurrent gastric adenocarcinoma (stage IV)	No	–	5-FU, leucovorin
5	42	Refractory acute lymphocytic leukemia	Yes	Hyper-CVAD Methotrexate 6-Mercaptopurine	Intrathecal cytarabine Autologous bone marrow transplant
6	41	Hodgkin lymphoma	No	–	No
7	29	Brain stem glioma	No	–	TMZ
8	28	Recurrent Hodgkin lymphoma	Yes	ABVD	ICE followed by cyclophosphamide and busulfan Autologous bone marrow transplant
9	33	Recurrent Hodgkin lymphoma	Yes	ABVD	ICE followed by cyclophosphamide and busulfan Brentuximab vedotin Autologous bone marrow transplant
10	37	Recurrent Hodgkin lymphoma	Yes	ABVD	ICE followed by cyclophosphamide and busulfan Autologous bone marrow transplant

Note:—ABVD indicates doxorubicin, bleomycin, vinblastine, dacarbazine; CHOP, cyclophosphamide, doxorubicin hydrochloride, vincristine, prednisone; Hyper-CVAD, cyclophosphamide, vincristine, doxorubicin, and dexamethasone; TMZ, temozolomide; CCNU, lomustine; ICE, ifosfamide, carboplatin, etoposide chemotherapy protocol; Vp-16, etoposide phosphate.

Table 4: Spine MRI findings at initial presentation of myelopathy

Mean time from symptom onset to first MRI (mo)	6 (Range, 0–41)
Level of longitudinally extensive myelitis (No. of patients) (%)	Cervical: 3 (27%) Thoracic: 5 (45%) Cervical and thoracic: 2 (18%) Entire spine: 1 (9%)
Level of vertebral T1 hyperintensities (No. of patients) (%)	Cervical: 2 (18%) Cervical and thoracic: 3 (27%) Thoracic: 1 (9%) Thoracic and lumbar: 1 (9%) Entire spine: 2 (18%) No changes: 2 (18%)
Location of axial T2 changes (No. of patients) (%)	Central (>2/3): 4 (36%) Central and posterior: 1 (9%) Entire cord: 5 (45%) Indeterminate: 1 (9%)
Cord expansion (No. of patients) (%)	Present: 6 (54%) Absent: 3 (27%) Indeterminate: 2 (18%)
Contrast enhancement (No. of patients) (%)	Enhancement present: 5 (45%) No enhancement: 5 (45%) Contrast not given: 1 (9%)

cord expansion in 3 (as evidenced by a completely effaced thecal sac circumferentially on axial T2-weighted images), and mild expansion in 3 patients. Contrast enhancement was variable and was seen in 45% of cases. Follow-up MR imaging (Table 5) was available for 8 (73%) patients (median, 14.5 months; range, 4–69 months). On follow-up MRIs, cord atrophy was noted in only 2 of 8 patients (25%). Persistent T2 abnormalities in the cord were noted in 4 of 8 (50%), while complete resolution of MR imaging findings was seen in 1 of 8 (12.5%). Hemorrhagic changes were noted in 1 of 8 (12.5%), with syringohydromyelia also noted in 1 patient (12.5%).

DISCUSSION

Our report is relevant considering the rarity of RM (only 11 cases during 20 years at a tertiary care institution). Our report reinforces the long latent period and variable clinical and imaging findings in RM.^{11,13,17-21} Our study also reaffirms that the longitudinally extensive cord signal pattern corresponding to the radiation field and the additional demonstration of T1-weighted hyperintense marrow signal changes noted in vertebrae included in the radiation field were useful imaging findings in incorporating RM in the differential diagnosis. These imaging findings may draw the investigator’s attention to the tissue alterations in the field of radiation, especially when there is a long latency before the development of symptoms or when radiation fields are not readily available and may give us helpful hints about the etiology of myelitis.^{22,23} Central aspect of spinal cord seemed to be predominantly involved because it contains spinal gray matter with myelinated tracts at the periphery and suggests a possible vascular etiology due to delayed regional vasculitis secondary to radiation rather than demyelination.²⁴ Our study, like most prior studies, suggests that MR imaging findings including cord expansion and contrast enhancement are seen initially at presentation and tend to resolve on follow-up. In our cohort, cord expansion was seen in 55% of patients, while no cord expansion was seen in 27% at initial presentation, with contrast enhancement being variable in our cohort, indicating temporal variability in the blood-cord barrier permeability. Hemorrhagic changes in the cord were associated with the most severe case of RM.

Prior reports have suggested that RM is a progressive and permanent disease.^{11,25} However, 45% of our patients reported some improvement in their neurologic symptoms on follow-up. The mechanism of neurologic recovery is unclear but may be due to



FIG 2. Longitudinally extensive myelitis. A, The cervical or thoracic cord or both were involved in all patients in a longitudinally extensive pattern. B, Maximum myelopathic changes (yellow arrows) correspond to the central field of radiation identified by apparent fatty vertebral bone marrow on T1-weighted images (yellow brackets).

resolution of cord edema and inflammation, which may manifest as cord expansion in the early phase. Other possible explanations for clinical improvement may include remyelination and revascularization associated with improvement in the MR imaging abnormalities as described in this report. Most patients in our cohort received steroids at presentation, while a smaller number received bevacizumab, immunoglobulin, plasmapheresis, or hyperbaric oxygen in addition to steroids. It is unclear whether the radiologic improvement in our series was due to these therapies or the natural history of this condition. Literature review suggests that some cases of RM may be steroid-responsive, while animal studies and case reports have demonstrated an anecdotal benefit with therapies such as hyperbaric oxygen and bevacizumab when used in the acute phase.²⁵⁻²⁷

The most important and concerning cause of myelopathy in a patient with cancer is still disease progression.²⁸ RM is a diagnosis of exclusion, and contrast-enhanced MR imaging is frequently used to help aid in this diagnosis and differentiate this entity from tumors or infections. The pathophysiology of radiation

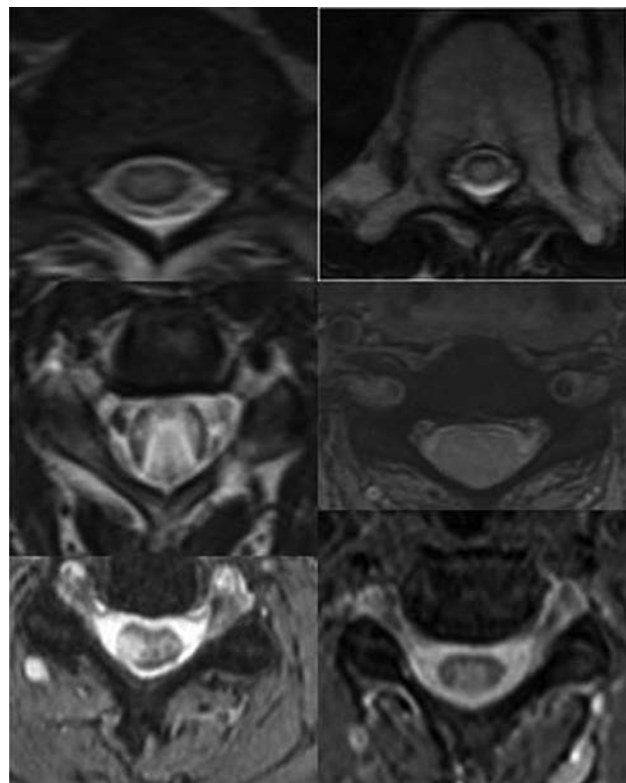


FIG 3. Central cord involvement. The central two-thirds of the cord on axial T2-weighted images was involved in 9 patients, and 1 patient presented with a small focal area of central and dorsal cord involvement.

Table 5: Findings on follow-up spine MRI

Radiographic follow-up available	Yes: 8 No: 3
Median follow-up (mo)	14.5 (4–69)
Cord atrophy (No. of patients) (%)	Present: 2 (25%) Absent: 6 (75%)
T2 findings (No. of patients) (%)	Decreased T2 abnormalities: 4 (50%) Resolved: 1 (12.5%) Hemorrhagic changes: 1 (12.5%) Syringohydromyelia: 1 (12.5%) Persistent T2 abnormalities: 4 (50%)

damage to the central nervous system is not well-defined, but oligodendrocytes and endothelial cells are considered major targets.²⁸⁻³² It is believed that endothelial cells are sensitive to radiation, but the effect has a longer latency in contrast to the glia, which is less sensitive but has a shorter latency.²⁰ Thus, early transient changes can be presumed to be due to demyelination, while more permanent changes are attributed to small-vessel ischemia with the extent of involvement dictating the severity and timing of symptoms.²⁴ The resulting evolving changes in the microvasculature and blood-cord barrier permeability have been historically held responsible for the temporal variability of presentation and inconsistent enhancement with contrast agents.²⁵

Another striking finding of this study is the high incidence of RM in patients with recurrent malignancies or patients who receive chemotherapy prior and/or concurrent with radiation. A cumulative radiation dose below 45 Gy in daily 1.8- to 2-Gy fractions is a widely accepted dose constraint for the spinal cord,²⁻⁶ and these dose constraints have certainly limited RM to a rare

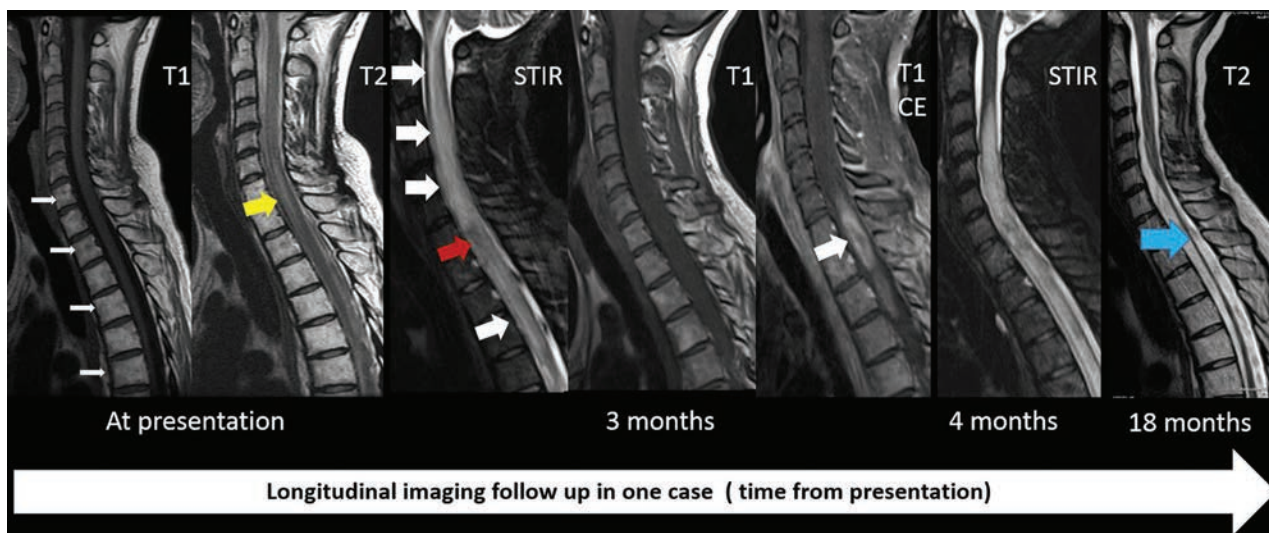


FIG 4. Sequential changes on imaging in a patient with severe radiation myelitis. Fatty bone marrow changes present with hyperintense T1 signal involving C7 and the upper thoracic vertebrae on the first image (*white arrows*). Less extensive longitudinally extensive myelitis at the C7, T1, and T2 levels is noted on the T2-weighted image with hyperintense signal at presentation (*yellow arrow*). At 3 months, cord expansion and extensive T2/STIR hyperintense signal changes involving the cervical and upper thoracic cord are noted (*white arrowhead*) with contrast enhancement at the C7, T1, and T2 levels (*single large white arrowhead*). The patient was paraplegic with urinary and bowel incontinence. She was treated with a high dose of steroids. Follow-up images at 18 months show cord atrophy (*blue arrow*). She eventually was able to ambulate with a walker after extensive physical therapy. CE indicates contrast enhancement.

complication. However, there is renewed interest in better understanding the clinical features, imaging findings, and underlying pathophysiology due to the re-emergence of RM with the increasing role of stereotactic radiosurgery and re-irradiation.²⁵ Our patients developed radiation myelitis even though they received a cumulative radiation dose well within the accepted tolerance limits for the spinal cord. Prior studies have indicated that tissue tolerance to radiation may be reduced with premedication with radiosensitizing chemotherapy.³³⁻³⁵ Most patients in our cohort were young (median age, 33 years), and this age may suggest that younger patients are at higher risk of developing RM, given the more intensive systemic therapy they generally receive.

This study suggests that there was a median delay of around 6 months before a firm diagnosis was made, highlighting the importance of time to correct diagnosis, with the start of and type of intervention possibly playing an important role in outcome. Prompt diagnosis may help avoid more invasive tests like biopsies.

Our study is unique because follow-up imaging and clinical history were available in most of our patients, and on follow-up, cord atrophy was seen in only 25% of our cases, which suggests that the timing of MR imaging after radiation may dictate the imaging findings. One of the interesting observations in this study is resolution or a decrease in T2 signal changes (Fig 4), affecting 12.5% and 50%, respectively, on follow-up, especially because RM is thought to be irreversible and permanent. Although formal statistical analysis was not possible due to the rarity of occurrence and small sample size, our series suggests that clinical improvement may correlate well with imaging findings on longitudinal follow-up. Hemorrhagic changes, cord expansion, and contrast enhancement were variable and were noted in patients who were scanned early during the disease process, and tended to resolve on follow-up. This finding has not been well-reported, and our correlation with clinical history suggests that the extent of hemor-

rhagic changes may dictate the severity of neurologic symptoms at presentation and disability at follow-up.

Limitation

We acknowledge that it is difficult to draw direct correlates between imaging findings and clinical outcomes because of the clinical data available being retrospective and issues related to recall bias due to the long latent period from symptom onset to diagnosis. Furthermore, patients were evaluated by a variety of providers (internists, medical oncologists, radiation oncologists, and neurologists) and the level of documentation varied between different specialties and clinical expertise of providers. Further studies should be performed to corroborate the findings of our study, including multicenter involvement to increase the sample size; however, the long-term follow-up and detailed clinical and radiologic data of this study are very informative.

Disclosures: Stephanie Terezakis—UNRELATED: Consultancy: L.E.K. Consulting; Employment: Johns Hopkins School of Medicine; Grants/Grants Pending: Elekta Instruments. Jaishri Blakeley—UNRELATED: Consultancy: AbbVie, Comments: through 2016 for 2 sessions of consultancy for a quality-of-life study. Izlem Izbudak—UNRELATED: Consultancy: Alexion Pharmaceuticals, Comments: neuromyelitis optica relapse adjudication committee MRI reads; Grants/Grants Pending: Siemens, Biogen, Comments: Siemens, DTI of the spinal cord prospective research grant; Biogen, MS PATHS scan-rescan brain MRI substudy.* *Money paid to the institution.

REFERENCES

1. Jin JY, Huang Y, Brown SL, et al. **Radiation dose-fractionation effects in spinal cord: comparison of animal and human data.** *J Radiat Oncol* 2015;4:225–33 CrossRef Medline
2. Breit A. **Radiation tolerance of the spinal cord.** *Int J Radiat Oncol Biol Phys* 1989;16:675–78 Medline
3. Emami B, Lyman J, Brown A, et al. **Tolerance of normal tissue to therapeutic irradiation.** *Int J Radiat Oncol Biol Phys* 1991;21:109–22 Medline
4. Kirkpatrick JP, van der Kogel AJ, Schultheiss TE. **Radiation dose-**

- volume effects in the spinal cord. *Int J Radiat Oncol Biol Phys* 2010; 76:S42–49 CrossRef Medline
5. Martel MK, Eisbruch A, Lawrence TS, et al. **Spinal cord dose from standard head and neck irradiation: implications for three-dimensional treatment planning.** *Radiother Oncol* 1998;47:185–89 CrossRef Medline
 6. Schultheiss TE. **Spinal cord radiation “tolerance”: doctrine versus data.** *Int J Radiat Oncol Biol Phys* 1990;19:219–21 Medline
 7. Dalmau J, Graus F, Rosenblum MK, et al. **Anti-Hu–associated paraneoplastic encephalomyelitis/sensory neuronopathy: a clinical study of 71 patients.** *Medicine (Baltimore)* 1992;71:59–72 CrossRef Medline
 8. Chamberlain MC. **Neoplastic myelopathies.** *Continuum (Minneapolis)* 2015;21(1 Spinal Cord Disorders):132–45 CrossRef Medline
 9. Payer S, Mende KC, Westphal M, et al. **Intramedullary spinal cord metastases: an increasingly common diagnosis.** *Neurosurg Focus* 2015;39:E15 CrossRef Medline
 10. Hrabalek L. **Intramedullary spinal cord metastases: review of the literature.** *Biomed Pap Med Fac Univ Palacky Olomouc Czech Repub* 2010;154:117–22 CrossRef Medline
 11. Reagan TJ, Thomas JE, Colby MY Jr. **Chronic progressive radiation myelopathy: its clinical aspects and differential diagnosis.** *JAMA* 1968;203:106–10 Medline
 12. Marcus RB Jr, Million RR. **The incidence of myelitis after irradiation of the cervical spinal cord.** *Int J Radiat Oncol Biol Phys* 1990;19:3–8 CrossRef Medline
 13. Komachi H, Tsuchiya K, Ikeda M, et al. **Radiation myelopathy: a clinicopathological study with special reference to correlation between MRI findings and neuropathology.** *J Neurol Sci* 1995;132:228–32 CrossRef Medline
 14. Wang PY, Shen WC, Jan JS. **Serial MRI changes in radiation myelopathy.** *Neuroradiology* 1995;37:374–77 Medline
 15. Michikawa M, Wada Y, Sano M, et al. **Radiation myelopathy: significance of gadolinium-DTPA enhancement in the diagnosis.** *Neuroradiology* 1991;33:286–89 CrossRef Medline
 16. Alfonso ER, De Gregorio MA, Mateo P, et al. **Radiation myelopathy in over-irradiated patients: MR imaging findings.** *Eur Radiol* 1997; 7:400–04 CrossRef Medline
 17. Koehler PJ, Verbiest H, Jager J, et al. **Delayed radiation myelopathy: serial MR-imaging and pathology.** *Clin Neurol Neurosurg* 1996;98: 197–201 CrossRef Medline
 18. Wang PY, Shen WC, Jan JS. **MR imaging in radiation myelopathy.** *AJNR Am J Neuroradiol* 1992;13:1049–55; discussion 1056–58 Medline
 19. Melki PS, Halimi P, Wibault P, et al. **MRI in chronic progressive radiation myelopathy.** *J Comput Assist Tomogr* 1994;18:1–6 CrossRef Medline
 20. Hopewell JW. **Late radiation damage to the central nervous system: a radiobiological interpretation.** *Neuropathol Appl Neurobiol* 1979; 5:329–43 CrossRef Medline
 21. Farrell BT, Hamilton BE, Dósa E, et al. **Using iron oxide nanoparticles to diagnose CNS inflammatory diseases and PCNSL.** *Neurology* 2013;81:256–63 CrossRef Medline
 22. Rubin P, Johnston CJ, Williams JP, et al. **A perpetual cascade of cytokines postirradiation leads to pulmonary fibrosis.** *Int J Radiat Oncol Biol Phys* 1995;33:99–109 CrossRef Medline
 23. Carmona R, Pritz J, Bydder M, et al. **Fat composition changes in bone marrow during chemotherapy and radiation therapy.** *Int J Radiat Oncol Biol Phys* 2014;90:155–63 CrossRef Medline
 24. Goertz O, Poettgen C, Akbari A, et al. **New model for long-term investigations of cutaneous microcirculatory and inflammatory changes following irradiation.** *J Radiat Res* 2015;56:456–61 CrossRef Medline
 25. Wong CS, Fehlings MG, Sahgal A. **Pathobiology of radiation myelopathy and strategies to mitigate injury.** *Spinal Cord* 2015;53: 574–80 CrossRef Medline
 26. Feldmeier JJ, Lange JD, Cox SD, et al. **Hyperbaric oxygen as prophylaxis or treatment for radiation myelitis.** *Undersea Hyperb Med* 1993;20:249–55 Medline
 27. Chamberlain MC, Eaton KD, Fink J. **Radiation-induced myelopathy: treatment with bevacizumab.** *Arch Neurol* 2011;68:1608–09 CrossRef Medline
 28. Schultheiss TE, Kun LE, Ang KK, et al. **Radiation response of the central nervous system.** *Int J Radiat Oncol Biol Phys* 1995;31:1093–112 CrossRef Medline
 29. Coderre JA, Morris GM, Micca PL, et al. **Late effects of radiation on the central nervous system: role of vascular endothelial damage and glial stem cell survival.** *Radiat Res* 2006;166:495–503 CrossRef Medline
 30. Okada S, Okeda R. **Pathology of radiation myelopathy.** *Neuropathology* 2001;21:247–65 CrossRef Medline
 31. Burns RJ, Jones AN, Robertson JS. **Pathology of radiation myelopathy.** *J Neurol Neurosurg Psychiatry* 1972;35:888–98 CrossRef Medline
 32. Lu FG, Wong CS. **Radiation-induced apoptosis of oligodendrocytes and its association with increased ceramide and down-regulated protein kinase B/Akt activity.** *Int J Radiat Biol* 2004;80:39–51 CrossRef Medline
 33. Seddon BM, Cassoni AM, Galloway MJ, et al. **Fatal radiation myelopathy after high-dose busulfan and melphalan chemotherapy and radiotherapy for Ewing’s sarcoma: a review of the literature and implications for practice.** *Clin Oncol* 2005;17:385–90 CrossRef Medline
 34. Rubin P. **The Franz Buschke lecture: late effects of chemotherapy and radiation therapy: a new hypothesis.** *Int J Radiat Oncol Biol Phys* 1984;10:5–34 Medline
 35. Chao MW, Wirth A, Ryan G, et al. **Radiation myelopathy following transplantation and radiotherapy for non-Hodgkin’s lymphoma.** *Int J Radiat Oncol Biol Phys* 1998;41:1057–61 CrossRef Medline

William G. Bradley Jr, MD, PhD, FACR

Perhaps more than any other single figure, Bill Bradley (1948–2017) both educated us regarding clinical MR imaging and popularized clinical MR imaging during its early days in setting the trajectory of the field. Bill was a larger-than-life figure with magnums of charisma, ebullience, and brilliance in such a unique blend that his passing leaves an undeniable gaping void in our collective family. Bill is survived by his devoted wife, pediatric neuroradiologist Dr Rosalind Dietrich; his son David; daughters Kristin Egan, India Homsy, and Felicity; and 5 grandchildren. Bill is also survived by his 2 brothers, Drs John Bradley and Thomas Bradley, and 6 nieces and nephews.

Bill was a self-proclaimed “Air Force brat,” born in Los Angeles on July 30, 1948, to Shirley Ann Premack and flight surgeon Dr William G. Bradley, Sr. He was an inveterate traveler, an unparalleled raconteur, and a remarkable creative force. Bill loved people, places, single malt scotch, laughing, and innovating. Bill left behind legions of fellows, residents, industry friends, and other acquaintances who consistently volunteer that he influenced, entertained, befriended, enriched, counseled, and guided them. Bill was irrepressible and uniquely unforgettable.

Bill lived his early years in Japan, was a proud Eagle Scout at 13, and graduated from high school in Bitberg, Germany, as Class President. Bill was an insatiable reader and learner and a lover of all things scientific from a very early age. His curiosity and creativity were manifest in his adolescent and teenage years by brilliant and innovative contributions to science fairs. Bill’s love of science and discovery was, in part, satisfied by his bachelor’s degree from the California Institute of Technology and his subsequent doctorate from Princeton, both in chemical engineering, as he sought the means to apply science and discovery for the common good. Bill found the means in medicine.

Bill completed his medical degree and radiology training at the University of California, San Francisco (UCSF), where radiology allowed his love of technology and science to simultaneously flourish. Bill’s insatiable curiosity and brilliance were focused and encouraged by his mentor and chair, Alex Margulis. Dr Margulis tasked Bill with making something practical of MR imaging, which at the time was a promising-yet-unproved new addition to the growing pantheon of imaging. At UCSF, Bill focused on translating and practically interpreting the complex physics of MR imaging into a language that other physicians could understand. Bill was equipped to handle this task by dint of his Cal Tech and Princeton training and his belief in the potential of the technology. Bill succeeded through his seminal landmark text written and edited with his friend David Stark, a brilliant radiologist in Boston at the time. This textbook led and taught the field for decades.

Bill’s mind was in perpetual motion, and the breadth of his curiosity and prodigious intellectual appetite encompassed such clinically and scientifically vital topics such as hydrocephalus, CSF flow, multiple sclerosis, blood breakdown products, and brain lymphatics and flow, among many topics. Bill pursued the science and phenomenology of MR imaging with unflagging determination and boundless energy during the next 3 decades. He initially



chose to discover and investigate in private practice settings. Bill joined Huntington Memorial Hospital in Pasadena, California, and then Long Beach Memorial Hospital, Long Beach, California, transforming both institutions with his delightful touch and his keen intellect. In private practice, Bill proved the headroom for discovery and novel implementation outside traditional academic centers while training outstanding fellows who would popularize and establish MR imaging. In private practice, Bill was a 1-man university, pursuing discovery, innovation, teaching, and clinical practice at a level that was the envy of fully established and broadly staffed world-class academic radiology departments.

In 2002, Bill started a new chapter in his professional life. Across the years, Bill’s insatiable thirst for knowledge, his unique ability to connect individuals, and his extroversion drew him to true university settings, where he could interact with engineers and scientists on a more sustained basis and deliver innovation as an expected and central product of his work. Bill enthusiastically accepted the charge of leading the Radiology Department at the University of California, San Diego, which he did for the next 13 years. During the first 8 years of his chairmanship, Bill intentionally and thoughtfully improved the rating of the radiology department in terms of National Institutes of Health funding from the mid-40s to the number 8 position. He achieved this by establish-

ing a team of world-famous faculty members within the department and as a brilliant talent scout, through identifying and recruiting inevitable future field leaders. Bill possessed a unique and infectious vision of the future and was able to share this vision with numerous industrial partners. Despite the competitive relationships among the industrial giants supplying radiology, Bill's charisma and imagination were such that he was central to all the vendors' conversations regarding their individual futures, whether the industrial friends were world leaders or new on the scene.

Attempting to quantify Bill's achievements is challenging because any such accounting fails to effectively convey his singular charisma and the subjective nature of his enduring impact on our field through each of us who knew and loved him. In addition, a distinguished Professor Emeritus, Bill published more than 200 articles, 54 chapters, and 20 additional textbooks. His accomplishments and service to organized radiology resulted in a collection of gold medals for distinguished and exceptional lifetime achievements from the most prestigious radiology societies, of which Bill was rightfully proud and grateful. Bill's gold medals were awarded by the Radiological Society of North America, the American College of Radiology, the International Society of Magnetic Resonance in Medicine, the American Roentgen Ray Society, and the Association of University Radiologists. For an individual to receive all 5 medals is truly exceptional and a testament to Bill's service and enduring impact on our field.

Bill's extensive contributions included his serving as President of the International Society of Magnetic Resonance in Medicine and serving on the Board of Trustees of the Radiological Society of North America Research and Education Foundation (1995–2001) and as the Chairman of the Fund Development Committee of that organization from 1996 to 2008. Bill was on the Board of Chancellors of the American College of Radiology, where he chaired the Commission on Neuroradiology and MR imaging from 1999 to 2005 and served as Vice President from 2005 to 2006. Bill was Chair of the Steering Committee for the Coalition for Imaging and Bioengineering Research and on the Boards of the Academy of Radiology Research, Association of University Radiologists, International Society for Strategic Studies in Radiology, and Academy of Radiology Leadership and Management. A simple tabulation of his offices fails to fully convey the impact and influence he had on every one of these organizations.

As with his other contributions, quantitating Bill's effect on organized radiology is akin to capturing lightning in a bottle. In pushing the analogy, even though the rest of us would never consider capturing lightning in a bottle, I imagine my friend Bill would be captivated by the idea, would imagine and iterate through myriad ways of doing just that, and would ultimately succeed. That, exactly, was our friend Bill.

A. Norbash

<http://dx.doi.org/10.3174/ajnr.A5712>

Medullary Edema and Enhancement with a Straight Upper Border in Cases of Dural Arteriovenous Fistulas

We read the recent article by Copelan et al,¹ “Dural Arteriovenous Fistulas: A Characteristic Pattern of Edema and Enhancement of the Medulla on MRI” with great interest. The authors describe an unusual but characteristic imaging appearance of patchy medullary edema and enhancement with areas of sparing in cases of dural arteriovenous (AV) fistulas.

We previously encountered a similar case of a patient with edema and abnormal patchy enhancement in the medulla on MR imaging with initial misdiagnosis and treatment for neuromyelitis optica. Subsequent DSA demonstrated an arteriovenous fistula with an arterial feeder from the posterior division of the right middle meningeal artery draining into a tortuous transcerebellar vein into a mildly distended varicose anterior spinal vein (Figs 1 and 2). We also note that similar to the cases described by Copelan et al, the edema and enhancement pattern in the medulla demonstrate a characteristically straight upper border (Fig 3). It has previously been reported that dural AV shunts develop at the site where the bridging veins penetrate the dura and then reflux into the pontomesencephalic and anterior medullary systems, potentially resulting in brain stem or cerebellar venous ischemia² and likely accounting for the straight upper border of edema due to a vascular etiology. We believe that the presence of medullary edema and enhancement with a straight upper border should alert the radiologist to the possibility of an underlying dural AV fistula.

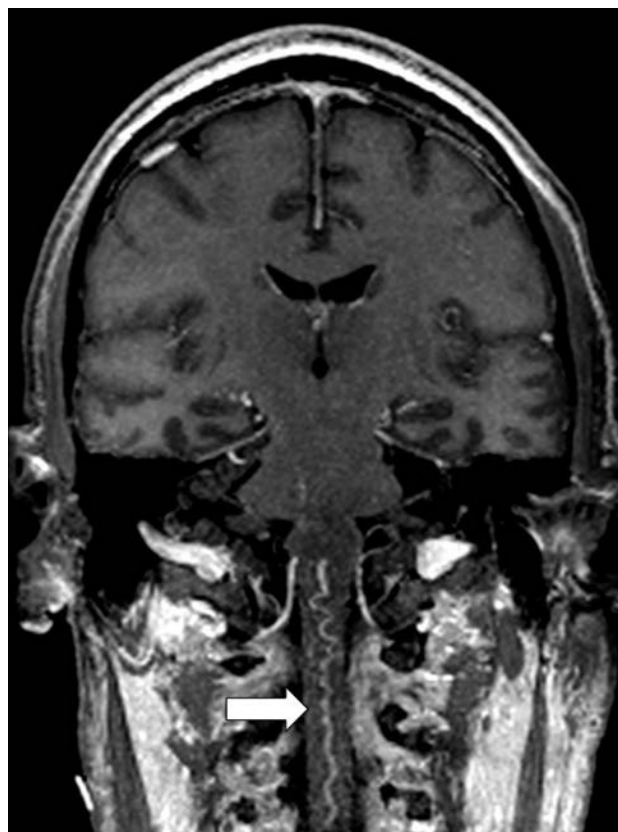


FIG 1. Coronal T1 postcontrast MIP image demonstrates the anterior spinal vein, which is distended and mildly varicose.

REFERENCES

1. Copelan AZ, Krishnan A, Marin H, et al. **Dural arteriovenous fistulas: a characteristic pattern of edema and enhancement of the medulla on MRI.** *AJNR Am J Neuroradiol* 2018;39:238–44 CrossRef Medline
2. Alvarez H, Sasaki-Adams D, Castillo M. **Resolution of brainstem edema after treatment of a dural tentorial arteriovenous fistula.** *Interv Neuroradiol* 2015;21:603–08 CrossRef Medline

● D. Byrne

● J.P. Walsh

Department of Radiology
Mater Misericordiae University Hospital
Dublin, Ireland

● T. Lynch

Dublin Neurologic Institute, Department of Neurology
Mater Misericordiae University Hospital
Dublin, Ireland

● E.C. Kavanagh

Department of Radiology
Mater Misericordiae University Hospital
Dublin, Ireland
School of Medicine
University College
Dublin, Ireland



FIG 2. Sagittal T1 postcontrast MIP image demonstrates the anterior spinal vein, which is distended and mildly varicose.

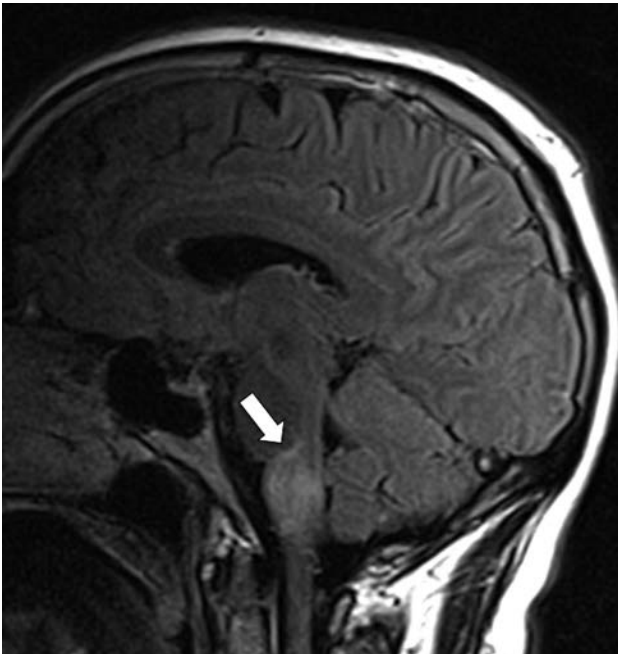


FIG 3. Sagittal FLAIR demonstrates medullary edema with a straight upper border.

Another Important Pitfall in the Diagnosis of Dural Sinus Thrombosis in Neonates

There are known diagnostic imaging pitfalls that may lead to signal changes in the dural sinuses during MR imaging. These pitfalls, which include in-plane flow, hypoplastic sinus, and slow flow,¹ require the administration of intravenous gadolinium to definitely exclude sinus thrombosis.

Flow void is usually observed in a patent dural sinus,¹ but due to the soft, flexible skull of neonates,² flattening and slight narrowing or compression of one of the transverse sinuses may be encountered, depending on the head position during the scan. Accordingly, the flow void may be absent, or the slow flow inside the flattened sinus may even result in a hyperintense signal on FLAIR images, which would resemble a thrombus. This narrowing or compression also leads to a loss of flow signal on the venous time-of-flight angiography. Failure to recognize such a cause may require gadolinium administration to exclude sinus thrombosis or may lead to recommendations of unnecessary follow-up scans, which might not be practical in neonates and could increase health care costs because neonates require adequate sedation before undergoing this procedure. Furthermore, this may lead to diagnostic delay, which could have implications for patient management and raise unnecessary parent concern due to the uncertainty of their child's diagnosis. Inspection of the head position on the scout and correlation with the other sequences are simple tactics for circumventing this pitfall, and if there is uncertainty, the sequence should be repeated after rotating the neonate's head to the contralateral side for confirmation (Figure).

Disclosures: Franca Wagner—UNRELATED: Grants/Grants Pending: MS Society,* Comments: not related to the submitted work. *Money paid to the institution.

REFERENCES

1. Poon CS, Chang JK, Swarnkar A, et al. Radiologic diagnosis of cerebral venous thrombosis: pictorial review. *AJR Am J Roentgenol* 2007; 189:S64–75 CrossRef Medline
2. Cho SM, Kim HG, Yoon SH, et al. Reappraisal of neonatal greenstick skull fractures caused by birth injuries: comparison of 3-dimen-

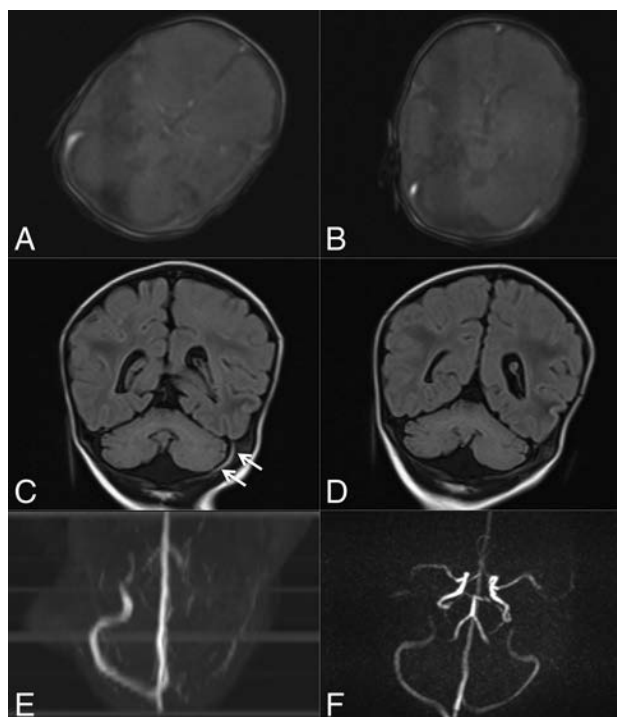


FIGURE. A 20-day-old female neonate with tonic-clonic epilepsy and perinatal asphyxia who underwent MR imaging to exclude cerebral venous thrombosis. The neonate was first placed with her head rotated to the left side, as observed in the scout (A). The FLAIR sequence (C) in this position showed hyperintense signal in the transverse and sigmoid sinuses (arrows). Furthermore, the venous TOF angiography showed no flow signal in the sinus (E). Before completion of the examination, the head rotation was corrected (see scout B), and the FLAIR sequence (D) was repeated; the hyperintense signal disappeared. A venous phase-contrast sequence was also performed (F) and showed normal flow in the left transverse sinus in this position. Therefore, no contrast was necessary to exclude cerebral venous thrombosis.

sional reconstructed computed tomography and simple skull radiographs. *World Neurosurg* 2018;109:e305–12 CrossRef Medline

● A. Hakim

● F. Wagner

University Institute of Diagnostic and Interventional Neuroradiology
Bern University Hospital, Inselspital, University of Bern
Bern, Switzerland

<http://dx.doi.org/10.3174/ajnr.A5674>

Rapid-Sequence MRI of the Brain: A Distinct Imaging Study

Rapid-sequence MRI of the brain (also known as “ultrafast brain,” “quick brain,” “fast brain,” and “one bang” MRI) has long been used in the evaluation of ventricular shunt catheters due to its ability to quickly evaluate intracranial fluid-containing spaces without anesthesia or the ionizing radiation of CT. Despite its value, there is no mention of the technique in the American College of Radiology Appropriateness Criteria (<https://www.acr.org/Clinical-Resources/ACR-Appropriateness-Criteria>), which do treat functional MRI and MR spectroscopy as distinct examinations, likely because these tests have distinct billable procedure codes.

When I moved from one large children’s hospital to another during my training, I saw firsthand a distinct difference in the use of rapid-sequence MRI. At my first institution, it was being ordered almost exclusively by neurosurgeons to guide neurosurgical management-specific decisions (shunt malfunction, hydrocephalus, cyst evaluation, and so forth). At my second, however, the technique had far greater reach among the gamut of pediatric specialists who were concerned about the possible neurotoxic effects of anesthesia and wanted to simply “rule out anything big” in patients with suspected neurologic pathology. In a count of 100 consecutive rapid MRI examinations read by a single radiologist from the same starting date at both sites, I found that rapid MRI had only composed about 15% of the total brain MRI at the restrictive hospital, while the figure was closer to 35% at the other. The permissive institution had about 8% of studies ordered for disorders unrelated to CSF-containing spaces (eg, developmental delay, altered mental status, family history of anomalies, and seizures), while the rate was only 3% at the more restrictive institution. Less than half of the examinations (46% at the restrictive site and 41% at the permissive site) were performed on children with shunts in place, similar to rates of 35% and 40% cited by prior authors.^{1,2} A notable difference in practice was that at the restrictive institution, all sedated MRI was checked by a radiologist before the examination was completed. Both sites partnered with privately contracted anesthesiologists.

Different pediatric specialists have different motivations for ordering rapid MRI. In extra-axial hematoma follow-up, for ex-

ample, a child abuse pediatrician may prefer a sedated conventional MRI, while a neurosurgeon may find rapid MRI suitable, even though this has been shown to be insensitive for evaluating abusive head trauma.³ A general pediatrician may be able to get rapid MRI more quickly than conventional MRI; thus, the rapid study becomes a tool to expedite discharge planning. Clinicians may move from one hospital to another without knowing which sequences are included in the study at the new site (eg, diffusion-weighted imaging, which makes the examination far more sensitive for ischemia and/or chemotherapy-related toxicity). The sequences used, specific techniques used during image acquisition, and detail of the reports issued have great consequences for patients. Uninformed pediatricians may accept rapid brain MRI “normal” findings as truly normal MRI examinations of the brain. What appears to be an arachnoid cyst on rapid MRI may be the cystic portion of a tumor, which the insensitive nature of the rapid MRI cannot detect.

Imaging centers associated with both institutions referenced above charged for rapid MRI using the same billable procedure code as a conventional MRI of the brain. Neuroradiologists must work to change this practice by designating the rapid-sequence MRI of the brain as a distinct limited study deserving its own charge. Not only is the interpretation of the examination less complex, but the acquisition of the images requires far less equipment-use time. At those centers where a rapid MRI is less expensive than a conventional MRI, how are insurers to know when they should pay for a rapid MRI and deny the order for a conventional MRI, which may incur an additional cost for general anesthesia? With regard to conventional pediatric MRI, what about requests for 3T and advanced sequences that require extra cost and training? How are we to decide who deserves these free extra services? Our billing system has simply not kept up with technology.

The appropriate use of rapid-sequence MRI falls somewhere between using it to screen all children with a suspected neurologic abnormality and using it exclusively to evaluate ventricular size. The problem is that without appropriate guidance from the imaging experts that we are, ordering providers are left ignorant of the true sensitivity and specificity of this valuable technique.

REFERENCES

1. Miller JH, Walkiwewicz T, Towbin RB, et al. **Improved delineation of ventricular shunt catheters using fast steady-state gradient recalled-**

echo sequences in a rapid brain MR imaging protocol in nonsedated pediatric patients. *AJNR Am J Neuroradiol* 2010;31:430–35 CrossRef Medline

2. Rozovsky K, Ventureyra EC, Miller E. **Fast-brain MRI in children is quick, without sedation, and radiation-free, but beware of limitations.** *J Clin Neurosci* 2013;20:400–05 CrossRef Medline
3. Kralik SF, Yasrebi M, Supakaul N, et al. **Diagnostic performance of**

ultrafast brain MRI for evaluation of abusive head trauma. *AJNR Am J Neuroradiol* 2017;38:807–13 CrossRef Medline

 **C.M. Pfeifer**

Department of Radiology
University of Texas Southwestern Medical Center
Dallas, Texas

Regarding: “Localized Marked Elongation of the Distal Internal Carotid Artery with or without PHACE Syndrome: Segmental Dolichoectasia of the Distal Internal Carotid Artery”

We read with interest the recently published article by Jia et al.¹ The authors reported a consecutive case series of 20 patients with striking arterial elongations with marked tortuosity and/or a conglomerated vascular mass involving the distal ICA. The authors reported that these lesions were associated with a striking female predominance (9:1, F/M) and a relatively young median age of 43.5 years. In general, the vascular lesions were incidental findings, and very few patients had any medical comorbidities. The authors reported a benign natural history for these lesions with slow progression of the lesions on follow-up imaging. Most interestingly, 9 of 20 patients had mild atrophy of the ipsilateral midbrain, and 4 of 20 patients met all the diagnostic criteria for PHACE syndrome.¹

The arterial lesions in the series of Jia et al¹ have been previously described as “pure arterial malformations,” defined as dilated, overlapping, and tortuous arteries forming a mass of arterial loops with a coil-like appearance in the absence of any arteriovenous connection.² In a recently published case series, our group identified 12 cases of pure arterial malformations.³ Similar to Jia et al, we found a striking female predominance (83.3%) and found that these patients were relatively young (mean age, 26.2 years). The lesions were incidental in all cases. Pure arterial malformations affected the anterior cerebral arteries in 25% of cases, the posterior communicating artery (PcomA) segment in 33.3% of cases, the MCA in 16.6% of cases, and posterior circulation arteries in 25% of cases. Four patients had focal aneurysms, and 5 lesions were partially calcified. Like Jia et al, we found that lesions affecting the PcomA segment of the ICA went on to affect the PcomA and posterior cerebral artery (PCA). Many of the lesions reported in our article had a striking resemblance to those reported by Jia et al. After 2.5 years of follow-up, none of the lesions had associated ischemia or hemorrhage, suggesting a benign natural history.³

We agree with the general assessment of Jia et al¹ that these lesions have a benign natural history and do not warrant treatment. However, imaging follow-up every few years may be beneficial so that we can better understand the natural history of these lesions. Our group suspects that these lesions likely form early in life or in utero.⁴ Potential etiologies that have been discussed in the literature include a congenital defect or insult resulting in arterial dysplasia; an insult such as

a viral infection or somatic mutation occurring later in life affecting a particularly vulnerable arterial segment (ie, segmental arterial vulnerability); or chronic healed dissection.

There have been at least 20 reported cases of pure arterial malformations reported in the literature before 2017.³ In general, these patients are younger, and most patients are female. More than 80% of cases are discovered incidentally. Lesions involving the distal anterior cerebral arteries (ACAs) are characterized as ectatic and moderately tortuous and have a looser coil configuration. Furthermore, calcifications of distal ACA lesions are relatively common in previously reported cases. These findings are like those we have seen with lesions involving the ACAs. Meanwhile, lesions of the MCA or PcomA-PCA are often composed of a tightly wound coil of vessels with superimposed clusters of aneurysms and calcifications. Previously reported lesions of the superior cerebellar artery and posterior inferior cerebellar artery also bear a remarkably similar resemblance to our cases in that the vessels have the appearance of a tightly wound coil without substantial ectasia or any associated aneurysm.

We are glad to see additional cases of pure arterial malformations reported in the literature. We encourage other authors to report their cases as they encounter them so the neurovascular community can be better informed regarding the appearance and natural history of these lesions.

REFERENCES

1. Jia ZY, Zhao LB, Lee DH. **Localized marked elongation of the distal internal carotid artery with or without PHACE syndrome: segmental dolichoectasia of the distal internal carotid artery.** *AJNR Am J Neuroradiol* 2018;39:817–23 CrossRef Medline
2. McLaughlin N, Raychev R, Duckwiler G, et al. **Pure arterial malformation of the posterior cerebral artery: importance of its recognition.** *J Neurosurg* 2013;119:655–60 CrossRef Medline
3. Brinjikji W, Cloft HJ, Flemming KD, et al. **Pure arterial malformations.** *J Neurosurg* 2017 Sep 29. [Epub ahead of print] CrossRef Medline
4. Sorenson TJ, Brinjikji W, Flemming KD, et al. **Pure arterial malformation (PAM) of the posterior inferior cerebellar artery (PICA) with interspersed adipose tissue: a case report.** *J Neurosurg Ped.* In press

W. Brinjikji

G. Lanzino

Departments of Neurosurgery and Radiology
Mayo Clinic
Rochester, Minnesota

REPLY:

We thank Dr Brinjikji and colleagues for the letter written in response to our recently published article, “Localized Marked Elongation of the Distal Internal Carotid Artery with or without PHACE Syndrome: Segmental Dolichoectasia of the Distal Internal Carotid Artery.”¹

We have read with interest the articles published by Brinjikji et al² and McLaughlin et al³ in recent years. In 2013, the latter reported “pure arterial malformations (PAM)” of the posterior cerebral artery in a young female adult and described them as dilated, overlapping, and tortuous arteries with a coil-like appearance and/or a mass of arterial loops without any associated venous component. Their reported lesion (showing a benign natural history) has a striking resemblance to lesions seen in some of our patients. In 2017, Brinjikji et al² reported a case series comprising 12 patients diagnosed with PAM located in different intracranial arteries.

To highlight the regionality of this phenomenon, we focused on cases of segmental involvement of the distal internal carotid artery. Although we have not drawn any pathogenetic conclusion about this morphologic aberration, we believe that publishing research about such lesions, including all intracranial locations, may improve the understanding of this type of lesion. Furthermore, we believe that the term “segmental intracranial dolichoec-

tasia” better represents these lesions than the term “malformation” because a malformation accompanies a functional defect, which is not applicable in our cases. However, further research is necessary to determine an appropriate name for this lesion.

We thank Dr Brinjikji and colleagues for their comments on our article, as well as for sharing their experience and encouraging others to report similar cases for promoting a deeper understanding of this disease entity.

REFERENCES

1. Jia ZY, Zhao LB, Lee DH. **Localized marked elongation of the distal internal carotid artery with or without PHACE syndrome: segmental dolichoectasia of the distal internal carotid artery.** *AJNR Am J Neuroradiol* 2018;39:817–23 CrossRef Medline
2. Brinjikji W, Cloft HJ, Flemming KD, et al. **Pure arterial malformations.** *J Neurosurg* 2017 Sep 29. [Epub ahead of print] CrossRef Medline
3. McLaughlin N, Raychev R, Duckwiler G, et al. **Pure arterial malformation of the posterior cerebral artery: importance of its recognition.** *J Neurosurg* 2013;119:655–60 CrossRef Medline

✉ **Z.Y. Jia**

✉ **L.B. Zhao**

Department of Radiology
The First Affiliated Hospital of Nanjing Medical University
Jiangsu Province, China

✉ **D.H. Lee**

Department of Radiology
Asan Medical Center
University of Ulsan College of Medicine
Seoul, Korea

<http://dx.doi.org/10.3174/ajnr.A5695>

Laryngeal Cartilage Invasion

In their article comparing MR imaging and dual-energy CT for the evaluation of cartilage invasion by laryngeal carcinoma,¹ the authors correctly stated in their introduction that the diagnosis of T4a disease—that is, tumor invading not just into but beyond the laryngeal cartilage and into the extralaryngeal soft tissues—constitutes a potential indication for laryngectomy. However, what follows appears to be an exercise in establishing whether there is merely tumor infiltration into the cartilage, a finding that may only establish T3 disease and that would not constitute grounds for surgery. Indeed, when the treatment goal is larynx conservation, the determination of tumor just within the cartilage is not critical, and whether dual-energy CT is better than MR imaging may be moot. In fact, the only imaging example pre-

sented in this article, Fig 1, shows a case in which there is no suggestion of extralaryngeal spread on either MR imaging or dual-energy CT. Much has been written on imaging of cartilage extension in laryngeal cancer, little of which, in my opinion, has bearing on real-world treatment, given the goal of organ preservation, in which laryngectomy is reserved for only advanced disease.

REFERENCE

1. Kuno H, Sakamaki K, Fujii S, et al. **Comparison of MR imaging and dual-energy CT for the evaluation of cartilage invasion by laryngeal and hypopharyngeal squamous cell carcinoma.** *AJNR Am J Neuroradiol* 2018;39:524–31 CrossRef Medline

©L.E. Ginsberg

MD Anderson Cancer Center
Houston, Texas

<http://dx.doi.org/10.3174/ajnr.A5723>

REPLY:

We appreciate Dr Ginsberg's interest and comments on our article, "Comparison of MR Imaging and Dual-Energy CT for the Evaluation of Cartilage Invasion by Laryngeal and Hypopharyngeal Squamous Cell Carcinoma."¹ We agree that the hypopharyngeal cancer case (presented in Fig 1) demonstrated lateral extralaryngeal tumor extension through wrapping around the posterior border of the thyroid cartilage on both MR imaging and dual-energy CT. Therefore, this case was defined as T4a disease, regardless of the cartilage invasion finding. We agree that determining both extralaryngeal extension and thyroid cartilage penetration is extremely important for treatment decision-making. Tumors that extend through potential spaces such as the thyrohyoid membrane and the thyroarytenoid gap might behave differently from those that penetrate through the cartilage, with the latter being more aggressive and potentially more likely to fail nonsurgical therapy.^{2,3} However, in clinical practice, patients with T4 disease do not always inevitably undergo laryngectomy, and patients without transcartilaginous tumor extension may be potential candidates for function-preserving treatment to some degree, and discussion with the patients forms part of the treatment decision-making process. Accurate diagnosis to avoid overestimation of thyroid cartilage invasion is important in the treatment decision-making process, irrespective of extralaryngeal spread. Beitler et al⁴ reported that extralaryngeal spread without thyroid cartilage penetration was more common than previously expected in patients with advanced laryngeal and hypopharyngeal cancers and that CT often involved an overdiagnosis in predicting cartilage penetration with a sensitivity of 75%.

In our study, extralaryngeal tumor extension was confirmed pathologically in 34 of 55 (62%) patients with advanced hypopharyngeal and laryngeal cancers; however, only 17 of 34 (50%) patients demonstrated cartilage invasion.¹ Extralaryngeal spread can be reasonably well identified on conventional CT, dual-energy CT,⁵ and MR imaging; however, extralaryngeal spread "with cartilage invasion" is sometimes overdiagnosed using conventional CT and MR imaging.⁵⁻⁷

As Dr Ginsberg has mentioned concerning laryngeal cancer, tumor erosion limited to the inner cortex of the thyroid cartilage indicates a T3 lesion, whereas erosion of the outer cortex of the thyroid cartilage defines a T4a tumor. However, unlike the larynx, thyroid or cricoid cartilage invasion in hypopharyngeal cancers

indicates a T4a lesion, even with localized cartilage invasion, and accurate staging requires a precise diagnosis of subtle cartilage invasion. Dual-energy CT may be helpful as a first-line technique for accurate staging to define the T-stage, particularly when distinguishing T4 from lower-stage lesions and to detect regional lymph nodes (N-staging) and distant metastasis (M-staging).⁸ Contrast-enhanced MR imaging remains useful for excluding cartilage invasion and for evaluation of prevertebral space invasion in patients with very advanced local disease.

REFERENCES

1. Kuno H, Sakamaki K, Fujii S, et al. **Comparison of MR imaging and dual-energy CT for the evaluation of cartilage invasion by laryngeal and hypopharyngeal squamous cell carcinoma.** *AJNR Am J Neuroradiol* 2018;39:524–31 CrossRef Medline
2. Lefebvre JL, Ang KK. **Larynx preservation clinical trial design: key issues and recommendations—a consensus panel summary.** *Head Neck* 2009;31:429–41 CrossRef Medline
3. Pfister DG, Laurie SA, Weinstein GS, et al; American Society of Clinical Oncology. **American Society of Clinical Oncology clinical practice guideline for the use of larynx-preservation strategies in the treatment of laryngeal cancer.** *J Clin Oncol* 2006;24:3693–704 CrossRef Medline
4. Beitler JJ, Muller S, Grist WJ, et al. **Prognostic accuracy of computed tomography findings for patients with laryngeal cancer undergoing laryngectomy.** *J Clin Oncol* 2010;28:2318–22 CrossRef Medline
5. Kuno H, Onaya H, Iwata R, et al. **Evaluation of cartilage invasion by laryngeal and hypopharyngeal squamous cell carcinoma with dual-energy CT.** *Radiology* 2012;265:488–96 CrossRef Medline
6. Li B, Bobinski M, Gandour-Edwards R, et al. **Overstaging of cartilage invasion by multidetector CT scan for laryngeal cancer and its potential effect on the use of organ preservation with chemoradiation.** *Br J Radiol* 2011;84:64–69 CrossRef Medline
7. Becker M, Zbären P, Casselman JW, et al. **Neoplastic invasion of laryngeal cartilage: reassessment of criteria for diagnosis at MR imaging.** *Radiology* 2008;249:551–59 CrossRef Medline
8. Kuno H, Onaya H, Fujii S, et al. **Primary staging of laryngeal and hypopharyngeal cancer: CT, MR imaging and dual-energy CT.** *Eur J Radiol* 2014;83:e23–35 CrossRef Medline

● **H. Kuno**

Department of Diagnostic Radiology
National Cancer Center Hospital East
Kashiwa, Chiba, Japan

● **O. Sakai**

Departments of Radiology, Otolaryngology–Head and Neck Surgery, and
Radiation Oncology
Boston Medical Center, Boston University School of Medicine
Boston, Massachusetts

● **R. Hayashi**

Department of Head and Neck Surgery
National Cancer Center Hospital East
Kashiwa, Chiba, Japan

<http://dx.doi.org/10.3174/ajnr.A5756>